IntechOpen

Mass Transfer in Chemical Engineering Processes

Edited by Jozef Markoš

MASS TRANSFER IN CHEMICAL ENGINEERING PROCESSES

Edited by **Jozef Markoš**

Mass Transfer in Chemical Engineering Processes
http://dx.doi.org/10.5772/659
Edited by Jozef Markoš

Contributors

Marisa Mendes, Mostafa Rahimnejad, Ali Asghar Ghoreyshi, Ghasem Najafpour, Vesna Rafajlovska, Jana Klopceska, Renata Slaveska-Raicki, Marija Srbinoska, Jose Ignacio Huertas, Nicolas Giraldo, Sebastian Izquierdo, Carlos Eduardo Nobrega, Nisio Brum, Giovanna Ferrari, Francesco Donsì, Gianpiero Pataro, Atsushi Makino, Guo Ping, Wang Zhouhua, Xu Yanmei, Du Jianfen, Mohammad Karimi, Madhumita Ray, Tarek J. Jamaleddine, Vladimir Tepliakov, Igor Beckman, Maxim Shalygin, Anchaleeporn Waritswat Lothongkum, Ura Pancharoen, Tatchanok Prapasawat

Notice

First published in Croatia, 2011 by INTECH d.o.o.
eBook (PDF) Published by IN TECH d.o.o.
Place and year of publication of eBook (PDF): Rijeka, 2019. IntechOpen is the global imprint of IN TECH d.o.o.
Printed in Croatia

Legal deposit, Croatia: National and University Library in Zagreb

Additional hard and PDF copies can be obtained from orders@intechopen.com

Mass Transfer in Chemical Engineering Processes
Edited by Jozef Markoš
p. cm.
ISBN 978-953-307-619-5
eBook (PDF) ISBN 978-953-51-4409-0

Meet the editor

Professor Jozef Markoš, born 1957 in Kremnica, Slovakia, is a full professor at Slovak University of Technology in Bratislava. He has over 30 years of research experience in the field of experimental and mathematical modelling, simulation, design and optimization of multiphase reactors and separations processes (heterogeneous catalysis, gas – liquid reactors, air lift bioreactors, reactive distillation, hybrid systems bioreactor – membrane separation) with several industrial realizations. His research and pedagogical activities are fully connected with Slovak University of Technology in Bratislava where he graduated in 1981, obtained his PhD in 1985 and became a full professor in 2005 (excluding 3 years, from 1991 to 1994 which he spent as postdoc at University of Cagliary, Italy and as senior researcher at research center C.R.S.4, Cagliary, Italy). Currently, Professor Markoš teaches Bc course "Basics of Chemical Reactors" and Ms courses "Theory of Multiphase Chemical Reactors" and "Mass Transfer and Separation processes". The research of professor Markoš has resulted in over 75 CC journal publications and over 100 conference publications.

Contents

Preface

Mass transfer in the multiphase multicomponent systems represents one of the most important problems to be solved in chemical technology, both in theoretical as well as practical point of view. In libraries all over the world, many books and articles can be found related to the mass transfer. Practically, all textbooks devoted to the separation processes or reaction engineering contain chapters describing the basic principles of the mass (and heat) transfer. It would be impossible (and also meaningless) to make the list of them; however, the most fundamental works of Bird, Steward and Lightfoot [1] and Taylor, Krishna and Wesseling, [2, 3, 4] have to be mentioned.

Unfortunately, the application of sophisticated theory still requires use of advanced mathematical apparatus and many parameters, usually estimated experimentally, or via empirical or semi-empirical correlations. Solving practical tasks related to the design of new equipment or optimizing old one is often very problematic. Prof. Levenspiel in his paper [5] wrote: "*...In science it is always necessary to abstract from the complexity of the real world....this statement applies directly to chemical engineering, because each advancing step in its concepts frequently starts with an idealization which involves the creation of a new and simplified model of the world around us. ...Often a number of models vie for acceptance. Should we favor rigor or simplicity, exactness or usefulness, the $10 or $100 model?"*

Presented book offers several "engineering" solutions or approaches in solving mass transfer problems for different practical applications: measurements of the diffusion coefficients, estimation of the mass transfer coefficients, mass transfer limitation in the separation processes like drying extractions, absorption, membrane processes, mass transfer in the microbial fuel cell design, and problems of the mass transfer coupled with the heterogeneous combustion.

I believe this book will provide its readers with interesting ideas and inspirations or with direct solutions of their particular problems. To conclude, let me quote professor Levenspiel again: "*May I end up by suggesting the following modeling strategy: always start*

by trying the simplest model and then only add complexity to the extent needed. This is the $10 approach."

Jozef Markoš
Institute of Chemical and Environmental Engineering,
Slovak University of Technology in Bratislava,
Slovak Republic

References

[1] Bird, R., B., Stewart, W., S., and Lightfoot, E., N., Transport Phenomena, Second Edition, John Wiley and Sons, Inc., New York, 2007
[2] Taylor, R. and Krishna, R., Multicomponent Mass Transfer, John Wiley and Sons, Inc., New York, 1993
[3] Wesselingh, J., A., and Krishna, R., Mass Transfer in Multicomponent Mixtures, Delft University Press, Delft, 2000
[4] Krishna, R. and Wesselingh, J.A., The Maxwell – Stefan approach to mass transfer, Chemical Engineering Science, 52, (1997), 861 – 911
[5] Levenspiel, O., Modeling in chemical engineering, Chemical Engineering Science, 57, (2002), 4691 – 4696

1

Research on Molecular Diffusion Coefficient of Gas-Oil System Under High Temperature and High Pressure

Ping Guo, Zhouhua Wang, Yanmei Xu and Jianfen Du
State Key Laboratory of Oil and Gas Reservoir Geology and Exploitation, Southwest Petroleum University, ChengDu, SiChuan, China

1. Introduction

As the technology of enhanced oil recovery by gas injection has already been applied worldwide, the research of the transmit mechanism between injected-gas and oil is important to the optimization of gas injection plan. Diffusion is an important phenomenon during the process of gas injection displacement. Because of diffusion, gas molecules will penetrate into the oil phase, while the oil will penetrate into the gas phase. Oil and gas could get balance with time. Diffusion affects the parameters of system pressure, component properties and balance time, which thus affect the efficiency of displacement. Molecular diffusion, which we usually refer to, includes mass transfer diffusion and self-diffusion. Mass transfer diffusion mainly occurs in non-equilibrium condition of the chemical potential gradient (μ_i) .The moleculars move from high chemical potential to low chemical potential of molecular diffusion until the whole system reaching equilibrium. The self-diffusion refers to free movement of molecules (or Brownian motion) in the equilibrium conditions. Mass transfer diffusion and self-diffusion can be quantitatively described by the diffusion coefficient. Up till now, there is no way to test the molecular diffusion coefficient directly. As for the question how to obtain the diffusion coefficient, it is a requirement to establish the diffusion model firstly, and then obtain the diffusion coefficient by analysis of experiments' results.

2. Traditional diffusion theory

2.1 Fick's diffusion law

Fick's law is that unit time per through unit area per the diffusive flux of materials is proportional directly to the concentration gradient, defined as the diffusion rate of that component A during the diffusion.

$$J_A \propto \frac{dc_A}{dz} \quad \text{or} \quad J_A = -D_{AB}\frac{dc_A}{dz} \tag{1}$$

Where, J_A — mole diffusive flux, $kmol \cdot m^{-2} \cdot s^{-1}$;
z — distance of diffusion direction;

$\frac{dc_A}{dz}$ —concentration gradient of component A at z-direction, $\left(kmol/m^3\right)/m$;

D_{AB} —the diffusion coefficient of component A in component B, $m^2 \cdot s^{-1}$.

Therefore, Fick's law says diffusion rate is proportional to concentration gradient directly and the ratio coefficient is the molecular diffusion coefficient. The Fick's diffusion law is called the first form.

Gas diffusion:

$$N_A = J_A = -D\frac{dc_A}{dz} \tag{2}$$

For:

$$c_A = \frac{n_A}{v} = \frac{p_A}{RT} \tag{3}$$

We can obtain:

$$N_A = -\frac{D}{RT}\frac{dp_A}{dz} \tag{4}$$

$$N_A \int_0^z dz = -\frac{D}{RT}\int_{p_A}^{p_i} dp_A \tag{5}$$

$$N_A \cdot z = \frac{D}{RT}\left(p_A - p_i\right) \tag{6}$$

$$N_A = \frac{D}{RTz}\left(p_A - p_i\right) \tag{7}$$

Define $\frac{D}{RTz} = k_G$ (k_G -mass transfer coefficient) ,then:

$$N_A = k_G\left(p_A - p_i\right) \tag{8}$$

Similarly, we can obtain the liquid phase diffusion, which is written as follows:

$$N_A = k_L\left(c_i - c_A\right) \tag{9}$$

Where $k_L = \frac{D}{z}$

Fick also presented a more general conservation equation:

$$\frac{\partial c_1}{\partial t} = D\left(\frac{\partial^2 c_1}{\partial z^2} + \frac{1}{A}\frac{\partial A}{\partial z}\frac{\partial c_1}{\partial z}\right) \quad t > 0, 0 < x < L \tag{10}$$

When area A is constant, eq. 10 become a basic equation of one-dimensional unsteady state diffusion, which is also known as Fick's second law.

Fick's second law describes the concentration change of diffusion material during the process of diffusion. From the first law and the second law, we can see that the diffusion coefficient D is independent of the concentration. At a certain temperature and pressure, it is a constant. Under such conditions, the concentration of diffusion equation can be obtained by making use of initial conditions and boundary conditions in the diffusion process, and then the diffusion coefficient could be gotten by solving the concentration of diffusion equation.

3. Molecular diffusion coefficient model

3.1 Establishment of diffusion model

In 2007, through the PVT experiments of molecular diffusion, Southwest Petroleum University, Dr. Wang Zhouhua established a non-equilibrium diffusion model and obtained a multi-component gas diffusion coefficient. The establishment of the model is shown in fig.1, with the initial composition of the known non-equilibrium state in gas and liquid phase. During the whole experiment process, temperature was kept being constant. The interface of gas - liquid always maintained a balance, considering the oil phase diffuses into the vapor phase. When the diffusion occurs, the system pressure, volume and composition of each phase will change with time until the system reaches balance.

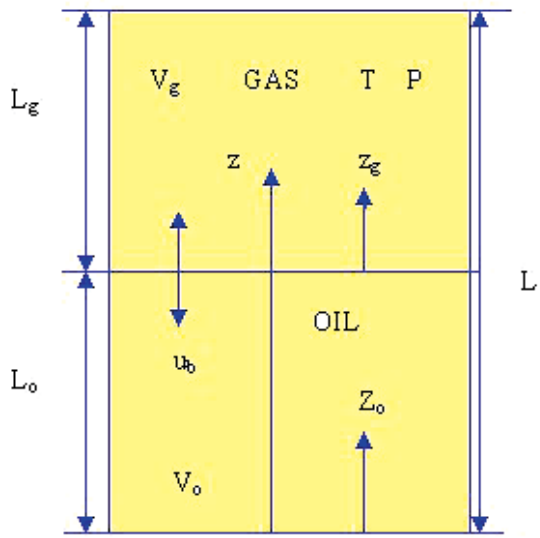

Fig. 1. Physical model schematic drawing

As shown in fig.1, x_i and y_i are i-composition molar fraction of liquid and gas phase respectively. C_{oi} and C_{gi} are i-composition mass fraction of liquid and gas phase respectively. ni is the total mole fraction of i-composition, mi is the total mass fraction of i-composition. L_o and L_g are the height of liquid and gas phase respectively. μ_b, defined as $\partial L_o / \partial t$, is the rate of movement of gas-liquid interface. z, z_o and z_g are coordinate axis as shown in fig.1.

If there is component concentration gradation, diffusion between gas and liquid phase will occur. Under the specific physical conditions of PVT cell, when gas phase diffuses into oil phase, the density of oil phase will decrease. According to the physical characteristics of diffusion, the concentration of light component in oil phase at the gas-liquid interface is higher than that of oil phase at the bottom of PVT cell, that is to say, the vector direction of concentration gradient of light component in oil phase is consistent with the coordinate direction of oil phase z_o. From the above analysis, we can see oil density along the coordinate direction is gradually decreasing, so there is no natural convection. The established models with specific boundary condition are as follows:
Oil phase:

$$\begin{cases} \dfrac{\partial C_{oi}}{\partial t} = \dfrac{\partial}{\partial z_o}\left[D_{oi} \dfrac{\partial C_{oi}}{\partial z_o} \right] \\ C_{oi}\left(z_o, 0\right) = C_{oi}^{1}\left(z_o\right) \\ \dfrac{\partial C_{oi}\left(0,t\right)}{\partial z_o} = 0 \\ C_{oi}\left(L_o, t\right) = C_{obi} \end{cases} \tag{11}$$

Gas phase:

$$\begin{cases} \dfrac{\partial C_{gi}}{\partial t} = \dfrac{\partial}{\partial z_g}\left[D_{gi} \dfrac{\partial C_{gi}}{\partial z_g} \right] \\ C_{gi}\left(z_g, 0\right) = C_{gi}^{1}\left(z_g\right) \\ C_{gi}\left(0,t\right) = C_{gbi} \\ \dfrac{\partial C_{gi}\left(L_g,t\right)}{\partial z_g} = 0 \end{cases} \tag{12}$$

C_{oi}^{1}, C_{gi}^{1} are i-component initial molar concentration of oil and gas phase, respectively, $kmol/m^3$.
C_{obi}, C_{gbi} are i-component molar concentration of oil and gas phase at oil-gas interface respectively, $kmol/m^3$.
In order to study the law of mutual diffusion between components, eq. 11 and 12 need to be solved. Because the velocity of gas-oil interface movement during the diffusion process is rather slow, we introduce a time step Δt. Then, we assume that gas-oil interface doesn't move, the height of oil and gas phase keeps the same, molar concentration at boundary and C_{obi}, C_{gbi} are constant during the whole time step,. And in the next time step, refresh the L_o, L_g and their values are the calculated result of the former time step, so each component concentration of oil and gas phase can be calculated. Continue the circular calculation like this way till gas and liquid phase reach balance. The detailed calculation procedure is as follows in fig. 2.

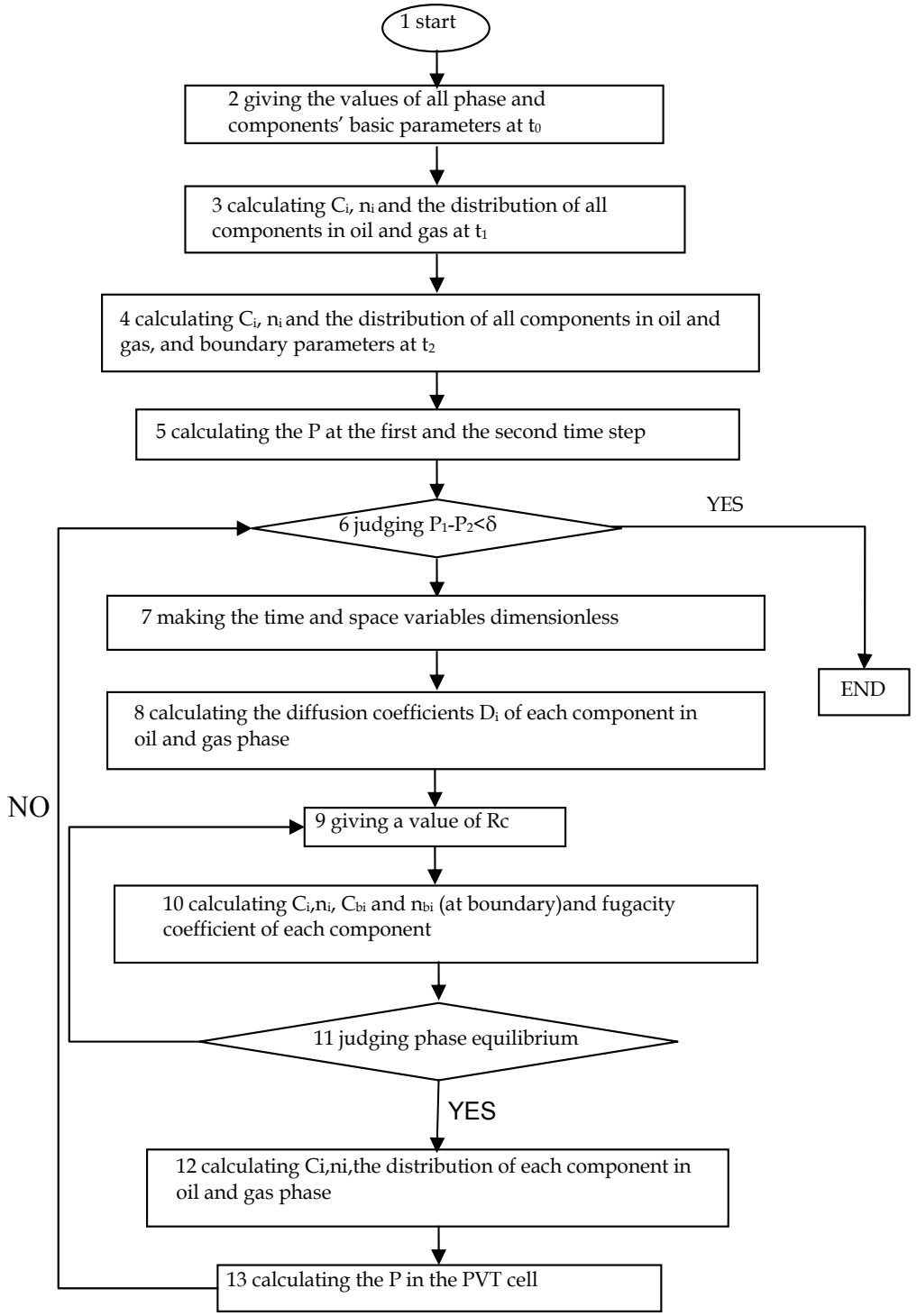

Fig. 2. Flow chart of calculation procedure

3.2 Model solution

Effective diffusion coefficient of each component directly affects the time to reach the balance for the whole system during the calculation procedure. There is no absolutely accurate general calculation equation to calculate the diffusion coefficient of i-component in oil phase and gas phase, except using the empirical equation which is a relatively accurate method. The diffusion factor of i-component in oil phase usually is usually calculated by Will—Chang(1955) and that in gas phase by Chapman-Enskog empirical formula (1972). The initial K value of each component is calculated by Wilson function, and corrected by fugacity coefficient in every time step, while fugacity coefficient is calculated by PR-EOS. Compared with the computation model proposed for single component, the model is much closer to the actual simulation, since it has taken interaction among the components into consideration.

4. The molecule diffusion experiment

The experiment tested the three different diffusion coefficients of hree different N_2, CH_4 and CO_2 gases and the diffusion coefficient of the actual oil separator. Using the mathematical model, we obtained diffusion coefficient of the gas molecules by fitting the experimental pressure changes or gas-oil interface position change.

4.1 Experimental fluid samples

The composition of gas sample is shown in Tab-1. The composition of oil sample is shown in Tab-2. The oil sample is taken from surface separator. The average molecular weight of oil sample is 231.5 and the density is 0.8305, g / cm^3 .

name	component name and molar percentage,%									
	N_2	CO_2	C_1	C_2	C_3	iC_4	nC_4	iC_5	nC_5	C_6
N_2	98.23	—	1.67	—	—	—	—	—	—	—
CO_2	0.0796	98.181	1.6939	—	—	—	—	—	—	—
Dry gas	3.1951	2.5062	92.7098	1.3957	0.1182	0.0141	0.0278	0.0129	0.0032	0.0169

Table 1. Components of gas samples

name	volume fraction,%	molar mass,kg/kmol	critical temperature,K	critical pressure,MPa	acentric factor
iC_4	0.057	58.124	408.1	3.600	0.1840
nC_4	0.094	58.124	425.2	3.750	0.2015
iC_5	0.405	72.151	460.4	3.340	0.2286
nC_5	0.337	72.151	469.6	3.330	0.2524
C_6	5.073	86.178	507.5	3.246	0.2998
C_7	4.578	100.250	543.2	3.097	0.3494
C_8	5.125	114.232	570.5	2.912	0.3513
C_9	3.625	128.259	598.5	2.694	0.3908
C_{10}	3.683	142.286	622.1	2.501	0.4438
C_{11+}	77.020	156.313	643.6	2.317	0.4775

Table 2. Components of oil samples used in diffusion experiments

4.2 Experimental temperature and pressure

Three groups of gas diffusion tests are conducted. The first one is the diffusion test of CO_2-Oil (20*MPa*, 60℃); the second is the diffusion test of CH_4-oil (20 *MPa*, 60℃); the third is the diffusion test of N_2-Oil (20 *MPa*, 60℃).

4.3 Experimental apparatus and experimental procedures

4.3.1 Experimental apparatus

Diffusion experiments are conducted mainly in DBR phase behavior analyzer. The other equipments include injection pump system, PVT cell, flash separator, density meter, temperature control system, gas chromatograph, oil chromatograph, electronic balance and gas booster pump. The flow chart is shown in fig.3.

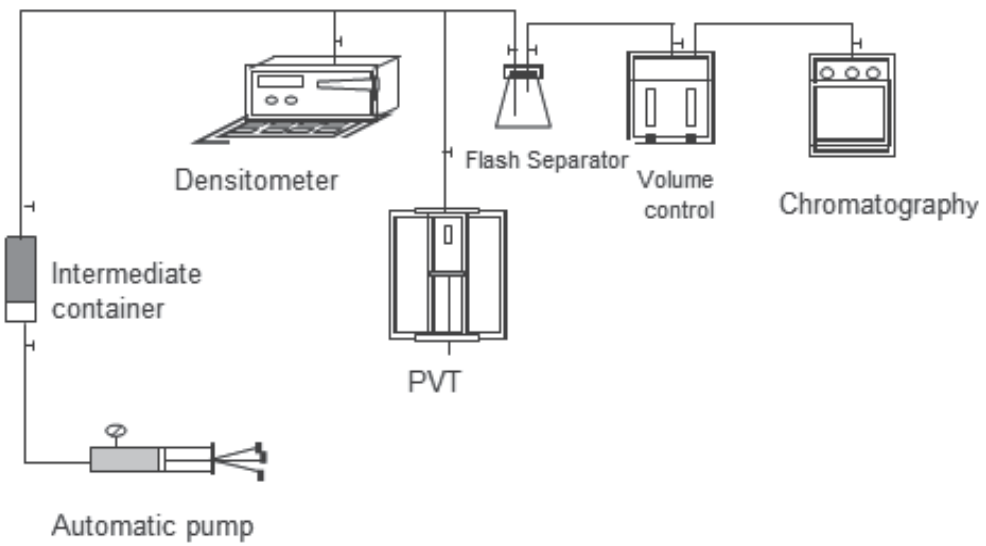

Fig. 3. The flow chart of diffusion experiment

4.3.2 Experimental procedures

Before testing, firstly, oil and gas sample under normal temperature are transferred into the intermediate container and put the middle container in a thermostatic oven. Then the oven is being heated up to 60℃ for 24 hours in general. The pressure of oil and gas sample under high-temperature is increased to the testing pressure—20*MPa*. Meanwhile, the temperature and pressure of PVT cell is increased to the experimental temperature and pressure, and then, the height of plunger is recorded. Secondly, transfer the oil sample into PVT cell and record the height of plunger again when the oil sample becomes steady. The difference of the two recorded heights is the oil volume. Thirdly, transfer the gas sample into PVT cell from the top of PVT cell. During the transferring process, it is necessary to keep a low sample transfer rate so that it would not lead to convection. Record the height of plunger and liquid level once completing sample transfer. Fourthly, start the diffusion test and make a record of time, pressure and liquid level. If variation of pressure is less than 1 psi during an interval of 30 minutes, it means gas-oil have reached the diffusive equilibrium and the

diffusion test is finished. And then, test the composition and density of oil phase and the composition of gas phase at different positions. Finally, wash the equipments with petroleum ether and nitrogen gas to prepare for the next experiment.

4.4 Experimental results and analysis

4.4.1 Experimental results

The test results are shown in Tab 3 and Fig 4.

Tab 3 has shown that the property of upper oil is different from that of lower oil in a certain extent. The component concentration of C_{11+} and flash density of the oil at upper position (upper oil) are lower than those at lower position (lower oil), but GOR of upper oil is obviously higher than that of the lower oil. Comparing the oil property of the three groups of experiment, it is found that the CO_2 concentration in oil phase and GOR in CO_2–oil diffusion experiment is higher than those of the other two gases diffusion experiments when the gas-oil system reaches balance. It shows that the high diffusion velocity, strong dissolving power and extraction to heavy components of CO_2 are the theory to explain the above phenomena.

component	upper oil phase			lower oil phase		
	N_2	CH_4	CO_2	N_2	CH_4	CO_2
CO_2	— —	1.1115	66.6284	— —	0.7231	66.3558
N_2	16.7464	0.8037	0.1354	10.8768	1.9091	0.0549
C_1	0.0256	34.3391	2.8402	0.0711	30.6201	1.9226
C_2	0.0052	0.7732	0.0231	0.0045	0.3081	0.0000
C_3	0.0394	0.1065	0.0397	0.0279	0.0240	0.0245
iC_4	0.1532	0.2481	0.1208	0.1084	0.1225	0.1035
nC_4	0.1981	0.3724	0.1715	0.1594	0.2431	0.1499
iC_5	0.4111	0.9540	0.4520	0.4545	0.4554	0.2850
nC_5	0.3091	0.7560	0.3594	0.3594	0.5611	0.2056
C_6	1.2669	5.6477	2.6848	1.6267	2.4097	0.8201
C_7	1.9029	5.6401	2.2140	2.9228	3.3796	1.0394
C_8	4.3693	7.1465	3.5759	5.7419	3.8080	2.1943
C_9	3.4355	5.2515	2.1883	4.9054	2.7312	1.6908
C_{10}	3.9898	4.6165	1.5017	4.5018	2.6389	1.9596
C_{11+}	67.1475	32.2331	17.0647	68.2393	50.0661	23.1940
GOR（m3/m3)	13.62	71.78	255	11.53	61	232.8
ρ_o（kg/m3）	822.6	821.9	825	823.8	822.9	830.2

Table 3. Comparision of oil component and composition at different position at the end of test

Fig4 has shown that system pressure drawdown curve due to diffusion displays that pressure is declining gradually with time. The pressure history curve of CO_2-oil diffusion test lies below, CH_4-oil lies middle, N_2-oil lies above. Hence, we can see that different diffusion tests have different rates of pressure drawdown. It shows that the diffusion velocity of CO_2 is the fastest, CH_4 is slower and N_2 is the slowest. For each group of diffusion experiment, the pressure drawdown is also different. The pressure drop of N_2-oil is 1.14MPa, CH_4-oil is 4.55*MPa* and CO_2-oil is 3.9*MPa*.

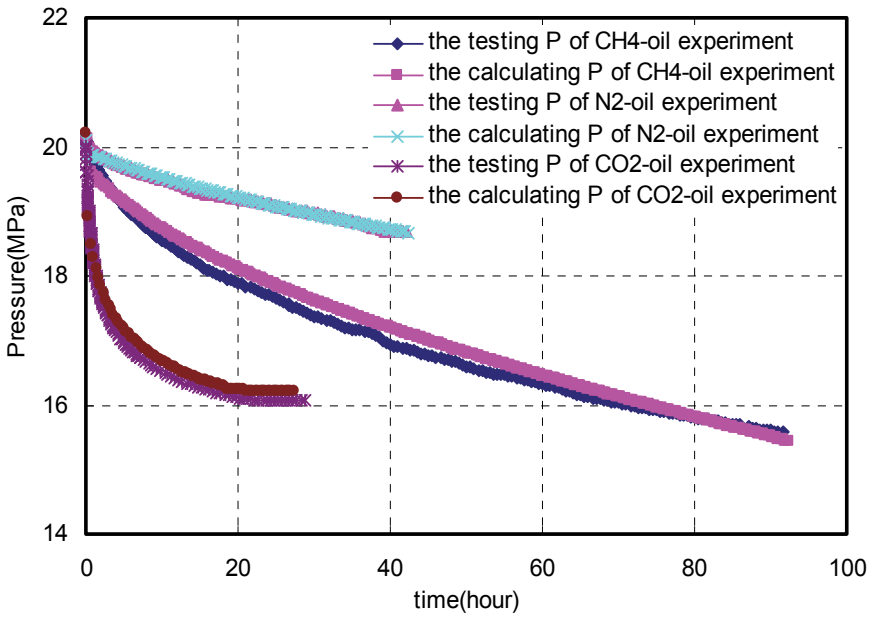

Fig. 4. Contrast of pressure variation of three groups of experiments

The diffusion coefficient is obtained by using established model to match the variation in pressure. Pressure matching is shown in fig.4. The matching result is fairly good. Normally, diffusion coefficient of gas in oil phase is most practical problem in engineering project; the diffusion coefficients of gas in oil phase of the three diffusion tests are shown in fig.5. Fig. 5 indicates that the diffusion coefficient, which increases with the decrease of pressure till the system reaches balance, is variable. The final calculated mole fraction of N_2 in oil phase when in balance is 12.86%, testing value varies from 16.7464%—10.8767% in the different positions at the end of the experiment; For CH_4-oil, the calculated result of CH_4 is 35.34%, the testing value ranges from 34.3391% to 37.6201%; and for CO_2-oil, the calculated result of CO_2 is 67.262% and the testing value ranges from 66.6284% to 66.3558%. The calculated value of component is close to the actual tested ones, which shows the established model and testing method are both reasonable.

4.4.2 Experimental analysis

4.4.2.1 Equilibrium time

The comparison of the equilibrium time of N_2-oil, CO_2-oil and CH_4-oil system under the condition of 20MPa, 60℃ is displayed in Tab 4 which shows that the equilibrium time of CO_2-oil system is obviously less than that of N_2-oil and CH_4-oil system, because the diffusion velocity of CO_2-oil is higher than that of the other two gases. The equilibrium time of N_2-oil is less than that of CH_4-oil; however, it doesn't mean that the diffusion velocity of N_2-oil is higher than CH_4-oil. In fact the main reason is that the solubility of N_2 in the oil is lower, and after a certain time, N_2-oil has reached saturated at the testing temperature and pressure so it appears that the equilibrium time of N_2 is less than that of CH_4. Another reason is that dry gas is used in the experiment instead of CH_4 and there are some heavy components, such as N_2 and C_3H_8 in the dry gas, so the diffusion equilibrium time increases.

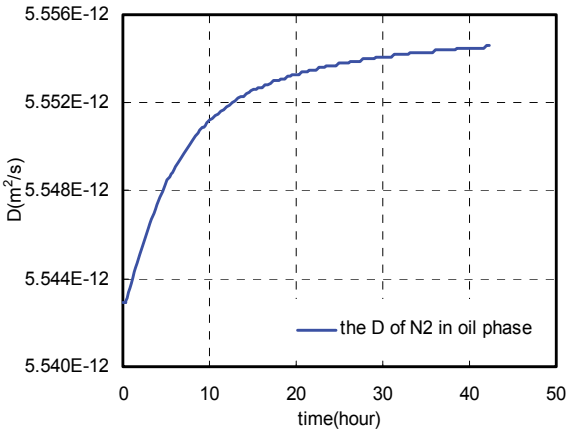

(a)

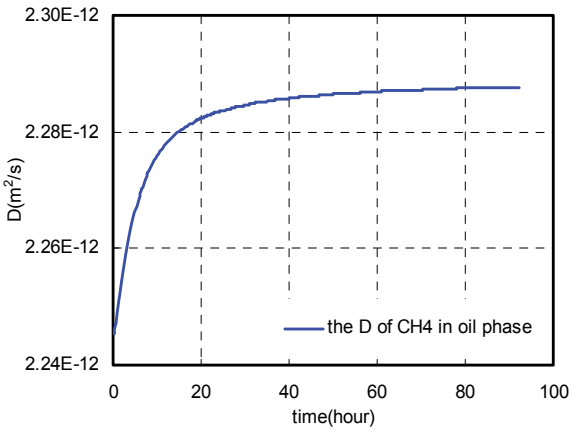

(b)

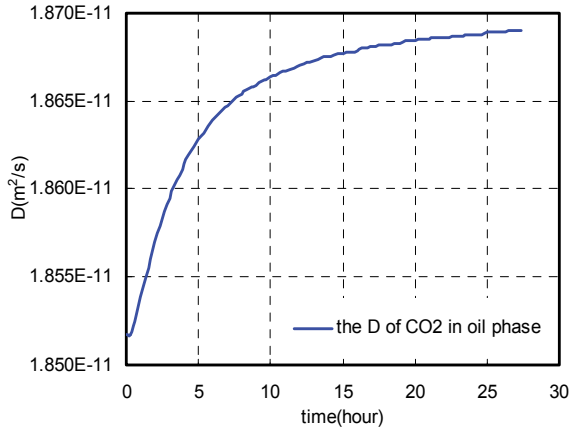

(c)

Fig. 5. Diffusion coefficient in liquid phase

The diffusion experiments of CO_2-dead oil have been conducted under the pressure of 1.36MPa, 0.8*MPa* and temperature of 20℃. abroad and the final equilibrium time was 35 and 27 minutes respectively. Compared with our test at high temperature and pressure, there is a great difference. It shows that pressure, temperature and oil composition have a dramatic influence on diffusion velocity. For the actual case of reservoir gas injection, the accurate shut-in time for the maximum oil recovery can be determined according to the testing results.

dissuasive gas	experimental condition	balance time, hour
N_2-oil	20*MPa*,60℃	42
CH_4-oil	20*MPa*,60℃	91.5
CO_2-oil	20*MPa*,60℃	27.33

Table 4. Balance time for different gas-oil systems

4.4.2.2 Pressure comparison

The comparison of pressure variation of the four diffusion experiments is shown in fig.6. It can be seen from fig.6, the pressure drop curve caused by the diffusion shows the pressure curve for CO_2 lies in the bottom, CH_4 lies in the middle, N_2 lies at the top. From the first phase of each pressure history curve, we can see, speed differences of different gases' pressure drop are significant. Therefore, the CO_2 diffusion rate is the fastest, CH_4 is second and N_2 is the slowest. Each diffusion experiment didn't have the same degree of pressure drop. The diffusion pressure drop of N_2-oil diffusion was 1.14MPa, diffusion pressure drop of CH_4-oil was 4.55MPa. CO_2-crude oil reduced to 3.7MPa; CO_2-crude oil diffusion pressure under the condition of 20MPa 80 ℃ reduced to 3.9MPa. The equilibrium pressure of four experiments was 18.68MPa, 15.57MPa, 16.4MPa and 16.3MPa respectively. CO_2-crude oil under the condition of 20MPa, 60 ℃, had a tendency of a period of diffusion pressure upward phase. From the two pressure curves of CO_2-crude oil, we can see that temperature on the early diffusion of CO_2 has some influence, the higher the temperature, the higher the rate of diffusion, but the final balance pressure has almost no difference. The shape of the pressure curves, except that of the pressure curve of CO_2-crude oil under the condition of 20MPa, 60℃ has abnormal pressure trend, the other three are essentially the same.

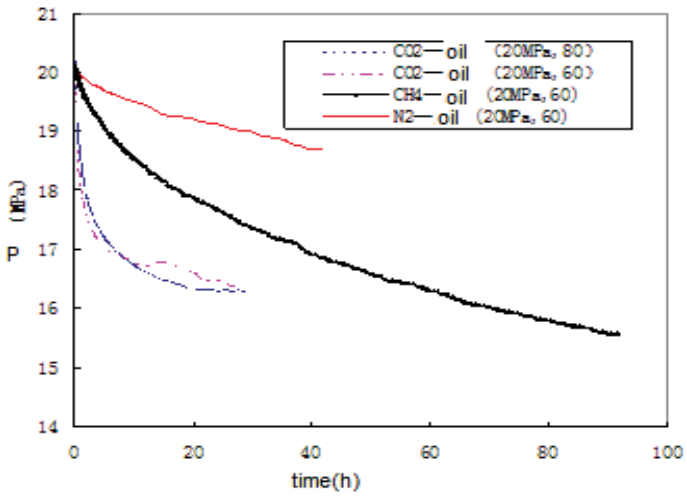

Fig. 6. The comparison of pressure variation of four diffusion experiments

4.4.2.3 Composition changes

The C_2-C_6 hydrocarbon compositions of four group of experiments are shown in Table 5, the comparison of oil phase composition is shown in Table 6.

experiment	upper gas,%	lower gas,%	remark
N_2—oil	0.3142	0.4740	20MPa,60℃
CH_4—oil	1.4974	5.5255	
CO_2—oil	1.1392	1.1524	
CO_2—oil	0.9445	1.7420	20MPa,80℃

Table 5. C_2—C_6 content contrast of gas phase

composition	upper oil				lower oil			
	N_2	CH_4	CO_2	CO_2 (80℃)	N_2	CH_4	CO_2	CO_2 (80 ℃)
CO_2		1.1115	74.6707	66.6284		0.7231	66.3558	66.5355
N_2	16.7464	0.8037	0.0606	0.1354	10.8768	1.9091	0.0549	0.0564
C_1	0.0256	34.3391	2.8120	2.8402	0.0711	37.6201	1.9226	1.8397
C_2	0.0052	0.7732	0.0000	0.0231	0.0045	0.3081	0.0000	0.0000
C_3	0.0394	0.1065	0.0252	0.0397	0.0279	0.0240	0.0245	0.0229
iC_4	0.1532	0.2481	0.1155	0.1208	0.1084	0.1225	0.1035	0.1274
nC_4	0.1981	0.3724	0.1666	0.1715	0.1594	0.2431	0.1499	0.1856
iC_5	0.4111	0.9540	0.3145	0.4520	0.4545	0.4554	0.2850	0.3851
nC_5	0.3091	0.7560	0.2260	0.3594	0.3594	0.5611	0.2056	0.2813
C_6	1.2669	5.6477	0.7177	2.6848	1.6267	2.4097	0.8201	0.7089
C_7	1.9029	5.6401	0.7219	2.2140	2.9228	3.3796	1.0394	0.8206
C_8	4.3693	7.1465	1.5241	3.5759	5.7419	3.8080	2.1943	1.9411
C_9	3.4355	5.2515	1.1743	2.1883	4.9054	2.7312	1.6908	1.5711
C_{10}	3.9898	4.6165	1.3611	1.5017	4.5018	2.6389	1.9596	1.8674
C_{11+}	67.1475	32.2331	16.1098	17.0647	68.2393	43.0661	23.1940	23.6572
GOR（m3/m3)	13.62	71.78	363.2	255	11.53	61	232.8	208.2
ρ_o（kg/m3）	822.6	821.9	827.7	825	823.8	822.9	830.2	831.4

Table 6. Oil content contrast of oil phase

4.4.2.4 Influence of system on diffusion coefficient

The calculated results of diffusion coefficient show that the diffusion coefficients of a certain component in different systems are not the same under the same temperature and pressure. Taking the injected gas for an example, as shown in Tab7, diffusion coefficient of each component of gas and liquid phase in the CO_2-oil system is higher than that of N_2-oil and CH_4-oil system, which is consistent with the diffusion phenomenon observed within the experiment. In the same system, diffusion coefficients of the identical component in different phases are not the same. The diffusion coefficient of gas phase is higher than that of liquid phase. For the phenomena above, there are two reasons, one is interaction between components; the other is the influence caused by the system's state. Molecular motion in gas phase is quicker than that in liquid phase, so diffusive velocity in gas phase is faster.

component	diffusion coefficient in gas phase (final value)			diffusion coefficient in oil phase (final value)		
	N_2-oil	CH_4-oil	CO_2-oil	N_2-oil	CH_4-oil	CO_2-oil
N_2	1.932E-11	8.281E-11	2.403E-10	5.555E-12	3.978E-12	1.082E-11
C_1	1.944E-11	6.081E-11	2.690E-10	3.559E-12	2.287E-12	1.263E-11
CO_2	— —	6.743E-11	2.723E-10	— —	3.985E-12	1.869E-11

Table 7. Diffusion coefficient of identical component in different systems

Table 5 and Table 6 shows that the contents of intermediate hydrocarbon components in lower gas is higher than those in upper gas. The content of C_{11+} components in upper oil, density of single-off oil is lower than the latter, but the upper part of the oil phase gas-oil ratio was significantly higher than the lower oil phase. From the component data of different locations, we can see that the oil and gas properties are not the same, the concentration difference of C_{11+} components of N_2, CH_4, CO_2 and CO_2 (80℃) between the upper and lower oil is respectively 10.8330%, 7.0842 % and 6.5924%, so during the phase calculation, we must consider physical heterogeneity which is caused by molecular diffusion and others of the oil and gas. From the content of the pseudo-component, we can also see that solubility in oil and extraction capacity of N_2 are very low. Since the cause, the property of N_2-oil experiment between upper and lower oil have little difference. Because of CH_4 and CO_2 have the higher solubility in the oil and powerful extraction capacity, the property between the upper and lower oil has great difference. In addition, the content of the diffusion gas are not the same, and their content of the same diffusion experiment in upper oil is higher than that in lower oil. For different experiments,CO_2 gas diffusion experiments is the highest content of gas diffusion(66% -74%), which is followed by CH_4 (34%-37%) and a minimum of N_2 (10%-16%), the final molar concentration differences of the gas diffusion reflect the size of the gas diffusion capacity, the stronger the diffusion capacity is, the higher the molar concentration would be, whereas the lower.

4.4.2.5 Influence of molar concentration on diffusion coefficient

According to literature review, there are two different opinions about the problem whether component concentration has an influence on diffusion coefficient or not at present. Some scholars think that there is an influence of component concentration on diffusion coefficient while others think that there is no influence. Taking the component of injected gas diffusing into liquid phase at 60℃ as an example, the relationship of content and diffusion coefficient is shown in fig7, 8 and 9. These figures show that diffusion coefficient of gas changes with the concentration variation of gas diffusing in the liquid phase. Compared with the initial values, the molar concentration changing level of N_2,CH_4,CO_2 are 12.86%,34.087% and 67.262% respectively and the changing level of the diffusion coefficient of the three gases is 0.211%,1.88% and 0.934% respectively at the end of tests. The data above show that the rate of change of concentration differs from that of diffusion coefficient in different systems. N_2 has the smallest rate of change while the rate of change of CH_4 diffusion coefficient is the largest. Theoretically, the component concentration does have a certain impact on diffusion coefficient. But in engineering application, the impact on the diffusion coefficient can be ignored due to the small rate of change (<2%) under this experimental condition.

The gas injection is applied widely not only in oil-field, but also in condensate gas-field. Hence, further researches need to be done to make sure whether the diffusion phenomena of gas-gas and gas-volatile oil agree with the research result in this paper. The porous media has impact on the phase state of oil and gas, the diffusion in porous media should be the

first step for the study of diffusion issue. The molecular diffusion coefficient tested in the paper is under static condition; nevertheless, how to evaluate the molecular diffusion under dynamic condition needs to develop new theories and testing method further.

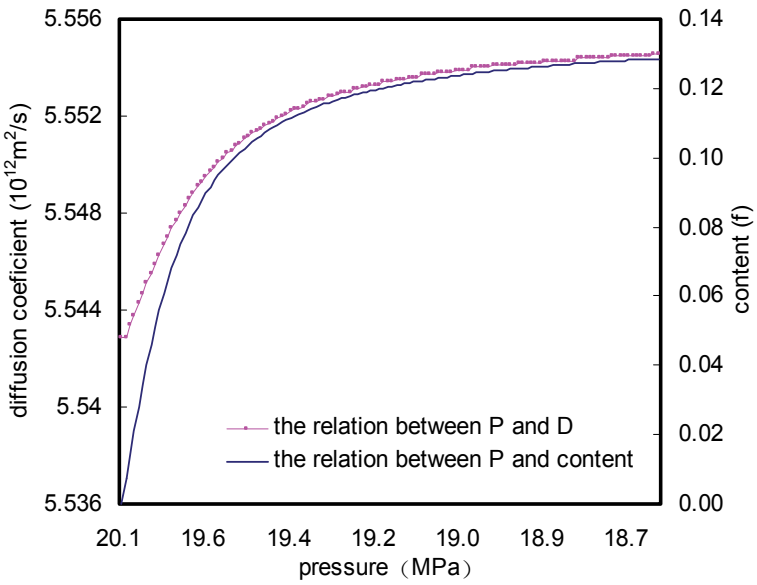

Fig. 7. Relationship of N_2 mole fraction in liquid phase and its diffusion coefficient in N_2-oil diffusion experiment

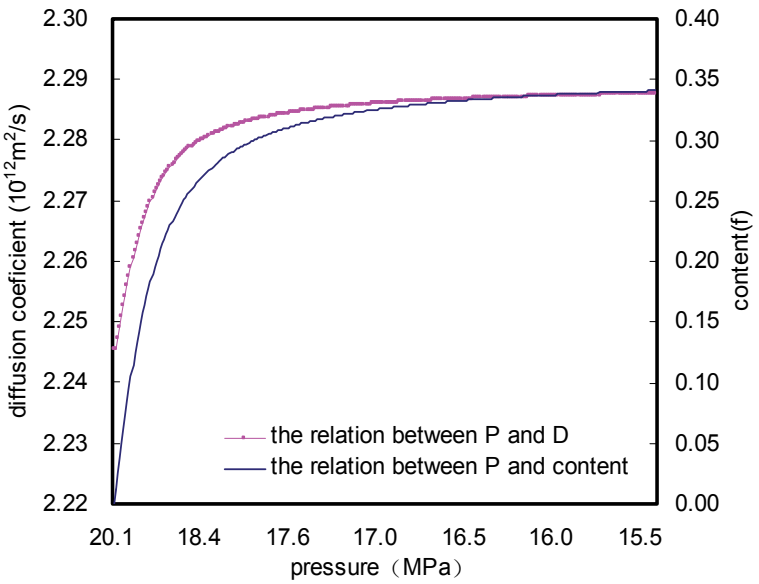

Fig. 8. Relationship of CH_4 mole fraction in liquid phase and its diffusion coefficient in CH_4-oil diffusion experiment

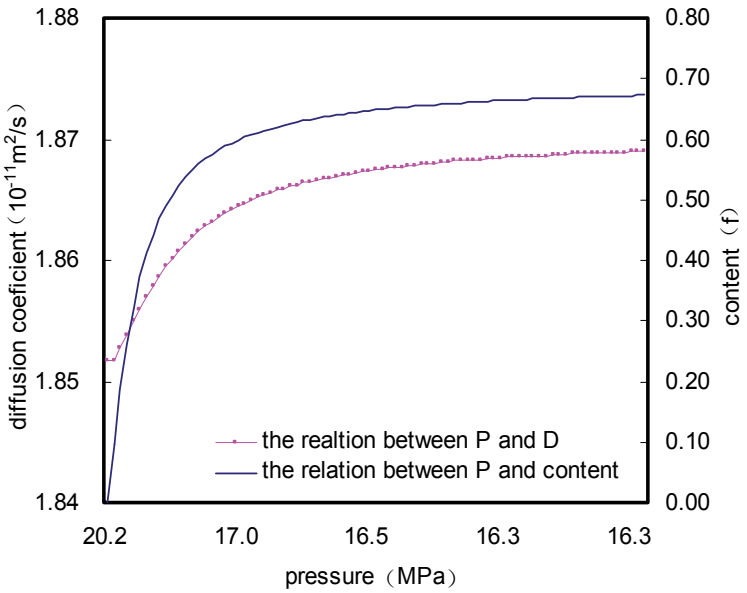

Fig. 9. Relationship of CO_2 mole fraction in liquid phase and its diffusion coefficient in CO_2-oil diffusion experiment

5. References

Reamer, H.H., Duffy, C.H., and Sage, B.H., Diffusion coefficients in hydrocarbon systems: methane – pentane in liquid phase[J]. Industrial Engineering Chemistry, 1958, 3:54-59

Gavalas, G.R., Reamer, H.H., Sage, B.H., Diffusion coefficients in hydrocarbon system. Fundaments, 1968, 7,306-312

Schmidt, T., Leshchyshyn, T.H., Puttagunta, V.R., Diffusion of carbon dioxide into Alberta bitumen.33d annual technical meeting of the petroleum society of CIM, Calgary, Canada,1982

Renner T A. Measurement and correlation of diffusion for CO_2 and rich gas applications[J]. SPE Res Eng, 1988,517-523

Nguyen, T.A., Faroup-Ali,S.M.,Role of diffusion and gravity segregation in oil recovery by immiscible carbon dioxide wag progress[C].In:UNITER international conference on heavy crude and tar sand, 1995, 12:393-403

Wang L S,Lang Z X and Guo T M. Measurements and correlation of the diffusion coefficients of carbon dioxide in liquid hydrocarbons under Elevated pressure[J]. Fluid phase equilibrium, 1996, 117:364-372

Riazi, M.R. A new method for experimental measurement of diffusion coefficients in reservoir fluids[J].SPEJ,1996,14 (5):235-250

Zhang, Y.P, Hyndman, C.L, Maini, B.B. Measuement of gas diffusivity in heavy oils[J]. SPEJ, 2000, 25 (4):37-475

Oballa, V.; Butler, R.M. An experimental-study of diffusion in the bitumen-toluene system. J. Can. Pet. Technol. 1989, 28 (2), 63-90

Das, S.K.; Butler, R.M. Diffusion coefficients of propane and butane in Peace River bitumen. Can. J. Chem. Eng. 1996, 74, 985-992

Wen, Y.; Kantzas, A.; Wang, G.J. Estimation of diffusion coefficients in bitumen solvent mixtures using low field NMR and X-ray CAT scanning, The 5th International Conference on Petroleum Phase Behaviour and Fouling, Banff, Alberta, Canada, June 13-17th, 2004

Chaodong Yang, Yongan GU.A new method for measuring solvent diffusivity in heavy oil by dynamic pendant drop shape analysis. SPE 84202,2003

R. Islas-Juarez, F. Samanego V., C. Perez-Rosales, et al. Experimental Study of Effective Diffusion in Porous Media.SPE92196,2004

Wilke C R and Chang P. Correlation of diffusion coefficients in dilute solutions[J]. AIChE Journal, 1955, 1(2):264-269

Chapman, EnskogThe Chapman-Enskog and Kihara approximations for isotopic thermal diffusion in gases[J]. Journal of Statistical Physics, 1975, 13(2):137-143

Riazi, M.R. A new method for experimental measurement of diffusion coefficients in reservoirfluids. SPEJ, 1996, 14(3-4): 235-250

2

Diffusion in Polymer Solids and Solutions

Mohammad Karimi
Amirkabir University of Technology, Department of Textile Chemistry
Iran

1. Introduction

The industrial importance of penetrable and/or impenetrable polymer systems is evident when one faces with a huge number of publications considering various aspects of diffusion phenomenon. Strong worldwide interest to realize more details about the fundamental of the process, generalize the governed laws to new findings, and find fast and reliable techniques of measurement, makes motivation to follow in this field of science.
Polymers are penetrable, whilst ceramics, metals, and glasses are generally impenetrable. Diffusion of small molecules through the polymers has significant importance in different scientific and engineering fields such as medicine, textile industry, membrane separations, packaging in food industry, extraction of solvents and of contaminants, and etc. Mass transfer through the polymeric membranes including dense and porous membranes depends on the factors included solubility and diffusivity of the penetrant into the polymer, morphology, fillers, and plasticization. For instance, polymers with high crystallinity usually are less penetrable because the crystallites ordered has fewer holes through which gases may pass (Hedenqvist and Gedde, 1996, Sperling, 2006). Such a story can be applied for impenetrable fillers. In the case of nanocomposites, the penetrants cannot diffuse through the structure directly; they are restricted to take a detour (Neway, 2001, Sridhar, 2006).
In the present chapter the author has goals of updating the theory and methodology of diffusion process on recent advances in the field and of providing a framework from which the aspects of this process can be more clarified. It is the intent that this chapter be useful to scientific and industrial activities.

2. Diffusion process

An enormous number of scientific attempts related to various applications of diffusion equation are presented for describing the transport of penetrant molecules through the polymeric membranes or kinetic of sorption/desorption of penetrant in/from the polymer bulk. The mass transfer in the former systems, after a short time, goes to be steady-state, and in the later systems, in all the time, is doing under unsteady-state situation. The first and the second Fick's laws are the basic formula to model both kinds of systems, respectively (Crank and Park, 1975).

2.1 Fick's laws of diffusion

Diffusion is the process by which penetrant is moved from one part of the system to another as results of random molecular motion. The fundamental concepts of the mass transfer are

comparable with those of heat conduction which was adapted for the first time by Fick to cover quantitative diffusion in an isotropic medium (Crank and Park, 1975). His first law governs the steady-state diffusion circumstance and without convection, as given by Equation 1.

$$J = -D\frac{\partial c}{\partial x} \tag{1}$$

where J is the flux which gives the quantity of penetrant diffusing across unit area of medium per unit time and has units of mol.cm^{-2}.s^{-1}, D the diffusion coefficient, c the concentration, x the distance, and $\partial c/\partial x$ is called the gradiant of the concentration along the axis. If J and c are both expressed in terms of the same unit of quantity, e.g. gram, then D is independent of the unit and has unit of cm^2.s^{-1}. Equation 1 is the starting point of numerous models of diffusion in polymer systems. Simple schematic representation of the concentration profile of the penetrant during the diffusion process between two boundaries is shown in Fig. 1-a. The first law can only be directly applied to diffusion in the steady state, whereas concentration is not varying with time (Comyn, 1985).

Under unsteady state circumstance at which the penetrant accumulates in the certain element of the system, Fick's second law describes the diffusion process as given by Equation 2 (Comyn, 1985, Crank and Park, 1968).

$$\frac{\partial c}{\partial t} = \frac{\partial}{\partial x}\left[D\frac{\partial c}{\partial x}\right] \tag{2}$$

Equation 2 stands for concentration change of penetrant at certain element of the system with respect to the time (t), for one-dimensional diffusion, say in the x-direction.

Diffusion coefficient, D, is available after an appropriate mathematical treatment of kinetic data. A well-known solution was developed by Crank at which it is more suitable to moderate and long time approximation (Crank, 1975). Sorption kinetics is one of the most common experimental techniques to study the diffusion of small molecules in polymers. In this technique, a polymer film of thickness $2l$ is immersed into the infinit bath of penetrant, then concentrations, c_t, at any spot within the film at time t is given by Equation 3 (Comyn, 1985).

$$\frac{c_t}{c_\infty} = 1 - \frac{4}{\pi}\sum_{n=0}^{\infty}\frac{(-1)^n}{2n+1}\exp\left[\frac{-D(2n+1)^2\pi^2 t}{4l^2}\right]\times\cos\left[\frac{(2n+1)\pi x}{2l}\right] \tag{3}$$

where c_∞ is the amount of accumulated penetrant at equilibrium, i.e. the saturation equilibrium concentration within the system. $L = 2l$ is the distance between two boundaries layers, x_0 and x_1 (Fig. 1-b).

Integrating Equation 3 yields Equation 4 giving the mass of sorbed penetrant by the film as a function of time t, M_t, and compared with the equilibrium mass, M_∞.

$$\frac{M_t}{M_\infty} = 1 - \sum_{n=0}^{\infty}\frac{8}{(2n+1)^2\pi^2}\exp\left[\frac{-D(2n+1)^2\pi^2 t}{4l^2}\right] \tag{4}$$

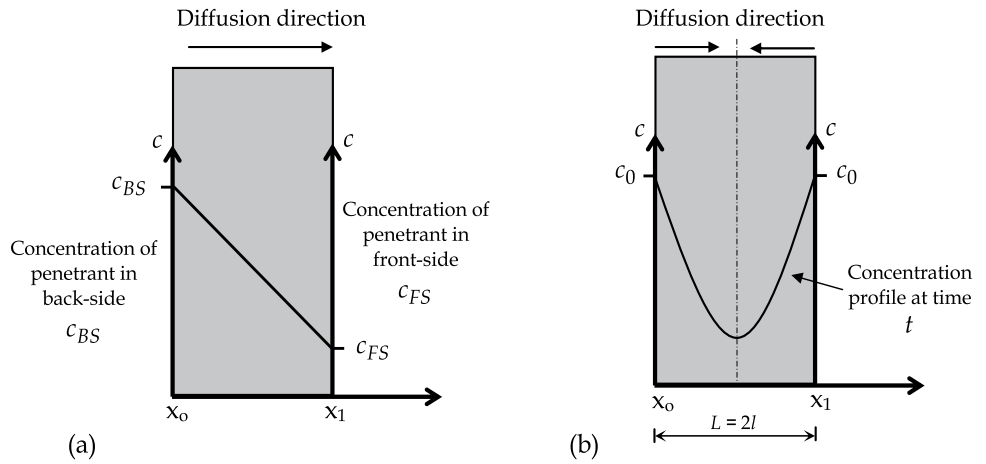

Fig. 1. Concentration profile under (a) steady state and (b) unsteady state condition.

For the processes which takes place at short times, Equation 4 can be written, for a thickness of $L = 2l$, as

$$\frac{M_t}{M_\infty} = \frac{2}{l}\left(\frac{D}{\pi}\right)^{1/2} t^{1/2} \tag{5}$$

Plotting the M_t / M_∞ as function of $t^{1/2}$, diffusion coefficient can be determine from the linear portion of the curve, as shown in Fig. 2. Using Equation 5 instead of Equation 4, the error is in the range of 0.1% when the ratio of M_t / M_∞ is lower than 0.5 (Vergnaud, 1991).

In the case of long-time diffusion by which there may be limited data at $M_t / M_\infty \leq 0.5$, Equation 4 can be written as follow:

$$\frac{M_t}{M_\infty} = 1 - \frac{8}{\pi^2}\exp\left[\frac{-D\pi^2 t}{4l^2}\right] \tag{6}$$

Equation 6 is usually used in the form of Equation 7, as given following,

$$\ln\left(1 - \frac{M_t}{M_\infty}\right) = \ln\left(\frac{8}{\pi^2}\right) - \frac{D\pi^2 t}{4l^2} \tag{7}$$

This estimation also shows similarly negligible error on the order of 0.1% (Vergnaud, 1991). Beyond the diffusion coefficient, the thickness of the film is so much important parameter affected the kinetics of diffusion, as seen in Equation 4. The process of dyeing by which the dye molecules accumulate in the fiber under a non-linear concentration gradient is known as the unsteady-state mass transfer, since the amount of dye in the fiber is continuously increasing. Following, Equation 8, was developed by Hill for describing the diffusion of dye molecules into an infinitely long cylinder or filament of radius r (Crank and Park, 1975, Jones, 1989).

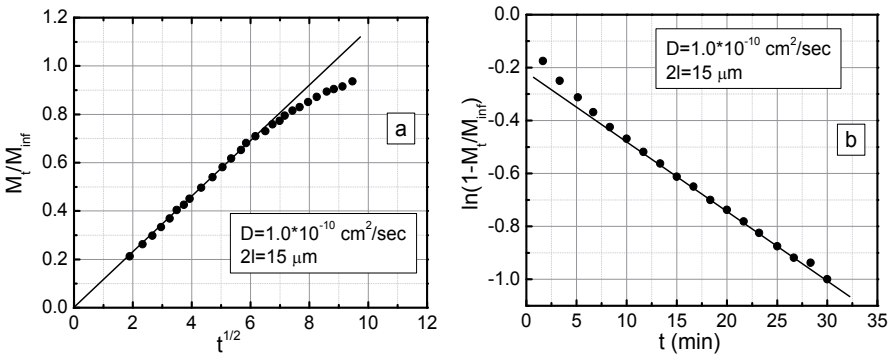

Fig. 2. Kinetics of mass uptake for a typical polymer. (a) M_t / M_∞ as function of $t^{1/2}$, (b) $\ln(1 - M_t / M_\infty)$ as function of t; data were extracted from literature (Fieldson and Barbari, 1993).

$$\frac{C_t}{C_\infty} = 1 - 0.692\left[\exp\left(-5.785Dt / r^2\right)\right] + 0.190\left[\exp\left(-30.5Dt / r^2\right)\right] + 0.0775\left[\exp\left(-74.9Dt / r^2\right)\right] + 0.0415\left[\exp\left(-139Dt / r^2\right)\right] + 0.0258\left[\exp\left(-223Dt / r^2\right)\right] + ...) \quad (8)$$

Variation of C_t / C_∞ for different values of radius of filaments are presented in Fig. 3. As seen in Fig.3, decreasing in radius of filament causes increasing in the rate of saturating.

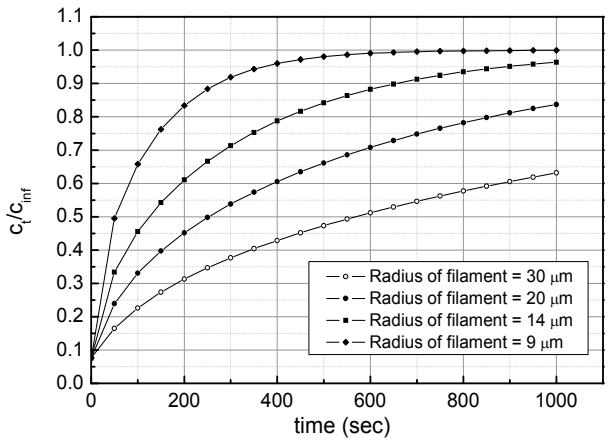

Fig. 3. C_t / C_∞ of dyeing versus t for different radius of fibers.

2.2 Permeability

The permeability coefficient, P, is defined as volume of the penetrant which passses per unit time through unit area of polymer having unit thickness, with a unit pressure diference across the system. The permeabilty depends on solubility coefficient, S, as well as the diffusion coefficient. Equation 9 expresses the permeabilty in terms of solubility and diffusivity, D, (Ashley, 1985).

$$P = D.S \tag{9}$$

Typical units for P are (cm^3 cm)/(s cm^2 Pa) (those units×10^{-10} are defined as the barrer, the standard unit of P adopted by ASTM).
Fundamental of diffusivity was discussed in the previous part and its measurement techniques will be discussed later. Solubility as related to chemical nature of penetrant and polymer, is capacity of a polymer to uptake a penetrant. The preferred SI unit of the solubility coefficient is (cm^3 [273.15; 1.013×10^5 Pa])/(cm^3.Pa).

2.3 Fickian and non-Fickian diffusion

In the earlier parts, steady-state and unsteady-state diffusion of small molecules through the polymer system was developed, with considering the basic assumption of Fickian diffusion. There are, however, the cases where diffusion is non-Fickian. These will be briefly discussed. Considering a simple type of experiment, a piece of polymer film is mounted into the penetrant liquid phase or vapor atmosphere. According to the second Fick's law, the basic equation of mass uptake by polymer film can be given by Equation 10 (Masaro, 1999).

$$\frac{M_t}{M_\infty} = kt^n \tag{10}$$

where the exponent n is called the type of diffusion mechanism, and k is constant which depends on diffusion coefficient and thickness of film.
Fickian diffusion (Case I) is often observed in polymer system when the temperature is well above the glass transition temperature of the polymer (T_g). Therefore it expects that the M_t / M_∞ is proportional to the square-root of time i.e. $n = 0.5$. Other mechanisms has been established for diffusion phenomenon and categorized based on the exponent n, as follow (Sperling, 2006);

$n > 1$	Supercase II
$n = 1$	Case II
$1 > n > \frac{1}{2}$	Anomalous
$\frac{1}{2} > n$	Pseudo-Fickian

The Case II diffusion is the second most important mechanism of diffusion for the polymer. This is a process of moving boundaries and a linear sorption kinetics, which is opposed to Fickian. A sharp penetration front is observed by which it advances with a constant rate. More detailed features of the process, as induction period and front acceleration in the latter stage, have been documented in the literatures (Windle, 1985).
An exponent between 1 and 0.5 signifies anomalous diffusion. Case II and Anomalous diffusion are usually observed for polymer whose glass transition temperature is higher than the experimental temperature. The main difference between these two diffusion modes concerns the solvent diffusion rate (Alfrey, 1966, as cited in Masaro, 1999).

2.4 Deborah number

A solid phase is generally considered as a glass or amorphous if it is noncrystalline and exhibits a second-order transition frequently referred to the glass transition (T_g) (Gibbs and Dimarzio, 1958), which is the transition between a glassy, highly viscous brittle structure,

and rubbery, less viscous and more mobile structure, states. The rubbery state ($T > T_g$), represents a liquid-like structure with high segmental motion resulting an increase of free volume with temperature. When the penetrant diffuses into the polymer, the plasticization occurs resulting a decrease of the T_g (Sperling, 2006) and increase of free volume of the mixture (Wang, 2000).

Since the mobility of polymer chain depends on temperature, it greatly decreases below and increases above the glass transition temperature. On the other hand, sorption and transport of penetrant into the polymer can change the mobility of the segments because of T_g depression. Consequently, the relaxation time of polymer decreases with increasing temperature or concentration of penetrant. The overall sorption process reflects all relaxation motions of the polymer which occur on a time scale comparable to or greater than the time scale of the concurrent diffusion process. Indeed, a Deborah number can be defined as the ratio of the relaxation time to the diffusion time. Originally introduced by Vrentas et al. (Vrentas, 1975), it is given by Equation 11.

$$D_e = \frac{\tau_e}{t} \tag{11}$$

where t is the characteristic time of diffusion process being observed and τ_e is the characteristic time of polymer. The Deborah number (D_e) is a useful scaling parameter for describing the markedly different behavior frequently being observed in diffusion process. For the experiments where that number is much less than unity ($D_e \ll 1$), relaxation is fast, penetrants are diffusing in where conformational changes in the polymer structure take place very quickly. Thus the diffusion mechanism will be Fickian. When the number is near unity, ($D_e \cong 1$), intermediate behavior is observed and can be called of 'coupled' diffusion-relaxation or just 'anomalous' (Rogers, 1985). If $D_e \gg 1$, the diffusing molecules are moving into a medium which approximately behaves as an elastic material. This is typical case of diffusion of small molecules into the glassy polymer. When the penetrantes diffuse into the polymer matrix until the concentration reaches an equilibrium value, a sharp diffusion front is formed that starts to move into the polymer matrix, where the glass transition of mixture drops down the experimental temperature. This process is the 'induction period' and represents the beginning of case II mechanism (Lasky, 1988).

2.5 Geometrical impedance factor

Diffusing penetrant through the polymer is greatly affected by the presence of impenetrable micro- and or nano-pieces which are located into the structure. Crystallites and micro and nano fillers are impenetrable and behave as barrier in advancing penetrant, causing to form a tortuosity in diffusion path, see Fig. 4. Considering the geometrical aspect of diffusion process, Michael et al. (Michaels and Parker, 1959, Michaels and Bixler, 1961, cited in Moisan, 1985, Hadgett, 2000, Mattozzi, 2007) proposed the following relationship between the overall diffusivity (D) and the diffusivity of the amorphous component (D_a).

$$D = \frac{D_a}{\tau\beta} \tag{12}$$

where β is an 'immobilization' factor and τ is a 'geometrical impedance' factor. β is almost equal to 1 for helium, that is a diffuser having very low atomic radius. It has been

recognized that τ increases very rapidly with increasing concentration of impenetrable pieces, and that the two factors increase much more rapidly in large molecules than in small ones (Moisan, 1985).

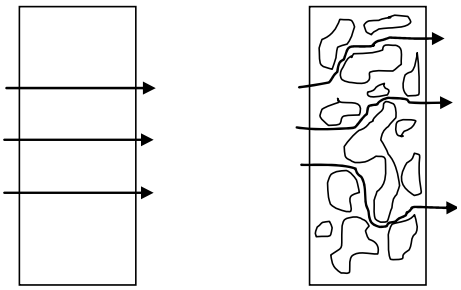

Fig. 4. Schematic demonstration of path through the structure; (a) homogeneous medium, (b) heterogeneous medium.

Filled polymer with nano-particles has lower diffusion coefficient than unfilled one. Poly(methyl methacrylate) (PMMA), for instance, is a glassy polymer, showing a non-Fickain diffusion for water with $D = 3.35 \times 10^{-8}\ cm^2.s^{-1}$. The diffusion coefficient of water is reduced to $D_e = 3.15 \times 10^{-9}\ cm^2.s^{-1}$ when the polymer is filled by silicate nanolayers of Cloisite 15A (Eyvazkhani and Karimi, 2009). Geometerical dimension, size distribution and amount of fillers as well as its level of dispersion into the polymer matrix are important factors controlling the rate of mass transfer through the filled polymer, especially nanocomposites.

As cleared, diffusing penetrants through a homogeneous polymer structure are advancing in a straight line, while they meander along the path, passing through the heterogeneous polymer structure such as nanocomposite. Polymer nanocomposites (PNCs) form by dispersing a few weight percent of nanometer-sized fillers, in form of tubular, spherical, and layer. Compared to neat polymer, PNCs have tendency to reduce the diffusion coefficient of penetrant through the increase in path length that is encountered by a diffusing molecule because of the presence of a huge number of barrier particles during the mass transfer. The largest possible ratio of the diffusivity of a molecule through the neat polymer (D) to that of the same molecule through the filled polymer (D_e) was formulated by several researchers whose equations were recently looked over by Sridhar and co-workers (Sridhar, 2006).

Block copolymers as well as polyblends are other interesting materials; have attracted the attention of a great number of scientists because of designable structure on a nanometer scale. These polymers have a multiphase structure, assembling at various textures. Sorption and transport in both have been approached along the lines discussed above. Tecoflex-EG72D (TFX), a kind of polyurethane, has potential to employ in medical application. Two-phase structure of this copolymer causes the path of penetrating into the TFX to be detour, not to be straight line. Generally, such materials have two different transition temperatures regarding to the phases, making them to be temperature sensitive incorporated with water vapor permeability. Fig. 5 shows the amount of water passing through the TFX membrane

as a function of time at different temperatures in steady state condition (Hajiagha and Karimi, 2010). Noticeably, an acceleration in permeability is observed above 40 °C concerning to glass transition temperature of soft phase. Controlling the microstructure of these multi-phase systems allows tuning the amount of permeability. Strong worldwide interest in using temperature sensitive materials shows these materials have potential to employ in textile industry, medicine, and environmental fields. For instance, combining these materials with ordinary fabrics provides variable breathability in response to various temperatures (Ding, 2006).

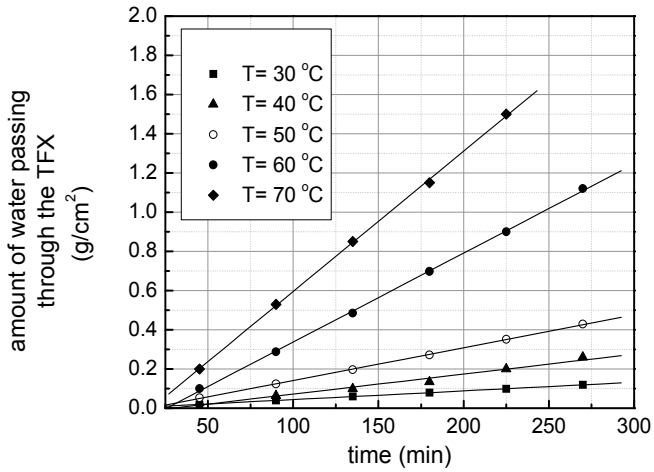

Fig. 5. Diffusion through the TFX film under steady-state conditions.

3. Thermodynamic of penetrant/polymer mixture

Thermodynamically describing the penetrant/polymer mixture is based on mobility of polymer chain during the diffusion process. Diffusion of penetrant into the polymer yeilds plasticization, resulting in significant depression of glass transition temperature. Indeed, a glassy polymer isothermally changes into a rubbery state only by diffusion of penetrant. Using classical thermodynamic theory, the glass transition temperature of the solvent and polymer mixture can be described by the following expression, which was derived by Couchman and Karasz (Couchman and Karasz, 1978).

$$T_{gm} = \frac{x_1 \Delta C_{p1} T_{g1} + x_3 \Delta C_{p3} T_{g3}}{x_1 \Delta C_{p1} + x_3 \Delta C_{p3}} \tag{13}$$

where T_{gm} and T_{gi} are the glass transition temperatures of the mixture and the pure component i, respectively. ΔC_{pi} is the incremental change in heat capacity at T_{gi}, and $x_i = n_i / (n_1 + n_3)$ represents the mole fraction defined on the basis of the repeat unit of the polymer. Most values of solvent glass transition have been published from free volume theory (Hong, 1995).

A solid phase of polymer is ordinarily designated as a glass if it is non-crystalline and if it exhibits at a certain higher temperature a second-order transition, often referred to as the

glass transition (Gibbs and Dimarzio, 1958). It was found that the specific volume of those polymers diminishes linearly with the temperature until the glass transition temperature T_g is achieved. Below this temperature the reduction continues but at a smaller rate. The difference between the volume observed at absolute zero temperature and the volume measured at transition temperature was considered as space, which, in the amorphous solid, is available for oscillations (Dimarzio, 1996). For the following model derivation, we assume that the state of the investigated polymer at the beginning is a glass. In this state the polymer chains are fixed on their location at least in comparison with the typical time constants of individual jump events of diffusing water molecules from one hole of the free volume to another. On the other hand, according to the free volume theory characterizing the excluded volume of a glassy polymer system, there is "free" space between atoms of the polymer chain, which can be occupied by small penetrant molecules. However, due to their size and shape, these penetrants can only "see" a subset of the total free volume, termed as the "accessible free volume". In this way accessible free volume depends on both, polymer and penetrant, whereas the total free volume depends only on the polymer. The situation is illustrated schematically in Fig. 6 on a lattice where it is assumed that the polymer chain consists of segments, which have the same volume as a penetrant particle.

This accessible free volume consists of the empty lattice sites and the sites occupied by the penetrant. For a corresponding lattice model, the primary statistical mechanical problem is to determine the number of combinatorial configurations available for the system (Sanchez and Lacombe, 1978, Prausnitz and Lichtenthaler, 1999). From the assumption of the glassy state, it follows that there is only one conformation for the polymer chain. This situation is different to the case of a polymer solution. Furthermore it is assumed for the thermodynamic model that also during the diffusion of penetrants through the polymer bulk, the conformation of the polymer chains does not change and remains as before (One should have in mind that diffusion is in reality only possible by rearrangement of polymer segments, i.e. by the opening of temporary diffusion channels. Therefore the zero-entropy is describing the extreme case of a completely stiff, i.e. ultra-glassy polymer, in which strictly speaking no diffusion could occur.). Therefore the number of possible conformations, for polymer chain, does not vary and is equal to one $(\Omega = 1)$. It results that the entropy change during the penetration is zero, $S_{polymer} = k\ln(\Omega) = 0$. Thus, if the situation is glassy, the Gibbs free energy of mixing (penetrant/polymer), ΔG_m, is given by Karimi and co-workers (Karimi, 2007),

$$\Delta G_m = \Delta H_m - T\Delta S_m = RT\left[\chi_{12}^{*} n_1 \phi_2 + n_1 \ln(\frac{\phi_1}{\phi_{FV}}) + n_0 \ln(\frac{\phi_0}{\phi_{FV}})\right] \tag{14}$$

where ϕ_{FV} is fractional free volume of pure polymer, ϕ_o volume fraction of holes, R the gas constant, T the absolute temperature, and n_1 and n_o are the number of moles of penetrant and holes respectively.

The GP model (Equation 14) represents, according to the definition, the thermodynamic state of a penetrant/polymer system where the polymer chains are completely inflexible and this stiffness will not be influenced by the sorption of the penetrant. In general such a condition will be only fulfilled if the quantity of penetrant in the polymer matrix is very small. Mainly hydrophobic polymers are candidates, which will meet these requirements

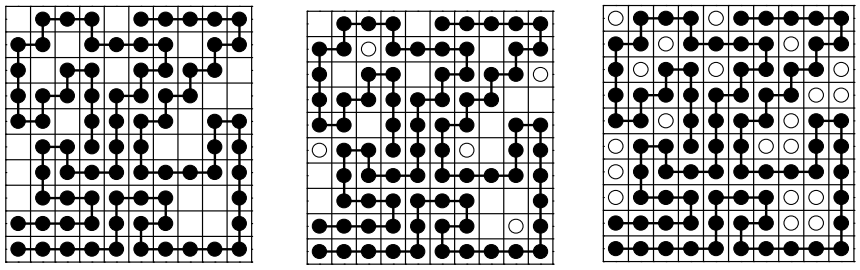

Fig. 6. Segments of a polymer molecule located in the lattice and penetrant molecules distributed within, schematically.

completely. However it cannot be expected that the GP model can also describe nonsolvent/polymer systems for hydrophilic membrane polymers. Therefore in order to extent the GP-model, it is assumed in the following that the status of the wetted polymer sample can be considered as a superposition of a glassy state and a rubber-like state (as well-described by Flory and Huggins, 1953), in general. We consider the polymer sample partly as a glass and partly (through the interaction with penetrant) as a rubber. The ratio of glassy and rubbery contributions will be assumed to be depending on the stiffness of the dry polymer sample (characterized e.g., by the glass temperature) and the quantity of sorbed penetrant. The glass temperature T_{gm} of a penetrant/polymer mixture can be estimated by Equation 13. Thus, the Gibbs free energy is given as follow (Karimi, 2007)

$$\frac{\Delta G_m}{RT} = \frac{\Delta H_m}{RT} - \frac{T\Delta S_m}{RT} = \chi_{12}^* n_1 \phi + \beta\left[n_1 \ln(\phi_1) + n_2 \ln(\phi_2)\right] + (1-\beta)\left[n_1 \ln(\frac{\phi_1}{\phi_{FV}}) + n_0 \ln(\frac{\phi_0}{\phi_{FV}})\right] \tag{15}$$

β is difinned according to $\beta = (T_{gm} - T_{g2}) / (T - T_{g2})$.

Actually, β represents a measure for the relative amount of "rubber-like regions" in the polymer at the temperature T of interest in the sorbed state. Per definition the β values vary between 0 and 1 for a completely glass-like and a completely rubber-like state, respectively, if both states are present. However β-values higher than 1 can be indicating a completely rubber-like state, well-describing by Flory-Huggins theory (Flory, 1956).

$$\frac{\Delta G_M}{RT} = n_1 \ln \phi_1 + n_2 \ln \phi_2 + \chi_{12} n_1 \phi_2 \tag{16}$$

In Equation 16, the first two terms is the combinatorial entropy computed by considering the possible arrangement of only polymer chains on the lattice.

With assumption of rubbery state, swelling of polymer by which the penetrant diffuses into the polymer more than free volume and the junction point is constant; Flory-Rehner equation (Flory, 1950, as cited in Prabhakar, 2005) is applicable.

$$\ln a_1 = \ln(1-\phi_2) + \phi_2 + \chi \phi_2^{\,2} + \frac{V_1 \rho_2}{\bar{M}_c}(\phi_2^{1/3} - \frac{1}{2}\phi_2) \tag{17}$$

where a_1 is penetrant activity and ϕ_2 volume fraction of polymer.

4. Measurement of diffusion

4.1 FTIR-ATR spectroscopy

Measuring the diffusion of small molecules in polymers using Fourier transform infrared-attenuated total reflection (FTIR-ATR) spectroscopy, is a promising technique which allows one to study liquid diffusion in thin polymer films in situ. This technique has increasingly been used to study sorption kinetics in polymers and has proven to be very accurate and reliable. Fig 7 shows schematic of the ATR diffusion experiment. In practice, the sample is cast onto one side of the ATR prism (optically dense crystal) and then the diffusing penetrants are poured on it. Various materials such as PTFE are used to seal the cell.

According to the principle of ATR technique (Urban, 1996), when a sample as rarer medium is brought in contact with totally reflecting surface of the ATR crystal (as a propagating medium), the evanescent wave will be attenuated in regions of the infrared spectrum where the sample absorbs energy. The electric field strength, E, of the evanescent wave decays exponentially with distance from interface, as shown in Fig 7. The distance, which is on the order of micrometers, makes ATR generally insensitive to sample thickness, allowing for dynamic measurement in a layer with certain thickness. The penetration depth of the IR beam in sample can be calculated by Equation 18.

$$dp = \frac{\lambda}{2\pi(n_1^2 \sin^2\theta - n_2^2)^{1/2}} \tag{18}$$

where depth of penetration of evanescent wave is shown by dp, λ is the wavelength of the infrared radiation, n_1 and n_2 are the refractive indices of flat crystals and polymer solutions respectively and θ is the angle of incidence beam. By increasing the refractive index of the ATR crystal, the depth of penetration will decrease (i.e changing from ZnSe to Ge, with refractive indices equal to 2.4 and 4, respectively). This will decrease the effective path length and therefore decrease the absorbance intensity of the spectrum. High index crystals are needed when analyzing high index materials. The refractive index of some ATR crystal is listed in Table 1.

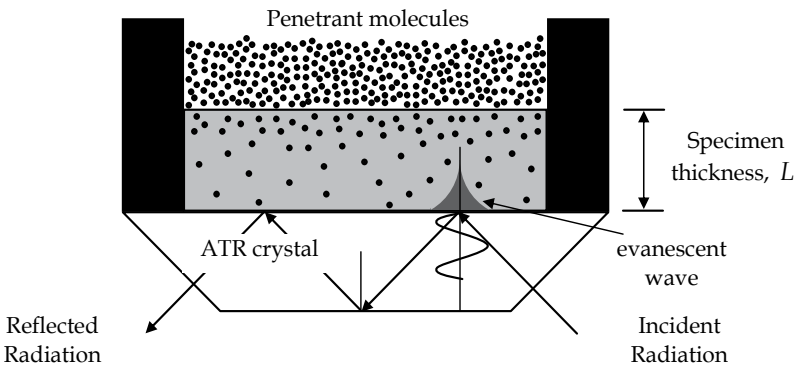

Fig. 7. Schematic representation of the ATR equipment for diffusion experiment.

ATR prism	Refractive index
ZnSe	2.4
Ge	4
ZnS	2.2
AMTIR	2.5
Si	3.4

Table 1. Refractive index of some ATR prism

As the goal of IR spectroscopic application is to determine the chemical functional group contained in a particular material, thus it is possible to measure the dynamic change of components containing such functional groups where they make a mixture. Considering water molecules as penetrant into the kind of polymer, the characteristic peak of water in region between 3800 cm^{-1} and 2750 cm^{-1} should be increase as results of increasing the concentration of water into the bottom layer of polymer, in contact with ATR prism. A representative sample of the spectra recorded is shown in Fig 8. This is a dynamic measurement of diffusing water into the PMMA uniformly thin film contacted on the ATR crystal.

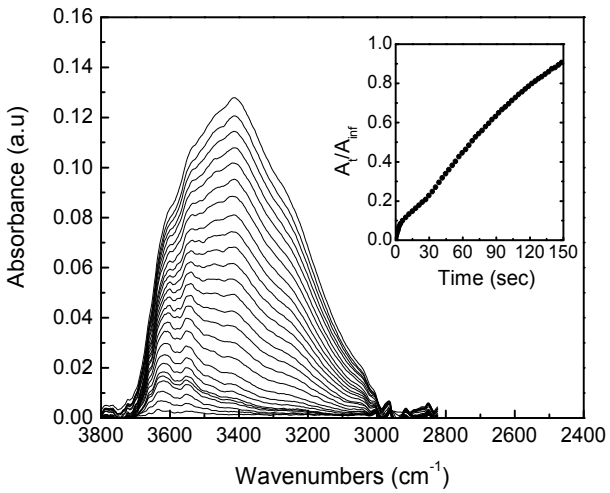

Fig. 8. Sequence of time-evolved spectra from PMMA sample treated at 25 °C.

To quantify the water concentration the simplest quantitative technique i.e. Beer-Lambert law, can be applied. Beer's law states that not only is peak intensity related to sample concentration, but the relationship is linear as shown in the following equation.

$$A = abc \tag{19}$$

where a is absorptivity of the component at the measured frequency, b pathlenght of the component, and c is the concentration of the component. Quantity of absorptivity, a, is determined based on certain calibration models. Various calibration models are available for quantifying unknown concentration of components. These models are simple Beer's law, classical least squares (CLS), stepwise multiple linear regression (SMLR), partial least squares (PLS), and principal component regression (PCR).

As a result, the Fickian concentration profile can be developed by Equation 20 (Fieldson, Barbari, 1993).

$$\frac{A_t}{A_\infty} = 1 - \frac{8\gamma}{\pi[1-\exp(-2\gamma l)]} \times \left[\frac{\exp\left(\frac{-D\pi^2 t}{4l^2}\right)\left(\frac{\pi}{2l}\exp(-2\gamma l) + (2\gamma)\right)}{\left(\frac{\pi^2}{4l^2} + 4\gamma^2\right)} \right] \tag{20}$$

where $\gamma = 1/dp$.

In Equation 20, it is assumed that the value of γ is constant. This is not entirly correct because it depends on the polymer refractive index, which can vary as the concentration of penetrant increases. Equation 20 could be simplified if following condition could be found in the experiment (Fieldson, Barbari, 1993):

$$4\gamma^2 \gg \frac{\pi^2}{4l^2} \quad \text{and} \quad 1 \gg \exp(-2\gamma l) \tag{21}$$

therefore

$$\ln(1 - \frac{A_t}{A_\infty}) = \ln(\frac{4}{\pi}) - \frac{D\pi^2}{4l^2}t \tag{22}$$

With Equation 22, the logarithm of the absorbance data is plotted as a function of time, and then the diffusion coefficient, D, is given by the slope of a linear least square regression. This is completely similar to the use of Equation 7 to determine the diffusion coefficient in gravimetric sorption experiments at long time. This technique has been increasingly employed in recent years (Fieldson and Barbari, 1993, Sammon, 2000, Yi and Pellegrino, 2002, Hua, 2004, Pereira, 2005, Doppers, 2006).

4.2 Other techniques of measuring

Beside with FTIR-ATR technique, a great variety of methods are available for measuring diffusion coefficients of penetrant into the polymeric systems. Gravimetric techniques that directly follow mass changes with time are frequently used for investigating the sorption kinetics (Chandra and Koros, 2009, Karimi, 2005, Cotugno, 2005). This is more applicable for gases and vapors which are almost condensable. The polymer thin film is hung on calibrated magnetic suspension balance; both are placed in a chamber maintained at the certain temperature. Sorption kinetics are obtained by recording the sample weight as function of time after introduction of the vapor into the chamber.

If non-condensable gases such as carbon dioxide, nitrogen, and methane are given to monitor sorption kinetics, pressure decay techniques are often employed (Liu and Tomasko, 2007). The polymer sample is loaded into the vessel conditioned at certain temperature. Then, penetrating gas is introduced to the vessel at a preset pressure. As the gas sorption proceeded, the detected system pressure gradually decreased from the initial reading. The saturation state reaches when no fluctuation in the pressure is observed.

'Wet cup' is the other most applicable technique to measure the diffusion coefficient as well as permeability of the polymer, not to measure sorption kinetics (Hubbell, 1975, Hu, 2007).

Based on the water cup method, referring to ASTM E96-00 standard, the vapor passing through the polymer film measured as function of time. That is, an open cup containing water sealed with the specimen membrane, and the assembly is placed in a test chamber at the certain temperature, with a constant relative humidity of 50%, and the water lost isrecorded after certain period of time

5. Mass transfer across the interface between polymer solution and nonsolvent bath

Polymer solutions are important for a variety of purposes, especially, for manufacturing fibers and membranes. Generally, solidification of polymer in shape of interest takes place by solvent evaporation from nonsolvent diffusion into the polymer solution. During the process, polymer solution is undergoing a change in the concentration of components. A schematic representation of mass transfer through the interface between polymer solution and nonsolvent bath is depicted in Fig. 9. During the quench period, solvent-nonsolvent exchange is doing with time and eventually polymer precipitation takes place. The ratio of solvent-nonsolvent exchange, predicting mass transfer paths on the thermodynamic phase diagram, is an important factor to control the ultimate structure of product (Karimi and Kish, 2009).

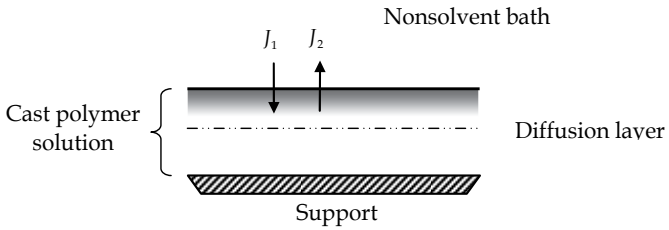

Fig. 9. Schematic presentation of mass transfer through the interface between polymer solution and nonsolvent bath.

Such a mass transfer process requires a consideration based on the thermodynamics of irreversible processes which indicates that the fundamental driving forces for diffusion through the interface of multiphase system are the gradients of the chemical potential of each of the system components. Here, considering polymer solution and nonsolvent bath as two-phase system, the amount of molecules passing through the interface could be described by Fick's law if the intrinsic mobility (M) of each component could be known. The flux (J) due to pure diffusion is:

$$J = -(\frac{\mathrm{M}\phi}{N})(\frac{\partial \mu}{\partial x}) \tag{23}$$

where N is Avogadro's number and μ is chemical potential (partial molar free energy). Replacing $\mu = RT\ln a$ in to the Equation 23 then,

$$J = -RT\frac{\mathrm{M}\phi}{N}(\frac{\partial \ln a}{\partial x}) \tag{24}$$

where a is the activity, R the gas constant, and T is the absolute temperature. Mobility coefficient some times are called self-diffusion coefficient (D^*), presenting the motion and diffusion of molecules without presence of concentration gradient and/or any driving force for mass transfer, given by $D^* = \mathrm{M}RT / N$. Then

$$J = -D^*\phi(\frac{\partial \ln a}{\partial x}) \tag{25}$$

Since it is difficult to measure the self-diffusion coefficient, a thermodynamic diffusion (D_T) is introduce to use in theories regarding the concentration and temperature dependence of diffusion, as given by

$$D_T = D(\frac{\partial \ln c_1}{\partial \ln a_1}) \tag{26}$$

According to Equation 25 to determine the mass transfer of solvent and or nonsolvent across the interface, it should be given their chemical potentials. Flory-Huggins (FH) model is well-established to use for describing the free energy of the polymer solution, as given in Equation 26. It should be noted that the FH model can be extended for multi-component system if more than one mobile component exists for mass transfer; more details for Gibbs free energy of multi-components system are documented in literatures (Karimi, 2005, Boom, 1994)

5.1 Mass transfer paths

Polymer membrane which is obtained by the so-called nonsolvent-induced phase separation (NIPS) (Fig. 9), has a structure determined by two distinct factors: (1) the phase separation phenomena (thermodynamics and kinetics) in the ternary system, and (2) the ratio and the rate of diffusive solvent-nonsolvent exchange during the immersion (Karimi, 2009, Wijmans, 1984). The exchange of the solvent and the nonsolvent across the interface initiates the phase separation of the polymer solution in two phases; one with a high polymer concentration (polymer-rich phase), and the other with a low polymer concentration (polymer-lean phase). The morphology of the membranes, the most favorable feature, is strongly related to the composition of the casting film prior and during the immersion precipitation. The compositional change during the phase separation has been frequently discussed theoretically (Tsay and McHugh, 1987), but the experimental results for the composition of the homogeneous polymer solution prior to precipitation of polymer are scarce (Zeman and Fraser, 1994, Lin, 2002). In particular, composition changes of all components prior to the demixing stage are necessary. In order to find out the change of composition during the phase inversion process it needs to determine the rate of solvent outflow (J_1) and nonsolvent inflow (J_2) through the diffusion layer. By this measurement the calculation of the changes in polymer content becomes possible.

As stated earlier, the flux for mobile components involved in the NIPS process can be described by Equation 27

$$J_i = -(RT)^{-1}D_i(\phi)\phi_i(\frac{\partial \mu_i}{\partial x}) \tag{27}$$

where J_i is the volume flux of component i. Here the self-diffusion coefficient (D_i) is considered as concentration-dependence.
To determine the mass transfer path for the polymer solution immersed into the nonsolvent bath the ratio of mass flaxes of nonsolvent to which of solvent should be plotted. Therefore we have

$$\frac{J_1}{J_2} = \sigma = \frac{\phi_1}{\phi_2} . \frac{d\mu_1}{d\mu_2} \tag{28}$$

The assumption made here is that the ratio of $D_1(\phi_1,\phi_2) / D_2(\phi_1,\phi_2)$ is constant and unity. If the differentials of the chemicals potential are expressed as functions of the volume fractions, one finds

$$\frac{d\phi_1}{d\phi_2} = \frac{\phi_1 \left(\partial\mu_1/\partial\phi_2\right)_{T,P,\phi_1} - k\phi_2 \left(\partial\mu_2/\partial\phi_2\right)_{T,P,\phi_1}}{k\phi_2 \left(\partial\mu_2/\partial\phi_1\right)_{T,P,\phi_2} - \phi_1 \left(\partial\mu_1/\partial\phi_1\right)_{T,P,\phi_2}} \tag{29}$$

This first order differential equation yields the relation between ϕ_1 and ϕ_2 in the diffusion layer as a function of the ratio $\sigma = J_1 / J_2$ and one of the boundary conditions.
With the aid of the Flory-Huggins expressions for the chemical potentials together with Equation 29, Cohen and co-workers (Cohen, 1979) calculated, for the first time, the composition paths within the ternary phase diagram and discussed them in relation to the formation of membranes. Equation 29 has been derived using the steady-state condition.
When a solution of a polymer in a solvent is immersed in a bath of a nonsolvent, there are, depending on the preparation condition, various possible outcomes as the solvent release from polymer solution and is replaced to a greater or lesser extent by nonsolvent (i.e. $d\phi_1 / d\phi_2 = ?$) (Karimi, 2009, Stropnik, 2000): *Region I,* as demonstrated in Fig. 10, the total polymer concentration decreases along the route. The change of composition in this region is a one-phase dilution of polymer solution without solidification. *Region II,* the routes intersect the binodal curve and enter the two-phase region. In this region there are two outcomes that depend on the location of the routes with respect to the route assigned by

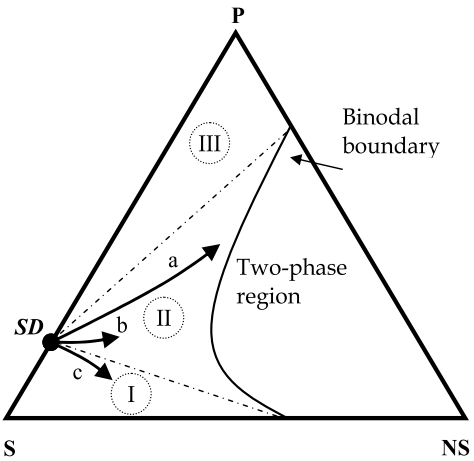

Fig. 10. Mass transfer paths in a triangle phase diagram.

$d\phi_1 / d\phi_2 = 1$, i.e. the path parallel to S~NS line. When $d\phi_1 / d\phi_2 > 1$, polymer content decreases along the route; Solidification of the system is possible as a result of phase transition, but loose heterogeneous structures result. In contrast, when $d\phi_1 / d\phi_2 < 1$, polymer concentration increases and solidification results from the increase of polymer content as well as from possible phase transitions. *Region III,* yields the most dense and homogeneous structures as located outside the two-phase region.

5.2 Measurement of mass transfer paths

Diffusion in polymer solution has been studied for decades using several techniques such as gravimetry (Hu, 1996), membrane permeation (Smith, 1988), fluorescence (Winsudel, 1996), and dynamic light scattering (Asten, 1996), Raman spectroscopy (Kim, 2000, Tsai and Torkelso, 1990), and recently ATR-FTIR (Karimi, 2009, Lin, 2002).

Through the FTIR spectroscopy a spot near the interface of a thin layer of casting solution has been examined. There are two problems with this method. One is the difficulty of introducing the nonsolvent (especially water) into the liquid cell by a syringe due to the capillary action of water. The other is the saturation of coagulation bath with solvent due to limitation of circulation in the nonsolvent bath. It seems that the investigations of the phase demixing processes by such arrangements limits the information about the compositional change prior the phase demixing step.

FTIR-ATR as a promising toll is recently used (Karimi and Kish, 2009) to measure the compositional path during the mass transfer of immersed polymer solution. A special arrangement to determine the concentration of components in the diffusion layers under quench condition prior to the phase separation and the concentration of all components in front of the coagulation boundary was introduced. This technique allows a simultaneous determination of solvent outflow and water inflow during the immersion time. Determination of the composition of all components becomes possible by using the calibration curves.

To measure the concentration of each component, polymer solution was cast directly on surface of the flat crystal (typically ZnSe, a 45o ATR prism), similar arrangement as shown in Fig. 7. The flat crystal is equipped with a bottomless liquid cell. The penetrant is

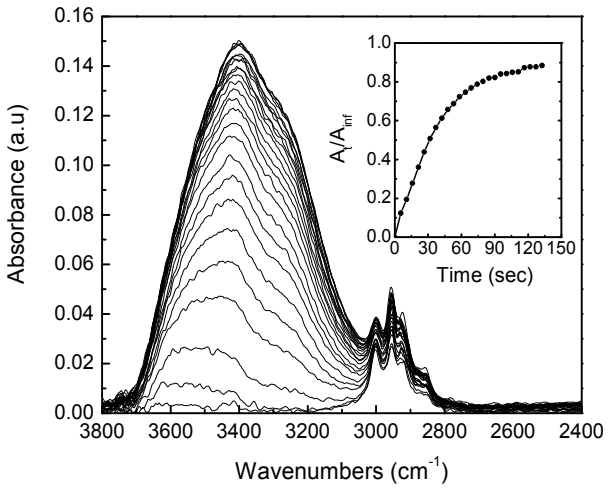

Fig. 11. Intensity (H2O/AC/PMMA system).

transferred into the cell, and simultaneously the recording of the spectrum is started. Fig 11 shows a series of recording spectra at wave number ranging from 2400 to 3800 cm^{-1} for the water/acetone/PMMA system.

Having the FTIR-ATR spectrum measured and the system calibrated, the composition of polymer solution at the layer close to ATR prism could be accurately determined if the method described in part 4.1 could be properly chosen. In the case of polymer solution, generally, simple Beer's law deosn't result correctly. Other methods are normally evaluated with standard solutions to choose the proper one. Advantage of these methods is found to be satisfactory for solving complex analytical problems where the component peaks overlap. The principle component regression (PCR) is succefully used by Karimi (Karimi and Kish, 2009) to resolve the bands in overlapped regions for water/acetone/PMMA and water/DMF/PMMA systems. Since there exists overlapped characteristic peaks the spectra, simple Beer's law deos not predict reliable results.

5.3 Composition path and structure formation

Undoubtedly, the rate of compositional change as well as the ratio of mass transfer of components across the interface of polymer solution are affecting factors controlling the ultimate structure, however, it should not be neglected that the thermodynamics is also the other affecting factor. Mass transfer paths can be derived from the model calculations defined in two different ways: The composition path can represent the composition range in the polymer solution between the support and the interface at a given time. The composition path can also be defined as the composition of a certain well defined element in the solution as a function of time. Some researchers have attempted to make relation between mass transfer and ultimate structure of polymer system. Many of them have referred to the rate of solvent and nonsolvent exchange, postulating instantaneous and delay demixing. This classification was clarified many observations about membrane morphologies. But there are several reports in the literatures that they didn't approve this postulation.

Direct measuring the time dependence of concentration of system components (for instance ϕ_1, ϕ_2, and ϕ_3) during the immersion precipitation process can clarify some obscure aspects of the structure formation. When the polymer solution comes to contact with nonsolvent bath, the solvent release may become higher than the nonsolvent penetration (i.e $d\phi_2 / d\phi_1 > 1$) that leads to an increase in polymer content of the dope and the solvent moves to mix with water in the water bath. The development of structure of this system will differ from which the solvent release is lower than the nonsolvent penetration (i.e $d\phi_2 / d\phi_1 < 1$). Different morphologies for PMMA membrane followed by different ratio of solvent and water exchange, $d\phi_2 / d\phi_1$, have been reported by Karimi (Karimi and Kish, 2009). Fig 12 shows such morphologies for PMMA membrane in which they developed from H_2O/DMF/PMMA and H_2O/AC/PMMA systems.

However the determination of mass transfer is very applicable to make clear some aspects of membrane morphologies, but there is a limitation regarding to the rate of data capturing. Some interesting morphologies were observed during the fast mass transfer in membrane-forming system. For example, Azari and et al. (Azari, 2010) have reported a structure transition when the thickness of cast polymer solution is changed. Fig 13 shows different structures of poly(acrylo nitrile) membrane preparing by same system (H_2O/DMF/PAN).

The authors believe that mass transfer during the process can describe the morphology development if it can be possible to measure.

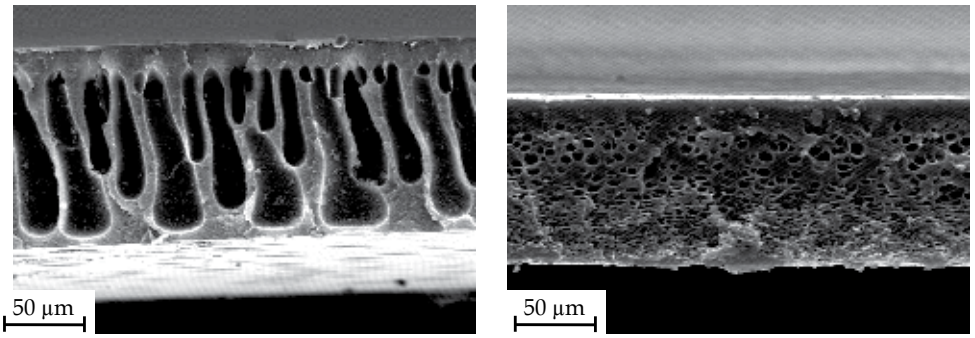

Fig. 12. SEM micrographs of PMMA membrane formed from different solvents; (a) Acetone, (b) N-dimethylformamide.

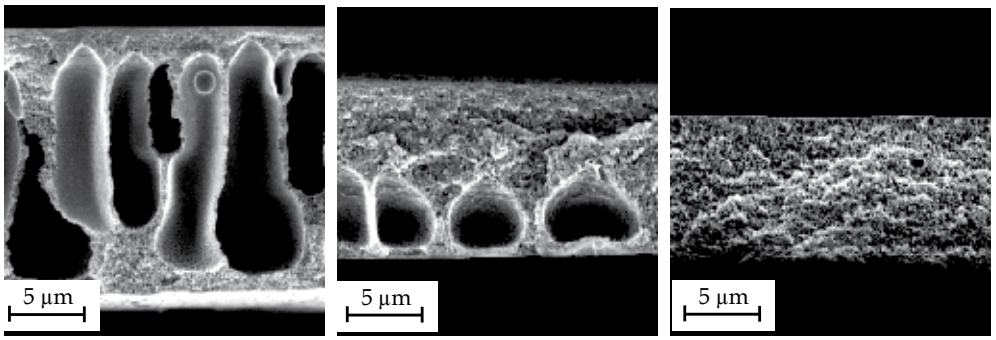

Fig. 13. Effect of membrane thickness on PAN membrane structure (dope, PAN/DMF: PAN 20 wt %: casting temperature 25 ^{o}C: coagulant, water).

6. Conclusion

Diffusion is an important process in polymeric membranes and fibers and it is clear that mass transfer through the polymeric medium is doing by diffusion. Analyzing the diffusion which is basically formulated by Fick's laws, lead to the following conclusions

1. Various mechanisms are considered for diffusion, which it is determined by time scale of polymer chain mobility
2. The rate of permeability can be controlled by loading impenetrable nano-fillers into the structure
3. Driving force for mass transfer across the interface of multiphase systems is chemical potential-base

As well described in this chapter, measuring the diffusion of small molecules in polymers using Fourier transform infrared-attenuated total reflection (FTIR-ATR) spectroscopy, is a promising technique which allows one to study liquid diffusion in thin polymer films in situ. This technique can be successfully employed for quantifying the compositional path during the mass transfer of immersed polymer solution, in which it is strongly involved to the structure development.

7. Acknowledgment

Helpful discussions with Prof. S. H. Amirshahi of Amirkabir University of Technology and Dr. N. Taheri of Tehran University are gratefully acknowledged.

8. List of symbols

A	absorption
a	activity
a	absorptivity
b	pathlenght of the component
c	concentration
ΔC	incremental change in heat capacity at T_g
D	diffusion coefficient
D^*	self-diffusion coefficient
D_T	thermodynamic diffusion
D_e	Deborah number
dp	depth of penetration
G	Gibbs free energy
H	Enthalpy
l	film thickness
M	intrinsic mobility
M	mass uptake
N	Avogadro's number
n	number of mole
P	permeability coefficient
R	gas constant
r	radius of filament
S	diffusivity coefficient
S	Entropy
T_g	glass transition
T	temperature
t	film thickness
x	mole fraction
J	flux
τ_e	characteristic time of polymer
β	immobilization factor
τ	geometrical impedance factor
ϕ_{FV}	fractional free volume
ϕ	volume fraction
χ	interaction parameter
ρ	density
υ	molar volume

λ wavelength
μ chemical potential

9. References

Ashley, R. J. (1985). Permeability and Plastics Packaging, In: *Polymer Permeability,* J. Comyn, 269-308, Elsevier Applied Science, ISBN 0-85334-322-5, Northern Ireland.

Azari, S.; Karimi, M. & Kish, M. H. (2010). Structural Properties of the Poly(acrylonitrile) Membrane Prepared with Different Thicknesses. *Industrial & Engineering Chemistry Research,* Vol.49, No. 5, (March 2005), pp. 2442-2448, ISSN 0888-5885

Boom, R. M.; Boomgaard, R. M. & Smolder, C. A. (1994). Equilibrium Thermodynamics of a Quaternary Membrane-Forming System with Two Polymers. I. Calculations. *Macromolecules,* Vol.27, No. 8, (April 1994), pp. 2034-2040, ISSN 0024-9297

Chandra, P. & Koros, W. J. (2009). Sorption and Transport of Methanol in Poly(ethylene terphthalate). *Polymer*, Vol. 50, No. 1, (January 2009), pp. 236-244, ISSN 0032-3861

Cohen, C.; Tanny, G. B. & Prager, S. (1979). Diffusion-Controlled Formation of Porous Structures in Ternary Polymer Systems. *Journal of Polymer Science: Part B: Polymer Physics*, Vol. 17, No. 3, (March 1979), pp. 477-489, ISSN 0887-6266.

Comyn J. (1985). Introduction to Polymer Permeability and the Mathematics of Diffusion, In: *Polymer Permeability,* J. Comyn, 1-10, Elsevier Applied Science, ISBN 0-85334-322-5, Northern Ireland.

Cotugno, S., Maio, E. D., Mensitieri, G., Iannace, S., Roberts, G. W., Carbonell, R. G. & Hopfenberg, H. B. (2005). Characterization of Microcellular Biodegradable Polymeric Foams Produced from Supercritical Carbon Dioxide Solutions. *Industrial & Engineering Chemistry Research,* Vol.44, No. 6, (March 2005), pp. 1795-1803, ISSN 0888-5885

Couchman, P. R. & Karasz, F. E. (1978). A classical thermodynamic discussion of the effect of composition on glass-transition temperature. *Macromolecules,* Vol.11, No. 1, (January 1978), pp. 117-119, ISSN 0024-9297

Crank, J. & Park, G. S. (1968). *Diffusion in Polymer* (First Edition), Academic Press, ISBN 0-12-197050-7, USA

Crank, J. (1975). *The Mathematics of Diffusion* (Second Edition), Claredon Press, ISBN 0-19-853344-6, England

Dimarzio, E. A., Castellano, C., & Yang, A. (1996). Glass temperature depression of polymers by use of mixed solvents: A colligative property. *Journal of Polymer Science: Part B: Polymer Physics*, Vol. 34, No. 3 , (February 1996), pp. 535-543, ISSN 0887-6266

Doppers, L. M., Sammon, C., Breen, C. & Yarwood, J (2006). FTIR-ATR Studies of the Sorption of Acetone/Water Mixtures in Poly(vinyl alcohol). *Polymer*, Vol. 47, No. 8, (April 2006), pp. 2714-2722, ISSN 0032-3861

Eyvazkhani, A. & Karimi M. (2009). Influence of Silica Nanolayers on the Water Diffusion through PMMA/Layered Silicate Nanocomposites. *Proceedings of the International Conference on Textile Engineering,* Rasht, Iran, October 27-29, 2009.

Fieldson, G. T. & Barbari, T. A. (1993). The Use of FTi.r.-a.t.r Spectroscopy to Characterize Penetrant Diffusion in Polymers. *Polymer*, Vol. 34, No. 6, (March 1993), pp. 1146-1153, ISSN 0032-3861

Flory, P. J. (1953). *Principle of Polymer Chemistry*, Cornell University Press, ISBN 0-8014-0134-8, USA

Gibbs, J. H. & DiMarzio, E. A. (1958). Nature of the Glass Transition and the Glassy State. *The Journal of Chemical Physics*, Vol. 28, No. 3 , (March 1958), pp. 373-383, ISSN 0021-9606

Hadgett, P. M., Goldbeck-Wood, G., Windle, A. H. (2000). Lattice Modelling of Penetrant Diffusion Through Heterogeneous Polymers. *Polymer*, Vol. 41 No. 16 , (Julay 2000), pp. 6151-6160, ISSN 0032-3861

Hajiagha, S., Karimi, M. & Ahmadzadeh, R. (2010). Use Different Solvents for Preparation of Temperature-Sensitive Polyurethane Membrane for Smart Textile, *Proceedings of the International Conference on Intelligent Textiles,* ISBN 978-89-92265-14-0, pp. 125-126, Seoul, Korea, June 17-18, 2010.

Hedenqvist, M. & Gedde, U. W. (1996). Diffusion of Small Molecule Penetrants in Semicrystalline Polymers. *Progress in Polymer Science,* Vol. 21, No. 2, (February 1996), pp. 299-333, ISSN 0079-6700

Hong, S. U. (1995). Prediction of Polymer/Solvent Diffusion Behavior Using Free-Volume Theory. *Industrial & Engineering Chemistry Research,* Vol.34, No. 7, (Julay 1995), pp. 2536-2544, ISSN 0888-5885

Hu, D. C. G. & Chou, K. J. N. (1996). Kinetics of Water Swelling and Development of Porous Structure in Ionic Poly(Acrylonitrile-Acrylamide-Acrylic Acid) Hydrogels. *Polymer,* Vol.37, No. 6, (February 1996), pp. 1019-1025, ISSN 0032-3861

Hu, J. (2007). *Shape Memory Polymers and Textiles* (First Edition), Woodhead Publishing, 978-1-84569-047-2, England

Hua, H. Rivard, T. & Dube, M. A. (2004). Off-line Monitoring of Styrene/Butyl Acrylate Copolymerizations in Toluene Using ATR-FTIR Spectroscopy. *Polymer*, Vol. 45, No. 2, (January 2004), pp. 345-354, ISSN 0032-3861

Hubbell, W. H., Brandt, H. & Munir, Z. A. (1975). Transient and Steady-State Water Vapor Permeation Through Polymer Films. *Journal of Polymer Science: Part B: Polymer Physics*, Vol. 13, No 3. , (March 1975), pp. 493-507, ISSN 0887-6266

Jones, F. (1989). Diffusion and Rate of Dyeing, In: *The Theory of Coloration of Textiles*, A. Johnson, pp. 373-427, Society of Dyers and Colourists, ISBN 0-901956-48-1, ?

Karimi M., Heuchel, M., Albrecht, W. & Hofmann, D. (2007). A Lattice-Fluid Model for the Determination of the Water/Polymer Interaction Parameter from Water Uptake Measurements. *Journal of Membrane Science*, Vol. 292, No. 1-2 , (April 2007), pp. 80-91, ISSN 0376-7388

Karimi M.; Albrecht, W.; Heuchel, M.; Kish M. H.; Frahn, J.; Weigel, Th.; Hofmann, D.; Modaress, H. & Lendlein, A. (2005). Determination of Water/Polymer Interaction Parameter for Membrane-Forming Systems by Sorption Measurements and Fitting Techniques. *Journal of Membrane Science*, Vol. 265, No 1-2, (November 2005), pp. 1-12, ISSN 0376-7388

Karimi, M. & Kish, M. H. (2009). Poly(methyl methacrylate) Membrane: Dynamic Measurement of Concentrations During Water-Induced Phase Separation. *Macromolecular Symposia,* Vol. 279, No. 6, (May 2009), pp. 210-220, ISSN 1521-3900

Kim, H. J.; Fouda, A. E. & Jonasson, K. (2000). In Situ Study on Kinetic Behavior during Asymmetric Membrane Formation via Phase Inversion Process Using Raman

Spectroscopy. *Journal of Applied Polymer Science*, Vol. 75, No. 1, (January 2000), pp.135-141 , ISSN 0021-8995

Lasky, R. C., Kramer, E. J., Hui, C. Y. (1988). The Initial Stages of Case II Diffusion at Low Penetrant Activities. *Polymer*, Vol. 29, No. 4 , (April 1988), pp. 673-679, ISSN 0032-3861

Lin, Y.; Wang, D. M. & Lai, J. Y. (2002). Nonsolvent induced gelation and its effect on membrane morphology. *Macromolecules,* Vol.35, No. 17, (August 2002), pp. 6697-6706, ISSN 0024-9297

Liu, D. & Tomasko, D. L. (2007).Carbon Dioxide Sorption and Dilation of Poly(lactide-co-glycolide). *Journal of Supercritical Fluids*, Vol. 39, No. 3, (January 2007), pp. 416-425, ISSN 0896-8446

Massaro, L. & Zhu, X. X. P (1999). Physical Models of Diffusion for Polymer Solutions, Gels and Solids. *Progress in Polymer Science,* Vol. 24, No. 5, (August 1999), pp. 731-775, ISSN 0079-6700

Mattozzi, A., Hedenqvist, M. S., Gedde, U. W. (2007). Diffusivity of n-hexane in Poly(ethylene-stat-octene)s Assessed by Molecular Dynamics Simulation. *Polymer*, Vol. 48, No. 17 , (August 2007), pp. 5174-5180, ISSN 0032-3861

Moisan, J. Y. (1985). Effects of Oxygen Permeation and Stabiliser Migration on Polymer Degradation, In: *Polymer Permeability,* J. Comyn, (Ed.), 11-73, Elsevier Applied Science, ISBN 0-85334-322-5, Northern Ireland.

Neway, B., Hedenqvist, M. S., Mathot, V. B. F. & Gedde, U. W. (2001). Free Volume and Transport Properties of Heterogeneous Poly(ethylene-co-octene)s. *Polymer*, Vol. 42, No. 12 , (June 2001), pp. 5307-5319, ISSN 0032-3861

Pereira, A. M., Lopes, M. C., Timmer, J. M. K. & Keurentjes, J. T. F. (2005). Solvent Sorption Measurements in Polymeric Membranes with ATR-IR Spectroscopy. *Journal of Membrane Science*, Vol. 260, No. 1-2, (September 2005), pp. 174-180, ISSN 0376-7388

Prabhakar, R. S.; Merkel, T. C.; Freeman, B. D.; Imizu T. and Higuchi, A. (2005). Sorption and Transport Properties of Propane and Perfluoropropane in Poly(dimethylsiloxane) and Poly(1-trimethylsilyl-1-propyne). *Macromolecules,* Vol.38, No. 5, (March 2005), pp. 1899-1910, ISSN 0024-9297

Prausnitz, J. M. & Lichtenthaler, E. G. A. (1999). *Molecular Thermodynamics of Fluid-Phase Equilibria*, (Tired Edition), Ptrntice Hall, ISBN ,

Rogers, C. B. (1985). Permeation of Gases and Vapours in Polymer, In: *Polymer Permeability,* J. Comyn, 11-73, Elsevier Applied Science, ISBN 0-85334-322-5, Northern Ireland.

Sammon, C., Yarwood, J. & Everall, N. (2000). A FTIR-ATR Study of Liquid Diffusion Processes in PET Films: Comparison of Water with Simple Alcohols. *Polymer*, Vol. 41 No. 7, (March 2000), pp. 2521-2534, ISSN 0032-3861

Smith, B. A. H. & Sefton, M. V. (1988). Permeability of Heparin-Polyvinyl alcohol Hydrogel to Thrombin and Antithrombin III. *Journal Biomedical Materials Research,* Vol.22, No. 8, (August 1988), pp. 673-685, ISSN 1549-3296

Sperling, L. H. (2006). *Introduction to Physical Polymer Science* (Fourth Edition), Wiley-Interscience, 13987-0-471-70606-9, USA

Sridhar, L. N., Gupta, R. K. & Bhardwaj, M. (2006). Barrier Properties of Polymer Nanocomposites. *Industrial & Engineering Chemistry Research*, Vol. 45, No. 25, (December 1996), pp. 8282-8289, ISSN 0888-5885

Stropnik, C.; Musil, V. & Brumen, M. (2000). Polymeric Membrane Formation by Wet-Phase Separation; Turbidity and Shrinkage Phenomena as Evidence for the Elementary Processes. *Polymer*, Vol. 41, No. 26, (December 2000), pp. 9227-9237, ISSN 0032-3861

Sunchez, I. C. & Lacombe, R. H. (1978). Statistical Thermodynamics of Polymer Solution. *Macromolecules*, Vol. 11, No. 6, (November 1978), pp. 1145-1156 , ISSN 0024-9297

Tsai F. J. & Torkelson, J. M. (1990). The Roles of Phase Separation Mechanism and Coarsening in the Formation of Poly(methyl methacrylate) Asymmetric Membranes. *Macromolecules*, Vol.23, No. 3, (February 1990), pp. 775-784, ISSN 0024-9297

Tsay, C. S. & McHugh A. J. (1990). Mass transfer modeling of asyinmetric membrane formation by phase inversion. *Journal of Polymer Science: Part B: Polymer Physics*, Vol. 28, No. 8, (July 1990), pp. 1327-1365, ISSN 0887-6266

Urban, M. W. (1996). *Attenuated Total Reflectance Spectroscopy of Polymers: Theory and Practice*, American Chemical Society, ISBN 13: 9780841233458, USA

Van Asten, A. C. ; Kok, W. T. ; Tilssen, R. & Roppe, H. (1996). Characterization of Thermal Diffusion of Polystyrene in Binary Mixtures of THF/Dioxane and THF/Cyclohexane. *Journal of Polymer Science: Part B: Polymer Physics,* Vol.34, No. 2, (January 1996), pp. 283-295, ISSN 0887-6266

Vergnaud, J. M. (1991). *Liquid Transport Processes in Polymeric Materials: Modeling and Industrial Applications*, Prentice Hall, 0-13-538315-3, USA

Vrentas, J. S., Jarzebski, C. M., & Duda, J. L. (1975). A Deborah number for diffusion in polymer-solvent systems. *AIchE Journal,* Vol. 21, No. 5, (September 1975), pp. 894-901, ISSN 0001-1541

Wang, B. G., Yamaguchi, T. & Nakao, S. I. (2000). Solvent Diffusion in Amorphous Glassy Polymers. *Journal of Polymer Science: Part B: Polymer Physics*, Vol. 38, No. 2 , (January 2000), pp. 346-356, ISSN 0887-6266

Wijmans, J. G.; Altena F. W. & Smolders C. A. (1984). Diffusion during the Immersion Precipitation Process. *Journal of Polymer Science: Part B: Polymer Physics*, Vol. 22, No. 3, (March 1984), pp. 519-524, ISSN 0887-6266

Windle, A. H. (1985). Case II Sorption, In: *Polymer Permeability,* J. Comyn, 75-118, Elsevier Applied Science, ISBN 0-85334-322-5, Northern Ireland.

Wisnudel, M. B. & Torkelson, J. M. (1996). Small-Molecule Probe Diffusion in Polymer Solution: Studies by Taylor Dispersion and Phosphorescence Quenching. *Macromolecules,* Vol.29, No. 19, (September 1996), pp. 6193-6207, ISSN 0024-9297

Yi, X., & Pellegrino, J. (2002).Diffusion Measurements with Fourier Transform Infrared Attenuated Total Reflectance Spectroscopy: Water Diffusion in Polypropylene. *Journal of Polymer Science: Part B: Polymer Physics*, Vol. 40, No. 10, (May 2002), pp. 980-991, ISSN 0887-6266

Zeman L. & Fraser T. (1994). Formation of air-cast cellulose acetate membranes. Part II. Kinetics of demixing and macrovoid growth. *Journal of Membrane Science*, Vol. 87, No. 3, (March 1994), pp. 267-279, ISSN 0376-7388

3

HETP Evaluation of Structured and Randomic Packing Distillation Column

Marisa Fernandes Mendes
Chemical Engineering Department, Technology Institute,
Universidade Federal Rural do Rio de Janeiro
Brazil

1. Introduction

Packed columns are equipment commonly found in absorption, distillation, stripping, heat exchangers and other operations, like removal of dust, mist and odors and for other purposes. Mass transfer between phases is promoted by their intimate contact through all the extent of the packed bed. The main factors involving the design of packed columns are mechanics and equipment efficiency. Among the mechanical factors one could mention liquid distributors, supports, pressure drop and capacity of the column. The factors related to column efficiency are liquid distribution and redistribution, in order to obtain the maximum area possible for liquid and vapor contact (Caldas and Lacerda, 1988).

These columns are useful devices in the mass transfer and are available in various construction materials such as metal, plastic, porcelain, ceramic and so on. They also have good efficiency and capacity, moreover, are usually cheaper than other devices of mass transfer (Eckert, 1975).

The main desirable requirements for the packing of distillation columns are: to promote a uniform distribution of gas and liquid, have large surface area (for greater contact between the liquid and vapor phase) and have an open structure, providing a low resistance to the gas flow. Packed columns are manufactured so they are able to gather, leaving small gaps without covering each other. Many types and shapes of packing can satisfactorily meet these requirements (Henley and Seader, 1981).

The packing are divided in random – randomly distributed in the interior of the column – and structured – distributed in a regular geometry. There are some rules which should be followed when designing a packed column (Caldas and Lacerda, 1988):

a. The column should operate in the loading region (40 to 80% flooding), which will assure the best surface area for the maximum mass transfer efficiency;
b. The packing size (random) should not be greater than 1/8 the column diameter;
c. The packing bed is limited to 6D (Raschig rings or sells) or 12D for Pall rings. It is not recommended bed sections grater than 10m;
d. Liquid initial distribution and its redistribution at the top of each section are very important to correct liquid migration to the column walls.

   A preliminary design of a packed column involves the following steps:

   1. Choice of packing;
   2. Column diameter estimation;

3. Mass transfer coefficients determination;
4. Pressure drop estimation;
5. Internals design.

This chapter deals with column packing efficiency, considering the main studies including random and structured packing columns. In packed columns, mass transfer efficiency is related to intimate contact and rate transfer between liquid and vapor phases. The most used concept to evaluate the height of a packed column, which is related to separation efficiency, is the HETP (Height Equivalent to Theoretical Plate), defined by the following equation:

$$Z = (HETP) \cdot (N) \tag{1}$$

in which Z is the height of the packed bed necessary to obtain a separation equivalent to N theoretical stages (Caldas and Lacerda, 1988).

Unfortunately, there are only a few generalized methods available in the open literature for estimating the HETP. These methods are empirical and supported by the vendor advice. The performance data published by universities are often obtained using small columns and with packing not industrially important. When commercial-scale data are published, they usually are not supported by analysis or generalization (Vital et al., 1984). Several correlations and empirical rules have been developed for HETP estimation in the last 50 years. Among the empirical methods, there is a rule of thumb for traditional random packing that says

$$HETP = column\ diameter \tag{2}$$

That rule can be used only in small diameter columns (Caldas and Lacerda, 1988).

The empirical correlation of Murch (1953) cited by Caldas and Lacerda (1988) is based on HETP values published for towers smaller than 0.3 m of diameter and, in most cases, smaller than 0.2 m. The author had additional data for towers of 0.36, 0.46 and 0.76 m of diameter. The final correlation is

$$HETP = K_1 G^{K_2} D^{K_3} Z^{1/3} \left(\frac{\alpha \mu_L}{\rho_L} \right) \tag{3}$$

K_1, K_2 and K_3 are constants that depend on the size and type of the packing.

Lockett (1998) has proposed a correlation to estimate HETP in columns containing structured packing elements. It was inspired on Bravo et al.'s correlation (1985) in order to develop an empirical relation between HETP and the packing surface area, operating at 80% flooding condition (Caldas and Lacerda, 1988):

$$HETP = \frac{\left(4.82 \left(\rho_L - \rho_G \right)^{0.5} \mu_r^{-0.06} \right)}{\alpha} \tag{4}$$

in which

$$\alpha = a_p \left[\left(1 + 0.78 e^{0.00058 a_p} \right) \left(\frac{\rho_G}{\rho_L} \right)^{0.25} \right]^2 \tag{5}$$

According to the double film theory, HETP can be evaluated more accurately by the following expression (Wang et al., 2005):

$$HETP = \frac{\ln \lambda}{\lambda - 1}\left[\frac{u_{Gs}}{k_G a_e} + \lambda \frac{u_{Ls}}{k_L a_e}\right] \quad (6)$$

Therefore, the precision to evaluate HETP by equation (6) depends on the accuracy of correlations used to predict the effective interfacial area and the vapor and liquid mass transfer coefficients. So, we shall continue this discussion presenting the most used correlations for wetted area estimation, both for random and structured packed columns. Wang et al. (2005) also presented a complete discussion about the different correlations mostly used for random and structured packing.

2. Literature review

The literature review will be divided in two sections, treating and analyzing separately random and structured distillation columns as the correlations for the effective area and HETP evaluation.

2.1 Part A: performance of random packing

Before 1915, packed columns were filled with coal or randomly with ceramic or glass shards. This year, Fredrick Raschig introduced a degree of standardization in the industry. Raschig rings, together with the Berl saddles, were the packing commonly used until 1965. In the following decade, Pall rings and some more exotic form of saddles has gained greater importance (Henley and Seader, 1981). Pall rings are essentially Raschig rings, in which openings and grooves were made on the surface of the ring to increase the free area and improve the distribution of the liquid. Berl saddles were developed to overcome the Raschig rings in the distribution of the liquid. Intalox saddles can be considered as an improvement of Berl saddles, and facilitated its manufacture by its shape. The packing Hypac and Super Intalox can be considered an improvement of Pall rings and saddles Intalox, respectively (Sinnott, 1999). In Figure 1, the packing are illustrated and commented.

The packing can be grouped into generations that are related to the technological advances. The improvements cited are from the second generation of packing. Today, there are packing of the fourth generation, as the Raschig super ring (Darakchiev & Semkov, 2008).

Tests with the objective to compare packing are not universally significant. This is because the efficiency of the packing does not depend, exclusively, on their shape and material, but other variables, like the system to be distilled. This means, for example, that a packing can not be effective for viscous systems, but has a high efficiency for non-viscous systems. Moreover, the ratio of liquid-vapor flow and other hydrodynamic variables also must be considered in comparisons between packing. The technical data, evaluated on packing, are, generally, the physical properties (surface area, free area, tensile strength, temperature and chemical stability), the hydrodynamic characteristics (pressure drop and flow rate allowable) and process efficiency (Henley and Seader, 1981). This means that Raschig rings can be as efficient as Pall rings, depending on the upward velocity of the gas inside the column, for example. These and other features involving the packing are extensively detailed in the study of Eckert (1970).

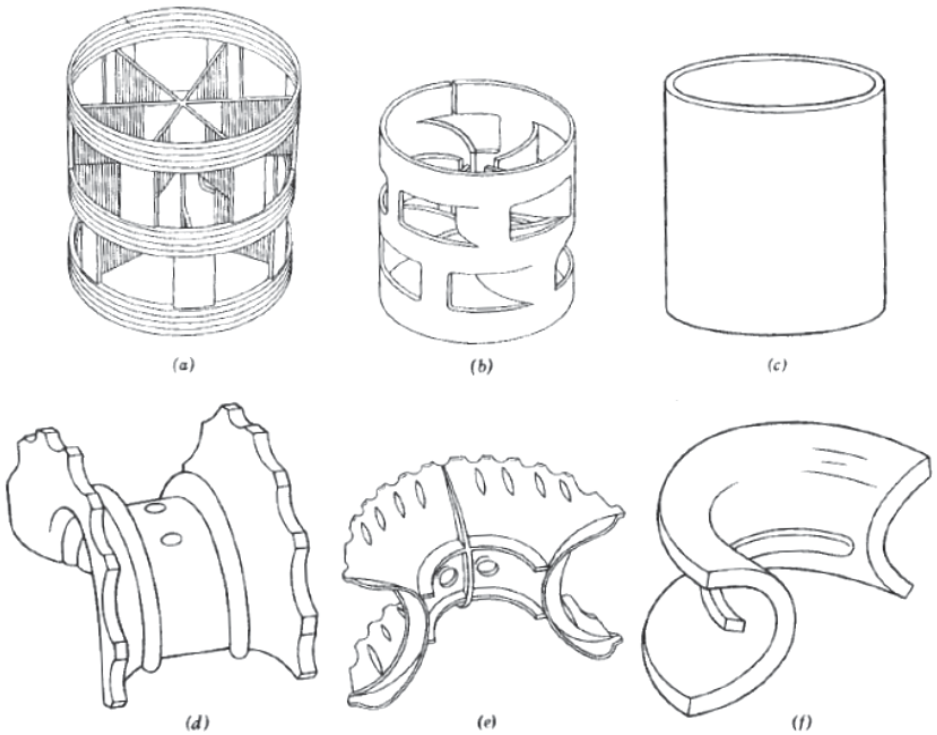

Ref: Henley & Seader (1981)

Fig. 1. Random packing: (a) plastic pall rings. (b) metal pall rings (Metal Hypac). (c) Raschig rings. (d) Intalox saddles. (e) Intalox saddles of plastic. (f) Intalox saddles

In literature, some studies on distillation show a comparison between various types of random and structured packing. Although these studies might reveal some tendency of the packing efficiency for different types and materials, it is important to emphasize that they should not generalize the comparisons.

Cornell et al. (1960) published the first general model for mass transfer in packed columns. Different correlations of published data of H_L and H_V, together with new data on industrial scale distillation columns, were presented to traditional packing, such as Raschig rings and Berl saddles, made of ceramic. Data obtained from the experimental study of H_L and H_V were analyzed and correlated in order to project packed columns. The heights of mass transfer for vapor and liquid phases, are given by:

$$H_V = \frac{\psi \cdot {S_{CV}}^{0,5}}{\left(G_L \cdot f_1 \cdot f_2 \cdot f_3\right)^n} \cdot \left(\frac{d_C}{12}\right)^m \cdot \left(\frac{Z}{10}\right)^{\frac{1}{3}} \tag{7}$$

$$H_L = \phi \cdot C_{fL} \cdot \left(\frac{Z}{10}\right)^{0,15} \cdot {S_{CL}}^{0,5} \tag{8}$$

which:

$$f_1 = \left(\frac{\mu_L}{\mu_W} \right)^{0,16} \tag{9}$$

$$f_2 = \left(\frac{\rho_W}{\rho_L} \right)^{1,25} \tag{10}$$

$$S_{CV} = \frac{\mu_G}{\rho_G \cdot D_G} \tag{11}$$

$$S_{CL} = \frac{\mu_L}{\rho_L \cdot D_L} \tag{12}$$

In the *f* factors, the liquid properties are done in the same conditions of the column and the water properties are used at 20 °C. The parameters *n* and *m* referred to the packing type, being 0.6 and 1.24, respectively, for the Raschig rings. C_{fL} represents the approximation coefficient of the flooding point for the liquid phase mass transfer. The values of φ and Ψ are packing parameters for the liquid and vapor phase mass transfer, respectively, and are graphically obtained. In this correlation, some variables don't obey a single unit system and therefore need to be specified: *dc*(in), *Z*(ft), *H*(ft), *G*(lbm/h.ft²).

Onda et al. (1968 a, b) presented a new model to predict the global mass transfer unit. In this method, the transfer units are expressed by the liquid and vapor mass transfer coefficients:

$$H_V = \frac{G_V}{k_V \cdot a_W \cdot P \cdot M_V} \tag{13}$$

$$H_L = \frac{G_L}{k_L \cdot a_W \cdot \rho_L} \tag{14}$$

In which:

$$k_V \cdot \left(\frac{R \cdot T}{a_P \cdot D_V} \right) = \Gamma \cdot \left(\frac{G_V}{a_P \cdot \mu_V} \right)^{0,7} \cdot \left(S_{CV} \right)^{\frac{1}{3}} \cdot \left(a_P \cdot d_P \right)^{-2} \tag{15}$$

$$k_L \cdot \left(\frac{\rho_L}{g \cdot \mu_L} \right)^{\frac{1}{3}} = 0,0051 \cdot \left(\frac{G_L}{a_w \cdot \mu_L} \right)^{\frac{2}{3}} \cdot \left(S_{CL} \right)^{-\frac{1}{2}} \cdot \left(a_P \cdot d_P \right)^{0,4} \tag{16}$$

where *Γ* is a constant whose values can vary from 5.23 (normally used) or 2, if the packing are Raschig rings or Berl saddles with dimension or nominal size inferior to 15 mm.

It can be noted, in these equations, the dependence of the mass transfer units with the wet superficial area. It is considered, in this model, that the wet area is equal to the liquid-gas interfacial area that can be written as

$$a_W = a_p \cdot \left\{ 1 - \exp\left[-1{,}45 \cdot \mathrm{Re}_L^{\,0,1} \cdot Fr_L^{\,-0,05} \cdot We_L^{\,0,2} \cdot \left(\frac{\sigma}{\sigma_C} \right)^{-0,75} \right] \right\} \tag{17}$$

where:

$$\mathrm{Re}_L = \frac{G_L}{a_P \cdot \mu_L} \tag{18}$$

$$We_L = \frac{G_L^{\,2}}{a_P \cdot \sigma \cdot \rho_L} \tag{19}$$

$$Fr_L = \frac{a_P \cdot G_L^{\,2}}{g \cdot \rho_L^{\,2}} \tag{20}$$

The ranges in which the equation should be used are: $0.04 < Re_L < 500$; $1.2\text{x}10^{-8} < We_L < 0.27$; $2.5\text{x}10^{-9} < Fr_L < 1.8\text{x}10^{-2}$; $0.3 < (\sigma_c/\sigma) < 2$.

The equation for the superficial area mentioned can be applied, with deviations of, approximately, 20% for columns packed with Raschig rings, Berl saddles, spheres, made of ceramic, glass, certain polymers and coatted with paraffin.

Bolles and Fair (1982) compiled and analyzed a large amount of performance data in the literature of packed beds, and developed a model of mass transfer in packed column. Indeed, the authors expanded the database of Cornell et al. (1960) and adapted the model to new experimental results, measured at larger scales of operation in another type of packing (Pall rings) and other material (metal). The database covers distillation results in a wide range of operating conditions, such as pressures from 0.97 to 315 psia and column diameters between 0.82 to 4.0 ft. With the inclusion of new data, adjustments were needed in the original model and the values of φ and Ψ had to be recalculated. However, the equation of Bolles and Fair model (1982) is written in the same way that the model of Cornell et al. (1960). The only difference occurs in the equation for the height of mass transfer to the vapor phase, just by changing the units of some variables:

$$H_V = \frac{\psi \cdot S_{CV}^{\,0,5}}{\left(3600 \cdot G_L \cdot f_1 \cdot f_2 \cdot f_3\right)^n} \cdot d'_C{}^{m} \cdot \left(\frac{Z}{10} \right)^{\frac{1}{3}} \tag{21}$$

In this equation, d'_C is the adjusted column diameter, which is the same diameter or 2 ft, if the column presents a diameter higher than that.

Unlike the graphs for estimating the values of φ and Ψ, provided by Cornell et al. (1960), where only one type of material is analyzed (ceramic) and the percentage of flooding, required to read the parameters, is said to be less than 50% in the work of Bolles and Fair (1982), these graphics are more comprehensive, firstly because they include graphics for Raschig rings, Berl saddles and metal Pall rings, and second because they allow variable readings for different flooding values.

The flooding factor, necessary to calculate the height of a mass transfer unit in the Bolles and Fair (1982) model, is nothing more than the relation between the vapor velocity, based on

the superficial area of the column, and the vapor velocity, based on the superficial area of the column at the flooding point. The Eckert model (1970) is used for the determination of these values. The authors compared the modified correlation with the original model and with the correlation of Onda et al. (1968 a, b), concluding that the lower deviations were obtained by the proposed model, followed by the Cornell et al. (1960) model and by the Onda et al. (1968 a, b) model.

Bravo and Fair (1982) had as objective the development of a general project model to be applied in packed distillation columns, using a correlation that don't need validation for the different types and sizes of packing. Moreover, the authors didn't want the dependence on the flooding point, as the model of Bolles and Fair (1982). For this purpose, the authors used the Onda et al. (1968 a, b) model, with the database of Bolles and Fair (1982) to give a better correlation, based on the effective interfacial area to calculate the mass transfer rate. The authors suggested the following equation:

$$a_e = \frac{\left(a_e \cdot H_V + \lambda \cdot a_e \cdot H_L\right)}{H_{OV}} \tag{22}$$

Evidently, the selection of k_V e k_L models is crucial, being chosen by the authors the models of Shulman et al. (1955) and Onda et al. (1968a, b), since they correspond to features commonly accepted. The latter equation has been written in equations 23 and 24. For the first, we have:

$$\frac{k_V \cdot \rho_V \cdot RT}{G_V} = 1.195 \cdot \left[\frac{d'_p \cdot G_V}{\mu_V \cdot (1-\varepsilon)}\right]^{-0.36} \cdot \left(S_{CV}\right)^{-\frac{2}{3}} \tag{23}$$

$$\frac{k_L \cdot d'_p}{D_L} = 25.1 \cdot \left[\frac{d'_p \cdot G_L}{\mu_L}\right]^{0.45} \cdot \left(S_{CL}\right)^{0.50} \tag{24}$$

The database used provided the necessary variables for the effective area calculation by the both methods. These areas were compared with the known values of the specific areas of the packing used. Because of that, the Onda et al. (1968 a, b) model was chosen to provide moderate areas values, beyond cover a large range of type and size packing and tested systems.

The authors defined the main points that should be taken in consideration by the new model and tested various dimensional groups, including column, packing and systems characteristics and the hydrodynamic of the process. The better correlation, for all the systems and packing tested is given by:

$$\frac{a_e}{a_p} = 0.498 \cdot \left(\frac{\sigma^{0.5}}{Z^{0.4}}\right) \cdot \left(Ca_L \cdot \mathrm{Re}_V\right)^{0.392} \tag{25}$$

which:

$$Ca_L = \frac{\mu_L \cdot G_L}{\rho_L \cdot \sigma \cdot g_C} \tag{26}$$

$$\mathrm{Re}_V = \frac{6 \cdot G_V}{a_P \cdot \mu_V} \tag{27}$$

Recently, with the emergence of more modern packing, other correlations to predict the rate of mass transfer in packed columns have been studied. Wagner et al. (1997), for example, developed a semi-empirical model, taking into account the effects of pressure drop and holdup in the column for the Nutter rings and IMTP, CMR and Flaximax packing. These packing have higher efficiency and therefore have become more popular for new projects of packed columns today. However, for the traditional packing, according to the author, only correlations of Cornell et al. (1960), Onda et al. (1968a, b), Bolles and Fair (1982) and Bravo and Fair (1982), presented have been large and viable enough to receive credit on commercial projects for both applications to distillation and absorption.

Berg et al. (1984) questioned whether the extractive distillation could be performed in a packed distillation column, or only columns with trays could play such a process. Four different packing were used and ten separation agents were applied in the separation of ethyl acetate from a mixture of water and ethanol, which results in a mixture that has three binary azeotropes and a ternary. A serie of runs was made in a column of six glass plates, with a diameter of 3.8 cm, and in two packed columns. Columns with Berl saddles and Intalox saddles (both porcelain and 1.27 cm) had 61 cm long and 2.9 cm in diameter. The columns with propellers made of Pyrex glass and with a size of 0.7 cm, and Raschig rings made of flint glass and size 0.6 cm, were 22.9 cm long and 1.9 cm in diameter. The real trays in each column were determined with a mixture of ethyl benzene and m-xylene. The cell, fed with the mixture, remained under total reflux at the bubble point for an hour. After, the feed pump was switched on and the separating agent was fed at 90 °C at the top of the column. Samples from the top and bottom were analyzed every half hour, even remain constant, two hours or less. The results showed, on average, than the packed column was not efficient as the columns of plates for this system. The best packing for this study were, in ascending order, glass helices, Berl saddles, Intalox saddles and Raschig rings. The columns with sieve plates showed the best results. Propellers glass and Berl saddles were not as effective as the number of perforated plates and Intalox saddles and Raschig rings were the worst packing tested. When the separating agent was 1,5-pentanediol, the tray column showed a relative volatility of ethyl acetate/ethanol of 3.19. While the packed column showed 2.32 to Propeller glass, 2.08 for Berl saddles, 2.02 for Intalox saddles and 2.08 for Raschig rings.

Through the years, several empirical rules have been proposed to estimate the packing efficiency. Most of the correlations and rules are developed for handles and saddle packing. Vital et al. (1984) cited several authors who proposed to develop empirical correlations for predicting the efficiency of packed columns (Furnas & Taylor, 1940; Robinson & Gilliand, 1950; Hands & Whitt, 1951; Murch, 1953; Ellis, 1953 and Garner, 1956).

According to Wagner et al. (1997), the HETP is widely used to characterize the ability of mass transfer in packed column. However, it is theoretically grounded in what concerns the mass transport between phases. Conversely, the height of a global mass transfer, H_{OV}, is more appropriate, considering the mass transfer coefficient (k) of the liquid phase (represented by subscript L) and vapor (represented by subscript V) individually. Thus, the knowledge of the theory allows the representation:

$$H_{OV} = H_V + \lambda \cdot H_L \tag{28}$$

$$H_V = \frac{G_V}{k_V \cdot a_e \cdot P \cdot M_V} \tag{29}$$

$$H_L = \frac{G_L}{k_L \cdot a_e \cdot \rho_L} \tag{30}$$

The effective interfacial mass transfer area, in a given system, is considered equal to the liquid and vapor phases, as is the area through which mass transfer occurs at the interface. It is important to also note that a_e is not composed only by the wet surface area of the packing (a_W), but throughout the area that allows contact between the liquid and vapor phases (Bravo and Fair, 1982). This area can be smaller than the global interfacial area, due to the existence of stagnant places, where the liquid reaches saturation and no longer participate in the mass transfer process. Due to this complicated physical configuration, the effective interfacial area is difficult to measure directly. The authors proposed a new model using high-efficiency random packing as IMTP, CMR, Fleximac and Nutter. The final model became

$$HETP = C_{pk}\frac{Z^{0.5}}{a_p}\left(\frac{\pi(\in -h)u_V}{4D_V}\right)^{0.5}\left[1+\left(\frac{hD_V M_L \rho_V}{(c-h)D_L M_V \rho_L}\frac{V}{L}\right)^{0.5}\right]\left[\left(\frac{1-\in +h}{1-c}\right)^{2/3}-1\right]^{-1} \tag{31}$$

After the test using 326 experimental data, the predicted values of HETP showed a deviation less than 25% from the experimental results. It was observed that physical properties have a little effect on mass transfer.

Four binary systems were tested (cyclohexane-heptane, methanol-ethanol, ethylbenzene-styrene and ethanol-water) from different database and different packing types and sizes. The only packing parameter needed was a packing characteristic which has a value of 0.030 for a 2 in Pall and Raschig rings and about 0.050 for 2 in nominal size of the high efficiency packing investigated.

The theoretical relations between the mass transfer coefficient and a packing efficiency definition, are not easily obtained, in a general manner. This is due to the divergence between the mechanisms of mass transfer in a packed section and the concept of an ideal stage. The theoretical relation deduced, applied in the most simple and commonly situation is described as:

$$HETP = H_{OV} \cdot \frac{\ln \lambda}{\lambda - 1} \tag{32}$$

Although validated only for the cases of dilute solutions, constant inclination of the equilibrium line, constant molar flow rates, binary systems and equimolar countercurrent diffusion, this equation has been applied to systems with very different conditions from these, and even for multicomponent systems (Caldas & Lacerda, 1988).

The design of packed columns by the method of the height of a global mass transfer unit is an established practice and advisable. For this, it is necessary to know the height of the mass transfer unit for both liquid and for vapor phases.

H_L values are usually experimentally obtained by absorption and desorption of a gas, slightly soluble, from a liquid film flowing over a packed tower, in a countercurrent mode with an air stream. Under these conditions, changes in gas concentration are neglected and

no resistance in the gas film is considered. The variables that affect the height of the liquid transfer unit are the height of the packed section, gas velocity, column diameter, the physical properties of liquid and the type and size of the packing.
The values of the height of a transfer unit of a gas film, H_V, need to be measured under the same conditions as the resistance of the liquid film is known. This can be done by the absorption of a highly soluble gas. An alternative method to determine H_V involves the vaporization of a liquid, at constant temperature, within a gas stream. In this case, the resistance of the liquid film is zero and H_V is equal to H_{OV}. The variables that affect the height of transfer unit of a gas film are the gas and liquid velocities, the physical properties of the gas, column diameter, the height, type and size of the packing (Cornell et al., 1960).
Linek et al. (2001) studied the hydraulic and mass transfer data measuring pressure drop, liquid hold-up, gas and liquid side volumetric mass transfer coefficients and the interfacial area for Rauschert-Metall-Sattel-Rings (RMSR) with 25, 40 and 50 mm. The shape and characteristics of the studied packing corresponded with the metal Pall rings and Intalox packing of Norton. The distillation experiments were performed using the systems methanol-ethanol, ethanol-water and isooctane-toluene at atmospheric pressure in a column of diameter 0.1 m and a height of packing 1.67 m, operated under total reflux. The measured values of HETP were compared with those calculated for the different sizes of RMSR packing for the distillation systems. The calculated values differ by less than ± 15% from the experimental values, with the exception for the data obtained at extremely low gas flow rates in the system ethanol-methanol for which the respective difference reached 46%. Figure 2, from the paper of Linek et al. (2001), shows the comparison of measured values of HETP with those calculated from absorption mass transfer data using the model described in Linek et al. (1995) cited by Linek et al. (2001).

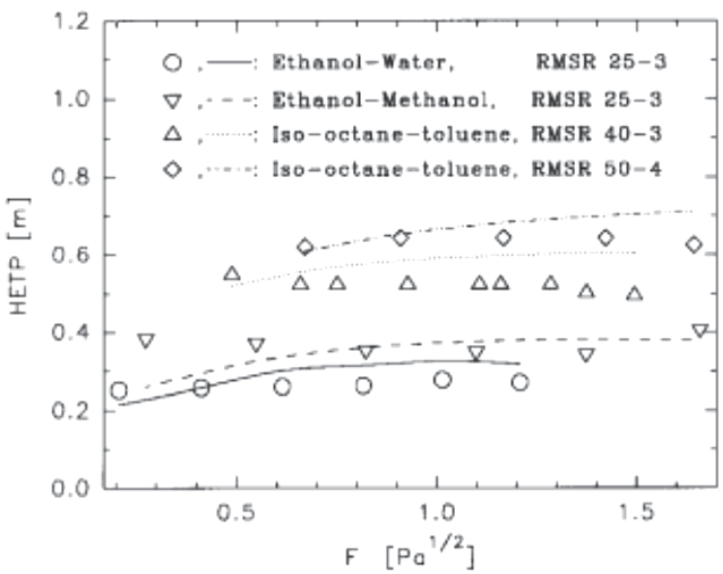

Fig. 2. Comparison of measured values of HETP with those calculated from absorption mass transfer data (Linek et al., 2001)

Senol (2001) studied the performance of a randomly packed distillation column depending on the effective vapor-liquid interfacial area and the flood ratio. The analysis were mainly focused optimizing HETP and effective interfacial areas as function of the flood ratio estimated by Eckert flooding model (Eckert, 1970 cited by Senol, 2001). The experiments were done in a pilot scale column of 9 cm inside diameter randomly filled to a depth of 1.90 m with Raschig-type ceramic rings under atmospheric pressure. The runs were conducted to determine the capacity and efficiency at total reflux for several pressure drops. The efficiency tests were made using three packings of 6.25, 9 and 10.8 mm nominal sizes and binary systems like trichloroethylene/heptane, methylcyclohexane/toluene, heptane/toluene and benzene/toluene. The HETP was obtained by the Fenske equation. The efficiency results gave evidence of two critical factors, the flood ratio and the packing geometry that affects significantly the magnitude of effective interfacial area.

A working database of 2350 measurements (under total molar reflux), in the work of Piché et al. (2003), were extracted from the open literature to generate height equivalent to a theoretical plate (HETP) calculations, essential for the design of randomly packed distillation columns. According to the authors, the HETP approaches more a rule of thumb concept than an exact science and can be calculated as:

$$HETP = \frac{\ln(m\,G'/L')}{m\,G'/L' - 1}\left(\frac{U_G}{k_G a_w} + m\frac{U_L}{k_L a_w}\right) \tag{33}$$

The database used included 325 measurements on the interfacial area, 1100 measurements on the liquid-film coefficient (k_La_w), 361 measurements on the gas-film coefficient (k_Ga_w), 1242 measurements on the liquid-overall coefficient (K_La_w) and 742 measurements on the gas-overall coefficient (K_Ga_w). The distillation database constituted 2357 HETP measurements taken from 22 different references, conducted at total molar reflux with standard binary mixtures (chlorobenzene-ethylbenzene, ethylbenzene-styrene, benzene-toluene, methanol/ethanol, trans-decalin/cis-decalin, ethanol-water, hexane-heptane, isopropanol-water, iso-octane-toluene, toluene-methylcyclohexane, cyclohexane-cyclohexanol, o-xylene-p-xylene, benzene-1,1-dichloroethylene, trichloroethylene-n-heptane, n-heptane-toluene). All the systems were distilled using 24 varieties of packing. After the construction of a new model based on a neural network, the deviations were calculated and were better than the original model of Piche et al. (2002) cited in Piche et al. (2003). The minimum deviation of HETP was 21.3%, including all the systems studied.

Darakchiev & Semkov (2008) studied the rectification of ethanol with three types of modern random packings, IMTP, Raschig Super Rings and Ralu Flow, in conditions close to real conditions of industrial operation. The experiments were performed in high and medium concentrations. The experimental unit consisted of a column of internal diameter of 21.3 cm, made of stainless steel, with reboiler of 80000 cm^3 of capacity and maximum resistance of 45 kW, condenser, pipes, devices for monitoring and measurement and a control panel. The column was built in separated sections and assembled by flanges. The packed section has a height of 2.8 m. To limit the damaging effect of preferential channels, reflectors rings were willing on 20 cm distance between the height of the packing. One type of disperser, a type of liquid distributor, with 21 holes of 3 mm with Teflon nozzle of 1.7 mm, was attached to the upper spine. To prevent clogging, a filter was placed before the distributor.

A diaphragm and a differential manometer were used to measure the discharge flow, which may be total or partial. The column was insulated by a layer of 50 mm glass fiber. The

experimental runs were done feeding 60000 cm^3 of the solution to reboiler. The minimum liquid flow rate in the distributor needed to ensure good distribution of liquid in the column was obtained, experimentally, in 58000 cm^3/h, which required a minimum output of 13 kW. After equilibrium, samples were taken before and after the packing. A densimeter was used to determine the concentration of the samples, applying temperature corrections. Eight types of random packings were studied: four metal Raschig Super Rings, with dimensions of 1.27, 1.52, 1.78 and 2.54 cm, a Raschig Super Ring, made of plastic, of 1. 52 cm, two kinds of IMTP packing and a Ralu Flow of plastic. The results showed good efficiency of the packing in ethanol dehydration. The best packing tested was Raschig Super Ring in the smaller dimension, producing a HETP with 28 cm. Comparing metal to plastic, there was a 6% lower efficiency for plastic packing.

Larachi et al. (2008) proposed two correlations to evaluate the local gas or liquids side mass transfer coefficient and the effective gas-liquid interfacial area. The study was done using structured and random packing, testing 861 experiments for structured packings and 4291 experiments for random packings. In order to reconstruct HETP values from the mass transfer parameters, 1192 HETP experiments for random packings and 127 experiments for structured packings were evaluated. All the distillation experiments were done at total molar reflux with standard binary mixtures as chlorobenzene/ethylbenzene, ethylbenzene/styrene, benzene/toluene, methanol/ethanol, etc. All the physical chemical properties unavailable were predicted according to the rules of Reid et al. (1987). According to the neural network weights, the relative deviation was 29.2% for the random packing and 18.2% for the experiments done with structured packings.

Soares (2010) studied the ethanol concentration using different salts, NaCl, $CaCl_2$, $Ca(NO_3)_2$, sodium acetate and potassium acetate, in a packed column, with 5.9 cm of internal diameter and 37 cm of packed section height, with Raschig rings (0.73 cm) made of glass. The HETP was evaluated operating the distillation column at total reflux ratio. Despite of the less efficiency compared with the more modern packing, this type of packing presented the lowest costs. The correlations used in this work were Bravo & Fair (1982), Bolles and Fair (1982) and Onda et al. (1968 a, b). The Cornell et al. (1960) correlation was not adopted, due to the fact that the model of Bolles and Fair (1982) is its improvement. All the physical-chemical properties were estimated by the different methods present in Reid et al. (1987). The thermodynamic modeling was done based on the work of Macedo et al. (1990), that introduced the Debye-Hückel term in UNIQUAC, to calculate the phase equilibrium for electrolytes. Two systems with different ethanol concentration were studied, 7 and 52 ºGL. The better results of predicted HETP were obtained using the Onda et al. (1968 a, b) and with the Bolles and Fair (1982) correlations. The results predicted by the correlation of Bravo and Fair (1982) modified by Onda et al. (1968 a, b) were much higher than the experimental HETP. According to Caldas and Lacerda (1988), the maximum deviation is 27% using Raschig rings made of ceramic.

The choice for a distillation column is based on the cost and on the properties of the studied system. In the past, except for the columns with small diameters, the trays are adopted in the most of the distillation columns. However, the development of high efficient packing and the need for the improvement of the capacity, efficiency, and to reduce the pressure drop, has led to a more use of the packing columns in a large wide of applications in an industrial scale (Perry and Green, 1999).

The difference in cost and height, between the tray and packed columns, are not significant, if operating conditions are providing efficiency close to maximal. In general, trays are used

in large diameter columns and in columns that need 20 to 30 stages. The packing are widely applied in the gas absorption, vacuum processes and pilot scale units (Henley and Seader, 1981). This can be explained, considering that: the packed columns can contain packing made of ceramic or plastic, desirable characteristics required for corrosive systems (very common in gas absorption processes), show characteristics of efficiency and pressure drop, critical factors in the vacuum distillation (often used to separate thermally sensitive mixtures, suffering decomposition and/or polymerization at high temperatures) are cheaper than the tray columns when employed less than 76 cm diameter. Another recommendation, for the preferential use of packed column, is made when you want separate systems with a tendency to form foams, since the tray columns have a higher degree of agitation (Perry and Green, 1999).

According to Perry & Green (1999), the main restrictions on the use of packed columns are: 1) when multiple feeds and/or multiple side streams and condensers and/or intermediary reboilers are required (tray valves are desirable in these cases); 2) when a periodic cleaning must be done inside the column due to certain characteristics of the system to be distilled (trays are easier to clean), 3) when data for the design of packed distillation columns are not available for certain mixtures (projects of tray columns are better established than for packed columns).

None of the three restrictions limit the use of packing to obtain anhydrous ethanol by extractive saline distillation. Doubts could arise with respect to the periodic cleaning of the interior of the column, needed for the alleged deposition of salt. This would not be necessary because the salt would tend strongly to remain in solution. Side devices are not required and the project data can be obtained through studies on a pilot scale, emphasizing the importance of this work.

The packed distillation columns must be fitted with a good distribution of liquid through the interior of the packing, to promote fluid turbulence and mass transfer by liquid dispersion. This allows for a greater contact between the liquid and vapor phases, increasing the efficiency of separation. At low flow rate of steam and/or liquids, or if the feeding of the liquid is not regular distributed over the packing, the liquid will tend to descend the walls of the column, forming preferential channels. Thus, the upward flow of steam is bypassed by the middle column, without a proper contact between the phases. In very small flow rates, the liquid may be insufficient to wet the packing surface. Therefore, it is strongly recommended an adjusted flow condition and the use of distributors, what can improve the wettability of the interior of the column (Henley and Seader, 1981).

The proposal of a generalized correlation for the HETP is a difficult task, because packed columns are equipments of continuous contact, so that the modeling of the phenomenon is more powerful when done by balances in the differential element of the packing. However, the use of HETP in specific situations provides reliable results and, in many cases, is the only possible systematic (Caldas & Lacerda, 1988).

2.2 Part B: performance of structured packing

In the field of distillation, structured packings have been established for several decades. They are preferred where liquid loads are acceptable, a high separation performance is required and low pressure drop is of importance (Fischer et al., 2003).

The first generation of structured packing was brought up in the early forties. In 1953, it was patented a packing named Panapak ™, made of a wavy-form expanded metal sheet, which was not successful may due to maldistribution or lack of good marketing (Kister, 1992).

The second generation came up at the end of 1950's with the highly efficient wire mesh packings, as Goodloe ™, Hyperfil ™ and Koch-Sulzer. Until the 70's, those packings were the most used in vacuum distillation due to their low pressure drop per theoretical stage. However, high cost, low capacity and high sensitivity to solids have prevented the utilization of wire mesh packings, except in vacuum distillation.
The corrugated structured packings, introduced by Sulzer by the end of the 70's, have initiated the third generation of structured packed columns. High capacity, lower cost, less sensitivity to solids while keeping a high performance, have made them competitive in relation to other column internals. The 1980's have perceived a growing popularity of those packings, especially on revamps in oil and petrochemical plants (Nicolaiewsky, 1999).
Those structured packings, made of corrugated metal sheets, had their surfaces treated, chemical or mechanically, in order to enhance their wettability and, consequently, their wetted area, improving their performance. The way wetted area is created, maintained and renewed, related to different surface geometry, has a remarkable effect not only on packing efficiency, but also on the performance of packed columns (Nicolaiewsky et al., 1999).
Spiegel and Meier (2003) summarized in the Figure 3 the evolution of the structured packings, concluding that no better performance was achieved with various packings of similar geometry. In 1994, a new geometry was developed and called as Optiflow and, in 1999, an improved structure of corrugated sheet packings, the MellapackPlus was developed based on CFD simulations and experimental tests. This new structure, compared with conventional Mellapak, has the pressure drop remarkably lowered and the maximum useful capacity could be extended uo to 50%.

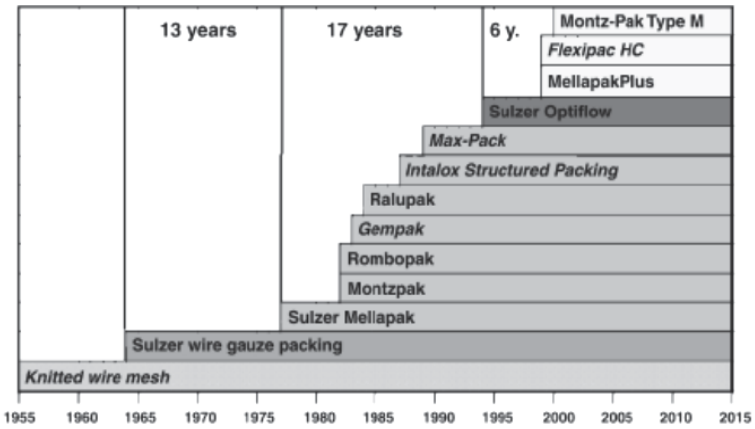

Fig. 3. History of structured packings (Spiegel and Meier, 2003)

According to Shi and Mersman (1985), the effective interfacial area includes not only films on the packing surface but also drops, jets and sprays which flow through the voids of the packed bed. In truth, wetted area can be divided into two parts: one occupied by the liquid film flowing over the surface of the packing and the other, the stagnant liquid. In gas absorption, the fraction of the wetted area occupied by the stagnant liquid soon becomes saturated with gas, and as renewal of that liquid is insignificant; it does not contribute to mass transfer. However, in distillation, these portions of stagnant liquid are also effective in the separation (Puranik and Vogelpohl, 1974).

The first fundamental model for structured packing efficiency is attributed to Bravo et al. (1985), applied to Sulzer gauze packings, in which the effective interfacial area should be considered equal to the nominal packing area. The pressure effect was not included in that model, due to the vacuum conditions on the tests, involving low liquid flow rates and films with lower resistance to mass transfer (Orlando Jr. et al., 2009).
Later, in 1987, Fair and Bravo proposed the following equations to predict the wetted area of corrugated structured packings:

$$a_e = \beta . a_p \quad (34)$$

where $\beta = 0.50 + 0.0059$ (% flood) and $\beta = 1.0$ for above 85% flood. The above equations mean that the effective interfacial area is always lower than the nominal packing area.
Based on measurements of widths of liquid films flowing over inclined surfaces, Shi and Mersmann (1985) have established a correlation for the estimation of wetted area. For the liquid film thickness, they used Nusselt's equation. The authors' correlation for the wetted area took into account the influence of physical properties like viscosity, surface tension and contact angle, with a great influence of the latter. The authors found out that a small variation on contact angle would cause a large influence on the wetted area, which is not reasonable according to findings of Nicolaiewsky et al. (1999), in which work correlations for the estimation of liquid film width and thickness were proposed to be used on a wetted area model in packed columns containing structured packing.
Shi and Mersmann's (1985) correlation for sheet metal structured packings can be written:

$$\frac{a_e}{a_p} = F_{SE} \frac{29.12\left(W_{eL}F_{rL}\right)^{0.15} S^{0.359}}{R_{eL}^{0.2}\varepsilon^{0.6}\left(1-0.93\cos\theta\right)\left(\sin\gamma\right)^{0.3}} \quad (35)$$

in which F_{SE} accounts for variations in surface enhancements and the contact angle θ accounts for surface material wettability. For sheet metal packing, the authors stated that:

$$\cos\theta = 0.9 \qquad \text{for } \sigma \le 0.055 \text{ N/m}$$

$$\cos\theta = 5.211x10^{-16.835\sigma} \qquad \text{for } \sigma \ge 0.055 \text{ N/m}$$

$$R_{eL} = \frac{4\delta u_{Le}\rho_L}{\mu_L} \quad (36)$$

$$F_{rL} = \frac{u_L^2}{Sg} \quad (37)$$

$$W_{eL} = \frac{u_L^2\rho_L S}{\sigma g_c} \quad (38)$$

Henriques de Brito and coworkers (1994) measured the effective interfacial area of sheet metal structured packings such as Mellapak 125Y, 250Y and 500Y. Their results have demonstrated that the effective area can be much higher than the packing surface area due to instabilities in liquid flow, such as ripples, waves, detachment of the film into liquid

showers, etc. The resulting correlation for all measurements is a function of the Reynolds number for the liquid phase, as follows:

$$\frac{a_e}{a_p} = 0.465 R_{eL}^{0.30} \tag{39}$$

It must be pointed out that the authors have not checked the correlation with fluids with different densities and viscosities.

Later on, Rocha et al. (1993, 1996) developed a mechanistic model aiming the design and optimization of CSSP (continuous separation structured packing) distillation columns of the metallic corrugated type, also applied to absorption and stripping processes. Liquid holdup prediction was the key to the development of correlations to measure pressure drop, capacity and mass transfer efficiency in the packing. In their model, Rocha and coworkers used Shi and Mersmann's (1985) correlation in order to evaluate the interfacial area available for mass transfer and the liquid holdup present in the packing. Those correlations involved parameters related to surface treatment, as contact angle on the packing surface, as well as packing geometry, liquid and vapor flow rates and physical properties of the system (Orlando Jr. et al., 2009). For the estimation of the liquid side mass transfer coefficient, Rocha et al. (1996) used a correlation developed by Brunazzi and coworkers (1995) for the evaluation of effective areas in absorption columns containing Mellapak 250Y and Sulzer BX.

Rocha et al. (1993) studied correlations to calculate flooding velocity and mass transfer efficiency by using the concept of HETP for distillation columns filled with structured packings. The authors observed that there are few correlations to predict HETP values amd most of them need empirical constants or exponents for their calculation. The disadvantage is that these values are not reported for all the packings and all the sizes available. It was used the Billet (Billet, 1987), Spiegel and Meier (Spiegel & Meier, 1987) and Bravo et al. (1985) correlations for the HETP calculation and the deviation between them was 11%.

Billingham and Lockett (1999) studied very small modifications to structured packing in order to increase the capacity. It was tested the air-water system and the cryogenic distillation. It was done three bricks of aluminum Flexipac 1Y in the initial experiments and in the other experiments, the packing was removed and the bricks disassembled and repinned together with each alternate sheet staggered in a vertical direction. For the cryogenic distillation, a larger specific surface area packing than Flexipac was used. The authors observed that the key is to reduce the pressure drop associated with vapour entry into the bricks, facilitating the passage of liquid from the bricks. Although the modified packings have increased capacity, HETP is about 25% higher than that the unmodified packings. To overcome this problem, another packing was used with the bricks having a flat top and a staggered base and were made from sheets of two different lenghs arranged alternatively. The modified packing had about 15% more capacity and the HETP has the same value of the unmodified packings.

None of those models mentioned so far considered the effect of vapor flow and thus can only be used with low vapor rates. However, since industrial columns often operate above the loading point, it was necessary to develop a correlation for effective interfacial area which was valid for a wide range of vapor rates (Xu et al., 2000). Using Billet and Schultes' model (1993) for effective interfacial area (which is very similar to Shi and Mersmann's model, but at least was validated with experimental data), Xu et al. (2000) introduced in that model the Marangoni effect. The authors considered that the surface tension positive

systems should have a higher interfacial area than the neutral and negative systems because the liquid films are more stable. This result is in agreement with measurements of contact angles formed by liquid films of diverse properties, in flat or textured surfaces (Nicolaiewsky and Fair, 1999), in which it was clear that texturing of surfaces would enhance wetting characteristics of positive systems. Xu et al's model (2000) was validated for three structured packing (Gempak 2.5A, AW7 and AW12), with three test systems (methanol-isopropanol, water-acetic acid and methanol-water), at two operating pressures (710 and 260 mmHg), having achieved an average 10.2% deviation of model prediction. The deviations are 20% approximately for 90% of the data points.

Olujic et al. (2003) made experimental studies in a distillation column at total reflux to report the capacity of a new generation of Montz structured packing. According to the authors, the major feature of Montz B1 is a smooth bend in the bottom third of the corrugation with continuously increasing corrugation base width. The experiments were done using a bed height of approximately 3.3 m and the system cyclohexane/heptanes was utilized, under different conditions of pressure, 0.17, 0.33, 1.03 and 4.14 bar. Five different dimensions of structured packing were investigated with a_p (m^2/m^3) of 244, 247, 250, 346 and 350. The number of equilibrium stages was calculated from the distillate and bottom compositions using the Fenske equation and an average relative volatility. Among the various results published by the authors, Figure 4 shows the dimensionless product of the specific surface area and HETP as a function of the operational pressure for both packing sizes. The figure concludes that larger surface area packing appear to use their available surface less efficiently. The performance enhancement in case of 350 series packings is 21% with respect to the standard size. The relatively high efficiency is similar as the original packing in its range of application. Because of that characteristic, columns equipped with B1-250 packing can be revamped with B1-250M packing.

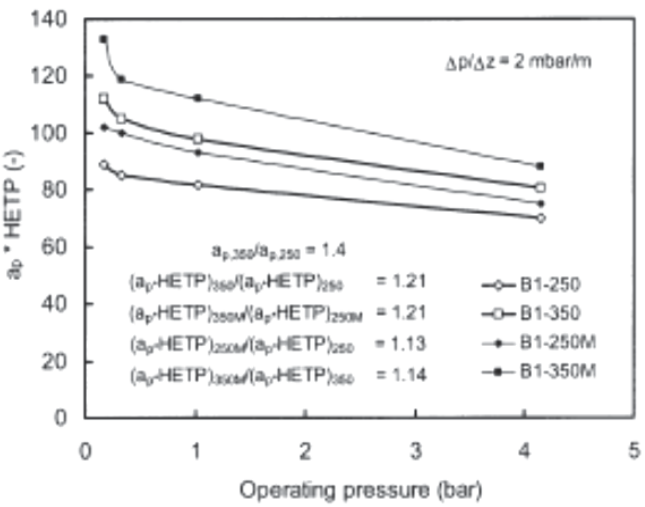

Fig. 4. Relative surface utilization efficiency as a function of operating pressure (total reflux)

In 2006, results from continuous feed and total reflux distillation experiments, carried out with a common type and size structured packing using two- and three-component mixtures of common alcohols and water, were published (Mori et al., 2006). The composition profiles

measured with the three component mixture were used to validate the rate-based (non-equilibrium) model developed at the Nagoya Institute of Technology (NIT), which appeared to be highly accurate, but also sensitive to the choice of the predictive method for the interfacial area. The rate-based, non-equilibrium (NEQ) approach adopted at NIT (Mori et al., 1996, 1999, 2002) includes Bravo et al. (1985) correlations for vapor and liquid side mass transfer coefficients that differ to some extent from those employed in the Delft model (Olujic et al., 1999). Two simple empirical models for effective specific area were considered in this work. First one is that introduced by Olujic and coworkers (1999) for Montz B1-250 packing and the other one is proposed by Henriques de Brito et al. (1994), for Mellapak packings. The authors concluded that the Delft model overpredicts the measurements at higher F factors to such an extent that it may be considered as safe or conservative. The NEQ model developed at NIT, in conjunction with Henriques de Brito et al. (1994) correlation for effective area, proved to be capable of reproducing all the measured composition profiles very well, regardless of the water content of the feed.

Also, in 2006, Mori et al. presented results of continuous feed and total reflux distillation experiments carried out with a common type and size structured packing, Montz-pack B1-250, using two (methanol-water) and three (methanol/ethanol/water) component mixtures of common alcohols and water. The packing is a conventional corrugated sheet metal structured packing with a regular shallow embossed unperforated surface, a corrugation inclination angle of 45º and an element height of 0.196 m. The experiments were done in a 210 mm diameter distillation column, with a total packed height of 2.156 m and the packed bed consisted of four sections. The experimental packing efficiency, expressed as HETP, under total reflux conditions, was calculated using the Fenske equation to estimate the number of equilibrium stages. The rate-based, non-equilibrium (NEQ) model was used because it does not require any empirically determined packing specific constant, just the main dimensions of corrugated sheets as well as the corrugation inclination angle. The model includes Bravo et al. (1985) correlations for vapor and liquid side mass transfer coefficients that differ from the Delft model. Two simple empirical model for the calculation of the effective specific area was considered: the first one, by Olujic et al. (1999) for B1-250 packing (equation 40) and the other one was proposed by Brito et al. (1994) for Mellapack packings (equation 41).

$$\frac{a_e}{a_p} = \frac{1}{1+\left(0.000002143 u^{-1.5}{}_{Ls}\right)} \tag{40}$$

$$\frac{a_e}{a_p} = 0.465\,\mathrm{Re}^{0.3}{}_{L} \tag{41}$$

Equation 40 was originally developed for Mellapak and is assumed here to be valid for other similar sheet metal packings, including Montzpak B1-250. The results, at total reflux conditions, is presented in Figure 5, that shows the mass transfer efficiency (the average HETP of B1-250) as a function of vapor load factor (F-factor). In the figure, Feed 1 refers to a low water content and the Feed 2 to a feed with relatively high water content. In both cases, the efficiency slowly decreases with increasing F-factor. According to the authors, a pronounced trend was observed with the B1-250 packing because is it an inherent characteristic of the Delft method (Olujic et al., 1999 cited by Mori et al., 2006).

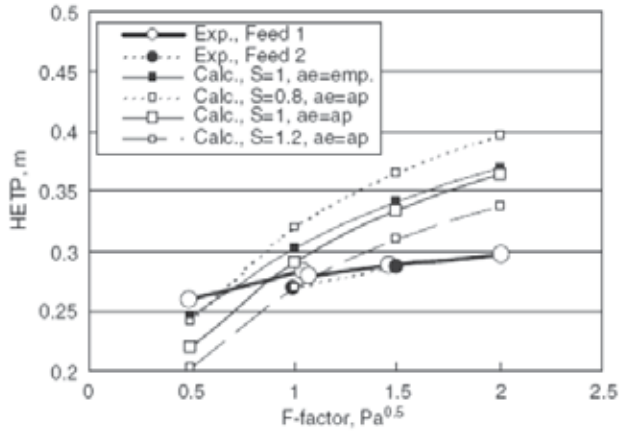

Fig. 5. Comparison of calculated and measured packing efficiencies at total reflux conditions

Ceramic foam packing has been known for many years and has a wide range of applications due to its low density and attractive thermal, mechanical, electrical, and acoustical properties. In a recent paper (Lévêque et al., 2009), its performance was evaluated as a distillation packing material. The hydraulic characteristics of the foam were experimentally determined for gas–liquid countercurrent flow using an air–water system. The performance in terms of pressure drop per unit height and flooding behavior was quite low compared with classical distillation packing materials (Sulzer M250Y, Sulzer CY and Pall rings). The liquid hold-up of the foam packing increased with increased liquid–gas loading in the loading zone, and the liquid hold-up was greater than other classical packing materials. Mass transfer efficiency was determined over the entire operating range using a cyclohexane/*n*-heptane system at atmospheric pressure under total reflux. The foam packing performance was very good, with a HETP of 0.2 m and increasing mass transfer with increasing gas and liquid superficial velocities inside the packing (Lévêque et al., 2009).
Last year, a French group from Université de Toulouse (Bessou et al., 2010), sponsored by Sulzer and Snecma Propulsion Solide, has developed a new structured packing, made of carbon, named The Sepcarb 4D packing, presenting its performance characteristics. The advantages of the packing rest on being inert, corrosion-resistant; has very low density (40 kg/m^3), with tubes of small thickness (0.2 mm). The separation efficiency has been determined using the HETP concept on distillation experiments with cyclohexane/n-heptane system at atmospheric pressure and total reflux. The best results were obtained with wall wipers, which improved liquid redistribution between packing cylinders and involved low wall effects. HETP calculated was 0.2 m, which corresponds to a good transfer performance when compared to classical packings such as Mellapak 250Y, Mellapak 425Y and Pall rings.
Performance of a distillation column, operating continuously with a mixture of known composition (C_8-C_{14}), containing Sulzer DX SS structured packing, has been evaluated. Prior to the experimental tests, simulation studies using commercial software PRO/II® were performed in order to establish the optimum operational conditions for the distillation, especially concerning operating pressure, top and bottom temperatures, feed location and reflux ratio. The results of PRO/II® were very similar to the analysis of the products obtained during continuous operation, therefore permitting the use of the properties

calculated by that software on the theoretical models investigated. Five theoretical models available in the literature (Bravo, Rocha and Fair, 1985; Rocha, Bravo and Fair, 1993, 1996; Brunazzi and Pagliant, 1997; Carlo, Olujić and Pagliant, 2006; Olujić et al., 2004) and an empirical model (Carrillo and coworkers, 2000) have been compared. Modifications concerning calculation of specific areas were performed on the correlations in order to fit them for gauze packing HETP evaluation. As the laboratory distillation column was operated continuously, different HETP values were found by the models investigated for each section of the column. The low liquid flow rates in the top section of the column are a source of error for HETP evaluation by the models; therefore, more reliable HETP values were found in the bottom section, in which liquid flow rates were much greater. Among the theoretical models, Olujić *et al*. (2004) has shown good results relatively to the experimental tests. In addition, the former model by Bravo, Rocha and Fair (1985) underestimates HETP values; however, with the modifications proposed in this work, it has achieved more realistic performance prediction, remaining a good choice for gauze packing HETP evaluation. Having the advantage of avoiding the calculation of effective area and mass transfer coefficients, an empirical model proposed by Carrillo and coworkers (2000) was also investigated, showing low deviations compared to the theoretical models tested.

Among the short-cut methods for the estimation of column efficiency, Carrillo and coworkers (2000) have proposed a modification of the Lockett equation (1998) to be used for HETP estimation of Sulzer BX packing. The correlation was proposed to be a function of the gas flow factor, densities of the liquid and vapor phases and the system pressure. The HETP values calculated by the modified equation have shown a good fit, compared to the published experimental data available.

Later, Carlo, Olujić and Pagliant (2006) used the absorption column studies developed by Brunazzi and Pagliant (1997), and made some modifications on the liquid side mass transfer coefficient, to adapt those correlations for HETP evaluation of distillation columns. Olujić's model (1997) was developed to predict hydraulic and separation performance of corrugated sheet structured packing in distillation systems. Since 1997, until its last version (Olujić et al. (2004), the model, named the Delft model, has been enhanced through tests using Montz B1 and BSH packings. A complete evaluation of Delft's model has been accomplished by Fair and coworkers (2000), showing that it overestimates the effective superficial area for structured packing column design. In order to compensate for that deviation, Olujić et al. (2004) have adapted Onda's correlation (1968) *apud* Olujić et al. (2004) to be used with structured packing columns.

In 2009, two works deal with the HETP evaluation using distinct base lube oil mixtures in a lab-scale distillation column, of 40 mm of nominal diameter, having 4 sections of 550 mm each containing Sulzer DX (gauze) structured packing, as the contacting device (Machado et al. and Orlando Jr. et al., 2009). Orlando Jr. et al. (2009) made several tests with a hydrocarbon mixture (C_8-C_{14}) to evaluate HETP using six HETP correlations to find out which is the most appropriate for structured packed columns with medium distillates. The theoretical models investigated are: Bravo et al. (1985), Rocha et al. (1993, 1996), Brunazzi and Pagliant (1997), Carlo et al. (2006) and Olujic et al. (2004). As the laboratory distillation column was operated continuously, different HETP values were found by the models for each section of the column. Olujic et al. (2004) was the best method, showing good results, together with the correlation of Carrillo et al. (2000), in which low deviations were obtained. The average deviation varied from 8 to 47%. The deviations can be explained by the fact that

most of the models have been proposed from testes using corrugated sheet structured packing elements, which performs differently from gauze type packing.
In the work of Machado and coworkers (2009), the authors worked with two mixtures, a heavier one composed of neutral medium and bright stock and another composed of spindle and neutral light. Simulation studies using the PRO II software had been performed in order to establish the best operating conditions in the distillation unit. Concerning the empirical models, a comparison between the Lockett (1998) and Carrillo et al. (2000) models was done. Among the theoretical models, Olujic et al. (2004) was chosen for being one of the most recent and robust. According to the authors, unfortunately, neither mass transfer model was able to properly describe the base lube oil distillation. Olujic et al. (2004) model yielded underestimated area values, by using Onda´s correlation (Onda et al., 1968), but a modified version proposed by Orlando Jr. et al. (2009) provided more realistic values for the effective areas. It was concluded that the nature of the mixtures had no influence on HETP deviations, pointing out that the low vapor flowrate inside the column was the most influential variable. Large deviations varying from 27 to 70% were obtained for all the mixtures and using all the methods.
Finally, Li et al. (2010) used a special high-performance structured packing, PACK-^{13}C, with a surface area of 1135 m^2/m^3 and the first stable isotope pilot-scale plant using structured packing was designed. The height and inner diameter of the distillation column were 20 m and 45 mm, respectively, and the height of the packing bed was 18 m. The raw materials utilized were only high purity CO gas and liquid notrogen. When the F-factor changes from 0.18 to 0.90 m/s, the number of theoretical plates per meter decreases from 30 to 20. The new structured packing was a combination of the advantages of structured and random packing, as showed in Figure 6. The inclination angle was 45^o, the height of corrugation was 2.5 mm, the porosity was 0.77 and the silk diameter was 0.085 mm.

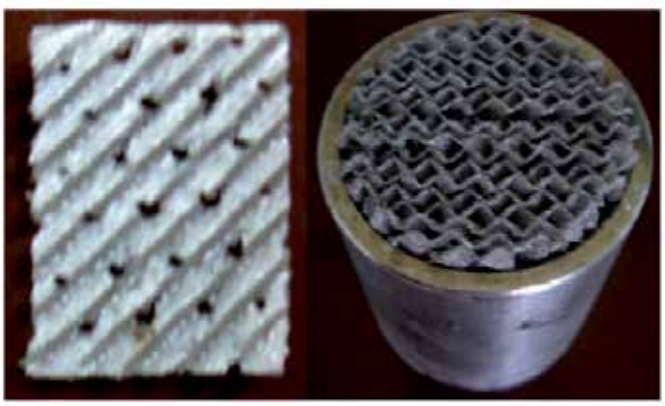

Fig. 6. Illustration of the structured packing PACK-^{13}C (Li et al., 2010)

The minimum theoretical plates, at total reflux, was calculated by the Fenske equation. The authors concluded that the PACK-^{13}C structured packing exhibits very high performance in isotope separation, combining the advantages of high theoretical plate numbers of the random packing and the excellent hydrodynamic properties of structured packing. Figure 7 confirms the characteristics of the structured packing relating the theoretical plates number and factor F.

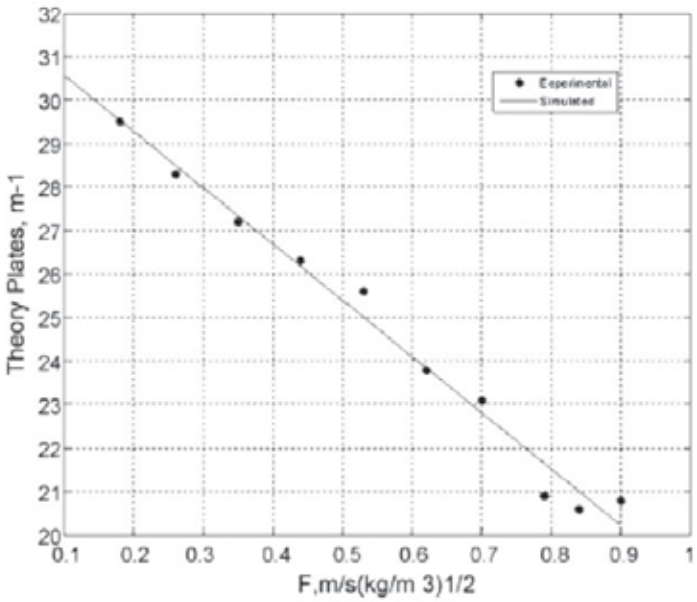

Fig. 7. The theoretical plates of PACK-^{13}C (Li et al., 2010)

3. Conclusions

The use of packed columns for continuous contacting of vapors and liquids is well established in the chemical industry, nowadays. The design of the columns require a knowledge of the height of a transfer unit and this chapter had as main objective the description of the present correlations, relating their advantages and disadvantages, for random and structured packing.

Among the researches encountered in the literature and cited in this chapter, it is important to have a model that describes the fluid dynamic relationships in packed columns with countercurrent flow of the gas and liquid phases to describe up the flood point. It is so important because above this point, the liquid accumulates to such an extent that column instability occurs. The disadvantage of some correlations relies on the fact that many parameter characteristics is only obtained graphically, what introduces deviations in the calculation of areas and HETP.

For the distillation in packed columns, it was ascertained that the resistance in both phases, liquid and vapor phases, should be taken into account in the HETP evaluation.

About the packing, new random and structured packing have been studied, but the difficulty in HETP representation remains the problem, due to the fact that it is so difficult to find a correlation that covers all systems with different physical properties and different nominal sizes of the packing.

Moreover, normally, HETP is substantially constant over a wide range of vapor flows; on the other hand, vapor flow varies increasing or decreasing the mass transfer depending on the liquid phase. Because of that, HETP is not constant along the column and it is convenient to define one value that which may be used for design purposes. Due to these factors, the correlations proposed, empirical or theoretical, do not reach the real value of HETP for any system studied.

Finally, to better evaluate HETP, it is also important to choose a thermodynamic model that can represent the behavior of the liquid-vapor equilibrium and complex methodologies to calculate the theoretical number of stages.

4. Nomenclature

d_P – nominal size of the packing
λ – inclination ratio between the equilibrium and operation straight
β – fraction of surface used for mass transfer
P – pressure of the system
G – mass flow of the phase
G_L – liquid mass flow
G_V – vapor mass flow
G - V – gas or vapor rate
L – liquid rate
M – molecular mass
M_L – molecular weight of liquid
M_V – molecular weight of vapor
ρ – density
H – height representation of the mass transfer unit
H_G – H_V – height of gas-side phase transfer unit (m)
H_L – height of liquid-side phase transfer unit (m)
H_{OG} - H_{OV} – height of an overall gas phase transfer unit (m)
g_C - conversion factor between strengh and mass
Ca_L – capilar number
C_{fL} – coefficient for effect of approach of flood point on liquid-phase mass transfer
C_{pk} – packing characteristic
h – operating holdup - m^3/m^3
c – void fraction
α – corrugation angle
γ – angle with the horizontal for falling film or corrugation channel
Θ - contact angle
g – gravity acceleration
R – universal constant of the gases
T – absolute temperature
S – side dimension of corrugation – m
u_{Ls} - liquid phase superficial velocity – m / s
u_{Gs} – vapor phase superficial velocity – m / s
μ_L – liquid viscosity – kg / m.s
μ_v – μ_G – vapor viscosity – kg / m.s
μ_w – water viscosity - kg / m.s
ρ_L - liquid density – kg / m^3
ρ_v – vapor density - kg / m^3
ρ_w – water density - kg / m^3
ε – void fraction of packing
Φ - packing parameter (function of packing type, size and G_L)

ψ - ratio (density of water/density of liquid)
d'_p – diameter of a sphere with the same superficial area of the packing element
dc – column diameter
S_C - Schmidt number
S_{CV} - Schmidt number of the vapor phase
S_{CL} - Schmidt number of the liquid phase
D – diffusivity
D_L – liquid diffusion coefficient – m^2/s
D_V – vapor diffusion coefficient - m^2/s
σ - liquid surface tension - N/m
σ_c – critical surface tension – N/m
Z – height of the packed bed
N – number of theoretical stages
m – slope of equilibrium line
a_e – effective interfacial area (m^2 / m^3)
a_w – wetted surface area of packing (m^2 / m^3)
a_p - specific surface of the packing (m^2 / m^3)
k_G - k_V – gas-phase mass transfer coefficient
k_L – liquid-phase mass transfer coefficient
μ_r – relation between liquid viscosity at the packing bed temperature and viscosity of the water at reference temperature of 20 °C

$$R_{eL} = \frac{4\delta u_{Le}\rho_L}{\mu_L}$$ (Reynolds number for liquid)

$$F_{rL} = \frac{u_L^2}{Sg}$$ (Froude number for liquid)

$$W_{eL} = \frac{u_L^2\rho_L S}{\sigma g_c}$$ (Weber number for liquid)

5. References

Berg, L., Ratanapupech, P., Yeh, A. I. (1984). Use of packed rectification columns in extractive distillation. *AIChE Journal*, v. 30, 5, pp. 845.

Bessou, V., Rouzineau, D., Prévost, M., Abbé, F., Dumont, C., Maumus, J. P., Meyer, M. (2010). Performance characteristics of a new structured packing. *Chemical Engineering Science*, v. 65, pp. 4855.

Billet, R. and Mackowiak, J. (1988). Application of Modern Packings in Thermal Separation Processes, *Chemical Engineering Technology*, v. 11, 2, pp. 213.

Billet, R., Schultes, M. (1993) Predicting Mass Transfer in Packed Towers, *Chemical Engineering Technology*, v. 16, 1.

Billingham, J.F., Lockett, M.J. (1999). Development a new generation of structured packings for distillation. *Trans IchemE*, v. 77 (A), pp. 583-587.

Bolles, W. L.; Fair, J. R. (1982). Improved mass-transfer model enhances packed column design. *Chemical Engineering*, v. 89(14), pp. 109-116.

Bravo, J. L., Fair, J. R. (1982). Generalazed correlation for mass transfer in packed distillation columns. *Ind. Eng. Chem. Proc. Des. Dev*., v.21, pp. 162.

Bravo, J. L., Patwardhan, A. A., Edgar, T. F. (1992). Influence of Effective Interfacial Areas in Operation and Control of Packed Distillation Columns, *Industrial Engineering Chemistry Research*, v. 31, pp. 604.

Bravo, J. L.; Rocha, J. A.; Fair, J. R. (1997). Mass-transfer in gauze packings. *Hydrocarbon Processing*, v. 64, n. 1, pp. 91-95.

de Brito, H. M., von Stockar, U. (1994). Effective mass-transfer area in a pilot plant column equipped with structured packings and with ceramic rings. *Industrial and Engineering Chemistry Research*, v. 33, pp. 647-656.

Brunazzi, E., Nardini, G., Paglianti, A., Petrarca, L. (1995). Interfacial Area of Mellapak Packing: Absorption of 1,1,1-Trichloroethane by Genosorb 300, *Chemical Engineering Technology*, v. 18, pp. 248.

Brunazzi, E., Pagliant, A. (1997). Liquid Film Mass-Transfer Coefficient in a Column Equipped with Structured Packings, *Ind. Eng. Chem. Res.*, 36, pp. 3792.

Caldas, J. N., de Lacerda, A. I. (1988). Torres Recheadas, JR Editora Técnica, Rio de Janeiro, Brazil.

Carlo, L. Del, Olujić, Ž., Pagliant, A. (2006). Comprehensive Mass Transfer Model for Distillation Columns Equipped with Structured Packings, *Ind. Eng. Chem. Res.*, 45, pp. 7967.

Carrillo, F., Martin, A., Rosello, A. (2000). A shortcut method for the estimation of structured packings HEPT in distillation. *Chemical Engineering & Technology*, v. 23, n. 5, pp. 425-428.

Cornell, D., Knapp, W. G., Close, H. J., Fair, J. R. (1960). Mass transfer efficiency packed columns (Part 2), *Chem. Eng. Progr.*, v. 56, 8, pp. 48.

Darakchiev, S., Semkov, K. (2008). A study on modern high-effective random packing for ethanol-water rectification, *Chemical Engineering Technology*, v. 31, 7, pp. 1.

Eckert, J. S. (1970). Selecting the proper distillation column packing. *Chemical Engineering Progress*, v. 66, 3, pp. 39.

Eckert, J. S. (1975). How tower packings behave. *Chemical Engineering*, v. 82, pp. 70.

Ellis, 1953

Fair, J. R., Bravo, J. L. (1987). Prediction of Mass Transfer Efficiencies and Pressure Drop for Structured Tower Packings in Vapor/Liquid Service, *Institution of Chemical Engineers Symposium Series*, n^0. 104, A183.

Fair, J. R., Seibert, F., Behrens, M., Saraber, P. P., Olujić, Ž. (2000). Structured packing performance – experimental evaluation of two predictive models, *Industrial & Engineering Chemistry Research*, v. 39, 6, pp. 1788.

Fischer, L., Bühlmann, U., Melcher, R. (2003). Characterization of high-performance structured packing. *Trans IchemE*, v. 81, pp. 79-84.

Henley, E. J., Seader, J. D. (1981). Equilibrium-stage separation operations in chemical engineering, New York, John Wiley & Sons.

Higbie, R. (1935). The Rate of Absorption of a Pure Gas into a Still Liquid During Short Period of Exposure, *Transactions of the American Institute of Chemical Engineers*, v. 31, pp. 365.

Kister, H. Z. (1992). *Distillation design*. New York, McGraw-Hill.

Laraqui, F., Lévesque, S., Grandjean, B.P.A. (2008). Seamless mass transfer correlations for packed beds bridging random and structured packings, *Ind. Eng. Chem. Res.*, v. 47, pp. 3274-3284.

Lévêque, J., Rouzineau, D., Prévost, M., Meyer, M. (2009). Hydrodynamic and mass transfer efficiency of ceramic foam packing applied to distillation. *Chemical Engineering Science*, v. 64, pp. 2607-2616.

Li, H. L., Ju, Y. L., Li, L. J., Xu, D. G. (2010). Separation of isotope ^{13}C using high-performance structured packing, *Chemical Engineering and Processing*, v. 49, pp. 255-261.

Linek, V., Petricek, P., Benes, P., Braun, R. (1984). Effective Interfacial Area and Liquid Side Mass Transfer coefficients in Absorption Columns Packed with Hydrophilised and Untreated Plastic Rings, *Chemical Research Design*, v. 62, pp. 13.

Linek, V., Moucha, T., Rejl, F.J. (2001). Hydraulic and mass transfer characteristics of packings for absorption and distillation columns. Rauschett-Metall-Sattel-Rings, *Trans IchemE*, v. 79, pp. 725-732.

Lockett, M. J. (1988). Easily predict structured-packing HETP, *Chemical Engineering Progress*, v. 94, 1, pp. 60.

Macedo, E. A., Skovborg, P., Rasmussen, P. (1990). Calculation of phase equilibria for solutions of strong electrolytes in solvent-water mixtures, *Chemical Engineering Science*, v. 45, 4, pp. 875.

Machado, R. S., Orlando Jr. A. E., Medina, L. C., Mendes, M.F., Nicolaiewsky, E. M. A. (2009). Lube oil distillation – Revamping and HETP Evaluation. *Brazilian Journal of Petroleum and Gas*, v. 3, 1, pp. 35.

Mori, H., Ito, C., Oda, A., Aragaki, T. (1999). Total reflux simulation of packed column distillation, *Journal of Chemical Engineering of Japan*, v. 32, pp.69.

Mori, H., Oda, A., Kunimoto, Y., Aragaki, T. (1996). Packed column distillation simulation with a rate-based method. *Journal of Chemical Engineering of Japan*, v. 29, pp. 307.

Mori, H., Ito, C., Taguchi, K., Aragaki, T. (2002). Simplified heat and mass transfer model for distillation column simulation. *Journal of Chemical Engineering of Japan*, v. 35, pp. 100.

Mori, H., Ibuki, R., Tagushi, K., Futamura, K., Olujić, Ž. (2006). Three-component distillation using structured packings: Performance evaluation and model validation, *Chemical Engineering Science*, v. 61. pp. 1760-1766.

Murrieta, C. R. et al. (2004). Liquid-side mass-transfer resistance of strucutured packings. *Industrial & Engineering Chemistry Research*, v. 43, 22, pp. 7113.

Nawrocki, P. A., Xu, Z. P. (1991). Chuang, K. T., Mass transfer in structured corrugated packing. *Canadian Journal of Chemical Engineering*, v. 69, 6, pp. 1336.

Nicolaiewsky, E. M. A. (1999). *Liquid Film Flow and Area Generation in Structured Packing Elements*. Ph.D. Dissertation, Escola de Quimica/UFRJ, Rio de Janeiro, Brazil.

Nicolaiewsky, E. M. A., Fair, J. R. (1999). Liquid flow over textured surfaces. 1. Contact angles. *Industrial and Engineering Chemistry Research*, v. 38, 1, pp. 284.

Nicolaiewsky, E. M. A., Tavares, F. W., Krishnaswamy, R., Fair, J. R. (1999). Liquid Film Flow and Area Generation in Structured Packed Columns, *Powder Technology*, v. 104, 84.

Olujić, Ž. (1997). Development of a Complete Simulation Model for Predicting the Hydraulic and Separation Performance of Distillation Columns Equipped with Structured Packings, *Chemical and Biochemical Engineering Quaterly*, v. 11, 1, pp. 31.

Olujić, Ž., Kamerbeek, A. B., Grauuk, J. (1999). A Corrugation Geometry Based Model for Efficiency of Structured Distillation Packing, *Chemical Engineering and Processing*, v. 38, pp. 683.

Olujić, Ž. (1999). Effect of column diameter on pressure drop of a corrugated sheet structured packing. *Trans IChemE*, 77, Part A.

Olujić, Ž., Seibert, A. F., Fair, J. R. (2000). Influence of corrugation geometry on the performance on structured packings: an experimental study, *Chemical Engineering and Processing*, v. 39, pp. 335.

Olujić, Ž., Seibert, A. F., Kaibel, B., Jansen, H., Rietfort, T., Zich, E. (2003). Performance characteristics of a new high capacity structured packing, *Chemical Engineeirng and Processing*, v. 42, pp. 55.

Olujić, Z., Behrens, M., Collo, L., Paglianti, A. (2004). Predicting the efficiency of corrugated sheet structured packings with large specific surface area. *Chemical and Biochemical Engineering Quarterly*, v. 18, pp. 89.

Onda, K., Takeuchi, H., Okumoto, Y. (1968a). Mass transfer coefficients between gas and liquid phases in packed columns. *Journal of Chemical Engineering of Japan*, v. 1, 1, pp. 56.

Onda, K., Sada, E., Takeuchi, H. (1968b). Gas absorption with chemical reaction in packed columns. *Journal of Chemical Engineering of Japan*, v. 1, 1, pp. 62.

Orlando Jr., A. E. (2007). Análise de desempenho de coluna de destilação contendo recheio estruturado, MSc. Dissertation, Escola de Química,UFRJ, Rio de Janeiro, Brazil.

Orlando Jr, A. E., Medina, L. C., Mendes, M. F., Nicolaiewsky, E. M. A. (2009). HETP evaluation of structured packing distillation column. Brazilian Journal of Chemical Engineering, v. 26, 3, pp.619.

Perry, R. H., Green D. (1997). Perry´s Chemical Engineering Handbook, 7th Edition, New York, McGraw-Hill.

Piché, S., Lévesque, S., Grandjean, B.P.A., Larachi, F. (2003). Prediction of HETP for randomly packed towers operation: integration of aqueous and non-aqueous mass transfer characteristics into one consistent correlation. *Separation and Purification Technology*, v. 33, pp. 145.

Puranik, S. S., Vogelpohl, A. (1974). Effective interfacial area in packed columns, *Chemical Engineering Science*, v. 29, pp. 501.

Reid, R. C., Prausnitz, J. M., Poling, B. E. (1987). The properties of gases and liquids, 4th Edition, New York, McGraw-Hill.

Rocha, J. A., Bravo, J. L., Fair, J. R. (1985). Mass Transfer in Gauze Packings, *Hydrocarbon Proc*essing, v. 64, 1, pp. 91.

Rocha, J. A., Bravo, J. L., Fair, J. R. (1993). Distillation columns containing structured packings: a comprehensive model for their performance. 1. Hydraulic models. *Industrial & Engineering Chemistry Research*, v. 32, 4, pp. 641.

Rocha, J.A., Escamilla, E.M., Martínez, G. (1993). Basic design of distillation columns filled with metallic structured packings. *Gas Separation & Purification*, v. 7 (1), pp. 57-61.

Rocha, J. A., Bravo, J. L., Fair, J. R. (1996). Distillation Columns Containing Structured Packings: A Comprehensive Model for their Performance. 2. Mass-Transfer Model, *Industrial Engineering Chemistry Research*, v. 35, pp. 1660.

Senol, A. (2001). Mass transfer efficiency of randomly-packed column: modeling considerations, *Chemical Engineering and Processing*, v. 40, pp. 41-48.

Shulman, H. J., Ullrich, C. F., Proulx, A. Z., Zimmerman, J. O. (1955). Performance of packed columns. II. Wetted and effective-interfacial areas, gas and liquid phase mass transfer rates. *AICHE Journal*, v. 1, 2, pp. 253.

Sinnott, R. K. (1999). Coulson and Richardson´s Chemical Engineering, *Chemical Engineering Design*, 3rd Edition, v. 6, Oxford, Butterworth-Heinemann.

Spiegel, L., Meier, W. (2003). Distillation columns with structured packings in the next decade, *Trans IchemE*, v. 81, pp. 39-47.

Shi, M. G., Mersmann, A. (1985). Effective Interfacial Area in Packed Columns. *German Chemical Engineering*, 8, 87.

Soares, R. B. (2010). Estudo da destilação extrativa salina em coluna recheada para a produção de etanol. Master Thesis, PPGEQ/UFRRJ, Seropédica, Rio de Janeiro, Brazil.

Suess P., Spiegel, L. (1992). Hold-up of mellapak structured packings. *Chemical Engineering and Processing*, v. 31, 2, pp. 119.

Xu, Z. P., Afacan, A., Chuang, K. T. (2000). Predicting mass transfer in packed columns containing structured packings. *Trans IChemE*, v. 78, pp. 91.

Wagner, I., Stichlmair, J., Fair, J. R. (1997). Mass transfer in beds of modern, high-efficiency random packings. *Industrial and Engineering Chemistry Research*, v. 36, pp. 227.

Wang, G. Q., Yuan, X. G., Yu, K. (2005). Review of Mass-Transfer Correlations for Packed Columns. *Industrial & Engineering Chemistry Research*, v. 44, 23, pp. 8715.

4

Mathematical Modelling of Air Drying by Adiabatic Adsorption

Carlos Eduardo L. Nóbrega[1] and Nisio Carvalho L. Brum[2]
[1]*Centro Federal de Educação Tecnológica, CEFET-Rio*
[2]*Universidade Federal do Rio de Janeiro, COPPE/UFRJ*
Brazil

1. Introduction

The careful control of ambient air moisture content is of concern in many industrial processes, with diverse applications such as in metallurgical processes or pharmaceutical production. In the air-conditioning field, the increasingly concern with sick building syndrome also brings humidity control into a new perspective. Underestimated ventilation rates might result in poor indoor air quality, with a high concentration of volatile organic compounds, smoke, bacteria and other contaminants. Epidemiological studies indicate a direct connection between inadequate levels of moisture and the incidence of allergies and infectious respiratory diseases. A popular method of lowering the concentration of contaminants is to increase the ventilation rates. In fact, the fresh air requirement per occupant/hour imposed by the current air-quality standard has doubled over the last three decades. Since the fresh air has to be brought to the thermal comfort condition, increased ventilation rates imply increased thermal loads, which in turn will demand chillers with increased cooling capacity. Accordingly, there is a trade-off between indoor air quality and energy consumption, which is also of main concern of private and public sectors.

Figure (1.a) shows an evaporative cooling system. It essentially consists of a chamber through which air is forced through a water shower. It is a sound system from air-quality, energy consumption and ecological viewpoints. The air quality is provided by a continuous air room change, with no air recirculation. Since the cooling effect is provided by evaporation of water into air, the energy consumption is restricted to the pumping power, which is usually low when compared to the energy needs of a compressor. Unlike vapor-compression systems, which usually employ ozone-depleting refrigerants, evaporative cooling systems exclusively employ water as the refrigerant.

Figure (1.b) shows that the evaporative cooling process is isenthalpic, which means that the air stream enthalpy remains unaltered as it flows through the evaporative cooler. Accordingly, the increase in the air stream humidity occurs at the expense of its own sensible energy, and the air stream is cooled and humidified as it crosses the evaporative cooler. Since the heat and mass transfer processes are mutually dependent, the air stream humidity at the inlet of the evaporative cooler has to be significantly low, if an appreciable cooling effect is to be achieved. Unfortunately this is not always the case, and this cooling technique is not as effective as traditional vapour-compression systems, being restricted to applications on low humidity areas (Khuen et al., 1998).

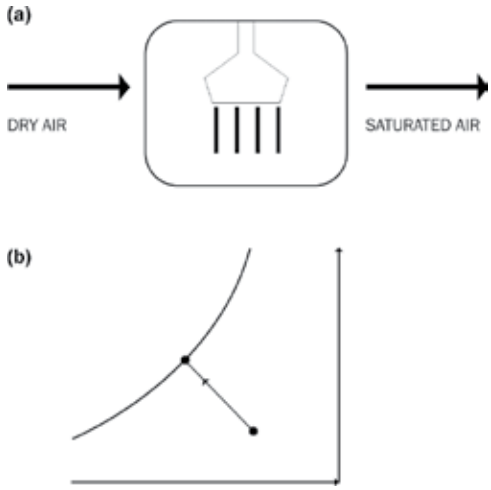

Fig. 1. Evaporative cooling system

One possible way to overcome this restriction would be artificially dry the air stream before it is admitted to the evaporative cooler, which can be accomplished by using a solid sorbent air dryer. Adsorption is primarily used for component separation from a gaseous mixture, and is widely employed in the chemical industry. The main advantage is that the adsorptive material pore size can be designed for selective adsorption of a given component, allowing even trace amounts to be removed (Chung and Lee, 2009). However, the removal of moisture from air for comfort cooling has distinguished features from gas separation usually practiced in the chemical industry.

Consider Figure (2.a), which shows an active desiccant rotor. It consists of a cylindrical drum, fitted with a micro-channel mesh, usually made of aluminum or plastic. The structure material is coated with silica-gel, which can be manufactured as a substrate. Silica-gel is a form of silicon dioxide derived from sodium silicate and sulfuric acid, which has good affinity to water vapor and an adsorbing capacity of as much as 40% of its own weight. Regular density silica gel typically offers an adsorptive area 400m^2 per cm^3, with an average porous radius corresponds to 11Å. The present model relies on the existence of an air layer in close contact with the solid, from which the adsorbed vapor molecules stem. The silica-gel affinity to water can be explained by considering that the state of any solid particle is considerably different, depending on its located on the core or on the solid surface. A particle located in the interior of the solid is neutral equilibrium, uniformly surrounded by other particles, and has minimum potential energy. Conversely, a particle on the surface is subjected to a greater potential energy, which is a representation of the required work to move the particle from the interior to the surface, agains the atractive molecules forces. The nearby vapor molecular are attracted form the air layer to the adsoprtive surface, in an effort to restore equilibrium (Masel, 1996). The desiccant wheel operates between two air streams, the process air stream, which is the stream to be dehumidified, and the regeneration stream, which is a high temperature air stream required to purge the humidity from the desiccant felt. At the process stream side, the humidity migrates from the air to the desiccant coated walls of the channel. Conversely, when the regeneration stream is forced through the micro-channels, the desiccant coat returns the humidity back to the air stream, which is dumped back to the atmosphere. Accordingly, the humidity at the outlet of the process stream can

become extremely low, enabling a much more significant temperature drop through the evaporative cooler. Similarly to the evaporative cooling process, the heat and mass transfer in the desiccant cooling process are also intimately connected: Consider the adsorption process, in which the humidity is attracted to the desiccant felt from the air stream. As the air is dehumidified, two factors contribute to increase its temperature, namely the heat of adsorption, which is the heat released as the vapor molecules are adsorbed, and ordinary heat transfer from the micro-channel walls, which have been exposed to the high temperature regeneration stream during the previous period of time. Since each micro-channel can be taken as an adiabatic cell, it can be concluded that the decrease in air humidity must exactly match the increase in air sensible energy, with mutually dependent effects as earlier described. Accordingly, the air crosses the desiccant rotor isenthalpically as shown in Figure (2.b), in the opposite direction of the evaporative cooling, which has been supported by numerical and experimental evidence (Nobrega and Brum, 2009a, 2009b).

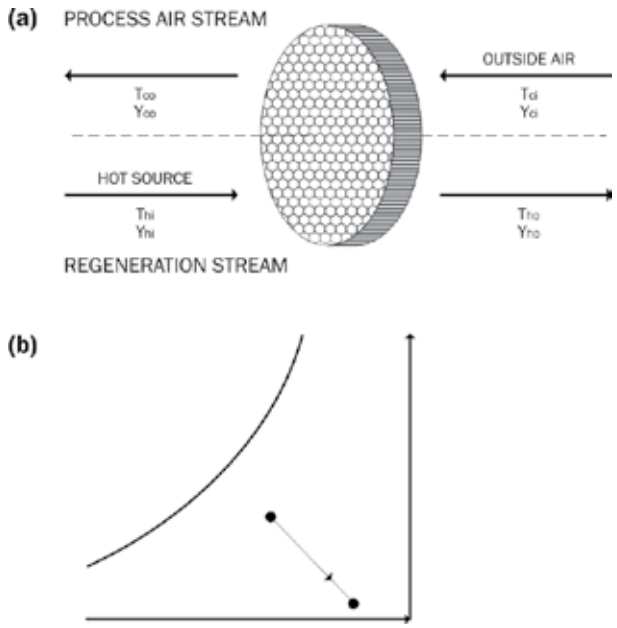

Fig. 2. Active desiccant rotor

The purpose of the modeling is to simulate what the process air outlet state would be, for given values of the inlet air state, length of the channel, period of revolution, desiccant material, regeneration temperature and other design parameters.

2. Mathematical model

The mathematical modelling of desiccant wheels is of key importance for equipment developers, so as to provide them with guidelines for improved design. It is also of importance to HVAC engineers, in order to access if the thermal comfort condition can be attained for a typical set of atmospheric conditions. The mathematical model relies on a number of simplifying assumptions, aiming at keeping the model (and its solution) as simple as possible, while retaining the physical meaning. An excellent review of the

mathematical modelling of adsorptive dehumidification can be found in the literature (Ge et al., 2008).

1. The micro-channels are perfectly insulated.
2. Heat and humidity transients within the air are negligible.
3. All thermo-physical properties for the fluid and the solid are considered constant.
4. The flow is hydro-dynamically and thermally developed.
5. The heat and mass transfer coefficients are assumed to be uniform along the micro-channel
6. Temperature and concentration distributions in the direction normal to the flow are taken to be uniform (lumped) within the channel and the solid.
7. The adsorption heat is modeled as a heat source within the solid material

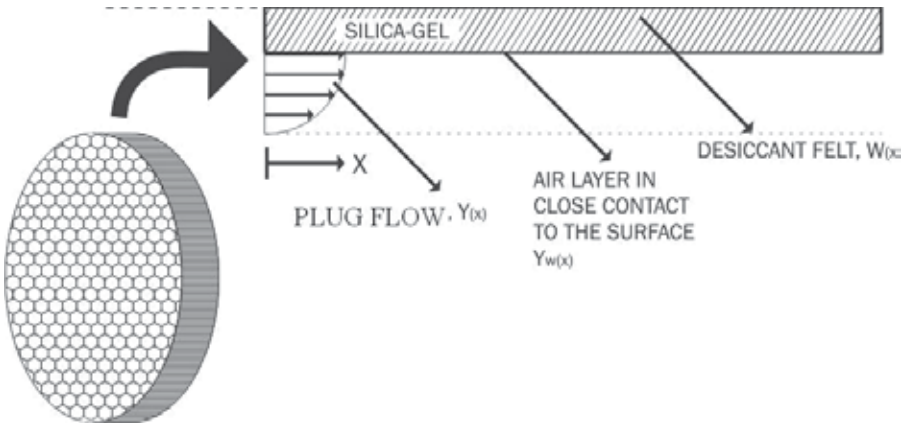

Fig. 3. Schematic of the flow channel with desiccant coating

Assumption (1) relies on symmetry between the cells, which can be represented by adiabatic surfaces. Assumption (6) is adopted in light of the small thickness of the desiccant layer (Shen & Worek, 1992), (Sphaier & Worek, 2006). Consider Figure (4.a), which represents a differential control volume which simultaneously encloses the desiccant layer and the flow channel. The mass conservation principle applied to the depicted control volume yields:

$$\dot{m}\left[\frac{1}{u_1}\frac{\partial Y}{\partial T}+\frac{\partial Y}{\partial x}\right]+f\frac{m_w}{L}\frac{\partial W}{\partial t}=0 \tag{1}$$

Consider Figure (4.b), which represents a differential control volume which solely encloses the desiccant layer. The mass conservation principle applied to the depicted control volume yields

$$f\frac{m_w}{d_h L}\frac{\partial W}{\partial t}=2h\left(Y-Y_w\right) \tag{2}$$

Figure (5.a) represents a differential control volume which simultaneously encloses the desiccant layer and the air stream. The energy conservation principle applied to the depicted control volume yields

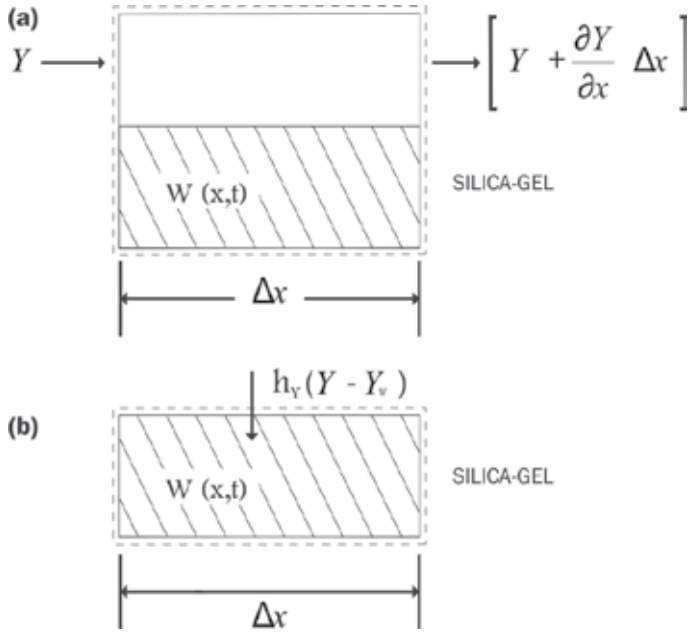

Fig. 4. Differential control volumes for mass balances

$$\dot{m}\left[\frac{1}{u_1}\frac{\partial H_1}{\partial T}+\frac{\partial H_1}{\partial x}\right]+\frac{m_w}{L}\frac{\partial H_w}{\partial t}=0 \tag{3}$$

Consider Figure (5.b), which represents a differential control volume which solely encloses the airstream. The mass conservation principle applied to the depicted control volume yields:

$$\dot{m}\left[\frac{1}{u_1}\frac{\partial H_1}{\partial T}+\frac{\partial H_1}{\partial x}\right]=2h\left(Y_w-Y\right)\frac{\partial H_1}{\partial Y}+2h_h\left(T_w-T_1\right) \tag{4}$$

In which the first term on the right hand side stands for the heat transfer between the sorbent and the air, whereas the second term represents the heat released during the adsorption. Defining the following non-dimensional parameters,

$$x^*=\frac{2h_h d_h x}{\dot{m}\dfrac{\partial H_1}{\partial T_1}} \tag{5}$$

$$t^*=\frac{2h_h d_h x t}{m_w C_{wr}} \tag{6}$$

After extensive algebra, Equations (1)-(4) can be rewritten as

$$\frac{\partial Y}{\partial x^*}=\left(Y_w-Y\right) \tag{7}$$

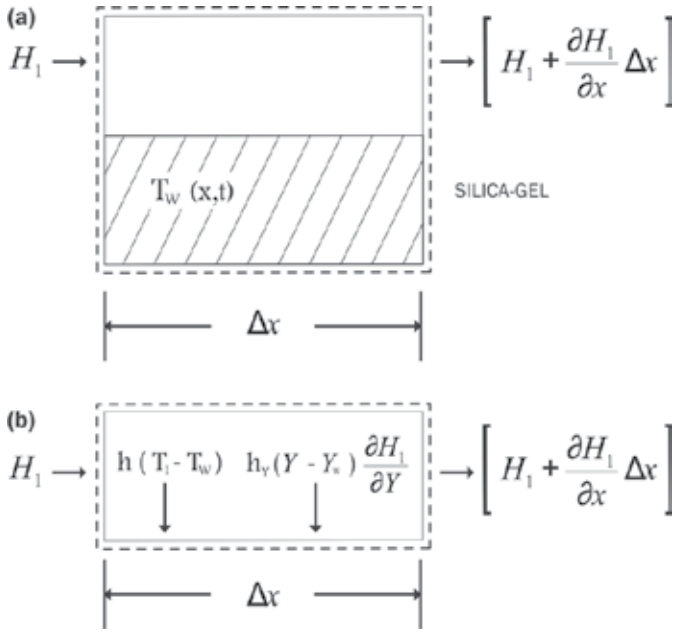

Fig. 5. Differential control volumes for energy balances

$$\frac{\partial W}{\partial t^*} = \lambda_2 \left(Y - Y_w \right) \tag{8}$$

$$\frac{\partial T_1}{\partial x^*} = \left(T_w - T \right) \tag{9}$$

$$\frac{\partial T_w}{\partial t^*} = \left(T - T_w \right) + \lambda_1 \left(Y - Y_w \right) \tag{10}$$

With

$$\lambda_2 = \frac{C_{wr}}{f \dfrac{\partial H_1}{\partial T_1}} \tag{11}$$

$$\lambda_2 = \frac{Q}{\dfrac{\partial H_1}{\partial T_1}} \tag{12}$$

Equation (12) represents the heat of adsoprtion, released as the vapor molecule is adsorbed within the silica-gel. The adsorption heat is comprised of the condensation heat plus the wettability heat, which accounts for reducing the degrees of movement freedom of a gas molecule from three to two, as it is captured by a surface. The current modeling allows different approaches to to the adsoprtion heat, as both analytical and experimentally obtained expressions for Q could be easily fitted to Eq. (12). For regular density siilica-gel, the following expression was experimentally obtained (Peasaran & Mills, 1987),

$$\begin{bmatrix} Q = -12400W + 3500\ ,\ W \le 0.05 \\ Q = -1400W + 2950\ ,\ W > 0.05 \end{bmatrix} \text{kJ/kg} \tag{13}$$

It shows that the heat release is not constant during the adsorption process, exhibiting a small reduction as the adsorption develops. This could be explained by observing that the first adsorbed molecules are attracted to the most energetically unbalanced sites. As the moisture uptake continues, the remaining spots to be occupied require less bonding energies, approaching ordinary latent heat as the solid becomes saturated. From the mathematical point of view, the problem is still undetermined, since there are five unknowns (T_1, T_w, Y, Y_w and W) and only four equations, (7) to (10). The missing equation is the adsorption isotherm, which is characteristic of each adsorptive material. For regular density silica-gel, the following expression was experimentally obtained,

$$\begin{aligned} \phi_w =& 0.0078 - 0.0579W + 24.16554W^2 \\ & -124.78W^3 + 204.2264W^4 \end{aligned} \tag{14}$$

Equations (15) and (16) are auxiliary equations, which relates the partial pressure of the air layer with the absolute humidity,

$$P_{ws} = \exp\left(23.196 - \frac{3816.44}{T_w - 46.13} \right) \tag{15}$$

$$Y_w = \frac{0.62188 p_w}{p_{atm} - p_w} = \frac{0.62188 \phi_w}{\frac{p_{atm}}{p_{ws}} - \phi_w} \tag{16}$$

The periodic nature of the problem implies an iterative procedure. Both initial distributions of temperature and humidity within the solid are guessed, and equations (7) to (10), assume the form of tridiagonal matrices, as a result of the discretization using the finite-volume technique, with a fully implicit scheme to represent the transient terms (Patankar, 1980).. By the end of the cycle, both calculated temperature and moisture fields are compared to the initially guessed. If there is a difference in any nodal point bigger than the convergence criteria established for temperature and moisture content,

$$Crit.\ \ Conv._{temp} = \frac{T_w(x,0) - T_w(guess)(x,0)}{T_w(x,0)} \tag{17}$$

$$Crit.\ \ Conv._{mass} = \frac{W(x,0) - W(guess)(x,0)}{W(x,0)} \tag{18}$$

the procedure is repeated, using the calculated fields as new guesses for the initial distributions. Figure (6) shows a simplified fluxogram for the numerical solution. Figures (7) and (8) show mass and temperature distributions along the desiccant felt, at selected angular positions. The curves relative to 0 and 2π are indistinguishable, as the periodic behaviour was attained. The average "hot outlet" enthalpy during a cycle is defined as

$$\overline{H_{ho}} = \frac{1}{P_h} \int_0^{p_h} H_{ho} dt^* \tag{19}$$

Since the wheel is to store neither energy nor mass after a complete cycle,

$$\sum \dot{m}_i H_i = \sum \dot{m}_o \bar{H}_o \tag{20}$$

$$\dot{m}_h H_{hi} + \dot{m}_c H_{ci} = \dot{m}_h \frac{1}{p_h} \int_0^{p_h} H_{ho}\, dt^* + \dot{m}_c \frac{1}{p_c} \int_0^{p_c} H_{co}\, dt^* \tag{21}$$

the normalized difference between the two sides of equation (21) is defined as the Heat Balance Error (HBE), which was found to be of the order of 0.1% for all simulations carried.

$$HBE = \frac{\dot{m}_h H_{hi} + \dot{m}_c H_{ci} - (\dot{m}_h \frac{1}{p_h} \int_0^{p_h} H_{ho}\, dt^* + \dot{m}_c \frac{1}{p_c} \int_0^{p_c} H_{co}\, dt^*)}{\dot{m}_h H_{hi} + \dot{m}_c H_{ci}} \tag{22}$$

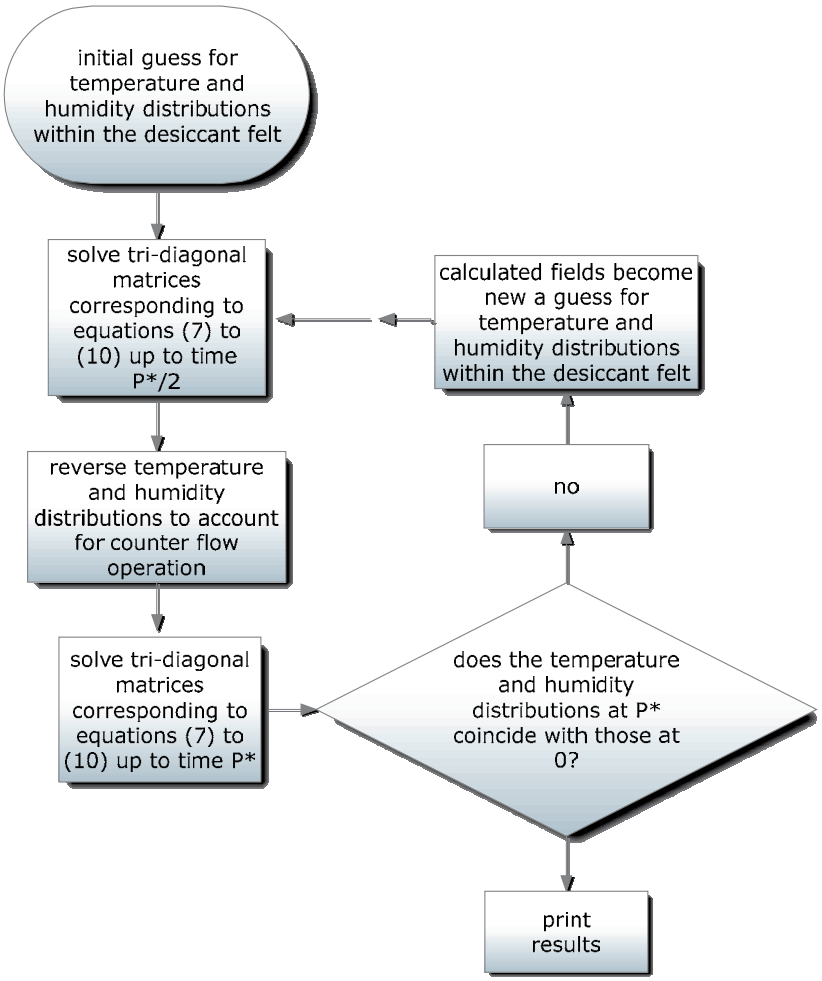

Fig. 6. Fluxogram of the numerical solution

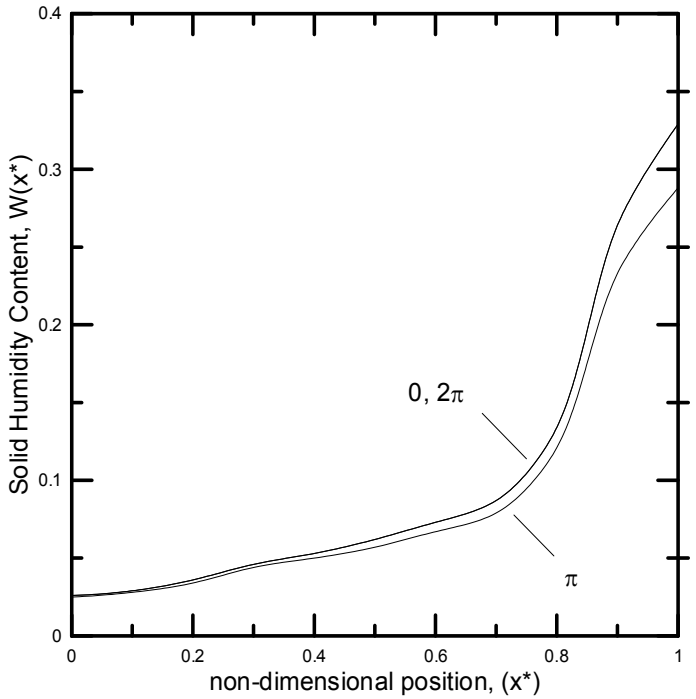

Fig. 7. Mass distributions at selected angular positions, P*40.0, NTU=16.0, T_{reg}=100°C.

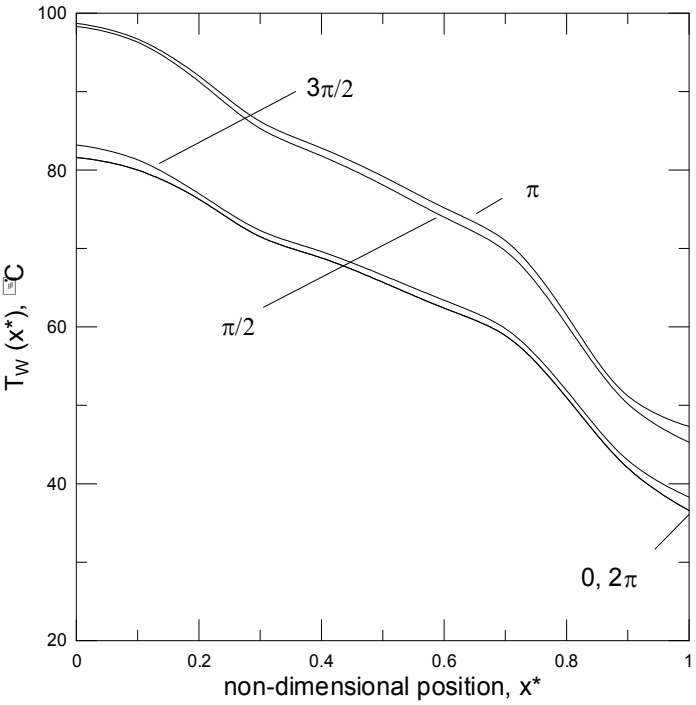

Fig. 8. Temperature distributions at selected angular positions P*40.0, NTU=16.0, T_{reg}=100°C.

3. Results

Since the active desiccant dehumidification is an isenthalpic process, it is not possible to establish a definition for the efficiency based on enthalpy. Accordingly, it is usual do define a dehumidification effectiveness as

$$\varepsilon_{dw} = \frac{Y_{ci} - Y_{co}}{Y_{ci}}$$

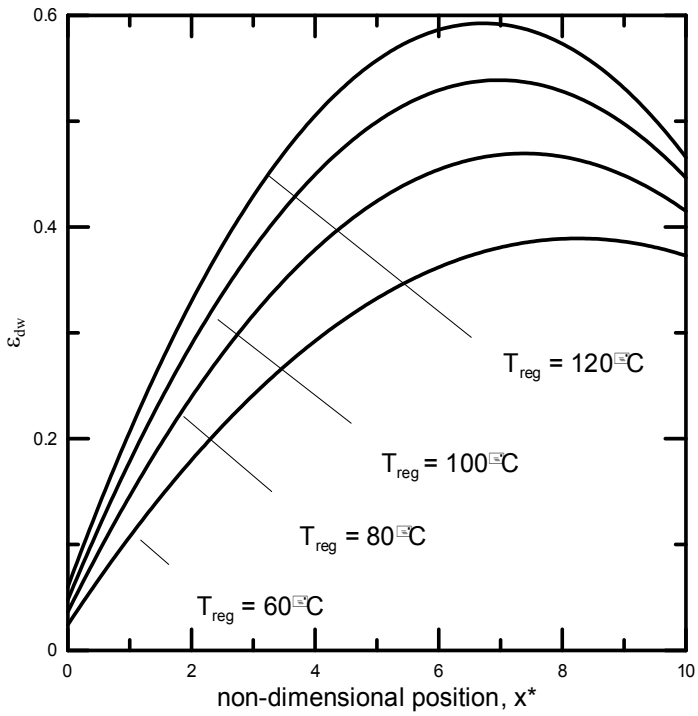

Fig. 9. Effectiveness-NTU chart, P*=10.0

The non-dimensional position defined by Eq. (5) has a remarkable similarity to the NTU parameter, commonly found in heat exchanger analysis. Accordingly, Figure (9) shows the influence of the micro-channel lentgh over the dehumidification effectiveness. It can be seen that the regeneration temperature has a significant influence over the moisture removal. Figure (9) shows the existence of an optimum micro-channel length, which can be explained by observing that the regeneration stream is admitted at x* = 0. Accordingly, the closer the position is to the end of the channel (x* =10.0), the lower will be the temperature, allowing for some of the moisture to be re-sorbed by the desiccant felt (Zhang et al., 2003). Figure (10) shows that, for higher non-dimesional periods of revolution P*, the optimum length is higher, due to the longer exposure to to regeneration stream and consequential higher average temperatures along the desiccant felt. Figure (11) shows the influence of the non-dimensional period of revolution over the effectiveness as a function of the regeneration temperature. It can be seen that for a moderate value for the non-dimensional period (P* = 10.0), the effectiveness is oblivious to an increase in regeneration temperature, due to an

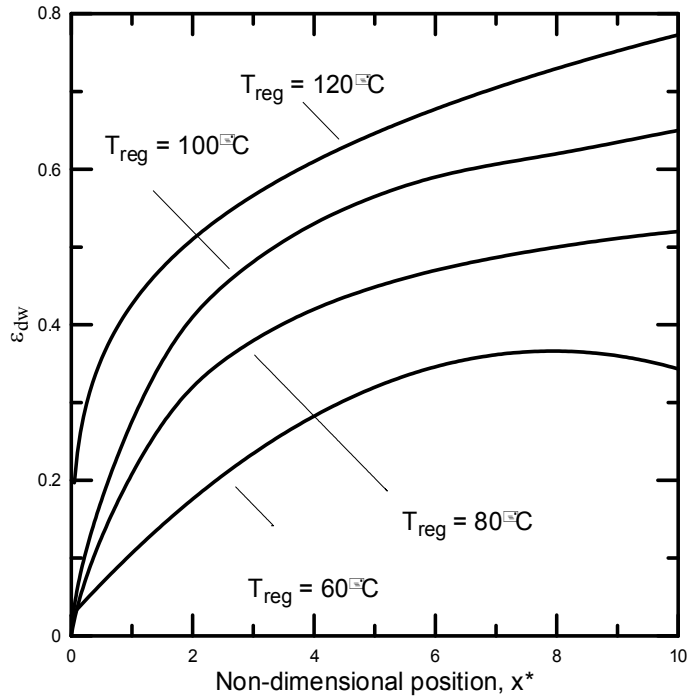

Fig. 10. Effectiveness-NTU chart, P*=80.0

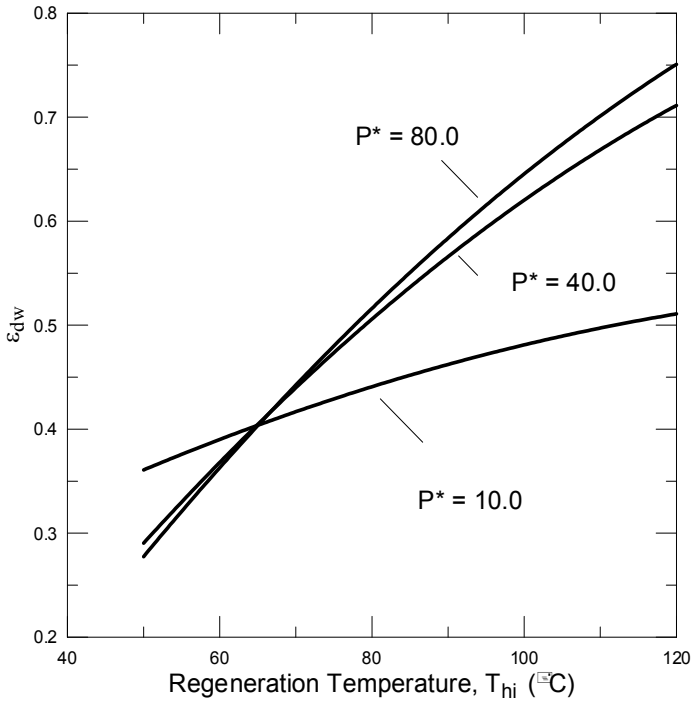

Fig. 11. Influence of P*, NTU=10.0, T_{hi} = 100°C

insufficient exposure to the hot source. Accordingly, larger values for P* will benefit from increased regeneration temperatures. Figure (12), however, shows that the dehumidification effectiveness will decrease after it reaches a maximum value, since for an infinite value for P* there would be no rotation and the heat and mass transport would completely cease.

Figure (13) shows the humidity distribution within the desiccant felt at the onset and at the end of the adsorptive process, for different regeneration temperatures. The area enclosed by these curves is a measure of the dehumidifying capacity of the equipment. It can be seen that the higher temperature enables a thorough drying of the material, resulting in a enhaced dehumidification capacity. Interesting to observe that different shapes for the moisture distribution arise, depending on the case. For the mild regeneration temperature, the moisture uptake is almost uniform aling x*, resulting in a smooth curve. Conversely, for the higher temperature, the moisture uptake is much more significant at the second half of the total length, as compared to the first half, resulting in an curve with exponential characteristic.

Figure (14) shows the humidity distribution within the desiccant felt at the onset and at the end of the adsorptive process, for different non-dimensional periods of revolution. It can be seen that for P* =10.0, the exposure to the regeneration stream is insufficient, resulting in a diminished dehumidification capacity, as the curves of minimum and maximum moisture content are undistinguishable. For a increased value of P*, represented by the dashed lines, the dehumidification capacity is enhanced, as illustrated by the greater enclosed area.

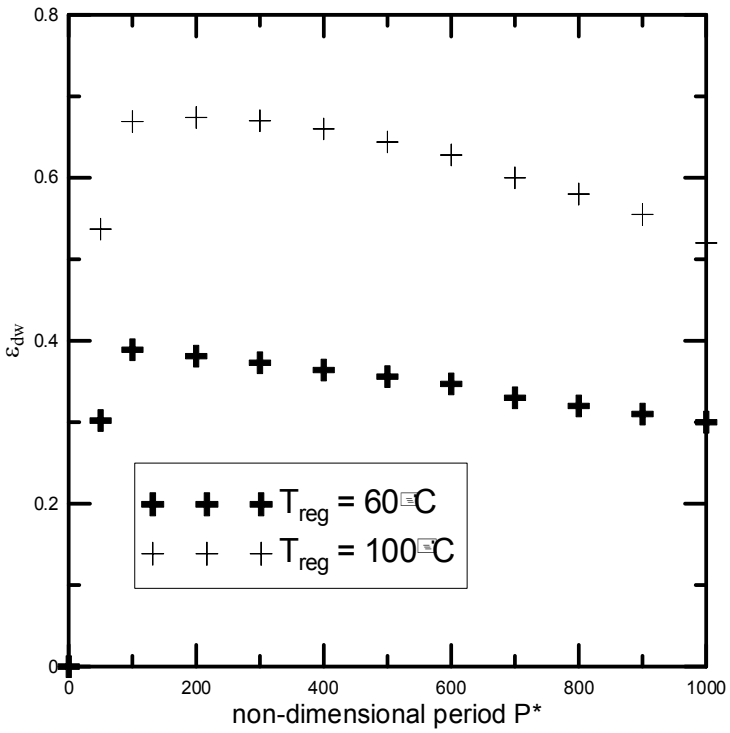

Fig. 12. Influence of P*, NTU=10.0.

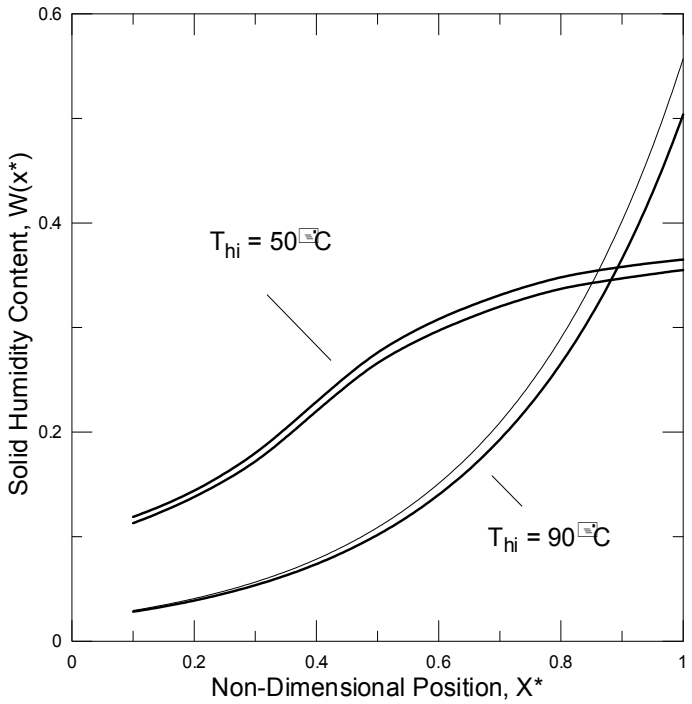

Fig. 13. Influence of T_{hi} on the Humidity Distribution, NTU=16.0, P* = 40.0

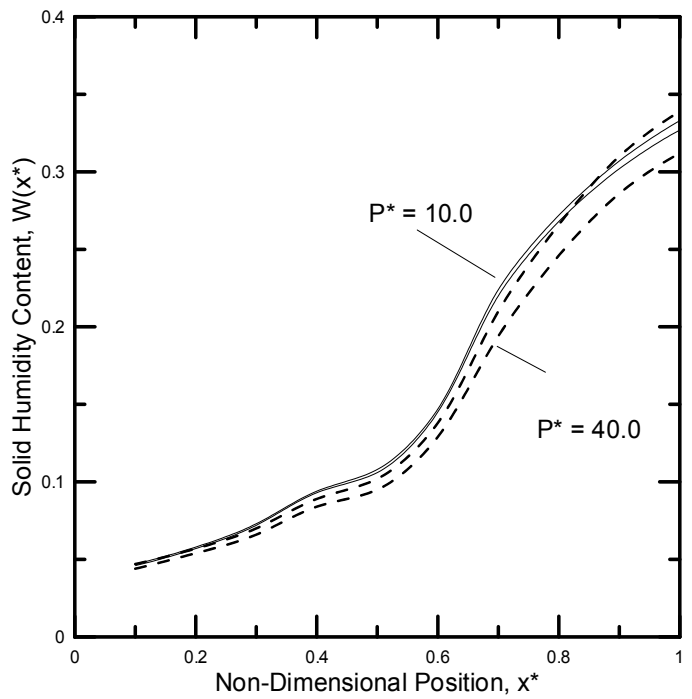

Fig. 14. Influence of P* on the Humidity Distribution, NTU=10.0, T_{hi} = 100°C

Bearing in mind that the outside air atmospheric conditions can present a significant variation throughout the day, it is usefull to define a dynamic control for the desiccant rotor operation. For instance, supposing a steady increase of 30% in outside air relative humidity, how much would be the required increase in P*, so as to obtain a constant humidity at the process air stream outlet? Figure (15) shows the results for different increasing values for the regeneration temperature. It can be seen that for T = 60°C, an increase in 10% of the process air stream inlet will require the period of revolution to double, being unable to respond to a further increase of the relative humidity. Conversely, a higher regeneration temperature such as T = 100°C will only require a small increase in the period P*, being able to respond to a relative humidity of process air stream inlet as high as 90%.

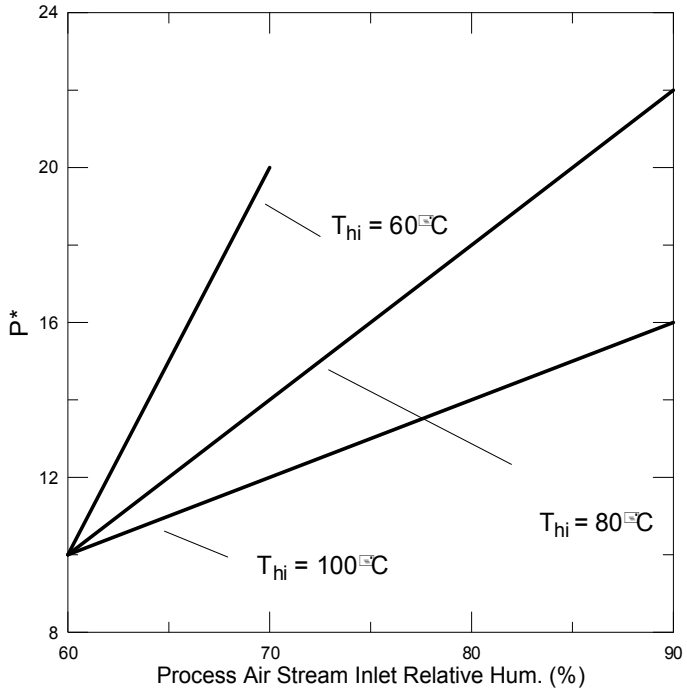

Fig. 15. Required increase in P*=10.0

4. Conclusion

A mathematical model for the heat and mass transfer on a hygroscopic material was developed, and resulting set of partial differential equations was solved using the finite-volume technique. The results showed that the process air stream outlet condition is strongly influenced by the regeneration temperature, as well as of the non-dimensional period of revolution. It was also shown that an increase on the outside air humidity can be easily handled by increasing the non-dimensional period of revolution, as long as a temperature of regeneration of at least 100°C is provided. The results for the humidity distribution along the desiccant felt show that the moisture removal capacity of silica-gel is limited, which opens an opportunity for the application of more selective materials. However, it shouldn´t be disregarded that a greater affinity to water vapour also implies a

greater amount of energy to remove the water vapour during the desorptive period. This could be of vital importance for the economic feasibility of this technology, unless an inexpensive thermal source is available.

5. Nomenclature

a	constant
c	constant
C_{wr}	wall specific heat (kJ/Kg K)
d	constant
d_h	hydraulic diameter (m)
f	desiccant mass fraction
h	heat transfer coefficient (KW/m^2)
h_y	convective mass transfer coefficient (kg/m^{2}s)
H	enthalpy of air (kJ/kg)
L	length of the wheel (m)
$\dot{m}_1$	air mass flow rate (kg/s)
m_w	mass of the wall (kg)
P	period of revolution
P_{atm}	atmospheric Pressure (Pa)
P_{ws}	saturation pressure (Pa)
Q	heat of adsorption (kJ/kg)
t	time (s)
T	temperature (°C)
u	air flow velocity (m/s)
Y	air absolute humidity (kg/kg air)
Y_L	adsorbed air layer absolute humidity (kg/kg air)
W	desiccant humidity content (kg of moisture/kg of desiccant)
x	coordinate (m)

Greek letters

λ_1	auxiliary parameter
λ_2	auxiliary parameter
ϕ_w	relative humidity of air layer
ε	effectiveness

Subscripts

ci	cold inlet
co	cold outlet
hi	hot inlet
ho	hot outlet
sat	saturation
w	desiccant channel wall
1	air

Superscript

*	non-dimensional

6. References

Chung, J.D.; Lee, D.Y., "Effect of Desiccant Isotherm on the Performance of Desiccant Wheel", International Journal of Refrigeration, 2009; (32), pp. 720-726.

Close, D.J., 1983. Characteristic Potentials for Heat and Mass Transfer Processes. *International Journal of Heat and Mass Transfer*, 1983, 26(7), pp.1098-1102.

Ge, T.S.; Li, Y.; Wang, R.Z., Dai, Y.J.., A Review of the Mathematical Models for Predicting Rotary Desiccant Wheel, *Renewable and Sustainable Energy Reviews*, 2008, (12), pp. 1485-1528.

Kuehn, R.I., (1996) *Principles of Adsorption and Reating Surfaces*, New York NY: J. Wiley & Sons, Unites States

Masel, T.H., Ramsey, J.W., Threlkeld, J.L., (1998) *Thermal Environmental Engineering*, 3rd Upper Saddle River, NJ: Prentice-Hall, Unites States

Niu, J.L.; Zhang, L.Z., (2002)Effects of Wall Thickness on Heat and Moisture Transfer in Desiccant Wheels for Air Dehumidification and Enthalpy Recovery, *International Communications in Heat and Mass Transfer*, 2002, (29), pp. 255-268.

Nobrega, C.E.L.; Brum, N.C.L., Influence of Isotherm Shape over Desiccant Cooling Cycle Performance, *Heat Transfer Engineering*, 2009, 30 (4), pp.302-308.

Nobrega, C.E.L.; Brum, N.C.L., Modeling and Simulation of Heat and Enthalpy Recovery Wheels, *Energy*, 2009, (34): 2063-2068.

Patankar, S., *Numerical Heat Transfer and Fluid Flow*, (1980) Boston, Ma: Hemisphere Publishing Co, United States.

Pesaran, A.A., Mills, A.F., Moisture Transport in silica Gel Packed Beds-Part I , *International Journal of Heat and Mass Transfer*, 1987; (30): 1051-1060.

Shen, C.M..; Worek, W.M., 1992. The Effect of Wall Conduction on the Performance of Regenerative Heat Exchangers, *Energy*, 1992, (17),pp.1199-1213.

Sphaier, C.M.; Worek, W.M., (2006), The Effect of Axial Diffusion on Enthalpy Wheels, *International Journal of Heat and Mass Transfer*, 2006, (49), pp. 1412-1419.

Zhang, X.J., Dai, Y.J., Wang, R.Z.; "A Simulation Study of Heat and Mass Transfer in a Honeycomb Structure Rotary Desiccant Dehumidifier", *Applied Thermal Engineering*, 2003, (23),pp. 989-1003.

5

Numerical Simulation of Pneumatic and Cyclonic Dryers Using Computational Fluid Dynamics

Tarek J. Jamaleddine and Madhumita B. Ray
Department of Chemical and Biochemical Engineering, University of Western Ontario, London, Ontario, Canada

1. Introduction

Drying is inherently a cross and multidisciplinary area because it requires optimal fusion of transport phenomena and materials science and the objective of drying is not only to supply heat and remove moisture from the material but to produce a dehydrated product of specific quality (Mujumdar, 2004)[1]. There are two main modes of drying used in the heat drying or pelletization processes; namely, direct and indirect modes. Each mode of drying has its merits and disadvantages and the choice of dryer design and drying method varies according to the nature of the material to be handled, the final form of the product, and the operating and capital cost of the drying process.

The drying of various materials at different conditions in a wide variety of industrial and technological applications is a necessary step either to obtain products that serve our daily needs or to facilitate and enhance some of the chemical reactions conducted in many engineering processes. Drying processes consume large amounts of energy; any improvement in existing dryer design and reduction in operating cost will be immensely beneficial for the industry.

With the advance in technology and the high demands for large quantities of various industrial products, innovative drying technologies and sophisticated drying equipment are emerging and many of them remain to be in a developmental stage due to the ever increasing presence of new feedstock and wetted industrial products. During the past few decades, considerable efforts have been made to understand some of the chemical and physical changes that occur during the drying operation and to develop new methods for preventing undesirable quality losses. It is estimated that nearly 250 U.S. patents and 80 European patents related to drying are issued each year (Mujumdar, 2004)[1]. Currently, the method of drying does not end at the food processing industry but extends to a broad range of applications in the chemical, biochemical, pharmaceutical, and agricultural sectors. In a paper by Mujumdar and Wu (2008)[2], the authors emphasized on the need for cost effective solutions that can push innovation and creativity in designing drying equipment and showed that a CFD approach can be one of these solutions. The collective effort of their research work along with other researchers in the drying industry using mathematical

modeling for the simulation of the drying mechanism in commercial dryers demonstrated the CFD capabilities and usefulness for the design and understanding of drying equipment.
In a recent paper by Jamaleddine and Ray (2010)[3], the authors presented a comprehensive review on the application of CFD for the design, study, and evaluation of lab-scale and industrial dryers. The use of different numerical methods such as the finite element, finite volume, and finite difference were fully discussed. Numerical models such as the Eulerian-Eulerian and Eulerian-Lagrangian, used for gas–solid multiphase flow systems were also discussed along with their merits, disadvantages, and the scope of their applicability. The application of Kinetic theory approach for granular flow was also discussed. The authors pointed out some of the merits and shortcomings of CFD methods in general, and the drying application, in particular. They argued that a key advantage of CFD methods in evaluating drying systems is that it makes it possible to evaluate geometric changes (different feed point layouts such as multiple entry points) and operating conditions with much less time (faster turnaround time) and expense (flexibility to change design parameters without the expense of hardware changes) than would be involved in laboratory testing. A second advantage is that CFD provides far more detailed output information (suited for trouble-shooting) and far better understanding of the dryer performance than can be obtained in a laboratory environment. By interpreting graphical predictions from a CFD solution, local conditions of all phases in the drying chamber can be evaluated and crucial information related to the dispersion of particulate material can be gathered.
Despite the fact that CFD methods can offer valuable information and a great deal of insight of the process, the use of CFD methods requires considerable expertise. Lack of in-depth knowledge of the CFD methods and insufficient proficiency in utilizing commercial CFD software packages are major concerns for implementing CFD solutions in unknown and unconventional systems. In addition, CFD models have inherent limitations and challenges. Massah et al. (2000)[4] indicated some of the computational challenges of CFD modeling in the drying applications of granular material as follows. First of all, most processes involve solids with irregular shapes and size distribution, which might not be easily captured by some models. Second, Eulerian-Eulerian CFD methods rely on the kinetic theory approach to describe the constituent relations for solids viscosity and pressure, which are based on binary collisions of smooth *spherical* particles and do not account for deviations in shape or size distribution. Finally, very little is known about the turbulent interaction between different phases; thus, CFD models might not have the ability of presenting the associated drag models for a specific case study especially when solids concentration is high. In addition to the above, note that CFD simulations of three-dimensional geometries are computationally demanding and might be costly and although in some cases, the computational effort can be reduced by modeling a two-dimensional representation of the actual geometry (mostly for axisymmetric systems), the realistic behaviour of the simulated system might not be fully captured. Some geometrical systems cannot be modeled using the above simplification and thus, the computational effort becomes a must. This argument also applies to models adopting the Eulerian-Lagrangian formulation for *dense systems* which determine the trajectories of particles as they travel in the computational domain. In addition, formulas describing cohesion and frictional stresses within solids assembly are also not well established in these models. Finally, changes in particle size due to attrition, agglomeration, and sintering are difficult to account for.

As for the heat- and mass-transfer correlations used in commercial CFD packages, very few are provided and the implementation of modified correlations or newly added ones to those already presented or provided by a commercial software demands the need for user defined function subroutines (UDF). This method can become very complicated and usually require many hours of coding and debugging. Although the heat-transfer model capabilities are well improved and capture the heat-transfer mechanism to a reasonable extent, average Nusselt number correlations are used instead of local values. This in turn, reduces the accuracy of the solution results. Additionally, the nature of the CFD equations is approximated which captures the solution results based on approximated assumptions and not on the exact solutions. From a mass-transfer capabilities point of view, mass-transfer models still lack robustness and are hardly included in the current available commercial software. The physics behind these transfer mechanisms is rich and complex, and not entirely captured by CFD methods due to its reliance on experimental observations and correlated equations. Thus, although *qualitative* predictions might be attainable to a reasonable extent, *quantitative* predictions are still the biggest challenge.

2. Numerical models

Multiphase flow models have improved substantially during the past years due to a better understanding of the physical phenomena occurring in multiphase flow systems. An extensive research has also led to a better understanding of the kinetic theory for granular flow and therefore, better implementation of the mathematical formulations pertaining to the flow, heat, and mass transfer mechanisms occurring in multiphase flow systems. The present numerical models for multiphase flows incorporate two approaches: the Eulerian-Eulerian approach, and the Eulerian-Lagrangian approach. A decision on whether the Eulerian-Eulerian or Eulerian-Lagrangian formulation of the governing equations is to be used should be made prior to the numerical solution, simply because each formulation has its limitations and constraints. Numerical predictions obtained from each formulation are not identical, and the choice of a convenient formulation for a specific model relies on whether a dense or dilute system is being considered and the objectives of the numerical study. For instance, if the objective of the numerical model is to follow the trajectories of individual particles, then the Eulerian-Lagrangian formulation appears more convenient for a dilute system (volume fraction of 1% and less). However, for a dense system, this approach is computationally expensive and time consuming and requires powerful and high-speed computers. On the contrary, the Eulerian-Eulerian formulation can handle both dense and dilute systems; however, it cannot predict the local behavior of particles in the flow field.

The theory behind the Eulerian-Eulerian approach is based on the macroscopic balance equations of mass, momentum, and energy for both phases. Eulerian models assume both phases as two interpenetrating continuum (Enwald et al., 1996)[5] and permit the solution of the Navier-Stokes equations with the assumption of incompressibility for both the gas and dispersed phases. The gas phase is the primary or continuous phase while the solid phase is termed as the dispersed phase. Both phases are represented by their volume fractions and are linked through the drag force in the momentum equation as given by Wen and Yu[6] correlation for a dilute system, Ergun[7] correlation for a dense system, and Gidaspow et al.[8], which is a combination of both correlations for transition and fluctuating systems. An averaging technique for the field variables such as the gas and solid velocities, solid volume

fraction, and solid granular temperature is adopted. With this approach, the kinetic theory for granular flow (KTGF) is adopted to describe the interfacial forces between the considered phases and between each of the phases and the boundaries of the computational domain. The KTGF is based on the flow of nonuniform gases primarily presented by Chapman and Cowling (1970)[9]. The model was then further matured through the work of Jenkins and Savage (1983)[10], Lun et al. (1984)[18], Ding and Gidaspow (1990)[11], Gidaspow et al. (1992)[8], and Gidaspow (1994)[12].

On the other hand, Lagrangian models, or discrete particle models, are derived from Newton's law of motion for the dispersed phase. This approach facilitates the ability to compute the trajectory (path) and motion of individual particles. The interactions between the particles are described by either a potential force (soft particle dynamics)[13] or by collision dynamics (hard particle dynamics)[14]. In the Lagrangian approach, the fluid phase is treated separately by solving a set of time averaged Navier-Stokes equations, whereas the dispersed phase is solved by tracking a large number of particles, bubbles, or droplets in the calculated flow field. By computing the temporal development of a sufficiently large sample of particles, ensemble average quantities describing system performance can be evaluated. Furthermore, using the Lagrangian approach, the dispersed phase can exchange mass, momentum, and energy with the fluid phase through a source term added to the conservation equations. These equations also account for the changes in volume fraction of each phase. As each individual particle moves through the flow field, its trajectory, mass, and heat transfer calculations are obtained from a force balance along with an updated local conditions of the continuous phase by solving mass and energy balance equations. Thus, external forces acting on the solid particle such as aerodynamic, gravitational, buoyancy, and contact due to collisions among the particles and between the particles and the domain boundaries, can be calculated simultaneously with the particle motion using local parameters of gas and solids.

Although the form of the Eulerian momentum equation can be derived from its Lagrangian equivalent by averaging over the dispersed phase, each model has its advantages and disadvantages depending on the objective of the study and the type of system used. With this and the above definitions in mind, we now discuss the merits and shortcomings of each formulation.

2.1 Merits and shortcomings of each approach

Some of the advantages and disadvantages of the Eulerian and Lagrangian formulations are discussed in this section. Examples of their use for actual physical systems are also provided to facilitate and enhance our understanding of the subject and to direct the reader to the appropriate formulation for the problem at hand.

For modeling spray dryers, coal and liquid fuel combustion, and particle-laden flows, the Lagrangian description of the governing equations is more suitable because these systems are considered dilute; that is, they are characterized by low concentration of particles with solid volume fractions on the order of 1% or less. It was previously mentioned that this characteristic of particles density allows the tracking of particles trajectories at different locations in the computational domain with less computational effort than the case for a dense system. Predicting the particles trajectories is the main distinctive advantage of the Lagrangian technique over the Eulerian formulation. This in turn provides the opportunity to evaluate interactions between particles, fluids, and boundaries at the microscopic level

using local flow parameters and gas properties, which is difficult to achieve using a continuum or steady-state model. The total number of particles is tractable from a computational point of view and modeling particle–particle and particle–wall interactions can be achieved with a great success. For additional information on the actual form of the conservation equations used in this approach, refer to Strang and Fix[15] and Gallagher[16].
In order to extend the applicability of single phase equations to multiphase flows, the volume fraction of each phase is implemented in the governing equations as was mentioned earlier. In addition, solids viscosities and stresses need to be addressed. The governing equations satisfying single phase flow will not be sufficient for flows where inter-particle interactions are present. These interactions can be in the form of collision between adjacent particles as in the case of a dilute system, or contact between adjacent particles in the case of dense systems. In the former, dispersed phase stresses and viscosities play a crucial role in the overall velocity and concentration distribution in the physical domain. The crucial factor attributed to this random distribution of particles in these systems is the gas phase turbulence. In cases where particles are light and small, turbulence eddies dominate the particles movement and the interstitial gas acts as a buffer that prevents collision between particles. However, in the case of heavy and large diameter particles (150 mm and higher), particle inertia is sufficient to carry them easily through the intervening gas film, and interactions occur by direct collision. Therefore, solids viscosities and stresses cannot be neglected, and the single phase fundamental equations need to be adjusted to account for the secondary phase interaction as shown in the next section.

2.2 Hydrodynamic model equations

In the previous section, it was mentioned that each phase is represented by its volume fraction with respect to the total volume fraction of all phases present in the computational domain. For the sake of simplicity, let us develop these formulations for a binary system of two phases, a gas phase represented by *g*, and a solid phase represented by *s*. Accordingly, the mass conservation equation for each phase *q*, such that *q* can be a gas= *g* or solid= *s* is:

$$\frac{\partial}{\partial t}\left(\rho_q \alpha_q\right) + \nabla \cdot \left(\rho_q \alpha_q \vec{U}_q\right) = \sum_{p=1}^{n} \dot{M}_{pq} \tag{1}$$

where $\dot{M}_{pq}$ (defined later) represents the mass transfer from the *p*th phase to the *q*th phase. When *q*=*g*, *p*=s, $\dot{M}_{pq} = \dot{M}_{sg} = -\dot{M}_{gs}$. Similarly, the momentum balance equations for both phases are:

$$\frac{\partial}{\partial t}\left(\rho_g \alpha_g \vec{U}_g\right) + \nabla \cdot \left(\rho_g \alpha_g \vec{U}_g \vec{U}_g\right) = -\alpha_g \nabla P + \nabla \cdot \bar{\bar{\tau}}_g + \rho_g \alpha_g \vec{g} + \vec{\beta}_{gs} + \dot{M}_{sg} \vec{U}_{gs} + \vec{F}_{vm} \tag{2}$$

$$\frac{\partial}{\partial t}\left(\rho_s \alpha_s \vec{U}_s\right) + \nabla \cdot \left(\rho_s \alpha_s \vec{U}_s \vec{U}_s\right) = -\alpha_s \nabla P_s + \nabla \cdot \bar{\bar{\tau}}_s + \rho_s \alpha_s \vec{g} - \vec{\beta}_{gs} - \dot{M}_{sg} \vec{U}_{gs} + \vec{F}_{vm} \tag{3}$$

such that $\vec{U}_{gs}$ is the relative velocity between the phases given by $\vec{U}_{gs} = \left(\vec{U}_g - \vec{U}_s\right)$.
In the above equations, $\vec{\beta}_{gs}$ represents the drag force between the phases and is a function of the interphase momentum coefficient K_{gs}, the number of particles in a computational cell N_d, and the drag coefficient C_D such that:

$$\begin{aligned}\vec{\beta}_{gs} &= K_{gs}\left(\vec{U}_g - \vec{U}_s\right) \\ &= N_d C_D \frac{1}{2}\rho_g \left(U_g - U_s\right)\left|\vec{U}_g - \vec{U}_s\right| A_{surface} \\ &= \frac{6\alpha_s}{\pi d_s^3} C_D \frac{1}{2}\rho_g \left(U_g - U_s\right)\left|\vec{U}_g - \vec{U}_s\right| \frac{\pi d_s^2}{4} \\ &= \frac{3}{4} C_D \frac{\alpha_s \rho_g}{d_s}\left(U_g - U_s\right)\left|\vec{U}_g - \vec{U}_s\right|\end{aligned} \tag{4}$$

The form of the drag coefficient in Equation (4) can be derived based on the nature of the flow field inside the computational domain. Several correlations have been derived in the literature. A well established correlation that takes into consideration changes in the flow characteristics for multiphase systems is Ossen drag model presented in Skuratovsky et al. (2003)[17] as follows:

$$\begin{aligned} C_d &= \frac{64}{\pi \mathrm{Re}_s}\left(1 + \frac{64}{2\pi}\right) && for\ \mathrm{Re}_s < 0.01 \\ C_d &= \frac{64}{\pi \mathrm{Re}_s}\left(1 + 10^x\right) && for\ 0.01 < \mathrm{Re}_s < 1.5 \\ x &= -0.883 + 0.906\ln\left(\mathrm{Re}_s\right) - 0.025\ln^2\left(\mathrm{Re}_s\right) \\ C_d &= \frac{64}{\pi \mathrm{Re}_s}\left(1 + 0.138\,\mathrm{Re}_s^{0.792}\right) for\ 1.5 < \mathrm{Re}_s < 133 \\ \ln C_d &= 2.0351 - 1.66\ln \mathrm{Re}_s + \ln^2 \mathrm{Re}_s - 0.0306\ln^3 \mathrm{Re}_s \\ & \quad for\ 40 < \mathrm{Re}_s < 1000 \end{aligned} \tag{5}$$

The form of Reynolds number defined in Equation (5) is a function of the gas properties, the relative velocity between the phases, and the solid phase diameter. It is given by:

$$\mathrm{Re}_s = \frac{\rho_g \left|\vec{U}_g - \vec{U}_s\right| d_s}{\mu_g} \tag{6}$$

The virtual-mass force $\vec{F}_{vm}$ in Equations (2) & (3) accounts for the force needed to accelerate the fluid surrounding the solid particle. It is given by:

$$\vec{F}_{vm} = \alpha_s \rho_g c_{vm}\left(\frac{d\vec{U}_g}{dt} - \frac{d\vec{U}_s}{dt}\right) \tag{7}$$

2.3 Complimentary equations – granular kinetic theory equations

When the number of unknowns exceeds the number of formulated equations for a specific case study, complimentary equations are needed for a solution to be possible. For a binary

system adopting the Eulerian formulation such that q= g for gas and s for solid, the volume fraction balance equation representing both phases in the computational domain can then be given as:

$$\sum_{q=1}^{n} \alpha_q = 1 \tag{8}$$

where $\alpha_q = \frac{V_q}{V}$

In the case of collision between the particles in the solid phase, the kinetic theory for granular flow based on the work of Gidaspow et al. (1992)[8] dictates that the solid shear viscosity μ_s can be represented by Equation (9) as follows:

$$\mu_s = \frac{10\rho_s d_s \sqrt{\theta_s \pi}}{96\alpha_s (1+e_{ss}) g_o}\left[1+\frac{4}{5}\alpha_s g_o (1+e_{ss})\right]^2 + \frac{4}{5}\alpha_s \rho_s d_s (1+e_{ss}) g_o \left(\frac{\theta_s}{\pi}\right)^{\frac{1}{2}} \tag{9}$$

where e_{ss} is a value between *0* and *1* dictating whether the collision between two solid particles is inelastic or perfectly elastic. When two particles collide, and depending on the material property, initial particle velocity, etc, deformation in the particle shape might occur. The resistance of granular particles to compression and expansion is called the solid bulk viscosity μ_b . According to Lun et al. (1984)[18] correlation, it is given by:

$$\mu_b = \frac{4}{3}\alpha_s \rho_s d_s g_o (1+e_{ss})\left(\frac{\theta_s}{\pi}\right)^{\frac{1}{2}} \tag{10}$$

In addition, the solid pressure P_s is given by Gidaspow and Huilin (1998)[19] as:

$$P_s = \alpha_s \rho_s \theta_s \left[1+2(1+e_{ss})\alpha_s g_o\right] \tag{11}$$

where θ_s is the granular temperature which measures the kinetic energy fluctuation in the solid phase written in terms of the particle fluctuating velocity c as:

$$\theta_s = c^2/3 \tag{12}$$

This parameter can be governed by the following conservation equation:

$$\begin{aligned} &\frac{3}{2}\left[\frac{\partial}{\partial t}(\rho_s \alpha_s \theta_s) + \nabla \cdot (\rho_s \alpha_s \vec{U}_s \theta_s)\right] \\ &= \left(-P_s \bar{\bar{I}} + \bar{\bar{\tau}}_s\right) : \nabla \cdot \vec{U}_s + \nabla \cdot (k_s \nabla \theta_s) - \gamma_s - 3\beta_{sg}\theta_s \end{aligned} \tag{13}$$

where the first term on the right hand side (RHS) is the generation of energy by the solid stress tensor; the second term represents the diffusion of energy; the third term represents the collisional dissipation of energy between the particles; and the fourth term represents the energy exchange (transfer of kinetic energy) between the gas and solid phases.

The diffusion coefficient for the solid phase energy fluctuation given by Gidaspow et al. (1992)[8] is:

$$k_s = \frac{150\rho_s d_s\sqrt{\theta_s\pi}}{384(1+e_{ss})g_o}\left[1+\frac{6}{5}\alpha_s g_o(1+e_{ss})\right]^2 + 2\alpha_s^2\rho_s d_s g_o(1+e_{ss})\left(\frac{\theta_s}{\pi}\right)^{\frac{1}{2}} \tag{14}$$

The dissipation of energy fluctuation due to particle collision given by Gidaspow et al. (1992)[8] is:

$$\gamma_s = 3\alpha_s^2\rho_s g_o\left(1-e_{ss}^2\right)\theta_s\left[\frac{4}{d_s}\left(\frac{\theta_s}{\pi}\right)^{\frac{1}{2}} - \nabla\cdot\vec{U}_s\right] \tag{15}$$

The radial distribution function g_o based on Ding and Gidaspow (1990)[11] model is a measure of the probability of particles to collide. For dilute phases, $g_o \to 1$; for dense phases, $g_o \to \infty$.

$$g_o = \frac{3}{5}\left[1-\left(\frac{\alpha_s}{\alpha_{s,\max}}\right)^{\frac{1}{3}}\right]^{-1} \tag{16}$$

2.4 Drying model equations – heat and mass transfer

The conservation equation of energy (q = g, s) is given by:

$$\frac{\partial}{\partial t}\left(\rho_q\alpha_q H_q\right) + \nabla\cdot\left(\rho_q\alpha_q\vec{U}_q H_q\right) = -\alpha_q\nabla P + \overline{\overline{\tau}}_q : \nabla\vec{U}_q + Q_{pq} + \dot{M}_{pq}H_q \tag{17}$$

By introducing the number density of the dispersed phase (solid in this case), the intensity of heat exchange between the phases is:

$$Q_{sg} = N_d\pi d_s^2 h\left(T_g - T_s\right) = \frac{6\alpha_s}{d_s}h\left(T_g - T_s\right) = \frac{6\alpha_s}{d_s}m_s c_p\frac{dT_s}{dt} \tag{18}$$

Many empirical correlations are available in the literature for the value of the heat- and mass-transfer coefficients. The mostly suitable for pneumatic and cyclone dryers are those given by Baeyens et al. (1995)[20] and De Brandt (1974)[21]. The Chilton and Colburn analogy for heat and mass-transfer are used as follows:

$$Nu_s = 0.15\,\mathrm{Re}_s \tag{19}$$

$$Nu_s = 0.16\,\mathrm{Re}_s^{1.3}\,\mathrm{Pr}^{0.67} \tag{20}$$

$$Sh = 0.15\,\mathrm{Re}_s \tag{21}$$

$$Sh = 0.16\,\mathrm{Re}_s^{1.3}\,Sc^{0.67} \tag{22}$$

where

$$h = \frac{Nu_s k_{cond}}{d_s} \qquad \Pr = \frac{c_p \mu_g}{k_{cond}} \qquad Sc = \frac{\mu_g}{\rho_g D_v} \tag{23}$$

The diffusion coefficient D_v defined in the above equations is assumed to be constant.
As the wet feed comes in contact with the hot carrier fluid, heat exchange between the phases occurs. In this stage, mass transfer is considered negligible. When the particle temperature exceeds the vaporization temperature, water vapor evaporates from the surface of the particle. This process is usually short and is governed by convective heat and mass transfer. This initial stage of drying is known as the constant or unhindered drying period (CDP). As drying proceeds, internal moisture within the particle diffuses to the surface to compensate for the moisture loss at that region, and diffusion mass transfer starts to occur. This stage dictates the transfer from the CDP to the second or falling rate drying period (FRP) and is designated by the critical moisture content. This system specific value is crucial in depicting which drying mechanism occurs; thus, it has to be accurate. However, it is not readily available and should be determined from experimental observations for different materials. An alternative approach that bypasses the critical value yet distinguishes the two drying periods is by drawing a comparison to the two drying rates. If the calculated value of diffusive mass transfer is greater than the convective mass transfer, then resistance is said to occur on the external surface of the particle and the CDP dominates. However, if the diffusive mass transfer is lower than the convective counterpart, then resistance occurs in the core of the particle and diffusion mass transfer dominates.
The governing equation for the CDP is expressed in Equation (24). This equation can be used regardless of the method adopted to determine the critical moisture content. In cases when the critical moisture content is known, the FRP can then be expressed as shown in Equation (25) such that $X_{eq} \le X \le X_{cr}$. When the critical value is not known, Equation (26) can then be used as shown below. This equation was derived based on Fick's diffusion equation[22] for a spherical particle averaged over an elementary volume.

$$\dot{M}_{CDR} = \frac{k_c M}{d_s}\left(\frac{P_{sat}(T_s)}{RT_s} - X_{H2O}\frac{P}{RT_g}\right) \tag{24}$$

$$\dot{M}_{FDR} = \frac{X - X_{eq}}{X_{cr} - X_{eq}}\dot{M}_{CDR} \tag{25}$$

$$\dot{M}_{Diffusion} = \frac{D_v \rho_s \pi^2}{R^2}\left(\overline{X} - X_{eq}\right) \tag{26}$$

In order to obtain the water vapor distribution in the gas phase, the species transport equation (convection-diffusion equation) is used as shown in Equation (27).

$$\frac{\partial}{\partial t}\left(\rho_g \alpha_g Y_g\right) + \nabla \cdot \left(\rho_g \alpha_g \vec{U}_g Y_g\right) = \nabla \cdot \left(\alpha_g \rho_g D_v \nabla Y_g\right) + \dot{M}_{sg} \tag{27}$$

During the drying process, liquid water is removed and the particle density gradually increases. With the assumption of no shrinkage, the particle density is expressed by:

$$\rho_s = \frac{\rho_{H_2O(l)}\rho_{ds}}{X\left(\rho_{ds} - \rho_{H_2O(l)}\right) + \rho_{H_2O(l)}} \tag{28}$$

2.5 Turbulence model equations

To describe the effects of turbulent fluctuations of velocities and scalar quantities in each phase, the $k-\varepsilon$ multiphase turbulent model can be used for simpler geometries. Advanced turbulence models should be used for cases with swirl and vortex shedding (*RANS*, $k-\omega$). In the context of gas-solid models, three approaches can be applied (FLUENT 6.3 User's guide)[23]: (1) modeling turbulent quantities with the assumption that both phases form a mixture of density ratio close to unity (mixture turbulence model); (2) modeling the effect of the dispersed phase turbulence on the gas phase and vice versa (dispersed turbulence model); or (3) modeling the turbulent quantities in each phase independent of each other (turbulence model for each phase). In many industrial applications, the density of the solid particles is usually larger than that of the fluid surrounding it. Furthermore, modeling the turbulent quantities in each phase is not only complex, but also computationally expensive when large number of particles is present. A more desirable option would then be to model the turbulent effect of each phase on the other by incorporating *source* terms into the conservation equations. This model is highly applicable when there is one primary phase (the gas phase) and the rest are dispersed dilute secondary phases such that the influence of the primary phase turbulence is the dominant factor in the random motion of the secondary phase.

2.5.1 Continuous phase turbulence equations

In the case of multiphase flows, the standard $k-\varepsilon$ model equations are modified to account for the effect of dispersed phase turbulence on the continuous phase as shown below:

$$\frac{\partial}{\partial t}\left(\rho_g\alpha_g k\right) + \nabla\cdot\left(\rho_g\alpha_g\vec{U}_g k\right) = \nabla\cdot\left(\alpha_g\frac{\mu_{t,g}}{\sigma_k}\nabla k_g\right) + \alpha_g G_{k,g} - \alpha_g\rho_g\varepsilon_g + \alpha_g\rho_g\Pi_{k_g} \tag{29}$$

and

$$\frac{\partial}{\partial t}\left(\rho_g\alpha_g\varepsilon_g\right) + \nabla\cdot\left(\rho_g\alpha_g\vec{U}_g\varepsilon_g\right) = \nabla\cdot\left(\alpha_g\frac{\mu_{t,g}}{\sigma_\varepsilon}\nabla\varepsilon_g\right) + \alpha_g\frac{\varepsilon_g}{k_g}\left(C_{1\varepsilon}G_{k,g} - C_{2\varepsilon}\rho_g\varepsilon_g\right) + \alpha_g\rho_g\Pi_{\varepsilon_g} \tag{30}$$

In the above equations, Π_{k_g} and Π_{ε_g} represent the influence of the dispersed phase on the continuous phase and take the following forms:

$$\Pi_{k_g} = \sum_{p=1}^{m}\frac{K_{gs}}{\alpha_g\rho_g}\left(k_{gs} - 2k_g + \vec{U}_{gs}\cdot\vec{U}_{dr}\right) \tag{31}$$

$$\Pi_{\varepsilon_g} = C_{3\varepsilon}\frac{\varepsilon_g}{k_g}\Pi_{k_g} \tag{32}$$

The drift velocity $\vec{U}_{dr}$ is defined in Equation (33). This velocity results from turbulent fluctuations in the volume fraction. When multiplied by the interchange coefficient K_{gs}, it serves as a correction to the momentum exchange term for turbulent flows:

$$\vec{U}_{dr} = -\left(\frac{D_s}{\sigma_{gs}\alpha_s}\nabla\alpha_s - \frac{D_g}{\sigma_{gs}\alpha_g}\nabla\alpha_g \right) \tag{33}$$

such that $D_g = D_s = D_{t,sg}$ for Tchen Theory of multiphase flow (FLUENT 6.3 User's guide)[23]. The generation of turbulence kinetic energy due to the mean velocity gradients $G_{k,g}$ is computed from:

$$G_{k,g} = \mu_{t,g}\left(\nabla\cdot\vec{U}_g + \left(\nabla\cdot\vec{U}_g\right)^T \right) : \nabla\vec{U}_g \tag{34}$$

The turbulent viscosity $\mu_{t,g}$ given in the above equation is written in terms of the turbulent kinetic energy of the gas phase as:

$$\mu_{t,g} = \rho_g C_\mu \frac{k_g^2}{\varepsilon_g} \tag{35}$$

The Reynolds stress tensor defined in Equation (13) for the continuous phase is based on the Boussinesq hypothesis[24] given by:

$$\overline{\overline{\tau}}_g = -\frac{2}{3}\left(\rho_g\alpha_g k_g + \rho_g\alpha_g\mu_{t,g}\nabla\cdot\vec{U}_g\right)\overline{\overline{I}} + \rho_g\alpha_g\mu_{t,g}\left(\nabla\cdot\vec{U}_g + \left(\nabla\cdot\vec{U}_g\right)^T \right) \tag{36}$$

2.5.2 Dispersed phase turbulence equations

Time and length scales that characterize the motion of solids are used to evaluate the dispersion coefficients, the correlation functions, and the turbulent kinetic energy of the particulate phase. The characteristic particle relaxation time connected with inertial effects acting on a particulate phase is defined as:

$$\tau_{F,sg} = \rho_g\alpha_s K_{gs}^{-1}\left(\frac{\rho_s}{\rho_g} + C_V \right) \tag{37}$$

The Lagrangian integral timescale calculated along particle trajectories is defined as:

$$\tau_{t,sg} = \frac{\tau_{t,g}}{\sqrt{\left(1 + C_\beta\xi^2\right)}} \tag{38}$$

where

$$\xi = \frac{\left|\vec{U}_{sg}\right|\tau_{t,g}}{L_{t,g}} \tag{39}$$

and

$$C_\beta = 1.8 - 1.35\left(\cos\theta\right)^2 \tag{40}$$

In Equation (40), θ is the angle between the mean particle velocity and the mean relative velocity. The constant term C_V = 0.5 is an added mass coefficient (FLUENT 6.3 User's guide)[23].
The length scale of the turbulent eddies defined in Equation (39) is given by:

$$L_{t,g} = \sqrt{\frac{3}{2}} C_\mu \frac{k_g^{3/2}}{\varepsilon_g} \tag{41}$$

The turbulence quantities for the particulate phase include

$$k_s = k_g \left(\frac{b^2 + \eta_{sg}}{1 + \eta_{sg}} \right) \tag{42}$$

$$k_{sg} = 2k_g \left(\frac{b + \eta_{sg}}{1 + \eta_{sg}} \right) \tag{43}$$

$$D_{t,sg} = \frac{1}{3} k_{sg} \tau_{t,sg} \tag{44}$$

such that

$$b = \left(1 + C_V\right) \left(\frac{\rho_s}{\rho_g} + C_V \right)^{-1} \tag{45}$$

$$\eta_{sg} = \frac{\tau_{t,sg}}{\tau_{F,sg}} \tag{46}$$

3. Grid generation

The development of a CFD model involves several tasks that are equally important for a feasible solution to exist with certain accuracy and correctness. A reliable model can only be possible when correct boundary and initial conditions are implemented along with a meaningful description of the physical problem. Thus, the development of a CFD model should involve an accurate definition of the variables to be determined; choice of the mathematical equations and numerical methods, boundary and initial conditions; and applicable empirical correlations. In order to simulate the physical processes occurring in any well defined computational domain, governing and complimentary equations are solved numerically in an iterative scheme to resolve the coupling between the field variables. With the appropriate set of equations, the system can be described in two- and three-dimensional forms conforming to the actual shape of the system. In many cases, it is

desirable to simplify the computational domain to reduce computational time and effort and to prevent divergence problems. For instance, if the model shows some symmetry as in the case of a circular geometry, it can be modeled along the plane of symmetry. However, for a possible CFD solution to exist, the computational domain has to be discretized into cells or elements with nodal points marking the boundaries of each cell and combining the physical domain into one computational entity.

It is a common practice to check and test the quality of the mesh in the model simply because it has a pronounced influence on the accuracy of the numerical simulation and the time taken by a model to achieve convergence. Ultimately, seeking an optimum mesh that enhances the convergence criteria and reduces time and computational effort is recommended. A widely used criterion for an acceptable meshing technique is to maintain the ratio of each of the cell-side length within a set number (x/y, y/z, $x/z < 3$). In practice, and for most computational applications, local residual errors between consecutive iterations for the dependent variables are investigated. In the case of high residual values, it is then recommended to modify the model input or refine the mesh properties to minimize these errors in order to attain a converged solution.

The choice of meshing technique for a specific problem relies heavily on the geometry of the domain. Most CFD commercial packages utilize a compatible pre-processor for geometry creation and grid generation. For instance, FLUENT utilizes Gambit pre-processor. Two types of technique can be used in Gambit, a uniform distribution of the grid elements, or what can be referred to as structured grid; and a nonuniform distribution, or unstructured grid. For simple geometries that do not involve rounded edges, the trend would be to use structured grid as it would be easier to generate and faster to converge. It should be noted that the number of elements used for grid generation also plays a substantial role in simulation time and solution convergence. The finer the mesh, the longer the computational time, and the tendency for the solution to diverge become higher; nevertheless, the higher the solution accuracy.

Based on the above, one tends to believe that it might be wise to increase the number of elements indefinitely for better accuracy in the numerical predictions on the expense of computational effort. In practice, this is not always needed. The modeller should always bear in mind that an optimum mesh can be attained beyond which, changes in the numerical predictions are negligible.

In the following, two case studies are discussed. In each case, the computational domain is discretized differently according to what seemed to be an adequate mesh for the geometry under consideration.

Case 1

Let us consider a 4-m high vertical pipe for the pneumatic drying of sand particles and another 25-m high vertical pipe for the pneumatic drying of PVC particles. For both cases, the experimental data, physical and material properties were taken from Paixao and Rocha (1998)[25] for sand, and Baeyens et al. (1995)[26] for PVC as shown in Table 1. Both models were meshed and simulated in a three-dimensional configuration as shown in Figures 1 and 2.

In Figure 1, hot gas enters the computational domain vertically upward, fluidizes and dries the particles as they move along the length of the dryer. As the gas meets the particles, particles temperature increases until it reaches the wet bulb temperature at which surface

Particle	**Sand**	**PVC**
Diameter (mm)	0.38	0.18
Density (g / cm^3)	2.622	1.116
Specific Heat [J / (kg ^{o}C)]	799.70	980.0
Drying Tube		
Height (m)	4.0	25.0
Internal Diameter (cm)	5.25	125.0
Gas Flow rate, W_g (kg/s)	0.03947	10.52
Solids Flow rate, W_s (kg/s)	0.00474	1.51
Inlet Gas Temperature, T_g (^{o}C)	109.4	126.0
Inlet Solids Temperature, T_s (^{o}C)	39.9	-
Inlet Gas Humidity, Y_g (kg/kg)	0.0469	-
Inlet Moisture Content of Particles, X_s (kg/kg)	0.0468	0.206

Paixao and Rocha (1998)[25]

Table 1. Conditions used in the numerical model simulation

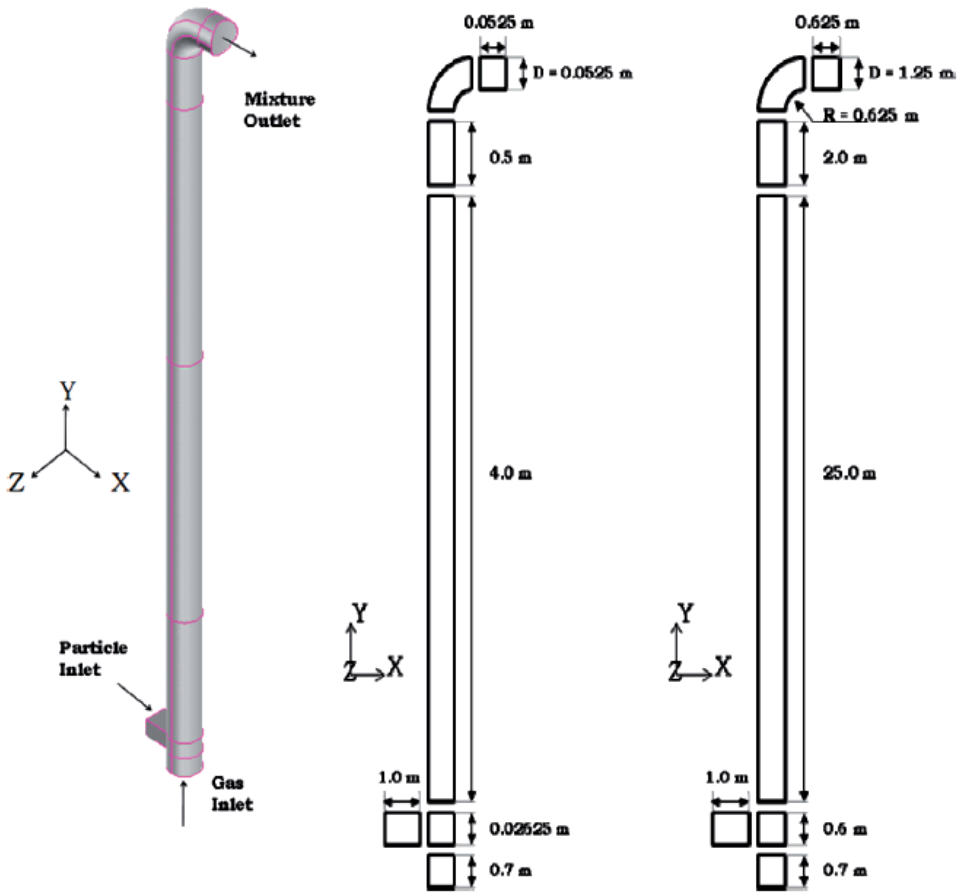

Fig. 1. (Left) Geometrical models; (middle) sand model; (right) PVC model

evaporation starts to occur. At this stage, convective mass transfer dominates the drying of surface moisture of particles during their residence time in the dryer. Since pneumatic drying is characterized by short residence times on the order of 1-10 seconds, mostly convective heat- and mass transfer occur. However, since experimental data for pore moisture evaporation were also provided in the independent literature, moisture diffusion or the second stage of drying was also considered.

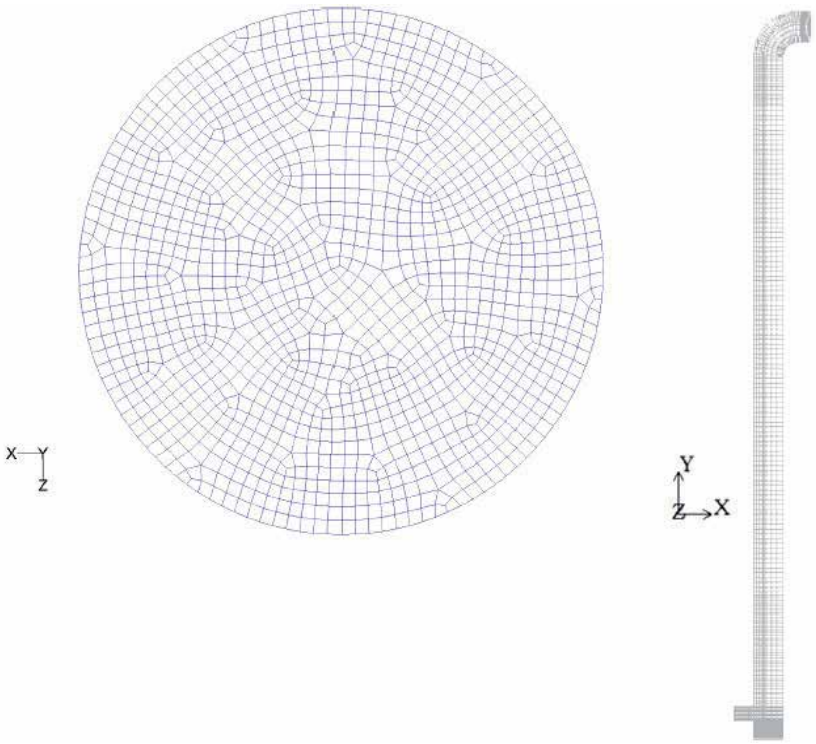

Fig. 2. Computational grid

The computational domain was discretized into hexahedral elements with unstructured mesh in the *x* and *z*-directions and nonuniform distribution in the *y*-direction. An optimized mesh with approximately 63 000 cells and 411 550 cells was applied for the sand and PVC models, respectively. The computational grid is shown in Figure 2. Grid generation was done in Gambit 4.6, a compatible pre-processor for FLUENT 6.3. A grid sensitivity study was performed on the large-scale riser using two types of grids, a coarse mesh with 160 800 elements, and finer mesh with 411 550 elements. All models were meshed based on hexahedral elements due to their superiority over other mesh types when oriented with the direction of the flow. Results obtained for the axial profiles of pressure and relative velocity yield a maximum of 15% difference between the predicted results up to 4.5 m above the dryer inlet; however, there was hardly any difference in the results at a greater length by changing the size of the grids. Therefore, the coarsest grid was used in all simulations.

Case 2

In this case, let us consider a different geometry as shown in Figure 3. This model discusses the drying of sludge material and linked to an earlier work presented by Jamaleddine and

Ray (2010)[3] for the drying of sludge in a large-scale pneumatic dryer. Material properties for sludge are shown in Table 2. The geometrical model is a large-scale model of a design presented by Bunyawanichakul et al. (2006)[28]. The computational domain consists of an inlet pipe, three chambers in the cyclone, and an outlet. Two parallel baffles of conical shape with a hole or orifice at the bottom divide the dryer chambers. As the gas phase and the particulate phase (mixture) enter the cyclone dryer tangentially from the pneumatic dryer, they follow a swirling path as they travel from one chamber to another through the orifice opening. This configuration allows longer residence times for the sludge thus enhancing heat- and mass-transfer characteristics.

Particle	**Sludge ***
Diameter (mm)	0.18
Density (kg / m^3)	998.0
Specific heat [J / (kg ^oC)]	4182.0
Thermal Conductivity [W / (m ^oC)]	0.6
Drying Tube	
Height (m)	8.0
Internal diameter (m)	6.0

*Sludge properties are taken from Arlabosse et al. (2005) [27]

Table 2. Conditions used in the numerical model simulation

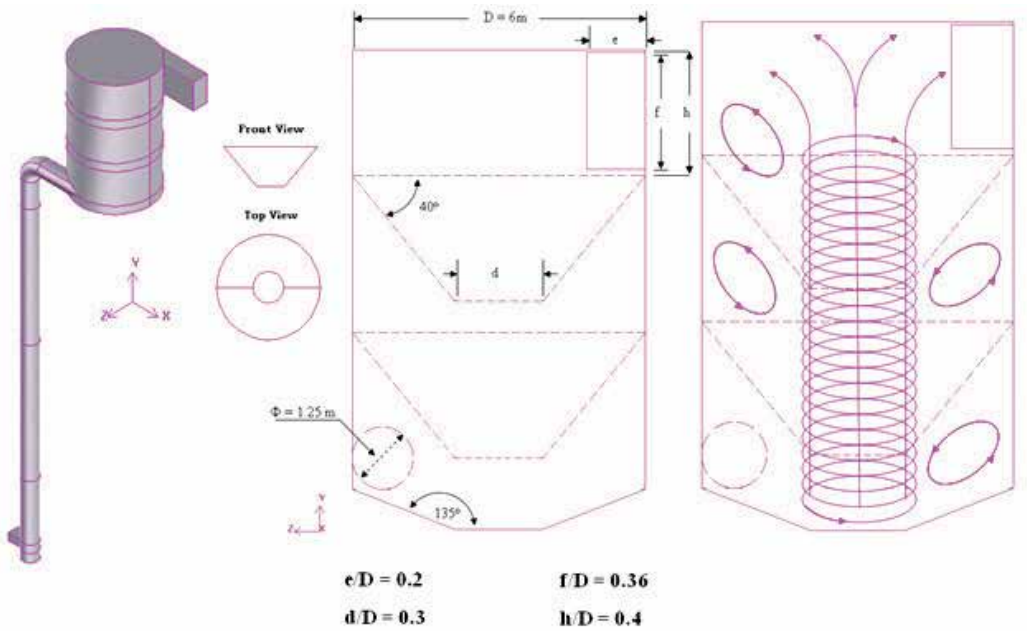

Fig. 3. Schematic of the pneumatic-cyclone dryer assembly

The numerical analysis is based on a 3D, Eulerian multiphase CFD model provided by FLUENT/ANSYS R12.0. Physical and material properties for the sludge material are shown in Table 2. The computational domain was discretized into hexahedral elements with approximately 230 385 cells. This element type was chosen as it showed better accuracy between the numerical predictions and experimental data than tetrahedral elements as shown in Bunyawanichakul et al. (2006)[28]. The computational grid is shown in Figure 4. Grid generation was done in Gambit 4.6, a compatible pre-processor for FLUENT.

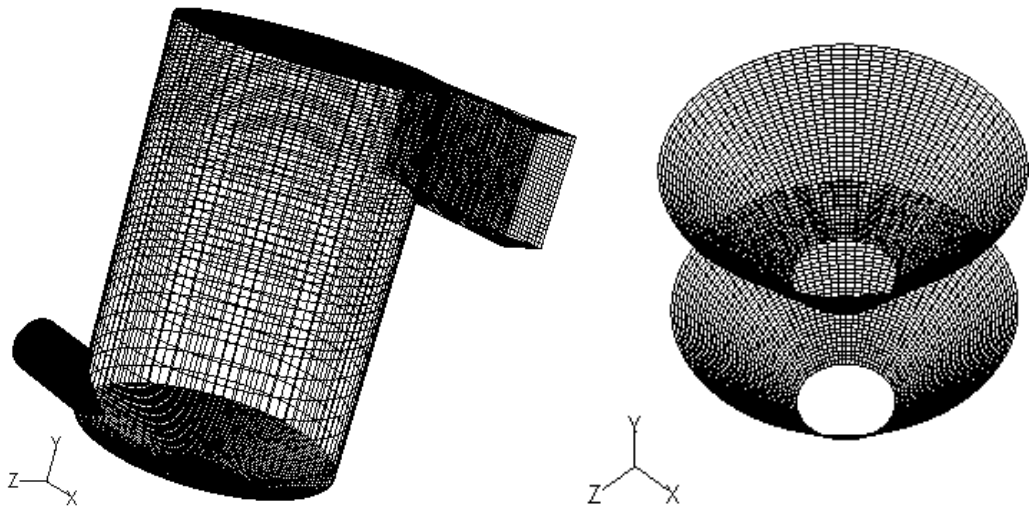

Fig. 4. Computational grid

4. Numerical parameters – numerical solvers

The governing equations along with the complementary equations are solved using a pressure based solution algorithm provided by FLUENT 6.3. This algorithm solves for solution parameters using a segregated method in such a manner that the equations are solved sequentially and in a separate fashion. Briefly stated, the solution parameters are initially updated. The *x*-, *y*-, and *z*-components of velocity are then solved sequentially. The mass conservation is then enforced using the pressure correction equation (SIMPLE algorithm) to ensure consistency and convergence of solution equations. The governing equations are spatially discretized using second-order upwind scheme for greater accuracy and a first-order implicit for time. This allows for the calculation of quantities at cell faces using a Taylor series expansion of the cell-centered solution about the cell centroid. More details related to this can be found in Patankar[29], or FLUENT 6.3 User Guide (2006)[23].

SAND AND PVC MODELS: A modified k-ε turbulence model is used along with the standard wall function for both phases in the vicinity of the wall. To avoid solution divergence, small time steps on the order of 1×10^{-4} to 1×10^{-6} are adopted. Solution convergence is set to occur for cases where scaled residuals for all variables fall below 1×10^{-3}, except for the continuity equation (1×10^{-4}) and the energy equation (1×10^{-6}).

SLUDGE MODEL: For this model, a RNG $k-\varepsilon$ turbulence model is used along with the standard wall function for both phases in the vicinity of the wall. Bunyawanichakul et al.[28] validated their numerical predictions with experimental data by adopting tetrahedral mesh

with Reynolds Stress Turbulence Model (RSTM), and hexahedral mesh with standard and RNG $k-\varepsilon$ turbulence models. It was found that the hexahedral mesh with the RNG $k-\varepsilon$ turbulence model predicted the pressure drop across the dryer chambers as well as the velocity distribution in the chambers reasonably well when used with the second-order advection scheme. In addition, RNG $k-\varepsilon$ turbulence model was successfully applied by Huang et al. (2004)[30,31] for modeling of spray dryers with different designs of atomizer. In order to avoid solution divergence in the current model, small time steps on the order of 1 x 10^{-3} - 1 x 10^{-4} are adopted. Solution convergence is set to occur for cases where scaled residuals far all variables fall below 1 x 10^{-3}, except for the continuity equation (1 x 10^{-4}) and the energy equation 1 x 10^{-6}. The maximum number of iterations per time step is set to 60. It took roughly 40 days for the solution to converge on Windows XP operating system with Core 2 Quad processor.

For all models, User Defined Functions subroutines (UDFs) are introduced to enhance the performance of the code. Accordingly, all UDFs are implemented directly from a source file written in a C programming language subsequently after the case file is read. This feature enables the macro functions to be visible or rather accessible by the user for them to be included in the solution where they should be applied. Equations implemented in UDFs are the following: a) properties pertaining to the drag force between the phases in Equations; b) the radial distribution function; c) the heat transfer coefficient; d) the mass transfer coefficient; and e) the particle density.

5. Results and discussion

In this section, some of the numerical predictions obtained from the CFD simulation for all cases considered in this chapter are shown. For case I, the numerical results agreed well with the experimental data with the following conditions: (i) the turbulent intensity is 5% at

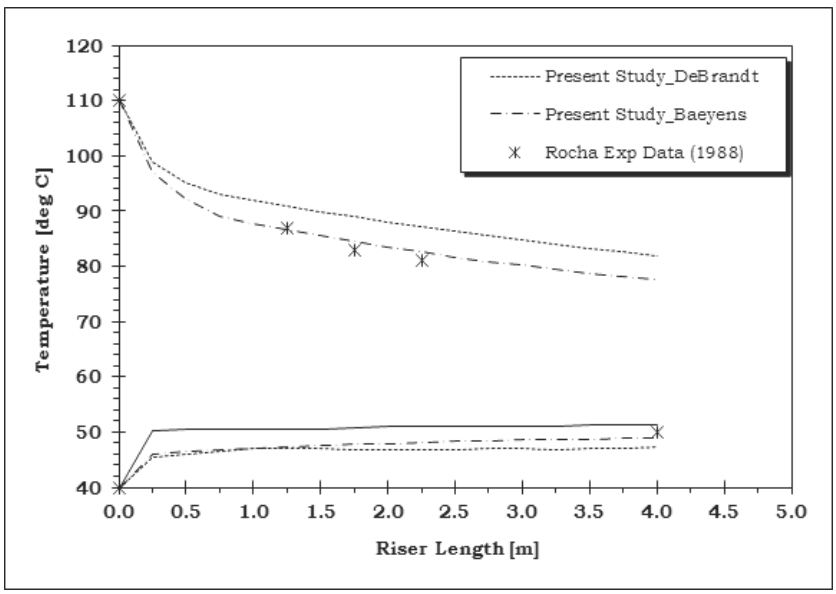

Fig. 5. Prediction of axial gas and particle temperatures along the length of the sand dryer (top lines, gas temperature; bottom lines, particle temperature)

the gas inlet; (ii) the turbulent intensity is 10% at the mixture inlet; (iii) the turbulent viscosity ratio was between 5-10%; (iv) particles were assumed to slip at the wall with specularity coefficient of 0.01; and (v) inelastic particle-wall collision with restitution coefficient of 0.6.

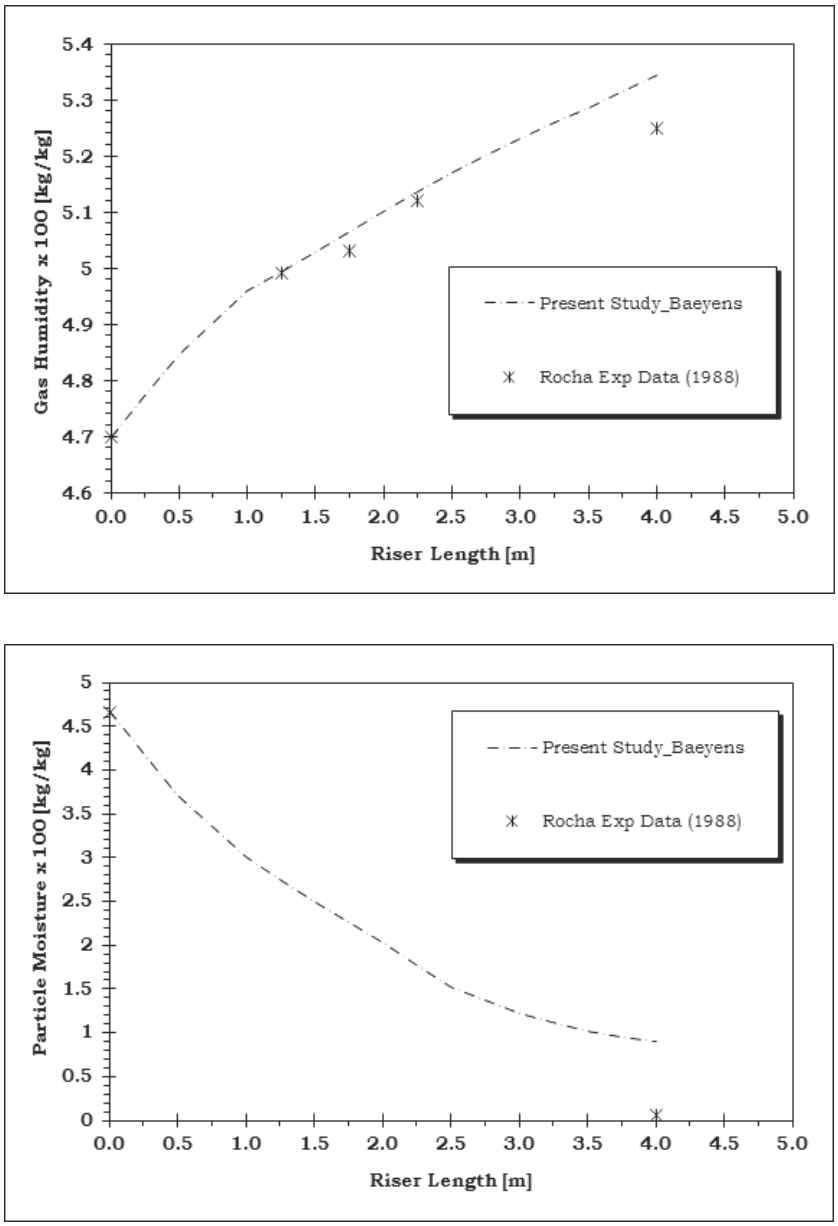

Fig. 6. Prediction of axial gas humidity (top) and particle moisture distribution (bottom) along the length of the sand dryer

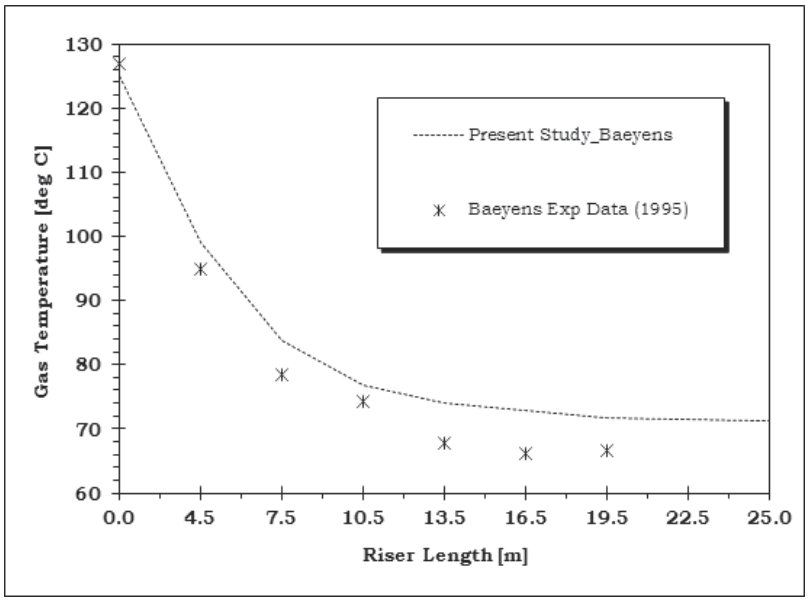

Fig. 7. Prediction of axial gas temperature along the length of the PVC dryer

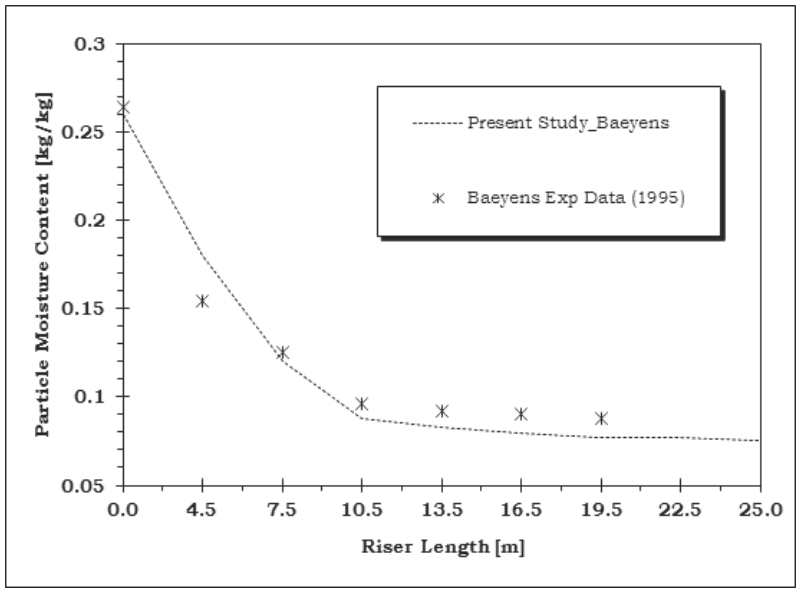

Fig. 8. Prediction of axial particle moisture distribution along the length of the PVC dryer

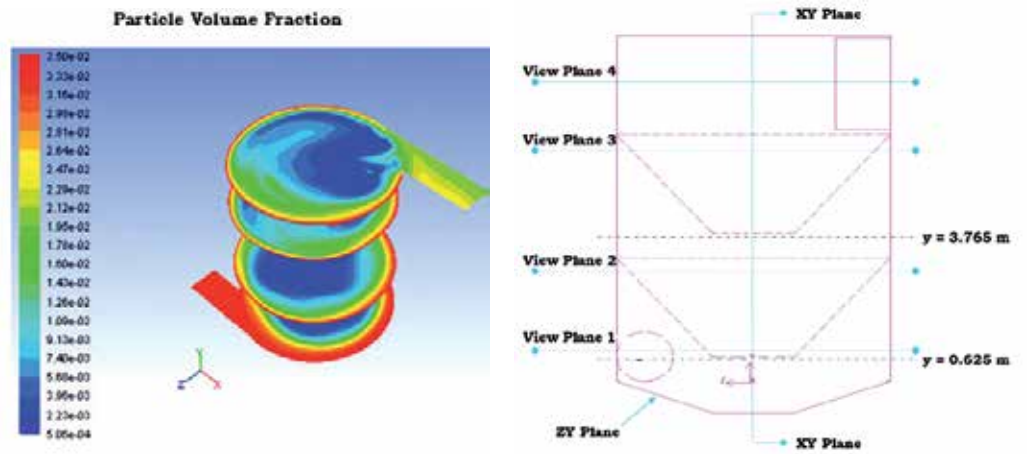

Fig. 9. Contour plot of particulate volume fraction (left) at selected view planes (right)

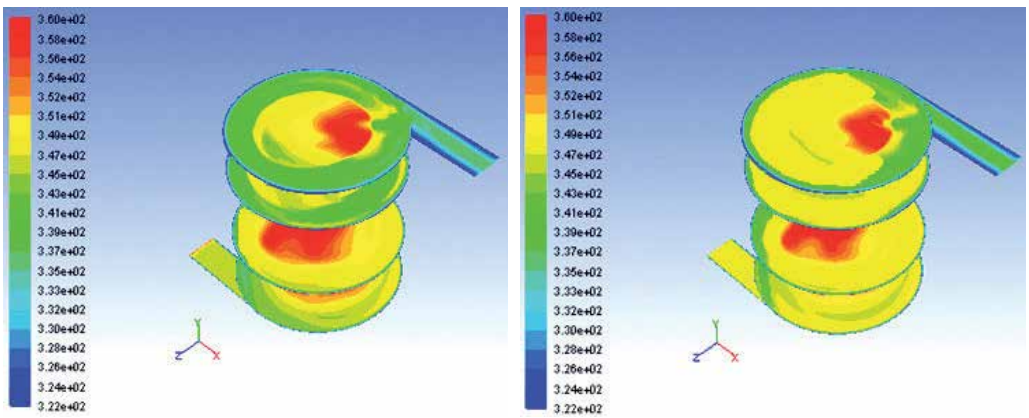

Fig. 10. Contour plot of gas (left) and particle (right) temperatures at selected view planes (Figure 9, right)

For case II, in absence of experimental data we relied more on the qualitative gas and solid velocity patterns in the cyclone dryer. In this case, the UDF capability in FLUENT/ANSYS R12.0 was enhanced by incorporating output data from a pneumatic dryer upstream of the cyclone dryer without facing any divergence or instability issues.

6. Concluding remarks

This chapter demonstrated a simple application of CFD for industrial drying processes. With careful consideration, CFD can be used as a tool to predict the hydrodynamic as well as the heat- and mass-transfer mechanisms occurring in the drying units. It can also be used to better understand and design the drying equipment with less cost and effort than laboratory testing. Although considerable growth in the development and application of CFD in the area of drying is obvious, the numerical predictions are by far still considered as qualitative measures of the drying kinetics and should be validated against experimental results. This is due to the fact that model approximations are used in association with CFD

methods to facilitate and represent complex geometries and reduce computational time and convergence problems.
Although CFD techniques are widely used, the modeller should bear in mind many of the pitfalls that characterize them. Some of these pitfalls are related to but not limited to the choice of the meshing technique; the numerical formulation; the physical correlations; the coding of meaningful and case specific UDFs; the choice from a spectrum of low and high order schemes for the formulation of the governing equations; and last but not least, the choice of iterative and solution dependent parameters.
In addition, due to the complex nature of the processes occurring in the drying systems, extensive simulations must be carried out to demonstrate that the solution is time- and grid-independent, and that the numerical schemes used have high level of accuracy by validating them with either experimental data or parametric and sensitivity analysis. This is particularly crucial in the approximation of the convective terms, as low order schemes are stable but diffusive, whereas high order schemes are more accurate but harder to converge.

7. Nomenclature

7.1 General

A	Surface area [m^2]
b	Coefficient in turbulence model [dimensionless]
c	Particle fluctuation velocity [m/s]
$C_{1\varepsilon}$,$C_{2\varepsilon}$,$C_{3\varepsilon}$	Turbulence coefficients [=1.42, 1.68, 1.2, respectively]
C_μ	Turbulence coefficient = 0.09 [dimensionless]
c_p	Specific heat capacity of the gas phase [J/kg K]
C_D	Drag coefficient, defined different ways [dimensionless]
c_{vm}	Virtual mass coefficient = 0.5 [dimensionless]
C_g	Vapor concentration in the gas phase [kmol/m^3]
$C_{p,s}$	Vapor concentration at the particle surface [kmol/m^3]
d_s	Particle diameter [m]
D_v	Diffusion Coefficient of water vapor in air [m^2/s]
D_s,$D_{t,sg}$	Turbulent quantities for the dispersed phase
e_{ss}	Particle-particle restitution coefficient [dimensionless]
e_w	Particle-wall restitution coefficient [dimensionless]
F_{vm}	Virtual mass force per unit volume [N/m^3]
$G_{k,g}$	Production of turbulence kinetic energy
g_o	Radial distribution function [dimensionless]
g	Gravitational acceleration constant [m/s^2] ; The gas phase
h	Heat transfer coefficient [W/m^{2}K]
H_{pq}	Interphase enthalpy [J/kg]
H_q	Enthalpy of the q phase [J/kg]
k	Turbulence kinetic energy [m^2/s^2]
K_{Ergun}	Fluid-particle interaction coefficient of the Ergun equation [kg/m^{3}s]
K_{gs}	Interphase momentum exchange coefficient [kg/m^{3}s]
k_{cond}	Thermal conductivity of gas phase [W/m K]
k_c	Convective mass transfer coefficient [m/s]
k_θ	Diffusion coefficient for granular energy

k_g	Turbulence quantity of the gas phase [m²/s²]
k_s	Turbulence quantity of the solid phase [m²/s²]
k_{sg}	Turbulence quantity of the inter-phase [m²/s²]
$L_{t,g}$	Length scale [m]
m_s	Solid mass [kg]
M	Molecular weight [kg/kmol]
$\dot{M}_{pq}$	Mass transfer between phases per unit volume [kg/m³s]
N_d	Number of particles per unit volume [1/m³]
Nu_s	Nusselt number [dimensionless]
P	Pressure [N/m²]
P_s	Solid pressure [N/m²]
P_{sat}	Saturated vapor pressure [Pa]
Pr	Prandtl number [dimensionless]
Q_{pq}	Heat exchange between the phases per unit volume [W/m³]
R	Gas constant [J/kmol K]; Particle radius [m]
Re_s	Solid Reynolds number [dimensionless]
Sc	Schmidt number [dimensionless]
Sh	Sherwood number [dimensionless]
t	Time [s]
T_g	Gas temperature [K]
T_s	Solid temperature [K]
$\vec{U}_q$	Velocity vector of phase q [m/s]
$\vec{U}_g$	Velocity vector of gas phase [m/s]
$\vec{U}_s$	Velocity vector of solid phase [m/s]
$\vec{U}_{sg}$	Relative velocity between the phases [m/s]
$\vec{U}_{dr}$	Drift velocity vector [m/s]
$\vec{U}_{s,\parallel}$	Particle slip-velocity parallel to the wall [m/s]
V	Volume [m³]
X	Particle moisture content [%]
X_{H2O}	Vapor mole fraction in the gas phase [dimensionless]
$\overline{X}$	Mean particle moisture content [%]
Y_q	Mass fraction of vapor in phase q [%]
$\overline{\overline{D}}_q$	Strain-rate tensor for phase q [1/s]

7.2 Greek symbols

α_q	Volume fraction of phase q (s = solid; g = gas)
$\alpha_{s,max}$	Maximum volume fraction of solid phase
β_{sg}	Drag force per unit volume between the phases [N/m³]
γ_s	Collisional dissipation of granular temperature [kg/m³ s]
ε	Turbulent dissipation rate [m²/s³]
ε_g	Turbulent dissipation rate of gas phase [m²/s³]
ε_s	Turbulent dissipation rate of solid phase [m²/s³]

η_{sg}	Turbulence quantity
θ_s	Granular temperature [m^2/s^2]
θ	Angle [rad]
μ_s	Solid shear viscosity [kg/m s] or [Pa s]
μ_b	Solid bulk viscosity [kg/m s] or [Pa s]
μ_g	Gas dynamic viscosity [kg/m s] or [Pa s]
$\mu_{t,q}$	Turbulence viscosity of phase q [kg/m s] or [Pa s]
K	Inter-phase drag coefficient [kg/m^3s]
$\Pi_{k,g}$, $\Pi_{s,g}$	Influence of dispersed phase on continuous phase
ρ_q	Density of phase q [kg/m^3]
ρ_g	Density of the gas phase [kg/m^3]
ρ_s	Density of the solid phase [kg/m^3]
σ_{gs}	Dispersion Prandtl number = 0.75
σ_k	Turbulent Prandtl number for the turbulent kinetic energy k
σ_ε	Turbulent Prandtl number for the turbulent dissipation rate ε
$\tau_{F,sg}$	Characteristic particle relaxation time connected with inertial effects [s]
$\overline{\overline{\tau}}_s$	Solid stress tensor [N/m^2]
$\tau_{t,g}$	Characteristic time of the energetic turbulent eddies [s]
$\tau_{t,sg}$	Lagrangian integral time scale [s]
$\overline{\overline{\tau}}_q$	Reynolds stress tensor [N/m^2] or [Pa]
∇	Rate of change in special coordinate [1/m]
$\overline{\overline{I}}$	Identity matrix

7.3 Subscripts

cr	Critical property
ds	Dry solid property
eq	Equilibrium property
g	Gas property
H2O(l)	Liquid water
o	Initial condition
q,p	Phase property (s = Solid; g = Gas)
s	Solid property
sat	Saturated condition
vm	Virtual mass

7.4 Superscripts

$\rightarrow$	Vector quantity
$=$	Tensor quantity

8. References

[1] Mujumdar, A.S. Research and development in drying: Recent trends and future prospects. Drying Technology 2004, *22* (1-2), 1 - 26.

[2] Mujumdar, A.S.; Wu, Z. Thermal drying technologies — Cost effective innovation aided by mathematical modeling approach. Drying Technology 2008, *26*, 146 - 154.
[3] Jamaleddine, T.J.; Ray, M.B. Application of computational fluid dynamics for simulation of drying processes: A review. Drying Technology 2010, *28* (2), 120 - 154.
[4] Massah, H.; Oshinowo, L. Advanced gas-solid multiphase flow models offer significant process improvements. Journal Articles by Fluent Software Users 2000, *JA112*, 1 - 6.
[5] Enwald, H.; Peirano, E.; Almstedt, A.E. Eulerian two-phase flow theory applied to fluidization. International Journal of Multiphase Flow 1996, *22* (suppl.), 21 - 66.
[6] Wen, C.Y.; Yu, Y.H. Mechanics of fluidization. Chemical Engineering Progress Symposium Series 1996, *62*, 100 – 111.
[7] Ergun, S. Fluid flow through packed columns. Chemical Engineering Progress 1952, *48*, 89 - 94.
[8] Gidaspow, D.; Bezburuah, R.; Ding, J. Hydrodynamics of circulating fluidized beds, kinetic theory approach. Fluidization VII Proceedings of the 7th Engineering Foundation Conference on Fluidization, Gold Coast, Australia 1992, 75 - 82.
[9] Chapman, S.; Cowling, T.G. *The mathematical theory of non-uniform gases*. 3rd ed., Cambridge University Press: Cambridge, U.K., 1970.
[10] Jenkins, J.T.; Savage, S.B. A theory for the rapid flow of identical, smooth, nearly elastic, spherical particles. J. Fluid Mech. 1983, *130*, 187 - 202.
[11] Ding, J.; Gidaspow, D. A bubbling fluidization model using kinetic theory of granular flow. AIChE J. 1990, *36*(4), 523 - 538.
[12] Gidaspow, D. *Multiphase Flow and Fluidization*. Academic Press, Inc., New York, 1994.
[13] Tsuji, Y.; Kawagushi, T.; Tanaka, T. Discrete particle simulation of two-dimensional fluidized bed. Powder Technology 1993, *77*, 79 - 87.
[14] Hoomans, B.P.B.; Kuipers, J.A.M.; Briels, W.J.; Van Swaaij, W.P.M. Discrete particle simulation of bubble and slug formation in a two-dimensional gas-fluidised bed: A hard-sphere approach. Chemical Engineering Science 1996, 51, 99–118.
[15] Strang, G.; Fix, G. *An Analysis of the Finite Element Method*. Prentice-Hall: Englewood Cliffs, NJ, 1973.
[16] Gallagher, R.H. *Finite Element Analysis: Fundamentals*. Prentice-Hall: Englewood Cliffs, NJ, 1975.
[17] Skuratovsky, I.; Levy, A.; Borde, I. Two-fluid two-dimensional model for pneumatic drying. Drying Technology 2003, *21*(9), 1649 – 1672.
[18] Lun, C.K.K.; Savage, S.B.; Jeffrey, D.J.; Chepurnity, N. Kinetic theories for granular flow: Inelastic particles in couette flow and slightly inelastic particles in a general flow field, J. Fluid Mechanics 1984, 140, 223 - 256.
[19] Gidaspow, D.; Huilin, L. Equation of State and Radial Distribution Function of FCC Particles in a CFB. AIChE J. 1998, 279.
[20] Baeyens, J.; Gauwbergen, D. van; Vinckier, I. Pneumatic drying: the use of large-scale experimental data in a design procedure. Powder Technology 1995, *83*, 139 – 148.
[21] De Brandt, IEC Proc. Des. Dev. 1974, *13*, 396.
[22] Fick, A. *Ueber Diffusion*. Poggendorff's Annals of Physics 1855, *94*, 59 - 86.
[23] FLUENT 6.3 User's Guide. Fluent Incorporated, Lebanon, NH, 2006.
[24] Hinze, J. O. *Turbulence*. McGraw-Hill Publishing Co., New York, 1975.

[25] Paixa˜o, A.E.A.; Rocha, S.C.S. Pneumatic drying in diluted phase: Parametric analysis of tube diameter and mean particle diameter. Drying Technology 1998, *16* (9), 1957 - 1970.

[26] Baeyens, J.; van Gauwbergen, D.; Vinckier, I. Pneumatic drying: The use of large-scale experimental data in a design procedure. Powder Technology 1995, *83*, 139 - 148.

[27] Arlabosse, P.; Chavez, S.; Prevot, C. Drying of municipal sewage sludge: From a Laboratory scale batch indirect dryer to the paddle dryer. Brazilian Journal of Chemical Engineering 2005, *22*, 227 - 232.

[28] Bunyawanichakul, P.; Kirkpatrick, M.; Sargison, J.E.; Walker, G.J. Numerical and experimental studies of the flow field in a cyclone dryer. Transactions of the ASME 2006, *128*, 1240 - 1250.

[29] Patankar, S.V. *Numerical Heat Transfer and Fluid Flow*. McGraw-Hill, New York, 1980.

[30] Huang, L.X.; Kumar, K.; Mujumdar, A.S. Simulation of a spray dryer fitted with a rotary disk atomizer using a three-dimensional computational fluid dynamic model. Drying Technology 2004, *22*(6), 1489 - 1515.

[31] Huang, L. X.; Kumar, K.; Mujumdar, A.S. A comparative study of a spray dryer with rotary disc atomizer and pressure nozzle using computational fluid dynamic simulations. Chemical Engineering and Processing 2006, *45*, 461 - 470.

6

Extraction of Oleoresin from Pungent Red Paprika Under Different Conditions

Vesna Rafajlovska[1], Renata Slaveska-Raicki[2],
Jana Klopcevska[1] and Marija Srbinoska[3]
[1]*Ss. Cyril and Methodius University in Skopje, Faculty of Technology and Metallurgy, Skopje*
[2]*Ss. Cyril and Methodius University in Skopje, Faculty of Pharmacy, Skopje*
[3]*University St. Kliment Ohridski-Bitola, Scientific Tobacco Institute, Prilep, Republic of Macedonia*

1. Introduction

The significance of and interest in pungent paprika have been growing over the years due to its high potential to provide a broad spectrum of products with important medicinal and commercial value (Govindarajan & Sathyanarayana, 1991; Guzman et al., 2011; Pruthi, 2003). As a rich source of characteristic phytocompounds, pungent paprika has a notable place in modern food and in pharmaceutical industries (De Marino et al., 2008).

As acknowledged, the principal pungent constituent of pungent paprika is capsaicin, an alkaloid or predominant capsaicinoid, followed by dihydrocapsaicin, nordihydrocapsaicin, homodihydrocapsaicin and homocapsaicin (Davis et al., 2007; Hoffman et al., 1983). Although there are two geometric isomers of capsaicin, only *trans*-capsaicin occurs naturally, and thus the term 'capsaicin' is generically used to refer to the *trans*-geometric isomer. The capsaicin content of pungent paprika ranges from 0.1 to 1%w/w (Barbero et al., 2006; Govindarajan & Sathyanarayana, 1991).

Over the years, capsaicin, a promising molecule with many possible clinical applications, has been comprehensively studied (experimentally, clinically and epidemiologically) owing to its prominent antioxidant, antimicrobial and anti-inflammatory properties (Dorantes et al., 2000; Materska & Peruska, 2005; Reyes-Escogido et al., 2011; Singh & Chittenden, 2008; Xing et al., 2006; Xiu-Ju et al., 2011). Many studies give evidence that capsaicin has been widely used as the potent active ingredient incorporated into a wide range of topical analgesic formulations (Weisshaar et al., 2003, Ying-Yue et al. 2001). Moreover, considerable interest has developed in expanding the usage of capsaicinoids in other forms such as natural product-based food additive, dietary supplements and as constituent in self-defense products (Dorantes et al., 2000; Materska & Perucka, 2005; Nowaczyk et al., 2008; Spicer & Almirall, 2005; Xing et al., 2006). In addition, the recent results showing their possible therapeutic effects in obesity treatment have further increased the importance of capsaicinoids (Ji-Hye et al., 2010).

One of the most common pungent paprika products is pungent capsicum oleoresin (PCO), an organic oily resin derived from the dried ripe fruits of pungent varieties of *Capsicum annuum* L., by means of solid-liquid extraction and subsequent solvent removal (Cvetkov &

Rafajlovska, 1992; Kense, 1970; Rajaraman et al., 1981). Basically, PCO contains pigments carotenoids predominantly capsanthin (Giovannucci, 2002, Hornero-Méndez et al., 2000; Matsufuji et al., 1998) and not less than eight percent of total capsacinoids. Furthermore, beside the pigments, chemical entities such as flavors, taste agents, vitamins and fatty oil are also present in the PCO components profile (Howard et al., 1994; Vinaz et al., 1992). However, a survey of literature reveals that, generally, the most commonly employed and a preferred method for extraction of compounds present in plant matrices is the conventional solid-liquid extraction using organic solvents. In later studies, these conventional methods were improved, modified or rationalized by varying different operating parameters (Boonkird et al., 2008; Toma et al., 2001; Vinatoru, 2001; Wang & Weller, 2006).

The paprika oleoresins are produced by solvent extraction of dried, ground red pepper fruits, using a solvent-system compatible with the lipophilic/hydrophilic characteristics of the extract sought and subsequent solvent-system removal. The solvents most commonly used for paprika oleoresin extraction are trichloroethylene, ethylacetate, acetone, propan-2-ol, methanol, ethanol and *n*-hexane (Cvetkov & Rafajlovska, 1992; Hornero-Méndez et al., 2000; Kense, 1970).

Although many studies have been published on the development and implementation of the different operating conditions for PCO recovery, little attention seems to have been given to the optimization of the various extraction variables (e.g. the appropriate solvent, temperature, dynamic extraction time, quantity of sample, etc.) nor has a systematic study for the optimization of the method been carried out. Therefore, in a situation, where multiple variables may influence the extraction yield, application of a response surface methodology (RSM) to optimize the extraction condition offers an effective technique for studying and optimizing the process and operating parameters (Acero-Ortega et al., 2005; Giovanni, 1983; Li & Fu, 2005; Montgomery, 2001).

As part of our contribution to the studies on extraction methods for pungent red paprika we have carried out organic solvent extraction procedure under different conditions, resulting in optimized conditions for the matrix compounds from *Capsicum annuum* L. Hence, the principal goals were to study the influence of the solvent type, extraction temperature and dynamic time on pungent red paprika extraction efficiency expressed by PCO yield and capsaicin and capsanthin content in it and to establish mathematical models to predict system responses.

2. Materials and methods

2.1 Plant material

Red pungent dried paprika fruits or, more precisely, pericarp (*Capsicum annuum* L., ssp. *microcarpum longum conoides*, convar. Horgos) used in this study were obtained from the Markova Ceshma region, Prilep, Republic of Macedonia. The pepper species was authenticated by Prof. Danail Jankulovski, Faculty of Agricultural Sciences and Food, Skopje, Republic of Macedonia. A voucher specimen (#1035) is deposited there. The dried pericarp was ground using Retsch ZM1 mill (Germany) and sieved (0.250 mm particle size). The paprika samples placed in dark glass bottles were stored at 4^{o}C in refrigerator.

2.2 Extraction procedure

The impact of three different solvents (ethanol, methanol and *n*-hexane) on the PCO yield, capsaicin and capsanthin content in it were explored using maceration by solid:liquid ratio 1:20 w/v. A 1 g paprika sample (0.0001 g accurately weighed) was used in preparation of

single extract. Furthermore, for extraction parameter study at different temperature and time, the extraction was carried out in thermostatic water bath at a temperature of 30, 40, 50, 60 and 70°C, respectively with the exception of 70°C when ethanol was utilized. The effect of dynamic extraction time on the analyte of interest was followed during 60, 120, 180 and 300 min, respectively. After extraction for selected time and at maintained temperature, the solvent was removed under vacuum (rotary vacuum evaporator, type Devarot, Slovenia, 35°C, atm. pressure). Solvent traces were discharged by drying the sample at 40°C, 105 mPa (vacuum drier, Heraeus Vacutherm VT 6025, Langenselbold, Germany). Each extraction procedure was performed in duplicate under the same operating conditions.

2.3 Determination of pungent capsicum oleoresin yield

Obtained PCOs were cooled in a desiccator and weighed. The steps of drying, cooling and weighing were repeated until the difference between two consecutive weights was smaller than 2 mg. The PCO yield was estimated according to dry matter weight in extracted quantity of red pungent paprika. The extract was transferred into a 100 mL volumetric flask and filled to 100 mL with ethanol (1st dissolution).

2.4 Determination of capsaicin content in pungent capsicum oleoresin

The capsaicin content in the extracts was determined by reading of the absorbance at 282 nm. Actually, 0.5 mL of 1st dissolution was dissolved and filled up to 10 mL with ethanol and the absorbance was measured. The concentration of capsaicin was estimated from the standard curve for capsaicin given by the Eq. (1).

$$y=9.64x+0.005 \quad R^2=0.9909 \tag{1}$$

where x = μg capsaicin/mL extract and y = absorbance.

2.5 Determination of capsanthin content in pungent capsicum oleoresin

Pigments concentration in red pungent paprika extract was calculated using the extinction coefficient of the major pigment capsanthin ($^{1\%}E_{460nm}$= 2300) in acetone (Hornero-Méndez et al., 2000).

2.6 Apparatus

The spectrophotometric measurements were carried out on a Varian Cary Scan 50 spectrophotometer (Switzerland) in 1cm quartz cells, at 25°C.

2.7 Statistical analysis

The statistical analysis and evaluation of the data were performed using STATISTICA 8 (StaSoft, Inc., Tulsa, USA) software. A two-predictors non linear regression model was used to evaluate the individual and interactive effects of two-independent variables, extraction temperature (x_1) and dynamic time (x_2). The responses measured were PCO yield, capsaicin and major pigment capsanthin present in the PCO.

The second order model includes linear, quadratic and interactive terms thus, in the responses function (Y)-Eq. 2, x_i and x_j are predictors; β_0 is the intercept; β_i are linear coefficients; β_{ii} are squared coefficients; β_{ij} are interaction coefficients and ε is an error term.

$$Y = \beta_o + \sum_{i=1}^{k} \beta_i X_1 + \sum_{i=1}^{k} \beta_{ii} X_2 + \sum_{i>1}^{k} \beta_{ij} X_i X_j + \varepsilon \quad (2)$$

ANOVA was used to evaluate the significances of the coefficients of the models judged by computing the *F*-value at a probability (*p*) of 0.001, 0.01 and 0.05.
The influence of the predictors on the responses was also presented using 3-D mesh plots and contour maps.

3. Results and discussion

As acknowledged, the selection of the most appropriate solvent for extracting the analytes of interest from the plant matrix is a basic step in the development of any method of solvent extraction. Theoretically, solvent would provide not only a background for the extraction process but it would also stabilize the analytes and the transition state species by solvating process. This solvation is due to solvent-analyte interactions during which a solvent acts either as a nucleophile or as an electrophile by donating or accepting electron pairs from the analyte. The research data evidence for hot pepper cultivars indicate that methanol and ethanol are solvents usually used in the extraction of capsaicinoids in various extraction techniques (Barbero et al., 2006; Kirschbamm-Titze et al., 2002; Williams et al. 2007). Studies on the solvent influence on pigments extraction from *Capsicum* fruits ascertained *n*-hexane and acetone as suitable solvent medium for pigments (Boyadzhiev et al., 1999; Feltl et al., 2005; Tepić et al., 2009).
Evidence provided by relevant literature positively confirm recent growing interest in the development of mathematical models that describe the extraction process as a function of various operational variables and, particularly, those that describe their combined effect (Acero-Ortega et al., 2005; Bo et al., 2008; Hismath et al., 2011; Liu et al., 2010).
In order to select the extraction solvent for pungent paprika matrix, experiments were performed with three solvents: ethanol, methanol and *n*-hexane. According to our previous experiences (Rafajlovska et al., 2007), the two variables that could potentially affect the extraction efficiency of the analytes of interest in chosen solvents are extraction temperature and dynamic time. Owing to the significance of interaction between time and temperature, their interactive influence on the extraction efficiency was also considered. Other parameters implicated in the extraction were kept constant, namely the solid:phase ratio and particles size.

3.1 Extraction of pungent capsicum oleoresin, capsaicin and capsanthin with ethanol

3.1.1 Model fitting

Table 1 shows the liner, quadratic and interactive coefficients of the independent variables in the models and their corresponding R^2 when ethanol was used as extraction solvent. It can be seen that the R^2 values for these response variables are higher than 0.97 where PCO and capsaicin are concerned, indicating that the regression models adequately explained the process. Therefore, the R^2 values are 0.9795 and 0.9810, respectively, for PCO yield and capsanthin. The probability (*p*) values of regression models for PCO and capsaicin show no lack-of-fit ($p < 0.001$). However, since the R^2 value of capsanthin is not acceptable (R^2=0.7890) this regression model is not suitable to explicate the extraction process for capsanthin, probably owing to the solvent characteristics.

	Yield (%)	Capsaicin (mg/100g)	Capsanthin (mg/100g)
b_o (intercept)	3.153322	186.625700	117.141400
b_1	0.260120***	- 0.262400	3.238900
b_2	0.025702**	0.063600	0.987800***
b_1^2	- 0.000452	0.010700	- 0.023000
b_2^2	- 0.000010	- 0.000500**	- 0.000800
b_{12}	- 0.000286**	0.004800***	- 0.012200***
R^2	0.9795	0.9810	0.7890
adjusted R^2	0.9722	0.9742	0.7138
p or probability	0.0000	0.0000	0.0002

Subscripts: 1 = temperature (°C); 2 = time (min);
*Significant at 0.05 level; **Significant at 0.0l level; ***Significant at 0.001 level.

Table 1. Regression coefficients, R^2, adjusted R^2 and *p* for three dependent variables for pungent capsicum oleoresin obtained by ethanol.

3.1.2 Influence of extraction temperature and time

The influence of extraction conditions on the PCO yield and capsaicin were presented by the coefficients of the second-order polynomials. As shown in Table 2, PCO yield was significantly affected by the positive linear effect ($p < 0.001$) of the temperature and the positive linear effect ($p < 0.01$) of the time. In this case, the temperature and time were relevant variables for the model. However, significant linear interaction between the temperature and time ($p < 0.01$) had a negative sign. Moreover, it was found that the influence in the second-order term for the both variables showed no significant effect ($p > 0.05$). These results suggest that the linear effect of the extraction temperature was the primary determining factor for PCO yield but there is no need for prolonged solid/liquid phase contact. The response surface and contour map were also developed to facilitate the visualization and latter, for predicting the optimum condition for PCO yield and capsaicin in ethanol (Fig. 1).

Fig. 1b shows that the PCO yield increased as the temperature increased. As for the capsaicin content in PCO, the positive interaction among the independent variables ($p < 0.001$) significantly influenced the capsaicin content. It was also found that quadratic effect of extraction time is negative at $p < 0.01$. However, the linear term of temperature and time showed no significant effect on capsaicin content in ethanolic PCO. Hence, when analyzing the interactive effect of temperature and time on the extraction efficiency of capsaicin (Fig. 2) in the model developed for ethanol as extraction solvent, it was observed that extended time of extraction is not appropriate under increased temperature condition.

Fig. 3 shows that owing to the capsanthin temperature liability (Ahmeda et al., 2002; Pérez-Gálvez et al., 2005; Schweiggert et al., 2007), capsanthin extraction in ethanolic medium should be performed at decreased temperature of about 40°C at most during extended time.

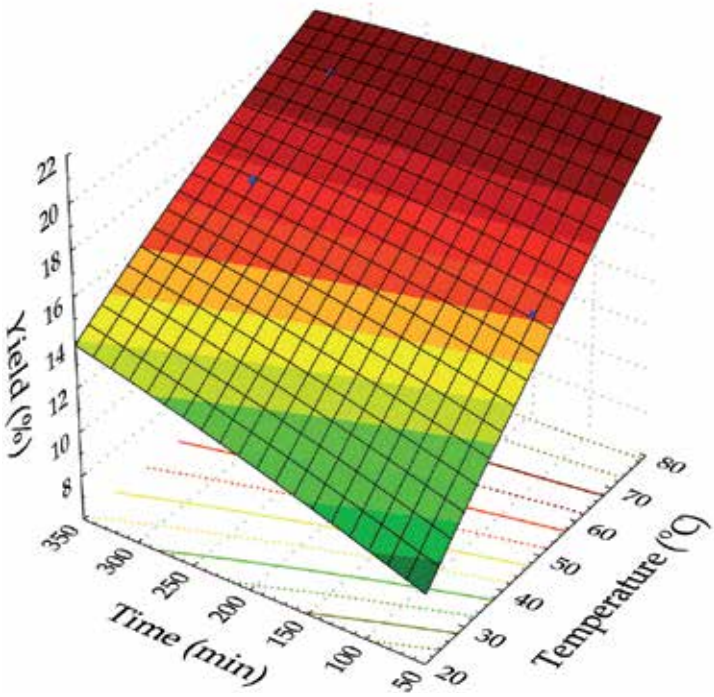

(a)

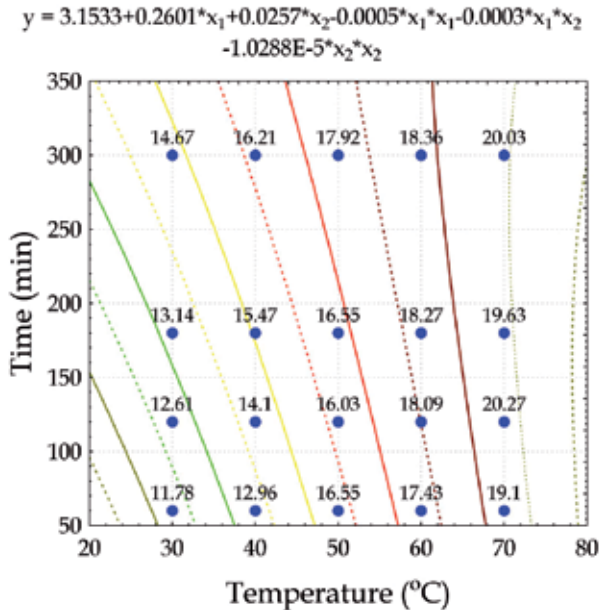

(b)

Fig. 1. 3-D mesh plot (a) and contour plot (b) of the effects of extraction temperature and time on PCO yield (%) in ethanol.

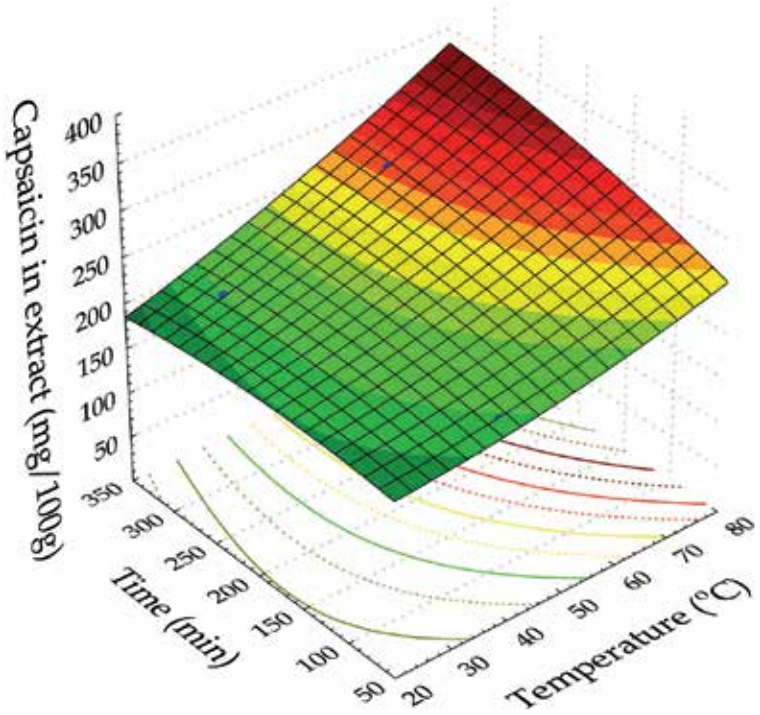

(a)

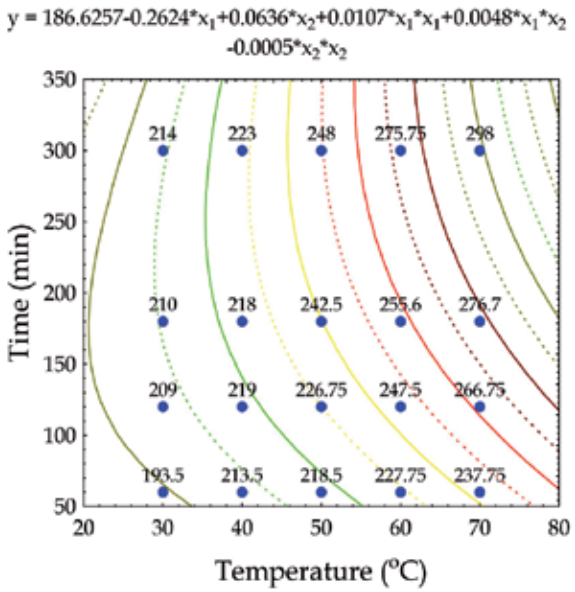

(b)

Fig. 2. 3-D mesh plot (a) and contour plot (b) of the effects of extraction temperature and time on capsaicin in ethanolic PCO.

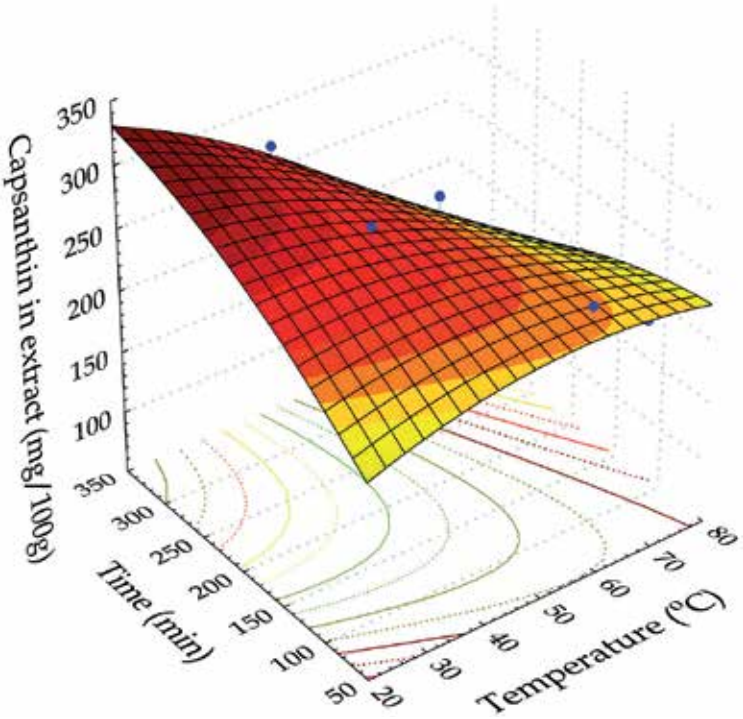

(a)

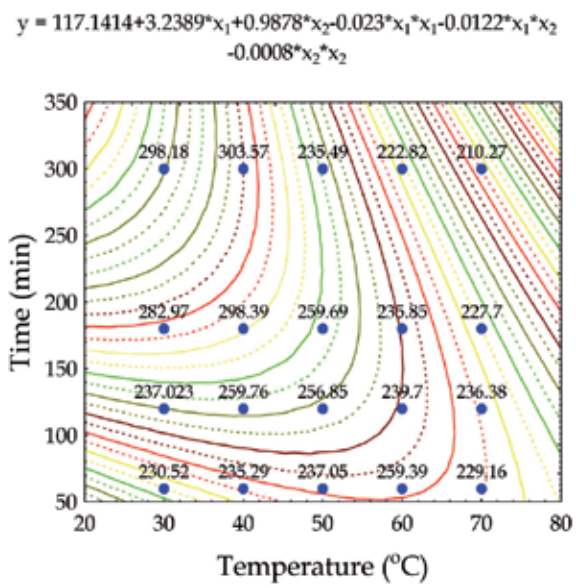

(b)

Fig. 3. 3-D mesh plot (a) and contour plot (b) of the effects of extraction temperature and time on capsanthin in ethanolic PCO.

3.2 Extraction of pungent capsicum oleoresin, capsaicin and capsanthin with methanol

3.2.1 Model fitting

The liner, quadratic and interactive coefficients of the independent variables in the models and their corresponding R^2 when methanol was used as extraction solvent are presented in Table 2.

	Yield (%)	Capsaicin (mg/100g)	Capsanthin (mg/100g)
b_o (intercept)	4.938929	16.501750	- 56.065700
b_1	0.282113	6.922010*	9.785980**
b_2	0.036924*	0.324730	0.808700**
b_1^2	- 0.002389	- 0.087330**	- 0.097400*
b_2^2	- 0.000051	- 0.001700**	- 0.001300*
b_{12}	0.000337	0.012620***	- 0.006600**
R^2	0.9702	0.9391	0.7228
adjusted R^2	0.9553	0.9087	0.5843
p or probability	0.0000	0.0000	0.0130

Subscripts: 1 = temperature (°C); 2 = time (min);
*Significant at 0.05 level; **Significant at 0.0l level; ***Significant at 0.001 level.

Table 2. Regression coefficients, R^2, adjusted R^2 and *p* for three dependent variables for pungent capsicum oleoresin obtained by methanol.

Table 2 clearly shows that the R^2 values for these response variables are higher than 0.93 for both PCO and capsaicin, indicating that the regression models adequately explain the process. Hence, the R^2 values are 0.9702 and 0.9391, respectively, for methanolic PCO yield and capsaicin. The *p* values of regression models for PCO yield and capsanthin show no lack-of-fit. However, as expected, the R^2 value of capsanthin is low, (R^2 = 0.7228) confirming that a high proportion of variability is not explained by the model. We therefore conclude that this regression model cannot offer a satisfactory explanation of the extraction process for capsanthin.

3.2.2 Influence of extraction temperature and time

The influence of extraction conditions on the PCO, capsaicin and capsathin are presented by the coefficients of the proposed model. As indicated by *p* value, positive linear ($p < 0.05$) effect of time is only confirmed to be significant for PCO yield, while positive linear ($p < 0.05$) effect of temperature is noticed for capsaicin content present in methanolic PCO. Furthermore, it is found that interactive influence of both variables has the prominent positive effect ($p < 0.001$) for capsaicin content. On the other hand, a negative quadratic effect ($p < 0.01$) has been verified for both variables for capsaicin.

Fig. 4 and 5 show the response surface and contour map for PCO yield and capsaicin. It was observed that the capsaicin content rises as the temperature and time increase, but prolonged phase contact at increased temperature will not be acceptable due to the negative quadratic terms at $p < 0.01$. Generally speaking, when a higher extraction temperature was applied to the process, a higher velocity and extraction efficacy were achieved. However, some degradation processes can easily occur at high temperature, resulting in lower analyte recovery.

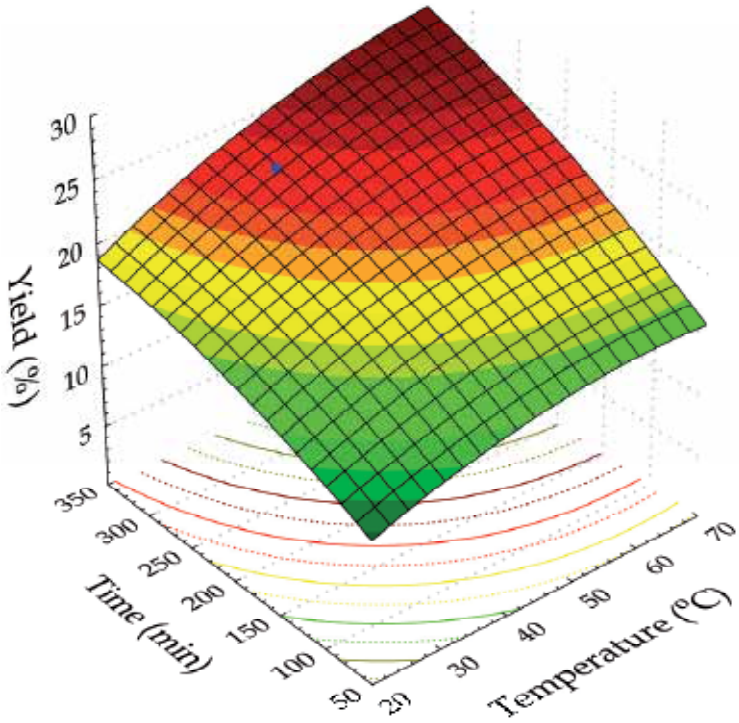

(a)

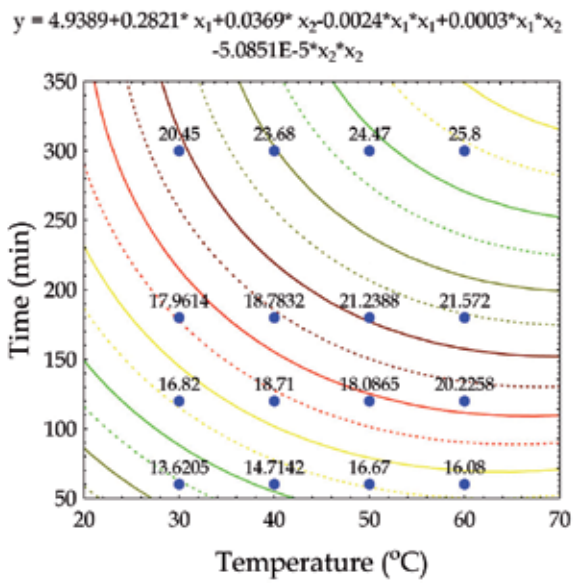

(b)

Fig. 4. 3-D mesh plot (a) and contour plot (b) of the effects of extraction temperature and time on PCO yield (%) in methanol.

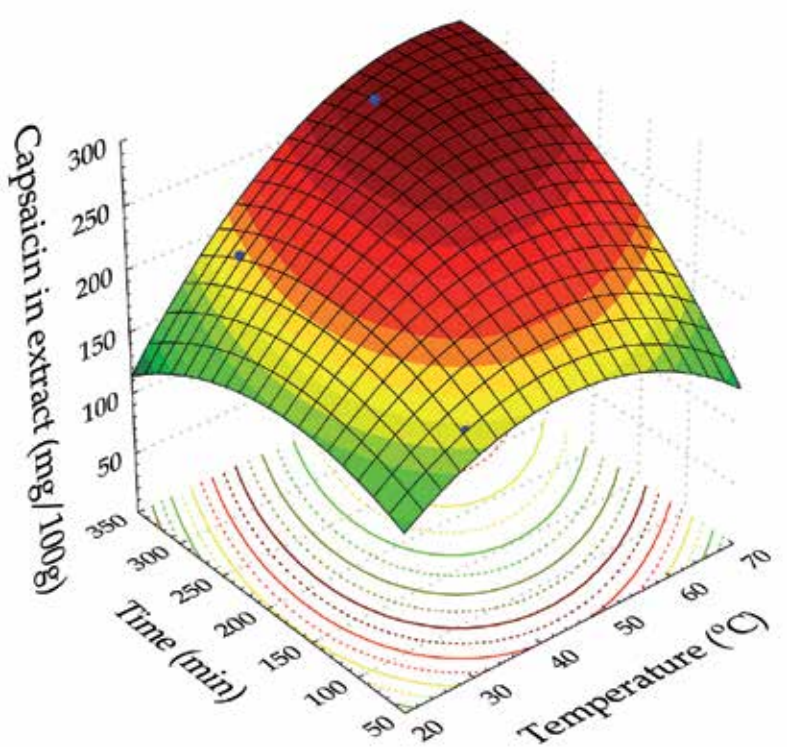

(a)

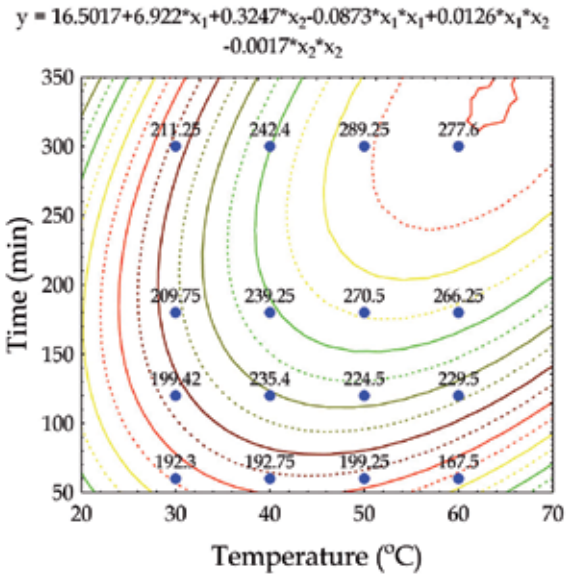

(b)

Fig. 5. 3-D mesh plot (a) and contour plot (b) of the effects of extraction temperature and time on capsaicin in methanolic PCO.

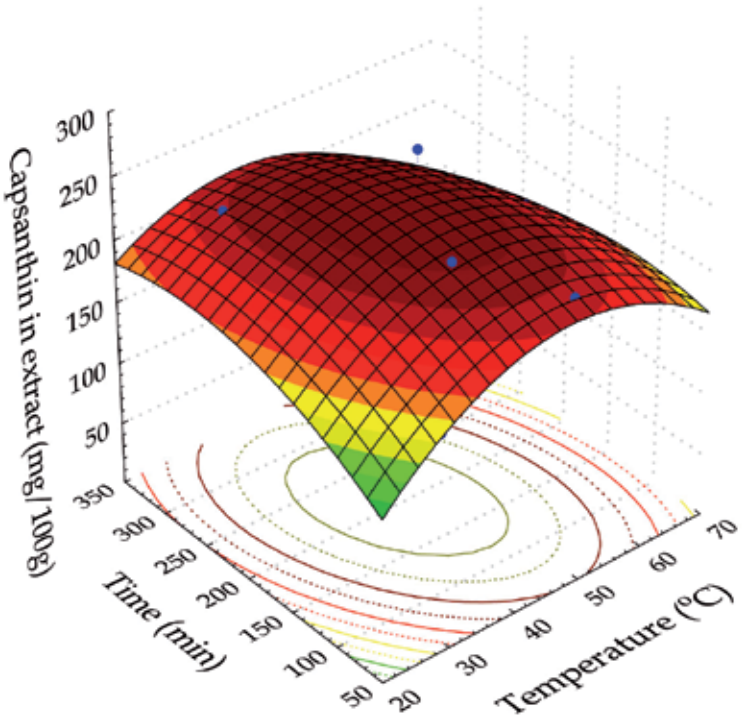

(a)

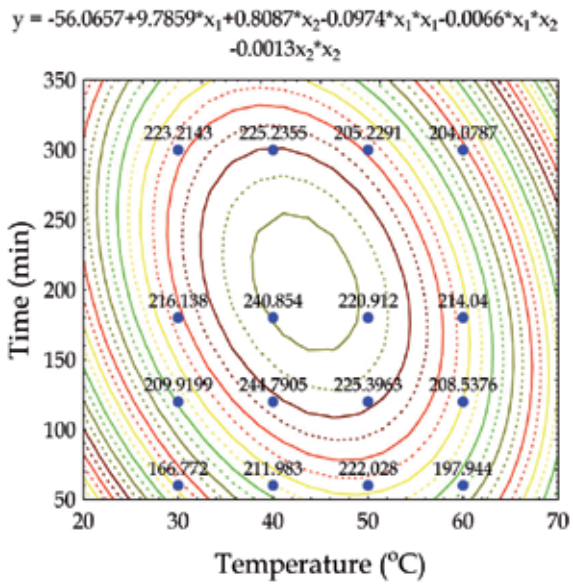

(b)

Fig. 6. 3-D mesh plot (A) and contour plot (B) of the effects of extraction temperature and time on capsanthin in methanolic PCO.

Consequently, Fig. 6 shows that the conditions for capsanthin extraction with methanol are unsuitable.

3.3 Extraction of pungent capsicum oleoresin, capsaicin and capsanthin with hexane

3.3.1 Model fitting

The data obtained by these models demonstrated how the independent variables in the models influenced the extraction efficiency of the analytes of interest when using *n*-hexane. Thus, the liner, quadratic and interactive coefficients of the independent variables in the models and their corresponding R^2 when *n*-hexane was used as extraction solvent presented in Table 3.

	Yield (%)	Capsaicin (mg/100g)	Capsanthin (mg/100g)
b_o (intercept)	3.922869*	- 27.952500	- 1912.489400
b_1	0.040339	3.445100*	88.014500**
b_2	0.007445	0.300400*	10.158300***
b_1^2	- 0.000234	- 0.028000	- 0.712100*
b_2^2	- 0.000013	- 0.000600*	- 0.001500
b_{12}	0.000105	- 0.001900	- 0.159800***
R^2	0.9482	0.7890	0.9013
adjusted R^2	0.9223	0.6836	0.8519
p or probability	0.0000	0.0037	0.0001

Subscripts: 1 = temperature (°C); 2 = time (min);
*Significant at 0.05 level; **Significant at 0.01 level; ***Significant at 0.001 level.

Table 3. Regression coefficients, R^2, adjusted R^2 and *p* for three dependent variables for pungent capsicum oleoresin obtained by *n*-hexane.

According to the *p*-value, the models appeared to be adequate for the observed data at a 99.9% confidence level for PCO yield and capsanthin when extraction process was carried out with *n*-hexane. The R^2 values, as a measure of the degree of fit, for these response variables, are higher than 0.90 where PCO and capsanthin are concerned, confirming that the regression models adequately explained the extraction process with *n*-hexane. Hence, the R^2 values are 0.9482 and 0.9013, respectively, for PCO yield and capsanthin. However, the R^2 value of capsaicin is low (R^2=0.7890) showing lack-of fit and has the less relevant dependent variable in the model. As expected, non-polar components are present in *n*-hexane extracts.

3.3.2 Influence of extraction temperature and time

The effect of extraction conditions on the PCO, capsaicin and capsathin are shown by the coefficients of the proposed model and confirmed by assessing the significance of the variables. As can be seen for capsanthin, both time ($p < 0.001$) and temperature ($p < 0.01$) are significant, being affected by the positive sign, while the interaction between temperature and time is significant ($p < 0.001$) with a negative sign. However, it is evident that negative quadratic effect ($p < 0.05$) of temperature is confirmed to be significant for capsanthin indicating that extended phase contact at increased temperature will be inappropriate. Obtained results also confirmed that *n*-hexane is the appropriate choice of solvent for capsanthin extraction. Fig. 7 and 9 show the response surface and contour map for PCO yield and capsanthin. Higher temperature and a longer phase contact decrease the capsanthin content in PCO.

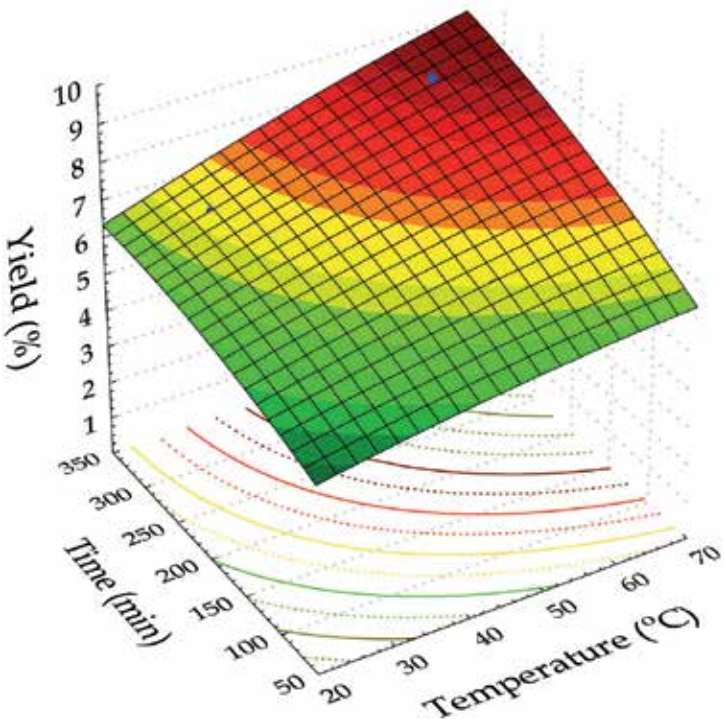

(a)

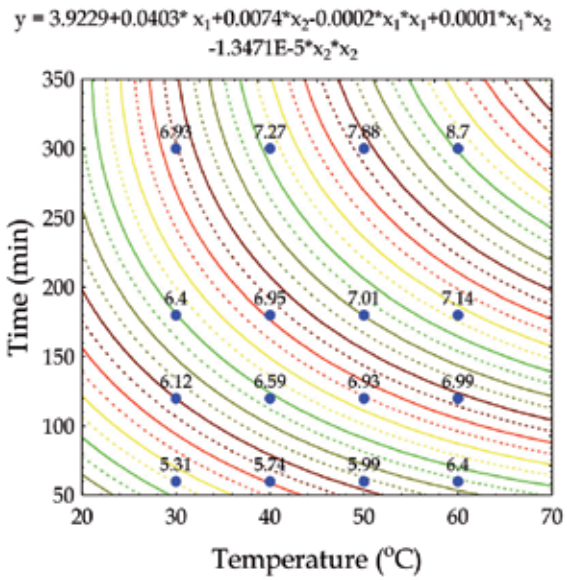

(b)

Fig. 7. 3-D mesh plot (a) and contour plot (b) of the effects of extraction temperature and time on PCO yield (%) in *n*-hexane.

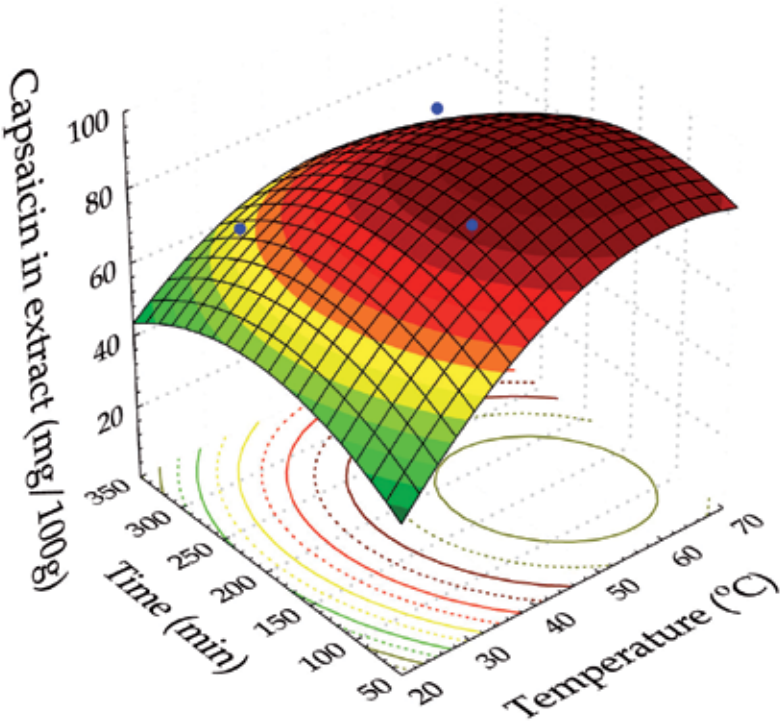

(a)

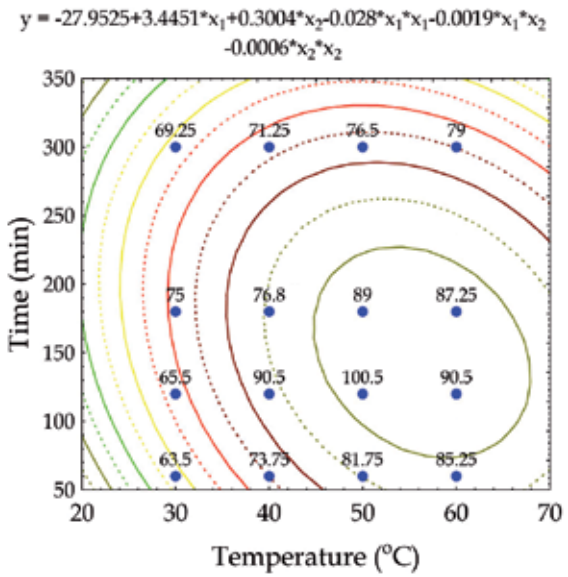

(b)

Fig. 8. 3-D mesh plot (a) and contour plot (b) of the effects of extraction temperature and time on capsaicin in *n*-hexane PCO.

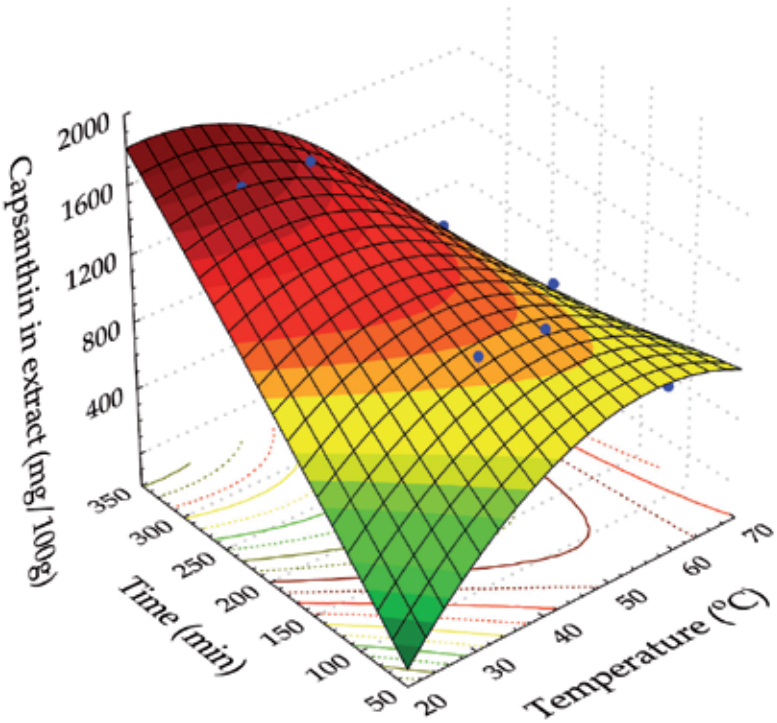

(a)

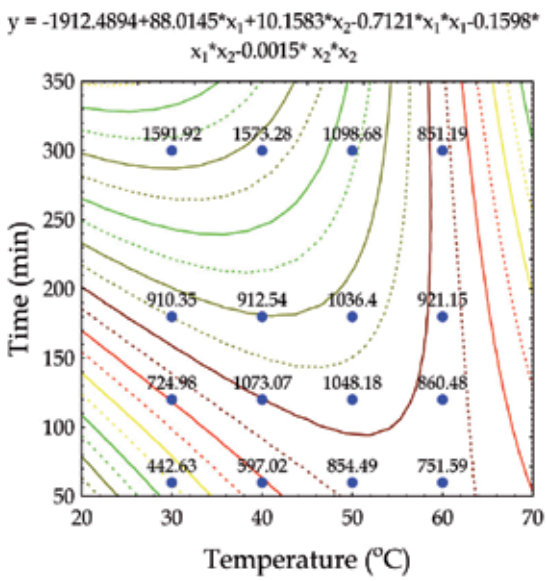

(b)

Fig. 9. 3-D mesh plot (a) and contour plot (a) of the effects of extraction temperature and time on capsanthin in *n*-hexane PCO.

Fig. 8 clearly shows that *n*-hexane is not the best solvent of choice for extraction of capsaicin.

3.4 Optimization of extraction conditions

RSM plays a key role in an efficient identification of the optimum values of the independent variables, under which depend variable could achieve a maximum response. In line with this, the set of optimum extraction conditions were determined by superimposing the contour plots of all the responses (Montgomery, 2001). The criteria applied for the optimization included maximum PCO yield and capsaicin in ethanol and methanol as well as maximum PCO yield and capsanhin in *n*-hexane. Data obtained from the profiles for predicted values and desirability are shown in Table 4. The desirability was calculated by simultaneous optimization of multiple responses, and ranges from low (0) to high (1). The optimum combined condition for PCO yield and capsaicin in ethanol was found to be at 68°C for 165 min. When methanol is used as extraction solvent, the lower temperature for protracted time contributes to maximum PCO yield and capsaicin. Therefore, the optimum combined condition in methanol is confirmed to be at 57°C for 256 min. The instability of capsanthin at increased temperature is again confirmed by optimum combined condition in *n*-hexane at 45°C for 256 min.

	Independent variable				
	Temperature (°C)	Time (min)	Low limit	High limit	Value
Dependent variable	**Ethanol**				
PCO yield (%)	68	165	11.28	21.63	19.12
Capsaicin (mg/100g)	68	165	118.45	290.71	269.00
Capsanthin (mg/100g)	35	256	195.85	303.75	293.46
Dependent variable	**Methanol**				
PCO yield (%)	57	256	12.38	26.23	23.73
Capsaicin (mg/100g)	57	256	158.04	297.82	283.10
Capsanthin (mg/100g)	45	165	178.93	250.71	210.65
Dependent variable	***n*-Hexane**				
PCO yield (%)	56	256	5.14	8.41	8.00
Capsaicin (mg/100g)	50	165	59.27	100.14	92.84
Capsanthin (mg/100g)	45	256	351.32	1554.66	1054.92

Table 4. The optimum combined condition predicted values for dependent variables at optimal values of variables.

3.5 Verification of predicted model

The PCO yield, capsaicin and capsanthin contents of the examined red pungent dried paprika fruit sample were calculated based on the optimized conditions of the proposed maceration method and compared with experimental values of the response variables. The verification of the obtained results requires good agreement between values calculated using the model equations and experimental value of the responses (Table 5).

	PCO yield (%)	Capsaicin (mg/100g)	Capsanthin (mg/100g)
Ethanol (time=165 min; temperature = 65°C)			
Predicted value	18.69	263.14	240.86
Experimental value	19.63	261.98	242.22
Methanol (time=256 min; temperature = 45°C)			
Predicted value	22.33	268.07	232.86
Experimental value	23.01	267.13	233.56
n-Hexane (time=256 min; temperature = 45°C)			
Predicted value	7.49	86.07	1267.49
Experimental value	6.72	87.22	1264.12

Table 5. Predicted and experimental value for the response at optimum conditions.

4. Conclusion

Surface plots were generated to describe the relationship between two operating variables and predicted responses.

Methanol and ethanol were confirmed to be superior and were chosen as the extraction solvents of first choice for the PCO and capsaicin under studied process condition. Regarding capsanthin, it is apparent that *n*-hexane offers optimal values with the highest desirability.

Process conditions, i.e. optimal extraction time and temperature with the highest desirability of analytes content of interest, were developed and verified.

5. References

Acero-Ortega, C.; Dorantes, L.; Hernández-Sánchez, H.; Tapia, M. S.; Gutiérrez-López, G.; Alzamora, S. & López-Malo, A. (2005). Response surface analysis of the effects of *Capsicum* extract, temperature and pH on the growth and inactivation of *Listeria monocytogenes*. *Journal of Food Engineering*, Vol.67, 247–252.

Ahmeda, J.; Shivhareb, U. S. & Ramaswamyc, H. S. (2002). A fraction conversion kinetic model for thermal degradation of color in red chilli puree and paste. *Lebensmittel-Wissenschaft und Technologie*, Vol.35, No.6, 497-503.

Barbero, G. F.; Palma, M. & Barroso C. G. (2006). Determination of capsaicinoids in peppers by microwave-assisted extraction–high-performance liquid chromatography with fluorescence detection. *Analytica Chimica Acta*, Vol.578, 227-233.

Bo, W.; Jianzhong, W.; Liangcheng, Z.; Xiaoping, G. & Guogang, M. (2008). Optimization for ultrasonic wave extraction of red pigment from paprika by response surface method. *Chinese Agricultural Science Bulletin*, Vol.6, 96-101.

Boonkird, S.; Phisalaphong, C. & Phisalaphong, M. (2008). Ultrasound-assisted extraction of capsaicinoids from *Capsicum* frutescens on a lab- and pilot-plant scale. *Ultrasonics Sonochemistry*, Vol.15, 1075–1079.

Boyadzhiev, L.; Kancheva, D.; Guiraud, P. & Gourdon, C. (1999). On carotenoids and capsaicin extraction from red paprika (*Capsicum annum* L.) fruits. *Hungarian Journal of Industrial Chemistry*, Vol.27, 37-41.

Cvetkov, Lj. & Rafajlovska, V. (1992). Choice of suitable solvent for oleoresin extraction from grinded spicy pepper. *Bulletin of the Chemists and Technologists of Macedonia*, Vol.11, 61-66.

Davis, C. B.; Markey, C. E.; Busch, M. A. & Busch, K. W. (2007). Determination of capsaicinoids in habanero peppers by chemometric analysis of UV spectral data. *Journal of Agricultural and Food Chemistry*, Vol. 55, 5925–593.

De Marino, S.; Iorizzi, M. & Zollo, F. (2008). Antioxidant activity and biological properties of phytochemicals in vegetables and spices (*Capsicum*, *Laurus*, *Foeniculum*). *Electronic Journal on Environmental, Agricultural and Food Chemistry* (*EJEAFChe),* Vol.7, No.10, 3174-3177.

Dorantes, L.; Colmenero, R.; Hernández, H.; Mota, L.; Jaramillo, M. E.; Fernández, E. & Solano, C. (2000). Inhibition of growth of some foodborne pathogenic bacteria by *Capsicum annum* extracts. *International Journal of Food Microbiology*, Vol.57, 125-128.

Feltl, L.; Pacáková, V.; [tulík K. & Volka, K. (2005). Reliability of carotenoid analyses: A Review, *Current Analytical Chemistry*, Vol.1, 93-102.

Giovanni, M. (1983). Response surface methodology and product optimization. *Food Technology*, Vol.37, 41–45.

Giovannucci, E. (2002). Lycopene and prostate cancer risk. Methodological considerations in the epidemiologic literature. *Pure Applied Chemistry*, Vol.74, 1427-1434.

Govindarajan, V. S. & Sathyanarayana, M. N. (1991). *Capsicum*: Production, technology, chemistry & quality; Part V. Impact on physiology, nutrition & metabolism, structure, pungency, pain and desensitisation sequences. *Critical Reviews in Food Science and Nutrition*, Vol.29, 435–474.

Guzman, I.; Bosland, P.W. & O'Connell, M.A. (2011). Heat, Color, and Flavor Compounds in *Capsicum* Fruit, In: The Biological Activity of Phytochemicals, Vol. 41, D. R. Gang, (Ed.), 109-126, Springer Science+Business Media, ISBN 978-1-4419-6961-3, Springer, New York, Dordrecht, Heidelberg, London.

Hismath, I.; Wan Aida, W. M. & Ho, C. W. (2011). Optimization of extraction conditions for phenolic compounds from neem (*Azadirachta indica*) leaves. *International Food Research Journal*, Vol.18, 59-67.

Hoffman, P. G.; Lego, M. C. &. Galetto, W.G. (1983). Separation and quantification of red pepper major heat principles by reverse-phase high pressure liquid chromatography. *Journal of Agricultural and Food Chemistry*, Vol.31, 1326-1330.

Hornero-Méndez, D.; Gómez-Ladrón de Guevara, R. & Mínguez- Mosquera, M. I. (2000). Carotenoid biosynthesis changes in five red pepper (*Capsicum annuum* L.) cultivars during ripening. Cultivar selection for breeding. *Journal of Agricultural and Food Chemistry*, Vol. 48, 3857-3864.

Howard, R. L.; Smith, T. R.; Waguer, B. A.; Villason, B. & Burns, E. E. (1994). Provitamin A and ascorbic acid content of fresh pepper cultivars *Capsicum annuum* and processed jalapenos. *Journal of Food Science*, Vol.59, No.2, 362-365.

Ji-Hye, K.; Goto, T.; In-Seob, H.; Teruo, K.; Young, M. K. & Rina,Y. (2010). Dietary capsaicin reduces obesity-induced insulin resistance and hepatic steatosis in obese mice fed a high-fat diet, *Obesity,* Vol.18, No.4, 780–787.

Kense, W. (1970). Solid-liquid extraction with a Carousel-type extractor. *Chemiker-Zeitung*, Vol.94, No.2, 56-62.

Kirschbaum-Titze, P.; Mueller-Seitz, E. & Petz, M. (2002). Pungency in paprika (*Capsicum annuum*). 2. Heterogeneity of capsaicinoid content in individual fruits from one plant. *Journal of Agricultural and Food Chemistry*, Vol.50, No.5, 1264–1266.

Li, Q. H. & Fu, C. L. (2005). Application of response surface methodology for extraction optimization of germinant pumpkin seeds protein. *Food Chemistry*, Vol.92, 701-706.

Liu, Q. M.; Yang, X. M.; Zhang, L. & Majetich, G. (2010). Optimization of ultrasonic-assisted extraction of chlorogenic acid from *Folium eucommiae* and evaluation of its antioxidant activity. *Journal of Medicinal Plants Research*, Vol.4, No.23, 2503-2511.

Materska, M. & Perucka, I. (2005). Antioxidant activity of the main phenolic compounds isolated from hot pepper fruit (*Capsicum annuum* L.). *Journal of Agricultural and Food Chemistry*, Vol.53, No.5, 1750-1756.

Matsufuji, H.; Nakaura, H.; Chino, M. & Takeda, M. (1998). Antioxidant activity of capsanthin and the fatty acids esters in paprika (*Capsicum annuum*). *Journal of Agricultural and Food Chemistry,* Vol.46, 3468-3472.

Montgomery, D.C. (2001). Fitting regression model, Response surface methods and other approaches to process optimization, In: Design and Analysis of Experiments, 392-510, John Wiley & Sons, Inc., ISBN 0-471-31649-0, New York.

Nowaczyk, P.; Nowaczyk, L.; Banach M. & Woźna A. (2008). The capsaicin and dihydrocapsaicin contents in soft-flesh fruit of *Capsicum frutescens* L. and *Capsicum annuum* L. hybrids. *Herba Polon*onica, Vol.52, No.1-2, 38-42.

Pérez-Gálvez, A.; Rios, J. J. & Mínguez-Mosquera, M. I. (2005). Thermal degradation products formed from carotenoids during a heat-induced degradation process of paprika oleoresins (*Capsicum annuum* L.). *Journal of Agricultural and Food Chemistry*, Vol.15, No.12, 4820-4826.

Pruthi, J. S. (2003). Chemistry and quality control of *Capsicum* and *Capsicum* products, In: *Capsicum*, genus *Capsicum*, Vol. 35, A. De Krishna, (Ed.), 25-70, Taylor and Francis Ltd., ISBN 0-415-29991-8, London and New York.

Rafajlovska, V.; Slaveska-Raicki, R.; Koleva-Gudeva, L. & Klopceska, J. (2007). Spice paprika oleoresin extraction under different conditions involving acetone and ethanol. *Journal of Food, Agriculture and Environment*, Vol.5, No.2, 65-69.

Rajaraman, K.; Kuty-Sumathy, A. M.; Sankarikutty, B. & Mathew, G. A. (1981.) Ethylacetat as solvent for extraction of spice oleoresins. *Journal of Food Science Technology*, Vol.18, 101-103.

Reyes-Escogido, M. L.; Gonzalez-Mondragon, E. G. & Vazquez-Tzompantzi. E. (2011). Chemical and pharmacological aspects of capsaicin. *Molecules*, Vol.16, 1253-1270.

Schweiggert, U.; Kurz, C.; Schieber, A. & Carle, R. (2007). Effects of processing and storage on the stability of free and esterified carotenoids of red peppers (*Capsicum annuum* L.) and hot chilli peppers (*Capsicum frutescens* L.). *European Food Research and Technology*, Vol.225, No.2, 261-270.

Singh, T. & Chittenden, C. (2008). In-vitro antifungal activity of chilli extracts in combination with *Lactobacillus casei* against common sapstain fungi. *International Biodeterioration and Biodegradation*, Vo.62, No.4, 364-367.

Spicer, Jr. O. L. & Almirall R. J. (2005). Extraction of capsaicins in aerosol defense sprays from fabrics. *Talanta*, Vol.67, 377–382.

Tepić, A.; Zeković, Z.; Kravić, S. & Mandić, A. (2009). Pigment content and fatty acid composition of paprika oleoresins obtained by conventional and supercritical carbon dioxide extraction, *Journal of Food*, Vol. 7, No.2, 95–10.

Toma, M.; Vinatoru, M.; Paniwnyk, L . & Mason, T. J. (2001). Investigation of the effects of ultrasound on vegetal tissues during solvent extraction. *Ultrasonics Sonochemistry*, Vol.8, 137-142.

Vinatoru, M. (2001). An overview of the ultrasonically assisted extraction of bioactive principles from herbs, *Ultrasonic Sonochemistry*, Vol.8, 303-313.

Vinaz, P.; Camoilo, N.; Gardia-Lopez, I. & Cordoba-Hernandez, M. (1992). Liquid chromatographic determination of fat-soluble vitamins in paprika and paprika oleoresin. *Food Chemistry*, Vol.45, 349-355.

Wang, L. & Weller, C. L. (2006). Recent advances in extraction of nutraceuticals from plants. *Trends in Food Science and Technology*, Vol.17, 300-312.

Weisshaar E., Dunker, N. & Gollnick, H. (2003). Topical capsaicin therapy in humans with hemodialysis-related pruritus. *Neuroscience Letters*, Vol.345, 192-194.

Willams, O. J.; Raghavan G. S. V.; Orsat, V. & Dai, J. (2007). Microwave-assisted extraction of capsaicinoids from *Capsicum* fruits. *Journal of Food Biochemistry*, Vol.28, No.2, 113-122.

Xing, F. B; Cheng, G. X. &, Yi, K. K. (2006). Study on the antimicrobial activities of the capsaicin microcapsules. *Journal of Applied Polymer Science*, Vol.102, No.2, 1318-1321.

Xiu-Ju, L.; Jun, P. & Yuan-Jian, Li. (2011). Recent advances in the study on capsaicinoids and capsinoids, *European Journal of Pharmacology*, Vol.650, 1-7.

Ying-Yue, W.; Chi-Tzong, H.; Wen-Ta, C. & Jia-You, F. (2001). In vitro and in vivo evaluations of topically applied capsaicin and nonivamide from hydrogels. *International Journal of Pharmaceutics*, Vol.224, 89-104.

7

Removal of H_2S and CO_2 from Biogas by Amine Absorption

J.I. Huertas, N. Giraldo and S. Izquierdo
Automotive Engineering Research Center-CIMA of Tecnologico de Monterrey, Mexico

1. Introduction

Due to strategic and environmental reasons, currently, there is an increasing interest in biofuels as alternative energy source. Bio-alcohols and biodiesel are the alternatives been considered for auto-motion while biomass and biogas are the alternatives been considered for electrical power generation.

Biogas is a medium-energy content fuel (~22 MJ/kg) derived from the organic material decomposition under anaerobic conditions (Horikawa et al, 2004). It can be obtained from landfills or from bio-digesters that transform manure and biomass into natural fertilizer in farms after 25-45 days of residence time. Due to its gaseous nature and the impossibility of producing it intensively, it is not attractive for large scale power generation.

However, recently, a new approach for electric power generation has been emerging. It consists of inter-connecting thousands of small and medium scale electrical plants powered by renewable energy sources to the national or regional electrical grids. It is considered to interconnect the hundreds of the existing small aero generators and solar panels (Pointon & Langan, 2002). Even though, there are still several technical issues to be resolved, this alternative of distributed electrical power generation is being considered as the best alternative to bring electricity to the rural communities located far away from the large urban centers.

In this case, the use of the biogas generated in the thousands of existing farms and landfills, as fuel for internal combustion engines connected to an electric generator becomes a very attractive alternative for electric power generation because of its very low cost, high benefit-cost ratio and very high positive impact on the environment.

Biogas is made up mainly of methane (CH_4) and carbon dioxide (CO_2). It also contains traces of hydrogen sulfide (H_2S). Its composition varies depending on the type of biomass. Table 1 shows its typical composition.

The biogas calorific power is proportional to the CH_4 concentration. To be used as fuel for internal combustion engines, it has been recommended a CH_4 concentration greater than 90% (Harasimowicz et al, 2007). However CO_2 has a typical concentration of ~ 40%. This high CO_2 concentration reduces the engine power output proportionally to its concentration, limiting the use of biogas in electrical power plants driven by internal combustion engines (Marchaim, 1992).

The high content of H_2S (~3500 ppm) causes corrosion in the metallic parts at the interior of the engine. The H_2S is an inorganic acid that attacks the surface of metals when they are

placed in direct contact. Sulfur stress cracking (SSC) is the most common corrosive mechanism that appears when the metal makes contact with H_2S. Sulfides of iron and atomic hydrogen are formed in this process. This mechanism starts to take place when the H_2S concentration is higher than 50 ppm (Gosh, 2007). The admission valves, bronze gears and the exhaust system are also attacked by the presence of H_2S. The degree of deterioration of the engines varies considerably. Results obtained experimentally on this regard are contradictory (Gonzalez et al, 2006; Marchaim, 1992). It has been found that H_2S in biogas diminishes the life time of the engine by 10 to 15% (Horikawa & Rossi, 2004). Finally, time between oil changes is reduced since lubricant oils contain H_2S and corrosion inhibitors to protect the engine. It increases the maintenance cost of the engine. Users consider the high maintenance cost as the main withdraw of these types of systems.

Component	Composition (%)			
	Agricultural waste	Landfills	Industrial Waste	Desired composition
CH_4	50-80	50-80	50-70	>70
CO_2	30-50	20-50	30-50	<10
H_2O	Saturation	Saturation	Saturation	N/S
H_2	0-2	0-5	0-2	N/S
H_2S	0.70	0.1	0.8	< 0.01
NH_3	Traces	Traces	Traces	N/S
CO	0-1	0-1	0-1	N/S
N_2	0-1	0-3	0-1	N/S
O_2	0-1	0-1	0-1	N/S

(N/S Not specified)

Table 1. Biogas composition. Most of the data from (Carrillo, 2003).

Typically, small scale power plants based on biogas range from 0.1 to 1 MW. This implies a volumetric biogas flows between 60 and 600 m^3/hr. For this small scale application an additional practical consideration arise. Out of the bio-digester or landfill, the biogas gauge pressure is negligible, and due to economical considerations the use of any device to increase pressure should be avoided. Engine suction is the only driving force available to make the biogas to flow from the bio-digester or landfill to the engine. Therefore, the pressure drop across the biogas treatment system should be the least possible.

To address this need, the present document describes the design, manufacturing and testing of a system to reduce H_2S and CO_2 content to less than 100 ppm and 10%, respectively, from 60 to 600 m^3/hr biogas streams, with minimum pressure drop, for applications in small scale power plants (0.1 to 1 MW) based on internal combustion engines fueled with biogas.

Initially, this document describes and compares the existing alternatives to trap H_2S and CO_2 from gaseous streams. From this analysis it is concluded that amines treatment is the most appropriate for this application. Since there is no reported data for the H_2S and CO_2 absorbing capacity of these substances, a method is proposed to measure it by means of a bubbler. This information is used in the design process of biogas treatment system. Details of the manufacturing process are also included. Then, results of the experimental work are reported, and finally, an economical analysis on the use of this type of systems is presented.

2. Biogas treatment methods

2.1 CO_2 removal from gas streams

CO_2 removal from gas streams has been of great interest, especially in large thermal power plants, due to its greenhouse effect (Romeo et al, 2006). Table 2 compares the different existing technologies.

2.1.1 Absorption

It refers to the process by which one substance, such as a solid or liquid, takes up another substance, such as a liquid or gas, through minute pores or spaces between its molecules. The absorption capacity of the absorber depends on the equilibrium concentrations between gaseous phase and the liquid phase. For diluted concentrations in many gases and in a wide interval of concentrations, the equilibrium relation is given by Henry's Law, which quantifies the gas absorption capacity in the fluid (Cengel & Boles, 2008). A gas absorbing unit should ensure complete contact between the gas and the solvent, in such a way that diffusion occurs at the inter-phase.

2.1.2 Adsorption

It refers to the process by which molecules of a substance, such as a gas or a liquid, collect on the surface of a solid. It differs from absorption, in which a fluid permeates or is dissolved by a liquid or solid (Tondeur & Teng, 2008). It could be physical or chemical. In physical adsorption processes, gas molecules adhere to the surface of the solid adsorbent as a result of the molecules attraction force (Van der Walls Forces). Chemical adsorption involves a chemical reaction. Usually, adsorbents are 12 μm to 120 μm high porosity solid grains, inert to the treated fluid. The most used adsorbents for CO_2 are activated charcoal, silica gel, zeolites and synthetic resins.

2.1.3 Condensation

It is the process of converting a gas into a liquid by reducing temperature and/or increasing pressure. Condensation occurs when partial pressure of the substance in the gas is lower than the vapor pressure of the pure substance at a given temperature.

2.1.4 Membranes

A membrane is a layer of material which serves as a selective barrier between two phases and remains impermeable to specific particles, molecules, or substances when exposed to the action of a driving force. The driving force is the pressure difference between both sides of the membrane. Gas permeability through a membrane is a function of the solubility and diffusivity of the gas into the material of the membrane. Membranes are expensive and their separation efficiencies are low (Ramírez, 2007).

2.2 H_2S removal from gas streams

Table 3 compares the different alternatives reported for H_2S removal from gas streams (Walsh et al, 1988).

2.2.1 Regenerative processes

It refers to processes where the cleaning reagent, once it becomes saturated, regains its removal capacity through a change in the external conditions.

Method	Option/Alternative	Advantages	Disadvantages
Absorption with water		High efficiency (>97% CH_4), Simultaneous removal of H_2S when H_2S < 300 cm_3 /m^3, Capacity is adjustable by changing pressure or temperature, Low CH_4 losses (<2%), tolerant to impurities	Expensive investment and operation, clogging due to bacterial growth, possible foaming, low flexibility toward variation of input gas
Absorption with polyethylene glycol		High efficiency (>97% CH_4), Simultaneous removal of organic S components, H_2S, NH_3, HCN and H_2O, Energetic more favorable than water, Regenerative, low CH_4 losses	Expensive investment and operation, difficult operation, Incomplete regeneration when stripping/vacuum (boiling required), reduced operation when dilution of glycol with water
Chemical absorption with amines		High efficiency (>99% CH_4), cheap operation, Regenerative, More CO_2 dissolved per unit of volume (compared to water), very low CH_4 losses (<0.1%)	Expensive investment, heat required for regeneration, corrosion, decomposition and poisoning of the amines by O_2 or other chemicals Precipitation of salts, possible foaming
PSA/VSA	Carbon molecular sieves Zeolites Molecular sieves Alumina silicates	Highly efficient (95-98% CH_4), H_2S is removed, low energy use: high pressure, compact technique, also for small capacities, tolerant to impurities	Expensive investment and operation, extensive process control needed, CH_4 losses when malfunctioning of valves
Membrane technology	Gas/gas Gas/liquid	H_2S and H_2O are removed, simple construction, Simple operation, high reliability, small gas flows treated without proportional increase of costs • Gas/gas: removal efficiency: <92% CH_4 (1 step) or > 96% CH_4, H_2O is removed • Gas/liquid: Removal efficiency: > 96% CH_4, cheap investment and operation, Pure CO_2 can be obtained	Low membrane selectivity: compromise between purity of CH_4 and amount of upgraded biogas, multiple steps required (modular system) to reach high purity, CH_4 losses.
Cryogenic separation		90-98% CH_4 can be reached, CO_2 and CH_4 in high purity, low extra energy cost to reach liquid biomethane (LBM)	Expensive investment and operation. CO_2 can remain in the CH_4
Biological removal		Removal of H_2S and CO_2, enrichment of CH_4, no unwanted end products	Addition of H_2, experimental - not at large scale

Table 2. Alternatives to remove CO_2 from gas streams (Ryckebosch et al, 2011).

	Alternative		Reactions	Range of application	Advantages	Disadvantages
Regenerative	Redox		$2Fe^{3+} + H_2S \rightarrow 2Fe^{2+} + S + 2H^+$ $2Fe^{2+} + 0.5O_2 + H_2O \rightarrow 2Fe^{3+} + 2OH^-$	0.5-15 ton/day of H_2S.	Elemental S is formed High removal efficiency Use of low toxicity solutions	Requires specialized supervision, Low quality product, high pressure problems.
	Amines		$2RNH_2 + H_2S \rightarrow (RNH_3)_2S$ $RNH_2 + H_2S \rightarrow RNH_3HS$	H_2S concentrations higher than 30 ppm and gas flows higher than 10000 m^3/day.	High removal efficiency for H_2S and CO_2	Cost
	Ferric oxide		$2Fe(OH) + 3H_2S \rightarrow Fe_2S_3 + 6H_2O$ $Fe(OH)_2 + H_2S \rightarrow FeS + 2H_2O$ $2Fe_2S_3 + 3O2 + 6H_2O \rightarrow 4Fe(OH)_3 + 3S_2$ $2FeS + O_2 + 2H_2O \rightarrow 2Fe(OH) + S_2$	Low scale	Most used. High removal efficiency(>99 %)	Inappropriate for medium scale application Reagent disposal
	Activated carbon		Adsorption	Low scale	Elemental S is formed	Absorbs CH_4
No regenerative	Solid reagents	Zinc oxides	$ZnO + H_2S \rightarrow ZnS + H_2O$	0.3-500 kg/day of H_2S.	Low cost high selectivity operational flexibility low CO2	Disposal of saturated reagent
		Iron oxides	$Fe_2O_3 + H_2S \rightarrow 2FeS + S + 3H_2O$ $FeO_4 + H_2S \rightarrow 3FeS + S + 4H_2O$			
		Sodium nitrite	$3H_2S + NaNO_2 \rightarrow NH_3 + 3S + NaOH + XNO_x$ $2NaOH + H_2S \rightarrow Na_2S + 2H_2O$			
	Solvents	Caustic wash	$CaO + H_2O \rightarrow Ca(OH)_2$ $Ca(OH) + H_2O \rightarrow Ca(CO)_3 + H_2O$ $CaO + H_2S \rightarrow CaS + H_2O$	0-300 ppm H_2S concentration	Elemental S is formed Low costs Low removal efficiency for H_2S and CO_2	Operational difficulties Disposal of saturated solution
		Permanganate solutions	$3H_2S + 2KMnQ \rightarrow 3S + 2H_2O + 2MnQ + 2KOH$			
		Water	Adsorption			
Biological			Uses bacteria or microorganisms under controlled ambient conditions	50-20000 kg/day of H_2S.	Elemental S is formed	Incomplete H_2S absorption, needs extra-treatment. Require strict control of bacterial conditions.
			Adsorption with filter.		High removal possible:>97% Low operational costs	

Table 3. Alternatives for H_2S removal from gas streams (EPRI, 1992; Freira, 2000; Ryckebosch et al, 2011).

- Amines: Monoethanolamine (MEA), Diethanolamine (DEA) and Methildiethanolamine (MDEA) are organic chemical compounds derived from ammonia as a result of the exchange of one hydrogen molecule by an alkyl radical (Kohl & Nielsen, 1997). The chemical reactions involved in the absorption process of H_2S are exothermic.
- Redox process: Through this process H_2S is physically absorbed in water and then, by the use of a chelating ferric solution, elemental sulphur is formed. After saturation, the reagent is regenerated in air (Horikawa & Rossi, 2004). It can be obtained more than 99% of H_2S absorption. Its main advantage is that it uses low toxicity solutions.
- Ferric oxide: Absorbent material must contain iron in form of oxides, hydrate oxides or hydroxides (Muche & Zimmermann, 1985). Reagent regeneration occurs by exposition to open atmosphere It is one of the most used methods in biogas treatment. It is very efficient at low scale. However, in high and medium scale applications this method becomes inefficient due to the labor costs involved. Reagent disposal is a serious environmental issue (Ramírez, 2007).
- Activated carbon: Activated carbon, also called activated charcoal or activated coal, is a form of carbon that has been processed to make it extremely porous and thus to have a very large surface area available for adsorption or chemical reactions (Horikawa &Rossi, 2004). It shows affinity to polar substances such as H_2O, H_2S, SO_2 among many others. In the case of H_2S, activated carbon absorbs and decomposes it to elemental sulphur (Garetto, 2000). It can be regenerated by temperature at around 400ºC. The main disadvantage of this alternative is its affinity for no polar substances such as methane, which makes the alternative inappropriate in pre-combustion processes (Ramírez, 2007).

2.2.2 Non regenerative processes

- Zinc oxides: It is based on the reaction of a metal oxide with H_2S to form the corresponding metal sulfide. Unlike iron oxides, zinc oxides treatment process is irreversible. Absorption reaction occurs at temperatures between 200ºC and 400ºC (Mabres et al, 2008).
- Iron oxides: It is based on the reaction of a ferric oxide and a triferric oxide with H_2S to form iron sulfide, sulphur and water. The absorption reaction occurs at temperatures between 30ºC to 60ºC (Svard, 2004; Steinfeld & Sanderson, 1998).
- Sodium nitrite: It is based in the reaction of H_2S with a solution of sodium nitrite. It produces a high percentage of H_2S removal. Its main drawback is the environmentally safe disposition of the saturated solution (Ramírez, 2007).
- Caustic wash: It is an effective method to remove H_2S y CO_2 from gas streams. Generally, it uses sodium hydroxide and calcium oxide (slaked lime) solutions to promote the chemical reactions showed in Table 3. Disposition of the saturated solutions should be performed according to environmental regulations (Zapata, 1998).
- Permanganate solutions: Potassium permanganate absorbs H_2S according to the reaction shown in Table 3. It has high removal efficiency but it is costly and requires special treatment of the saturated solutions (Ramírez, 2007).
- Water: It can be used to remove H_2S y CO_2 by physical adsorption. It is rarely used because water consumption is high and removal efficiency is low for large volumes of biogas (Kapdi et al, 2007).

2.2.3 Biological methods

It uses microorganisms under controlled ambient conditions (humidity, oxygen presence, H_2S presence and liquid bacteria carrier) (Fernández & Montalvo, 1998). Microorganisms are highly sensitivity to changes in pressure, temperature, PH and certain compounds. It requires moderate investments.

2.3 Selection

To select a methodology for H_2S and CO_2 removal it should be taken into account (Treybal, 1996):

- The volumetric flow of biogas
- The amount of H_2S and CO_2 to be removed and their desired final concentrations
- Availability of environmentally safe disposal methods for the saturated reagents
- Requirements regarding the recovery of valuable components such as S
- Cost

Table 2 and table 3 show that most of the existing methods for H_2S and CO_2 removal are appropriate for either small scale with low H_2S and CO_2 concentration or large scale with high pressure drops. Applications with intermediate volumetric flows, high H_2S and CO_2 content and minimum pressure drop, as in the present case, are atypical. Table 3 shows that for the case of H_2S, in the present application, the most appropriate methods are amines and iron oxides, which also absorb CO_2. Iron oxides are meant for small to medium scale applications while amines are meant for large scale applications. Amines have higher H_2S and CO_2 absorbing efficiency than iron oxides. Both methods have problems with disposition of saturated reagents. Even though amines are costly, they can be regenerated, and depending on the size of the application they could become economically more attractive than iron oxides. Both methods were selected for the present applications. However in this document, results only for the case of amines are reported.

3. Determination of the amines H_2S and CO_2 absorbing capacity

Several works have been developed to model mass transfer in gas-liquid chemical absorbing systems and especially for simultaneous amine H_2S and CO_2 absorption (Little et al, 1991; Mackowiak et al, 2009; Hoffmann et al, 2007). It has been concluded that the reaction of H_2S with amines is essentially instantaneous, and that of CO_2 with amine is slow relatively (Qian et al, 2010). Therefore, for amine H_2S and CO_2 absorption in packed columns mass transfer is not limited by chemical reaction but by the mechanical diffusion or mixing of the gas with the liquid and by the absorbing capacity of the amine.

The Henry's constant defines the capacity of a solvent to absorb physically gas phase components. Under these circumstances of instantaneous reaction it can be extended to chemical absorption. The Henry´s law states than under equilibrium conditions (Treybal, 1996; Hvitved, 2002).

$$P_A = y_A \cdot P = H_A \cdot x_A \tag{1}$$

Where:

P_A Partial pressure of component A in gas phase

P Total pressure

H_A Henry's constant of component A
y_A Molar concentration of component A in gas phase
x_A Mass concentration of component A in liquid phase

It is determined in a temperature and pressure controlled close box by measuring the equilibrium concentration of the component in both gas and liquid phase. Therefore, it requires spectrophotometric or chromatographic analysis to determine component concentration in the liquid phase (Wark, 2000). It has been observed that H_2S concentrations in amines solutions are highly sensible to pressure and temperature, making spectrophotometric or chromatographic analysis hardly suitable for this application. For this reason literature does not report amines H_2S and CO_2 absorbing capacity.

As an alternative it was proposed to determine the H_2S and CO_2 absorbing capacity of the amines by using the gas bubbler setup illustrated in figure 1. This set up looks for a full interaction of the gas stream with the absorbing substance such that it can be assumed thermodynamic equilibrium at the liquid-gas inter phase. Experiments are conducted under standard conditions of pressure and temperature (101 kPa, 25°C). To ensure constant temperature for exothermic or endothermic reactions the set up is placed inside a controlled temperature water bath.

Temperature, pressure, gas flow and degree of water dilution of the absorbing substance are measured. The amount of solution in the bubbler is kept constant in 0.5 L. Table 4 describes the variables measured and their requirements in terms of resolution and range.

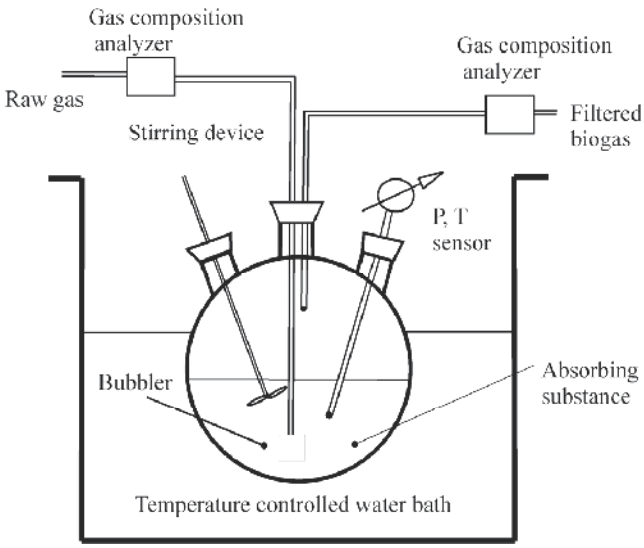

Fig. 1. Setup to determine the absorbing capacity of gas-phase components by liquid phase absorbers in the bubbling method.

Several tests were conducted to verify reproducibility of the method. Figure 2 shows the results obtained in terms of absorbing efficiency vs. time. Absorbing efficiency (η_f) is defined as:

$$\eta_f = \frac{y_i - y_o}{y_i} \tag{2}$$

Where

y_i H_2S molar concentration at the inlet

y_o H_2S molar concentration at the outlet

Variable	*Resolution*	*Range*
Molar concentration at the inlet and outlet	CO_2 ±3% CH_4 ±3% O_2 ±1% H_2S 35ppm	CO_2 0-100% CH_4 0-100% O_2 0-25% H_2S 0-5000ppm
Temperature inside and outside of the bubbler	0.1ºC	0-50 ºC
Volumetric gas flow	0.1 slpm	0-2 slpm
Time	0.1 s	N/A

(N/A Not applies)

Table 4. Variables to be monitored during the determination of the absorbing capacity of gas-phase components by liquid phase absorbers in the bubbling method.

Figure 2 shows that any of the amines solutions can remove 100% of the H_2S biogas content in the initial part of the test. However it is required at least 50% of amine concentration to remove 100% of the CO2 biogas content in this first stage.

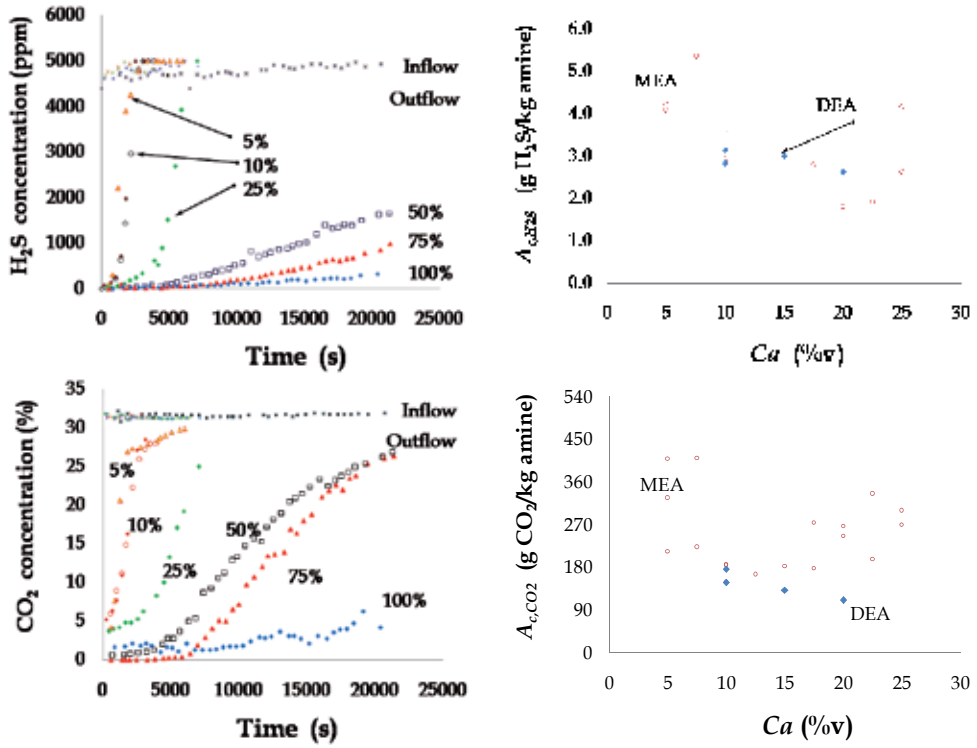

Fig. 2. Evolution of the H_2S and CO_2 concentration during bubbling tests with MEA (left) and H_2S and CO_2 absorbing capacity of MEA and DEA as function of their concentration in water (right).

Figure 2 also shows that absorbing efficiencies depend on the degree of saturation of the absorbing substance and on the ratio of the gas flow and the mass of absorbing substance in the bubbler. Additionally, this figure shows that the saturation profiles are similar and have an S type shape. The absorbing capacity under quasi-equilibrium conditions ($A_{c,e}$) is defined as:

$$A_{c,e} = \frac{M}{R^o T m}\int_0^{t_s}(y_o - y_i)Q\,dt \tag{3}$$

Where:

M H_2S or CO_2 molecular weight
R^o Universal gas constant
T Absolute temperature
m Mass of the absorbing substance within the bubbler
Q Gas volumetric flow measured at standard conditions

Figure 2 shows that MEA and DEA exhibit similar H_2S and CO_2 absorbing capacities and that they depend on their concentration in water. They exhibit a minimum around 20% and a maximum around 7.5% of volumetric concentration. These results indicate that scrubbing systems should work around 7.5% for applications where H_2S removal is the main concern or higher than 50% where CO_2 removal is the main objective. However at this high concentration it was observed that amines traces cause corrosion on metallic components, especially when they are made of bronze. Finally, figure 2 shows that on average at 7.5% of MEA or DEA concentration in water their absorbing capacity is of 5.37 and 410.1 g of H_2S and CO_2, respectively, per Kg of MEA or DEA.

4. Amine based H_2S and CO_2 biogas scrubber

Figure 3 illustrates the general configuration of an amine based biogas scrubber. It consists of an absorption column, a desorption column and a water wash scrubber. Initially, raw biogas enters the absorption column where the amine solution removes H_2S and CO_2. Then, the biogas passes through the water wash scrubber where amines traces are removed and

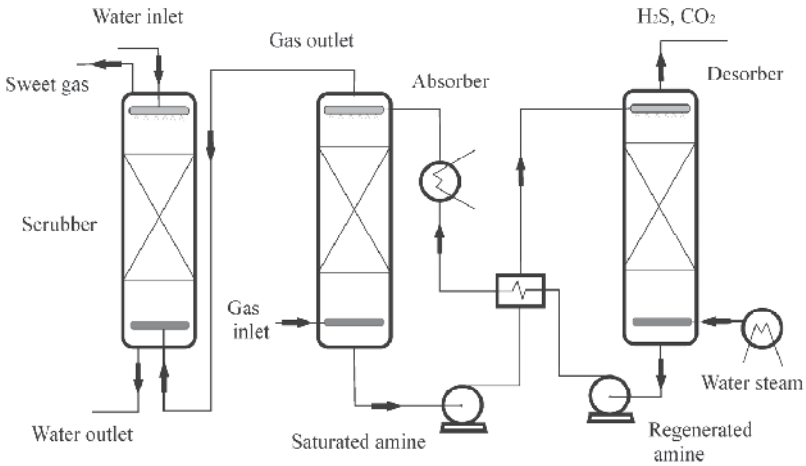

Fig. 3. Illustration of the amine based biogas H_2S and CO_2 scrubber.

the saturated amine passes through the desorption column where it is regenerated. A heat exchanger is used to cool the regenerated amine before it re-enters the absorption column.

4.1 Absorption column

A H_2S and CO_2 amine wash biogas scrubber was designed to meet the design parameters specified in section 1 (final H_2S and CO_2 concentration lower than 100 ppm and 10%, respectively, 60 m^3/s of biogas flow and minimum pressure drop). It is a counter flow column where amine solution fall down due to gravity and raw biogas flows from the bottom towards the top of the column due to pressure difference. The column is fully packed with inert polyetilene jacks to enhance the contact area between the gas and liquid phases. In addition several disks are incorporated to ensure the uniform distribution of both flows through the column.

The length of the column is designed to obtain the specified final H_2S and CO_2 concentration and the diameter is designed to meet a minimum pressure drop with the specified gas flow. This procedure is well established and reported in references (Wiley, 2000; Wark, 2000). It requires as data input the results reported in section 3. Table 5 shows the technical characteristics of the absorption column.

Parameter	Column	
	Absorption	**Desorption**
Material	PVC	SS
Gas flow [m^3/h]	7.6	8.25
Liquid flow [l/h]	33.3	69
Packing material	Jacks	SS rasching rings
Diámeter [cm]	6.7	6.7
Height [cm]	240	240
Pressuere drop [in.c.a]	0.28	0.2-3
Working reagent	MEA at 10%	H_2O
Qr	230	N/A
η_{H2S}	98%	N/A
η_{CO2}	75%	N/A
YH_2S start	>5000 ppm	N/A
YH_2S final	<100 ppm	N/A
YCO_2 start	>40%	N/A
YCO_2 final	<10%	N/A

(N/A Not applies)

Table 5. Technical characteristics of the columns used in the amine based biogas scrubber

The absorption column was instrumented with temperature and pressure sensors at the inlet and outlet. Flow meters were used for both the biogas and the liquid phase absorbing substance. Biogas CH_4, CO_2, O_2, and H_2S concentration were measured at the inlet and outlet of the column by gas detector tubes and electro chemical cells with the technical characteristic specified in Table 4.

The absorption column was evaluated with MEA, DEA, and MDEA. Initially all amines were diluted at 30% (C_a=30%) in water as recommended by manufacturer (Romeo et al, 2006). However, later on, results from section 3 were incorporated and therefore it was used 7.5% and several other levels of dilution.

Figure 4 shows that pressure drop along the column increases quadratically with the volumetric ratio biogas to amine solution (Q_r). For a biogas volumetric flow of 7.6 m³/h, the pressure drop is about 3 inches of water column, which is acceptable for this application. This result implies that the final diameter of the column should be 18.8 cm to meet the condition of 60 m³/h of biogas flow.

Figure 5 shows the results obtained in terms of H_2S and CO_2 removing efficiencies (η_{H2S} and η_{CO2}) as function of Q_r. It shows that the different types of amines produce similar results and that the column with all the amines is able to reach η_{H2S}>98% (final Y_{H2S}=100 ppm) for $Q_r \leq 230$ when C_a=9%. Under this circumstances η_{CO2} >75% (final Y_{CO2}<10%). Since MEA is the cheapest amine, it was selected as the working reagent for the absorption column.

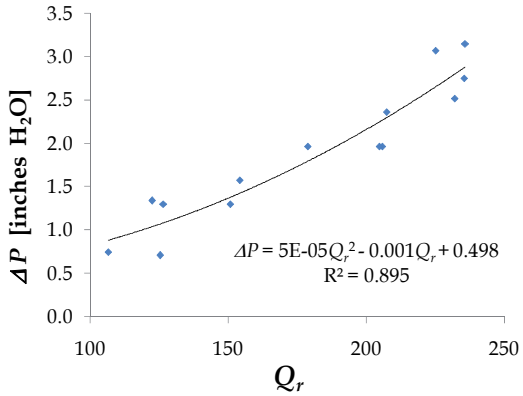

Fig. 4. Pressure drop along the absorption column as function of Q_r. Amine solution flow was kept constant at 26.5 L/h.

Removing efficiency is a metric to evaluate the performance of the column reaching the final specified concentration. It evaluates under which conditions of Q_r and C_a the biogas exits with the final specified concentration. However it does not evaluate the performance of the column in terms of mass transfer. In other words, it does not evaluate the column length (L). Amine solution can leave the absorption column unsaturated, which is an undesirable condition since it will increase the total amount of amine required, and therefore the operational costs of the system. Figure 5 shows this effect as a high removing efficiency obtained when the amine solution is passed for a second time along the same column. To quantify this effect, here, it is proposed to define the mass transfer efficiency of the column for component i ($\eta_{m,i}$) as:

$$\eta_{m,i} = \frac{A_{cr,i}}{A_{c,i}} \tag{4}$$

$$A_{cr,i} = \frac{P}{R_i T} \frac{Y_{i,o}\,\eta_i}{\rho_a\, C_a} Q_r \tag{5}$$

Where:

$A_{cr,i}$ Component *i* real absorbing capacity of the column

$A_{c,i}$ Component *i* amine absorbing capacity as reported in section 3.

P Pressure
T Temperature
R_i Component i gas constant
ρ_a Amine density

Using this definition, it was found that $\eta_{m,CO2}$=86% for Q_r=230. For practical applications this value is acceptable. Higher mass transfer efficiencies can be obtained increasing the length of the column or using more appropriate filling materials. Table 5 summarizes the final operational conditions of the absorption column.

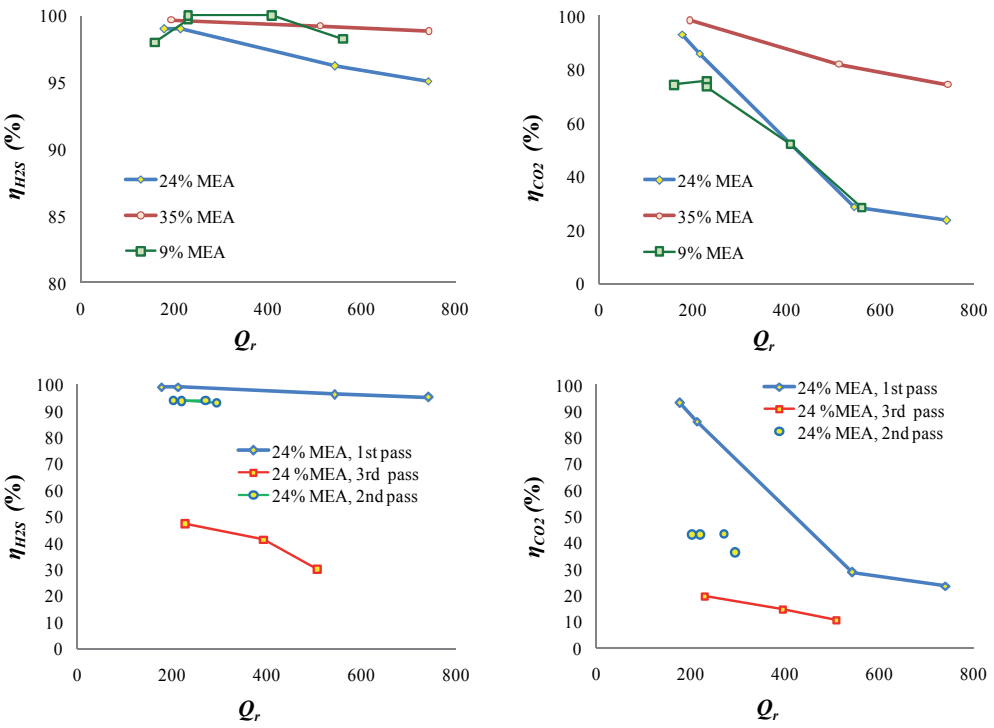

Fig. 5. H_2S and CO_2 removing efficiencies of the absorption column as function of volumetric ratios of biogas to amine flows for the case of MEA.

4.2 Regenerative column

Amines desorb H_2S and CO_2 when they are heated up to 120°C at atmospheric pressure (Kolh & Nielsen, 1997). For the present application, this heat addition can be obtained in a counter flow heat exchanger between the amine and the engine exhaust gases. Alternatively, exhaust gases can be used to generate saturated steam and then heat the amines by direct mixing with this steam in a desorbing column. Attending literature recommendations on this matter the latest alternative was chosen (Kolh & Nielsen, 1997).

A desorbing column was designed, manufactured and tested to regenerate amines solutions by mixing with steam. Figure 3 illustrates its operation. Preheated saturated amine solution fall down through the desorption column due to gravity while steam moves in counter-flow due to pressure difference. Under steady conditions the energy requirements for the

desorption column are the heats of desorption, sensible and latent for the amine solution and for the steam. They are influenced by pressure and flow rates (Chakravarti et al, 2001).
For larger scale applications the CO_2 and H_2S -rich vapor stream that leaves the desorption column can be passed through a reflux condenser where H_2O is partially condensed, CO_2 sequestrated and H_2S recovered for industrial applications.
On the other side, regenerated amine solutions should be cooled before reentering the absorption column because temperature reduces the amine absorbing capacity. For this purpose it is used a heat exchanger between regenerated amine and saturated amine coming out of the absorption column. The regenerative column was made of 2.5 inches stainless steel pipe to avoid corrosive problems. It was fully packed with stainless steel rashing rings to increase the contact area between the amine solution and the steam. Additionally it was thermally isolated with a heavy layer of fiberglass to avoid heat losses. Table 5 shows its technical specification.
It was instrumented with temperature and pressure sensors at the inlet, middle and outlet of the column. Amines solution flow rate was measured. Steam flow was adjusted to obtain maximum temperature. However, since the column is an open atmosphere system, the maximum temperature that can be reached is the water boiling temperature (98°C for atmospheric pressure of 85 KPa).

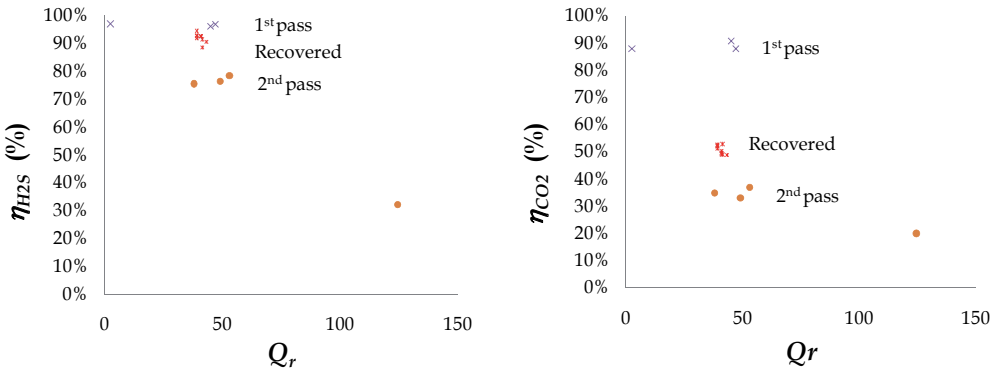

Fig. 6. H_2S and CO_2 removing efficiencies of the absorption column as function of volumetric ratios of biogas to amine flows for the case of regenerated MEA at 15% of volumetric concentration.

Fully saturated amines solutions were passed through the desorption column and collected at the bottom. Then they were cooled and used again in the absorption column under the same conditions as they were initially saturated (Q_r=230). Figure 6 shows results obtained in terms of removing efficiency. It shows that the H_2S removing efficiencies change from 98% to 95% when the amine is regenerated. Similarly, it changes from 87% to 50% for the case of CO_2. Even though these results are encouraging, they are still partial results in the sense that further work is required to ensure maximum amines regeneration before evaluating its removing efficiency. Literature reports that amines can be regenerated 25 times before being degraded.

5. Economical evaluation

An economical analysis was performed to evaluate the economical feasibility of implementing this type of amine based H_2S and CO_2 biogas scrubber. It was assumed a

horizon time of 10 years and a scale of power generation of 1 kW in a typical farm in Mexico without any governmental subsidy or benefits from green bonuses. It was also assumed an annual interest rate of 5%. From the engine manufacturer experience it is known that oil change period is reduced from 1000 to 250 hr and that overhaul maintenance is reduced from 84000 hr to 24000 hr when using biogas without any treatment. Additionally it was considered in the analysis that power output increases ≈30% when using the amine treatment system. Under these circumstances it was found that electric power generation from biogas currently has a cost of 0.024 USD/kW-h and that this cost can be reduced up to 61% (0.015 USD/kW-h) when the amine based H_2S and CO_2 biogas scrubber is included. Then, it was found that the turnover of the initial investment is of about 1 year.

6. Conclusions

Recently, a new approach for electric power generation has been emerging as a consequence of the need of replacing traditional hydrocarbon fuels by renewable energies. It consists of inter-connecting thousands of small and medium scale electric plants powered by renewable energy sources to the national or regional electric grid. In this case, typical small scale (0.1 to 1 MW) plants consisting of internal combustion engines coupled to electric generator and fueled by biogas become as one of the most attractive alternatives because of its very low cost, high benefit-cost ratio and very high positive impact on the environment.

However, the use of biogas to generate electricity has been limited by its high content of H_2S (1800-5000 ppm) and CO_2 (~40%). The high content of H_2S corrodes important components of the engine like the combustion chamber, bronze gears and the exhaust system. CO_2 presence reduces the energy density of the fuel and therefore the power output of the system. Therefore there is a need for a system to reduce H_2S and CO_2 biogas content to less than 100 ppm and 10%, respectively, from 60 to 600 m^3/hr biogas streams.

To address this need, several existing alternatives to remove H_2S and CO_2 content from gaseous streams were compared in terms of their range of applicability, removing efficiency, pressure drop across the system, feasibility of reagent regeneration and availability of methods environmentally safe for final disposal of saturated reagents. It was found that the existing methods are appropriate for either small scale applications with low H_2S and CO_2 concentration or large scale with high pressure drops. Applications with intermediate volumetric flows, high H_2S and CO_2 content and minimum pressure drop, as required in the present case, are atypical. It was also found that the most appropriate methods for the present application are amines and iron oxides, which absorb both H_2S and CO_2. Iron oxides are meant for small to medium scale applications while amines are meant for large scale applications. Amines have higher H_2S and CO_2 absorbing efficiencies than iron oxides. Both methods have problems with disposition of saturated reagents. Even though amines are costly, they can be regenerated, and depending on the size of the application they could become economically more attractive than iron oxides. Both methods were selected for the present applications. However in this document, only results for the case of amines were reported.

To design the scrubbing system based on amines it is necessary to know its H_2S and CO_2 absorbing capacity. Since there is not reported data on this regard, it was proposed a method to measure it by means of a bubbler. It is an experimental setup where the gas stream passes through a fixed amount of the absorbing substance until it becomes saturated. Results showed that MEA and DEA exhibit similar H_2S and CO_2 absorbing capacities and

that they depend on their concentration in water. They exhibit a minimum around 20% of volumetric concentration. These results indicate that scrubbing systems should work around 7.5% for applications where H_2S removal is the main concern or higher than 50% where CO_2 removal is the main objective. On average at 7.5% of MEA or DEA concentration in water their absorbing capacity is of 5.37 and 410.1 g of H_2S and CO_2, respectively, per Kg of MEA or DEA.

Using this information, it was designed an absorbing gas-liquid column to reduce the H_2S and CO_2 content to 100 ppm and 10%, respectively, from ~60 m^3/hr biogas streams, with negligible pressures drop. The manufactured column was tested with three different types of amines: MEA, DEA, and MDMEA. Results permitted to identify the ratio of amines to biogas flow (Q_r=230) required to obtain the highest H_2S and CO_2 removing efficiencies (98% and 75% respectively) along with the highest mass transfer in the column (86%) when it is used MEA at 9%.

Then, an amine regenerative system was designed, manufactured and tested. Exhaust hot gases from the engine were used to heat the diluted amine up to 95ºC. Tests showed that the H_2S removing efficiencies change from 98% to 95% when the amine is regenerated. Similarly, it changes from 87% to 50% for the case of CO_2. Even though these results are encouraging, they are still partial results in the sense that further work is required to ensure maximum amines regeneration before evaluating its removing efficiencies.

Finally, an economical analysis was performed assuming a horizon time of 10 years and a scale of power generation of 1 kW in a typical farm in Mexico without any governmental subsidy or benefits from green bonuses. It was found that under these circumstances, electric power generation from biogas has a cost of 0.024 USD/kW-h. This cost can be reduced up to 61% (0.015 USD/kW-h0 when the amine based H2S and CO2 biogas scrubber is included). Then, it was found that the turnover of the initial investment is of about 1 year.

7. Acknowlegments

This project was partially financed by the Mexican council of science and technology-COMECYT and the company MOPESA. The authors also express their gratitude to engineer Jessica Garzon for their contributions to this project.

8. References

Carrillo, L. (2003). *Microbiología Agrícola*, Universidad Nacional de Salta, ISBN 987-9381-16-5, Salta, Argentina

Cengel, Y. & Boles, A. (2008). *Thermodynamics. An Engineering Approach* (6th Ed.), McGraw-Hill, ISBN 9780073305370, New York, New York, USA

Chakravarti, S.; Gupta, A. & Hunek, B. (2001). Advanced Technology for the Capture of Carbon Dioxide, *First National Conference on Carbon Sequestration*, Washington, DC, USA, May 15-17, 2001

Montes, M.; Legorburu, I. & Garetto, T. (2008). *Eliminación de Emisiones Atmosféricas de COVs por catálisis y adsorción*, CYTED, ISBN 978-84-96023-64-2, Madrid, Spain

Davis, W. (2000). *Air Pollution Engineering Manual*, Wiley Interscience Publication, ISBN 978-0-471-33333-3

DePriest, W. & Van Laar, J. (1992). *Engineering Evaluation of PRENFLO-based Integrated-gasification-combined-cycle (IGCC) power plant designs*, Chicago, Illinois, USA

Fernández, E. & Montalvo, S. (1998). *Métodos económicos y ecológicamente viables para purificar gases contaminantes*, 26.04.2011, Available from: http://www.bvsde.ops-oms.org/bvsaidis/caliaire/peru/cubpca004.pdf

Gosh, D. P. (2007). Wet H_2S Cracking Problem in Oil Refinery Processes - Material selection and operation control issues, *The 2007 Tri-Service Corrosion Conference*, December 3-7, 2007, Denver, Colorado, USA

Harasimowicz, M.; Orluk, P.; Zakrzewska-Trznadel, G. & Chmielewski, A. (2007). Application of polyimide membranes for biogas purification and enrichment, *Journal of Hazarous Materials*, Vol. 144, No. 3, June 2007, pp. 698-702, ISSN 0304-3894

Horikawa, M.S.; Rossi, M.L.; Gimenes, M.L.; Costa, C.M.M. & da Silva, M.G.C. (2004). Chemical Absorption of H_2S for biogas purification, *Brazilian Journal of Chemical Engineering,* Vol. 21, No. 3, July-September 2004, pp. 415-422

Hvitved, J. (2002). *Sewer Processes: Microbial and Chemical Process Engineering of Sewer Networks*, CRC Press, ISBN 1-56676-926-4, Florida, USA

Kapdi, S.S., Vijay, V.K., Rajesh, S.K. & Prasad, R. (2007). Biogas Scrubbing, Compression and Storage: Perspective and Prospectus in Indian Context, *Renewable Energy*, Vol. 30, No. 8, July 2005, pp. 1195-1202, ISSN 0960-1481

Kolh, A. & Nielsen, R. (1997). *Gas Purification*, Gulf Publishing Company, ISBN 978-0-88415-220-0, Houston, Texas, USA

Hoffmann, A.; Mackowiak, J. F.; Górak, A.; Haas, M.; Löning, J.-M.; Runowski,T. & Hallenberger, K. (2007). Standardization of mass transfer measurements: A basis for the description of absorption processes, *Chemical Engineering Research and Design*, Vol. 85, A1, (January 2007), pp. 40- 49

Littel, R. J.; Filmer, B.; Versteeg, G. F. & Van Swaaij, W. P. M. (1991). Modelling of simultaneous absorption of H2S and CO2 in alkanolamine solutions: the Influence of parallel and consecutive reversible reactions and the coupled diffusion of ionic species, *Chemical Engineering Science*, Vol. 46, No. 9, (1991), pp. 2303-2313

Mabres, A., Freire, D. & Bevilacqua, L. (2003). Eliminación de Sulfuro de Hidrógeno en Emisiones Gaseosas Atmosféricas, *5tas. Jornadas de Preservación de Agua, Aire y Suelo en la Ind. del Petróleo y del Gas*, Buenos Aires, Argentina, November 5-7, 2003

Mackowiak, J. F.; Górak, A.; Kenig, E. Y. (2009). Modelling of combined direct-contact condensation and reactive absorption in packed columns, *Chemical Engineering Journal*, No. 146, (2009), pp. 362- 369

Marchaim, U. (1992). *Biogas processes for sustainable development*, FAO, ISBN 92-5-103126-6, Rome, Italy

Muche, H. & Zimmermann, H. (1985). *The Purification of Biogas*, ISBN 3-528-02015-6, Munich, Germany

Pointon, K. & Langan, M. (2002). *Distributed Power Generation Using Biogas Fuelled Microturbines*, 26.04.2011, Available from: www.berr.gov.uk/files/file14934.pdf

Qian, Z.; Xu, L.; Li, Z.; Li, H. & Guo, K. (2010). Selective Absorption of H2S from a Gas Mixture with CO2 by Aqueous N-Methyldiethanolamine in a Rotating Packed Bed, *Industrial & Engineering Chemistry Research*, Vol. 49, No. 16, (May 2010), pp. 6196-6203

Ramírez, M. (2007). *Viabilidad de un proceso para la eliminación conjunta de H_2S y NH_3 contenido en efluentes gaseosos*. Universidad de Cádiz, Cádiz, Spain.

Romeo, L. M.; Escosa, J. & Bolea, I. (2006). *Postcombustion CO_2 sequestration,* Universidad de Zaragoza, Zaragoza, Spain

Steinfeld, G., & Sanderson, R. (1998). *Landfill Gas Cleanup for Carbonate Fuel Cell Power Generation,* National Renewable Energy Laboratory, Morgantown, West Virginia, USA

Svärd, T. (2004). *Adsorption of Hydrogen Sulfide at low temperature*, Lund University, Lund, Sweden

Tondeur, D. & Teng, F. (2008). Carbon capture and storage for greenhouse effect mitigation. In *Future Energy: Improved, sustainable and clean options for our planet*, T. M. Letcher (Ed.), pp. 305-330, Elsevier, ISBN 978-0-08-054808-1, China

Treybal, R. E. (1996). *Operaciones de Transferencia de Masa* (2nd ed.), Mc Graw Hill, ISBN 968-6046-34-8, Mexico

Walsh, J.; Ross, C.; Smith, M.; Harper, S. & Wilkins, W. (1988). *Biogas Utilization Handbook,* Georgia Tech Research Institute, ISBN 0962464740, Atlanta, Georgia, USA

Wark, K. & Warner, C.F. (1981). *Air Pollution: Its Origin and Control*, Harper and Row Publishers, New York, New York, USA

www.textoscientificos.com. (December 2nd, 2005). *Usos del biogas,* April 5th, 2011, Available from: http://www.textoscientificos.com/energia/biogas/usos

8

Mass Transfer Enhancement by Means of Electroporation

Gianpiero Pataro[1], Giovanna Ferrari[1,2] and Francesco Donsì[1]
[1]Department of Industrial Engineering,
[2]ProdAl scarl,
University of Salerno,
Italy

1. Introduction

PEF treatment involves the application of repetitive ultra-short pulses (from ns to μs) of a high-strength electric field (0.1-10 kV/cm) through a material located between two electrodes. The application of the external electric field induces the permeabilization of cytoplasmatic membranes. The main advantages of PEF with respect to other treatments addressed to disrupt the cell membranes, such as the application of heat or the addition of pectolytic enzymes, are as follows:

- Cost reduction due to lower energy consumption and unnecessary enzyme addition
- Higher purity of the extracts, since upon the PEF treatment the permeabilized cell membranes maintain their structural integrity and are not disrupted in small fragments
- Lower processing times thanks to the increased mass transfer rates.

The application of PEF as a permeabilization treatment to increase the rates of mass transfer of valuable compounds from biological matrices was demonstrated to be effective in drying, extraction, and diffusion processes.

This chapter reviews the basic mechanisms of PEF-induced permeabilization of plant tissues, discusses the methods of detection of electrically induced cell damages and analyses the influence of PEF process parameters on mass transfer. Furthermore, mathematical models to describe the mass transfer rates from PEF-treated vegetable tissue are discussed and some criteria of energy optimization are given as well as some examples on the recovery of polyphenolic compounds from food matrices and on the integration of PEF treatments in the winemaking industry.

2. Basic considerations and mechanism

The application of pulsed electric fields to biological cells (plant or animal) mainly affects the cell membranes, inducing local changes in their structures and promoting the formation of pores. This phenomenon, named electroporation (or elecropermeabilization), causes a drastic increase in the permeability of cell membranes, which lose their semipermeability, either temporarily or permanently (Weaver & Chizmadzhed, 1996). Electroporation is today widely used in biotechnology and medicine to deliver drugs and genes into living cells

(Neumann et al., 1982; Fromm et al., 1985; Mir, 2000; Serša et al., 2003; Miklavčič et al., 2006). Recently, the interest in electropermeabilization has considerably grown, as it offers the possibility to develop different non-thermal alternatives to the traditional processing methods of the food industry requiring the disintegration of cell membrane. For example, the complete damage of the microbial cell membrane induced by the application of intensive PEF process conditions has been intensively studied in the last twenty years as a new non-thermal method of food preservation (Barsotti and Cheftel, 1999; Mosqueda-Melgar et al., 2008; Pataro et al., 2011). More interestingly, it has been also reported by several research teams that the application of a pulsed electric fields pre-treatment of moderate intensity to biological tissue may considerably increase the mass and heat transfer rates between plant cells and the surroundings, making it suitable for enhancing the efficiency of the pressing, extraction, drying and diffusion processes of the food industry (Angersbach, 2000; Vorobiev et al., 2005; Vorobiev and Lebovka, 2006; Donsì et al., 2010b).

The exact mechanism of electroporation is not yet fully understood. Several theories (Chang, 1992; Neumann et al., 1992; Zimmermann, 1986) based on the experiments carried out on model systems such as liposomes, planar bilayers, and phospholipid vescicles were proposed to explain the mechanism of the reversible electroporation and/or the electrical membrane breakdown. All of these theories in their differences are characterized by advantages and disadvantages, but they share a common feature: the cell membrane plays a significant role in amplifying the applied electric field, as the conductivity of intact membrane is several orders of magnitude lower than the conductivities of extra cellular medium and cell cytoplasm (Weaver and Chizmadzhev, 1996). Hence, when the biological cells are exposed to an external electric field E, the trans-membrane potential (u_m) increases as a result of the charging process at the membrane interfaces. In Fig. 1 the simple case of a sphere shaped biological cell is considered. The trans-membrane potential u_m can be derived from the solution of Maxwell's equation in spherical coordinates, assuming several simplifying restrictions (Neumann, 1996), according to Eq. 1, where r_{cell} is the radius, and θ is the angle between the site on the cell membrane where u_m is measured and the direction of the vector E.

$$E_m = 1.5 \cdot r_{cell} \cdot E \cdot \cos(\theta) \tag{1}$$

The highest drop of potential occurs at the cell poles (θ = 0, π), and decreases to 0 at $\theta = \pm\pi/2$. That is why the maximum membrane damage probability occur at the poles of the cell exposed to the electric field facing the electrodes (Fig. 1). Being the membrane thickness h (≈ 5 nm) significantly smaller than the plant cell radius (≈100 μm), a selective concentration of the electric field on the membrane occurs, creating a trans-membrane electric field, $E_m = u_m/h$, which is about 10^5 times higher than the applied field strength (Vorobiev and Lebovka, 2008; Weaver and Chizmadzhev, 1996).

If a critical value of the field strength E_c is exceeded, a critical trans-membrane potential can be induced (typically 0.2-1.0 V for most cell membranes) that leads to the formation of reversible or irreversible pores in the membrane (Zimmermann and Neil, 1996). The occurrence of reversible or irreversible permeabilization of the cell membranes depends on the intensity of the external electric fields, pulse energy and number of pulses applied. The greater the value of these parameters, the higher is the extent of the membrane damage (Angersbach et al., 2002). When a mild PEF treatment is applied, either because the electric

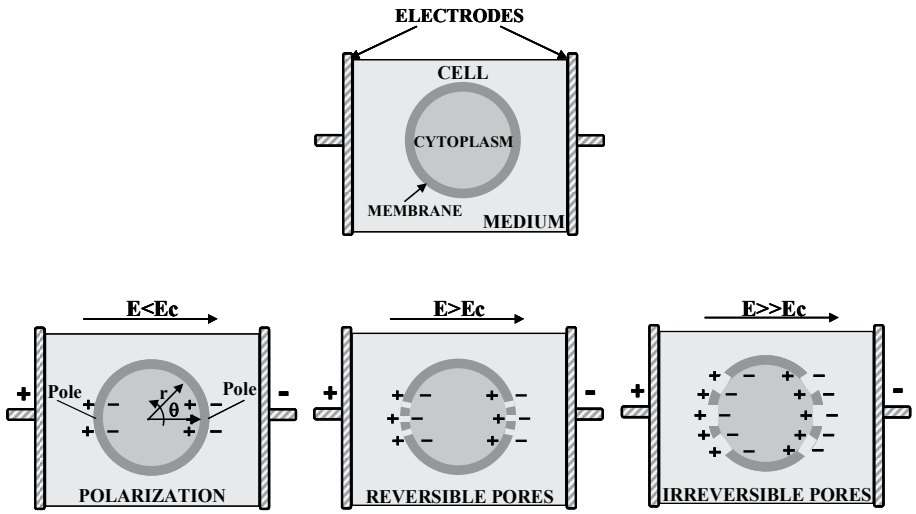

Fig. 1. Schematic depiction of the permeabilization mechanism of a biological cell membrane exposed to an electric field *E*. Electroporated area is represented with a dashed line. E_c: critical electric field strength.

field applied is below the critical value E_c or the number of pulses is too low, reversible permeabilization occurs, allowing the cell membrane to recover its structure and functionality over time. On the contrary, when more intense PEF treatment is applied, irreversible electroporation takes place, resulting in cell membrane disintegration as well as loss of cell viability (Zimmerman, 1986). According to Eq. 1, the external electric field to be applied in order to reach the critical trans-membrane potential decreases with the cell radius increasing. Being the plant tissue cells rather larger (≈100 μm) than microbial cells (≈1-10 μm), the electric field strength required for elecroplasmolysis in plant cells (0.5-5 kV/cm) (Knorr, 1999) is lower than that required for inactivation microorganisms (10-50 kV/cm) (Barbosa-Canovas et al., 1999). However, modifications of the properties of the cell membranes occurring during the PEF treatment cause the critical electric field, required to cause disruptive effects on biological cells, to decrease. Experimental results have demonstrated that the rupture (critical) potential of the lipid-proteins membranes ranges from 2 V at 4°C to 1 V at 20 °C and 500 mV at 30-40°C (Zimmermann, 1986). The increase in temperature promotes greater ions mobility through the cell membranes, which become more fluid, and decreases their mechanical resistance (i.e. elastic modules) (Coster and Zimmermann, 1975).

Overall, the electroporation process consists of different phases. The first of them, which does not contribute to molecular transport, is the temporal destabilization and creation of pores (reported as occurring on time scales of 10 ns), during the charging and polarization of the membranes. The charging time constant (1 μs), defined as the time between electric field application and the moment when the membrane acquires a stable electric potential, is a parameter specific for each treated vegetable or animal tissue, which depends on cellular size, membrane capacitance, the conductivity of the cell and the extracellular electrolyte (Knorr et al., 2001). The second phase is a time-dependent expansion of the pores radii and aggregation of different pores (in a time range of hundred of microseconds to milliseconds, lasting throughout the duration of pulses). The last phase, which takes place after electric

pulse application, consist of pores resealing and lasts seconds to hours. Molecular transport across the permeabilized cell membrane associated with electroporation is observed from the pore formation phase until membrane resealing is completed (Kandušer and Miklavčič, 2008). Therefore, in PEF treatment of biological membranes, the induction and development of the pores is a dynamic and not an instantaneous process (Angersbach et al., 2002).

3. Detection and characterization of cell disintegration in biological tissue

The first studies on the degree of cell membrane permeabilization were based on quantifying the release of intracellular metabolites (i.e. pigments) from vegetable cells after electroporation induced by the application of PEF (Brodelius et al., 1988; Dörnenburg and Knorr, 1993). The irreversible permeabilization of the cells in vegetable tissue was demonstrated for the first time for potato tissue (exposed to PEF treatment), determining the release of the intracellular liquid from the treated tissue using a centrifugal method. A liquid leakage from the tissue of PEF-treated samples was detected, while no-release occurred from the control samples. This leakage was therefore interpreted as a consequence of the cellular damage by the electrical pulses inside the cells of the tissue (Angersbach and Knorr, 1997). However, in order to obtain a quantitative measure of the induced cell damage degree P, defined as the ratio of the damaged cells and the total number of cells, several methods have been defined. The direct estimation of the damage degree can be carried out through the microscopic observation of the PEF-treated tissue (Fincan and Dejmek, 2002). However, the procedure is not simple and may lead to ambiguous results (Vorobiev and Lebovka, 2008). Therefore, experimental techniques based on the evaluation of the indicators that macroscopically register the complex changes at the membrane level in real biological systems have been introduced. For example, the value of P could be related to a diffusivity disintegration index Z_D estimated from diffusion coefficient measurements of PEF-treated biological materials during the following extraction process (Jemai and Vorobiev, 2001; Lebovka et al., 2007b), where D is the measured apparent diffusion coefficient, with the subscript i and d referring to the values for intact and totally destroyed material, respectively.

$$Z_D = \frac{D - D_i}{D_d - D_i} \tag{2}$$

The apparent diffusion can be determined from solute extraction or convective drying experiments. Unfortunately, diffusion techniques are not only indirect and invasive for biological objects, but they may also have an impact on the structure of the tissue. Furthermore, also the validity of the Eq. 2 is still controversial (Vorobiev et al., 2005; Lebovka et al., 2007b).

Measurements of the changes in the electrophysical properties such as complex impedance of untreated and treated biological systems have been suggested as a simple and more reliable method to obtain a measurement of the extent of damaged cells (Angersbach et al., 2002). Intact biological cells have insulated membranes (the plasma membrane and the tonoplast) which are responsible for the characteristic alternating current-frequency dependence on the biological material's impedance. These membranes are faced on both sides with conductive liquid phases (cytosol and extracellular liquid), as illustrated in Fig. 2. Therefore, the electrical behavior of a single intact plant cell is equivalent to an ohmic-capacitive circuit in which insulated cell membranes can be assumed to be a capacitor

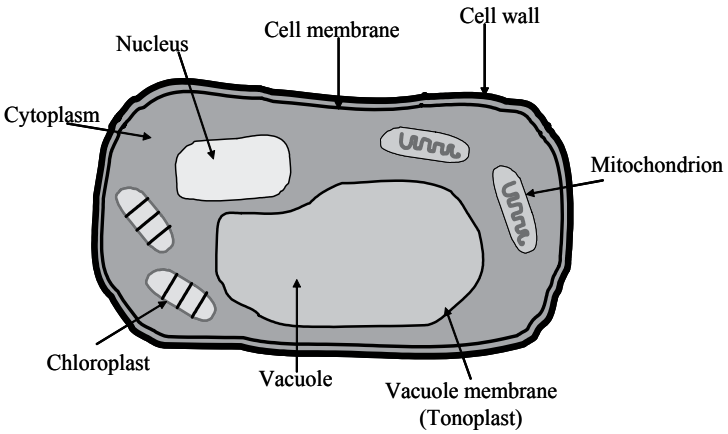

Fig. 2. Simplified scheme of anatomy of plant cells.

connected in parallel to a resistor, while the conductive liquid on both sides of the membranes can be introduced to this circuit as two additional resistors (Fig. 3a) (Angersbach et al., 1999). Hence, the electrophysical properties of cell systems, as characterized by the Maxwell-Wagner polarization effect at intact membrane interfaces, can be determined on the basis of impedance measurements in a frequency range between 1 kHz and 100 MHz, which is called β-dispersion (Angersbach et al., 2002). The complete disintegration of the cytoplasm membranes and tonoplast of plant cells reduces the equivalent circuit to a parallel connection of three ohmic resistor, formed by electrolyte of the cytoplasm, the vacuole, and the extracellular compartments, respectively (Fig. 3b).

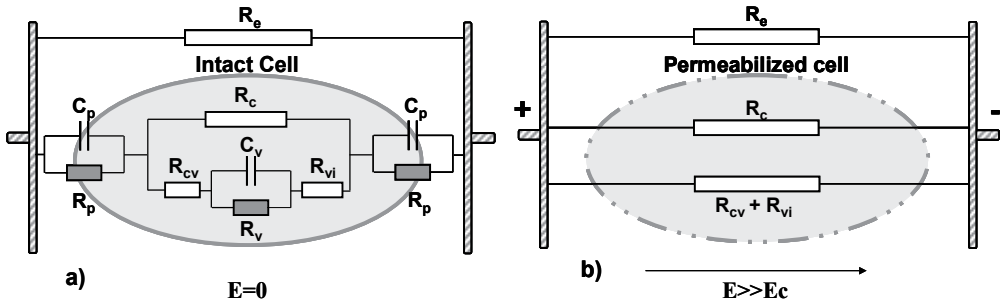

Fig. 3. Equivalent circuit model of (a) an intact and (b) ruptured plant cell. R_p, R_v, plasma and vacuole membrane (tonoplast) resistance; C_p, C_v, plasma and vacuole membrane (tonoplast) capacitance; R_c, cytoplasmic resistance surrounding the vacuole in the direction of current; R_{cv}, cytoplasmic resistance in vacuole direction; R_{vi}, resistance of the vacuole interior; R_e, resistance of the extracellular compartment (Adapted from Angersbach et al., 1999).

The impedance-frequency spectra of intact and treated samples are typically determined with an impedance measurement equipment in which a sample, placed between two parallel plate cylindrical electrodes, is exposed to a sinusoidal or wave voltage signal of alternative polarity with a fixed amplitude (typically between 1 and 5 V peak to peak) and frequency (f) in the range of 3 kHz to 50 MHz. However, the range of characteristic low and high frequencies used depends on the cell size in relation to the conductivity of cell liquid and neighboring fluids, as shown in Table 1 (Angersbach et al., 2002).

Biological material	Low frequency (kHz)	High frequency (MHz)
Large cells		
Animal muscle tissue	≤3	≥15
Fish tissue (mackerel or salmon)	≤3	≥3
Plant cells (apple, potato, or paprika)	≤5	≥5
Small cells		
Yeast cells (*S. cerevisiae*)	≤50	≥25

Table 1. Characteristic low and high frequency values for different biological material.

Electrical impedance is determined as the ratio of the voltage drop across the sample and the current crossing it during the test. The complex impedance $Z(j\omega)$ is expressed according to Eq. 3, where j is the imaginary unit, $\omega = 2\pi f$ is the angular frequency, $|Z(j\omega)|$ is the absolute value of the complex impedance, and φ the phase angle between voltage across the sample and the current through it.

$$Z(j\omega) = |Z(j\omega)| \cdot e^{j\phi} \tag{3}$$

As the complex impedance $Z(j\omega)$ depends on the geometry of the electrode system, the specific conductivity $\sigma(\omega)$ can be instead used (Knorr and Angersbach, 1998; Lebovka et al., 2002; Sack and Bluhm, 2008). For the plate electrode system it has been calculated according to Eq. 4, where l_s is the length of the sample and A_s is the area perpendicular to the electric field.

$$\sigma(\omega) = \frac{l_s}{A_s |Z(j\omega)|} \tag{4}$$

The results of numerous experiments indicate that the impedance or conductivity-frequency spectra of intact and processed plant tissue in a range between 1 kHz and 50 MHz can typically be divided into characteristic zones (Angersbach et al., 1999).
Fig. 4a shows a typical frequency-impedance spectra for artichoke bracts and the transition from an intact to ruptured state in the frequency range of the measured current of 100 Hz to 10 MHz. The results show that the absolute value of the impedance of the intact biological tissue is strongly frequency dependent. This is because in the low frequency field the cell membrane acts as a capacitor preventing the flow of the electric current in the intracellular medium (ohmic-capacitive behavior). Upon increasing the frequency, the cell membrane becomes less and less resistant to the current flow in the intracellular liquid.
At very high frequency values, the membrane is totally shorted out and the absolute value of the complex impedance is representative of the contribution of both extra and intracellular medium (pure ohmic behavior). Thus, the tissue permeabilization induced by an external stress such as PEF treatment, is detectable in the low frequency range. In the high frequency range, because the cell membrane does not show any resistance to the current flow, there is practically no difference between the impedance of intact cells and cells with ruptured membranes. As PEF treatment intensity (field strength and energy input) increases, the extent of membrane permeabilization also increases, thus leading to a significant lowering of the impedance value. When the cells are completely ruptured, the impedance reaches a constant value, exhibiting no frequency dependence (pure ohmic

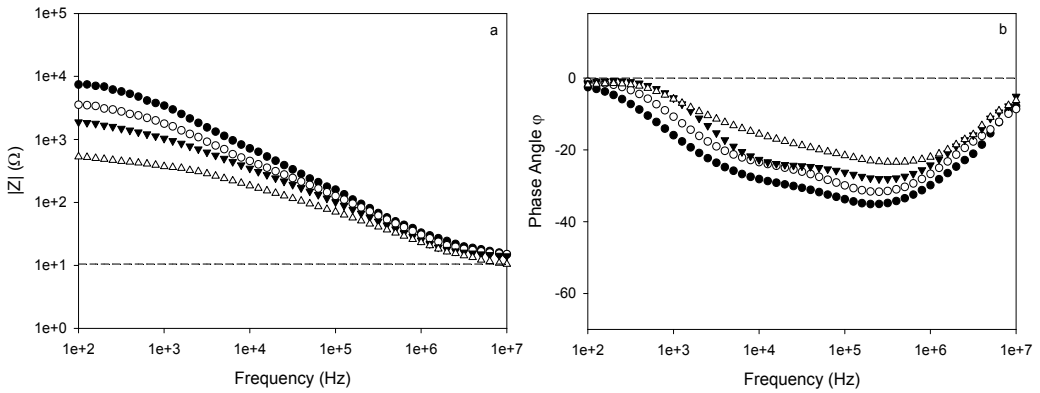

Fig. 4. (a) Absolute value (|*Z*|) and (b) phase angle (φ) of the complex impedance of control and PEF-treated artichoke bracts as a function of frequency (Unpublished data). (●) Control; (○) 3 kV/cm, 1 kJ/kg; (▼) 3 kV/cm, 10 kJ/kg; (△) 7 kV/cm, 10 kJ/kg; (---) theoretical trend of completely ruptured cells.

behavior) (Battipaglia et al., 2009; Pataro et al., 2009). However, the typical electrical behaviour of intact and processed plant tissue can be also analysed in terms of frequency-phase angle spectra (Pataro et al., 2009; Battipaglia et al., 2009; Sack and Bluhm, 2008; Sack et al., 2009). Fig. 4b shows a typical frequency-phase angle spectra for artichoke bracts and the transition from intact to ruptured state in the frequency range of the measured current of 100 Hz to 10 MHz. According to the ohmic-capacitive behavior of intact biological tissue, a negative value of the phase angle is detected. In particular, at characteristic low and high frequencies, the imaginary component of the cell impedance is equal to zero (Angersbach et al., 1999; Angersbach et al., 2002). Hence, the phase angle between voltage and current approaches zero, which is the typical behavior of a pure ohmic system.

At medium frequencies, the influence of the capacitive current through the cell membranes on the phase angle is quite high and a minimum value of the phase angle is detected. As reported in Table 2, the minimum phase angle varies with the type of plant material. During the PEF treatment, the capacitances of the cell membranes become more and more shortened, and the increase of the phase angle can be taken as a measure for the degree of electroporation. If all cells are opened completely, the phase angle approaches zero in the ideal case (Pataro et al., 2009; Sack et al., 2009).

In order to quantify the cellular degree of permeabilization, a coefficient Z_p, the cell disintegration index, has been defined on the basis of the measurement of the electrical complex conductivity of intact and permeabilized tissue in the low (≈1-5 kHz) and high (3-50 MHz) frequency ranges (Angersbach et al., 1999), as shown in Eq. 5, where σ is the electrical conductivity, the superscripts *i* and *t* indicate intact and treated material, respectively, and the subscripts *l* and *h* the low and high frequency field of measurement, respectively.

$$Z_p = \frac{\left(\sigma_h^i / \sigma_h^t\right)\sigma_l^t - \sigma_l^i}{\sigma_h^i - \sigma_l^i} \tag{5}$$

Biological material	Frequency (kHz)(*)	Reference
Apple	50	(Sack et al. 2009)
Carrots	100	(Sack et al. 2009)
Potato	90	(Sack et al. 2009)
Artichoke	200	(Battipaglia et al. 2009)
Sugar beet	50	(Sack and Bluhm 2008)
Pinot noir grapes	100	(Sack et al. 2009)
Alicante grapes	400	(Sack et al. 2009)
Aglianico grapes	300	(Donsì et al., 2010a)
Piedirosso grapes	900	(Donsì et al., 2010a)
Muskateller mash	300	(Sack et al. 2009)
Riesling mash	700	(Sack et al. 2009)

Table 2. Typical frequency value of minimum phase angle for different biological material.

The disintegration index characterizes the proportion of damaged (permeabilized) cells within the plant product (Knorr and Angersbach, 1998). It is the average cell disintegration characteristic in the sample and describes the transition of a cell from an intact to ruptured state (Ade-Omowaye et al., 2001). For intact cells, Z_p=0; for total cell disintegration, Z_p=1.
Another definition of the cell disintegration index Z_p was given by Lebovka et al. (2002), based on the work of Rogov and Gorbatov (1974) according to Eq. 6, where σ is the measured electrical conductivity value at low frequencies (1–5 kHz) and the subscripts i and d refer to the conductivities of intact and totally destroyed material, respectively

$$Z_p = \frac{\sigma - \sigma_i}{\sigma_d - \sigma_i} \tag{6}$$

Therefore, σ_i and σ_d can be estimated as the conductivity value of untreated material in low frequency range and the conductivity value of treated material in the high frequency range, respectively (Donsì et al., 2010b). As in the previous case, Z_p=0 for intact tissue and Z_p=1 for totally disintegrated material. This method has proved to be a useful tool for the determination of the status of cellular materials as well as the optimization of various processes regarding minimizing cell damage, monitoring the improvement of mass transfer, or for the evaluation of various biochemical synthesis reactions in living systems (Angersbach et al., 1999; Angersbach et al., 2002). Unfortunately, there exists no exact relation between the disintegration index Z_p and damage degree P, though it may be reasonably approximated by the empirical Archie's equation (Eq. 7) (Archie, 1942), where exponent m falls within the range of 1.8-2.5 for biological tissue, such as apple, carrot and potato (Lebovka et al. 2002).

$$Z_p \approx P^m \tag{7}$$

In summary, electroporation of biological tissue and the consequent mass transfer process are complex functions of material properties which, in turn, are spatially dependent and highly inhomogeneous. The use of methods based on the evaluation of macroscopic indicators, such as those described above, can help to better understand the complex

changes occurring at the membrane level during the electropermeabilization processes as well as clarify how the subsequent leaching phenomena are affected by the degree of membrane rupture. However, all these methods are indirect and do not allow the exact evaluation of the damage degree. In addition, it should be also considered that, depending on the type of process and on the food matrices used, not all the indicators are able to accurately quantify the release of intracellular metabolites from plant tissue in relation to the cell damage induced by PEF. Probably, the use of multiple indicators such as those evaluated by the simultaneous diffusion and electrical conductivity measurements during solid-liquid leaching process assisted by PEF, should be used to provide a more simple and effective way of monitoring the extraction process.

4. Influence of PEF process parameters

According to electroporation theory, the extent of cell membrane damage of biological material is mainly influenced by the electric treatment conditions. Typically, electric field strength E, pulse width τ_p and number of pulses n_p (or treatment time $t_{PEF} = \tau_p \cdot n_p$) are reported as the most important electric parameters affecting the electroporation process. In general, increasing the intensity of these parameters enhances the degree of membrane permeabilization even if, beyond a certain value, a saturation level of the disintegration index is generally reached (Lebovka et al., 2002). For example, the disintegration index of potato tissue was reported to be markedly increased when increasing either the field strength or the number of pulses (Angersbach et al., 1997; Knorr and Angersbach, 1998; Knorr, 1999). The effect of the applied field strength (between 0.1 and 0.4 kV/cm) and pulse width (between 10 and 1000 μs) on the efficiency of disintegration of apple tissue by pulsed electric fields (PEF) has also been studied (De Vito et al., 2008). The characteristic damage time τ, estimated as a time when the disintegration index Z_p attains one-half of a maximal value, i.e. $Z_p = 0.5$ (Lebovka et al., 2002), decreased with the increase of the field strength and pulse width. In particular, longer pulses were more effective, and their effect was particularly pronounced at room temperature and moderate electric fields ($E = 0.1$ kV/cm). However, Knorr and Angersbach (1998), utilizing the disintegration index Z_p for the quantification of cell permeabilization of potato tissue, found that, at a fixed number of pulses, the application of variable electric field strength and pulse width, but constant electrical energy per pulse W, resulted in the same degree of cell disintegration. Thus, the authors suggested that the specific energy per pulse should be considered as a suitable process parameter for the optimization of membrane permeabilization as well as for PEF-process development.

For exponential decay pulses, W (kJ/kg·pulse) can be calculated by Eq. 8, where E_{max} is the peak electric field strength (kV/m), k is the electrical conductivity (S/m), τ_p is the pulse width (s), and ρ is the density of the product (kg/m^3).

$$W = \frac{kE_{\max}^2 \tau_p}{\rho} \tag{8}$$

The relationship between W and cell permeabilization was evaluated systematically by examining the variation of specific energy input per pulse (from 2.5 to 22000 J/kg) and the number of pulses (n_p =1-200; pulse repetition = 1 Hz). The Z_p value induced by the treatment increased continuously with the specific pulse energy as well as with the pulse numbers.

Theoretically, the total cell permeabilization of plant tissue was obtained by applying either one very high energy pulse or a large number of pulses of low energy per pulse (Knorr and Angersbach, 1998). Based on these results, the total specific energy input W_T, defined as $W_T = W \cdot n_p$ (kJ/kg), should be used, next to field strength, as a fundamental parameter in order to compare the intensities of PEF- treatments resulting from different electric pulse protocols and/or PEF devices. In addition, the use of the total energy input required to achieve complete cell disintegration for any given matrix also provides an indication of the operational costs. Utilizing the disintegration index Z_p evaluated by Eq. (6) for the quantification of cell membrane permeabilization of the outer bracts of artichokes heads, the relationship between total specific energy input ranging from 1 to 20 kJ/kg and cell permeabilization, evaluated for different field strength applied in the range from 1 to 7 kV/cm, is reported in Fig. 5.

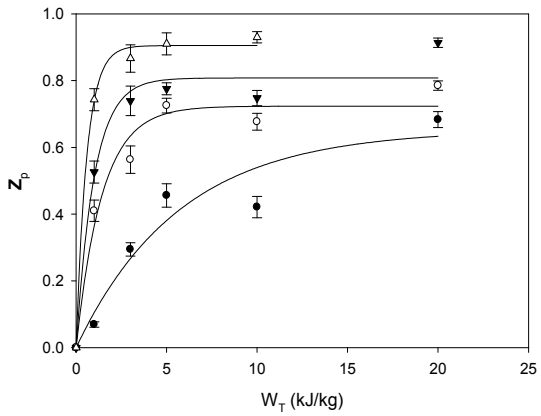

Fig. 5. Disintegration index Z_p of outer bracts of artichoke head versus total specific energy input at different electric filed strength applied: (●) 1 kV/cm; (○) 3 kV/cm; (▼) 5 kV/cm; (△) 7 kV/cm (unpublished data).

The extent of damaged cells grows with both energy input and field strength applied during PEF treatment. However, for each field strength applied, the values of Z_p usually reveal an initial sharp increase in cell disintegration with increasing in energy input, after which any further increase causes only marginal effects, being a saturation level reached. The higher is the field strength applied, the higher the saturation level reached. In particular, as clearly shown by the results reported in Fig. 5, the energy required to reach a given permeabilization increases with decreasing the field strength applied. The characteristic electrical damage energy $W_{T,E}$, estimated as the total specific energy input required for Z_p to attain, at each field strength applied, one-half of its maximal value, i.e. Z_p=0.5, is presented in Fig. 6. The $W_{T,E}$ values decrease significantly with the increase of the electric field strength from 1 to 3 kV/cm and then tend to level-off to a relatively low energy value with further increase of E up to 7 kV/cm. Based on these results, the use of higher field strength should be preferred in order to obtain the desired degree of permeabilization with the minimum energy consumption. However, the estimation of the optimal value of the electric field intensity must take into account that beyond a certain value of E no appreciable reduction in the energy value required to obtain a given permeabilization effect can be achieved. From

the results reported in Fig. 6, an electric field intensity in the range between 3-4 kV/cm can be estimated as optimal (E_{opt}), from the balance between the maximization of the degree of ruptured cells in artichoke bracts tissue and the minimum energy consumption, which impacts on the operative costs, at the minimum possible electric field intensity, which impacts on the investment costs.

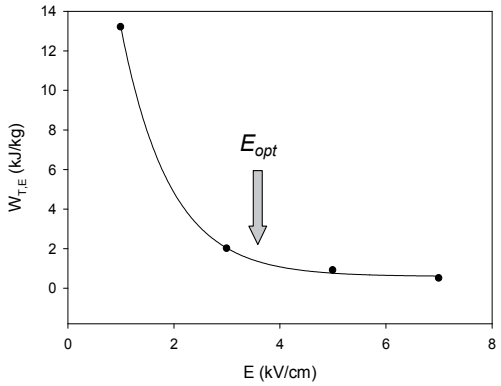

Fig. 6. Characteristic electrical damage energy $W_{T,E}$ of outer bracts of artichoke versus electric field strength applied (unpublished data).

A further criterion for energy optimization, based on the relationship between the characteristic damage time τ and the electric field intensity E, has been proposed by Lebovka et al. (2002). A PEF treatment capable of achieving a Z_p value of 0.5, is characterized by a duration t_{PEF} corresponding to the characteristic damage time $\tau(E)$, which is in turn a function of the electric field. Therefore, the energy input required will be proportional to the product $\tau(E) \cdot E^2$, as shown by Eq. 8. Since the $\tau(E)$ value decreases by increasing the electric field intensity E, the product of $\tau(E) \cdot E^2$ goes through a minimum (Fig. 7). Criteria of energy optimization require a minimum of this product. This minimum corresponds to the minimum power consumption for material treatment during characteristic time $\tau(E)$. A further increase of E results in a progressive increase of the product $\tau(E) \cdot E^2$ and of the energy input, but gives no additional increase in conductivity disintegration index Z_p. An

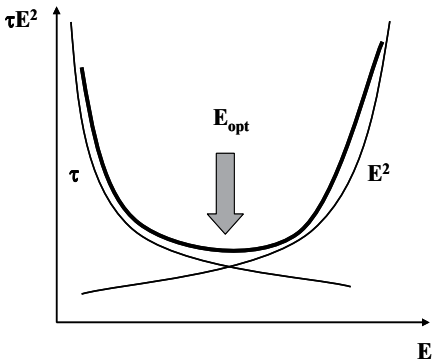

Fig. 7. Schematic presentation of optimization product $\tau(E) \cdot E^2$ versus electric field intensity E dependence (adapted from Lebovka et al., 2002).

optimal value of the electric field intensity $E_{opt} \approx 400$ V/cm, that results in maximal material disintegration at the minimal energy input, was estimated for apple, carrot and potato tissue. Based on this value the characteristic time τ was estimated as $2 \cdot 10^{-3}$ s for apple, $7 \cdot 10^{-4}$ s for carrot and $2 \cdot 10^{-4}$ s for potato and the energy consumption decreased in the same order: apple → carrot → potato (Lebovka et al., 2002).

5. Effect of PEF treatment of mass transfer rate from vegetable tissue

5.1 Models for mass transfer from vegetable tissue

Mass transfer during moisture removal for shrinking solids can be described by means of the Fick's second law of diffusion, reported in Eq. 9, also when PEF-pretreatment was applied to increase tissue permeabilization (Arevalo et al., 2004; Lebovka et al., 2007b; Ade-Omowaye et al., 2003). In Eq. 9, ω is the average concentration of soluble substances in the solid phase as a function of time (ω_0 is the initial concentration) and D_{eff} (m²/s) is the effective diffusion coefficient.

$$\frac{\partial \omega}{\partial t} = D_{eff} \frac{\partial^2 \omega}{\partial x^2} \tag{9}$$

The most commonly used form of the solution of Eq. 9 is an infinite series function of the Fourier number, Fo = (4 *Deff t*)/L^2, which can be written according to Eq. 10 (Crank, 1975). The solution of Eq. 10 is based on the main assumptions that D_{eff} is constant and shrinkage of the sample is negligible (Ade-Omowaye et al., 2003).

$$\vartheta = \frac{\omega}{\omega_o} = \frac{8}{\pi} \sum_{n=0}^{\infty} \frac{1}{(2n+1)} \exp\left[-(2n+1)^2 \pi^2 F_o \right] \tag{10}$$

The application of Eq. 10 to the drying of PEF-treated vegetable tissue, was reported for the ideal case of an infinite plate (disks of tissue with diameter >> thickness), according to the form of Eq. 11 (Arevalo et al., 2004), where M_r = (M - M_e)/(M_0 - M_e) is the adimensional moisture of the vegetable tissue at time t, M_0 is the initial moisture content, M_e is the equilibrium moisture content, M is the moisture content at any given time, D_{eff} is the effective coefficient of moisture diffusivity (m²/s), t is the drying time (s), and L is half-thickness of the plate (m).

$$M_r = \frac{M - M_e}{M_o - M_e} = \frac{8}{\pi^2} \sum_{n=0}^{\infty} \frac{1}{(2n+1)^2} \exp\left[-(2n+1)^2 \frac{\pi^2 D_{eff} t}{L^2} \right] \tag{11}$$

For long drying times, Eq. 11 is expected to converge rapidly and may be approximated by a one-term exponential model, reported in Eq. 12, which can be used for the estimation of the moisture effective diffusivity (Arevalo et al., 2004; Ade-Omowaye et al., 2003).

$$M_r = \frac{M - M_e}{M_o - M_e} = \frac{8}{\pi^2} \exp\left[-\frac{\pi^2 D_{eff} t}{L^2} \right] \tag{12}$$

In other cases, the first five terms of the series of Eq. 11 were used for the estimation of the moisture effective diffusivity, by means of the least square fitting of the experimental data

(Loginova et al., 2010; Lebovka et al., 2007b). Due to the simplifying assumptions taken, the solution reported in Eq. 10 applies well to the extraction of soluble matter from PEF-treated vegetable tissue, which is considered to be dependent on an effective diffusion coefficient D_{eff}, but also takes into account the maximum amount of extractable substances. Eq. 13 represents the modified form of the Crank solution that was applied to the extraction of soluble matter from vegetable tissue (Loginova et al., 2010).

$$1-\frac{y}{y_\infty}=\frac{8}{\pi^2}\alpha\sum_{n=0}^{\infty}\frac{1}{(2n+1)^2}\exp\left[-(2n+1)^2\frac{\pi^2 D_{eff}t}{L^2}\right] \tag{13}$$

In Eq. 13, y is the solute concentration in the extracting solution, y_∞ is the concentration at equilibrium (t=∞) and α is the solid/liquid ratio. The values of the effective diffusion coefficient D_{eff} exhibit a strong dependence on the temperature, at which the mass transfer process, such as drying, extraction or expression, occurs. In particular, the dependence of D_{eff} on temperature can be expressed through an Arrhenius law, reported in Eq. 14, where D_∞ is the effective diffusion coefficient at an infinitely high temperature (m²/s); E_a is the activation energy (kJ/mol), R is the universal gas constant (8.31 10^{-3} kJ/mol K) and T is the temperature (K) (Amami et al., 2008).

$$D_{eff}=D_\infty\exp\left[-\frac{E_a}{RT}\right] \tag{14}$$

Frequently, the kinetics of extraction of PEF treatments was expressed through a simplified form of Eq. 12, which is reported in Eq. 15 and which can be used for the estimation of a kinetic constant of extraction k_d. The kinetic constant k_d includes the diffusion coefficient of the extracted compound, the velocity of the agitation, the total surface area, the volume of solvent and the size and geometry of solid particles (Lopez et al., 2009a; Lopez et al., 2009b). In Eq. 15, y is again the solute concentration in the extracting solution and y_∞ is the concentration at equilibrium (t=∞).

$$\frac{y}{y_\infty}=\left[1-\exp(-k_d t)\right] \tag{15}$$

Some authors reported that mass transfer from vegetable tissue subjected to extraction, pressing or osmotic dehydration may occur according to two different regimes, corresponding to convective fluxes of surface water and diffusive fluxes of intracellular liquids (Amami et al., 2006). The convective or "washing" regime occurs in the initial stages of the mass transfer process and is associated to higher mass fluxes, with its importance further increasing for the tissue that is humidified electrically. The pure diffusion regime is instead characterized by a lower rate of transfer and becomes significant when the washing stage is completed (El-Belghiti and Vorobiev, 2004). The mathematical model that can be used to describe the combination of the washing and pure diffusion regimes is reported in Eq. 16 (El-Belghiti and Vorobiev, 2004; Amami et al., 2006).

$$\frac{y}{y_\infty}=\frac{y_w}{y_\infty}\left[1-\exp(-k_w t)\right]+\frac{y}{y_\infty}\left[1-\exp(-k_d t)\right] \tag{16}$$

In Eq. 16, y represents is the solute concentration in the solution at any time during the extraction process, y_∞ is the equilibrium solute concentration, y_w is the final solute concentration in the solution due to the washing stage alone, y_d is the final solute concentration in the solution due to the diffusion stage alone. Moreover, k_w and k_d represent the rate constants for the washing stage and for the diffusion stage, respectively and give indications about the characteristic times $\tau_w = 1/k_w$ and $\tau_d = 1/k_d$ of the two phenomena.

5.2 Effect of PEF pretreatment on mass transfer rates during drying processes

The reported effect of PEF treatment on mass transfer rates during drying of vegetable tissue is typically an increase in the effective diffusion coefficient D_{eff}. For example, Fig. 8 reports the D_{eff} values estimated from drying data of untreated and PEF-treated potatoes (Fig. 8a) and bell peppers (Fig. 8b). In particular, Fig. 8a shows the Arrhenius plots of $\ln(D_{eff})$ vs. $1/T$ for convective drying of intact, freeze-thawed and PEF-treated potato tissue. In the Arrhenius plot, the activation energy can be calculated from the slope of the plotted data, according to Eq. 17.

$$\ln D_{eff} = \ln D_\infty - \frac{E_a}{R}\frac{1}{T} \tag{17}$$

Remarkably, PEF treatment did not significantly affected the activation energy E_a in comparison to untreated potato samples ($E_a \approx 21$ and 20 kJ/mol, respectively), but caused a significant reduction of the estimated D_∞ values (intercept with y-axis). In comparison, freeze-thawed tissue exhibited a significantly different diffusion behavior, with the D_{eff} value being similar to that of the PEF-treated tissue at low temperature (30°C) and increasing more steeply at increasing temperature ($E_a \approx 27$ kJ/mol) (Lebovka et al., 2007b).
Similarly, the application of PEF increased the effective water diffusivity during the drying of carrots, with only minor variations of the activation energies. More specifically, a PEF treatment conducted at E = 0.60 kV/cm and with a total duration t_{PEF} = 50 ms, increased the values of D_{eff}, estimated according to Eq. 11, from $0.3 \cdot 10^{-9}$ and $0.93 \cdot 10^{-9}$ m²/s at 40 to 60°C drying temperatures, respectively, for intact samples, to $0.4 \cdot 10^{-9}$ and $1.17 \cdot 10^{-9}$ m²/s at the same temperatures for PEF-treated samples. In contrast, the activation energies, estimated from Eq. 14, were only mildly affected, being reduced from ≈ 26 kJ/mol to ≈ 23 kJ/mol by the PEF treatment (Amami et al., 2008).
The increase of PEF intensity, achieved by applying a higher electric field and/or a longer treatment duration, causes the D_{eff} values to increase until total permeabilization is achieved. For example, Fig. 8b shows the D_{eff} values estimated from fluidized bed-drying of bell peppers, PEF treated with an electric field ranging between 1 and 2 kV/cm and duration of the single pulses longer than the duration applied in the previous cases (400 μs vs. 100 μs). The total specific applied energy W_T was regulated by controlling the number of pulses and the electric field applied. Interestingly, the D_{eff} values increased from $1.1 \cdot 10^{-9}$ to an asymptotic value of $1.6 \cdot 10^{-9}$ m²/s when increasing the specific PEF energy up to 7 kJ/kg, probably corresponding to conditions of complete tissue permeabilization. As a consequence, further PEF treatment did not cause any effect on D_{eff} values (Ade-Omowaye et al., 2003).

5.3 Effect of PEF on mass transfer rates during extraction processes

In the case of extraction of soluble matter from vegetable tissue, the PEF treatments affected the mass transfer rates not only by increasing the effective diffusion coefficient D_{eff}, but also

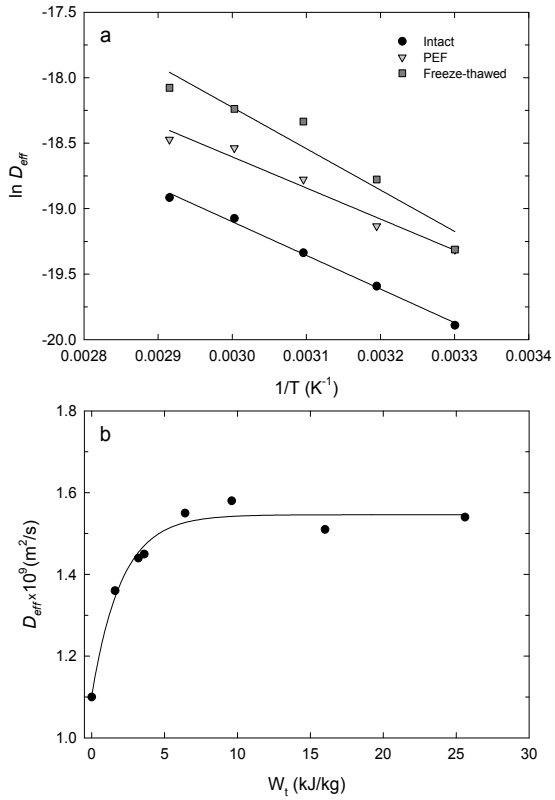

Fig. 8. Dependence of diffusion coefficients of PEF-treated samples on drying temperature and on the specific PEF energy. (a) Dependence on temperature of diffusion coefficients during drying of untreated, freeze-thawed and PEF treated potatoes. PEF treatment conditions were E=0.4 kV/cm and t_{PEF} = 500 ms. Drying was carried at variable temperature in a drying cabinet with an air flow rate of 6 m^3/h (Lebovka et al., 2007b). (b) Dependence on the specific applied energy of PEF treatment of diffusion coefficients during drying of bell peppers. PEF treatment conditions were E=1-2 kV/cm and t_{PEF} = 4-32 ms. Drying was carried at 60 °C in a fluidized bed with air velocity of 1 m/s (Ade-Omowaye et al., 2003).

inducing a significant decrease in the activation energy E_a, which translates in smaller dependence of D_{eff} on extraction temperature. Fig. 9a reports the activation energies of intact, PEF-treated and thermally-treated apple slices, estimated from the data of sugar concentration in the extraction medium through Eq. 13 and 14. Apple samples treated by PEF (E=0.5 kV/cm and t_{PEF} = 0.1 s) exhibited an intermediate activation energy ($E_a \approx$ 20 kJ/mole), which was significantly lower than for intact samples ($E_a \approx$ 28 kJ/mole) and measurably higher than for samples that were previously subjected to a thermal treatment at 75 °C for 2 min ($E_a \approx$ 13 kJ/mole). Moreover, PEF treatment also induced an increase of the D_{eff} value in comparison to untreated tissue for all the different temperatures tested (Jemai and Vorobiev, 2002). For example, at 20 °C D_{eff} estimated from PEF-treated samples ($3.9 \cdot 10^{-10}$ m^2/s) was much closer to the D_{eff} value of denatured samples ($4.4 \cdot 10^{-10}$ m^2/s) than to the D_{eff} of intact tissue ($2.5 \cdot 10^{-10}$ m^2/s). In addition, at 75 °C the D_{eff} value of PEF-treated samples was $13.4 \cdot 10^{-10}$ m^2 s^{-1}, compared with $10.2 \cdot 10^{-10}$ m^2/s for thermally denatured

samples, indicating that the electrical treatment had a greater effect on the structure and permeability of apple tissue than the thermal treatment (Jemai and Vorobiev, 2002).
PEF treatment of sugar beets affected the diffusion of sugar through the cell membranes by decreasing the activation energy of the effective diffusion coefficients. Fig. 9b shows the Arrhenius plots of the effective sugar diffusion coefficient D_{eff} of PEF treated sugar beets from two independent experiments (Lebovka et al., 2007a; El-Belghiti et al., 2005). For example, PEF treatment conducted at E=0.1 kV/cm and t_{PEF} = 1 s caused the reduction of the activation energy from ≈ 75 kJ/mol (untreated sample) to ≈ 21 kJ/mol, with the D_{eff} values being always larger for PEF treated samples (Lebovka et al., 2007a). Interestingly, a different experiment resulted in similar values of the activation energy (≈ 21 kJ/mol) of D_{eff} for sugar extraction from sugar beet after a PEF treatment conducted at E = 0.7 kV/cm and t_{PEF} = 0.1 s. Similarly, the values of the effective diffusion coefficient D_{eff}, estimated for extraction of soluble matter from chicory, were significantly higher for PEF-treated samples (E = 0.6 kV/cm and t_{PEF} = 1 s) than for untreated samples in the low temperatures range, while at high temperature (60 – 80 °C) high D_{eff} values were observed for both untreated and PEF-pretreated samples. In particular, the untreated samples exhibited a non-Arrhenius behavior, with a change in slope occurring at ≈ 60 °C. For T > 60 °C, the diffusion coefficient activation energy was similar to that of PEF treated samples, while for T < 60 °C the activation energy was estimated as high as ≈ 210 kJ/mol, suggesting an abrupt change in diffusion mechanisms. In particular, the authors proposed that below 60 °C, the solute matter diffusion is controlled by the damage of cell membrane barrier and is therefore very high for untreated samples (≈ 210 kJ/mol) and much smaller for PEF treated samples (≈ 19 kJ/mol). Above 60 °C, the extraction process is controlled by unrestricted diffusion with small activation energy in a chicory matrix completely permeabilized by the thermal treatment (Loginova et al., 2010).

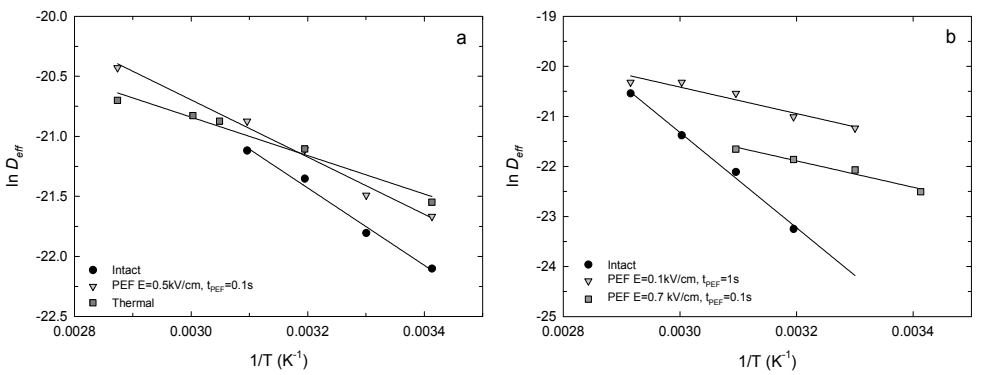

Fig. 9. Dependence on temperature of diffusion coefficients during extraction of soluble matter. (a) Diffusion of soluble matter from untreated, thermally treated (75 °C, 2 min) and PEF treated apples. PEF treatment conditions were E=0.5 kV/cm and t_{PEF} = 0.1 s (Jemai and Vorobiev, 2002). (b) Diffusion of sugar from sugar beets. PEF treatment conditions were E=0.1 kV/cm and t_{PEF} = 1 s (Lebovka et al., 2007a) and E=0.7 kV/cm and t_{PEF} = 0.1 s (El-Belghiti et al., 2005).

Apparently, the intensity of the PEF treatment may significantly affect the D_{eff} values and the equilibrium solute concentration. Fig. 10 shows the values of the effective diffusion

coefficients D_{eff} (Fig. 10a) and the equilibrium sugar concentration y_∞ (Fig. 10b), estimated through data fitting with Eq. 15 and 13, for a PEF treatment significantly different from those reported in Fig. 8 and 9, due to the electric field being significantly higher (up to 7 kV/cm) and the treatment duration shorter (40 μs) (Lopez et al., 2009b).
Interestingly, for low temperature extraction (20 and 40 °C), both D_{eff} and y_∞ values significantly increased upon PEF treatment. In particular, most of the variation of both D_{eff} and y_∞ occurred when increasing the applied electric field from 1 to 3 kV/cm, with E = 1 kV/cm only mildly affecting the mass diffusion rates, suggesting that for E ≥ 3 kV/cm the sugar beet tissue was completely permeabilized. At higher extraction temperature (70 °C), both D_{eff} and y_∞ values are independent on PEF treatment, being the thermal permeabilization the dominant phenomenon (Lopez et al., 2009b).

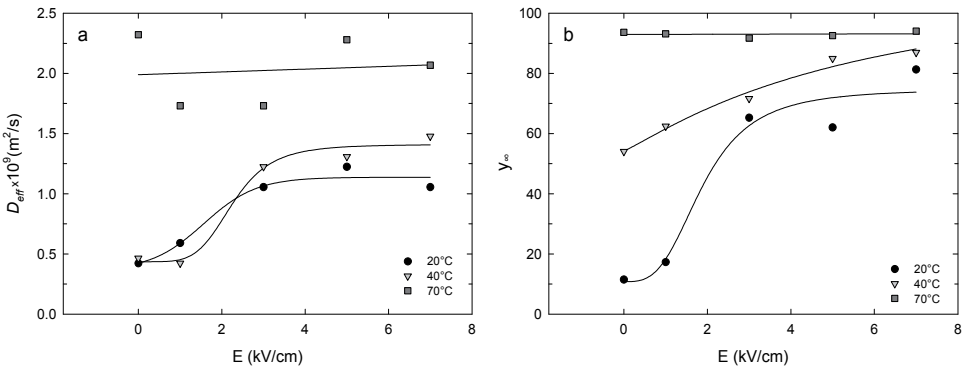

Fig. 10. Dependence on PEF treatment intensity of diffusion coefficient D_{eff} (a) and maximum sugar yield y_∞ (b) during sugar extraction from sugar beets. PEF treatment conditions were E=0-7 kV/cm and $t_{PEF} = 4 \cdot 10^{-5}$ s (Lopez et al., 2009b).

6. A case study - red wine vinification

A promising application of PEF pretreatment of vegetable tissue is in the vinification process of red wine. Grapes contain large amounts of different phenolic compounds, especially located in the skin, that are only partially extracted during traditional winemaking process, due to the resistances to mass transfer of cell walls and cytoplasmatic membranes. In red wine, the main phenolic compounds are anthocyanins, responsible of the color of red wine, tannins and their polymers, that instead give the bitterness and astringency to the wines (Monagas et al., 2005). In addition, polyphenolic compounds also contribute to the health beneficial properties of the wine, related to their antioxidant and free radical-scavenging properties (Nichenametla et al., 2006).
The phenolic content and composition of wines depends on the initial content in grapes, which is a function of variety and cultivation factors (Jones and Davis, 2000), but also on the winemaking techniques (Monagas et al., 2005). For instance, increasing fermentation temperature, thermovinification and use of maceration enzymes can enhance the extraction of phenolic compounds through the degradation or permeabilization of the grape skin cells (Lopez et al., 2008b). Nevertheless, permeabilization techniques suffer from some drawbacks, such as higher energetic costs and lower stability of valuable compounds at higher temperature (thermovinification), or the introduction of extraneous compounds and

general worsening of the wine quality (Spranger et al., 2004). Therefore, PEF treatment may represent a viable option for enhancing the extraction of phenolic compounds from skin cells during maceration steps, without altering wine quality and with moderate energy consumption.

From a technological prospective, great interest was recently focused on the application of PEF for the permeabilization of the grape skins prior to maceration. The enhancement of the rate of release of phenolic compounds during maceration offers several advantages. In case of red wines obtained from grapes poor in polyphenols, it can avoid blending with other grape varieties richer in phenolic compounds, or use of enzymes. Moreover, it can reduce significantly the maceration times (Donsì et al., 2010a; Donsì et al., 2010b).

The main effect of PEF treatment of grape skins or grape mash is the increase of color intensity, anthocyanin content and of total polyphenolic index with respect to the control during all the vinification process on different grape varieties (Lopez et al., 2008a; Lopez et al., 2008b; Donsì et al., 2010a). Furthermore, it was reported that PEF did not affect the ratio between the components of the red wine color (tint and yellow, red and blue components) and other wine characteristics such as alcohol content, total acidity, pH, reducing sugar concentration and volatile acidity (Lopez et al., 2008b). In particular, Fig. 11 shows the evolution of total polyphenols concentration in the grape must during the fermentation/maceration stages of two different grape varieties, Aglianico and Piedirosso. Prior to the fermentation/maceration step, the grape skins were treated at different PEF intensities ($E = 0.5 - 3$ kV/cm and total specific energy from 1 to 25 kJ/kg), with their permeabilization being characterized by electrical impedance measurements. Furthermore, the release kinetics of the total polyphenols were characterized during the fermentation/maceration stage by Folin-Ciocalteau colorimetric methods. It is evident that on Aglianico grape variety the PEF treatment caused a significant permeabilization that enhanced the mass transfer rates of polyphenols through the cellular barriers. Moreover, higher intensity of PEF treatment resulted in both faster mass transfer rates and higher final concentration of polyphenols (Fig. 11a). In contrast, the PEF treatment of Piedirosso variety did not result in any effect on the release kinetics of polyphenols, with very slightly differences being observable between untreated and treated grapes (Fig. 11b).

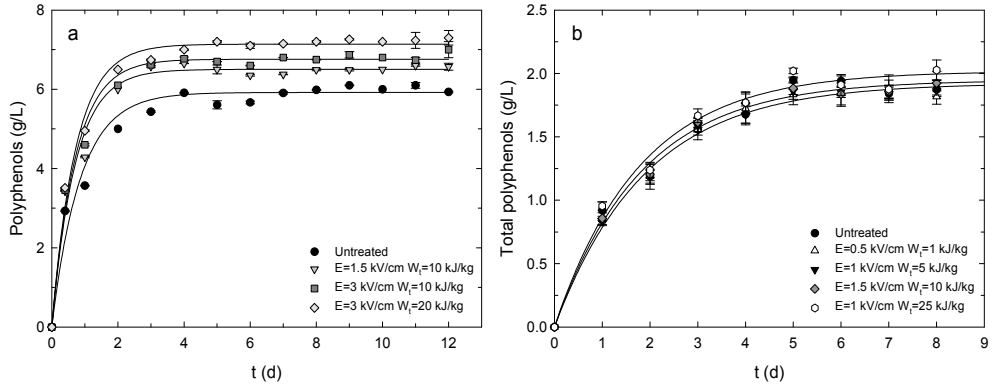

Fig. 11. Evolution over time of total polyphenols concentration in the grape must during fermentation/maceration of two Italian grape varieties: Aglianico (a) and Piedirosso (b) (Donsì et al., 2010a).

This is particularly evident in Fig. 12, where the kinetic constant k_d (Fig. 12a) and the equilibrium concentration y_∞ (Fig. 12b) are reported as a function of the total specific energy delivered by the PEF treatment. While both k_d and y_∞ increased for Aglianico grapes at increasing the specific energy, for Piedirosso the estimated values of both k_d and y_∞ remained constant and independent on the PEF treatments. This is even more remarkable if considering that PEF treatments, under the same operative conditions, caused a significant increase of the permeabilization index Z_p on both grape varieties, as shown in Fig. 12c. In particular, for a total specific energy W_T> 10 kJ/kg a complete permeabilization ($Z_p \approx 1$) was obtained for Piedirosso and an almost complete permeabilization for Aglianico ($Z_p \approx 0.8$).

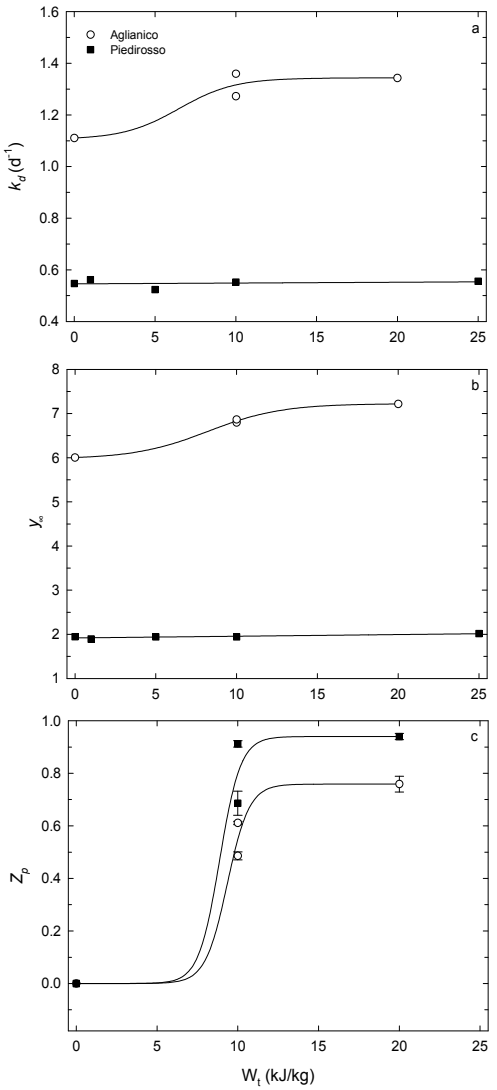

Fig. 12. Kinetic constant k_d (a), equilibrium polyphenolic concentration y_∞ (b) estimated through Eq. 15 from maceration data and permeabilization index Z_p (c) of different untreated and PEF-treated grape varieties, Aglianico and Piedirosso (Donsì et al., 2010a).

Fig. 13, which reports a scheme of a grape skin cell, may help in clarifying the discrepancies observed between measured permeabilization and mass transfer rates in the case of Piedirosso and to explain the mechanisms of PEF-assisted enhancement of polyphenols extraction. Polyphenols and anthocyanins are mainly contained within the vacuoles of the cells, and therefore their extraction encounters two main resistances to mass transfer, which are formed respectively by the vacuole membrane and the cell membrane. PEF treatment causes permanent membrane permeabilization provided that a critical trans-membrane potential is induced across the membrane by the externally applied electric field (Zimmermann, 1986). Since for a given external electric field the trans-membrane potential increases with cell size (Weaver and Chizmadzhev, 1996), the critical value of the external electric field E_{cr} required for membrane permeabilization will be lower for larger systems. Therefore, it can be assumed that the critical electric field for cell membrane permeabilization, E_{cr1}, will be lower than the one for vacuole membrane permeabilization, E_{cr2}. Therefore, in agreement with the reported data, it can be assumed that the applied electric field $E > E_{cr1}$ already at $E = 1$ kV/cm and that the extent of cell membrane permeabilization depends only on the energy input. Whereas, in the case of the vacuole membrane permeabilization, the critical value E_{cr2} is probably in the range of the applied electric field, and the increase of the intensity of E (from 0.5 to 3 kV/cm) can also increase the permeabilization of the membrane of smaller vacuoles. For the above reasons, it can be concluded that the permeabilization index Z_p takes into account the permeabilization of the cell membrane and therefore suggests that cell permeabilization occurred both for Aglianico and Piedirosso grapes.

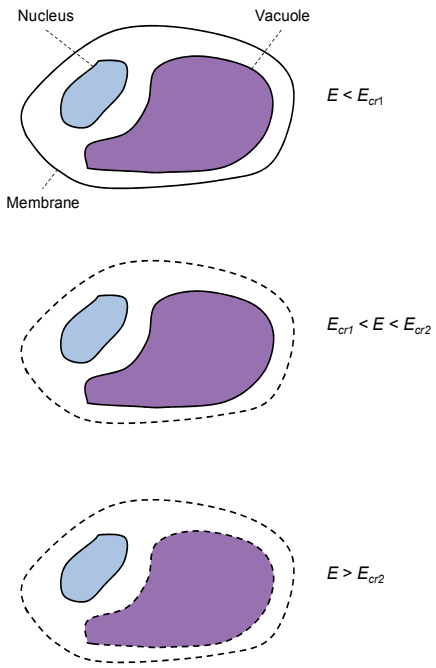

Fig. 13. Simplified scheme of the effect of PEF treatments with electric field intensity E on the structure of a grape skin cell. E_{cr1}: critical electric field for cell membrane permeabilization; E_{cr2}: critical electric field for vacuole membrane permeabilization.

Assuming that the resistance to mass transfer through the vacuole membrane is the rate determining step, the fact that the mass transfer rates are enhanced only for Aglianico and not for Piedirosso can be explained only inferring that, due to biological differences, the applied PEF treatments were able to permeabilize the vacuole membrane only of Aglianico grape skin cells and not of Piedirosso grape skin cells.
In summary, PEF treatments of the grape skins resulted able to affect the content of polyphenols in the wine after maceration, depending on the grape variety. For Piedirosso grapes, the PEF treatment did not increase the release rate of polyphenols. On the other hand, PEF treatment had significant effects on Aglianico grapes, with the most effective PEF treatment inducing, in comparison with the control wine, a 20% increase of the content of polyphenols and a 75% increase of anthocyanins, with a consequent improvement of the color intensity (+20%) and the antioxidant activity of the wine (+20%). Moreover, in comparison with the use of a pectolytic enzyme for membrane permeabilization, the most effective PEF treatment resulted not only in the increase of 15% of the total polyphenols, of 20% of the anthocyanins, of 10% of the color intensity and of 10% of the antioxidant activity, but also in lower operational costs. In fact, the cost for the enzymatic treatment is of about 4 € per ton of grapes (the average cost of the enzyme is about 200 €/kg, and the amount used is 2 g per 100 kg of grapes), while the energy cost for the PEF treatments, calculated as (specific energy) ·(treatment time) ·(energy cost), was estimated in about 0.8 € per ton of grapes (with the energy costs assumed to be 0.12 €/kWh) in the case of the most effective treatment (Donsì et al., 2010a).

7. Conclusions and perspectives

PEF technology is likely to support many different mass transfer-based processes in the food industry, directed to enhancing process intensification. In particular, the induction of membrane permeabilization of the cells through PEF offers the potential to effectively enhance mass transfer from vegetable cells, opening the doors to significant energy savings in drying, to increased yields in juice expression, to the recovery of valuable cell metabolites, with functional properties, or even to the functionalization of foods. For instance, PEF treatment of the grape pomaces during vinification can significantly increase the polyphenolic content of the wine, thus improving not only the quality parameters (i.e. color, odor, taste…) but also the health beneficial properties (i.e. antioxidant activity). Furthermore, PEF treatments can also be applied to enhance mass transfer into the food matrices, by permeabilization of the cell membranes and enhanced infusion of functional compounds or antimicrobial into foods, minimally altering their organoleptic attributes.
In consideration of the fact that energy requirements for PEF-assisted permeabilization are in the order of about 10 kJ/kg of raw material, it can be concluded that PEF pretreatments can represent an economically viable option to other thermal or chemical permeabilization techniques. However, further research and development activities are still required for the optimization of PEF technology in process intensification, especially in the development of industrial-scale generators, capable to provide the required electric field.

8. References

Ade-Omowaye B.I.O, Angersbach A., Eshtiaghi N.M., Knorr D. (2001). Impact of high intensity electric field pulses on cell permeabilisation and as pre-processing step in coconut processing. *Innovative Food Science & Emerging Technologies*, 1, 203-209.

Ade-Omowaye, B.I.O., Rastogi, N.K., Angersbach, A. & Knorr, D. (2003). Combined effects of pulsed electric field pre-treatment and partial osmotic dehydration on air drying behaviour of red bell pepper. *Journal of Food Engineering*, 60, 89-98.

Amami, E., Khezami, L., Vorobiev, E. & Kechaou, N. (2008). Effect of pulsed electric field and osmotic dehydration pretreatment on the convective drying of carrot tissue. *Drying Technology*, 26, 231-238.

Amami, E., Vorobiev, E. & Kechaou, N. (2006). Modelling of mass transfer during osmotic dehydration of apple tissue pre-treated by pulsed electric field. *Lwt-Food Science and Technology*, 39, 1014-1021.

Angersbach A., Heinz V. & Knorr, D. (1997). Effects of pulsed electric fields on cell membranes in real food systems. *Innovative Food Science & Emerging Thecnologies* (IFSET), 1, 135-149.

Angersbach, A., Heinz, V. & Knorr, D. (1999). Electrophysiological model of intact and processed plant tissues: Cell disintegration criteria. *Biotechnology Progress*, 15, 753-762.

Angersbach, A., Heinz, V. & Knorr, D. (2002). Evaluation of Process-Induced Dimensional Changes in the Membrane Structure of Biological Cells Using Impedance Measurement. *Biotechnology Progress*, 18, 597-603.

Angersbach, A., Heinz, V. & Knorr, D. (2000). Effects of pulsed electric fields on cell membranes in real food systems. *Innovative Food Science & Emerging Technologies*, 1, 135–149.

Archie G.E. (1942). The electrical resistivity log as an aid in determining some reservoir characteristics. *Transactions of AIME*, 146, 54–62.

Arevalo, P., Ngadi, M. O., Bazhal, M. I. & Raghavan, G. S. V. (2004). Impact of pulsed electric fields on the dehydration and physical properties of apple and potato slices. *Drying Technology*, 22, 1233-1246.

Barbosa-Canovas, G.V., Gongora-Nieto, M.M., Pothakamury, U.R. & Swanson, B.G. (1999). Preservation of foods with pulsed electric fields In: *Food Science and Technology*, S.L. Taylor (ed.), Academic Press, San Diego.

Barsotti, L. & Cheftel, J.C. (1999). Food processing by pulsed electric fields. II. Biological aspects. *Food Review Interantional*, 15,181-213.

Battipaglia, G., De Vito, F., Donsì, F., Ferrari, G. & Pataro, G. (2009). Enhancement of polyphenols extraction from involucral bracts of artichokes. In: Vorobiev, E., Lebovka, N., Van Hecke, E. & Lanoisellé, J.-L. (Eds.) BFE 2009, International Conference on Bio and Food Electrotechnologies. Compiègne, France: Université de Technologie de Compiègne (pp. 40-44).

Brodelius, P.E., Funk, C. & Shillito, R.D. (1988). Permeabilization of cultivated plant cells by electroporation for release of intracellularly stored secondary products. *Plant Cell Reports*, 7, 186-188.

Chang D.C. (1992). Structure and dynamics of electric field–induced membrane pores as revealed by rapid-freezing electron microscopy, In: *Guide to electroporation and Electrofusion*, D.C. Chang, B.M. Chassy, J.A. Saunders, and A.E. Sowers (eds.), Academic Press, California, pp. 9-28.

Coster, H.G.L. & Zimmermann, U. (1975). The mechanism of electrical breakdown in the membranes of Valonia utricularis. *Journal of Membrane Biology* 22, 73-90.

Crank, J. (1975). The mathematics of diffusion, New York, Oxford University Press.

De Vito F., Ferrari G., Lebovka N.I., Shynkaryk N.V. & Vorobiev E. (2008). Pulse Duration and Efficiency of Soft Cellular Tissue Disintegration by Pulsed Electric Fields. *Food Bioprocess Technology*, 1, 307-313.

Donsì, F., Ferrari, G. & Pataro, G. (2010b). Applications of Pulsed Electric Field Treatments for the Enhancement of Mass Transfer from Vegetable Tissue. *Food Engineering Reviews*, 2, 109-130.

Donsì, F., Ferrari, G., Fruilo, M. & Pataro, G. (2010a). Pulsed Electric Field-Assisted Vinification of Aglianico and Piedirosso Grapes. *Journal of Agricultural and Food Chemistry*, 58, 11606-11615.

Dörnenburg H. & Knorr D. (1993). Cellular Permeabilization of Cultured Plant Tissues by High Electric Field Pulses of Ultra High Pressure for the Recovery of Secondary Metabolites. in Food Biotechnolology, 7,35-48.

El-Belghiti, K. & Vorobiev, E. 2004. Mass transfer of sugar from beets enhanced by pulsed electric field. *Food and Bioproducts Processing*, 82, 226-230.

El-Belghiti, K., Rabhi, Z. & Vorobiev, E. (2005). Kinetic model of sugar diffusion from sugar beet tissue treated by pulsed electric field. *Journal of the Science of Food and Agriculture*, 85, 213-218.

Fincan, M., Dejmek, P. (2002). In situ visualization of the effect of a pulsed electric field on plant tissue. *Journal of Food Engineering*, 55, 223-230.

Fromm, M.E., Taylor, M.P. & Walbot, V. (1985). Expression of genes transferred into monocot and dicot plant cells by electroporation. Proceedings of the National Academy of Sciences of the United States of America, 82, 5824-5828.

Jemai, A. B. & Vorobiev, E. (2001). Enhancement of the diffusion characteristics of apple slices due to moderate electric field pulses (MEFP). In Proceedings of the 8th International Congress on Engineering and Food; Welti-Chanes J., Barbosa-Canovas G.V., Aguilera J.M. (eds.); ICEF 8 :Puebla City, México, 2001a; Vol. II, 1504–1508.

Jemai, A. B. & Vorobiev, E. (2002). Effect of moderate electric field pulses on the diffusion coefficient of soluble substances from apple slices. *International Journal of Food Science and Technology*, 37, 73-86.

Jones, G. V. & Davis, R. E. (2000). Climate influences on grapevine phenology, grape composition, and wine production and quality for Bordeaux, France. *American Journal of Enology and Viticulture*, 51, 249-261.

Kandušer, M. & Miklavčič, D. (2008). Electroporation in Biological Cell and Tissue: An Overview. In: *Electrotechonologies for Extraction from Food Plants and Biomaterial*, E. Vorobiev, N. I. Lebovka (Eds.), (pp. 1–37). New York, USA: Springer.

Knorr, D. (1999). Novel approaches in food-processing technology: new technologies for preserving foods and modifying function. Current Opinion in Biotechnology, 10,485–491.

Knorr, D., Angersbach, A. (1998). Impact of high-intensity electrical field pulses on plant membrane permeabilization. *Trends in Food Science & Technology*, 9,185-191.

Knorr, D., Angersbach, A., Eshtiaghi, M.N., Heinz, V. & Dong-Un Lee, D.U. (2001). Processing concepts based on high intensity electric field pulses. *Trends in Food Science & Technology*, 12:129–135.

Lebovka, N.I., Bazhal, M.I. & Vorobiev, E. (2002). Estimation of characteristic damage time of food materials in pulsed-electric fields. *Journal of Food Engineering*, 54,337–346.

Lebovka, N. I., Shynkaryk, M. V., El-Belghiti, K., Benjelloun, H. & Vorobiev, E. (2007a). Plasmolysis of sugarbeet: Pulsed electric fields and thermal treatment. *Journal of Food Engineering*, 80, 639-644.

Lebovka, N. I., Shynkaryk, N. V. & Vorobiev, E. (2007b). Pulsed electric field enhanced drying of potato tissue. *Journal of Food Engineering*, 78, 606-613.

Loginova, K. V., Shynkaryk, M. V., Lebovka, N. I. & Vorobiev, E. (2010). Acceleration of soluble matter extraction from chicory with pulsed electric fields. *Journal of Food Engineering*, 96, 374-379.

Lopez, N., Puertolas, E., Condon, S., Alvarez, I. & Raso, J. (2008a). Application of pulsed electric fields for improving the maceration process during vinification of red wine: influence of grape variety. *European Food Research and Technology*, 227, 1099-1107.

Lopez, N., Puertolas, E., Condon, S., Alvarez, I. & Raso, J. (2008b). Effects of pulsed electric fields on the extraction of phenolic compounds during the fermentation of must of Tempranillo grapes. *Innovative Food Science & Emerging Technologies*, 9, 477-482.

Lopez, N., Puertolas, E., Condon, S., Raso, J. & Alvarez, I. (2009a). Enhancement of the extraction of betanine from red beetroot by pulsed electric fields. *Journal of Food Engineering*, 90, 60-66.

Lopez, N., Puertolas, E., Condon, S., Raso, J. & Alvarez, I. (2009b). Enhancement of the solid-liquid extraction of sucrose from sugar beet (Beta vulgaris) by pulsed electric fields. Lwt-Food Science and Technology, 42, 1674-1680.

Miklavčič, D., Čorović, S., Puchihar, G. & Pavšelj, N. (2006). Importance of tumor coverage by sufficiently high local electric field for effective electrochemotherapy. *European Journal of Cancer Supplement* ,4, 45-51.

Mir, L.M. (2000). Therapeutical perspective of in vivo cells electropermeabilization. *Bioelectro-chemistry*, 53, 1-10.

Monagas, M., Bartolome, B. & Gomez-Cordoves, C. (2005). Updated knowledge about the presence of phenolic compounds in wine. *Critical Reviews in Food Science and Nutrition*, 45, 85-118.

Mosqueda-Melgar, J., Elez-Martinez, P., Raybaudi-Massilia, R.M. & Martín-Belloso, O. (2008). Effects of pulsed electric fields on pathogenic microorganisms of major concern in fluid foods: a review. *Critical Reviews in Food Science and Nutrition*, 13, 747–759.

Neumann, E. (1996). Gene delivery by membrane electroporation. In P. T. Lynchm & M. R. Davey (Eds), Electrical manipulation of cells (pp.157-184). New York: Chapman and Hall.

Neumann, E., Sprafke, A., Boldt, E. & Wolf, H. (1992). Biophysical considerations of membrane electroporation. In: *Guide to Electroporation and Electrofusion*, Chang, D., Chassy, B., Saunders, J., Sowers, A., (ed), Academic Press: California, 77–90.

Neumann, E., Schafer-Ridder, M., Wang, Y. &Holschneider, P.H. (1982). Gene transfer into mouse lyomas cells by electroporation in high electric fields. The EMBO Journal, 1, 841-845.

Nichenametla, S. N., Taruscio, T. G., Barney, D. L. & Exon, J. H. (2006). A review of the effects and mechanisms of polyphenolics in cancer. *Critical Reviews in Food Science and Nutrition*, 46, 161-183.

Pataro, G., Donsì, G., Ferrari, G. (2009). The effect of conventional and ohmic heating on the permeability of cell membrane in vegetables tissue. In: Vorobiev, E., Lebovka, N., Van Hecke, E. & Lanoisellé, J.-L. (Eds.) BFE 2009, International Conference on Bio and Food Electrotechnologies. Compiègne, France: Université de Technologie de Compiègne, (pp. 246-250).

Pataro, G., Senatore, B., Donsì, G. & Ferrari, G. (2011). Effect of electric and flow parameters on PEF treatment efficiency. *Journal of Food Engineering*, 105, 79–88.

Rogov, I.A. & Gorbatov, A.V. (1974). Physical methods of food treatment. Moscow: *Pischevaya promyshlennost* (in Russian).

Sack, M., & Bluhm, H. (2008). New Measurement Methods for an Industrial Scale Electroporation Facility for Sugar Beets, IEEE Trans. Industry Applications, Vol 44, No 4, July-August 2008: 1074-1083.

Sack, M., Eing, C., Stangle, R., Wolf, A., Muller, G., Sigler, J. & Stukenbrock, L. (2009). Electric Measurement of the Electroporation Efficiency of Mash from Wine Grapes. *IEEE T Dielect El In*, 16, 1329-1337.

Serša, G., Čemaar & Rudolf, Z. (2003). Electrochemotherapy: advantages and drawbacks in treatment of cancer patients. *Cancer Therapy*, 1, 133-142.

Spranger, M. I., Climaco, M. C., Sun, B. S., Eiriz, N., Fortunato, C., Nunes, A., Leandro, M. C., Avelar, M. L. & Belchior, A. P. (2004). Differentiation of red winemaking technologies by phenolic and volatile composition. *Analytica Chimica Acta*, 513, 151-161.

Vorobiev, E. & Lebovka, N.I. (2008). Pulsed-Electric-Fields-Induced Effects in Plant Tissues: Fundamental Aspects and Perspectives of Applications.. In: *Electrotechonologies for Extraction from Food Plants and Biomaterial,*. E. Vorobiev, & N. I. Lebovka (Eds.), In (pp. 39–82). New York, USA: Springer.

Vorobiev, E., Jemai, A.B., Bouzrara, H., Lebovka, N.I. & Bazhal, M.I. (2005). Pulsed electric field assisted extraction of juice from food plants. In: *Novel food processing technologies*, G. Barbosa-Canovas, M. S. Tapia & M. P. Cano (Eds.), (pp. 105–130). New York, USA: CRC.

Vorobiev, E. & Lebovka, N.I. (2006). Extraction of intercellular components by pulsed electric fields. In: *Pulsed electric field technology for the food industry. Fundamentals and applications,* J Raso & H Heinz (Eds.), (pp. 153–194). New York, USA: Springer.

Vorobiev, E. & Lebovka, N. I. (2008). Pulsed-Electric-Fields-Induced Effects in Plant Tissues: Fundamental Aspects and Perspectives of Applications. In: *Electrotechonologies for Extraction from Food Plants and Biomaterial,* E. Vorobiev, & N. I. Lebovka (Eds.), (pp. 39–82). New York, USA: Springer.

Weaver, J. C. & Chizmadzhev, Y. A. (1996). Theory of electroporation: A review. *Bioelectrochemistry and Bioenergetics*, 41, 135-160.

Zimmermann, U. & Neil, G.A. (1996). Electromanipulation of Cells, pp. 1-106, CRC Press, Boca Ration, New York.

Zimmermann, U. (1986). Electrical breakdown, electropermeabilization and electrofusion. *Reviews of Physiology, Biochemistry and Pharmacology,* 105, 175–256.

9

Roles of Facilitated Transport Through HFSLM in Engineering Applications

A.W. Lothongkum[1], U. Pancharoen[2] and T. Prapasawat[1]
[1]*Department of Chemical Engineering, Faculty of Engineering, King Mongkut's Institute of Technology Ladkrabang, Bangkok,*
[2]*Department of Chemical Engineering, Faculty of Engineering, Chulalongkorn University, Bangkok, Thailand*

1. Introduction

For a number of manufacturing processes, separation, concentration and purification are important to handle intermediates, products, by-products and waste streams. In this regards mass and heat transfer play a significant role to attain efficient results. Concern to the separation operations, they can be classified as energy-intensive interphase mass transfer processes and less energy- or less material-intensive intraphase mass transfer processes (Henley & Seader, 1981). With environmental and energy constraints in these days, for sustainability it is of much concern the requirements of process intensification and looking for the most effective operation based on green chemistry concepts (Badami, 2008; Escobar & Schäfer, 2010; Matthews, 2007). Membrane technologies are a potential sustainable solution in this point of view. In contrast to the energy-intensive interphase mass transfer processes as distillation and extraction, membrane separation is an intraphase-mass-transfer process without the energy-intensive step of creating or introducing a new phase. It involves the selective diffusion of target species through the membrane at different rates. Although membrane operations are a relatively new type of separation process, several of them are fast-growing and successfully not only in biological systems but also a large industrial scale, e.g., food and bioproduct processing (Jirjis & Luque, 2010; Lipnizki, 2010). They can apply for a wide range of applications and provide meaningful advantages over conventional separation processes. In applications of controlling drug delivery, a membrane is generally used to moderate the permeation rate of a drug from its reservoir to the human body. In applications for safety regulations of food packaging, the membrane controls the permeation of undesirable constituents completely. In separation purposes, the membrane allows one component in a feed mixture to permeate itself but prohibits permeation of others. Among several membrane types, supported liquid membranes (SLMs) or immobilized liquid membranes (ILMs) containing carriers or extractants to facilitate selective transport of gases or ions draw high interest of the researchers and users in the industry as they are advanced economical feasible for pre-concentration and separation of the target species. So far, four types of supported liquid membrane modules (spiral wound, hollow fiber, tubular and flat sheet or plate and frame) have been used in the industry (Baker, 2007; Cui et al., 2010). The

hollow fiber supported liquid membrane (HFSLM) is renowned as a favorable system to separate valuable compounds or pollutants at a very low concentration and has specific characteristics of simultaneous extraction and stripping of the low-concentration target species in one single stage, non-equilibrium mass transfer, high selectivity and low solvent used.

This chapter describes transport mechanisms in HFSLM and shows some applications with reference to our up-to-date publications, for example

- the effective extraction and recovery of praseodymium from nitrate solutions of mixed rare earths, $RE(NO_3)_3$. Mass transfer phenomena in the system, the extraction equilibrium constant (K_{ex}), distribution ratio (D), permeability coefficient (P), aqueous-phase mass-transfer coefficient (k_i) and organic-phase mass-transfer coefficient (k_m) were reported (Wannachod et al., 2011).
- the enhancement of uranium separation from trisodium phosphate (a by-product from monazite processing) by consecutive extraction with synergistic extractant via HFSLM (Lothongkum et al., 2009).
- a mathematical model describing the effect of reaction flux on facilitated transport mechanism of Cu(II) through the membrane phase of the HFSLM system. The model was verified with the experimental separation results of Cu(II) in ppm level by LIX84I dissolved in kerosene. The model results were in good agreement with the experimental data at the average percentage of deviation of 2%. (Pancharoen et al., in press).

2. Principles of liquid membranes

New technologies and developments in membranes can be accessed from journals (e.g., J. Membr. Sci., Sep. Sci. Technol., Sep. Purif. Technol., J. Alloy. Compd.), vendor communications (via websites), patents and conference proceedings, e.g., annual ACS (Prudich et al., 2008). Theories and applications of liquid membranes (LMs) are stated in (Baker, 2007; Baker & Blume (1990); Kislik, 2010; Scott & Hughes, 1996). Refer to Kislik (Kislik, 2010), LMs are classified in different criteria as follows:

- Classification based on module design configurations

1. Bulk liquid membrane (BLM)
2. Supported or immobilized liquid membrane (SLM or ILM)
3. Emulsion liquid membrane (ELM)

- Classification based on transport mechanisms

1. Simple support
2. Facilitated or carrier-mediated transport (The chemical aspects of complexation reactions to the performance of facilitated transport will be discussed later.)
3. Coupled counter- or cotransport
4. Active transport

- Classification based on carrier types

1. Water-immiscible, organic carriers
2. Water-soluble polymers
3. Electrostatic, ion-exchange carriers
4. Neutral, but polarizable carriers

- Classification based on membrane support types

1. Neutral hydrophobic, hydrophilic membranes
2. Electrically charged or ion exchange membranes

3. Flat sheet, spiral wound module membranes
4. Hollow fiber membranes
5. Capillary hollow fiber membranes

- Classification based on applications

1. Metal-separation concentration
2. Biotechnological products recovery-separation
3. Pharmaceutical products recovery-separation
4. Organic compounds separation, organic pollutants recovery from wastewaters
5. Gas separations
6. Fermentation or enzymatic conversion-recovery-separation (bioreactors)
7. Analytical applications
8. Wastewater treatment including biodegradable-separation techniques

2.1 Membrane structures, materials and modules

The performance of membrane relates closely to its structure, material and module. It is known that porous membranes can be classified according to their structures into microporous and asymmetric membranes. Microporous membranes are designed to reject the species above their ratings. They can get blocked easily compared to asymmetric membranes.

In case of membrane materials, polymeric or organic membranes made of various polymers (e.g., cellulose acetate, polyamide, polypropylene, etc) are cheap, easy to manufacture and available of a wide range of pore sizes. However, some limitations like pH, temperature, pressure, etc can impede the applications of polymeric membranes. On the other hand, ceramic or inorganic membranes have advantages of high mechanical strength, high chemical and thermal stability over the polymeric membranes but they are brittle and more expensive.

In terms of membrane modules, the development of membrane module with large surface areas of membrane at a relatively low manufacturing cost is very important. Resistance to fouling, which is a particularly critical problem in liquid separation, depends on the membrane module. Of four types of the SLM modules (spiral wound, hollow fiber, tubular and flat sheet or plate and frame), hollow fiber module (Fig.1) has the greatest surface area-to-volume ratio resulting in high mass transfer coefficient and is the most efficient type of

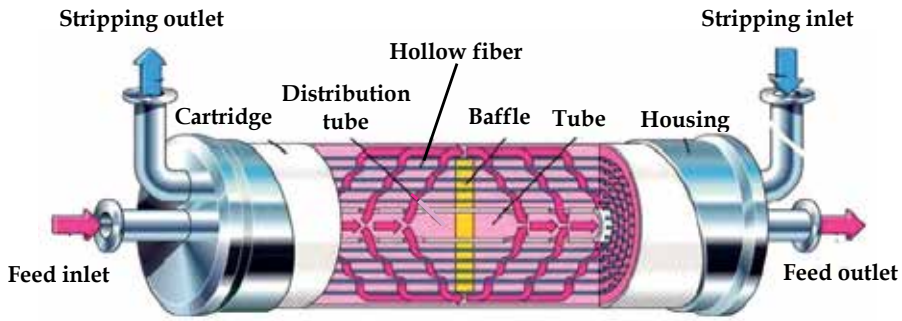

Fig. 1. The hollow fiber module (http://www.liquicel.com/product-information/gas-transfer.cfm)

membrane separation. Hollow fiber module is obviously the lowest cost design per unit membrane area. Compared to flat sheet modules, hollow fiber modules can be operated at higher pressure operation and their manufacturing cost is lower. However, the resistance to fouling of the hollow fibers is poor so the module requires feed pretreatment to reduce large particle sizes. The properties of module designs are shown in Table 1.

Properties	Hollow fibers	Spiral-wound	Flat sheet	Tubular
Manufacturing cost	moderate	high	high	high
Resistance to fouling	very poor	moderate	good	very good
Parasitic pressure drop	high	moderate	low	low
High pressure operation	yes	yes	difficult	difficult
Limit to specific membranes	yes	no	no	no

Table 1. Properties of membrane module designs (modified from Table 2. p. 419, Baker, 2007)

In principle, important performance characteristics of membranes are 1) permeability, 2) selectivity and retention efficiency, 3) electrical resistance, 4) exchange capacity, 5) chemical resistance, 6) wetting behavior and swelling degree, 7) temperature limits, 8) mechanical strength, 9) cleanliness, and 10) adsorption properties (Kislik, 2010). We will discuss in section 3 relevant to permeability, resistance and mass transfer across the HFSLM.

2.2 Hollow fiber supported liquid membrane (HFSLM)

The characteristics of the hollow fiber module are shown in Table 2.

Characteristics	Description
Material	Polypropylene
Fiber ID (μm)	140
Fiber OD (μm)	300
Number of fibers	10,000
Module diameter (cm)	6.3
Module length (cm)	20.3
Effective surface area or contact area (m^2)	1.4
Area per unit volume (cm^2/cm^3)	29.3
Pore size (μm)	0.03
Porosity (%)	30
Tortuosity	2.6

Table 2. Characteristics of hollow fiber module

Hollow fiber modules are recommended to operate with the Reynolds number from 500-3,000 in the laminar flow region. They are one of high economical modules in terms of energy consumption. Other advantages of HFSLM over conventional separations are:

1. high selectivity based on a unique coupled facilitated transport mechanisms and sometimes by using synergistic extractant;

2. simultaneous extraction and stripping of very low-concentration target species (either precious species or toxic species) in one single stage;
3. mild product treatment due to moderate temperature operation;
4. compact and modular design for easy installation and scaling up for industrial applications;
5. low energy consumption;
6. lower capital cost;
7. lower operating cost (consuming small amounts of extractant and solvent and low maintenance cost due to a few moving parts);
8. higher flux;
9. non-equilibrium mass transfer.

As stated, the extremely important disadvantage of HFSLM is the fouling of the hollow fibers causing a reduction in the active area of the membrane and therefore a reduction in flux and process productivity over time. Fouling can be minimized by regular cleaning intervals. The concepts of membrane fouling and cleaning were explained by Li & Chen (Li & Chen, 2010). Active research includes, for example, membrane surface modification (to reduce fouling, increase flux and retention), new module designs (to increase flux, cleanability), etc should be further studied. In short, flux enhancement and fouling control were suggested by different approaches separately or in combination (Cui et al., 2010; Scott & Hughes, 1996):

1. hydrodynamic management on feed side;
2. back flushing or reversed flow and pulsing;
3. membrane surface modification;
4. feed pretreatment;
5. flux control;
6. regular effective membrane cleaning.

3. Mass transfer across HFSLM

Mass transfer plays significant role in membrane separation. The productivity of the membrane separation processes is identified by the permeate flux, which represents rate of target species transported across the membrane. In general practice, high selectivity of membranes for specific solutes attracts commercial interest as the membranes can move the specific solutes from a region of low concentration to a region of high concentration. For example, membranes containing tertiary amines are much more selective for copper than for nickel and other metal ions. They can move copper ions from a solution whose concentration is about 10 ppm into a solution whose concentration is 800 times higher. The mechanisms of these highly selective membranes are certainly different from common membranes which function by solubility mechanism or diffusion. The selectivity of these membranes is, therefore, dominated by differences in solubility. These membranes sometimes not only function by diffusion and solubility but also by chemical reaction. In this case, the transport combines diffusion and reaction, namely facilitated diffusion or facilitated transport or carrier-mediated transport (Cussler, 1997).

For an in-depth understanding of the facilitated transport through liquid membrane, we recommend to read (Kislik, 2010). The facilitated transport mechanisms can be described by solute species partitioning (dissolving), ion complexation, and diffusion. The detailed steps are as follows:

Step 1. Metal ions or target species in feed solution or aqueous phase are transported to a contact surface between feed solution and liquid membrane, subsequently react with the organic extractant at this interface to form complex species.

Step 2. The complex species subsequently diffuse to the opposite side of liquid membrane by the concentration gradient. It is assumed that no transport of target species passes this interface.

Step 3. The complex species react with the stripping solution at the contact surface between liquid membrane and the stripping solution and release metal ions to the stripping phase.

Step 4. Metal ions are transferred into the stripping solution while the extractant moves back to liquid membrane and diffuses to the opposite side of liquid membrane by the concentration gradient to react again with metal ions in feed solution.

The facilitated transport mechanisms through the hollow fiber module are shown in Fig. 2. The facilitated transport through an organic membrane is used widely for the separation applications. The selectivity is controlled by both the extraction/ stripping (back-extraction) equilibrium at the interfaces and the kinetics of the transported complex species under a non-equilibrium mass-transfer process (Yang, 1999).

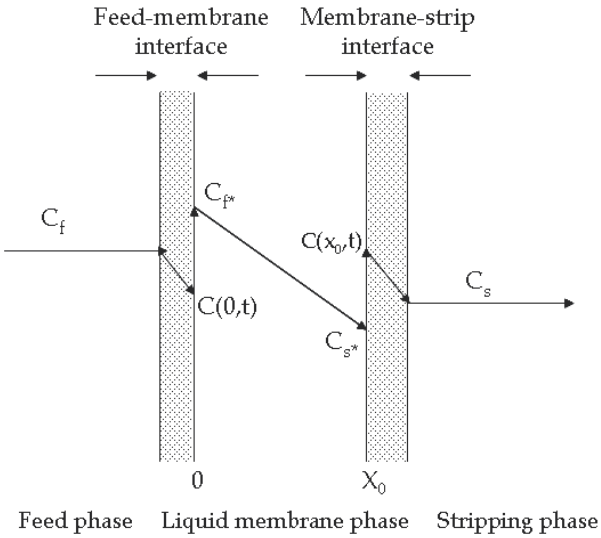

Fig. 2. Facilitated transport mechanisms through the HFSLM

The chemical reaction at the interface between feed phase and liquid membrane phase takes place when the extractant $(\overline{RH})$ reacts with the target species (M^{n+}) in the feed Eq. (1).

$$M^{n+} + \overline{nRH} \rightleftharpoons \overline{MR_n} + nH^+ \tag{1}$$

$\overline{MR_n}$ is the complex species in liquid membrane phase.

The extraction equilibrium constant (K_{ex}) of the target species is

$$K_{ex} = \frac{[\overline{MR_n}]\cdot[H^+]^n}{[M^{n+}]\cdot[\overline{RH}]^n} \tag{2}$$

The distribution ratio (D) is

$$D = \frac{\overline{[MR_n]}}{[M^{n+}]} \tag{3}$$

The distribution ratio should be derived as a function of the extraction equilibrium constant as

$$D = \frac{K_{ex}\overline{[RH]}^n}{[H^+]^n} \tag{4}$$

Mass transfer through HFSLM for the separation of the target species in terms of permeability coefficient (P) depends on the overall mass transfer resistance. To determine the overall mass transfer coefficient for the diffusion of the target species through HFSLM, the relationship between the overall mass transfer coefficient and the permeability coefficient is deployed. The permeability coefficient is reciprocal to the mass transfer coefficients as follows (Urtiaga et al., 1992; Kumar et al., 2000; Rathore et al., 2001)

$$\frac{1}{P} = \frac{1}{k_i} + \frac{r_i}{r_{lm}}\frac{1}{P_m} + \frac{r_i}{r_o}\frac{1}{k_s} \tag{5}$$

where k_i and k_s are the feed-phase and stripping-phase mass transfer coefficients, r_{lm} is the log-mean radius of the hollow fiber in tube and shell sides, r_i and r_0 are the inside and outside radius of the hollow fiber, P_m is membrane permeability coefficient relating to the distribution ratio (D) in Eq. (4) and can be defined in terms of the mass transfer coefficient in liquid membrane (k_m) as

$$P_m = Dk_m \tag{6}$$

Three mass transfer resistances in Eq. (5) are in accordance with three steps of the transport mechanisms. The first term represents the resistance when the feed solution flows through the hollow fiber lumen. The second resistance relates to the diffusion of the complex species through liquid membrane that is immobilized in the porous wall of the hollow fibers. The third resistance is due to the stripping solution and liquid membrane interface outside the hollow fibers. The mass transfer resistance at the stripping interface can be disregarded as the mass transfer coefficient in the stripping phase (k_s) is much higher than that in the feed phase (k_i) according to the following assumptions (Uedee et al., 2008):

1. The film layer at feed interface is much thicker than that at the stripping interface. This is because of a combination of a large amount of target species in feed and co ions in buffer solution at the feed interface while at the stripping interface, a few target species and stripping ions exist. In Eqs. (7) and (8), thick feed interfacial film (l_{if}) makes the mass transfer coefficient in feed phase (k_i) much lower than that in the stripping phase (k_s).

Feed-mass transfer coefficient $$k_i = \frac{D}{l_{if}} \tag{7}$$

Stripping-mass transfer coefficient $$k_s = \frac{D}{l_{is}} \tag{8}$$

2. The difference in the concentration of target species in feed phase (C_f) and the concentration of feed at feed-membrane interface (C_f*) is higher than the difference in

the concentration of stripping phase at membrane-stripping interface (C_s*) and the concentration of target species in stripping phase (C_s). At equal flux by Eq. (9), k_i is, therefore, much lower than k_s.

$$J = k_i(C_f - C_f^*) = k_s(C_s^* - C_s) \tag{9}$$

3. From Eq. (5), we can ignore the third mass transfer resistance. This is attributed to the direct contact of stripping ions with the liquid membrane resulting in rapid dissolution and high mass transfer coefficient of the stripping phase.

P_m in Eq. (5) can be substituted in terms of the distribution ratio (D) and the mass transfer coefficient in liquid membrane (k_m) in Eq. (6) as

$$\frac{1}{P} = \frac{1}{k_i} + \frac{r_i}{r_{lm}}\frac{1}{Dk_m} \tag{10}$$

In addition, from the permeability coefficient (P) by Danesi (Danesi, 1984):

$$-V_f \ln\left(\frac{C_f}{C_{f,0}}\right) = AP\frac{\beta}{\beta+1}t \tag{11}$$

where

$$\beta = \frac{Q_f}{PLN\varepsilon\pi r_i} \tag{12}$$

We can calculate the permeability coefficient from the slope of the plot between $-V_f \ln\left(\frac{C_f}{C_{f,0}}\right)$ against t.

Table 3 shows some applications of HFSLM and their mass transfer related.

4. HFSLM in engineering applications

Compared to conventional separations, membrane separations are attractive for the processing of food, bioproducts, etc where the processed products are sensitive to temperature since most membrane separations involve no chemical, biological, or thermal changes (or moderate temperature changes) of the target component during processing. For environmental-related applications, membrane separation has developed into an important technology for separating volatile organic compounds (VOCs), e.g., acetaldehyde, BTXs, ethylene oxide, trichloroethylene, etc and other gaseous air pollutants from gas streams (Schnelle and Brown, 2002; Simmon et al., 1994).

The following works show the applications of using HFSLM and the role of facilitated transport in separation of praseodymium from nitrate solution of mixed rare earths $RE(NO_3)_3$ (Wannachod et al., 2011), separation of uranium from trisodium phosphate from monazite ores processing (Lothongkum et al., 2009) supplied by the Rare Earth Research and Development Center, Office of Atoms for Peace, Bangkok, Thailand, and separation of Cu(II) by LIX84I.

4.1 Effective extraction and recovery of praseodymium from mixed rare earths

Praseodymium (Pr), one of the elements recovered from mixed rare earths (REs), is very useful, e.g., as a composition in mischmetall alloy and a core material for carbon arcs in film

Authors	Species	Extractants	Solvents	P (10^5 m/s)	D 10^3 (-)	k_i (10^3 m/s)	k_m (10^5 m/s)	Results
(Ortiz et al., 1996)	Cr(VI) in synthetic water	Aliquat 336	Kerosene	-	-	-	0.0022	The model results agree well with the experiment
(Marcese & Camderros, 2004)	Cd(II) in synthetic water	D2EHPA	Kerosene	0.1-0.26	-	-	-	The model results reasonably agree with the experiment
(Huang et al., 2008)	D-Phe and L-Phe in synthetic water	Cu(II) N-decyl-(L)-hydroxy proline	Hexanol/ Decane	-	-	$4.5x10^{-5}$	Rapid diffusion (very low k_m)	The model results agree well with the experiment
(Prapasawat et al., 2008)	As(III), As(V) in synthetic water	Cyanex 923	Toluene	-	-	0.072 0.107	34.5 17.9	The mass transfer in the film layer between the feed phase and liquid membrane is the rate controlling step
(Wannachod et al., 2011)	Pr(III) from $RE(NO_3)_3$ solution	Cyanex 272	Kerosene	27-77.5	4.6-15.5	0.103	7.88	The mass transfer in the membrane is the rate controlling step
(Lothongkum et al., 2011)	As from produced water	Aliquat 336 Bromo-PADAP, Cyanex 471, Cyanex 923	Toluene	5.5-11.5	0.63-1.5	0.392	0.102	The mass transfer in the membrane is the rate controlling step
	Hg from produced water	Aliquat 336 Bromo-PADAP, Cyanex 471, Cyanex 923	Toluene	34-53.1	4.5-8.7	22.1	0.013	The mass transfer in the membrane is the rate controlling step

Table 3. Applications of HFSLM and mass transfer related

studio light and searchlights. Praseodymium produces brilliant colors in glasses and ceramics. The composition of yellow didymium glass for welding goggles derived from infrared-heat absorbed praseodymium. Currently, the selective separation and concentration of mixed rare earths are in great demand owing to their unique physical and chemical properties for advanced materials of high-technology devices. Several separation techniques are in limitations, for example, fractionation and ion exchange of REs are time consuming. Solvent extraction requires a large number of stages in series of the mixer settlers to obtain high-purity REs. Due to many advantages of HFSLM and our past successful separations of cerium(IV), trivalent and tetravalent lanthanide ions, etc by HFSLM (Pancharoen et al., 2005; Patthaveekongka et al., 2006; Ramakul et al., 2004, 2005, 2007), we again approached the HFSLM system for extraction and recovery of praseodymium from mixed rare earth solution. The system operation is shown in Fig. 3. Of three extractants, Cyanex 272 in kerosene found to be more suitable for high praseodymium recovery than Aliquat 336 and Cyanex 301 as shown in Fig. 4. Higher extraction of 92% and recovery of 78% were attained by 6-cycle continuous operation about 300 min as shown in Fig. 6.

In this work, the extraction equilibrium constant (K_{ex}) obtaining from Fig. 7 was 1.98×10^{-1} ($L \cdot mol^{-1}$)[4]. The distribution ratio (D) at Cyanex 272 concentration of 1.0-10 (%v/v) were calculated and found to be increased with the extractant concentration and agreed with Pancharoen et al., 2010. We obtained the permeability coefficients for praseodymium at Cyanex 272 concentration of 1.0-10 (%v/v) from Fig.8. The mass transfer coefficients in feed phase (k_i) and in liquid membrane (k_m) of 0.0103 and 0.788 cm s^{-1}, respectively were

obtained from Fig.9. Because k_m is much higher than k_i, it indicates that the diffusion of praseodymium ions through the film layer between the feed phase and liquid membrane is the rate-controlling step.

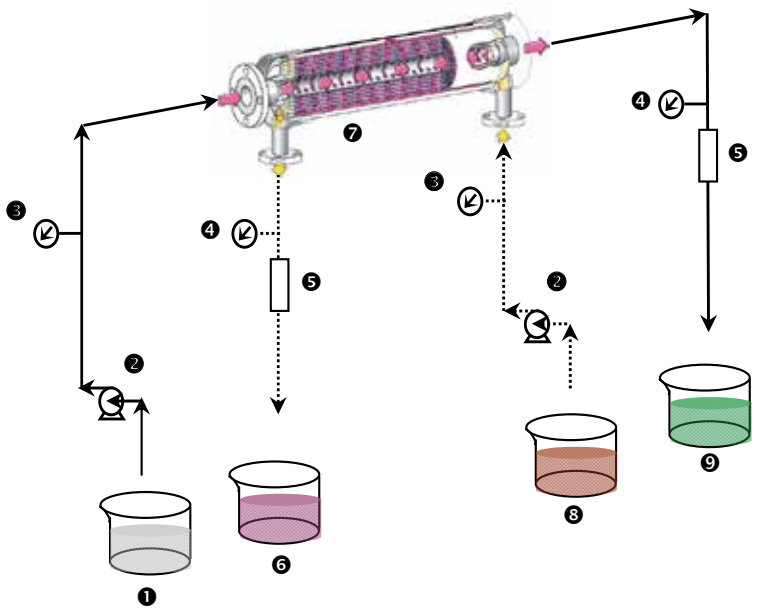

Fig. 3. Schematic counter-current flow diagram for one-through-mode operation of the HFSLM system (❶ inlet feed solution, ❷ gear pumps, ❸ inlet pressure gauges, ❹ outlet pressure gauges, ❺ outlet flow meters, ❻ outlet stripping solution, ❼ the hollow fiber module, ❽ inlet stripping reservoir, and ❾ outlet feed solution)

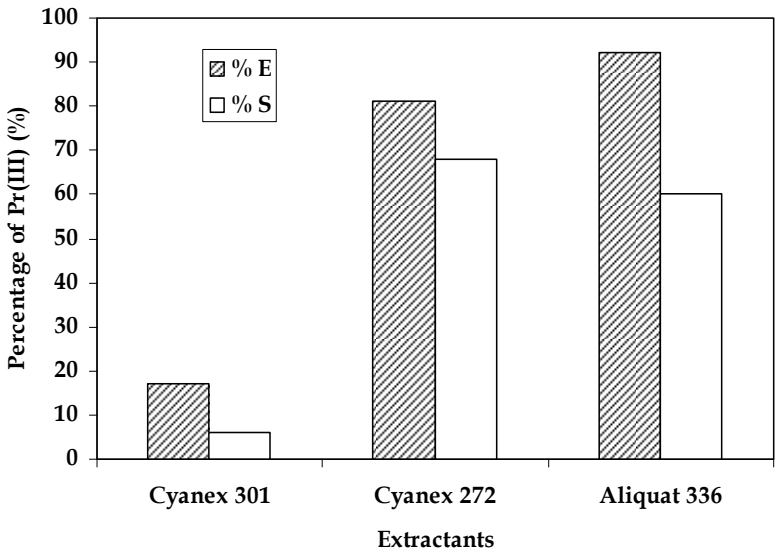

Fig. 4. The percentages of the Pr(III) extraction and stripping from one-through-mode operation

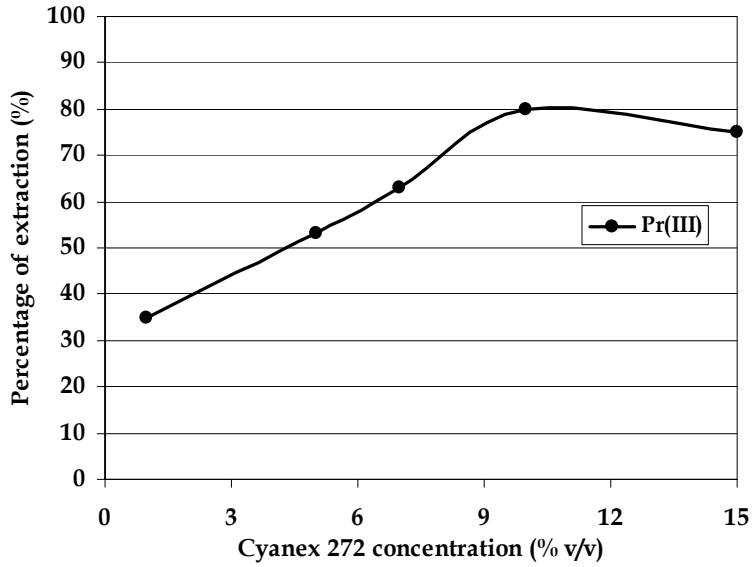

Fig. 5. The percentage of Pr(III) extraction against Cyanex 272 concentration

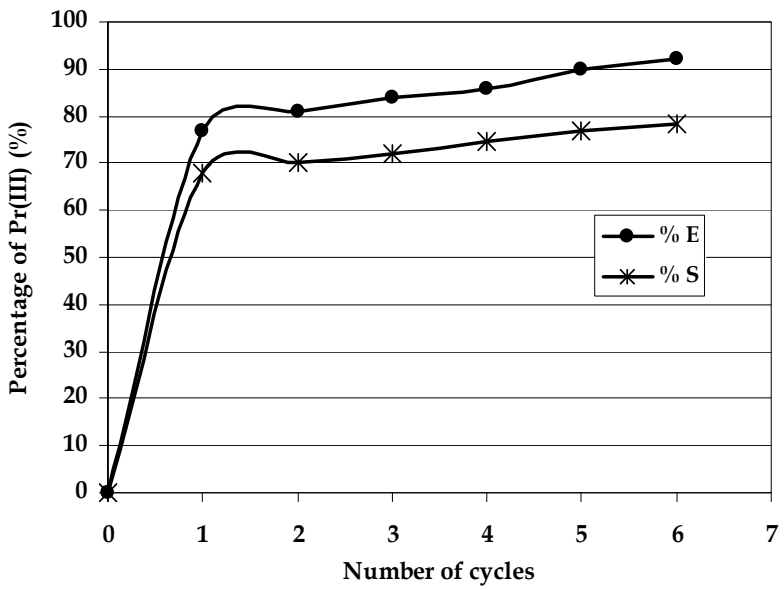

Fig. 6. The percentages of Pr(III) extraction by 10 (%v/v) Cyanex 272 and stripping against the number of separation cycles

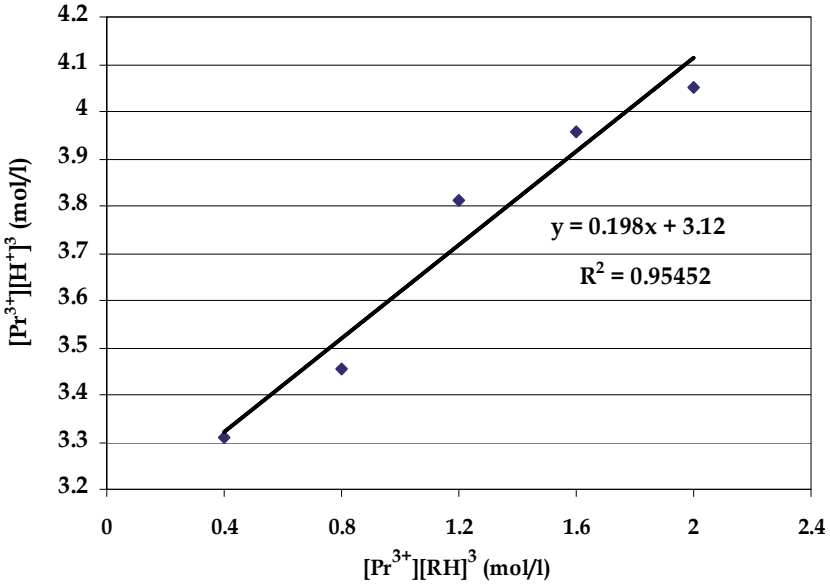

Fig. 7. Extraction of Pr(III) by Cyanex 272 as a function of equilibrium $[Pr^{3+}][RH]^3$

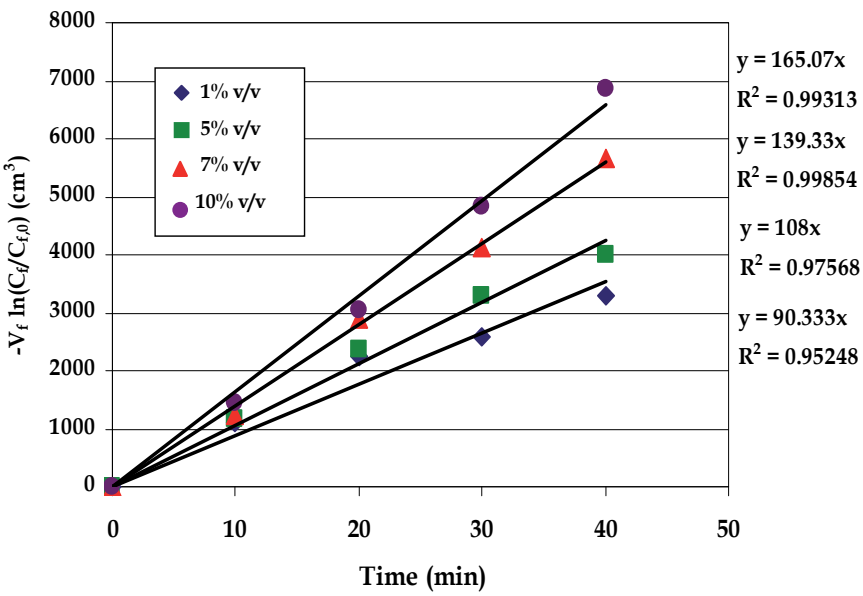

Fig. 8. Plot of $-V_f \cdot \ln(C_f / C_{f,0})$ of Pr(III) at different Cyanex 272 concentrations against time

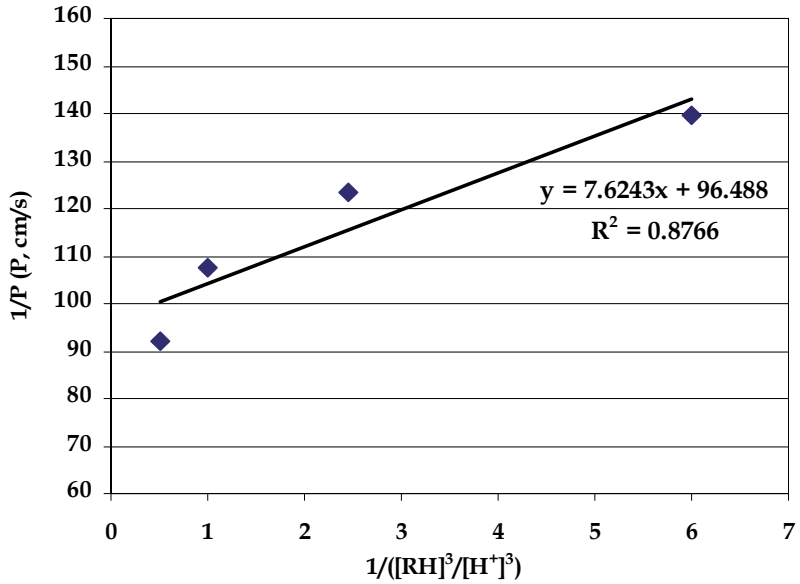

Fig. 9. Plot of 1/P as a function of $1/([RH]^3 / [H^+]^3)$

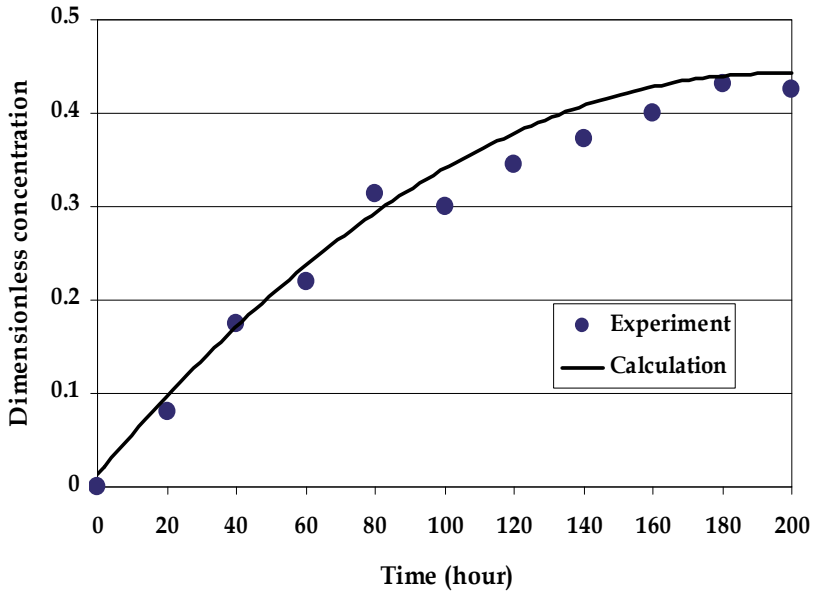

Fig. 10. The model prediction of dimensionless recovery concentration of Pr(III) and experimental results

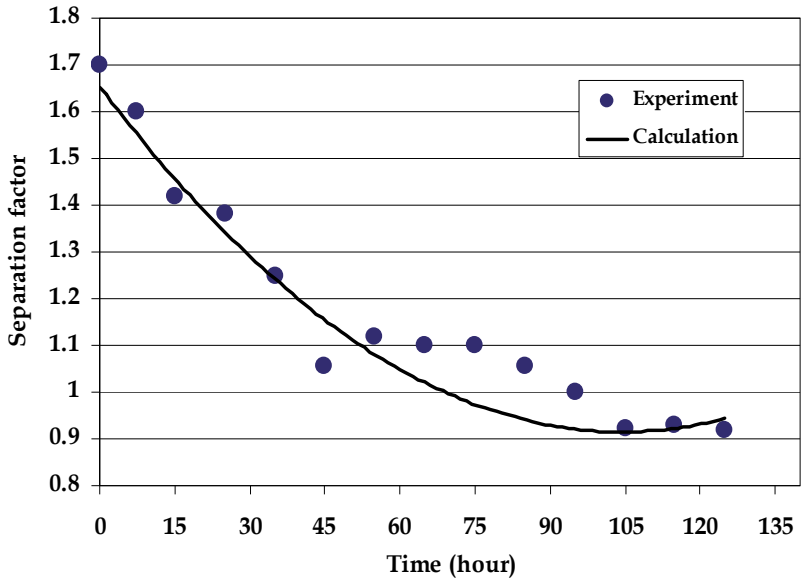

Fig. 11. The model prediction of separation factor and experimental results

From Figs. 10 and 11, we can see that the predictions of dimensionless concentration in stripping phase and the separation factor agreed with the experimental results.

4.2 Enhancement of uranium separation from trisodium phosphate

Two grades of trisodium phosphate, food and technical grades, are extensively used for various purposes. Food grade is used as an additive in cheese processing. Technical grade is used for many applications, e.g., in boiler-water treatment, testing of steel parts after pickling, industrial detergents such as degreasers for steels, and heavy-duty domestic cleaners. As trisodium phosphate is a by-product from the separation of desired rare earths in monazite processing, it is contaminated by some amount of uranium which is often found with the monazite. Uranium is a carcinogen on the other hand it is useful as a radioactive element in the front and back ends of the nuclear fuel cycle, therefore the separation method to recover uranium from trisodium phosphate is necessary. For 45-ppm-uranium-contaminated trisodium phosphate solution, HFSLM is likely a favorable method as it can simultaneously extract the ions of very low concentration and can recover them in one single operation. Undoubtedly, the facilitated transport across the HFSLM accelerates the extraction and recovery of uranium.

Eq. 13 shows that uranium species form complex species with Aliquat 336 (tri-octyl methyl ammonium chloride: $CH_3R_3N^+Cl^-$) in modified leaching and extraction of uranium from monazite (El-Nadi et al., 2005).

$$[UO_2(CO_3)_3]^{4-} + \overline{2(NR_4)^+Cl^-} \rightleftharpoons \overline{(NR_4)_2[UO_2(CO_3)_2^{2-}]} + 2Cl^- + CO_3^{2-} \quad (13)$$

$[UO_2(CO_3)_3]^{4-}$ represents the uranium species, $\overline{2(NR_4)^+Cl^-}$ represents general form of Aliquat 336 in liquid membrane and $\overline{(NR_4)_2[UO_2(CO_3)_2^{2-}]}$ represents the complex species of Aliquat 336 and uranium species in liquid membrane.

Fig. 12 shows percentage of uranium extraction by different extractants. We can see that D2EHPA (di (2-ethylhexyl) phosphoric acid) obtained high percentage of extraction, however its extractability abruptly decreased with time. Thus, Aliquat 336, of which its extractability followed D2EHPA and decreased slightly with time, was considered the most appropriate extractant for uranium. It can be attributed that uranium ions in trisodium phosphate solution are in $[UO_2(CO_3)_3]^{4-}$ and Aliquat 336, a basic extractant, is good for cations while D2EHPA, an acidic extractant, is good for anions form of UO_2^{2+}. The percentage of uranium extraction at different concentrations of Aliquat 336 is shown in Fig. 13.

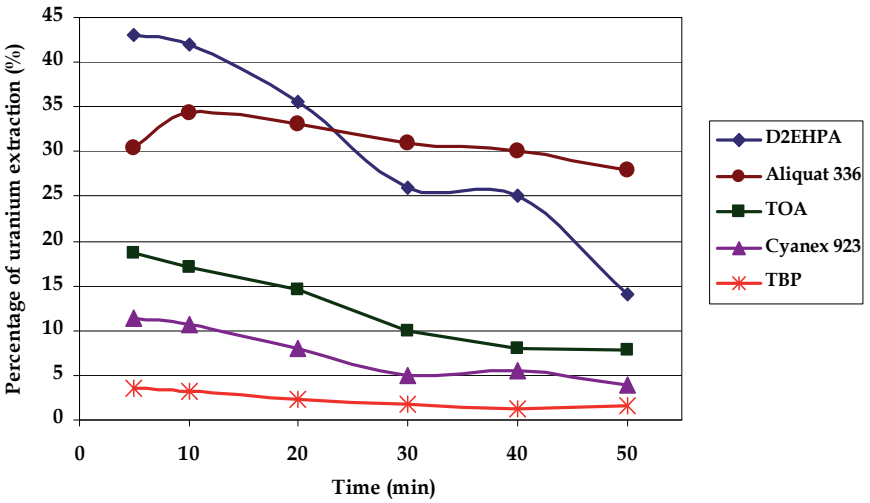

Fig. 12. Percentage of uranium extraction against time using different extractants of 0.1 M, stripping solution [HNO_3] of 0.5 M, equal Q_{feed} and $Q_{stripping\ solution}$ of 100 ml/min

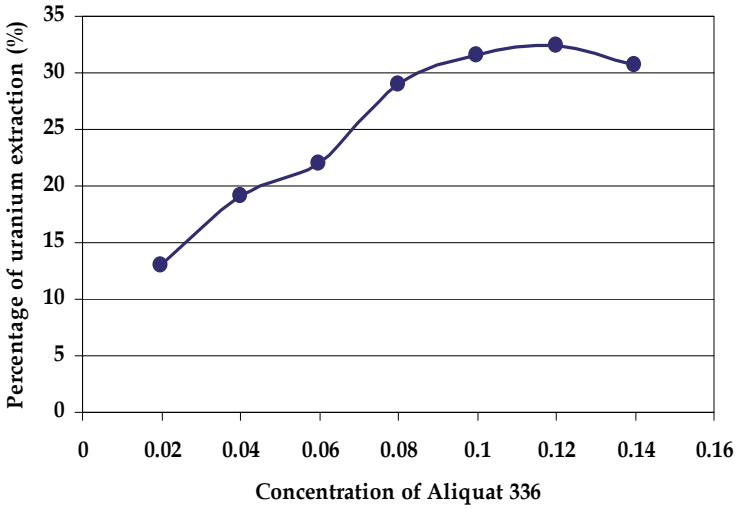

Fig. 13. Percentage of uranium extraction at different concentrations of Aliquat 336, stripping solution [HNO_3] of 0.5 M, equal Q_{feed} and $Q_{stripping\ solution}$ of 100 ml/min

To enhance the extraction of uranium, a mixture of Aliquat 336 and TBP (tributylphosphate) showed synergistic effect as can be seen in Fig. 14. The percentage of uranium extraction using the synergistic extractant was higher than that by a single extractant of Aliquat 336 and TBP. The highest extraction of uranium from trisodium phosphate solution was obtained by a synergistic extractant of 0.1 M Aliquat 336 and 0.06 M TBP. (The extraction increased with the concentration of TBP upto 0.06 M.)

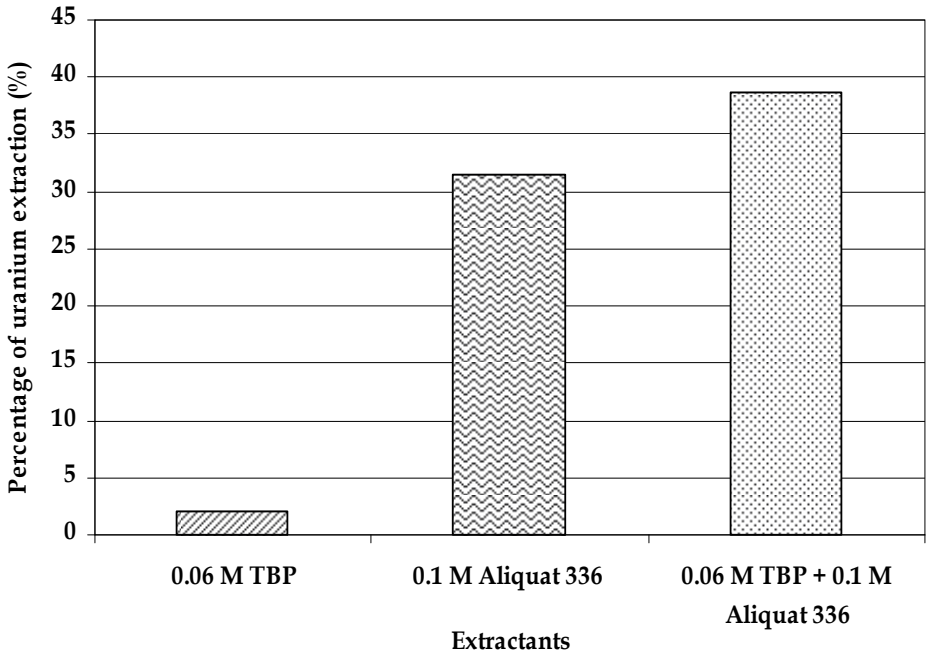

Fig. 14. Percentage of uranium extraction against single and synergistic extractants: stripping solution [HNO_3] of 0.5 M, equal Q_{feed} and $Q_{stripping\ solution}$ of 100 ml/min

The reaction by the synergistic extractant of Aliquat 336 and TBP is proposed in this work.

$$[UO_2(CO_3)_3]^{4-} + \overline{2(NR_4)^+Cl^-} + x\overline{TBP} \rightleftharpoons \overline{(NR_4)_2[UO_2(CO_3)_2^{2-}]\cdot TBP_x} + 2Cl^- + CO_3^{2-} \qquad (14)$$

From Fig. 15, by using the synergistic extractant of 0.1 M Aliquat 336 mixed with 0.06 M TBP, the stripping solution of 0.5 M HNO_3 with equal flow rates of feed and stripping solutions of 100 ml/min, the percentages of extraction and stripping reached 99% (equivalent to the remaining uranium ions in trisodium phosphate solution of 0.22 ppm) and 53%, respectively by 7-cycle separation in 350 min. The percentage of uranium stripping was much lower than the percentage of extraction presuming that uranium ions accumulated in liquid membrane phase of the hollow fiber module. This is a limitation of the HFSLM applications. For higher stripping, a regular membrane service is needed. In conclusion, the remaining amount of uranium ions in trisodium phosphate solution was 0.22 ppm, which stayed within the standard value 3-ppm uranium of the technical-grade trisodium phosphate. Further study on a better stripping solution for uranium ions is recommended.

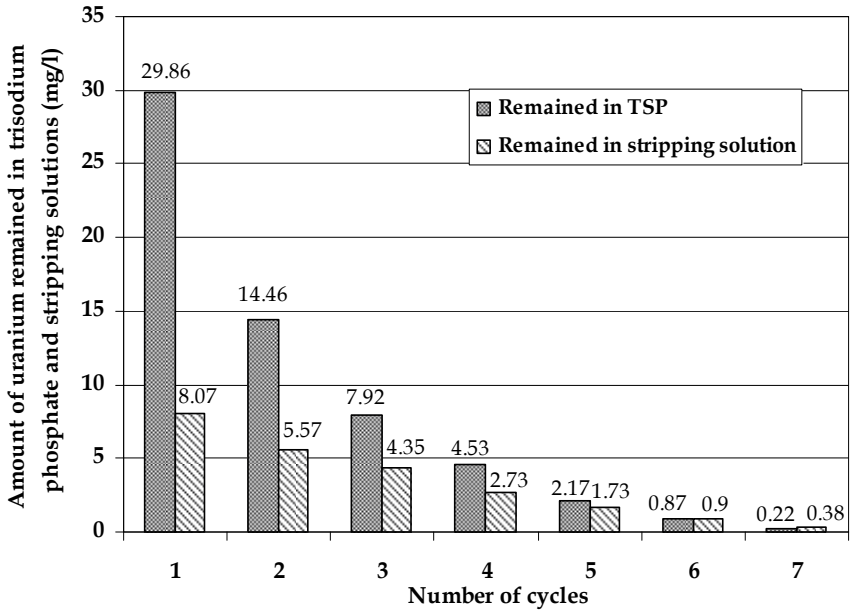

Fig. 15. Amount of uranium ions remained in trisodium phosphate and stripping solutions of one-module operation against the number of separation cycles by 0.1 M Aliquat 336 mixed with 0.06 M TBP, stripping solution [HNO_3] of 0.5 M, equal Q_{feed} and $Q_{stripping\ solution}$ of 100 ml/min

4.3 Reaction flux model for extraction of Cu(II) with LIX84I

In regard to apply the hollow fiber contactor for industrial scale, the reliable mathematical models are required. The model can provide a guideline of mass transfer describing the transport mechanisms of the target species through liquid membrane, and predict the extraction efficiency. Normally, different types of the extractants, their concentration and transport mechanisms (diffusion and facilitated transport or carrier-mediated transport) play important roles on the extraction efficiency. The facilitated transport mechanism relates to the reaction flux of chemical reaction between the target species and the selected single extractant or synergistic extractant to form complex species (Bringas et al., 2009; Kittisupakorn et al., 2007; Ortiz et al., 1996). In principle, the metal-ion transport through the membrane phase occurs when the metal ions react with the selected extractant at the interface between feed phase or aqueous phase and liquid membrane phase, consequently the generated complex species diffuse through the membrane phase. In this work, we developed a mathematical model describing the effect of reaction flux on facilitated transport mechanism of copper ions through the HFSLM system because copper is used extensively in many manufacturing processes, for example, electroplating, electronic industry, hydrometallurgy, etc. Therefore, copper ions, which are toxic and non-biodegradable, may contaminate wastewaters and cause environmental problems and health effects if no appropriate treatment is taken (Lin & Juang, 2001; Ren et al., 2007). The model was verified with the experimental extraction of copper ions in ppm level using LIX84I dissolved in kerosene by continuous counter-current flow through a single-hollow

fiber module. It is known that LIX-series compounds are the most selective extractants of high selectivity and widely used for copper ions (Breembroek et al., 1998; Campderros et al., 1998; Lin & Juang, 2001; Parhi & Sarangi, 2008; Sengupta, et al., 2007). The schematic flow diagram of the separation via HFSLM is shown in Fig. 16. The transport mechanism of copper ion in micro porous hollow fiber is presented schematically in Fig. 17. The chemical reaction at the interface between feed phase and liquid membrane phase takes place when the extractant $(\overline{RH})$ reacts with copper ions in feed (Eq. (15)).

$$Cu^{2+}_{(aq)} + 2\overline{RH}_{(org)} \rightleftharpoons \overline{CuR}_{2(org)} + 2H^{+}_{(aq)} \tag{15}$$

$(\overline{RH})$ is LIX84I in liquid membrane phase.
$\overline{CuR_2}$ is the complex species of copper ion in liquid membrane phase.

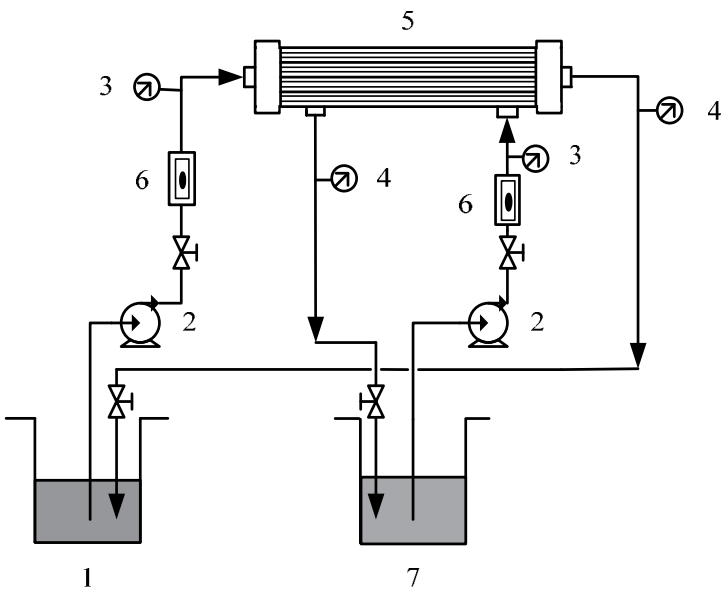

Fig. 16. Schematic diagram for counter-current flow of Cu(II) separation by a single-hollow fiber module (1 = feed reservoir, 2 = gear pumps, 3 = inlet pressure gauges, 4 = outlet pressure gauges, 5 = hollow fiber module, 6 = flow meters and 7 = stripping reservoir

Eq. (15) can be simplified as follows:

$$aA + bB \xrightarrow{k_f} cC + dD \tag{16}$$

where A is copper ion, B is LIX84I, C is complex species of copper ion and LIX84I, D is hydrogen ion, and a, b, c, d are stoichiometric coefficients of A, B, C and D, respectively.
The reaction rate (r_A) is

$$-r_A = k_f C^{n}_{A\ (x,t)} \tag{17}$$

k_f is the forward reaction rate constant and n is the order of reaction.

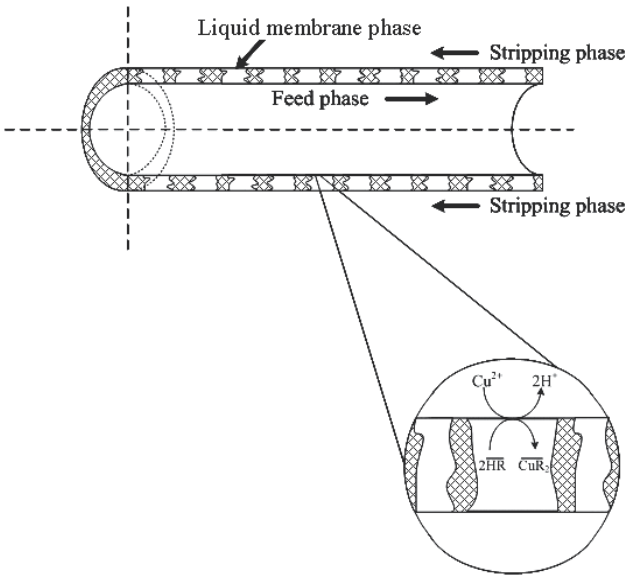

Fig. 17. Schematic transport mechanism of copper ion in liquid membrane phase

The transport of copper ions through a cylindrical hollow fiber is considered in the axial direction or bulk flow direction and radial direction. In order to develop the model, the following assumptions are made:

1. The inside and outside diameters of a hollow fiber are very small. Thus, the membrane thickness is very thin; therefore the radial concentration profile of copper ions is constant.
2. Only the complex species occurring from the reaction, not copper ions, diffuse through liquid membrane phase.
3. The extraction reaction is irreversible that means only the forward reaction of Eq. (15) is considered.
4. Due to very thin membrane thickness, it is presumed that the reaction occurs only in the axial direction of the hollow fibers. Mass flux of copper ions exists in the axial direction.

The conservation of mass for copper ion transport in the hollow fiber is considered as shown in Fig. 18.

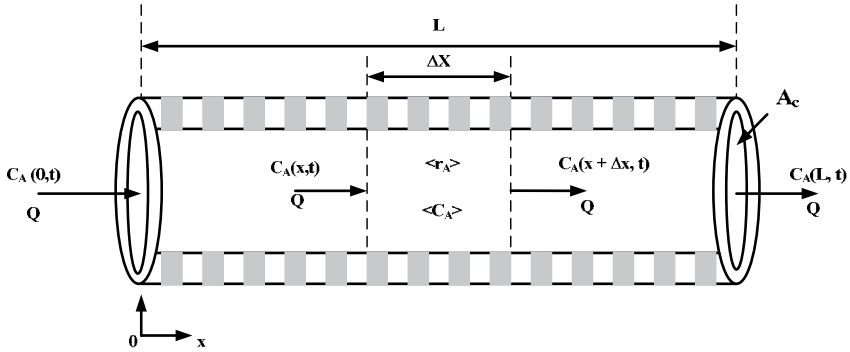

Fig. 18. Transport of copper ions in the hollow fiber

At a small segment Δx, the conservation of mass can be described below:

$$QC_{A\ (x,t)} - QC_{A\ (x+\Delta x,t)} - \langle r_A \rangle \Delta x A_c = \frac{d\langle C_A \rangle}{dt} \Delta x A_c \tag{18}$$

$\langle r_A \rangle$ and $\langle C_A \rangle$ are the average values of the reaction rate and the concentration of copper ions, respectively

Dividing Eq. (18) by $\Delta x A_c$ and taking a limit $\Delta x \rightarrow 0$, obtains

$$-\frac{Q}{A_c}\frac{\partial C_{A\ (x,t)}}{\partial x} - r_{A\ (x,t)} = \frac{\partial C_{A\ (x,t)}}{\partial t} \tag{19}$$

At the initial condition (t = 0), the conservation of mass in Eq. (19) is considered with regard to 3 cases of the reaction orders as follows:

Case 1: n = 0

$$C_{A\ (L,0)} = C_{A\ (0,0)} + \frac{k_f A_c}{Q} L \tag{20}$$

Case 2: n = 1

$$C_{A\ (L,0)} = C_{A\ (0,0)} e^{\frac{k_f A_c}{Q} L} \tag{21}$$

Case 3: n ≠ 0, 1

$$C_{A\ (L,0)} = \left[C_{A\ (0,0)}^{1-n} + \frac{(1-n) k_f A_c}{Q} L \right]^{\frac{1}{1-n}} \tag{22}$$

At time t (t ≠ 0), the conservation of mass in Eq. (19) in the differential form is

$$-\frac{Q}{A_c}\frac{\partial \overline{C}_{A\ (x,t)}}{\partial x} - \bar{r}_{A\ (x,t)} = \frac{\partial \overline{C}_{A\ (x,t)}}{\partial t} \tag{23}$$

where $\overline{C}_{A\ (x,t)} = C_{A\ (x,t)} - C_{A\ (x,0)}$

$$\bar{r}_{A\ (x,t)} = r_{A\ (x,t)} - r_{A\ (x,0)} = -\left(\frac{k_f n}{\lambda - \gamma x} \right) \overline{C}_{A\ (x,t)}$$

Linearize Eq. (23) by taking Laplace transforms and considering 3 cases of reaction orders, we obtain:

Case 1: n = 0

$$\overline{C}_{A\ (L,t)} = \overline{C}_{A\ (0,t-\tau_0)} + k_f (t - \tau_0) - k_f t \tag{24}$$

Case 2: n = 1

$$\overline{C}_{A\ (L,t)} = e^{\alpha} \overline{C}_{A\ (0,t-\tau_0)} \tag{25}$$

Case 3: $n \neq 0, 1$

$$\overline{C}_{A\ (L,t)} = e^{\beta}\overline{C}_{A\ (0,t-\tau_0)} \tag{26}$$

Let $\tau_0 = \frac{A_c L}{Q}$, $\alpha = \frac{k_f A_c L}{Q}$, $\beta = \left(\frac{A_c k_f n}{Q\gamma}\right)\ln\left(\frac{\gamma L + \lambda}{\lambda}\right)$, $\gamma = \frac{(1-n)k_f A_c}{Q}$ and $\lambda = C_{A(0,0)}^{1-n}$

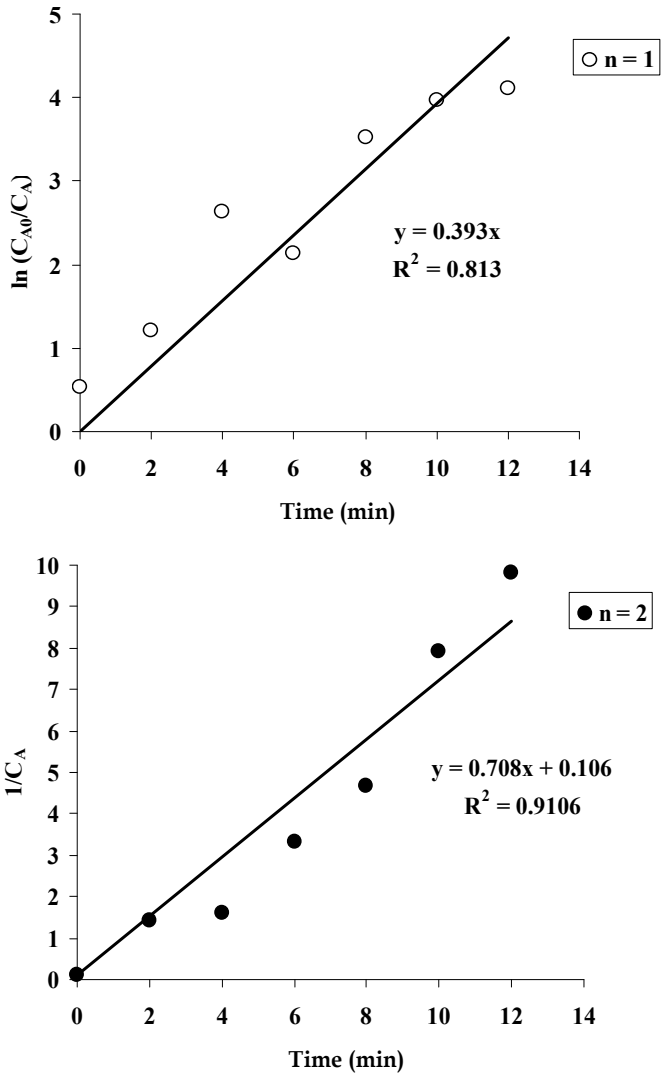

Fig. 19. The integral concentrations of Cu(II) and separation time, ○ for n = 1 and ● for n = 2

The reaction rate constant of the second order is taken into consideration for a better curve fitting between the model and the experimental results, as shown in Table 4 by higher R-squared and less deviation.

The optimum separation time and separation cycles of the extraction can be estimated. The model was verified with the experimental extraction results and other literature.
Fig. 19 is a plot of the integral concentrations of Cu(II) against time to determine the reaction order (n) and the forward reaction rate constant (k_f). The rate of diffusion and/or rates of chemical changes may control the kinetics of transport through liquid membrane depending on transport mechanisms (diffusion or facilitated). The reaction rate constants of first-order (n = 1) and second-order (n = 2) are 0.393 min^{-1} and 0.708 L/mg·min, respectively.

Reaction order (n)	Reaction rate constant (k_f)	R-squared	% Deviation
First-order	0.393 min^{-1}	0.813	61.233
Second-order	0.708 L/mg·min	0.911	1.453

Table 4. R-squared and percentages of deviation for first-order and second-order reactions

The percentage of copper ion extraction is calculated by Eq. (27). The percentage of deviation is calculated by Eq. (28).

$$\% \text{ extraction} = \frac{C_{f,in} - C_{f,out}}{C_{f,in}} \times 100 \tag{27}$$

$$\% \text{ deviation} = \frac{\sum_{i=1}^{j} \left(\frac{C_{Expt.} - C_{Theo.}}{C_{Expt.}} \right)_i}{j} \times 100 \tag{28}$$

The optimum separation time for the prediction of separation cycles can be estimated by the model based on the optimum conditions from the plot of percentage of extraction as a function of initial concentration of the target species in feed and also feed flow rate.
In this work, at the legislation of Cu(II) concentration in waste stream of 2 mg/L, the calculated separation time is 10 min for about 15-continuous cycles. The percentage of extraction calculated from this reaction flux model is much higher than the results from other works which applied different extractants and transport mechanisms. Types of extractants and their concentrations are significant to the separation of metal ions. For example, a hard base extractant can extract both dissociated and undissociated forms in a basic or weak acidic condition but dissociated forms are high favorable. While a neutral extractant normally reacts with undissociated forms, but in an acidic condition it can react with dissociated forms. It is noteworthy to be aware that not only types of the extractants (single or synergistic), in this case LIX84I for Cu(II), but also the transport mechanism, e.g., facilitated transport mechanism attributes to the extraction efficiency. The model results are in good agreement with the experimental data at the average percentage of deviation of 2%.

5. Conclusions

Facilitated transport of the solutes or target species benefits the separation process by liquid membrane with a non-equilibrium mass transfer and uphill effect. It is more drastic chemical changes of the target species with the presence of a suitable extractant or carrier (sometimes by synergistic extractant) in liquid membrane to form new complex species

(dissociated and undissociated forms) to diffuse through the liquid membrane phase. As a result, the efficiency and selectivity of the transport across liquid membrane markedly enhance. Factors that affect the facilitated transport and diffusion through the membrane are, for example, extractant types and properties (e.g., proton donors, electron donors), solvent characteristics, stripping types and properties, life time of membrane due to fouling, operating temperature. Many outstanding advantages of the HFSLM make it the most efficient type of membrane separation for several applications. It is worth to note that the HFSLM can simultaneously extract the target species of very low concentration and recover them in one single operation. For favorable ions (e.g., precious metals), high percentage of recovery is desirable.

Despite many advantages, at present the HFSLM is not often used in a large-scale industry because the major drawbacks of hollow fibers are not only fouling but also mechanical stability of the support. However, in regard to apply the HFSLM in industrial scale, the reliable mathematical model is required as the model can foretell the effect of mass transfer as the functions of operating parameters, membrane properties and feed properties on the separation efficiency. However, due to the limitations of applications or unclear phenomena around the membrane surface, no model so far is fully satisfactory and universally applicable. Even though, the model can help to understand and predict the operation as well as the separation performance. In case the separation of metal ions by the HFSLM, as there are several parameters involved, e.g., types of metal ions, extractants and stripping solutions, and the transport mechanisms, therefore the model probably has implications for other metals but it may need some modifications corresponding to such parameters.

6. Acknowledgments

The authors are highly grateful to the Royal Golden Jubilee Ph.D. Program (Grant No. PHD50K0329) under the Thailand Research Fund, the Rare Earth Research and Development Center of the Office of Atoms for Peace (Thailand), Thai Oil Public Co., Ltd., the Separation Laboratory, Department of Chemical Engineering, Chulalongkorn University, Bangkok, Thailand. Kind contributions by our research group are deeply acknowledged.

7. Nomenclature

A	Membrane area (cm^2)
A_C	Cross-sectional area of hollow fiber (cm^2)
BLM	Bulk liquid membrane
BTXs	Benzene, toluene, xylenes
C_A	Concentration of copper ions
$<C_A>$	Average value of the concentration of copper ions
C_f	Concentration of target species in feed phase (moles per unit volume)
C_{f^*}	Concentration of target species at feed-membrane interface (moles per unit volume)
$C_{f,0}$	Initial concentration of target species in feed phase (moles per unit volume)
$C_{f,in}$, $C_{f,out}$	Concentration of target species at feed inlet and feed outlet (moles per unit volume)

C_s	Concentration of target species in the stripping solution (moles per unit volume)
C_{s^*}	Concentration of target species at membrane-stripping interface (moles per unit volume)
C(0,t)	Concentration of target species at liquid membrane thickness = 0 and any time (moles per unit volume)
$C(x_0,t)$	Concentration of target species at liquid membrane thickness of x_0 and any time (moles per unit volume)
D	Distribution ratio
ELM	Emulsion liquid membrane
H^+	Hydrogen ion representing pH gradient
HFSLM	Hollow fiber supported liquid membrane
ILM	Immobilized liquid membrane
J	Flux (mol/cm^2 s)
K_{ex}	Extraction equilibrium constant
k_f	Forward reaction rate constant (cm^3/mg·min)
k_i	Feed- or aqueous-phase mass transfer coefficient or mass transfer coefficient in feed phase
k_m	Organic-phase mass transfer coefficient or mass transfer coefficient in liquid membrane phase
k_s	Stripping-phase mass transfer coefficient or mass transfer coefficient in stripping phase
L	Length of the hollow fiber (cm)
LMs	Liquid membranes
l_{if}	Feed interfacial film thickness
l_{is}	Stripping interfacial film thickness
$\overline{M}$	Target species
$\overline{MR_n}$	Complex species in the membrane phase
N	Number of hollow fibers in the module
n	Order of the reaction
P	Permeability coefficient
P_m	Membrane permeability coefficient
Q	Volumetric flow rate (cm^3/min)
Q_f, Q_{feed}	Volumetric flow rate of feed solution (cm^3/s)
Q_s, $Q_{stripping\ solution}$	Volumetric flow rate of stripping solution (cm^3/s)
r_A	Reaction rate
$\langle r_A \rangle$	Average value of the reaction rate of copper ions
$\overline{RH}$	General form of the extractant
r_i	Inside radius of the hollow fiber (cm)
r_{lm}	Log-mean radius of the hollow fiber
r_o	Outside radius of the hollow fiber (cm)
SLMs	Supported liquid membranes
t	Time (min)
V_f	Volume of the feed phase (cm^3)
VOCs	Volatile organic compounds
x	Spatial coordinate, direction of fiber axis

x_0	Membrane thickness (cm)

Greek letters

ε	Porosity of the hollow fibers (%)
α	Parameter in Eq. (25)
β	Parameter in Eqs. (11-12) and (26)
γ, λ	Parameters for β in Eq. (26)
τ_0	Parameter in Eqs. (24)-(26)

Symbol

< >	average value
Δ	difference between exit and entry values

Subscripts

aq	In aqueous phase
f	At feed phase
f,in and f,out	At feed inlet and feed outlet
h	Hollow fiber
m	At liquid membrane phase
org	In organic phase (liquid membrane phase)
s	At stripping phase
Expt.	Experimental values
Theo.	Modeled or theoretical values

8. References

Badami, B.V. (2008). Concept of green chemistry redesigning organic synthesis. *Resonance*, Vol. 13, No. 11, (Nov. 2008), pp. 1041-1048.

Baker, R.W. (2007). Membrane Technology *in* Seidl, A. (ed.), *Kirk-Othmer Chemical Technology and the Environment,* John Wiley & Sons Inc., ISBN 978-0-470-10540-5, New Jersey, USA., pp. 4-8, 419.

Baker, R.W. & Blume, I. (1990). Coupled Transport Membranes, *in* Porter, M.C. (ed.), *Handbook of Industrial Membrane Technology,* Noyes Publication, ISBN 0-8155-1205-8, Park Ridge, N.J. USA., pp. 511-588.

Breembroek, G.R.M., Straalen, A., Witkamp, G.J. & Rosmalen, G.M. (1998). Extraction of cadmium and copper using hollow fiber supported liquid membranes. *J. Membr. Sci.*, Vol.146, No.2, (Aug. 1988), pp. 185-195.

Bringas, E., Roman, M.F.S., Irabien, J., & Ortiz, I. (2009). An overview of the mathematical modeling of liquid membrane separation processes in hollow fiber contactors. *J. Chem. Technol. Biotechnol.*, Vo.84, (May 2009), pp. 1583-1614.

Campderros, M.E., Acosta, A. & Marchese J. (1998). Selective separation of copper with LIX 864 in a hollow fiber module. *Talanta*, Vol.47, No.1, (Sept. 1988), pp. 19-24.

Cui, Z.F., Jiang, Y. & Field, R.W. (2010). Fundamentals of Pressure-Driven Membrane Separation Processes, *in* Cui, Z.F. & Muralidhara, H.S. (eds.), *Membrane Technology: A Practical Guide to Membrane Technology and Applications in Food and Bioprocessing* , Butterworth-Heinemann, Elsevier, ISBN 978-1-85671-632-3, USA., pp. 5-8, 16.

Cussler, E.L. (1997). *Diffusion of Mass Transfer in Fluid Systems (2nd edition)*, Cambridge University Press, ISBN 0-521-45078-0, Cambridge, UK., p. 460.

Danesi, P.R. (1984). A simplified model for the couple transport of metal ions through hollow-fiber supported liquid membranes. *J. Membr. Sci.*,**.** Vol.20, No.3, (Sept. 1984), pp. 231-248.

El-Nadi, Y. A., Daoud, J. A. & Aly, H. F. (2005). Modified leaching and extraction of uranium from hydrous oxide cake of Egyptian monazite. *Int. J. Miner. Process*., Vol.76, (Apr. 2005), pp. 101-110.

Escobar, I.C. & Schäfer A.I. (2010). *Sustainable Water for the Future: Water Recycling versus Desalination,* Elsevier, ISBN 978-0-444-53115-5, Amsterdam, The Netherlands, pp. 160-178.

Jirjis, B.F. & Luque, S. (2010). Practical Aspects of Membrane System Design in Food and Bioprocessing Applications, *in* Cui, Z.F. & Muralidhara, H.S. (eds.), Butterworth-Heinemann, Elsevier, ISBN 978-1-85671-632-3, USA., pp. 179-212.

Henley, E.J. & Seader, J.D. (1981). *Equilibrium-Stage Separation Operations in Chemical Engineering*, Wiley & Sons Inc., ISBN 0-471-37108-4, USA., pp. 1-24.

Huang, D., Huang, K., Chen, S., Liu, S. & Yu, J. (2008). Rapid reaction-diffusion model for the enantioseparation of phenylalanine across hollow fiber supported liquid membrane. *Sep. Sci. Tech*., Vol. 43, (Sept. 2007), pp. 259-272.

Kislik, V.S. (2010). Introduction, General Description, Definitions, and Classification. Overview, *in* Kislik, V.S. (ed.), *Liquid Membranes Principle and Applications in Chemical Separations and Wastewater Treatment,* Elsevier, ISBN 978-0-444-53218-3, Amsterdam, The Netherlands, pp. 3-8, 17-71.

Kittisupakorn, P., Weerachaipichaskul, W. & Thitiyasook, P. (2007). Modeling and simulation of copper-ion extraction with hollow fiber supported liquid membrane. *J. Ind. Eng. Chem*., Vol.13, No.6, (Aug. 2007), pp. 903-910.

Kumar, A., Haddad, R., Benzal, G., Ninou, R., & Sastre, A.M. (2000). Use of modified membrane carrier system for recovery of gold cyanide from alkaline cyanide media using hollow fiber supported liquid membranes: feasibility studies and mass transfer modeling. *J. Membr. Sci.*, Vol.174, No.1, (Feb. 2000), pp. 17-30.

Li, H. & Chen, V. (2010). Membrane Fouling and Cleaning in Food and Bioprocessing, *in* Cui, Z.F. & Muralidhara, H.S. (eds.), *Membrane Technology: A Practical Guide to Membrane Technology and Applications in Food and Bioprocessing*, Butterworth-Heinemann, Elsevier, ISBN 978-1-85671-632-3, USA., pp. 213-249.

Lin, S.H. & Juang, R.S. (2001). Mass-transfer in hollow-fiber modules for extraction and back-extraction of copper(II) with LIX64N carriers. *J. Membr. Sci.*, Vol.188, No.2, (Jul. 2001), pp. 251-262.

Lipnizki, F. (2010). Cross-Flow Membrane Applications in the Food Industry, *in* Peinemann, K.-V., Nunes, S.P. & Giorno, L. (2010). *Membranes for Food Applications,* Wiley-VCH, ISBN 978-3-527-31482-9, Weinheim, Germany, pp. 1-24.

Lothongkum, A.W., Ramakul, P., Sasomsub, W., Laoharochanapan, S. & Pancharoen, U. (2009). Enhancement of uranium ion flux by consecutive extraction via hollow fiber supported liquid membrane. *J. Taiwan Inst. Chem. Eng*., Vol.40, No.5, (Sept. 2009), pp. 518-523.

Lothongkum, A.W., Suren, S. Chaturabul, S. Thamphiphit, N. & Panchareon, U. (2011). Simultaneous removal of arsenic and mercury from natural-gas-co-produced water

from the Gulf of Thailand using synergistic extractant via HFSLM. *J. Membr. Sci.*, Vol. 369, (Dec. 2010), pp. 350-358.

Marcese, J. & Camderros, M.(2004). Mass transfer of cadmium ions in a hollow-fiber module by pertraction. *Desalination*, Vol.164, (Sept. 2004), pp. 141-149.

Matthews, M.A. (2007). Green Chemistry, *in* Seidl, A. (ed.), *Kirk-Othmer Chemical Technology and the Environment,* John Wiley & Sons Inc., ISBN 978-0-470-10540-5, New Jersey, USA., pp. 4-8.

Ortiz, I., Galán, B & Irabien, A. (1996). Membrane mass transfer coefficient for the recovery of Cr(VI) in hollow fiber extraction and back-extraction modules. *J. Membr. Sci.*, Vol.18, (Mar. 1996), pp. 213-231.

Pancharoen, U., Ramakul, P. & Patthaveekongka, W. (2005). Purely extraction and separation of mixure of cerium(IV) and lanthanum(III) via hollow fiber supported liquid membrane. *J. Ind. Eng. Chem*., Vol.11, No.6, (Sept. 2005), pp. 926- 931.

Pancharoen, U., Somboonpanya, S., Chaturabul, S. & Lothongkum, A.W. (2010). Selective removal of mercury as $HgCl_4^{2-}$ from natural gas well produced water by TOA via HFSLM. *J. Alloy Compd.*, Vol.489, No.1, (Jan. 2010), pp. 72-79.

Pancharoen, U., Wongsawa, T. & Lothongkum, A. W. (2011). Reaction flux model for extraction of Cu(II) with LIX84I in HFSLM. *Sep. Sci. Tech.*, (in press).

Parhi, P.K. & Sarangi, K. (2008). Separation of copper, zinc, cobalt and nickel ions by supported liquid membrane technique using LIX 84I, TOPS-99 and Cyanex 272. *Sep. Purif. Technol.*, Vol.59, No.2, (Feb. 2008), pp. 169-174.

Patthaveekongka, W., Ramakul, P., Assabumrungrat, S. & Pancharoen, U. (2006). Transport of cerium, lanthanum, neodymium and palladium via hollow fiber supported liquid membrane based on equilibrium theory. *J. Chin. Inst. Chem. Engrs*., Vol.37, No.3, pp. 227-238.

Polypore Company, MEMBRANA Underline Performance, Liqui-Cel membrane contactors, 15.05.2011, Available from: http://www.liquicel.com/product-information/gas-transfer.cfm

Prapasawat, T., Ramakul, P., Satayaprasert, C., Pancharoen, U. & Lothongkum, A. W. (2008). Separation of As(III) and As(V) by hollow fiber supported liquid membrane based on the mass transfer theory. *Korean J. Chem. Eng*., Vol.25, No.1, (May 2008), pp. 158-163.

Prudich, M.E., Chen, H., Gu, T., Gupta, R.M., Johnston, K.P., Lutz, H., Ma, G. & Su, Z. (2008). Alternative Solid/Liquid Separations, *in* Green, D. W. & Perry, R. H. (eds.), *Perry's Chemical Engineers'Handbook (8th edition),* McGraw-Hill, ISBN 978-0-07-142294-9, New York, USA., pp. 20-36-20-37.

Ramakul, P., Nakararueng, K. & Pancharoen, U. (2004). One-through selective separation of copper, chromium and zinc ions by hollow fiber supported liquid membrane. *Korean J. Chem. Eng*., Vol.21, No.6, (Aug. 2004), pp. 1212- 1217.

Ramakul, P., Pattaweekongka, W. & Pancharoen, U. (2005). Selective separation of trivalent and tetravalent lanthanide from mixture by hollow fiber supported liquid membrane. *J. Chin. Inst. Chem. Engrs*., Vol.36, No.5, pp. 459-465.

Ramakul, P., Prapasawad, T., Pancharoen, U. & Pattaveekongka, W. (2007). Separation of radioactive metal ions by hollow fiber-supported liquid membrane and permeability analysis. *J. Chin. Inst. Chem. Engrs*., Vol.38, (Apr. 2007), pp. 489- 494.

Rathore, N.S., Sonawane, J.V., Kumar, A., Venugopalan, A. K., Singh, R. K., Bajpai, D. D. & Shukla, J. P. (2001). Hollow fiber supported liquid membrane: a novel technique for separation and recovery of plutonium from aqueous acidic wastes. *J. Membr. Sci.*, Vol.189, No.1, (Mar. 2001), pp. 119-128.

Ren, Z., Zhang, W., Lui, Y., Dai, Y. & Cui, C. (2007). New liquid membrane technology for simultaneous extraction and stripping of copper(II) from wastewater. *Chem. Eng. Sci.*, Vol.62, No.22, (Nov. 2007), pp. 6090-6101.

Schnelle, K.B. & Brown, C.A. (2002). *Air Pollution Control Technology Handbook,* CRC Press, ISBN 0-8493-9588-7, USA., pp. 237-239.

Scott, K. & Hughes, R. (1996). *Industrial Membrane Separation Technology*, Blackie Academic & Professional, ISBN 0-7514-0338-5, UK., pp. 93-107, 258-270.

Sengupta, B., Bhakhar, M.S. & Sengupta, R. (2007). Extraction of copper from ammoniacal solutions into emulsion liquid membranes using LIX 84 I. *Hydrometallurgy*, Vol.8, No.3-4, (Dec. 2007), pp. 311-318.

Simmons, V., Kaschemekat, J., Jacobs, M.L. & Dortmudt, D.D. (1994). Membrane system offer a new way to recover volatile organic air pollutants. *Chem. Eng*., Vol.101, No.9, (Sept. 1994), pp.92-94.

Urtiaga, A.M., Ortiz, M.I. & Salazar, E. (1992). Supported liquid membranes for the separation-concentration of phenol. 2. mass-transfer evaluation according to fundamental equations. *Ind. Eng. Chem. Res.*, Vol.31, No.7, (Jul. 1992), pp. 1745-1753.

Wannachod, P., Chaturabul, S., Pancharoen, U., Lothongkum, A.W. & Patthaveekongka, W. (2011). The effective recovery of praseodymium from mixed rare earths via a hollow fiber supported liquid membrane and its mass transfer related. *J. Alloy. Compd.*, Vol.509, No.2, (Sept. 2011), pp. 354–361.

Yang, J. & Fane, A.G. (1999). Facilitated transport of copper in bulk liquid membranes containing LIX984N. *Sep. Sci. Tech.*, Vol.34, No.9, (Jun. 1999), pp. 1873–1890.

10

Particularities of Membrane Gas Separation Under Unsteady State Conditions

Igor N. Beckman[1,2], Maxim G. Shalygin[1] and Vladimir V. Tepliakov[1,2]
[1]*A.V.Topchiev Institute of Petrochemical Synthesis, Russian Academy of Sciences*
[2]*M.V.Lomonosov Moscow Sate University, Chemical Faculty*
Russia

1. Introduction

Membranes become the key component of modern separation technologies and allow exploring new opportunities and creating new molecular selective processes for purification, concentration and separation of liquids and gases (Baker, 2002, 2004). Particularly the development of new highly effective processes of gas separation with application of existing materials and membranes takes specific place. In present time special attention devotes to purification of gas and liquid waste streams from ecologically harmful and toxic substances such as greenhouse gases, VOCs and others. From the fundamental point of view the development on new highly effective processes of gas separation demands the investigation of mass transfer in the unsteady (kinetic) area of gas diffusion through a membrane. This approach allows in some cases to obtain much higher selectivity of separation (using the same membrane materials) compared to traditional process where steady state conditions are applied. First studies of membrane separation processes under unsteady state conditions have demonstrated both opportunities and problems of such approach (Beckman, 1993; Hwang & Kammermeyer, 1975; Paul, 1971).

It was shown that effective separation in unsteady membrane processes is possible if residence times of mixture components significantly differ from each other that is the rare situation in traditional polymeric materials but well known for liquid membranes with chemical absorbents (Shalygin et al., 2006). Nevertheless similar behavior is possible in polymeric membranes as well when functional groups which lead to partial or complete immobilization of diffusing molecules are introduced in polymer matrix. Moreover the functioning of live organisms is related with controllable mass transfer through cell membranes which "operate" in particular rhythms. For example scientific validation of unsteady gas transfer processes through membranes introduces particular interest for understanding of live organisms' breathing mechanisms.

It can be noticed that development of highly effective unsteady membrane separation processes is far from systematic understanding and practical evaluation. Therefore the evolution of investigations in this area will allow to accumulate new knowledge about unsteady gas separation processes which can be prototypes of new pulse membrane separation technologies.

Theoretical description of unsteady mass transfer of gases in membranes is presented in this work. Examples of binary gas mixture separation are considered for three cases of gas

concentration variation on membrane: step function, pulse function and harmonic function. Unsteady gas flow rates and unsteady separation factors are calculated for all cases. Amplitude-frequency, phase-frequency and amplitude-phase characteristics as well as Lissajous figures are calculated for harmonic functions. The comparison of mixture separation efficiency under steady and unsteady mass transfer conditions is carried out. Calculations were performed for oxygen-nitrogen and oxygen-xenon gas mixtures separation by membranes based on polyvinyltrimethylsilane and for CO_2 transfer in liquid membrane with chemical absorbent of CO_2.

2. Regimes of unsteady gas transfer in membranes

The basis for mathematical modeling was taken from (Crank, 1975; Beckman et. al, 1989, 1991, 1996). According to the tradition scheme the gas flux at output of membrane in permeation method is defined by 1st Fick's law:

$$J(t) = -DA\left.\frac{\partial C(x,t)}{\partial x}\right|_{x=H} \tag{1}$$

where J – gas flux through membrane, A – area of membrane, D – diffusivity coefficient, H – thickness of membrane, C – concentration of gas molecules inside of membrane, t – time of diffusion, x – coordinate.
After some transient period of time the flux is achieving the steady-state condition:

$$J_{SS} = ADS\frac{p_u - p_d}{H}, \tag{2}$$

where S – solubility coefficient of gas in polymer, p_u and p_d – partial pressure of gas in upstream and downstream, respectively. Usually $p_u >> p_d$ and the steady-state gas flux through membrane (J_{ss}) can be expressed as:

$$J_{SS} = ADS\frac{p_u}{H} = AP\frac{p_u}{H}, \tag{3}$$

where $P = DS$ is the permeability coefficient.
Three steady-state selectivity factors can be defined for understanding of consequent detailed analysis: general (on the permeability coefficients) α_{SS}, kinetic (on the diffusivity coefficients) α_D and thermodynamic (on the solubility coefficients) α_S. Ideal selectivity for a pair of gases is described by equation (4):

$$\alpha_{SS} = \frac{P_A}{P_B} = \frac{D_A S_A}{D_B S_B} = \alpha_D \alpha_S, \tag{4}$$

where P_A, P_B the permeability coefficients of gases A and B, respectively; D_A, D_B are the diffusivity coefficients; S_A, S_B are the solubility coefficients.

2.1 Step function variation of gas concentration in upstream

In traditional permeability method at the input membrane surface at given moment of time the step function variation of gas concentration (high partial gas pressure) is created and at

the output membrane surface the partial gas pressure is keeping close to zero during whole diffusion experiment. At the beginning the gas transfer is unsteady and then after definite time the steady-state gas transfer is achieved.

In the frames of "classical" diffusion mechanism (that is the diffusion obedient to Fick's law and the solubility – to Henry's law) the unsteady distribution of concentration of diffusing gas $C(x,t)$ across the flat membrane with thickness H, is determined by the 2nd Fick's law:

$$\frac{\partial C(x,t)}{\partial t} = D\frac{\partial^2 C(x,t)}{\partial x^2} \tag{5}$$

Standard initial and boundary conditions are: $C(0,t)=C_u$; $C(H,t)=0$; $C(x,0)=0$, where C_u is the concentration of gas in membrane respected to partial pressure of gas at the upstream side in accordance with Henry's law:

$$C_u = Sp_u\,, \tag{6}$$

where S is solubility coefficient of gas in polymer.

The unsteady gas flux through membrane follows from the solution of Eq. (5) and can be expressed in two forms:

$$J(t) = J_{ss}\frac{4}{\sqrt{\pi}}\sqrt{\frac{H^2}{4Dt}}\sum_{m=0}^{\infty}\left\{-\frac{(2m+1)^2 H^2}{4Dt}\right\} \tag{7}$$

$$J(t) = J_{ss}\left[1+2\sum_{n=1}^{\infty}(-1)^n \exp\left\{-\left(\frac{n\pi}{H}\right)^2 Dt\right\}\right], \tag{7'}$$

where $J_{SS} = \frac{DC_u A}{H} = \frac{PAp_u}{H}$ is steady-state gas flux.

The series of the Eq. (7) is converged at small values of time and the series of the Eq. (7') is converged at high values of time.

Traditionally, membrane gas transfer parameters P, D and S can be found from two types of experimental time dependencies: (1) the dependence of gas volume $q(t)$ or (2) the dependences of gas flow rate $J(t)$, permeated through a membrane. The pulse function variation of gas concentration in upstream is applied enough rare in experimental studies and corresponding response function $j(t)$ in downstream relates with other functions as follows:

$$j(t) = \frac{dJ(t)}{dt} = \frac{d^2 q(t)}{dt^2} \tag{8}$$

The unsteady selectivity for a gas pair can be expressed using Eq. (7) as follows:

$$\alpha_{US} = \frac{D^A S^A\left\{1+2\sum_{n=1}^{\infty}(-1)^n \exp\left(-\frac{n^2\pi^2 D^A t}{H^2}\right)\right\}}{D^B S^B\left\{1+2\sum_{n=1}^{\infty}(-1)^n \exp\left(-\frac{n^2\pi^2 D^B t}{H^2}\right)\right\}} \tag{9}$$

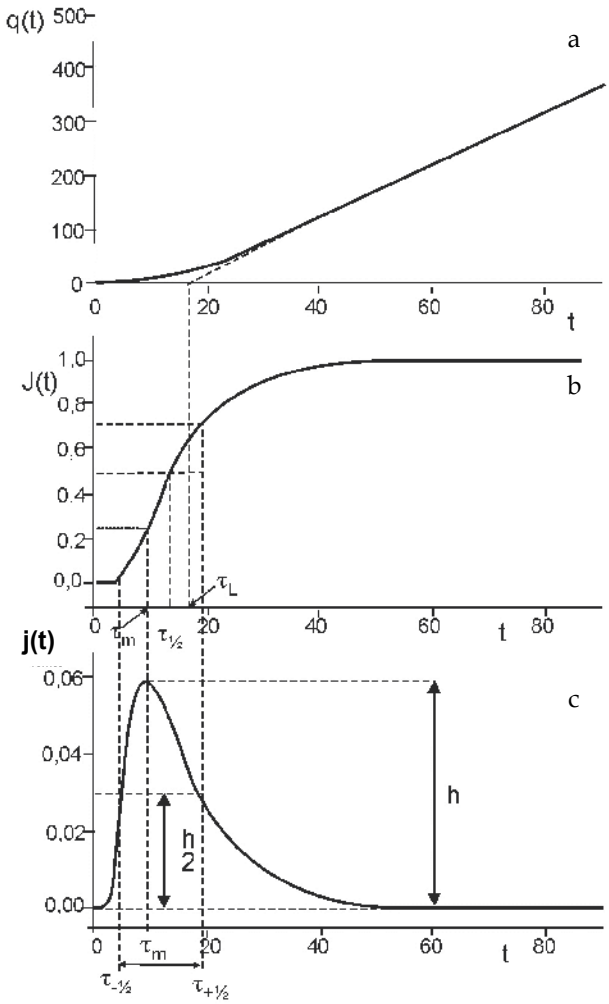

Fig. 1. Typical kinetic curves for different experimental methods of measurements of unsteady gas transfer: a – integral method (variation of gas volume in downstream after step function variation of gas concentration in upstream), b – differential method (variation of gas flux in downstream after step function variation of gas concentration in upstream), c – pulse method (variation of gas flux in downstream after pulse function variation of gas concentration in upstream).

As it is seen from eq. (9) the non steady-state selectivity factor (α_{US}) depends on diffusion time. Accordingly to Eq. (9) when $t \to \infty$, $\alpha_{US} \to \alpha_{SS}$ and the highest value of selectivity can be achieved at short times. The unsteady-state regime allows to rich infinitely high selectivity of separation but at the same time permeation fluxes dramatically go down. It means that for real application of unsteady separation regime the compromise time intervals need to be selected for appropriate balance between permeance and selectivity values.

2.2 Pulse function variation of gas concentration in upstream

In the case of pulse permeation method the measurement of the gas flux permeating through membrane as response on the short square pulse of feed concentration is considered (Beckman et al., 1989, 1991). In the case of the square pulse of concentration with duration Δt in upstream the response function of gas flux can be described as follows:

$$J(t) = J_{SS}\left[f_1(t) - \gamma f_2(t-\Delta t)\right], \tag{10}$$

where γ=0 for $t<\Delta t$ (the rising branch of curve) and γ=1 for $t>\Delta t$ (the descending branch of curve):

$$f_1(t) = 1 + 2\sum_{n=1}^{\infty}(-1)^n \exp\left(-n^2\pi^2 D\frac{t}{H^2}\right) \tag{11}$$

$$f_2(t) = 1 + 2\sum_{n=1}^{\infty}(-1)^n \exp\left(-n^2\pi^2 D\frac{t-\Delta t}{H^2}\right) \tag{12}$$

The distortion of pulse concentration at $\Delta t \to 0$ for the permeation through membrane is described by Eq. (13):

$$j(t) = \frac{dJ(t)}{dt} = 2J_{SS}\frac{\pi^2 D}{H^2}\sum_{n=1}^{\infty}(-1)^{n+1} n^2 \exp\left\{-\left(\frac{n\pi}{H}\right)^2 Dt\right\} \tag{13}$$

The permeation flux through the membrane is decreasing with decreasing of the pulse duration. As to compare with other permeability methods the pulse method requires shorter time of experiment and possesses higher resolution and dynamics.

The transfer of square pulse of concentration of binary gas mixture is considered below. If permeability coefficients of both components are similar (for example, hydrogen and carbon dioxide permeability as it can be found for main part of polymers) the separation of such gas mixture at steady-state condition is actually impossible. However, if values of diffusivity coefficients are not similar (for example $D_A > D_B$), the separation can be possible though at definite interval of time with very high selectivity factors. In this case the membrane acts as chromatography column. During this process at short times penetrate flux is enriched by component A, at average times both components are presented and at long times the component B is dominated in downstream. It should be noted that the resolution between two peaks is strongly depends on the pulse duration (Δt) and it decreases with increasing of Δt. Thus, the selectivity of separation can be controlled by the duration of pulse.

For the quantitatively description of the membrane separation process the differential unsteady selectivity factor can be introduced:

$$\alpha(t) = \frac{J_A(t)}{J_B(t)} = \frac{J_{SS\,A}F_A}{J_{SS\,B}F_B} = \alpha_{SS}K_\alpha, \tag{14}$$

where $F = J(t)/J_{SS}$, $\alpha_{SS} = S_A D_A/(S_B D_B)$ is the steady-state selectivity factor, $K_\alpha = F_A/F_B$ is the parameter of selectivity, and $\alpha(t)$ is the differential unsteady selectivity factor. It is evident that unsteady selectivity factor is transformed to the steady-state one if duration of the pulse increasing ($\Delta t \to \infty$, $K_\alpha \to 1$, $\alpha(t) \to \alpha_{SS}$). It should be noted that α_{SS} is determined by relation

of the permeability coefficients P_A and P_B, whereas K_α depends only on diffusivity coefficients. It allows controlling the penetrated gas mixture composition by variation of pulse duration and/or time of recovery.

It should be noted that in case of evident resolution of two concentration peaks after membrane the task of gas transfer parameters determination can be easily solved by using non-linear Least Squares Method (LSM): the diffusivity coefficients are determined by the time of peak's maximum achievement, and the solubility coefficients are estimated by heights of peaks.

In case of non-resolved peaks the following algorithm based on assumption of simple peak function can be suggested. First of all the time of maximal flux achievement (t_m) and maximal height of peak (I_m) have to be determined. Then the peak should be divided into n parts by height (for example n=10 and height of each part is h_i, Fig. 2). Each part has two characteristic points of intersection with curve $I(t)$: at time t_i^- and at time t_i^+, which determine width of peak at height h_i as $d_i = t_i^+ - t_i^-$ and two segments: left half-width $d_i^- = t_m - t_i^-$ and right half-width $d_i^+ = t_i^+ - t_m$. In such a way the ensemble of asymmetry parameters $\Delta_i = d_i^+ - d_i^-$ can be determined.

The advantage of suggested method is that it can be applied for the determination of diffusivity coefficients of gases for binary gas mixture of unknown composition. Such analysis can be important, for example, for applications where gas sensors with selective membrane layer are used. Particular nomographs for determination of gas diffusivities were calculated and are represented in Fig. 3. In this case the right half-widths of peak are used.

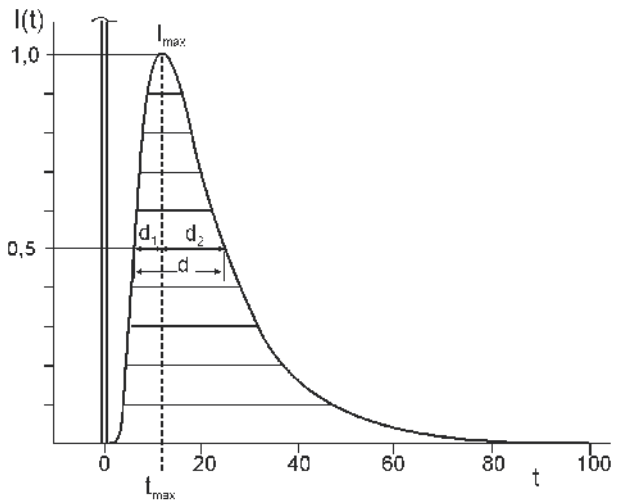

Fig. 2. The analysis of non-resolved peaks after membrane (infinitely short concentration pulse in upstream).

So, if to find these parameters from experimental peak and to fix the time of the peak maximum t_m, then to draw on diagram the experimental point, then to find the relation of the diffusion coefficients for binary gas mixture along with parallel, so, the relative contribution of D values can be found along with meridian. If to know the thermodynamic properties of gases considered and the diffusivity of main component the composition of the feed gas mixture and D value of second component can be determined.

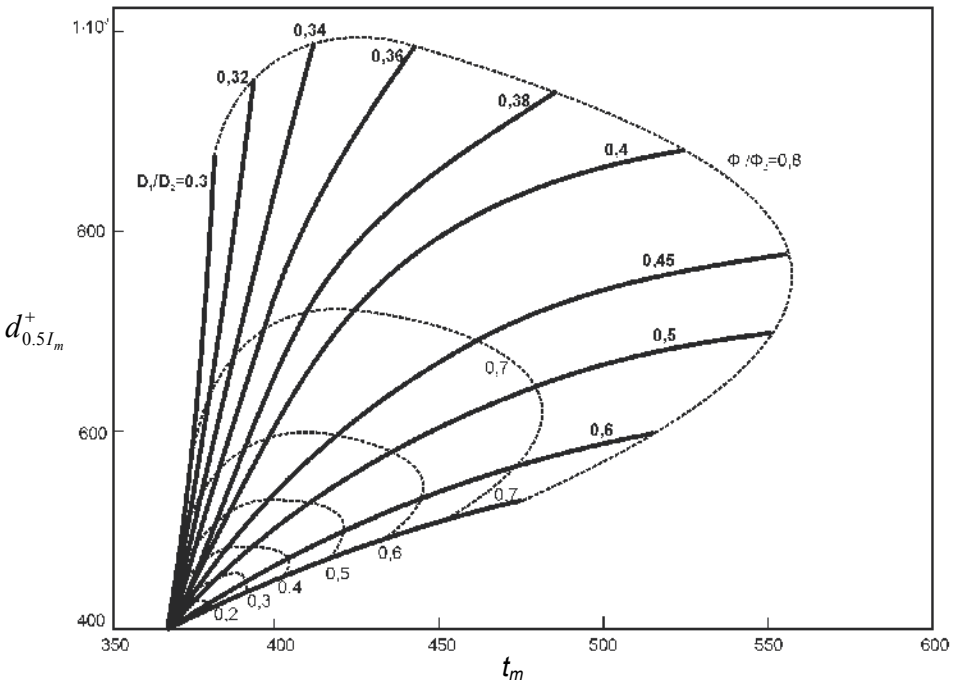

Fig. 3. Nomographs for the determination of the gas diffusivity coefficients and the composition of binary gas mixture. The parameters for the calculation are: H=0.02 cm, S_1/S_2=0.5, A_S=100 см², p=76 cm Hg. Φ_1 and Φ_2 are corresponding contributions into permeation flux of components A and B.

2.3 Harmonic function variation of gas concentration in upstream

Method of the concentration wave is based on study of wave deformation during penetration through a membrane. The variation of gas flux at the downstream is usually measured. Measurements should be carried out at several frequencies of harmonic function. Obtained dependencies of amplitude and phase variation on frequency are used for the characterization of membrane. The existing of five degrees of freedom (steady-state condition relatively of which the harmonic function takes place; time of the steady-state achieving; change of the amplitude and phase characteristics after transfer through membrane and their dependences on the frequency) allows to control the diffusion of gas and consequently the separation process (Beckman et al., 1996).
In case of variation of gas concentration in upstream as harmonic function:

$$C = 0.5C_0\left[1+\sin(\omega t)\right], \tag{15}$$

the variation of gas flux after membrane can be described by the following equation:

$$J_1 = \frac{DAC_0}{2H}\left\{\sin(\omega t) + 2\omega\sum_{n=1}^{\infty}\frac{(-1)^n\left\{\frac{n^2\pi^2 D}{H^2}\left[\cos(\omega t)-\exp\left(-\frac{n^2\pi^2 Dt}{H^2}\right)\right]+\omega\sin(\omega t)\right\}}{\frac{n^4\pi^4 D^2}{H^4}+\omega^2}\right\} \tag{16}$$

where $C_0 = Sp_0$, p_0 is maximal partial pressure of gas, ω is frequency.
Harmonic variation of gas flux after membrane will have the same frequency but lower amplitude and phase shift (Fig. 4).
If concentration of gas in upstream fluctuate with amplitude A_0:

$$C(0,t) = A_0 \sin(\omega t), \tag{17}$$

harmonic vibrations take place around stable level that can be calculated as follows:

$$J_R = \frac{A_0}{2}\left\{1 + 2\sum_{n=1}^{\infty}(-1)^n \exp\left(-\frac{n^2\pi^2 Dt}{H^2}\right)\right\} \tag{18}$$

At high values of time a quasi-stationary flux through membrane can be described as follows:

$$J(t) = \frac{DAC_0}{H}\left(\sin(\omega t) + 2\omega\sum_{n=1}^{\infty}\frac{(-1)^n\left\{\frac{n^2\pi^2 D}{H^2}\cos(\omega t) + \omega\sin(\omega t)\right\}}{\frac{n^4\pi^4 D^2}{H^4} + \omega^2}\right) \tag{19}$$

Eq. (19) represents the simple harmonic vibration that has the same frequency but lower amplitude and phase shift:

$$J_\infty(\omega) = A(\omega)\sin\left[\omega t + \varphi(\omega)\right], \tag{20}$$

where the amplitude of passed wave is:

$$A(\omega) = \frac{A_0 H\sqrt{\frac{\omega}{D}}}{\left[\mathrm{sh}^2\left(H\sqrt{\frac{\omega}{2D}}\right) + \sin^2\left(H\sqrt{\frac{\omega}{2D}}\right)\right]^{1/2}} \tag{21}$$

and the phase shift is:

$$\varphi(\omega) = \mathrm{arctg}\left[\frac{\mathrm{tg}\left(H\sqrt{\frac{\omega}{2D}}\right) - \mathrm{th}\left(H\sqrt{\frac{\omega}{2D}}\right)}{\mathrm{tg}\left(H\sqrt{\frac{\omega}{2D}}\right) + \mathrm{th}\left(H\sqrt{\frac{\omega}{2D}}\right)}\right] \tag{22}$$

Concentration waves decay strongly as a rule, however they possess all properties of waves, in particularly, interference and diffraction.
The diagram shown in Fig. 5 allows carrying out relatively simple estimation of diffusivity coefficient by measuring the ratio between the amplitude and the phase shift of the incident and the transmitted waves at definite frequency: the crossing point of the respective curves can be used for determination of D values. For small values of frequency following

simplified equation can be used: $\varphi=\omega H^2/6D$. For high values of frequency ($H\sqrt{\omega/2D} > \pi/2$) phase shift can be calculated as $\varphi \approx H\sqrt{\omega/2D} - \pi/4$.

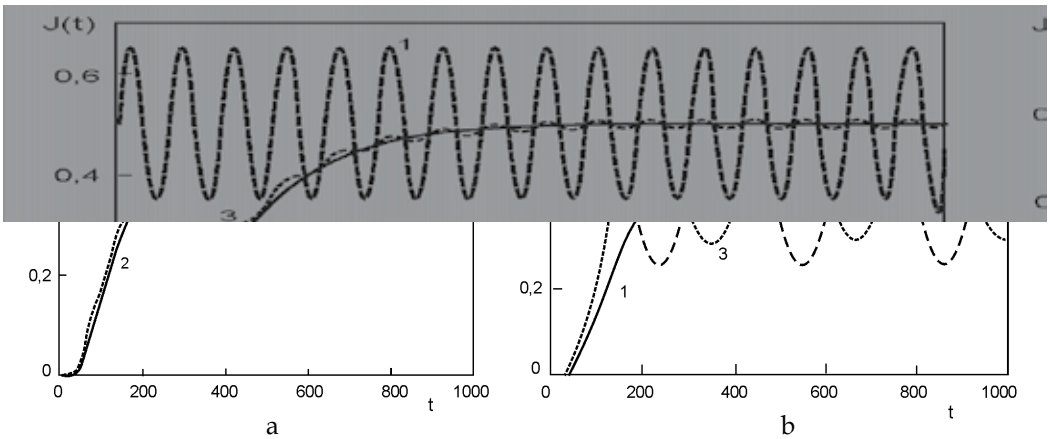

Fig. 4. The permeation of concentration wave through membrane (H=0.01 cm; D=10^{-7} cm^2/s) at two frequencies: $\omega = 0.1$ (a) and $\omega = 0.02$ (b). 1 – kinetic permeability curve (step function variation of the gas concentration in upstream); 2 – variation of the gas concentration in upstream; 3 – variation of the gas flux in downstream.

Thus, quasi-stationary gas flux value is determined by membrane permeance; the amplitude of the transmitted wave depends on permeability (i.e., on diffusivity and solubility coefficients), thickness of membrane and frequency. However, the ratio between the amplitude of the oscillations in upstream and downstream does not depend on the permeability coefficient. The phase shift depends on the diffusivity coefficient which determines the rate of the periodical stationary state achievement as well.

From experimental data treatment point of view this method possesses more degrees of freedom: time of the periodical stationary condition, the equilibrium position, the amplitude of wave and the phase shift. Diffusivity coefficient can be calculated by using of any of these parameters. Additional degree of freedom is changing of frequency.

For the classical diffusion mechanism the amplitude function $A(\omega)$ decreases with increasing of the frequency of waves (membrane passes the lower frequency waves and cut off the higher frequency ones); the phase shift function $\varphi(\omega)$ passes through minimum and then becomes as the periodical wave.

The particularity of permeation of the concentration waves through membrane is suitable to present as amplitude-phase diagram where the amplitude value represents the length of vector and the phase shift is the angle of slope. The swing of spiral is defined by the permeability coefficient P. If the amplitude-phase diagram to imagine as reduced value A/A_0, where A is the amplitude of transmitted wave and A_0 is the amplitude of the incident one then obtained curve will not depend on P and represents unique form for all variety of the situations of "classical" mechanism of diffusion.

It is evident that the membrane can be considered as the filter of high frequencies the higher diffusivity providing the wider the transmission band.

The permeation of concentration waves through non-homogeneous membrane media can be considered as a particular case. The example of gas diffusion by two parallel independent

channels (two-component medium) is considered below (corresponding parameters are: diffusivity coefficients D_1, D_2; solubility coefficients S_1, S_2; contributions to total flux through membrane $\Phi_1=S_1/S$, $\Phi_2=S_2/S$, where $S_1+S_2=S$, $\Phi_1+\Phi_2=1$.
The results of modeling are presented in Fig.6. It is seen that the presence of two ways of diffusion considerably changes the curve form of amplitude-phase characteristic. It can be used for the detection of additional channels of diffusion (e.g., pores) and for determination of values of local transport parameters.

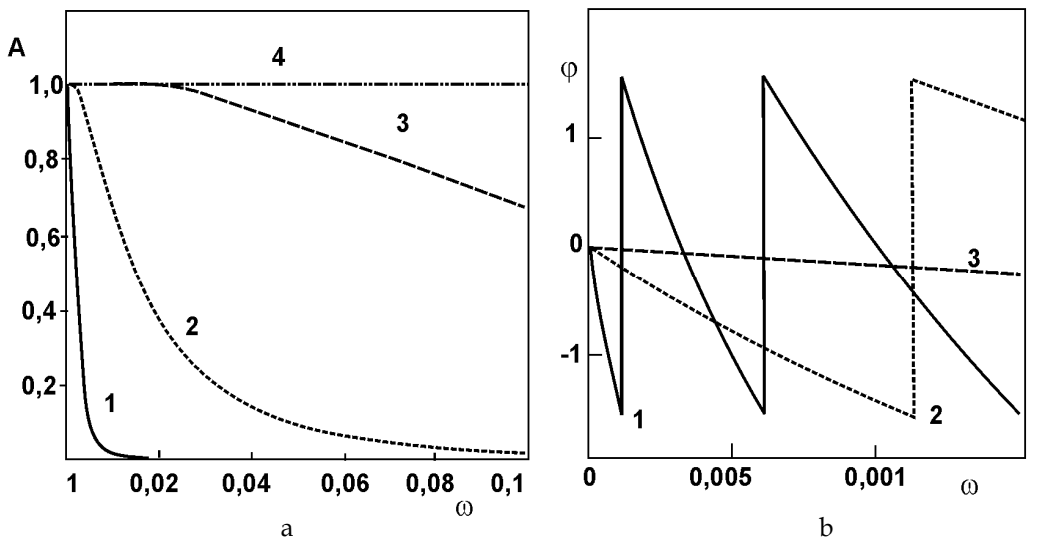

Fig. 5. The dependences of the amplitude and the phase shift of the transmitted wave on the frequency of the incident wave at the different diffusivity values (cm^2/s): 1 – 10^{-8}, 2 – 10^{-7}, 3 – 10^{-6}, 4 – 10^{-5}; (a) relative amplitude (A_d / A_0), (b) phase shift.

Other representation of results of the concentration wave method is the Lissajous figures. These figures are built in coordinates: the ordinate is the amplitude of transmitted concentration wave; the abscissa is the amplitude of incident wave (Fig. 7). In case of homogeneous diffusion medium (classical mechanism of diffusion) the Lissajous figure has the appearance of straight line passing through origin of coordinates and angular with 45° in relation to the abscissa axis. Lissajous figure does not depend on the vibration frequency for classical diffusion mechanism.
If concentration wave consists of two gases A and B the input of membrane is as following:

$$c^A = \frac{C_0^A}{2}\left[1+\sin(\omega t)\right] \text{ and } c^B = \frac{C_0^B}{2}\left[1+\sin(\omega t)\right] \tag{23}$$

The flux at the output of membrane:

$$J = J^A + J^B \tag{24}$$

The periodic stationary condition is achieved after some intermediate time the amplitude being:

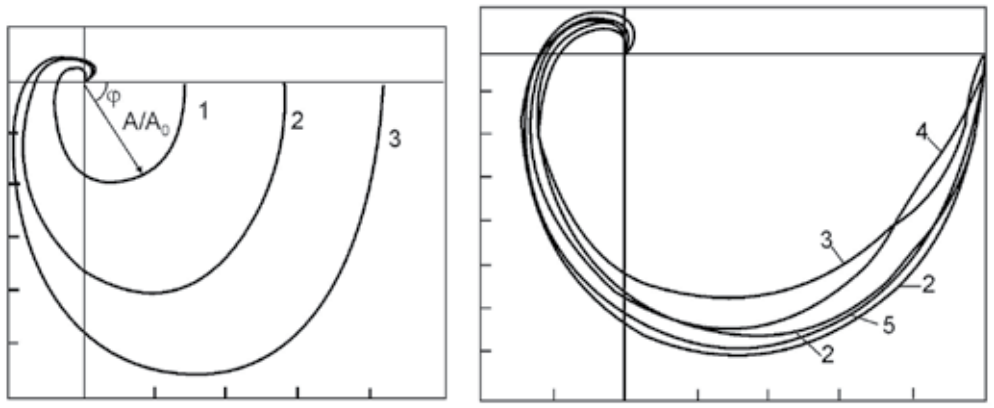

Fig. 6. The amplitude-phase diagrams obtained by the method of the concentration waves: a – (initial scale) homogeneous medium: 1 – D_1=l·10^{-5} cm^2/s, 2 – D_2=2·10^{-6} cm^2/s, 3 – parallel diffusion with D_1 and D_2 (Φ_1=Φ_2=0,5); b – reduced scale: 1 – homogeneous medium with any D, parallel diffusion with D_1= l·10^{-5} cm^2/s and D_2 (cm^2/s): 2 – 2·10^{-5}, 3 – 5·10^{-5}, 4 – 1·10^{-4}, 5 – 5·10^{-4}.

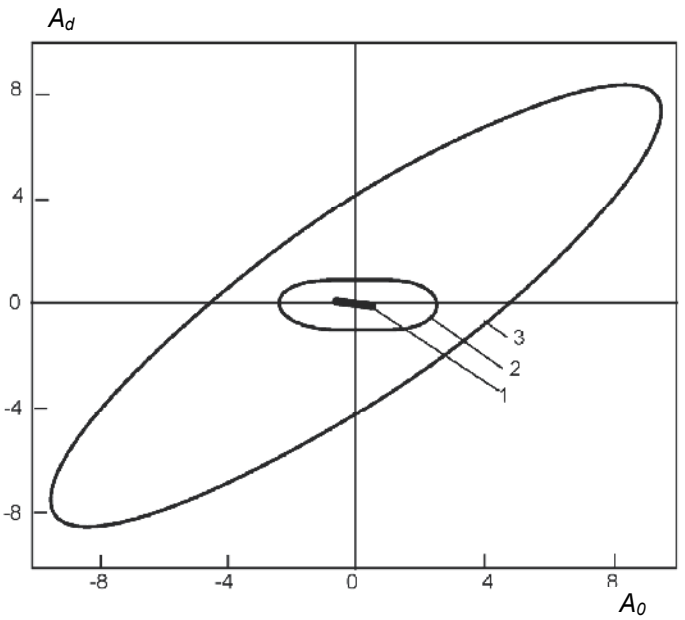

Fig. 7. Lissajous figure for the parallel diffusion through bicomponent membrane medium (D_1 = 1·10^{-5}, D_2 = 2·10^{-5} cm^2/s; Φ_1 = Φ_2 = 0.5): 1 – ω = 0.1 s^{-1}; 2 – ω = 0.5 s^{-1}; 3 – ω = 1 s^{-1}.

$$A = A^A \sin\left(\omega t + \varphi^A\right) + A^B \sin\left(\omega t + \varphi^B\right) = A^{AB} \sin\left(\omega t + \varphi^{AB}\right), \quad (25)$$

where $A^{AB} = \sqrt{\left(A^A\right)^2 + \left(A^B\right)^2 + 2A^A A^B \cos\left(\varphi^B - \varphi^A\right)}$ and the phase shift is:

$$\varphi^{AB} = \operatorname{arctg}\left(\frac{\varphi^B \sin\left(\varphi^B - \varphi^A\right)}{A^A + A^B \cos\left(\varphi^B - \varphi^A\right)}\right), \quad (26)$$

It should be noted that for lower frequency the amplitude of wave at output of membrane is defined by the both gas components. With increasing of the frequency the relative amplitude passes through minimum. This minimum on the curve $A^{AB}(\omega)/A^A$ via ω is defined by fact that the phase shift between output waves of components $\varphi^{AB} = |\varphi^A - \varphi^B| \rightarrow \pi/2$ leads to decreasing of total value of the amplitude at output of membrane. For enough high frequency ω, the amplitude A^B of the frequency with lower D value is small and total amplitude of output waves A is mainly defined by the amplitude of the component possessing high D value.

3. Separation of gas mixtures

Let's consider the separation of ternary gas mixtures at the different non-steady state regimes of permeation. The gas mixture will consist of oxygen, nitrogen and xenon (gaseous mixture of this kind is used in medicine). Traditionally, we have deal with the step function variation of gas concentration on input surface of membrane while the concentration is keeping to zero at output surface of membrane during whole duration of experiment. The calculation was carried out for the following parameters: H=0.01 cm, A=10 cm^2, p=1 bar, t=1 – 8000 sec, the diffusivity coefficients D are: $7.6\cdot10^{-7}$ (O_2), $3.6\cdot10^{-7}$ (N_2), $2.7\cdot10^{-8}$ (Xe); the solubility coefficients S are: $5.79\cdot10^{-3}$ (O_2), $3.06\cdot10^{-3}$ (N_2), $6.3\cdot10^{-2}$ (Xe); the permeability coefficients P are: $4.4\cdot10^{-9}$ (O_2), $1.102\cdot10^{-9}$ (N_2), $1.795\cdot10^{-9}$ (Xe), the steady state fluxes at output of membrane are: $3.344\cdot10^{-4}$(O_2), $8.372\cdot10^{-5}$(N_2), $1.293\cdot10^{-4}$ (Xe).

The steady state selectivity for the above mentioned gases are $\alpha_{O2/N2}$=4, $\alpha_{Xe/N2}$=1.54, $\alpha_{O2/Xe}$=2.59. From kinetic curves presented in Fig. 8(a) it is seen that the steady state condition is earlier achieved for oxygen and later on for xenon. It should be noted that the flux of nitrogen lower than one for xenon. The variation of the selectivity factors with time is shown in Fig. 8(b). For short-delay the selectivity can rich very high values but fluxes are very small. With time the non-stationary selectivity are tended to the stationary ones.

The calculation for the pulse function variation of gas concentration was carried out for ternary gas mixture oxygen-nitrogen-xenon (Fig.9). Xenon passes through membrane substantially later then oxygen and nitrogen though the steady state flux of xenon is higher than one for nitrogen. The steady state fluxes are 79.2 (oxygen), 19.8 (nitrogen) and 30.6 (xenon).

It should be noted that for the pulse variation of concentration the earlier fractions of oxygen and nitrogen are depleted by xenon but the final fractions involve a small content of oxygen and xenon being more than nitrogen. It is important that during permeation process the inversion of the selectivity occurs for pair nitrogen/xenon. For example, at time t = 1000 s

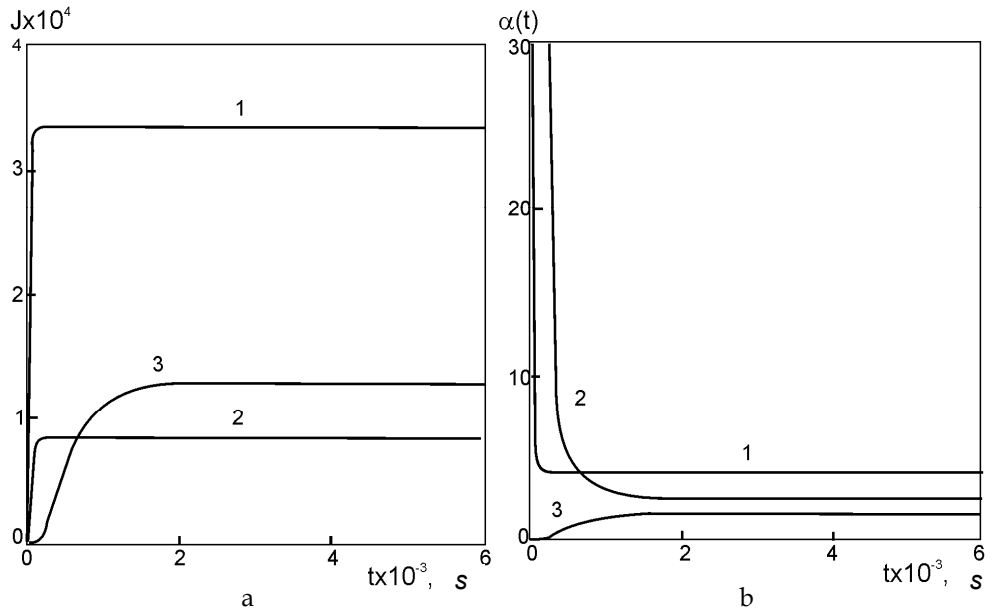

Fig. 8. Non-steady state permeability of oxygen (1), nitrogen (2) and xenon (3) through film of PVTMS: a – changing of gas fluxes with time at output of membrane; b – changing of separation selectivity with time: 1 – O_2/N_2, 2 – O_2/Xe, 3 – Xe/N_2.

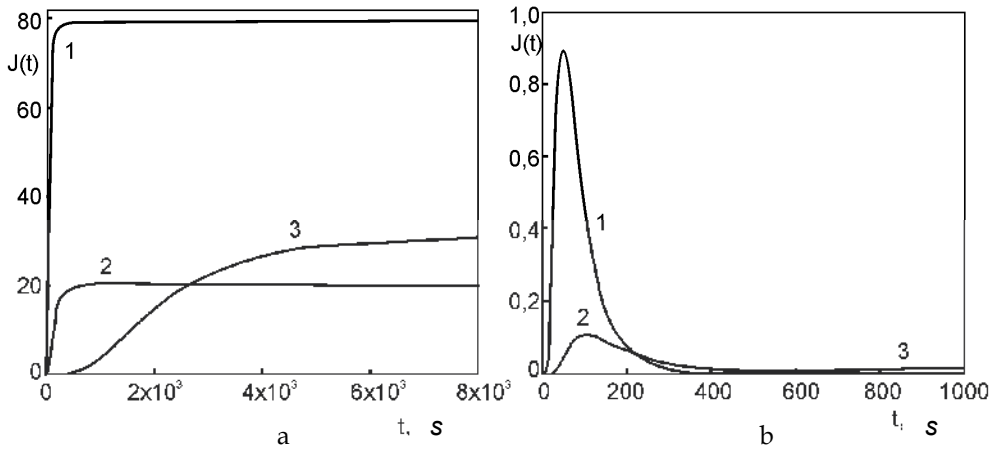

Fig. 9. Non-steady state permeability of oxygen (1), nitrogen (2) and xenon (3) through the film of PVTMS: a – the step variation of concentration; b – the pulse variation of concentration.

$\alpha(t) = J_{N_2} / J_{Xe}$ = 6.05, and at $t \to \infty$ α=0.65. It is evident that at time 2500-3000 s the separation of nitrogen/xenon mixture does not occur (α=1). In the whole, for the pulse variation of concentration xenon is well separated from air that we can clearly see in Fig. 10 where peaks are well resolved.

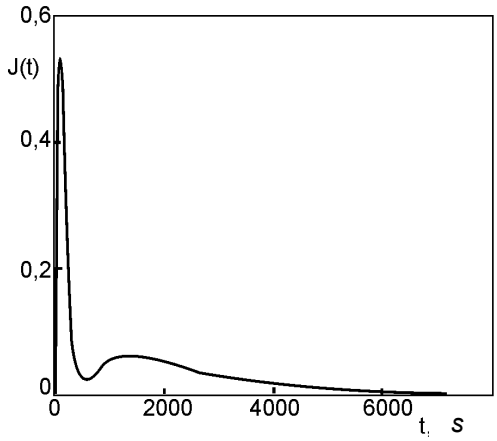

Fig. 10. The view of the output pulse function of gas mixture (nitrogen-xenon) permeation through PVTMS film.

The separation of considered ternary gas mixture is possible under the concentration wave regime as well. The results of mathematical modeling of permeation of the concentration wave (of nitrogen, oxygen or xenon) were obtained for PVTMS film. Following values of parameters were used for calculations: thickness of film H=0.01 cm; area A=10 cm^2; reference frequency: ω_0= 0.01 s^{-1} (range of frequency 0-0.04 s^{-1}); time interval: t=0-4000 s; feed pressure p_u=76 cm Hg; amplitude of the pressure variation in upstream is 15.2 cm Hg. (i.e., the feed pressure is 1 bar and harmonic changing is Δp=20%); transport parameters for oxygen: S=5.79·10^{-3} cm^3(STP)/(cm^3·cmHg), D=7.6·10^{-7} cm^2/s, P=4.4·10^{-9} cm^3(STP)·cm/(cm^3·s·cmHg); transport parameters for nitrogen: S=3.06·10^{-3} cm^3(STP)/(cm^3·cmHg), D=3.6·10^{-7} cm^2/s, P=1.1·10^{-9} cm^3(STP)·cm/(cm^3·s·cmHg). The flux is presented as cm^3(STP)/(s·cmHg) for all cases.

If to consider the separation of binary mixtures xenon-oxygen and xenon-nitrogen that the calculations were carried out using the same parameters as the above mentioned but the reference frequency was chosen lower: ω=0.001, the range of frequency was 0-0.003 s^{-1}, time range t=0-10000 s, D_{Xe} 2.7·10^{-8}, S_{Xe}=0.63, P_{Xe}=1.7·10^{-9}. The stationary selectivity for oxygen/xenon α=2.59. Since for PVTMS we have P_{O2}>P_{Xe}>P_{N2}, the maximal flux is for oxygen (3.34·10^{-3}), then for xenon (8.37·10^{-5}) and then for nitrogen (1.28·10^{-4}). The oscillations of output waves of gas fluxes with amplitudes 6.69·10^{-5}, 1.67·10^{-5}, 2.41·10^{-5} and with the phase shift 0.022, 0.046 and 0.685 for oxygen, xenon and nitrogen, respectively (since D_{O2}>D_{N2}>D_{Xe}).

Fig. 11 demonstrates the particularity of the flux fluctuations for mixtures xenon-oxygen as transmitted waves for PVTMS film. It was found that the fluxes relatively of which the harmonic vibration occurs are varied from 1.623·10^{-4} for mixture with 10% Xe till 3.166·10^{-4} for mixture with 90%Xe; the wave amplitude from 2.593·10^{-5} for mixture with 10% Xe till 6.154·10^{-5} for mixture with 90%Xe, the phase shift from 0.505 for mixture with 10% Xe till 0.043 for mixture with 90%Xe. In the range of given interval of frequency the wave amplitudes of oxygen and nitrogen do not practically depend on the frequency whereas the xenon amplitude decreases. The selectivity factor fluctuates on periodical (but not sinusoidal) low: the fluctuations are substantial for gas mixtures enriched by Xe and lower for ones with lower content of Xe.

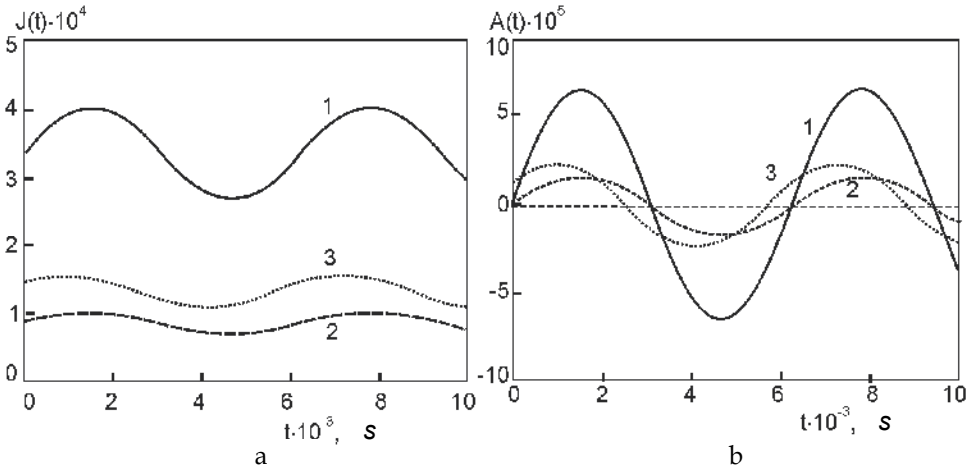

Fig. 11. The concentration waves at the output of membrane for mixture oxygen (30%), xenon (30%) and nitrogen (40%): a – flux fluctuation, b – the variation of the oscillation swing for different gases: 1 – oxygen, 2 – nitrogen, 3 – xenon.

4. Control of gas transfer in membranes

Previously there were considered methods of influence on membrane separation characteristics by variation of conditions at the upstream membrane side. Another group of methods is based on the modification of a membrane i.e. introduction of functional groups into membrane material that leads to acceleration or slowing down of diffusion of one of gas mixture components. Demonstration of application of these methods is presented below.

4.1 Acceleration of diffusion of a component

The improvement of separation can be achieved under as steady as unsteady state conditions by introduction of additional diffusion channel for one of gas mixture components. The model of dissociation diffusion can be applied for this case. The model considers two diffusion channels with diffusion coefficients D_1 and D_2 for a component transfer and possibility of molecules exchange between channels with transition rate constants k_1 and k_2 for transition from channel 1 to 2 and vice versa respectively (equilibrium constant of transition $K = k_1/k_2$). In this case differential equation system of component transfer is as follows:

$$\begin{cases} \dfrac{\partial C_1}{\partial t} = D_1 \dfrac{\partial^2 C_1}{\partial x^2} - k_1 C_1 + k_2 C_2 \\ \dfrac{\partial C_2}{\partial t} = D_2 \dfrac{\partial^2 C_2}{\partial x^2} + k_1 C_1 - k_2 C_2 \end{cases}, \tag{27}$$

where C_1 and C_2 – gas concentration in channels 1 and 2, D_1 and D_2 – diffusion coefficients of gas in channels 1 and 2, k_1 – probability of transition 1→2, k_2 – probability of transition 2→1.
The solution of the system for flat thin film with thickness H and traditional boundary conditions is:

1. Gas flow rate in channel 1:

$$J_1(t) = J_{SS1}\left[1 - \sum_{n=1}^{\infty} \frac{(-1)^n}{A}\left\{\left(\alpha_1 - D_2\omega_n^2 - k_1 - k_2\right)e^{-\alpha_1 t} - \left(\alpha_2 - D_2\omega_n^2 - k_1 - k_2\right)e^{-\alpha_2 t}\right\}\right] \quad (28)$$

2. Gas flow rate in channel 2:

$$J_2(t) = J_{SS2}\left[1 - \sum_{n=1}^{\infty} \frac{(-1)^n}{A}\left\{\left(\alpha_1 - D_1\omega_n^2 - k_1 - k_2\right)e^{-\alpha_1 t} - \left(\alpha_2 - D_1\omega_n^2 - k_1 - k_2\right)e^{-\alpha_2 t}\right\}\right] \quad (29)$$

where $\omega = \pi n / H$,

$$J_{SS1} = \frac{AD_1S_1p_u}{H} \quad (30)$$

$$J_{SS2} = \frac{AD_2S_2p_u}{H} \quad (31)$$

$$\alpha_1(\omega) = 0.5\left[\left(D_1 + D_2\right)\omega^2 + k_1 + k_2\right] - A(\omega) \quad (32)$$

$$\alpha_2(\omega) = \alpha_1(\omega) + 2A(\omega) \quad (33)$$

$$A(\omega) = 0.5\sqrt{\left(D_1 - D_2\right)^2\omega_n^4 + 2\left(D_1 - D_2\right)\left(k_1 - k_2\right)\omega_n^2 + \left(k_1 + k_2\right)^2}\ , \quad (34)$$

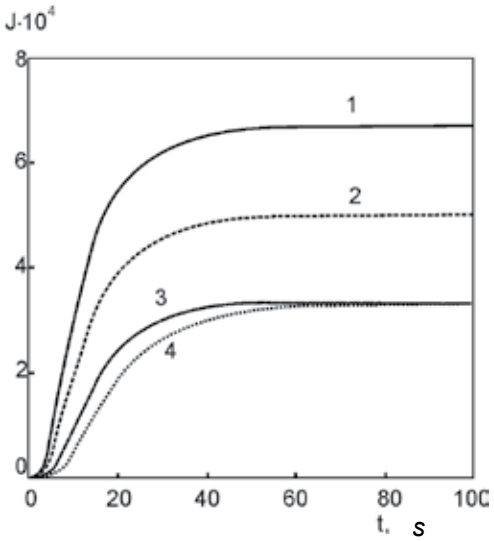

Fig. 12. Unsteady oxygen flow rate through PVTMS membrane: 1 – oxygen flow rate in channel 1, 2 – overall flow rate (individual flow rates are involved with weight 0.5), 3 – oxygen flow rate in channel 2, 4 – oxygen flow rate for classical diffusion mechanism.

Overall flow rate through membrane (with contribution of each flux 0.5) is:

$$J(t) = 0.5\left[J_1(t) + J_2(t)\right] \tag{35}$$

Calculation was carried out with following values of parameters: A=10, H=0.01, p=76, t=1-200. It was assumed that dissociation diffusion mechanism is realized for oxygen while transfer of nitrogen occurs by classical diffusion mechanism. Parameters for oxygen: D_1=7.6x10^{-7}, D_2=D_1, S_2=S_1=5.79x10^{-3}, k_1=0.1 and k_2=0.1 (K=1). Parameters for nitrogen: D=3.6x10^{-7}, S=3.06x10^{-3}. Obtained dependencies are presented in Fig. 12. One can see that additional channel decreases the time of unsteady state.

Fig. 13 represents unsteady separation factor for oxygen/nitrogen gas pair. Introduction of additional diffusion channel increases value of separation factor α (steady state value increases from 4 to 6). Transition rate constants have no influence on steady state separation factor value. At initial time increasing of K leads to increasing of separation factor but these effects are relatively small.

The influence of introduction of additional diffusion channel on separation when pulse function variation of gas concentration in upstream is applied is shown in Fig. 14. Calculation was carried out for the same parameters determined above except D_2=5D_1. Oxygen transfer by dissociation diffusion mechanism (diffusion in two parallel channels with reversible exchange of gas molecules among them) leads to drastic increase of peak height and its displacement to lower times compared to classical diffusion mechanism.

Fig. 15 represents similar data for air (21% of O_2, 78% of N_2). In case of diffusion by classical mechanism there is no clear separation while in case of dissociation diffusion of oxygen (and classical diffusion of nitrogen) at k_1=k_2=0.1 (K=1) the bimodal shape of overall peak is noticeable due to displacement of oxygen peak to lower times. When transition rate constants are k_1=1 and k_2=0,1 (K=10) overall peak clearly expands to two components so that almost pure oxygen passes through membrane at lower times and nitrogen at higher times.

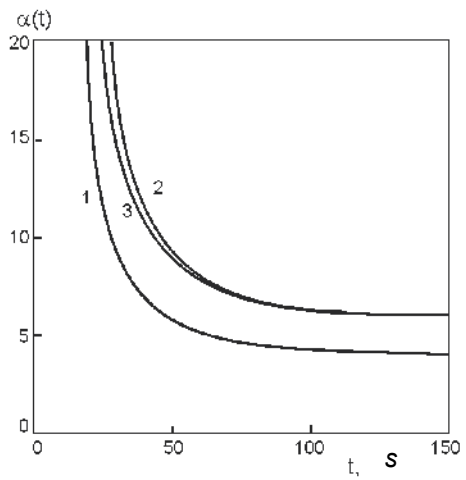

Fig. 13. Unsteady separation factor $\alpha_{O2/N2}$: 1 – "classical" diffusion, 2 – K=1, 3 – K=10.

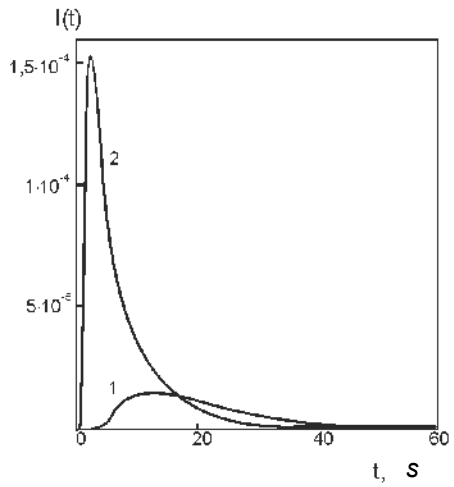

Fig. 14. Comparison of oxygen concentration peaks deformation for delta-function impulse transfer through PVTMS membrane: 1 – oxygen diffusion by classical mechanism, 2 – oxygen diffusion by dissociation mechanism.

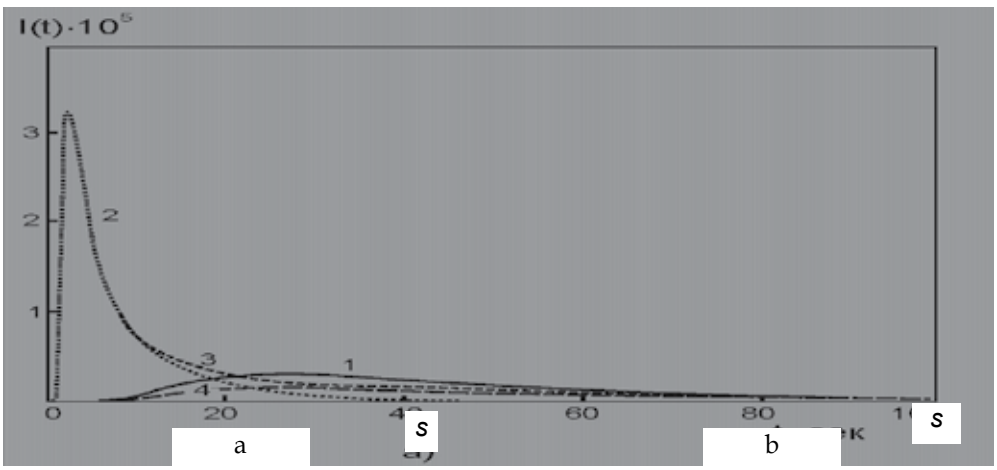

Fig. 15. Separation of air, pulse function variation of gas concentration in upstream: a – transition rate constants k_1=k_2=0.1 (K=1), b – transition rate constants k_1=1, k_2=0.1 (K=10). 1 – air transfer by classical diffusion mechanism; dissociation diffusion of oxygen: 2 – oxygen flow rate, 3 – overall flow rate, 4 – nitrogen flow rate.

4.2 Slowing down of diffusion of a component

Another approach of improvement of membrane separation characteristics under unsteady mass transfer conditions is slowing down of diffusion of one of gas mixture components. Such effect can be achieved by introduction of chemically active centers (functional groups) into membrane material which one of gas mixture components reacts with. In case of the first order reversible chemical reaction the mass transfer of reacting component is described by following differential equation system:

$$\begin{cases} \dfrac{\partial C_1}{\partial t} = D_1 \dfrac{\partial^2 C_1}{\partial x^2} - k_1 C_1 + k_2 C_2 \\ \dfrac{\partial C_2}{\partial t} = k_1 C_1 - k_2 C_2 \end{cases}, \tag{36}$$

where C_1 and C_2 – component concentration in membrane medium and chemically active centers, respectively, D – diffusion coefficient, k_1 and k_2 – primary and reversible chemical reaction rate constants, respectively.

System (36) has analytical solution. Unsteady gas flow rate trough membrane can be expressed as follows:

$$J = \frac{DSAp_u}{H}\left\{1 - \sum_{n=1}^{\infty} \frac{(-1)^n}{A}\left[\left(\alpha_1 - k_1 - k_2\right)e^{-\alpha_1 t} - \left(\alpha_2 - k_1 - k_2\right)e^{-\alpha_2 t}\right]\right\}, \tag{37}$$

where $\omega = n\pi/H$, n=1, 2, ...,

$$\alpha_1 = 0.5\left(k_1 + k_2 + D\omega^2\right) - A \tag{38}$$

$$\alpha_2 = 0.5\left(k_1 + k_2 + D\omega^2\right) + A \tag{39}$$

$$A = \sqrt{k_1 k_2 + 0.25\left(k_1 - k_2 + D\omega^2\right)^2} \tag{40}$$

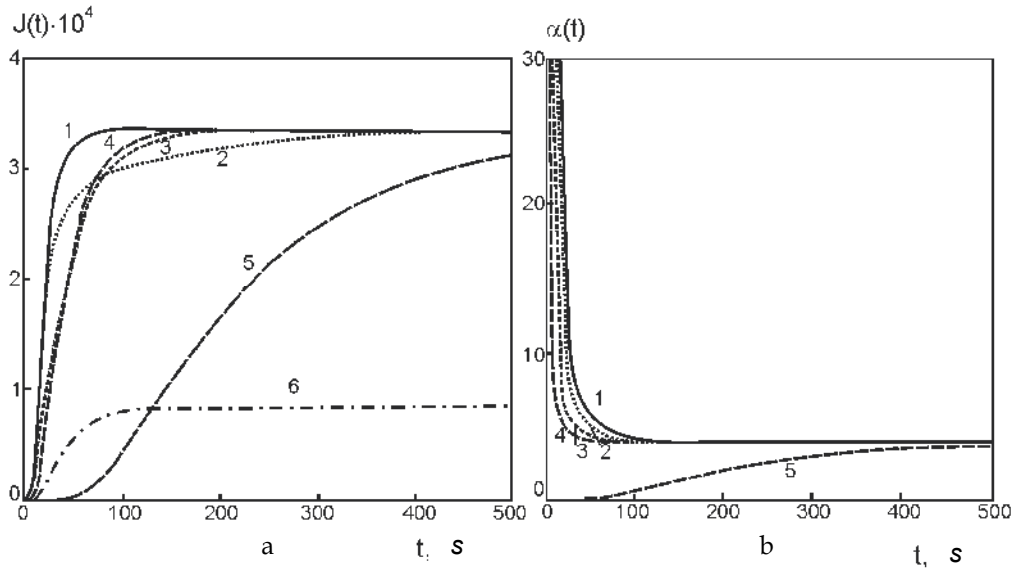

Fig. 16. The influence of reversible chemical sorption on unsteady oxygen transfer: a – unsteady oxygen flow rate; b – unsteady separation factor (1 – diffusion of oxygen by classical mechanism; diffusion with chemical sorption: 2 – k_1=k_2=0.01; 3 – k_1=k_2=0.1; 4 – k_1=k_2=1; 5 – k_1=10, k_2=1; 6 – unsteady nitrogen transfer).

Calculation was carried out with the same main parameters which were defined in previous section. Fig. 16(a) represents the influence of chemical sorption and values of reaction rate constants on unsteady oxygen flow rate through membrane, and Fig. 16(b) represents the influence of these parameters on unsteady oxygen/nitrogen separation factor. Figures demonstrate that capture of oxygen by chemically active centers significantly affect the shape of flow rate curves, especially at high values of chemical equilibrium constant ($K=k_1/k_2$). Capture of oxygen leads to slowing down of its diffusion and decreasing of efficiency of oxygen from nitrogen separation.

4.3 Example of modeling of unsteady CO2 transfer in liquid membrane with chemical absorbent

It is known that insertion of practically interesting quantities of immobilization centers into polymer matrix can be difficult. At the same time there is a class of membranes where insertion of desirable substances in membrane media is very simple. This class is represented by liquid membranes (LMs). In spite of their disadvantages such as degradation, complexity of preparation, sensitivity to pressure drop etc., LMs show extremely high selectivity for particular gas pares and are interesting as an object of fundamental studies. Practical example of theoretical description and calculation of unsteady CO_2 transfer in LM and the comparison of theoretical results with experimental data is presented in this section.

It was shown experimentally that step function supply of CO_2/N_2 gas mixture over LM with aqueous potassium carbonate (chemical absorbent of CO_2) results in establishing of the steady N_2 flux through the membrane after 50 seconds while CO_2 flux through the membrane rises only up to 10% of the steady state value after 250 seconds in spite of almost equal magnitudes of N_2 and CO_2 diffusion coefficients. Such slow increasing of CO_2 flow rate is caused by interaction of CO_2 with carbonate ions that leads to formation of bicarbonate ions. This situation is simultaneously similar to both ones described in previous sections: capture of CO_2 molecules on the one hand and its additional transfer due to diffusion and reversible reaction of bicarbonate ions with releasing of CO_2 on the other side of membrane on the other hand. Therefore the time of achievement of the steady state of CO_2 transfer is higher (due to CO_2 capture) and final value of CO_2 flow rate is also higher (due to additional CO_2 transfer in bicarbonate ion form) compared to the case where chemical absorption is absent. This example shows that under unsteady state conditions such membrane provides N_2-rich permeate at the beginning and CO_2-rich permeate after certain time (since steady-state CO_2 permeance is higher).

The description and analysis of CO_2 transfer in this case is more complex than described in previous sections because carbonate ions are mobile and can be considered as CO_2 "carriers" that introduces the necessity to take into account their transfer in LM as well as transfer of CO_2 in the form of bicarbonate ions and interactions between all reactants. Another particularity of considered example is that reaction of CO_2 with aqueous potassium carbonate is the second order reversible chemical reaction therefore analytical solution of differential equation system of mass transfer can not be obtained. Numerical methods of the differential equation system solution are the only that can be applied for calculations. The scheme and coordinates of considered LM is shown in Fig. 17. LM is formed between two polymeric membranes which are asymmetric with thin dense layer turned to the liquid phase. The permeance of polymeric membranes is two orders higher than permeance of LM and thickness of dense layer is three orders lower than thickness of LM. The time of establishing of steady state mass transfer through polymeric membranes is four orders

lower than for LM, therefore unsteady mass transfer in polymeric membranes can be neglected. Presented below mathematical model of CO_2 transfer in LM with aqueous potassium carbonate is based on the following assumptions: isothermal conditions; diffusion and solubility coefficients of the components are independent from concentration changes caused by diffusion and chemical reactions; components of gas phase (i.e. CO_2, N_2 etc.) are the only volatile species; a negligible change in the liquid phase volume during absorption of volatile components; concentration of volatile components in molecular form in the membrane and the liquid phase obeying Henry's law.

The approach of CO_2 interaction with aqueous potassium carbonate can be found in numerous studies (Cents et al., 2005; Chen et al., 1999; Danckwerts & Sharma, 1966; Dindore et al., 2005; Lee et al., 2001; Morales-Cabrera et al., 2005; Otto & Quinn, 1971; Pohorecki & Kucharski, 1991; Suchdeo & Schultz 1974; Ward & Robb, 1967).

The mechanism is based on accounting of four reactions. When potassium carbonate dissolves in water it dissociates with formation of metal and carbonate ions. The reaction of carbonate ions with water gave rise to bicarbonate and hydroxyl ions:

$$CO_3^{2-} + H_2O \overset{K'_C}{\Leftrightarrow} HCO_3^- + OH^- \tag{41}$$

Almost in all the studies mentioned above this reaction (and corresponding expression for calculation of the reaction equilibrium constant) is given in the following alternative form:

$$HCO_3^- + H_2O \overset{K_C}{\Leftrightarrow} H_3O^+ + CO_3^{2-} \tag{42}$$

These two reactions are interconnected by the reaction of dissociation of water:

$$2H_2O \overset{K_W}{\Leftrightarrow} H_3O^+ + OH^- \tag{43}$$

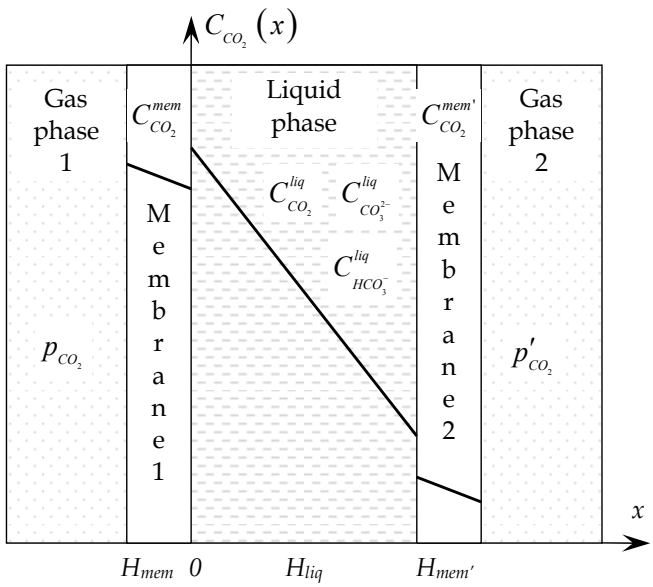

Fig. 17. The scheme and coordinates of LM used in mathematical model.

The interaction of CO_2 with the potassium carbonate solution occurs by two parallel reactions:

$$CO_2 + 2H_2O \underset{k_{-1}}{\overset{k_1}{\Leftrightarrow}} H_3O^+ + HCO_3^- \tag{44}$$

$$CO_2 + OH^- \underset{k_{-2}}{\overset{k_2}{\Leftrightarrow}} HCO_3^- \tag{45}$$

The overall reaction of CO_2 with carbonate ion can be represented as follows:

$$CO_2 + CO_3^{2-} + H_2O \Leftrightarrow 2HCO_3^- \tag{46}$$

Reactions (44) and (45) are rate controlling reactions and reactions (41) and (43) can be considered as instantaneous reactions. Therefore concentrations of H_3O^+, OH^- and CO_3^{2-} are assumed to be always in equilibrium that allows to define reaction rate term of CO_2 as follows:

$$R_{CO_2}^{liq} = C_{HCO_3^-}^{liq}\left(k_{-1}K_C\frac{C_{HCO_3^-}^{liq}}{C_{CO_3^{2-}}^{liq}} + k_{-2}\right) - C_{CO_2}^{liq}\left(k_1 + k_2\frac{K_W C_{CO_3^{2-}}^{liq}}{K_C C_{HCO_3^-}^{liq}}\right) \tag{47}$$

Reaction rate terms of CO_3^{2-} and HCO_3^- are following from Eq. (46):

$$R_{CO_3^{2-}}^{liq} = R_{CO_2}^{liq} \tag{48}$$

$$R_{HCO_3^-}^{liq} = -2R_{CO_2}^{liq} \tag{49}$$

Here it is assumed that the activity coefficients of all species are equal to unity. Equations permitting calculations of the reaction rate and equilibrium constants can be found in the literature and are presented in Table 1.

Thus, in addition to the CO_2 transfer in the liquid phase it is necessary to take into account the transfer and interaction of carbonate ions and bicarbonate ions. The differential equation system of unsteady mass transfer in liquid phase can be represented as follows:

$$\begin{cases} \dfrac{\partial C_{CO_2}^{liq}(x,t)}{\partial t} = D_{CO_2}^{liq}\dfrac{\partial^2 C_{CO_2}^{liq}(x,t)}{\partial x^2} + R_{CO_2}^{liq}(x,t) \\ \dfrac{\partial C_{CO_3^{2-}}^{liq}(x,t)}{\partial t} = D_{CO_3^{2-}}^{liq}\dfrac{\partial^2 C_{CO_3^{2-}}^{liq}(x,t)}{\partial x^2} + R_{CO_2}^{liq}(x,t) \\ \dfrac{\partial C_{HCO_3^-}^{liq}(x,t)}{\partial t} = D_{HCO_3^-}^{liq}\dfrac{\partial^2 C_{HCO_3^-}^{liq}(x,t)}{\partial x^2} - 2R_{CO_2}^{liq}(x,t) \end{cases} \tag{50}$$

Boundary conditions at the membrane-gas phase interface:

$$C_{CO_2}^{m}(-H_m,t) = p_{CO_2}(t)S_{CO_2}^{m} \tag{51}$$

Constant	Equation	Units	Ref.
k_1	$\log_{10} k_1 = 329.85 - 110.541 \log_{10} T - 17265.4 / T$	s^{-1}	Danckwerts & Sharma, 1966
k_2	$\log_{10} k_2 / k_2^{\infty} = 0.08I$	l/(mol·s)	Rahimpour & Kashkooli, 2004
	$\log_{10} k_2^{\infty} = 13.635 - 2895 / T$	l/(mol·s)	Danckwerts & Sharma, 1966
K_1	$\log_{10} K_1 = 14.843 - 0.03279T - 3404.7 / T$	mol/l	Danckwerts & Sharma, 1966
K_2	$K_2 = K_1 / K_4$	l/mol	Danckwerts & Sharma, 1966
K_C	$\log_{10} K_C^{\infty} = 6.498 - 0.0238T - 2902.4 / T$	mol/l	Danckwerts & Sharma, 1966
K_W	$\log_{10} K_W = -23.5325 + 0.03184T$	mol^2/l^2	Lee et al., 2001
D_{CO_2}	$D_{CO_2} = \frac{0.0235 \times \exp(-2119 / T)}{(1 + 0.354M)^{0.82}}$	cm^2/s	Lee et al., 2001
$D_{HCO_3^-}$	$D_{HCO_3^-} = D_{CO_3^{2-}} = D_{CO_2} \sqrt{\mu_{CO_2} / \mu_{HCO_3^-}}$	cm^2/s	Otto & Quinn, 1971
S_{CO_2}	$\log_{10} S_{CO_2} = -5.30 + 1140 / T - 0.125M$	mol/(l·atm)	Lee et al., 2001

Table 1. Values employed in the calculations.

$$C_{CO_2}^{m'}(H_{liq} + H_{m'}, t) = p'_{CO_2}(t) S_{CO_2}^{m'} \tag{52}$$

Boundary conditions at the membrane-liquid phase interface:

$$\frac{C_{CO_2}^{liq}(0,t)}{S_{CO_2}^{liq}} = \frac{C_{CO_2}^{m}(0,t)}{S_{CO_2}^{m}} \tag{53}$$

$$\frac{C_{CO_2}^{m'}(H_{liq},t)}{S_{CO_2}^{m'}} = \frac{C_{CO_2}^{liq}(H_{liq},t)}{S_{CO_2}^{liq}} \tag{54}$$

$$D_{CO_2}^{liq} \frac{\partial C_{CO_2}^{liq}(0,t)}{\partial x} = D_{CO_2}^{m} \frac{C_{CO_2}^{m}(0,t) - C_{CO_2}^{m}(-H_m,t)}{H_m} \tag{55}$$

$$D_{CO_2}^{liq} \frac{\partial C_{CO_2}^{liq}(H_{liq},t)}{\partial x} = D_{CO_2}^{m'} \frac{C_{CO_2}^{m'}(H_{liq} + H_{m'},t) - C_{CO_2}^{m'}(H_{liq},t)}{H_{m'}} \tag{56}$$

$$\frac{\partial C_{CO_3^{2-}}^{liq}(0,t)}{\partial x} = \frac{\partial C_{CO_3^{2-}}^{liq}(H_{liq},t)}{\partial x} = \frac{\partial C_{HCO_3^-}^{liq}(0,t)}{\partial x} = \frac{\partial C_{HCO_3^-}^{liq}(H_{liq},t)}{\partial x} = 0 \tag{57}$$

Initial conditions:

$$C^{liq}_{CO_2}(x,0) = \overline{C}^{liq}_{CO_2} \tag{58}$$

$$C^{liq}_{CO_3^{2-}}(x,0) = \overline{C}^{liq}_{CO_3^{2-}} \tag{59}$$

$$C^{liq}_{HCO_3^-}(x,0) = \overline{C}^{liq}_{HCO_3^-} \tag{60}$$

This model can be extended for the description of gas mixture transfer by addition of mass transfer equations of other components. The comparison between calculation and experimental data is shown in Figs. 18 and 19.

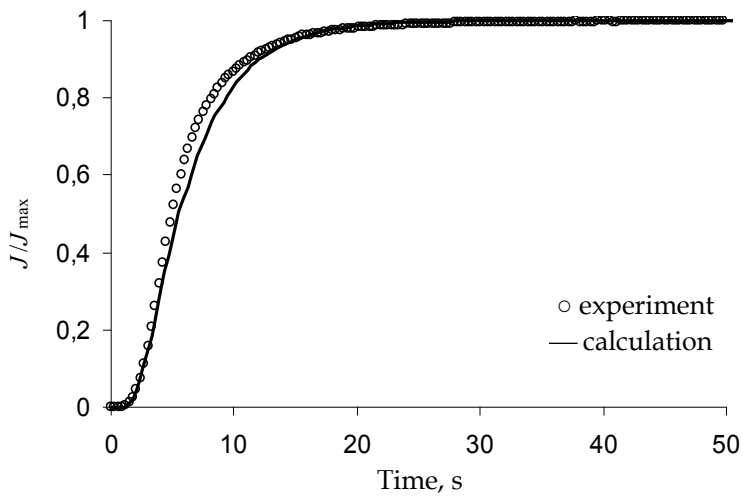

Fig. 18. Unsteady CO_2 transfer through LM with distilled water.

Theoretical and experimental dependencies are almost identical for the LM with distilled water (Fig. 18) and the time of unsteady CO_2 transfer is about 30 seconds. In case of LM with potassium carbonate theoretical and experimental dependencies show a significant increase in the time of unsteady transfer for highly concentrated solutions up to 800 seconds. This is the result of the CO_2 consumption by a non-saturated potassium carbonate solution during its diffusion through the liquid phase. The more concentrated the solution, the more time is needed for its saturation. Theoretical dependencies in Fig. 19 display faster increase in CO_2 flux as compared to their experimental counterparts. The explanation of this behavior can be the influence of heat effects during CO_2 absorption by non-saturated solution that was not taken into account.

Unsteady transfer of other gases such as N_2, O_2 etc. through LM is very close to one represented in Fig. 18 even at high concentration of potassium carbonate in liquid phase, therefore at initial time effective separation of such components as N_2, O_2 etc. from CO_2 is possible.

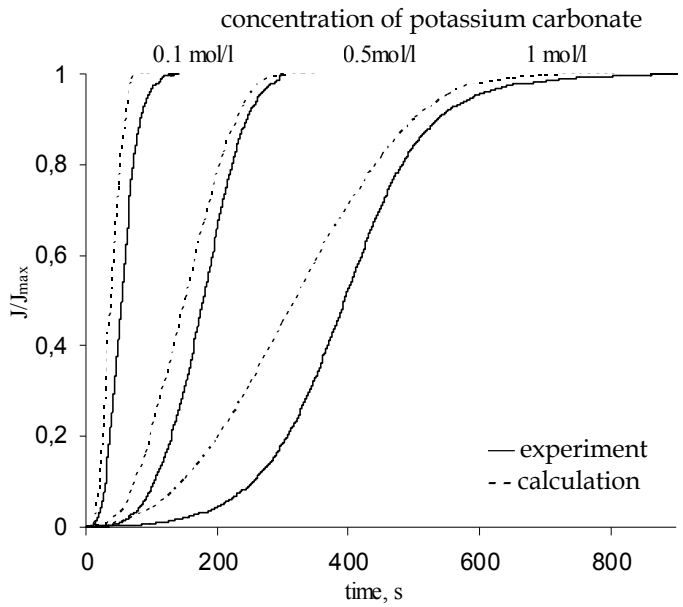

Fig. 19. Unsteady CO_2 transfer through LM with potassium carbonate.

5. Conclusion

As it follows from results of mathematical modeling the application of unsteady mass transfer regimes allows effectively control the selectivity of gas mixture separation by membrane. Particularly, the application of pulse and harmonic oscillations of gas concentration permits to adjust separation process by variation of frequency causing variation of amplitude and phase of the concentration waves passing through a membrane and therefore variation of productivity and selectivity of separation. This technique can provide extremely high separation factors at initial times but unfortunately at low productivity. For O_2/N_2 gas mixture concentration wave method is low effective but for Xe/N_2 and Xe/O_2 good separation can be obtained. The study of unsteady mass transfer is important for development of gas sensors with membrane coating since they have low selectivity and therefore respond to all components of gas mixture. Important task in this case is restoring of initial composition of gas at the registration system inlet and actual function of variation of composition during the time based on the sensor response after membrane. Increasing or decreasing of unsteady selectivity can be controlled by creation of new membrane materials and systems with partial or complete immobilization on functional groups introduced in membrane medium. Suggested mathematical apparatus allows to solve these tasks and to formulate requirements to the system "membrane-gas mixture" for realization of unsteady highly effective gas separation processes.

The development of mathematical apparatus of selective unsteady transfer of gas mixtures through membranes is necessary for development of phenomenological description of dynamics of mass transfer of O_2, N_2 and CO_2 in breathing apparatus of humans and animals for understanding of functioning of live organisms.

6. List of symbols

A	membrane area [m^2] or concentration wave amplitude
C	concentration [kmol/m^3]
D	diffusivity [m^2/s]
d	width/half-width of peak
H	thickness of membrane [m]
I	ionic strength of solution [kg ion/m^3]
J	gas flow rate [kmol/s] or [m^3/s]
j	pulse response function [kmol/(m^2·s^2)]
k	reaction rate constant
K	reaction equilibrium constant
L	length [m]
M	initial concentration of K_2CO_3 in solution [kmol/m^3]
m, n	integer number
P	permeability coefficient
p	gas partial pressure [Pa]
q	volume of gas [m^3]
R	formation/consumption rate of a component [kmol/(m^3·s)]
S	solubility [kmol/(m^3·Pa)]
T	temperature [K]
t	time [s]
x	coordinate [m]

Subscripts/Superscribts

∞	infinite dilution
A, B	gas mixture components
d	downstream
liq	liquid phase
mem	membrane phase
SS	steady state
US	unsteady state
u	upstream
W	water

Greek

a	selectivity/separation factor
γ	parameter
Δ	asymmetry parameter
Φ	contributions of a component into permeation flux
φ	phase shift
μ	molar mass [kg/kmol]
ω	frequency

7. References

Baker, R. (2002). Future direction of membrane gas separation technology. *Ind. Eng. Chem. Res.*, Vol.41, pp. 1393-1411

Baker, R. (2004). *Membrane technology and application*, *2nd ed.*, John Wiley & Sons Ltd., California, USA

Beckman, I.; Shelekhin, A. & Teplyakov, V. (1989). Membrane separation of gas mixture under unsteady state conditions. *DAN USSR*, Vol.308, No.3, pp. 635-637 (In Russian)

Beckman, I.; Shelekhin, A. & Teplyakov, V. (1991). Separation of gas mixtures in unsteady-state conditions. *J. Membrane Sci.,* Vol.55, pp. 283-297

Beckman, I. (1993). Unusual membrane processes: non-steady state regimes, nonhomogeneous and moving membranes, In: *Polymeric Gas Separation membranes*, D.R. Paul & Yu.P. Yampolskii, (Eds.), 301-352, CRC Press, Boca Raton, Florida, USA

Beckman, I.; Zheleznov, A. & Loza, K. (1996). Concentration wave method in diagnostics of inhomogeneity of material structure, *Vestnik MGU, Series 2: Chemistry*, Vol.37, No.2, pp. 173-176 (In Russian)

Cents, A.; Brilman, D. & Versteeg, G. (2005). CO_2 absorption in carbonate/bicarbonate solutions: the Danckwerts-criterion revisited. *Chem. Eng. Sci.,* Vol.60, pp. 5830-5835

Chen, H.; Kovvali, A., Majumdar, S. & Sirkar, K. (1999). Selective CO_2 separation from CO_2-N_2 mixtures by immobilized carbonate-glycerol membranes. *Ind. Eng. Chem. Res.,* Vol.38, pp. 3489-3498

Crank, J. (1975). *The mathematics of diffusion*, Clarendon Press, Oxford, UK

Danckwerts, P. & Sharma, M. (1966). The absorption of carbon dioxide into solutions of alkalis and amines (with some notes on hydrogen sulphide and carbonyl sulphide). *Chem. Eng.*, Vol.44, pp. CE244-CE280

Dindore, V.; Brilman, D. & Versteeg, G. (2005). Modelling of cross-flow membrane contactors: mass transfer with chemical reactions. *J. Membrane Sci.,* Vol.255, pp. 275-289

Hwang, S.-T. & Kammermeyer, K. (1975). *Membranes in Separations*, John Wiley & Sons, New York, USA

Lee, Y.; Noble, R., Yeomb, B., Park, Y. & Lee, K. (2001). Analysis of CO_2 removal by hollow fiber membrane contactors. *J. Membrane Sci.,* Vol.194, No.1, pp. 57-67

Morales-Cabrera, M.; Perez-Cisneros, E. & Ochoa-Tapia J. (2005). An approximate solution for the CO_2 facilitated transport in sodium bicarbonate aqueous solutions. *J. Membrane Sci.,* Vol.256, pp. 98-107

Otto, N. & Quinn, J. (1971). The facilitated transport of carbon dioxide through bicarbonate solutions. *Chem. Eng. Sci.,* Vol.26, pp. 949-961

Paul, D. (1971). Membrane separation of gases using steady cyclic operation. *Ind. Eng. Chem. Process Des. Develop.*, Vol.10, No.3, pp. 375-379

Pohorecki, R. & Kucharski, E. (1991). Desorption with chemical reaction in the system CO_2-aqueous solution of potassium carbonate. *Chem. Eng. J.,* Vol.46, pp. 1-7

Rahimpour, M. & Kashkooli, A. (2004). Enhanced carbon dioxide removal by promoted hot potassium carbonate in a split-flow absorber. *Chem. Eng. and Processing,* Vol.43, pp. 857

Shalygin, M.; Okunev, A., Roizard, D., Favre, E. & Teplyakov, V. (2006). Gas permeability of combined membrane systems with mobile liquid carrier. *Colloid Journal* Vol.68, pp. 566-574 (In Russian)

Suchdeo, S. & Schultz, J. (1974). The permeability of gases through reacting solutions: the carbon dioxide-bicarbonate membrane system. *Chem. Eng. Sci.,* Vol.29, No.1, pp. 13-23

Ward, W. & Robb, W. (1967). Carbon dioxide-oxigen separation: facilitated transport of carbon dioxide across a liquid film. *Science* Vol.156, pp. 1481-1484

11

Effect of Mass Transfer on Performance of Microbial Fuel Cell

Mostafa Rahimnejad, Ghasem Najafpour and Ali Asghar Ghoreyshi
Babol Noshirvani University
Iran

1. Introduction

As the energy sources decrease and the climate conditions change, demand for new and clean sources of energy has increased (Hong et al., 2009; Li et al., 2010a). Fuel cells , as a high efficiency energy converting device, have attracted more and more attention recently with low/zero emission (Liu et al., 2006). Moreover, conventional sewage treatment requires high energy and capital cost so there is great interest for finding clean and sustainable energy with very low or zero emission and cost effective that is an alternative for treatment technology (Appleby, 1988; Min et al., 2005).

Microbial fuel cells (MFCs) are one kind of fuel cell and also new source of energy. In MFCs, electrons are supplied from chemical bonds with the aids of microorganisms. Then the produced electrons are transported to anode surfaces and protons are moved through proton exchange membrane or salt bridge toward cathode (Wen et al., 2009). The electron flows through an electrical external circuit while anode is connected to cathode. The flow of electron has a current (I) and power (P) is resulted. The reduction of organic substances in anode was catalyzed by the living organism in anode chamber (Chen et al., 2008; Rahimnejad et al., 2009)

Traditional MFC is consist of two separated chambers named cathode and anode ones. Oxidation of substrate by microorganisms leads to generation of electrons and protons in anaerobic anode compartment. (Rahimnejad et al., 2009). A typical biological fuel cell is shown schematically in Fig.1.

Several parameters affect on the performance of MFC, namely microbial inoculums, chemical substrates, mass transfer area, absence or existence of proton exchange materials, mechanism of electron transfer to the anode surface ,cell internal and external resistance, solution ionic strength, electrode materials and the electrode spacing (Park and Zeikus, 2000; Gil et al., 2003; Rosenbaum et al., 2007; Zhang et al., 2007; Li et al., 2010b)

Direct electron transfers from anaerobic anode chamber to anode surface had shown to take place only at very low efficiency (Park et al., 2000; Lovley, 2006) . Electron transfer efficiencies in MFCs would be improved with the use of suitable electron mediators. Most MFCs use electron mediator component to improve the output of the cells. It has been reported in the literature that mediators are artificially added to anode chamber, such as Methylen blue (MB), Neutral red (NR), Thionin, Ferricyanide, Humic acid or Methyl viologen (Kim and Lee). The presence of artificial electron mediators are essential in some of MFCs to improve the performance of MFCs (Park and Zeikus, 1999; 2000) . But recently,

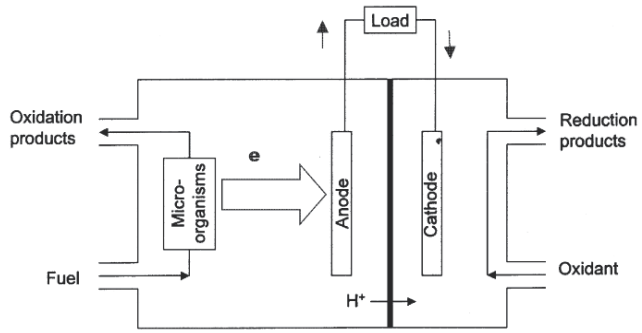

Fig. 1. A typical MFC representing current generation with the help of microorganisms (Shukla et al., 2004)

mediators less MFCs became an interesting issue for many researchers (Kim et al., 2002; Chaudhuri and Lovley, 2003; Venkata Mohan et al., 2007; Huang et al., 2008; Venkata Mohan et al., 2008) . Table 1 shows a list of MFCs were examined with or without mediators used as component along with substrate.

Microorganism	Substrate	Mediators	Reference
Geobacter sulfurreducens	Acetate	Without mediator	(Bond and Lovley, 2003)
Saccharomyces cerevisiae	Hydrolyzed Lactose	MB, NR	(Najafpour et al.)
Saccharomyces cerevisiae	Glucose	NR	(RAHIMNEJAD et al.; Rahimnejad et al., 2009)
Saccharomyces cerevisiae	Glucose	Resorufin	(Ganguli and Dunn, 2009)
Aeromonas hydrophila	Glucose, Acetate	Without mediator	(Pham et al., 2003)
Enterococcus faecium	Glucose	Pyocyanin	(Rabaey et al., 2005a)
Streptococcus lactis	Glucose	Ferric Chelate complex	(Vega and Fernández, 1987)
Proteus vulgaris	Glucose, Maltose, Galactose	Thionin	(Lee et al., 2002)
Gluconobacter oxydans	Glucose	HNQ, Resazurin, Thioninee	(Lee et al., 2002)
Shewanella putrefaciens	Lactate	Without mediator	(Kim et al., 2002)
Domestic wste water	Glucose, Xylose	Humic acid	(Thygesen et al., 2009)
Geobacter sulfurreducens	Acetate	Without mediator	(Yi et al., 2009)
Rhodoferax ferrireducens	Glucose	Without mediator	(Chaudhuri and Lovley, 2003)
Activated sludge	Waste water	Without mediator	(Kim et al., 2004)
Mixed consortium	Glucose, Sucrose	Without mediator	(Rabaey et al., 2005b)
Actinobacillus succinogenes	Glucose	NR, Thionine	(Park and Zeikus, 2002)
Klebsiella pneumoniae	Glucose	HNQ	(Rhoads et al., 2005)
Micrococcus luteus	Glucose	Thionine	(Choi et al., 2007)
Shewanella oneidensis	Lactate	Anthraquinone-2,6-disulfonate (AQDS)	(Ringeisen et al., 2006)
Escherichia coli	Glucose, Acetate	NR, 2-Hydroxy-1,4-Naphthoquinone, MB	(Bennetto, 1990; Park et al., 2000; Schröder et al., 2003; Grzebyk and Pozniak, 2005; Ieropoulos et al., 2005)
Proteus vulgaris	Glucose, Sucrose	Thioninee	(Bennetto et al., 1985; Thurston et al., 1985; Shin et al., 2006)
Proteus mirabilis	Glucose	Thionine	(Choi et al., 2003)
Shewanella putrefaciens	Glucose, Lactate	Without mediator	(Kim et al., 2002)

Table 1. Microorganisms used in MFC

Commonly oxygen as terminal electron acceptor was used in cathode compartment. Consumption of electrons and protons that are combined with oxygen, forms water at last, and end this transfer cycle. Oxidized mediators, can also accelerate reaction of forming water in cathode chamber (Heitner-Wirguin, 1996).
The objective of this chapter was to demonstrate the power production from glucose as sole electron donors in MFC. But the main purpose of this present research was to investigated the effect of mass transfer area on MFCs performance.

2. Materials and methods

2.1 Microorganism and cultivation

Saccharomyces cerevisiae PTCC 5269 was supplied by Iranian Research Organization for Science and Technology (Tehran, Iran). The microorganisms were grown at anaerobic condition in an anaerobic jar vessel. The prepared medium for seed culture consisted of glucose, yeast extract, NH_4Cl, NaH_2PO_4, $MgSO_4$ and $MnSO_4$: 10, 3, 0.2, 0.6, 0.2 and 0.05 $g.l^{-1}$, respectively.
The medium pH was initially adjusted to 6.5 and the inoculums were introduced into the media at ambient temperature. The inoculated cultures were incubated at 30°C. The bacteria were fully grown in a 100ml flask without any agitation for the duration of 24 hours. Substrate consumption was calculated based on determination of the remaining sugars in the culture. Growth was monitored by measuring the optical density (OD at 620_{nm}). Substrate consumption was calculated based on determination of the remained sugars in the culture according to Sadasivam and Manickam(Sadasivam and Manickam, 2005).

2.2 Chemical and analysis

All chemicals and reagents used for the experiments were analytical grades and supplied by Merck (Darmstadt, Germany). The pH meter, HANA 211(Romania) model glass-electrode was employed to measure pH values of the aqueous phase. The initial pH of the working solution was adjusted by addition of diluted HNO3 or 0.1M NaOH solutions. Dinitrosalicylic acid [3, $5(NO_2)_2C_6H_2$-2OH-COONa.H_2O] (DNS) method was developed to detect and measure substrate consumption using colorimetric method. Before analysis, liquid samples were filtered by a 0.45 µm syringe membrane (Sartorius Minisart).
Scan Electron Microscope (SEM): The anode electrode before and at the end of the experiment was examined by a Scanning Electronic Microscope (SEM) (Phillips XL30, Holland). Finally, images of the samples were taken under SEM at magnifications of 5000. SEM images were used to demonstrate the physical characteristics of the electrode surface and to examine the growth of yeast on the anode surface.

2.3 MFC

Different kinds of MFCs were made up to investigation of mass transfer area on performance of MFC. All MFCs fabricated from Plexiglas material were used as MFCs in laboratory scale. The volume of each chamber (anode and cathode chambers) was 800 ml with a working volume of 615 ml. The sample port was provided for the anode chamber, wire point input and inlet port. The selected electrodes in MFC were graphite plates, size of 40×70×1.2mm. Proton exchange membrane (PEM; NAFION 117, Sigma–Aldrich) was used to separate two compartments. Proton exchange membrane, nafion, was subjected to a course of pretreatment to take off any impurities that was boiling for 1h in 3% H_2O_2, washed with deionized water, 0.5 M H_2SO_4, and finally washed with deionized water. In order to maintain membrane for good conductivity, the anode and cathode compartments were filled with deionized water

when the MFC was not in use. Neutral red and potassium permanganate were also supplied by Merck Company (Darmstadt, Germany) as mediators and oxidizer agent in continues mode, respectively. The schematic diagram, photographic images and auxiliary equipments of the fabricated MFC cell in batch and continuous systems are shown in Fig. 2. In continuous operation, the MFC was continuously fed with the prepared media in an up-flow mode using an adjustable peristaltic pump (THOMAS, Germany).

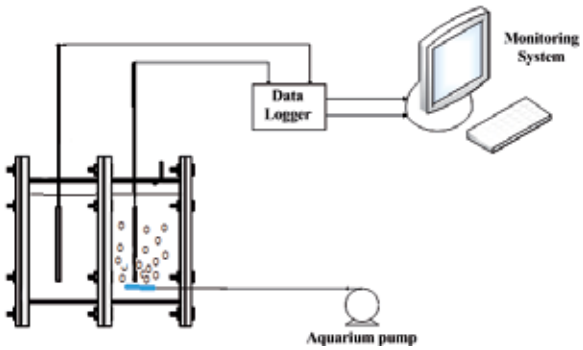

(a)

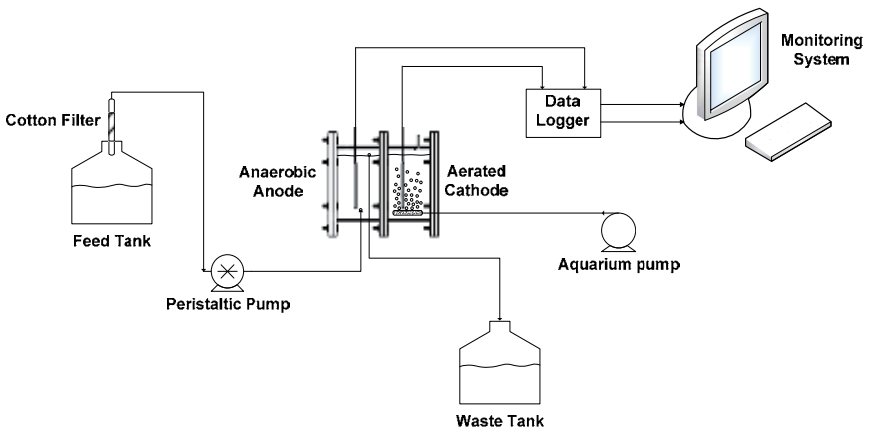

(b)

Fig. 2. Schematic diagram of cubic two chamber MFC in batch (a) and continues (b) mode

2.4 Analytical method

Two protocols, polarity and cyclic voltammetry techniques, were adopted to analyze experimental data in terms of voltage and current density.

2.4.1 Polarity curve

Polarization curves were obtained using an adjustable external resistance. Power and current were calculated based on following equations:

$$P=I\times E \tag{1}$$

$$I=(E/R_{ext}) \quad (2)$$

where P is generated power and E measured cell voltage; R_{ext} denotes external resistance and I indicates produced current. The online recorded produced current and power were normalized by the surface area of the used membrane. Analog digital data acquisition was fabricated to record data point in every 4 min. Measurements were carried out at variable resistances which were imposed to the MFC. The current in the MFC was automatically calculated and recorded dividing the obtained voltage by the specified resistance. Then, the system provides power calculation by multiplication of voltage and current. The provisions were provided for online observation of polarization curve showing the variation of power density and MFC voltage with respect to current. The online system had the ability to operate automatically or manually. While it operates in auto-mode, the assembled relays were able to regulate automatically the resistances. Voltage of MFC was amplified and then data were transmitted to a microcontroller by an accurate analog to digital converter. The microcontroller was also able to send the primary data to a computer by serial connection. In addition, a special function of MATLAB software (7.4, 2007a) was used to store and display synchronically the obtained data. The power, current and voltage were automatically recorded by the computer connected to the system.

Columbic efficiency can be calculated by division of total coulombs obtained from the cell and theoretical amount of coulombs that can be produced from glucose (Equation 3):

$$CE= (C_p/C_T)\times 100 \quad (3)$$

Total coulombs are obtained by integrating the current variation over time (C_p), where C_T is the theoretical amount of coulombs that can be produced from carbon source, calculated as follows:

$$C_T= (FbSV.M^{-1}) \quad (4)$$

For continuous flow through the system, CE can be calculated on the basis of generated current at steady state conditions as follows (Logan et al., 2006):

$$CE = MI/Fbq\Delta S \quad (5)$$

In equation (4), *F* is Faraday's constant , b the number of moles of electrons produced per mole of substrate (24 mol of electrons were produced in glucose oxidation in anaerobic anode chamber), *S* the substrate concentration, *q* flow rate of substrate and *M* the molecular weight of used substrate (*M*= 180.155 g.mol^{-1}) (Allen and Bennetto, 1993; Oh and Logan, 2006).

In batch mode, polarization curves were obtained at steady state condition by setting an adjustable resistance in data logger. When the MFC was operated in continuous mode, the concentration of glucose in the feed tank solution was kept constant at 30 g.l^{-1}. Several hydraulic retention times (HRT) were examined in continuous operation. The HRT was measured from the volume of medium and the inward flow rate to the anode compartment of MFC.

2.4.2 Cyclic Voltammetry (CV)

Beside the polarity curve, cyclic Voltammeter (IVUM soft, Ivium Technology, Netherland) was also used to analyze for testing oxidation and reduction of organic materials. The potential range of -400 mV to 1000 mV was applied. The working electrode and sense

electrode were joined together to measure oxidation and reduction peaks. Carbon paper (NARA, Guro-GU, Seoul, Korea) was used as the working electrode and Platinum (Platinum, gauze, 100 mesh, 99.9% meta basis, Sigma Aldrich) as the counter electrode. Also, Ag/AgCl (Ag/AgCl, sat KCl, Sensortechnik Meinsberg, Germany) electrode was utilized as reference electrode. Voltage rate of 50 $mV.S^{-1}$ was chosen as scan rate in CV analysis.

3. Result and discussion

Microorganism can be used in MFCs to catalyze the conversion of organic matter into electricity. The performance of the MFC was evaluated by the polarization curve and power density. The main goal of research to work on MFC is to increase output power and receive maximum generated current under optimum potential conditions.

Polarization behavior of the fabricated cell was recorded for several external resistances to determine maximum power generation. Polarization curve and power density vs. current density of the cell after 12 hours incubation and also reaching to steady state (SS) condition are presented in Fig. 3. The maximum produced power without any electron shuttle in anode was 4 $mW.m^{-2}$. The produced power and current were very low to use in a small device and it must be improved.

Mediators are normally used to enhance the performance of MFCs (Najafpour et al.). Mediators are artificial compounds or produced by the microorganism itself. Some microorganisms produce nanowires to transmit electrons directly without using any mediator but other organisms need to add artificial electron shuttle into anode chamber (Mathuriya and Sharma, 2009). Yeast cannot transfer the produced electrons to the anode surface without addition of mediators. In orther to improve the power density and also current density several mediators with several concentrations were selected to enhance the power generation and current in the fabricated MFC. The maximum power, maximum current and also the obtained OCV at the best concentration of each mediator are summarized in Table 2. The data indicated that the mediators were essential when yeast was used as active biocatalyst in the MFC. Also this table indicated NR with concentration of 200 $\mu mol.l^{-1}$ had the best ability for transferring the generated electrons in the anode chamber to the anode surface. The indicated concentration of NR in anaerobic anode compartment increased the produced power was 46 times more than the case without mediators in the MFC.

Type of mediators	Optimum concentration (μ $mol.l^{-1}$)	P_{max} ($mW.m^{-2}$)	I_{max} in P_{max} ($mA.m^{-2}$)	OCV at SS condition (mV)
Without mediators	---	0.8	11	280
Ferric chelate	400	7.3	67	285
Thionine	500	12	79	460
NR	200	37	151	505
MB	300	8.3	71	410

Table 2. Optimum condition obtained from this study at several concentrations of mediators

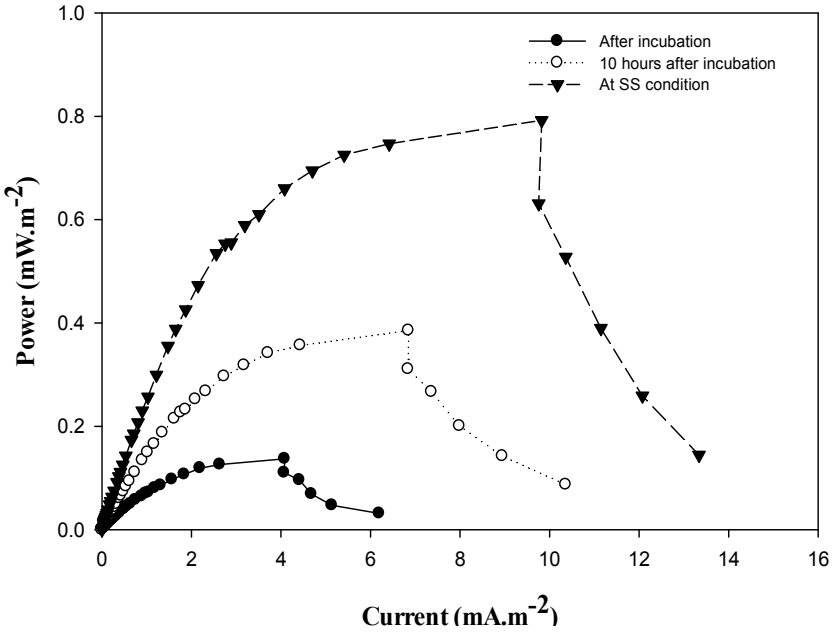

(a)

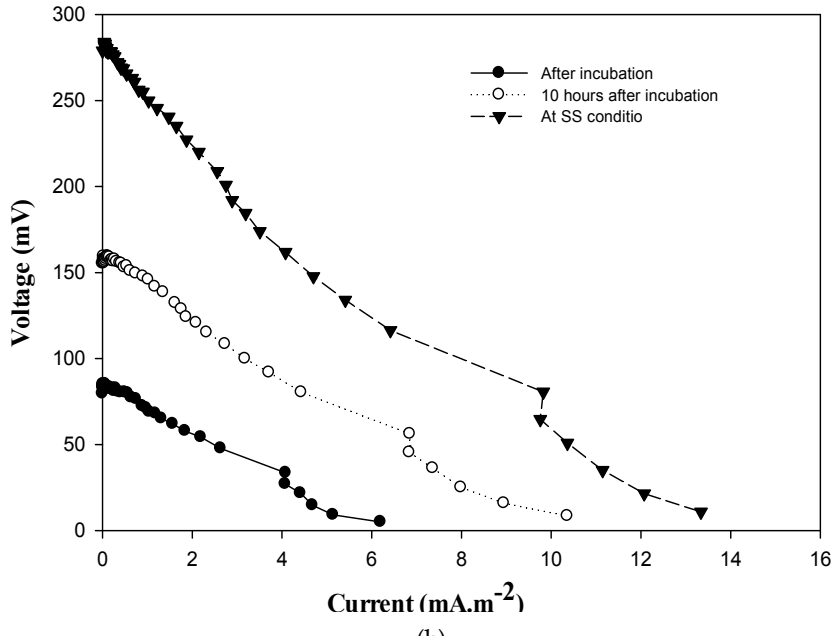

(b)

Fig. 3. Generated power density (a) and voltage (b) as function of current density at start up, 10 hours after incubation and at steady state condition

In order to obtain the best oxidizer in cathode compartment, several oxidizers were analyzed. Table 3 summarized the optimum conditions obtained for distilled water, potassium ferricyanide and potassium permanganate. The maximum power, current and OCV was obtained with potassium permanganate.

Type of Oxidizer	Optimum concentration (μ mol.l^{-1})	P_{max} (mW.m^{-2})	I_{max} in P_{max} (mA.m^{-2})	OCV at SS condition (mV)
Distillated water	---	7.6	68	404
H_2O_2	---	41	155	610
Potassium ferricyanide	200	49	177	508
Potassium Permanganate	300	110	380	860

Table 3. Optimum conditions obtained from several oxidizers

Glucose consumption and cell growth with respect to incubation time at 200µmol.l^{-1} of NR as electron mediators are presented in Fig. 4. Figure 4 demonstrated that *S. cerevisiae* had the good possibility for consumption of organic substrate at anaerobic condition and produce bioelectricity.

The aim of this research was to found optimum effect of mass transfer area on production of power in the fabricated MFC. Figure 5 shows the effect of mass transfer area on performance

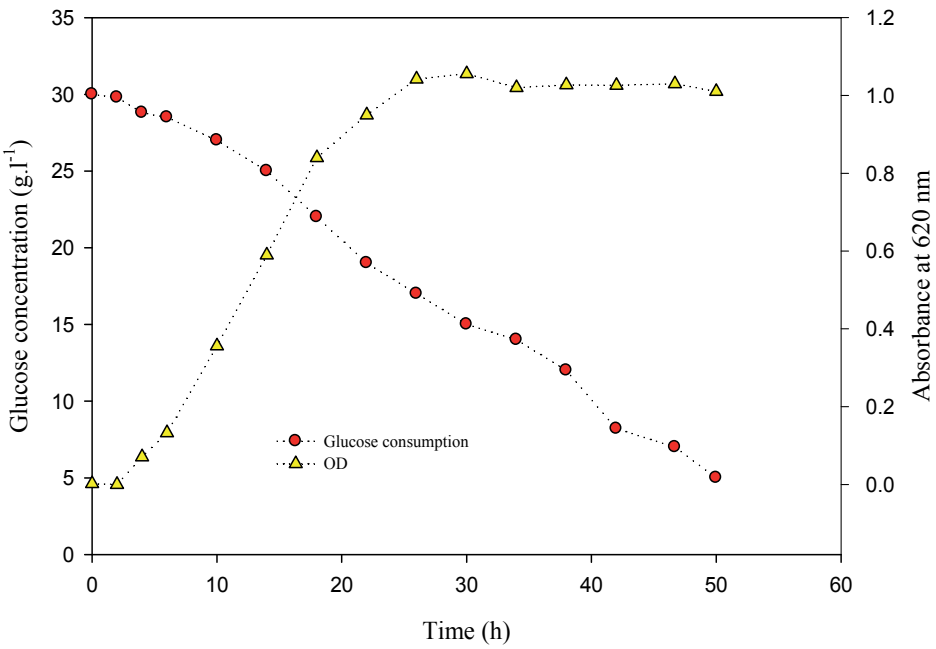

Fig. 4. Cell growth profiles and glucose consumption by *S. cerevisiae*

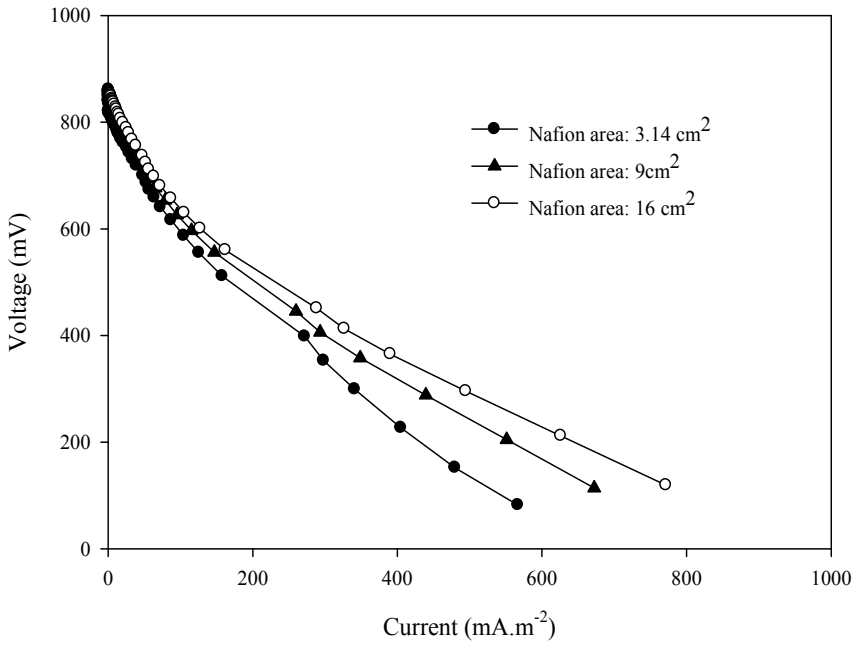

(a)

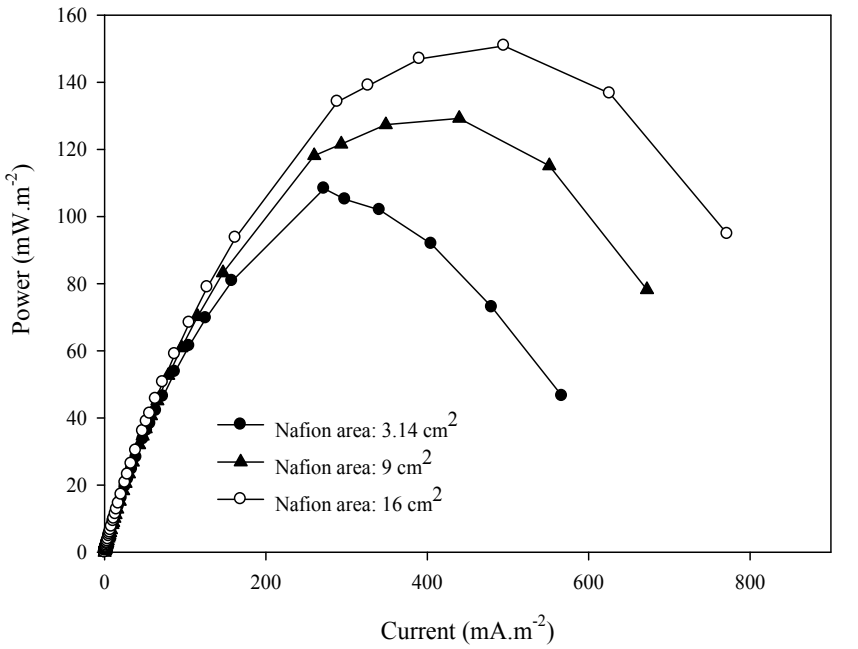

(b)

Fig. 5. Effect of mass transfer area on performance of MFC.

of MFC. Three different mass transfer area (3.14, 9and 16 cm^2) were experimented and the results in polarization curve presented in Fig. 5 a and b. Membrane in MFC allows the generated hydrogen ions in the anode chamber pass through the membrane and then to be transferred to cathode chamber (Rabaey et al., 2005a; Cheng et al., 2006; Venkata Mohan et al., 2007; Aelterman et al., 2008). The obtained result shows the maximum current and power were obtained at Nafion area of 16 cm^2. The maximum power and current generated were 152 $mW.m^{-2}$ and 772 $mA.m^{-2}$, respectively.

Figure 6 depicts an OCV recorded by online data acquisition system connected to the MFC for duration of 72 hours. At the starting point for the experimental run, the voltage was less than 250mV and then the voltage gradually increased. After 28 hours of operation, the OCV reached to a maximum and stable value of 8mV. The OCV was quite stable for the entire operation, duration of 72 hours.

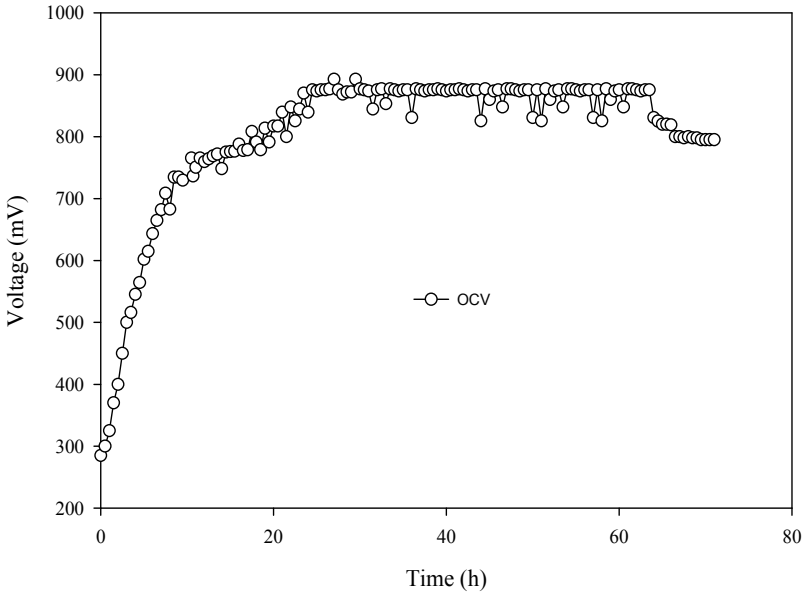

Fig. 6. Stability of OCV.OCV recorded by online data acquisition system connected to the MFC for duration of 72 hours

There are several disadvantages of batch operation for the purpose of power generation in MFCs. The nutrients available in the working volume become depleted in batch mode. The substrate depletion in batch MFCs results in a decrease in bioelectricity production with respect to time. This problem is solved in continuous MFCs that are more suitable than batch systems for practical applications (Rabaey et al., 2005c). The advantages of continuous culture are that the cell density, substrate and product concentrations remain constant while the culture is diluted with fresh media. The fresh media is sterilized or filtered and there are no cells in the inlet stream.

The batch operation was switched over to continuous operation mode by constantly injection of the prepared substrate to the anode compartment. The other factors were kept constant based on optimum conditions determined from the batch operation. For the MFC operated under continuous condition, substrate with initial glucose concentration of 30 $g.l^{-1}$

was continuously injected from feed tank to the anode chamber using a peristaltic pump. Four different HRT were examined in this research to determine the optimum HRT for maximum power and current density. The polarization curve at each HRT at steady state condition was recorded with online data acquisition system and the obtained data are presented in table 4. The optimum HRT was 6.7 h with the maximum generated power density of 274 mW.m^{-2}.

HRT (h)	P_{max} (mW.m^{-2})	I_{max} in P_{max} (mA.m^{-2})	OCV at SS condition (mV)
16	161	420	801
12.34	182	600	803
6.66	274	850	960
3.64	203	614	975

Table 4. Effect of different HRT on production of power and current in fabricated MFC

The growth kinetics and kinetic constants were determined for continuous operation of the fabricated MFC. The growth rate was controlled and the biomass concentration was kept constant in continuous system through replacing the old culture by fresh media. The material balance for cells in a continuous culture is defined by equation 5 (Bailey and Ollis, 1976):

$$F.x_i - F.x + V.r_x = V.{}^{dx}/_{dt} \tag{5}$$

where, F is volumetric flow rate of feed and effluent liquid streams, V is volume of liquid in system, r_x is the rate of cell growth, xi represents the component i molar concentration in feed stream and x is the component i molar concentration in the reaction mixture and in the effluent stream. The rate of formation of a product is easily evaluated at steady-state condition for inlet and outlet concentrations. The dilution rate, D, is defined as D=V/F which characterizes the inverse retention time. The dilution rate is equal to the number of fermentation vessel volumes that pass through the vessel per unit time. D is the reciprocal of the mean residence time(Najafpour, 2007).

At steady-state condition, there is no accumulation. Therefore, the material balance is reduced to:

$$F.x_i - F.x + V.r_x = 0 \quad \rightarrow {}^{V}/_{F} = {}^{(x - x_0)}/_{r_x} \tag{6}$$

When feed is steriled, there is no cell entering the bioreactor, which means x_0=0. Using the Monod equation for the specific growth rate in equation 6, the rate may be simplified and reduced to following equation:

$$r_x = {}^{dx}/_{dt} = \mu x = {}^{(\mu_{max}.S.x)}/_{K_s + S} \tag{7}$$

HRT (h)	16	12.34	6.66	3.64
X (g.l-1)	1.94	1.74	1.728	1.5
S(g.l-1)	6.95	9.13	12.86	22.8

Table 5. Biomass and substrate concentration in outlet of MFC at different HRT

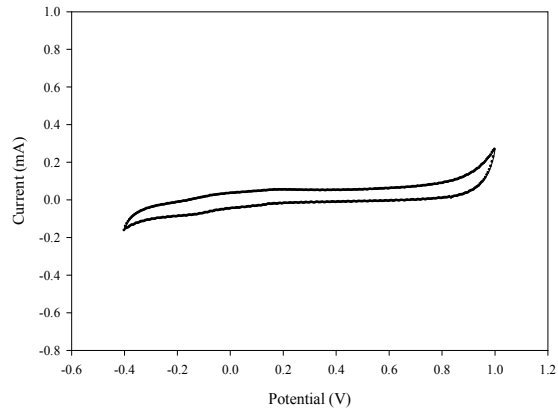

(a)

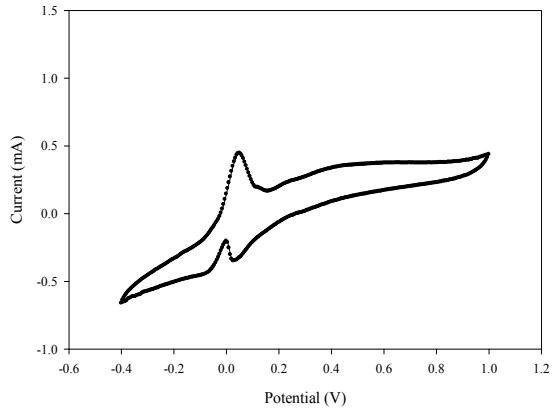

(b)

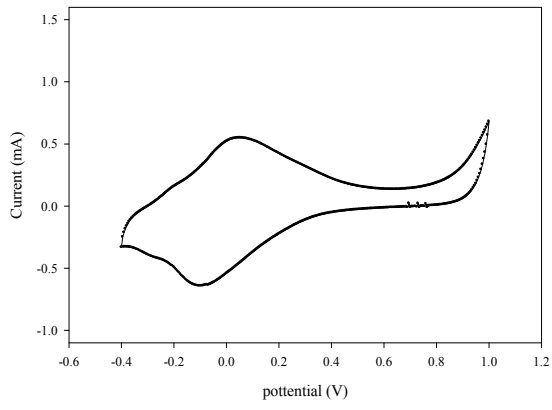

(c)

Fig. 7. Effect of active biofilm on anode surface with CV analysis. (a) absence of biofilm ,(b) after formation of biofilm with out mediators and (c) after formation of biofilm with 200 µmol.l^{-1} NR as electron mediators .scan rate was 0.01 V.S^{-1}

Biomass and substrate concentration in outlet stream of MFC at different HRT are shown in Table 4. To evaluate kinetic parameters, the double reciprocal method was used for linearization. The terms μ_{max} and K_s were recovered from a linear fit of the experimental data by Plotting 1/D versus 1/S. The values obtained for μ_{max} and K_s were 0.715 h and 59.74 g/l, respectively. Then, the kinetic model is defined as follows:

$$r_x = {}^{(0.715\, S.x)}/_{59.74 + S} \tag{8}$$

In the next stage, anode electrode with attached microorganisms was analyzed with CV in. The system was analyzed in anaerobic anode chamber. Before formation of active biofilm on anode surface, oxidation and reduction peak was not observed in CV test (Fig. 7a). Current-potential curves by scanning the potential from negative to positive potential after formation of active biofilm are shown in Fig. 7b. Two oxidation and one reduction peak was obtained with CV test. One peak was obtained in forward scan from -400 to 1000 mV and one oxidation and reduction peak was obtained in reverse scan rate from 1000 to -400 mV. The similar result by alcohol as electron donors in anode chamber was reported(Kim et al., 2007). The first peak was observed in forward scan rate between -0.087 to 1.6 V. Also 200 μmol.l^{-1} NR was added to anode chamber and then this system was examined with CV (Fig. 7 c)

Graphite was used as electrode in the MFC fabricated cells. The normal photographic image of the used electrode before employing in the MFC as anode compartment is shown in Fig. 8a. Scanning electronic microscopy technique has been applied to provide surface criteria and morphological information of the anode surface. The surface images of the graphite plate electrode were successfully obtained by SEM. The image from the surface of graphite electrode before and after experimental run was taken. The sample specimen size was 1cm×1cm for SEM analysis. Fig. 8b and 8c show the outer surface of the graphite electrode prior and after use in the MFC, respectively. These obtained images demonstrated that microorganisms were grown on the graphite surface as attached biofilm. Some clusters of microorganism growth were observed in several places on the anode surface.

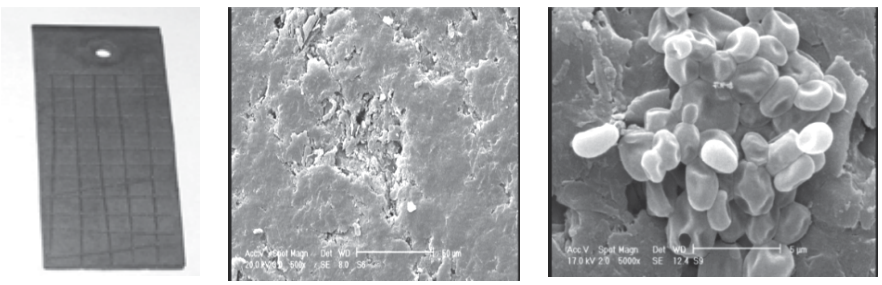

(a) (b) (c)

Fig. 8. Photography image (a) and SEM images from anode electrode surface before (b) and after (c) using in anode compartment

Yeast as biocatalyst in the MFC consumed glucose as carbon source in the anode chamber and the produced electrons and protons. In this research, glucose was used as fuel for the MFC. The anodic and catholic reactions are taken place at the anode and cathode as summarized below:

$$C_6H_{12}O_6 + 6H_2O \longrightarrow 6CO_2 + 24\ e^- + 24H^+ \quad (9)$$

$$6O2 + 24\ e^- + 24H^+ \longrightarrow 12H_2O \quad (10)$$

24 mol electrons and protons are generated by oxidation of one mole of glucose in an anaerobic condition. To determine CE (Columbic Efficiency), 1 KΩ resistance was set at external circuit for 25 h and the produced current was measured. The average obtained current was 105.85 $mA.m^{-2}$. In this study, CE was calculated using equations 3 and 4. CE was 26% at optimum concentration of NR as mediator. CE at continues mode was around 13 percent and this efficiency is considered as very low efficiency. The similar results with xylose in fed-batch and continuous operations were also reported (Huang and Logan, 2008b; a). This may be due to the breakdown of sugars by microorganisms resulting in production of some intermediate products such as acetate, butyrate, and propionate, which can play a significant role in decrease of CE.

4. Chapter conclusion

MFC produce current through the action of bacteria that can pass electrons to an anode, the negative electrode of a fuel cell. The electrons flow from the anode through a wire to a cathode The idea of making electricity using biological fuel cell may not be new in theory, certainly as a practical method of energy production it is quite new. Some of MFCs don't need mediators for transfer electrons but some of others need mediators in anode chamber for transfer electrons to anode surface.

Bioelectricity production from pure glucose by *S cerevisiae* in dual chambered MFC was successfully carried out in batch and continuous modes. Potassium permanganate was used as oxidizing agent in cathode chamber to enhance the voltage. NR as electron mediator with low concentration (200 $\mu mol.l^{-1}$) was selected as electron mediator in anode side. The highest obtained voltage was around 900 mV in batch system and it was stable for duration time of 72 h. The mass transfer area is one of the most critical parameter on MFCs performances.

5. Acknowledgments

The authors wish to acknowledge Biotechnology Research Center, Noshirvani University of Technology, Babol, Iran for the facilities provided to accomplish the present research.

6. References

Aelterman, P., Versichele, M., Marzorati, M., Boon, N., Verstraete, W. (2008). *Loading rate and external resistance control the electricity generation of microbial fuel cells with different three-dimensional anodes*. Bioresource Technology 99, 8895-8902.

Allen, R., Bennetto, H.(1993). *Microbial fuel-cells*. Applied Biochemistry and Biotechnology 39, 27-40.

Appleby, A., 1988. Fuel cell handbook.

Bailey, J., Ollis, D.(1976). *Biochemical engineering fundamentals*. Chemical Engineering Education.

Bennetto, H.(1990). *Electricity generation by microorganisms*. Biotechnology 1, 163-168.

Bennetto, H., Delaney, G., Mason, J., Roller, S., Stirling, J., Thurston, C.(1985). T*he sucrose fuel cell: efficient biomass conversion using a microbial catalyst*. Biotechnology Letters 7, 699-704.

Bond, D.R., Lovley, D.R.(2003). *Electricity production by Geobacter sulfurreducens attached to electrodes*. Applied and environmental microbiology 69, 1548.

Chaudhuri, S.K., Lovley, D.R.(2003). *Electricity generation by direct oxidation of glucose in mediatorless microbial fuel cells*. Nature Biotechnology 21, 1229-1232.

Chen, G., Choi, S., Lee, T., Lee, G., Cha, J., Kim, C.(2008). *Application of biocathode in microbial fuel cells: cell performance and microbial community*. Applied Microbiology and Biotechnology 79, 379-388.

Cheng, S., Liu, H., Logan, B.E.(2006). *Increased power generation in a continuous flow MFC with advective flow through the porous anode and reduced electrode spacing*. Environmental Science and Technology 40, 2426-2432.

Choi, Y., Jung, E., Kim, S., Jung, S.(2003). *Membrane fluidity sensoring microbial fuel cell*. Bioelectrochemistry 59, 121-127.

Choi, Y., Jung, E., Park, H., Jung, S., Kim, S.(2007). *Effect of initial carbon sources on the performance of a microbial fuel cell containing environmental microorganism micrococcus luteus*. Notes 28, 1591.

Ganguli, R., Dunn, B.S.(2009). *Kinetics of Anode Reactions for a Yeast-Catalysed Microbial Fuel Cell*. Fuel Cells 9, 44-52.

Gil, G., Chang, I., Kim, B., Kim, M., Jang, J., Park, H., Kim, H.(2003). *Operational parameters affecting the performannce of a mediator-less microbial fuel cell*. Biosensors and Bioelectronics 18, 327-334.

Grzebyk, M., Pozniak, G.(2005). *Microbial fuel cells (MFCs) with interpolymer cation exchange membranes*. Separation and Purification Technology 41, 321-328.

Heitner-Wirguin, C.(1996). *Recent advances in perfluorinated ionomer membranes: Structure, properties and applications*. Journal of Membrane Science 120, 1-33.

Hong, S., Chang, I., Choi, Y., Kim, B., Chung, T.(2009). *Responses from freshwater sediment during electricity generation using microbial fuel cells*. Bioprocess and biosystems engineering 32, 389-395.

Huang, L., Logan, B.(2008a). *Electricity generation and treatment of paper recycling wastewater using a microbial fuel cell*. Applied microbiology and biotechnology 80, 349-355.

Huang, L., Logan, B.(2008b). *Electricity production from xylose in fed-batch and continuous-flow microbial fuel cells*. Applied microbiology and biotechnology 80, 655-664.

Huang, L., Zeng, R.J., Angelidaki, I.(2008). *Electricity production from xylose using a mediator-less microbial fuel cell*. Bioresource Technology 99, 4178-4184.

Ieropoulos, I., Greenman, J., Melhuish, C., Hart, J.(2005). *Comparative study of three types of microbial fuel cell*. Enzyme and Microbial Technology 37, 238-245.

Kim, B.H., Park, H.S., Kim, H.J., Kim, G.T., Chang, I.S., Lee, J., Phung, N.T.(2004). *Enrichment of microbial community generating electricity using a fuel-cell-type electrochemical cell*. Applied Microbiology and Biotechnology 63, 672-681.

Kim, H.J., Park, H.S., Hyun, M.S., Chang, I.S., Kim, M., Kim, B.H.(2002). A *mediator-less microbial fuel cell using a metal reducing bacterium, Shewanella putrefaciens*. Enzyme and Microbial Technology 30, 145-152.

Kim, J., Jung, S., Regan, J., Logan, B.(2007). *Electricity generation and microbial community analysis of alcohol powered microbial fuel cells*. Bioresource technology 98, 2568-2577.

Kim, M.S., Lee, Y.j.(2007). *Optimization of culture conditions and electricity generation using Geobacter sulfurreducens in a dual-chambered microbial fuel-cell.* International Journal of Hydrogen Energy.

Lee, S., Choi, Y., Jung, S., Kim, S.(2002). *Effect of initial carbon sources on the electrochemical detection of glucose by Gluconobacter oxydans.* Bioelectrochemistry 57, 173-178.

Li, J., Liu, G., Zhang, R., Luo, Y., Zhang, C., Li, M.(2010a). *Electricity generation by two types of microbial fuel cells using nitrobenzene as the anodic or cathodic reactants.* Bioresource technology 101, 4013-4020.

Li, W., Sheng, G., Liu, X., Yu, H.(2010b). *Recent advances in the separators for microbial fuel cells*. Bioresource technology.

Liu, H., Song, C., Zhang, L., Zhang, J., Wang, H., Wilkinson, D.P.(2006). *A review of anode catalysis in the direct methanol fuel cell*. Journal of Power Sources 155, 95-110.

Logan, B., Hamelers, B., Rozendal, R., Schr◌der, U., Keller, J., Freguia, S., Aelterman, P., Verstraete, W., Rabaey, K.(2006). *Microbial Fuel Cells: Methodology and Technology†*. Environ. Sci. Technol 40, 5181-5192.

Lovley, D.R.(2006). *Erratum: Bug juice: Harvesting electricity with microorganisms*. Nature Reviews Microbiology 4, 797.

Mathuriya, A., Sharma, V.(2009). *Bioelectricity production from paper industry waste using a microbial fuel cell by Clostridium species.* J Biochem Tech 1, 49-52.

Min, B., Cheng, S., Logan, B.(2005). *Electricity generation using membrane and salt bridge microbial fuel cells*. Water research 39, 1675-1686.

Najafpour, G.(2007). *Biochemical engineering and biotechnology*. Elsevier Science Ltd, ISBN-10: 0-444-52845-8,Netherland.

Najafpour, G., Rahimnejad, M., Mokhtarian, N., Daud, W., Ghoreyshi, A.(2010). B*ioconversion of Whey to Electrical Energy in a Biofuel Cell Using Saccharomyces cerevisiae*. World Applied Sciences Journal 8, 1-5.

Oh, S.E., Logan, B.E.(2006). *Proton exchange membrane and electrode surface areas as factors that affect power generation in microbial fuel cells*. Applied Microbiology and Biotechnology 70, 162-169.

Park, D., Kim, S., Shin, I., Jeong, Y.(2000). *Electricity production in biofuel cell using modified graphite electrode with neutral red*. Biotechnology Letters 22, 1301-1304.

Park, D., Zeikus, J.(1999). *Utilization of electrically reduced neutral red by Actinobacillus succinogenes: physiological function of neutral red in membrane-driven fumarate reduction and energy conservation*. Journal of Bacteriology 181, 2403.

Park, D., Zeikus, J.(2000). *Electricity generation in microbial fuel cells using neutral red as an electronophore*. Applied and Environmental Microbiology 66, 1292.

Park, D., Zeikus, J.(2002). *Impact of electrode composition on electricity generation in a single-compartment fuel cell using Shewanella putrefaciens*. Applied Microbiology and Biotechnology 59, 58-61.

Pham, C.A., Jung, S.J., Phung, N.T., Lee, J., Chang, I.S., Kim, B.H., Yi, H., Chun, J.(2003). *A novel electrochemically active and Fe(III)-reducing bacterium phylogenetically related to Aeromonas hydrophila, isolated from a microbial fuel cell.* FEMS Microbiology Letters 223, 129-134.

Rabaey, K., Boon, N., Hofte, M., Verstraete, W.(2005a). *Microbial phenazine production enhances electron transfer in biofuel cells*. Environ. Sci. Technol 39, 3401-3408.

Rabaey, K., Ossieur, W., Verhaege, M., Verstraete, W.(2005b). C*ontinuous microbial fuel cells convert carbohydrates to electricity*, Water Science and Technology, pp. 515-523.

Rabaey, K., Ossieur, W., Verhaege, M., Verstraete, W., Guiot, S., Pavlostathis, S., van Lier, J.(2005c). *Continuous microbial fuel cells convert carbohydrates to electricity*, IWA Publishing, Alliance House 12 Caxton Street London SW 1 H 0 QS UK, pp. 515-523.

Rahimnejad, M., Jafari, T., Haghparast, F., Najafpour, G.D., Goreyshi, A.A. (2011), *Nafion as a nanoproton conductor in microbial fuel cells*. Turkish J. Eng. Env. Sci 34, 289-292.

Rahimnejad, M., Mokhtarian, N., Najafpour, G., Daud, W., Ghoreyshi, A.(2009). *Low Voltage Power Generation in aBiofuel Cell Using Anaerobic Cultures*. World Applied Sciences Journal 6, 1585-1588.

Rhoads, A., Beyenal, H., Lewandowski, Z.(2005). *Microbial fuel cell using anaerobic respiration as an anodic reaction and biomineralized manganese as a cathodic reactant*. Environmental Science and Technology 39, 4666-4671.

Ringeisen, B.R., Henderson, E., Wu, P.K., Pietron, J., Ray, R., Little, B., Biffinger, J.C., Jones-Meehan, J.M.(2006). *High power density from a miniature microbial fuel cell using Shewanella oneidensis DSP10*. Environmental Science and Technology 40, 2629-2634.

Rosenbaum, M., Zhao, F., Quaas, M., Wulff, H., Schröder, U., Scholz, F.(2007). *Evaluation of catalytic properties of tungsten carbide for the anode of microbial fuel cells*. Applied Catalysis B: Environmental 74, 261-269.

Sadasivam, S., Manickam, A., 2005. Biochemical Methods New Age International (P) Ltd., Publishers, New Delhi.

Schröder, U., Nießen, J., Scholz, F.(2003). *A generation of microbial fuel cell with current outputs boosted by more than one order of magnitude* (Angew Chem Int Ed 42: 2880–2883). Angew Chem 115, 2986-2989.

Shin, S., Choi, Y., Na, S., Jung, S., Kim, S.(2006). *Development of bipolar plate stack type microbial fuel cells*. BULLETIN-KOREAN CHEMICAL SOCIETY 27, 281.

Shukla, A., Suresh, P., Berchmans, S., Rajendran, A.(2004). *Biological fuel cells and their applications*. Curr Sci 87, 455-468.

Thurston, C., Bennetto, H., Delaney, G., Mason, J., Roller, S., Stirling, J.(1985). G*lucose metabolism in a microbial fuel cell. Stoichiometry of product formation in a thionine-mediated Proteus vulgaris fuel cell and its relation to coulombic yields*. Microbiology 131, 1393.

Thygesen, A., Poulsen, F.W., Min, B., Angelidaki, I., Thomsen, A.B.(2009). *The effect of different substrates and humic acid on power generation in microbial fuel cell operation*. Bioresource Technology 100, 1186-1191.

Vega, C., Fernández, I.(1987). *Mediating effect of ferric chelate compounds in microbial fuel cells with Lactobacillus plantarum, Streptococcus lactis, and Erwinia dissolvens*. Bioelectrochemistry and Bioenergetics 17, 217-222.

Venkata Mohan, S., Veer Raghavulu, S., Sarma, P.N.(2008). *Influence of anodic biofilm growth on bioelectricity production in single chambered mediatorless microbial fuel cell using mixed anaerobic consortia*. Biosensors and Bioelectronics 24, 41-47.

Venkata Mohan, S., Veer Raghavulu, S., Srikanth, S., Sarma, P.N.(2007). *Bioelectricity production by mediatorless microbial fuel cell under acidophilic condition using wastewater as substrate: Influence of substrate loading rate*. Current Science 92, 1720-1726.

Wen, Q., Wu, Y., Cao, D., Zhao, L., Sun, Q.(2009). *Electricity generation and modeling of microbial fuel cell from continuous beer brewery wastewater*. Bioresource Technology 100, 4171-4175.

Yi, H., Nevin, K.P., Kim, B.C., Franks, A.E., Klimes, A., Tender, L.M., Lovley, D.R.(2009). *Selection of a variant of Geobacter sulfurreducens with enhanced capacity for current production in microbial fuel cells*. Biosensors and Bioelectronics 24, 3498-3503.

Zhang, T., Zeng, Y., Chen, S., Ai, X., Yang, H.(2007). *Improved performances of E. coli-catalyzed microbial fuel cells with composite graphite/PTFE anodes*. Electrochemistry Communications 9, 349-353.

12

Mass Transfer Related to Heterogeneous Combustion of Solid Carbon in the Forward Stagnation Region - Part 1 - Combustion Rate and Flame Structure

Atsushi Makino
Japan Aerospace Exploration Agency
Japan

1. Introduction

Carbon combustion has been a research subject, relevant to pulverized coal combustion. However, it is not limited to basic research on coal/char combustion, but can benefit various aerospace applications, such as propulsion due to its high energy density and evaluation of protection properties of carbon-carbon composites (C/C-composites) used as high-temperature, structural materials for atmospheric re-entry, gas-turbine blades, scram jet combustors, etc., including ablative carbon heat-shields. Because of practical importance, extensive research has been conducted experimentally, theoretically, and/or numerically, as summarized in several comprehensive reviews (Batchelder, et al., 1953; Gerstein & Coffin, 1956; Walker, et al., 1959; Clark, et al., 1962; Khitrin, 1962; Mulcahy & Smith, 1969; Maahs, 1971; Rosner, 1972; Essenhigh, 1976, 1981; Annamalai & Ryan, 1993; Annamalai, et al., 1994). Nonetheless, because of complexities involved, further studies are required to understand basic nature of the combustion. Some of them also command fundamental interest, because of simultaneous existence of surface and gas-phase reactions, interacting each other.

Generally speaking, processes governing the carbon combustion are as follows: (i) diffusion of oxidizing species to the solid surface, (ii) adsorption of molecules onto active sites on the surface, (iii) formation of products from adsorbed molecules on the surface, (iv) desorption of solid oxides into the gas phase, and (v) migration of gaseous products through the boundary layer into the freestream. Since these steps occur in series, the slowest of them determines the combustion rate and it is usual that steps (ii) and (iv) are extremely fast.

When the surface temperature is low, step (iii) is known to be much slower than steps (i) or (v). The combustion rate, which is also called as the mass burning rate, defined as mass transferred in unit area and time, is then determined by chemical kinetics and therefore the process is kinetically controlled. In this kinetically controlled regime, the combustion rate only depends on the surface temperature, exponentially. Since the process of diffusion, being conducted through the boundary layer, is irrelevant in this regime, the combustion rate is independent of its thickness. Concentrations of oxidizing species at the reacting surface are not too different from those in the freestream. In addition, since solid carbon is more or less porous, in general, combustion proceeds throughout the sample specimen.

On the other hand, when the surface temperature is high, step (iii) is known to be much faster than steps (i) and (v). The combustion rate is then controlled by the diffusion rate of oxidizing species (say, oxygen) to the solid surface, at which their concentrations are negligibly small. In this diffusionally controlled regime, therefore, the combustion rate strongly depends on the boundary layer thickness and weakly on the surface temperature ($\propto T^{0.5\sim1.0}$), with exhibiting surface regression in the course of combustion.

Since oxygen-transfer to the carbon surface can occur via O_2, CO_2, and H_2O, the major surface reactions can be

$$C + O_2 \rightarrow CO_2 , \tag{R1}$$

$$2C + O_2 \rightarrow 2CO , \tag{R2}$$

$$C + CO_2 \rightarrow 2CO , \tag{R3}$$

$$C + H_2O \rightarrow CO + H_2 . \tag{R4}$$

At higher temperatures, say, higher than 1000 K, CO formation is the preferred route and the relative contribution from (R1) can be considered to be negligible (Arthur, 1951). Thus, reaction (R2) will be referred to as the C-O_2 reaction.

Comparing (R2) and (R3), as alternate routes of CO production, the C-O_2 reaction is the preferred route for CO production at low temperatures, in simultaneous presence of O_2 and CO_2. It can be initiated around 600 K and saturated around 1600 K, proceeding infinitely fast, eventually, relative to diffusion. The C-CO_2 reaction of (R3) is the high temperature route, initiated around 1600 K and saturated around 2500 K. It is of particular significance because CO_2 in (R3) can be the product of the gas-phase, water-catalyzed, CO-oxidation,

$$2CO + O_2 \rightarrow 2CO_2 , \tag{R5}$$

referred to as the CO-O_2 reaction. Thus, the C-CO_2 and CO-O_2 reactions can form a loop.

Similarly, the C-H_2O reaction (R4), generating CO and H_2, is also important when the combustion environment consists of an appreciable amount of water. This reaction is also of significance because H_2O is the product of the H_2-oxidation,

$$2H_2 + O_2 \rightarrow 2H_2O , \tag{R6}$$

referred to as the H_2-O_2 reaction, constituting a loop of the C-H_2O and H_2-O_2 reactions.

The present monograph, consisting of two parts, is intended to shed more light on the carbon combustion, with putting a focus on its heat and mass transfer from the surface. It is, therefore, not intended as a collection of engineering data or an exhaustive review of all the pertinent published work. Rather, it has an intention to represent the carbon combustion by use of some of the basic characteristics of the chemically reacting boundary layers, under recognition that flow configurations are indispensable for proper evaluation of the heat and mass transfer, especially for the situation in which the gas-phase reaction can intimately affect overall combustion response through its coupling to the surface reactions.

Among various flow configurations, it has been reported that the stagnation-flow configuration has various advantages, because it provides a well-defined, one-dimensional flow, characterized by a single parameter, called the stagnation velocity gradient. It has even been said that mathematical analyses, experimental data acquisition, and physical

interpretations have been facilitated by its introduction. Therefore, we will confine ourselves to studying carbon combustion in the axisymmetric stagnation flow over a flat plate and/or that in the two-dimensional stagnation flow over a cylinder. From the practical point of view, we can say that it simulates the situations of ablative carbon heat-shields and/or strongly convective burning in the forward stagnation region of a particle.

In this Part 1, formulation of the governing equations is first presented in Section 2, based on theories on the chemically reacting boundary layer in the forward stagnation field. Chemical reactions considered include the surface C-O_2 and C-CO_2 reactions and the gas-phase CO-O_2 reaction, for a while. Generalized species-enthalpy coupling functions are then derived without assuming any limit or near-limit behaviors, which not only enable us to minimize the extent of numerical efforts needed for generalized treatment, but also provide useful insight into the conserved scalars in the carbon combustion. In Section 3, it is shown that straightforward derivation of the combustion response can be allowed in the limiting situations, such as those for the Frozen, Flame-detached, and Flame-attached modes.

In Section 4, after presenting profiles of gas-phase temperature, measured over the burning carbon, a further analytical study is made about the ignition phenomenon, related to finite-rate kinetics, by use of the asymptotic expansion method to obtain a critical condition. Appropriateness of this criterion is further examined by comparing temperature distributions in the gas phase and/or surface temperatures at which the CO-flame can appear. After having constructed these theories, evaluations of kinetic parameters for the surface and gas-phase reactions are conducted in Section 5, in order to make experimental comparisons, further.

Concluding remarks for Part 1 are made in Section 6, with references cited and nomenclature tables. Note that the useful information obtained is further to be used in Part 2, to explore carbon combustion at high velocity gradients and/or in the High-Temperature Air Combustion, with taking account of effects of water-vapor in the oxidizing-gas.

2. Formulation

Among previous studies (Tsuji & Matsui, 1976; Adomeit, et al., 1976; Adomeit, et al., 1985; Henriksen, et al., 1988; Matsui & Tsuji, 1987), it may be noted that Adomeit's group has made a great contribution by clarifying water-catalyzed CO-O_2 reaction (Adomeit, et al., 1976), conducting experimental comparisons (Adomeit, et al., 1985), and investigating ignition/extinction behavior (Henriksen, et al., 1988). Here, an extension of the worthwhile contributions is made along the following directions. First, simultaneous presence of the surface C-O_2 and C-CO_2 reactions and the gas-phase CO-O_2 reaction are included, so as to allow studies of surface reactions over an extended range of its temperatures, as well as examining their coupling with the gas-phase reaction. Second, a set of generalized coupling functions (Makino & Law, 1986) are conformed to the present flow configuration, in order to facilitate mathematical development and/or physical interpretation of the results. Third, an attempt is made to identify effects of thermophysical properties, as well as other kinetic and system parameters involved.

2.1 Model definition

The present model simulates the isobaric carbon combustion of constant surface temperature T_s in the stagnation flow of temperature T_∞, oxygen mass-fraction $Y_{O,\infty}$, and carbon dioxide mass-fraction $Y_{P,\infty}$, in a general manner (Makino, 1990). The major reactions

considered here are the surface C-O_2 and C-CO_2 reactions and the gas-phase CO-O_2 reaction. The surface C+O_2→CO_2 reaction is excluded (Arthur, 1951) because our concern is the combustion at temperatures above 1000 K. Crucial assumptions introduced are conventional, constant property assumptions with unity Lewis number, constant average molecular weight, constant value of the product of density ρ and viscosity μ, one-step overall irreversible gas-phase reaction, and first-order surface reactions. Surface characteristics, such as porosity and internal surface area, are grouped into the frequency factors for the surface reactions.

2.2 Governing equations

The steady-state two-dimensional and/or axisymmetric boundary-layer flows with chemical reactions are governed as follows (Chung, 1965; Law, 1978):

Continuity:
$$\frac{\partial\left(\rho u R^j\right)}{\partial x}+\frac{\partial\left(\rho v R^j\right)}{\partial y}=0\,, \tag{1}$$

Momentum:
$$\rho u\frac{\partial u}{\partial x}+\rho v\frac{\partial u}{\partial y}-\frac{\partial}{\partial y}\left(\mu\frac{\partial u}{\partial y}\right)=\rho_\infty u_\infty\left(\frac{\partial u}{\partial x}\right)_\infty\,, \tag{2}$$

Species:
$$\rho u\frac{\partial Y_i}{\partial x}+\rho v\frac{\partial Y_i}{\partial y}-\frac{\partial}{\partial y}\left(\rho D\frac{\partial Y_i}{\partial y}\right)=-w_i \quad (i = \mathrm{F, O}), \tag{3}$$

$$\rho u\frac{\partial Y_\mathrm{P}}{\partial x}+\rho v\frac{\partial Y_\mathrm{P}}{\partial y}-\frac{\partial}{\partial y}\left(\rho D\frac{\partial Y_\mathrm{P}}{\partial y}\right)=w_\mathrm{P}\,, \tag{4}$$

$$\rho u\frac{\partial Y_\mathrm{N}}{\partial x}+\rho v\frac{\partial Y_\mathrm{N}}{\partial y}-\frac{\partial}{\partial y}\left(\rho D\frac{\partial Y_\mathrm{N}}{\partial y}\right)=0\,, \tag{5}$$

Energy:
$$\rho u\frac{\partial\left(c_\mathrm{p}T\right)}{\partial x}+\rho v\frac{\partial\left(c_\mathrm{p}T\right)}{\partial y}-\frac{\partial}{\partial y}\left(\lambda\frac{\partial T}{\partial y}\right)=q w_\mathrm{F}\,, \tag{6}$$

where T is the temperature, c_p the specific heat, q the heat of combustion per unit mass of CO, Y the mass fraction, u the velocity in the tangential direction x, v the velocity in the normal direction y, and the subscripts C, F, O, P, N, g, s, and ∞, respectively, designate carbon, carbon monoxide, oxygen, carbon dioxide, nitrogen, the gas phase, the surface, and the freestream.

In these derivations, use has been made of assumptions that the pressure and viscous heating are negligible in Eq. (6), that a single binary diffusion coefficient D exists for all species pairs, that c_p is constant, and that the CO-O_2 reaction can be represented by a one-step, overall, irreversible reaction with a reaction rate

$$w_\mathrm{F}=\left(\nu_i W_i\right)B_\mathrm{g}\left(\frac{\rho Y_\mathrm{F}}{W_\mathrm{F}}\right)^{\nu_\mathrm{F}}\left(\frac{\rho Y_\mathrm{O}}{W_\mathrm{O}}\right)^{\nu_\mathrm{O}}\exp\left(-\frac{E_\mathrm{g}}{R^o T}\right), \tag{7}$$

where B is the frequency factor, E the activation energy, R^0 the universal gas constant, ν the stoichiometric coefficient, and W the molecular weight. We should also note that R^j in Eq. (1) describes the curvature of the surface such that j = 0 and 1 designate two-dimensional and axisymmetric flows, respectively, and the velocity components u_∞ and v_∞ of the frictionless flow outside the boundary layer are given by use of the velocity gradient a as

$$u_\infty = ax\,, \qquad v_\infty = -(j+1)ay \tag{8}$$

2.3 Boundary conditions

The boundary conditions for the continuity and the momentum equations are the well-known ones, expressed as

$$\begin{aligned} &\text{at } y{=}0: && u = 0\,, && v = v_s\,, \\ &\text{as } y\to\infty: && && v = v_\infty\,. \end{aligned} \tag{9}$$

For the species conservation equations, we have in the freestream as

$$(Y_\mathrm{F})_\infty = 0, \quad (Y_i)_\infty = Y_{i,\infty} \quad (i = \mathrm{O, P, N}). \tag{10}$$

At the carbon surface, components transported from gas to solid by diffusion, transported away from the interface by convection, and produced/consumed by surface reactions are to be considered. Then, we have

$$(\rho v Y_\mathrm{F})_\mathrm{s} - \left(\rho D \frac{\partial Y_\mathrm{F}}{\partial y}\right)_\mathrm{s} = 2W_\mathrm{F}\left(\frac{\rho Y_\mathrm{O}}{W_\mathrm{O}}\right)_\mathrm{s} B_{\mathrm{s,O}} \exp\left(-\frac{Ta_{\mathrm{s,O}}}{T_\mathrm{s}}\right) + 2W_\mathrm{F}\left(\frac{\rho Y_\mathrm{P}}{W_\mathrm{P}}\right)_\mathrm{s} B_{\mathrm{s,P}} \exp\left(-\frac{Ta_{\mathrm{s,P}}}{T_\mathrm{s}}\right), \tag{11}$$

$$(\rho v Y_\mathrm{O})_\mathrm{s} - \left(\rho D \frac{\partial Y_\mathrm{O}}{\partial y}\right)_\mathrm{s} = -W_\mathrm{O}\left(\frac{\rho Y_\mathrm{O}}{W_\mathrm{O}}\right)_\mathrm{s} B_{\mathrm{s,O}} \exp\left(-\frac{Ta_{\mathrm{s,O}}}{T_\mathrm{s}}\right), \tag{12}$$

$$(\rho v Y_\mathrm{P})_\mathrm{s} - \left(\rho D \frac{\partial Y_\mathrm{P}}{\partial y}\right)_\mathrm{s} = -W_\mathrm{P}\left(\frac{\rho Y_\mathrm{P}}{W_\mathrm{P}}\right)_\mathrm{s} B_{\mathrm{s,P}} \exp\left(-\frac{Ta_{\mathrm{s,P}}}{T_\mathrm{s}}\right), \tag{13}$$

$$(\rho v Y_\mathrm{N})_\mathrm{s} - \left(\rho D \frac{\partial Y_\mathrm{N}}{\partial y}\right)_\mathrm{s} = 0\,. \tag{14}$$

2.4 Conservation equations with nondimensional variables and parameters

In boundary layer variables, the conservation equations for momentum, species i, and energy are, respectively,

$$\frac{d^3 f}{d\eta^3} + f\frac{d^2 f}{d\eta^2} + \frac{1}{2^j}\left\{\frac{\rho_\infty}{\rho} - \left(\frac{df}{d\eta}\right)^2\right\} = 0\,, \tag{15}$$

$$L\left(\tilde{Y}_\mathrm{F} + \tilde{Y}_\mathrm{P}\right) = L\left(\tilde{Y}_\mathrm{O} + \tilde{Y}_\mathrm{P}\right) = L\left(\tilde{Y}_\mathrm{P} - \tilde{T}\right) = L\left(\tilde{Y}_\mathrm{N}\right) = 0\,, \tag{16}$$

$$L\left(\tilde{T}\right) = -Da_{\mathrm{g}}\omega_{\mathrm{g}}, \tag{17}$$

where the convective-diffusive operator is defined as

$$L = \frac{d^2}{d\eta^2} + f\frac{d}{d\eta}. \tag{18}$$

The present Damköhler number for the gas-phase CO-O_2 reaction is given by

$$Da_{\mathrm{g}} = \left(\frac{B_{\mathrm{g}}}{2^j a}\right)\left(\frac{\rho_\infty}{\nu_{\mathrm{P}} W_{\mathrm{P}}}\right)^{\nu_{\mathrm{F}}+\nu_{\mathrm{O}}-1}(\nu_{\mathrm{F}})^{\nu_{\mathrm{F}}}(\nu_{\mathrm{O}})^{\nu_{\mathrm{O}}}, \tag{19}$$

with the nondimensional reaction rate

$$\omega_{\mathrm{g}} = \left(\frac{\tilde{T}_\infty}{\tilde{T}}\right)^{\nu_{\mathrm{F}}+\nu_{\mathrm{O}}-1}\left(\tilde{Y}_{\mathrm{F}}\right)^{\nu_{\mathrm{F}}}\left(\tilde{Y}_{\mathrm{O}}\right)^{\nu_{\mathrm{O}}}\exp\left(-\frac{\tilde{T}a_{\mathrm{g}}}{\tilde{T}}\right). \tag{20}$$

In the above, the conventional boundary-layer variables s and η, related to the physical coordinates x and y, are

$$s = \int_0^x \rho_\infty(x)\,\mu_\infty(x)\,u_\infty(x)\,R^{2j}\,dx, \tag{21}$$

$$\eta = \frac{u_\infty(x)R^j}{\sqrt{2s}}\int_0^y \rho(x,y)\,dy. \tag{22}$$

The nondimensional streamfunction $f(s,\eta)$ is related to the streamfunction $\psi(x, y)$ through

$$f(s,\eta) = \frac{\psi(x,y)}{\sqrt{2s}}, \tag{23}$$

where $\psi(x, y)$ is defined by

$$\rho u R^j = \frac{\partial\psi}{\partial y}, \qquad \rho v R^j = -\frac{\partial\psi}{\partial x}, \tag{24}$$

such that the continuity equation is automatically satisfied. Variables and parameters are:

$$\tilde{T} = \frac{T}{q/(c_p\alpha_{\mathrm{F}})}, \qquad \tilde{T}a = \frac{E/R^o}{q/(c_p\alpha_{\mathrm{F}})}, \qquad \alpha_{\mathrm{F}} = \frac{\nu_{\mathrm{P}}W_{\mathrm{P}}}{\nu_{\mathrm{F}}W_{\mathrm{F}}},$$

$$\tilde{Y}_{\mathrm{F}} = \frac{\nu_{\mathrm{P}}W_{\mathrm{P}}}{\nu_{\mathrm{F}}W_{\mathrm{F}}}Y_{\mathrm{F}}, \qquad \tilde{Y}_{\mathrm{O}} = \frac{\nu_{\mathrm{P}}W_{\mathrm{P}}}{\nu_{\mathrm{O}}W_{\mathrm{O}}}Y_{\mathrm{O}}, \qquad \tilde{Y}_{\mathrm{N}} = Y_{\mathrm{N}}, \qquad \delta = \frac{W_{\mathrm{P}}}{W_{\mathrm{C}}}.$$

Here, use has been made of an additional assumption that the Prandtl and Schmidt numbers are unity. Since we adopt the ideal-gas equation of state under an assumption of constant, average molecular weight across the boundary layer, the term (ρ_∞/ρ) in Eq. (15) can be

replaced by (T/T_∞). As for the constant $\rho\mu$ assumption, while enabling considerable simplification, it introduces 50%-70% errors in the transport properties of the gas in the present temperature range. However, these errors are acceptable for far greater errors in the chemical reaction rates. Furthermore, they are anticipated to be reduced due to the change of composition by the chemical reactions.
The boundary conditions for Eq. (15) are

$$f(0)=f_s, \qquad \left(\frac{df}{d\eta}\right)_s=0, \qquad \left(\frac{df}{d\eta}\right)_\infty=1, \tag{25}$$

whereas those for Eqs. (16) and (17) are

$$\begin{aligned} &\text{at } \eta=0: \quad \tilde{T}=\tilde{T}_\mathrm{s}, \qquad \tilde{Y}_i=\left(\tilde{Y}_i\right)_\mathrm{s} \qquad (i=\mathrm{F, O, P, N}), \\ &\text{as } \eta\to\infty: \ \tilde{T}=\tilde{T}_\infty, \qquad \tilde{Y}_\mathrm{F}=0, \qquad \tilde{Y}_i=\left(\tilde{Y}_i\right)_\infty \qquad (i=\mathrm{O, P, N}), \end{aligned} \tag{26}$$

which are to be supplemented by the following conservation relations at the surface:

$$-\left(\frac{d\tilde{Y}_\mathrm{F}}{d\eta}\right)_\mathrm{s}+\left(-f_\mathrm{s}\right)\tilde{Y}_{\mathrm{F,s}}=\delta\left(-f_{\mathrm{s,O}}\right)+2\delta\left(-f_{\mathrm{s,P}}\right)=\delta\left(-f_\mathrm{s}\right)+\delta\left(-f_{\mathrm{s,P}}\right), \tag{27}$$

$$-\left(\frac{d\tilde{Y}_\mathrm{O}}{d\eta}\right)_\mathrm{s}+\left(-f_\mathrm{s}\right)\tilde{Y}_{\mathrm{O,s}}=-\delta\left(-f_{\mathrm{s,O}}\right)=-\delta\left(-f_\mathrm{s}\right)+\delta\left(-f_{\mathrm{s,P}}\right), \tag{28}$$

$$-\left(\frac{d\tilde{Y}_\mathrm{P}}{d\eta}\right)_\mathrm{s}+\left(-f_\mathrm{s}\right)\tilde{Y}_{\mathrm{P,s}}=-\delta\left(-f_{\mathrm{s,P}}\right), \tag{29}$$

$$-\left(\frac{d\tilde{Y}_\mathrm{N}}{d\eta}\right)_\mathrm{s}+\left(-f_\mathrm{s}\right)\tilde{Y}_{\mathrm{N,s}}=0, \tag{30}$$

where

$$\delta\left(-f_\mathrm{s}\right)=\delta\left(-f_{\mathrm{s,O}}\right)+\delta\left(-f_{\mathrm{s,P}}\right)=A_{\mathrm{s,O}}\tilde{Y}_{\mathrm{O,s}}+A_{\mathrm{s,P}}\tilde{Y}_{\mathrm{P,s}}\ ; \tag{31}$$

$$A_{\mathrm{s,O}}\equiv Da_{\mathrm{s,O}}\left(\frac{\tilde{T}_\infty}{\tilde{T}_\mathrm{s}}\right)\exp\left(-\frac{\tilde{T}a_{\mathrm{s,O}}}{\tilde{T}_\mathrm{s}}\right); \quad Da_{\mathrm{s,O}}\equiv\frac{B_{\mathrm{s,O}}}{\sqrt{2^j a(\mu_\infty/\rho_\infty)}},$$

$$A_{\mathrm{s,P}}\equiv Da_{\mathrm{s,P}}\left(\frac{\tilde{T}_\infty}{\tilde{T}_\mathrm{s}}\right)\exp\left(-\frac{\tilde{T}a_{\mathrm{s,P}}}{\tilde{T}_\mathrm{s}}\right); \quad Da_{\mathrm{s,P}}\equiv\frac{B_{\mathrm{s,P}}}{\sqrt{2^j a(\mu_\infty/\rho_\infty)}},$$

and $Da_{\mathrm{s,O}}$ and $Da_{\mathrm{s,P}}$ are the present surface Damköhler numbers, based only on the frequency factors for the C-O_2 and C-CO_2 reactions, respectively. Here, these heterogeneous

reactions are assumed to be first order, for simplicity and analytical convenience.[1] As for the kinetic expressions for non-permeable solid carbon, effects of porosity and/or internal surface area are considered to be incorporated, since surface reactions are generally controlled by combinations of chemical kinetics and pore diffusions.
For self-similar flows, the normal velocity v_s at the surface is expressible in terms of $(-f_s)$ by

$$(\rho v)_s = (-f_s)\sqrt{2^j a\, \rho_\infty \mu_\infty} \ . \tag{32}$$

Reminding the fact that the mass burning rate of solid carbon is given by $\dot{m} = (\rho v)_s$, which is equivalent to the definition of the combustion rate [kg/(m²·s)], then $(-f_s)$ can be identified as the nondimensional combustion rate. Note also that the surface reactions are less sensitive to velocity gradient variations than the gas-phase reaction because $Da_s \sim a^{-1/2}$ while $Da_g \sim a^{-1}$.

2.5 Coupling functions

With the boundary conditions for species, cast in the specific forms of Eqs. (27) to (29), the coupling functions for the present system are given by

$$\tilde{Y}_F + \tilde{Y}_P = \frac{\left(\tilde{Y}_{P,\infty} + \delta\beta\right) + \left(\tilde{Y}_{P,\infty} - \delta\right)\beta\xi}{1+\beta}, \tag{33}$$

$$\tilde{Y}_O + \tilde{Y}_P = \frac{\left(\tilde{Y}_{O,\infty} + \tilde{Y}_{P,\infty} - \delta\beta\right) + \left(\tilde{Y}_{O,\infty} + \tilde{Y}_{P,\infty} + \delta\right)\beta\xi}{1+\beta}, \tag{34}$$

$$\tilde{Y}_O + \tilde{T} = \tilde{Y}_{O,s} + \tilde{T}_s + \left(\tilde{Y}_{O,\infty} - \tilde{Y}_{O,s} + \tilde{T}_\infty - \tilde{T}_s\right)\xi; \qquad \tilde{Y}_{O,s} = \frac{\tilde{Y}_{O,\infty} + \tilde{T}_\infty - \tilde{T}_s - \gamma}{1+\beta+A_{s,O}\left[\beta/(-f_s)\right]}, \tag{35}$$

$$\tilde{Y}_P - \tilde{T} = \tilde{Y}_{P,s} - \tilde{T}_s + \left(\tilde{Y}_{P,\infty} - \tilde{Y}_{P,s} - \tilde{T}_\infty + \tilde{T}_s\right)\xi; \qquad \tilde{Y}_{P,s} = \frac{\tilde{Y}_{P,\infty} - \tilde{T}_\infty + \tilde{T}_s + \gamma}{1+\beta+A_{s,P}\left[\beta/(-f_s)\right]}, \tag{36}$$

$$\tilde{Y}_N = \tilde{Y}_{N,\infty}\frac{1+\beta\,\xi}{1+\beta}, \tag{37}$$

where

$$\xi = \frac{\int_0^\eta \exp\left(-\int_0^\eta f\, d\eta\right) d\eta}{\int_0^\infty \exp\left(-\int_0^\eta f\, d\eta\right) d\eta}, \tag{38}$$

$$\gamma = \frac{\left(\tilde{T}'\right)_s}{(\xi')_s}, \qquad \beta = \frac{(-f_s)}{(\xi')_s}, \qquad (\xi')_s = \frac{1}{\int_0^\infty \exp\left(-\int_0^\eta f\, d\eta\right) d\eta}, \tag{39}$$

[1]The surface C-O_2 reaction of half-order is also applicable (Makino, 1990).

and a prime indicates $d/d\eta$. Using the new independent variable ξ, the energy conservation Eq. (17) becomes

$$\left(\frac{d^2\tilde{T}}{d\xi^2}\right) = -\frac{Da_g \omega_g}{(d\xi/d\eta)^2} \,. \tag{40}$$

Therefore, the equations to be solved are Eqs. (15) and (40), subject to the boundary conditions in Eq. (25) and

$$\left(\tilde{T}\right)_{\xi=0} = \tilde{T}_s, \qquad \left(\tilde{T}\right)_{\xi=1} = \tilde{T}_\infty \,, \tag{41}$$

by use of $(-f_s)$ given by Eq. (31) and the coupling functions in Eqs. (33) to (36). Key parameters in solving those are Da_g, $Da_{s,O}$, $Da_{s,P}$, and $(-f_s)$.

2.6 Transfer number and combustion rate

The influence of finite rate gas-phase kinetics is studied here. The global rate equation used has the same form as that of Howard, et al. (1973), in which the activation energy and the frequency factor are reported to be E_g=113 kJ/mol and B_g=1.3×10^8 [(mol/m^3)·s]$^{-1}$, respectively. The combustion response is quite similar to that of particle combustion (Makino & Law, 1986), as shown in Fig. 1(a) (Makino, 1990). The parameter β, indispensable in obtaining the combustion rate, is bounded by limiting solutions to be mentioned, presenting that the gas-phase CO-O_2 reaction reduces the surface C-O_2 reaction by consuming O_2, while at the same time initiating the surface C-CO_2 reaction by supplying CO_2, and that with increasing surface temperature the combustion rate can first increase, then decrease, and increase again as a result of the close coupling between the three reactions. In addition, the combustion process depends critically on whether the gas-phase CO-O_2 reaction is activated. If it is not, the oxygen in the ambience can readily reach the surface to participate in the C-O_2 reaction. Activation of the surface C-CO_2 reaction depends on whether the environment contains any CO_2. However, if the gas-phase CO-O_2 reaction is activated, the existence of CO-flame in the gas phase cuts off most of the oxygen supplied to the surface such that the surface C-O_2 reaction is suppressed. At the same time, the CO_2 generated at the flame activates the surface C-CO_2 reaction.

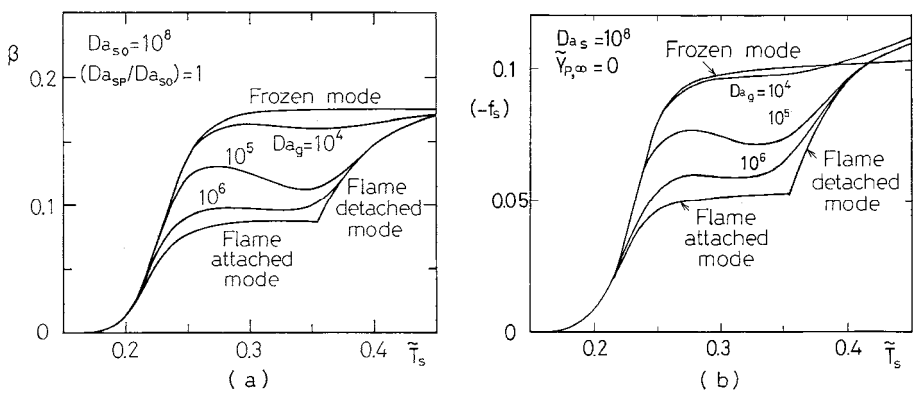

Fig. 1. Combustion behavior as a function of the surface temperature with the gas-phase Damköhler number taken as a parameter; $Da_{s,O}$= $Da_{s,P}$=10^8 and $Y_{P,\infty}$=0 (Makino, 1990). (a) Transfer number. (b) Nondimensional combustion rate.

It may informative to note that the parameter β, defined as $(-f_s)/(\xi')_s$ in the formulation, coincides with the conventional transfer number (Spalding, 1951), which has been shown by considering elemental carbon, $(W_C/W_F)Y_F+(W_C/W_P)Y_P$, taken as the transferred substance, and by evaluating driving force and resistance, determined by the transfer rate in the gas phase and the ejection rate at the surface, respectively (Makino, 1992; Makino, et al., 1998). That is,

$$\frac{\left(\frac{W_C Y_F}{W_F}+\frac{W_C Y_P}{W_P}\right)_s-\left(\frac{W_C Y_F}{W_F}+\frac{W_C Y_P}{W_P}\right)_\infty}{1-\left(\frac{W_C Y_F}{W_F}+\frac{W_C Y_P}{W_P}\right)_s}=\frac{\left(\tilde{Y}_F+\tilde{Y}_P\right)_s-\left(\tilde{Y}_F+\tilde{Y}_P\right)_\infty}{\delta-\left(\tilde{Y}_F+\tilde{Y}_P\right)_s}\equiv\beta\,. \tag{42}$$

Figure 1(b) shows the combustion rate in the same conditions. At high surface temperatures, because of the existence of high-temperature reaction zone in the gas phase, the combustion rate is enhanced. In this context, the transfer number, less temperature-sensitive than the combustion rate, as shown in Figs. 1(a) and 1(b), is preferable for theoretical considerations.

3. Combustion behavior in the limiting cases

Here we discuss analytical solutions for some limiting cases of the gas-phase reaction, since several limiting solutions regarding the intensity of the gas-phase CO-O_2 reaction can readily be identified from the coupling functions. In addition, important characteristics indispensable for fundamental understanding is obtainable.

3.1 Frozen mode

When the gas-phase CO-O_2 reaction is completely frozen, the solution of the energy conservation Eq. (17) readily yields

$$\tilde{T}=\tilde{T}_s+\gamma\,\xi\,;\quad \gamma=\tilde{T}_\infty-\tilde{T}_s\,. \tag{43}$$

Evaluating Eqs. (35) and (36) at ξ=0 for obtaining surface concentrations of O_2 and CO_2, and substituting them into Eq. (31), we obtain an implicit expression for the combustion rate $(-f_s)$

$$\delta\left(-f_s\right)=A_{s,O}\frac{\tilde{Y}_{O,\infty}}{1+\beta+A_{s,O}\left[\beta/\left(-f_s\right)\right]}+A_{s,P}\frac{\tilde{Y}_{P,\infty}}{1+\beta+A_{s,P}\left[\beta/\left(-f_s\right)\right]}\,, \tag{44}$$

which is to be solved numerically from Eq. (15), because of the density coupling. The combustion rate in the diffusion controlled regime becomes the highest with satisfying the following condition.

$$\beta_{max}=\frac{\tilde{Y}_{O,\infty}+\tilde{Y}_{P,\infty}}{\delta} \tag{45}$$

3.2 Flame-detached mode

When the gas-phase CO-O_2 reaction occurs infinitely fast, two flame-sheet burning modes are possible. One involves a detached flame-sheet, situated away from the surface, and

the other an attached flame-sheet, situated on the surface. The Flame-detached mode is defined by

$$\tilde{Y}_{\mathrm{O}}\left(0 \le \xi \le \xi_f\right) = \tilde{Y}_{\mathrm{F}}\left(\xi_f \le \xi \le \infty\right) = 0\,. \tag{46}$$

By using the coupling functions in Eqs. (33) to (36), it can be shown that

$$\delta\left(-f_{\mathrm{s}}\right) = A_{\mathrm{s,P}}\,\frac{\tilde{Y}_{\mathrm{O},\infty} + \tilde{Y}_{\mathrm{P},\infty} - \delta\beta}{1+\beta} \tag{47}$$

$$\tilde{T}_f = \tilde{T}_{\mathrm{s}} + \left(\tilde{Y}_{\mathrm{O},\infty} + \tilde{T}_{\infty} - \tilde{T}_{\mathrm{s}}\right)\xi_f\,; \qquad \xi_f = \frac{2\delta\beta - \tilde{Y}_{\mathrm{O},\infty}}{\left(2\delta + \tilde{Y}_{\mathrm{O},\infty}\right)\beta}, \tag{48}$$

Once ($-f_{\mathrm{s}}$) is determined from Eqs. (47) and (15), ξ_f can readily be evaluated, yielding the temperature distribution as

$$0 \le \xi \le \xi_f : \quad \tilde{T} = \tilde{T}_{\mathrm{s}} + \left(\tilde{Y}_{\mathrm{O},\infty} + \tilde{T}_{\infty} - \tilde{T}_{\mathrm{s}}\right)\xi\,, \tag{49}$$

$$\xi_f \le \xi \le \infty : \quad \tilde{T} = \tilde{T}_{\infty} - \left\{\tilde{T}_{\infty} - \tilde{T}_{\mathrm{s}} + \left(\frac{\tilde{Y}_{\mathrm{O},\infty} - 2\delta\beta}{1+\beta}\right)(1-\xi)\right\}. \tag{50}$$

In addition, the infinitely large Da_{g} yields the following important characteristics, as reported by Tsuji & Matsui (1976).

1. The quantities Y_{F} and Y_{O} in the reaction rate ω_{g} in Eq. (20) becomes zero, suggesting that fuel and oxygen do not coexist throughout the boundary layer and that the diffusion flame becomes a flame sheet.
2. In the limit of an infinitesimally thin reaction zone, by conducting an integration of the coupling function for CO and O_2 across the zone, bounded between $\eta_{f-} < \eta < \eta_{f+}$, where η_f is the location of flame sheet, we have

$$-\left(\frac{d\tilde{Y}_{\mathrm{F}}}{d\eta}\right)_{f-} = \left(\frac{d\tilde{Y}_{\mathrm{O}}}{d\eta}\right)_{f+} \quad \text{or} \quad -\left(\frac{dY_{\mathrm{F}}}{d\eta}\right)_{f-} = \frac{\nu_{\mathrm{F}} W_{\mathrm{F}}}{\nu_{\mathrm{O}} W_{\mathrm{O}}}\left(\frac{dY_{\mathrm{O}}}{d\eta}\right)_{f+}, \tag{51}$$

   suggesting that fuel and oxidizer must flow into the flame surface in stoichiometric proportions. Here the subscript $f+$ and $f-$, respectively, designate the oxygen and fuel sides of the flame. Note that in deriving Eq. (51), use has been made of an assumption that values of the individual quantities, such as the streamfunction f and species mass-fraction Y_i, can be continuous across the flame.
3. Similarly, by evaluating the coupling function for CO and enthalpy, we have

$$\left(\frac{d\tilde{T}}{d\eta}\right)_{f-} - \left(\frac{d\tilde{T}}{d\eta}\right)_{f+} = -\left(\frac{d\tilde{Y}_{\mathrm{F}}}{d\eta}\right)_{f-} \quad \text{or} \quad \lambda\left(\frac{dT}{d\eta}\right)_{f-} - \lambda\left(\frac{dT}{d\eta}\right)_{f+} = -q\rho D\left(\frac{dY_{\mathrm{F}}}{d\eta}\right)_{f-}, \tag{52}$$

   suggesting that the amount of heat generated is equal to the heat, conducted away to the both sides of the reaction zone.

3.3 Flame-attached mode

When the surface reactivity is decreased by decreasing the surface temperature, then the detached flame sheet moves towards the surface until it is contiguous to it ($\xi_f = 0$). This critical state is given by the condition

$$\beta_a = \frac{\tilde{Y}_{O,\infty}}{2\delta}, \tag{53}$$

obtained from Eq. (48), and defines the transition from the detached to the attached mode of the flame. Subsequent combustion with the Flame-attached mode is characterized by $Y_{F,s} = 0$ and $Y_{O,s} \geq 0$ (Libby & Blake, 1979; Makino & Law, 1986; Henriksen, et al., 1988), with the gas-phase temperature profile

$$\tilde{T} = \tilde{T}_s + \left(\tilde{T}_\infty - \tilde{T}_s\right)\xi, \tag{54}$$

given by the same relation as that for the frozen case, because all gas-phase reaction is now confined at the surface. By using the coupling functions in Eqs. (33) to (36) with $Y_{F,s} = 0$, it can be shown that

$$\delta\left(-f_s\right) = A_{s,O}\frac{\tilde{Y}_{O,\infty} - 2\delta\beta}{1+\beta} + A_{s,P}\frac{\tilde{Y}_{P,\infty} + \delta\beta}{1+\beta}. \tag{55}$$

which is also to be solved numerically from Eq. (15). The maximum combustion rate of this mode occurs at the transition state in Eq. (53), which also corresponds to the minimum combustion rate of the Flame-detached mode.

3.4 Diffusion-limited combustion rate

The maximum, diffusion-limited transfer number of the system can be achieved through one of the two limiting situations. The first appears when both of the surface reactions occur infinitely fast such that $Y_{O,s}$ and $Y_{P,s}$ both vanish, yielding Eq. (45). The second appears when the surface C-CO_2 reaction occurs infinitely fast in the limit of the Flame-detached mode, which again yields Eq. (45). It is of interest to note that in the first situation the reactivity of the gas-phase CO-O_2 reaction is irrelevant, whereas in the second the reactivity of the surface C-O_2 reaction is irrelevant. While the transfer numbers β are the same in both cases, the combustion rates, thereby the oxygen supply rates, are slightly different each other, as shown in Fig, 1(b), because of the different density coupling, related to the flame structures. Note that the limiting solutions identified herein provide the counterparts of those previously derived (Libby & Blake, 1979; Makino & Law, 1986) for the carbon particle, and generalize the solution of Matsui & Tsuji (1987) with including the surface C-CO_2 reaction.

4. Combustion rate and flame structure

A momentary reduction in the combustion rate, reported in theoretical works (Adomeit, et al., 1985; Makino & Law, 1986; Matsui & Tsuji, 1987; Henriksen, 1989; Makino, 1990; Makino & Law, 1990), can actually be exaggerated by the appearance of CO-flame in the gas phase, bringing about a change of the dominant surface reactions from the faster C-O_2 reaction to the slower C-CO_2 reaction, due to an intimate coupling between the surface and gas-phase

reactions. In spite of this theoretical accomplishment, there are very few experimental data that can support it.

In the literature, in general, emphasis has been put on examination of the surface reactivities with gaseous oxidizers, such as O_2, CO_2, and H_2O (*cf.* Essenhigh, 1981) although surface reactivities on the same solid carbon are limited (Khitrin & Golovina, 1964; Visser & Adomeit, 1984; Harris & Smith, 1990). As for the gas-phase CO-O_2 reactivity, which is sensitive to the H_2O concentration, main concern has been put on that of the CO-flame (Howard, et al., 1973), called the "strong" CO-oxidation, which is, however, far from the situation over the burning carbon, especially for that prior to the appearance of CO-flame, because some of the elementary reactions are too slow to sustain the "strong" CO-oxidation. Furthermore, it has been quite rare to conduct experimental studies from the viewpoint that there exist interactions between chemical reactions and flow, so that studies have mainly been confined to obtaining combustion rate (Khitrin & Golovina, 1964; Visser & Adomeit, 1984; Matsui, et al., 1975; Matsui, et al., 1983, 1986).

In order to examine such interactions, an attempt has been made to measure temperature profiles over the burning graphite rod in the forward stagnation flowfield (Makino, et al., 1996). In this measurement, N_2-CARS[2] thermometry (Eckbreth, 1988) is used in order to avoid undesired appearance and/or disappearance of the CO-flame. Not only the influence due to the appearance of CO-flame on the temperature profile, but also that on the combustion rate is investigated. Measured results are further compared with predicted results (Makino, 1990; Makino & Law, 1990; Makino, et al., 1994).

4.1 Combustion rate and ignition surface-temperature

Here, experimental results for the combustion rate and the temperature profiles in the gas phase are first presented, which are closely related to the coupled nature of the surface and gas-phase reactions. The experimental setup is schematically shown in Fig. 2. Air used as an oxidizer is supplied by a compressor and passes through a refrigerator-type dryer and a surge tank. The dew point from which the H_2O concentration is determined is measured by a hygrometer. The airflow at room temperature, after passing through a settling chamber (52.8 mm in diameter and 790 mm in length), issues into the atmosphere with a uniform velocity (up to 3 m/s), and impinges on a graphite rod to establish a two-dimensional stagnation flow. This flowfield is well-established and is specified uniquely by the velocity gradient a ($=4V_\infty/d$), where V_∞ is the freestream velocity and d the diameter of the graphite rod. The rod is Joule-heated by an alternating current (12 V; up to 1625 A). The surface temperature is measured by a two-color pyrometer. The temperature in the central part (about 10 mm in length) of the test specimen is nearly uniform. In experiment, the test specimen is set to burn in airflow at constant surface temperature during each experimental run. Since the surface temperature is kept constant with external heating, quasi-steady combustion can be accomplished. The experiment involves recording image of test specimen in the forward stagnation region by a video camera and analyzing the signal displayed on a TV monitor to obtain surface regression rate, which is used to determine the combustion rate, after having examined its linearity on the combustion time.

Figure 2(a) shows the combustion rate in airflow of 110 s^{-1} (Makino, et al., 1996), as a function of the surface temperature, when the H_2O mass-fraction is 0.003. The combustion rate, obtained from the regression rate and density change of the test specimen, increases

[2] CARS: Coherent Anti-Stokes Raman Spectroscopy

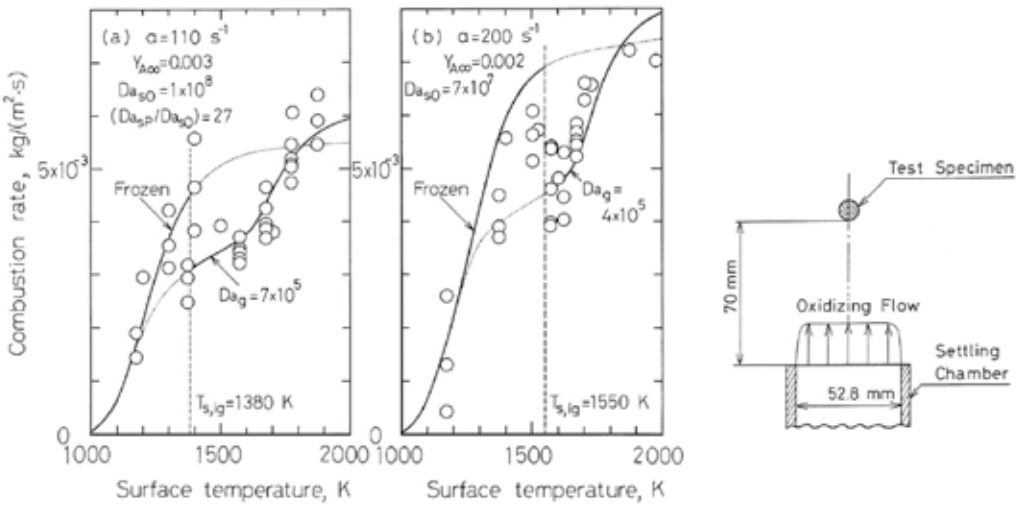

Fig. 2. Combustion rate of graphite rod (ρ_C=1.25×10^3 kg/m^3) as a function of the surface temperature; (a) for the velocity gradient of 110 s^{-1} in airflow with the H_2O mass-fraction of 0.003; (b) for the velocity gradient of 200 s^{-1} in airflow with the H_2O mass-fraction of 0.002. Data points are experimental (Makino, et al., 1996) and curves are calculated for the theory (Makino, 1990). The gas-phase Damköhler number corresponds to that for the "strong" CO-oxidation. The ignition surface-temperature $T_{s,ig}$ is calculated, based on the ignition analysis (Makino & Law, 1990). Schematical drawing of the experimental setup is also shown.

with increasing surface temperature, up to a certain surface temperature. The combustion in this temperature range is that with negligible CO-oxidation, and hence the combustion rate in Frozen mode can fairly predict the experimental results. A further increase in the surface temperature causes the momentary reduction in the combustion rate, because appearance of the CO-flame alters the dominant surface reaction from the C-O_2 reaction to the C-CO_2 reaction. The surface temperature when the CO-flame first appears is called the ignition surface-temperature (Makino & Law, 1990), above which the combustion proceeds with the "strong" CO-oxidation. The solid curve is the predicted combustion rate with the surface kinetic parameters (Makino, et al., 1994) to be explained in the next Section, and the global gas-phase kinetic parameters (Howard, et al., 1973). In numerical calculations, use has been made of the formulation, presented in Section 2.

The same trend is also observed in airflow of 200 s^{-1}, as shown in Fig. 2(b). Because of the reduced thickness of the boundary layer with respect to the oxidizer concentration, the combustion rate at a given surface temperature is enhanced. The ignition surface-temperature is raised because establishment of the CO-flame is suppressed, due to an increase in the velocity gradient.

4.2 Temperature profile in the gas phase

Temperature profiles in the forward stagnation region are shown in Fig. 3(a) when the velocity gradient of airflow is 110 s^{-1} and the H_2O mass-fraction is 0.002. The surface temperature is taken as a parameter, being controlled not to exceed ±20 K from a given value. We see that the temperature profile below the ignition surface-temperature (*ca.* 1450 K) is completely different from that above the ignition surface-temperature. When the

surface temperature is 1400 K, the gas-phase temperature monotonically decreases, suggesting negligible gas-phase reaction. When the surface temperature is 1500 K, at which CO-flame can be observed visually, there exists a reaction zone in the gas phase whose temperature is nearly equal to the surface temperature. Outside the reaction zone, the temperature gradually decreases to the freestream temperature. When the surface temperature is 1700 K, the gas-phase temperature first increases from the surface temperature to the maximum, and then decreases to the freestream temperature. The existence of the maximum temperature suggests that a reaction zone locates away from the surface. That is, a change of the flame structures has certainly occurred upon the establishment of CO-flame.

It may be informative to note the advantage of the CARS thermometry over the conventional, physical probing method with thermocouple. When the thermocouple is used for the measurement of temperature profile corresponding to the surface temperature of 1400 K (or 1500 K), it distorts the combustion field, and hence makes the CO-flame appear (or disappear). In this context, the present result suggests the importance of using thermometry without disturbing the combustion fields, especially for the measurement at the ignition/extinction of CO-flame. In addition, the present results demonstrate the high spatial resolution of the CARS thermometry, so that the temperature profile within a thin boundary layer of a few mm can be measured.

Predicted results are also shown in Fig. 3(a). In numerical calculations, use has been made of the formulation mentioned in Section 2 and kinetic parameters (Makino, et al., 1994) to be explained in the next Section. When there exists CO-flame, the gas-phase kinetic parameters used are those for the "strong" CO-oxidation; when the CO-oxidation is too weak to establish the CO-flame, those for the "weak" CO-oxidation are used. Fair agreement between experimental and predicted results is shown, if we take account of measurement errors (±50 K) in the present CARS thermometry.

Our choice of the global gas-phase chemistry requires a further comment, because nowadays it is common to use detailed chemistry in the gas phase. Nonetheless, because of its simplicity, it is decided to use the global gas-phase chemistry, after having examined the fact that the formulation with detailed chemistry (Chelliah, et al., 1996) offers nearly the same results as those with global gas-phase chemistry.

Figure 3(b) shows the temperature profiles for the airflow of 200 s^{-1}. Because of the increased velocity gradient, the ignition surface-temperature is raised to be *ca.* 1550 K, and the boundary-layer thickness is contracted, compared to Fig. 3(a), while the general trend is the same.

Figure 3(c) shows the temperature profiles at the surface temperature 1700 K, with the velocity gradient of airflow taken as a parameter (Makino, et al., 1997). It is seen that the flame structure shifts from that with high temperature flame zone in the gas phase to that with gradual decrease in the temperature, suggesting that the establishment of CO-flame can be suppressed with increasing velocity gradient.

Note here that in obtaining data in Figs. 3(a) to 3(c), attention has been paid to controlling the surface temperature not to exceed ±20 K from a given value. In addition, the surface temperature is intentionally set to be lower (or higher) than the ignition surface-temperature by 20 K or more. If we remove these restrictions, results are somewhat confusing and gas-phase temperature scatters in relatively wide range, because of the appearance of unsteady combustion (Kurylko & Essenhigh, 1973) that proceeds without CO-flame at one time, while with CO-flame at the other time.

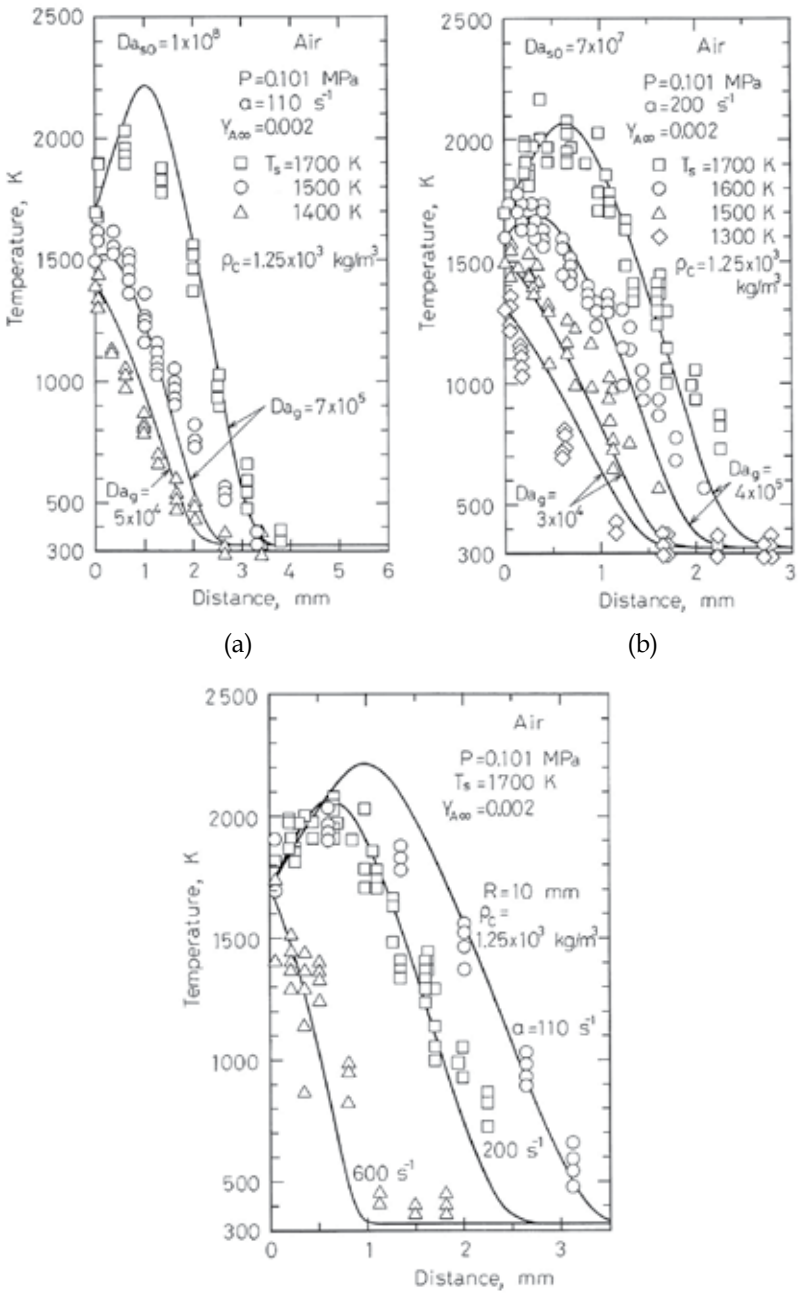

Fig. 3. Temperature profiles over the burning graphite rod in airflow at an atmospheric pressure. The H_2O mass-fraction is 0.002. Data points are experimental (Makino, et al., 1996; Makino, et al., 1997) and solid curves are theoretical (Makino, 1990); (a) for the velocity gradient 110 s^{-1}, with the surface temperature taken as a parameter; (b) for 200 s^{-1}; (c) for the surface temperature 1700 K, with the velocity gradient taken as a parameter.

4.3 Ignition criterion

While studies relevant to the ignition/extinction of CO-flame over the burning carbon are of obvious practical utility in evaluating protection properties from oxidation in re-entry vehicles, as well as the combustion of coal/char, they also command fundamental interests because of the simultaneous existence of the surface and gas-phase reactions with intimate coupling (Visser & Adomeit, 1984; Makino & Law, 1986; Matsui & Tsuji, 1987). As mentioned in the previous Section, at the same surface temperature, the combustion rate is expected to be momentarily reduced upon ignition because establishment of the CO-flame in the gas phase can change the dominant surface reactions from the faster C-O_2 reaction to the slower C-CO_2 reaction. By the same token the combustion rate is expected to momentarily increase upon extinction. These concepts are not intuitively obvious without considering the coupled nature of the gas-phase and surface reactions.

Fundamentally, the ignition/extinction of CO-flame in carbon combustion must necessarily be described by the seminal analysis (Liñán, 1974) of the ignition, extinction, and structure of diffusion flames, as indicated by Matalon (1980, 1981, 1982). Specifically, as the flame temperature increases from the surface temperature to the adiabatic flame temperature, there appear a nearly-frozen regime, a partial-burning regime, a premixed-flame regime, and finally a near-equilibrium regime. Ignition can be described in the nearly-frozen regime, while extinction in the other three regimes.

For carbon combustion, Matalon (1981) analytically obtained an explicit ignition criterion when the O_2 mass-fraction at the surface is O(l). When this concentration is O(ε), the appropriate reduced governing equation and the boundary conditions were also identified (Matalon, 1982). Here, putting emphasis on the ignition of CO-flame over the burning carbon, an attempt has first been made to extend the previous theoretical studies, so as to include analytical derivations of various criteria governing the ignition, with arbitrary O_2 concentration at the surface. Note that these derivations are successfully conducted, by virtue of the generalized species-enthalpy coupling functions (Makino & Law, 1986; Makino, 1990), identified in the previous Section. Furthermore, it may be noted that the ignition analysis is especially relevant for situations where the surface O_2 concentration is O(ε) because in order for gas-phase reaction to be initiated, sufficient amount of carbon monoxide should be generated. This requires a reasonably fast surface reaction and thereby low O_2 concentration. The second objective is to conduct experimental comparisons relevant to the ignition of CO-flame over a carbon rod in an oxidizing stagnation flow, with variations in the surface temperature of the rod, as well as the freestream velocity gradient and O_2 concentration.

4.3.1 Ignition analysis

Here we intend to obtain an explicit ignition criterion without restricting the order of $Y_{O,s}$. First we note that in the limit of $Ta_g \to \infty$, the completely frozen solutions for Eqs. (16) and (17) are

$$\left(\tilde{T}\right)_0 = \tilde{T}_s + \left(\tilde{T}_\infty - \tilde{T}_s\right)\xi \tag{56}$$

$$\left(\tilde{Y}_i\right)_0 = \tilde{Y}_{i,s} + \left(\tilde{Y}_{i,\infty} - \tilde{Y}_{i,s}\right)\xi \qquad (i = \mathrm{F, O, P}) \tag{57}$$

For finite but large values of Ta_g, weak chemical reaction occurs in a thin region next to the carbon surface when the surface temperature is moderately high and exceeds the ambient

temperature. Since the usual carbon combustion proceeds under this situation, corresponding to the condition (Liñán, 1974) of

$$\tilde{T}_{\mathrm{s}} + \tilde{Y}_{\mathrm{F,s}} > \tilde{T}_{\infty}\,, \tag{58}$$

we define the inner temperature distribution as

$$\left(\tilde{T}\right)_{\mathrm{in}} = \left(\tilde{T}\right)_0 + \varepsilon\,\tilde{T}_{\mathrm{s}}\lambda\theta(\xi) + O\left(\varepsilon^2\right) = \tilde{T}_{\mathrm{s}}\left[1-\varepsilon(\chi-\lambda\theta)\right] + O\left(\varepsilon^2\right) \tag{59}$$

where

$$\varepsilon = \frac{\tilde{T}_{\mathrm{s}}}{\tilde{T}a_{\mathrm{g}}}\,, \quad \lambda = \frac{\tilde{Y}_{\mathrm{O},\infty}}{\tilde{T}_{\mathrm{s}}-\tilde{T}_{\infty}}\,, \quad \xi = \varepsilon\left(\frac{\tilde{T}_{\mathrm{s}}}{\tilde{T}_{\mathrm{s}}-\tilde{T}_{\infty}}\right)\chi\,. \tag{60}$$

In the above, ε is the appropriate small parameter for expansion, and χ and θ are the inner variables.

With Eq. (59) and the coupling functions of Eqs. (33) to (36), the inner species distributions are given by:

$$\left(\tilde{Y}_{\mathrm{O}}\right)_{\mathrm{in}} = \tilde{Y}_{\mathrm{O,s}} + \varepsilon\,\tilde{T}_{\mathrm{s}}\lambda(\chi-\theta) \tag{61}$$

$$\left(\tilde{Y}_{\mathrm{F}}\right)_{\mathrm{in}} = \left(\frac{2\delta\beta-\tilde{Y}_{\mathrm{O},\infty}}{1+\beta}\right) + \tilde{Y}_{\mathrm{O,s}} + \varepsilon\left(\frac{\tilde{T}_{\mathrm{s}}}{\tilde{T}_{\mathrm{s}}-\tilde{T}_{\infty}}\right)\left(\frac{\tilde{Y}_{\mathrm{O},\infty}-2\delta\beta}{1+\beta}\chi - \tilde{Y}_{\mathrm{O},\infty}\theta\right). \tag{62}$$

Thus, through evaluation of the parameter γ, expressed as

$$\gamma \equiv \left(\frac{d\tilde{T}}{d\xi}\right)_{\mathrm{s}} = \left[\frac{d\chi}{d\xi}\frac{d\left(\tilde{T}\right)_{\mathrm{in}}}{d\chi}\right]_{\mathrm{s}} = -\left(\tilde{T}_{\mathrm{s}}-\tilde{T}_{\infty}\right) + \tilde{Y}_{\mathrm{O},\infty}\left(\frac{d\theta}{d\chi}\right)_{\mathrm{s}} + O(\varepsilon)\,, \tag{63}$$

the O_2 mass-fraction at the surface is obtained as

$$\tilde{Y}_{\mathrm{O,s}} = \frac{\tilde{Y}_{\mathrm{O},\infty}}{1+\beta+A_{\mathrm{s,O}}\left[\beta/\left(-f_{\mathrm{s}}\right)\right]}\left\{1-\left(\frac{d\theta}{d\chi}\right)_{\mathrm{s}}\right\}. \tag{64}$$

Substituting χ, Eqs. (59), (61), and (62) into the governing Eq. (17), expanding, and neglecting the higher-order convection terms, we obtain

$$\frac{d^2\theta}{d\chi^2} = -\Delta(\chi-\theta+\eta_{\mathrm{O}})^{1/2}\exp(\lambda\theta-\chi), \tag{65}$$

where

$$\Delta = Da_{\mathrm{g}}\exp\left(-\frac{\tilde{T}a_{\mathrm{g}}}{\tilde{T}_{\mathrm{s}}}\right)\left\{\left(\frac{\beta}{\left(-f_{\mathrm{s}}\right)}\right)\left(\frac{\tilde{T}_{\mathrm{s}}}{\tilde{T}_{\mathrm{s}}-\tilde{T}_{\infty}}\right)\right\}^2\left(\frac{\tilde{T}_{\mathrm{s}}}{\tilde{T}a_{\mathrm{g}}}\right)^{3/2}\left(\frac{\tilde{T}_{\infty}}{\tilde{T}_{\mathrm{s}}}\right)^{1/2}\frac{\tilde{Y}_{\mathrm{F,s}}}{\left(\lambda\tilde{T}_{\mathrm{s}}\right)^{1/2}}\,, \tag{66}$$

$$\eta_O = \frac{\tilde{Y}_{O,s}}{\varepsilon \tilde{T}_s \lambda} . \tag{67}$$

Note that the situation of $Y_{F,s} = O(\varepsilon)$ is not considered here because it corresponds to very weak carbon combustion, such as in low O_2 concentration or at low surface temperature.
Evaluating the inner temperature at the surface of constant T_s, one boundary condition for Eq. (65) is

$$\theta(0)=0 \tag{68}$$

This boundary condition is a reasonable one from the viewpoint of gas-phase quasi-steadiness in that its surface temperature changes at rates much slower than that of the gas phase, since solid phase has great thermal inertia.
For the outer, non-reactive region, if we write

$$\left(\tilde{T}\right)_{\text{out}} = \tilde{T}_s + \left(\tilde{T}_\infty - \tilde{T}_s\right)\xi + \varepsilon\, \tilde{T}_s \Theta(\xi) + O\left(\varepsilon^2\right), \tag{69}$$

we see from Eq. (17) that Θ is governed by $L(\Theta) = 0$ with the boundary condition that $\Theta(\infty) = 0$. Then, the solution is $\Theta(\xi) = -C_I(1 - \xi)$, where C_I is a constant to be determined through matching.
By matching the inner and outer temperatures presented in Eqs. (59) and (69), respectively, we have

$$\lambda\theta(\infty) = -C_I, \qquad \left(\frac{d\theta}{d\chi}\right)_\infty = 0 . \tag{70}$$

the latter of which provides the additional boundary condition to solve Eq. (65), while the former allows the determination of C_I.
Thus the problem is reduced to solving the single governing Eq. (65), subject to the boundary conditions Eqs. (68) and (70). The key parameters are Δ, λ, and η_O. Before solving Eq. (65) numerically, it should be noted that there exists a general expression for the ignition criterion as

$$2\Delta_I\lambda = \frac{1}{\sqrt{\eta_O} + \frac{\sqrt{\pi/\lambda}}{2} e^{\lambda\eta_O}\left\{erfc(\lambda\eta_O) + (\lambda - 1)\int_{\chi_I}^{\infty} e^{(\lambda-1)\chi} erfc(z)d\chi\right\}} ; \; erfc(z) = \frac{2}{\sqrt{\pi}}\int_z^\infty \exp\left(-t^2\right)dt , \tag{71}$$

corresponding to the critical condition for the vanishment of solutions at

$$\left(\frac{d\theta}{d\chi}\right)_s = \frac{1}{\lambda} \quad \text{or} \quad \left(\frac{d\left(\tilde{T}\right)_{in}}{d\xi}\right)_s = 0 , \tag{72}$$

which implies that the heat transferred from the surface to the gas phase ceases at the ignition point. Note also that Eq. (71) further yields analytical solutions for some special cases, such as

$$\text{at } \lambda = 1: \quad 2\Delta_I = \frac{1}{\sqrt{\eta_O} + \frac{\sqrt{\pi}}{2} e^{\eta_O} erfc(\lambda\eta_O)} , \tag{73}$$

$$\text{as } \eta_O \to \infty: \quad 2\Delta_I \lambda = \frac{1}{\sqrt{\eta_O}}, \tag{74}$$

the latter of which agrees with the result of Matalon (1981).
In numerically solving Eq. (65), by plotting $\theta(\infty)$ vs. Δ for a given set of λ and η_O, the lower ignition branch of the S-curve can first be obtained. The values of Δ, corresponding to the vertical tangents to these curves, are then obtained as the reduced ignition Damköhler number Δ_I. After that, a universal curve of $(2\Delta_I\lambda)$ vs. $(1/\lambda)$ is obtained with η_O taken as a parameter. Recognizing that $(1/\lambda)$ is usually less than about 0.5 for practical systems and using Eqs. (71), (73), and (74), we can fairly represent $(2\Delta_I\lambda)$ as (Makino & Law, 1990)

$$2\Delta_I \lambda = \frac{1}{\sqrt{\eta_O} + \frac{\sqrt{\pi}}{2}\left[e^{\eta_O}\, erfc\left(\sqrt{\eta_O}\right) + \left\{ \frac{1}{F(\lambda)} - 1 \right\} \exp\left(-\frac{\sqrt{\eta_O}}{2} \right) \right]}, \tag{75}$$

where

$$F(\lambda) = 0.56 + \frac{0.21}{\lambda} - \frac{0.12}{\lambda^2} + \frac{0.35}{\lambda^3} \tag{76}$$

Note that for large values of $(1/\lambda)$, Eq. (75) is still moderately accurate. Thus, for a given set of λ and η_O, an ignition Damköhler number can be determined by substituting the values of Δ_I, obtained from Eq. (75), into Eq. (66).
It may be informative to note that for some weakly-burning situations, in which O_2 concentrations in the reaction zone and at the carbon surface are O(1), a monotonic transition from the nearly-frozen to the partial-burning behaviors is reported (Henriksen, 1989), instead of an abrupt, turning-point behavior, with increasing gas-phase Damköhler number. However, this could be a highly-limiting behavior. That is, in order for the gas-phase reaction to be sufficiently efficient, and the ignition to be a reasonably plausible event, enough CO would have to be generated at the surface, which further requires a sufficiently fast surface C-O_2 reaction and hence the diminishment of the surface O_2 concentration from O(l). For these situations, the turning-point behavior can be a more appropriate indication for the ignition.

4.3.2 Experimental comparisons for the ignition of CO flame

Figure 4 shows the ignition surface-temperature (Makino, et al., 1996), as a function of the velocity gradient, with O_2 mass-fraction taken as a parameter. The velocity gradient has been chosen for the abscissa, as originally proposed by Tsuji & Yamaoka (1967) for the present flow configuration, after confirming its appropriateness, being examined by varying both the freestream velocity and graphite rod diameter that can exert influences in determining velocity gradient. It is seen that the ignition surface-temperature increases with increasing velocity gradient and thereby decreasing residence time. The high surface temperature, as well as the high temperature in the reaction zone, causes the high ejection rate of CO through the surface C-O_2 reaction. These enhancements facilitate the CO-flame, by reducing the characteristic chemical reaction time, and hence compensating a decrease in the characteristic residence time. It is also seen that the ignition surface-temperature

decreases with increasing $Y_{O,\infty}$. In this case the CO-O_2 reaction is facilitated with increasing concentrations of O_2, as well as CO, because more CO is now produced through the surface C-O_2 reaction.

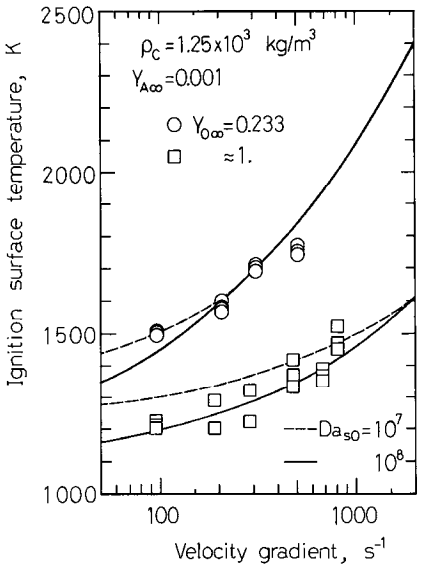

Fig. 4. Surface temperature at the establishment of CO-flame, as a function of the stagnation velocity gradient, with the O_2 mass-fraction in the freestream and the surface Damköhler number for the C-O_2 reaction taken as parameters. Data points are experimental (Makino, et al., 1996) with the test specimen of 10 mm in diameter and 1.25×10^3 kg/m^3 in graphite density; curves are calculated from theory (Makino & Law, 1990).

Solid and dashed curves in Fig. 4 are predicted ignition surface-temperature for $Da_{s,O}=10^7$ and 10^8, obtained by the ignition criterion described here and the kinetic parameters (Makino, et al., 1994) to be explained, with keeping as many parameters fixed as possible. The density ρ_∞ of the oxidizing gas in the freestream is estimated at T_∞= 323 K. The surface Damköhler numbers in the experimental conditions are from 2×10^7 to 2×10^8, which are obtained with $B_{s,O}$ = 4.1×10^6 m/s. It is seen that fair agreement is demonstrated, suggesting that the present ignition criterion has captured the essential feature of the ignition of CO-flame over the burning carbon.

5. Kinetic parameters for the surface and gas-phase reactions

In this Section, an attempt is made to extend and integrate previous theoretical studies (Makino, 1990; Makino and Law, 1990), in order to further investigate the coupled nature of the surface and gas-phase reactions. First, by use of the combustion rate of the graphite rod in the forward stagnation region of various oxidizer-flows, it is intended to obtain kinetic parameters for the surface C-O_2 and C-CO_2 reactions, based on the theoretical work (Makino, 1990), presented in Section 2. Second, based on experimental facts that the ignition of CO-flame over the burning graphite is closely related to the surface temperature and the

stagnation velocity gradient, it is intended to obtain kinetic parameters for the global gas-phase CO-O_2 reaction prior to the ignition of CO-flame, by use of the ignition criterion (Makino and Law, 1990), presented in Section 4. Finally, experimental comparisons are further to be conducted.

5.1 Surface kinetic parameters

In estimating kinetic parameters for the surface reactions, their contributions to the combustion rate are to be identified, taking account of the combustion situation in the limiting cases, as well as relative reactivities of the C-O_2 and C-CO_2 reactions. In the kinetically controlled regime, the combustion rate reflects the surface reactivity of the ambient oxidizer. Thus, by use of Eqs. (31) and (34), the reduced surface Damköhler number is expressed as

$$A_i = \frac{\delta(-f_s)(1+\beta)}{\tilde{Y}_{i,\infty} - \delta\beta} \qquad (i = \mathrm{O}, \mathrm{P}) \tag{77}$$

when only one kind of oxidizer participates in the surface reaction.
In the diffusionally controlled regime, combustion situation is that of the Flame-detached mode, thereby following expression is obtained:

$$A_\mathrm{P} = \frac{\delta(-f_s)(1+\beta)}{\tilde{Y}_{\mathrm{O},\infty} - \delta\beta} \tag{78}$$

Note that the combustion rate here reflects the C-CO_2 reaction even though there only exists oxygen in the freestream.

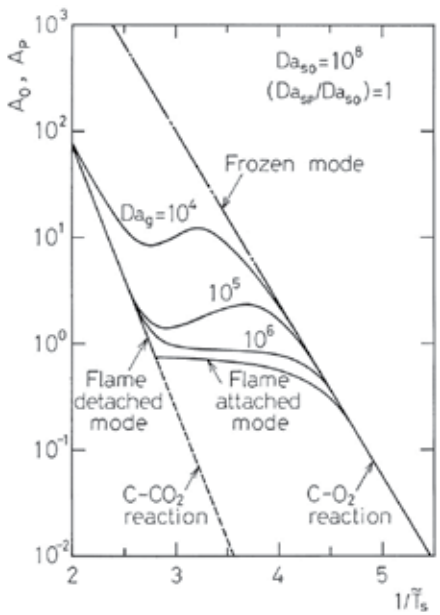

Fig. 5. Arrhenius plot of the reduced surface Damköhler number with the gas-phase Damköhler number taken as a parameter; $Da_{s,O}$= $Da_{s,P}$=10^8; $Da_{s,P}/Da_{s,O}$=1; $Y_{O,\infty}$=0.233; $Y_{P,\infty}$=0 (Makino, et al., 1994).

In order to verify this method, the reduced surface Damköhler number A_i is obtained numerically by use of Eq. (77) and/or Eq. (78). Figure 5 shows the Arrhenius plot of A_i with the gas-phase Damköhler number taken as a parameter. We see that with increasing surface temperature the combustion behavior shifts from the Frozen mode to the Flame-detached mode, depending on the gas-phase Damköhler number. Furthermore, in the present plot, the combustion behavior in the Frozen mode purely depends on the surface C-O_2 reaction rate; that in the Flame-detached mode depends on the surface C-CO_2 reaction rate. Since the appropriateness of the present method has been demonstrated, estimation of the surface kinetic parameters is conducted with experimental results (Makino, et al., 1994), by use of an approximate relation (Makino, 1990)

$$\left(\xi_s'\right) = 0.4\widetilde{T}_s + 0.56 \tag{79}$$

for evaluating the transfer number β from the combustion rate through the relation $\beta=(-f_s)/(\xi'_s)$ in Eq. (39). Values of parameters used are q = 10.11 MJ/kg, c_p = 1.194 kJ/(kg·K), $q/(c_p\alpha_F)$ = 5387 K, and T_∞ = 323 K. Thermophysical properties of oxidizer are also conventional ones (Makino, et al., 1994).

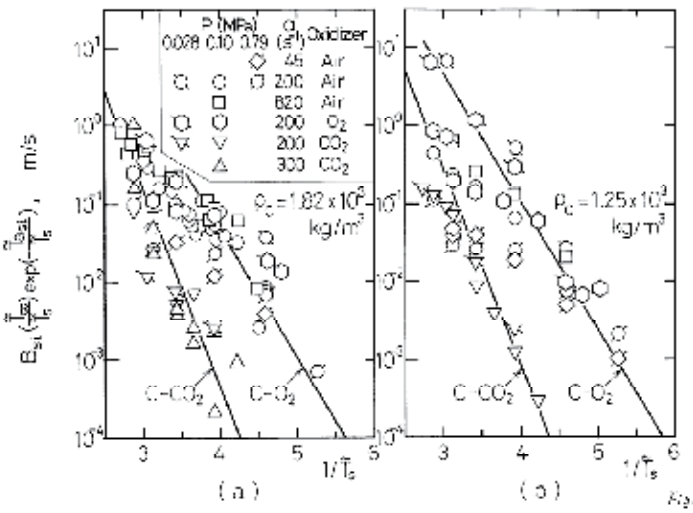

Fig. 6. Arrhenius plot of the surface C-O_2 and C-CO_2 reactions (Makino, et al., 1994), obtained from the experimental results of the combustion rate in oxidizer-flow of various velocity gradients; (a) for the test specimen of 1.82×10^3 kg/m^3 in graphite density; (b) for the test specimen of 1.25×10^3 kg/m^3 in graphite density.

Figure 6(a) shows the Arrhenius plot of surface reactivities, being obtained by multiplying A_i by $[a(\mu_\infty/\rho_\infty)]^{1/2}$, for the results of the test specimen with 1.82×10^3 kg/m^3 in density. For the C-O_2 reaction $B_{s,O}$ =2.2×10^6 m/s and $E_{s,O}$ = 180 kJ/mol are obtained, while for the C-CO_2 reaction $B_{s,P}$ = 6.0×10^7 m/s and $E_{s,P}$ = 269 kJ/mol. Figure 6(b) shows the results of the test specimen with 1.25×10^3 kg/m^3. It is obtained that $B_{s,O}$ = 4.1×10^6 m/s and $E_{s,O}$= 179 kJ/mol for the C-O_2 reaction, and that $B_{s,P}$ = 1.1×10^8 m/s and $E_{s,P}$ = 270 kJ/mol for the C-CO_2 reaction. Activation energies are respectively within the ranges of the surface C-O_2 and C-

CO_2 reactions; *cf.* Table 19.6 in Essenhigh (1981). It is also seen in Figs. 6(a) and 6(b) that the first-order Arrhenius kinetics, assumed in the theoretical model, is appropriate for the surface C-O_2 and C-CO_2 reactions within the present experimental conditions.

5.2 Global gas-phase kinetic parameters

Estimation of gas-phase kinetic parameters has also been made with experimental data for the ignition surface-temperature and the ignition criterion (Makino & Law, 1990) for the CO-flame over the burning carbon. Here, reaction orders are *a priori* assumed to be $n_F = 1$ and $n_O = 0.5$, which are the same as those of the global rate expression by Howard et al. (1973). It is also assumed that the frequency factor B_g is proportional to the half order of H_2O concentration: that is, $B_g = B_g^*(\rho Y_A/W_A)^{1/2}$ $[(\mathrm{mol/m^3})^{1/2}\cdot\mathrm{s}]^{-1}$, where the subscript A designates water vapor. The H_2O mass-fraction at the surface is estimated with $Y_{A,s} = Y_{A,\infty}/(1+\beta)$, with water vapor taken as an inert because it acts as a kind of catalyst for the gas-phase CO-O_2 reaction, and hence its profile is not anticipated to be influenced. Thus, for a given set of λ and η_O, an ignition Damköhler number can be determined by substituting Δ_I in Eq. (75) into Eq. (66).

Figure 7 shows the Arrhenius plot of the global gas-phase reactivity, obtained as the results of the ignition surface-temperature. In data processing, data in a series of experiments (Makino & Law, 1990; Makino, et al., 1994) have been used, with using kinetic parameters for the surface C-O_2 reaction. With iteration in terms of the activation temperature, required for determining Δ_I with respect to η_O, E_g = 113 kJ/mol is obtained with $B_g^* = 9.1\times10^6$ $[(\mathrm{mol/m^3})^{1/2}\cdot\mathrm{s}]^{-1}$. This activation energy is also within the range of the global CO-O_2 reaction; *cf.* Table II in Howard, et al. (1973).

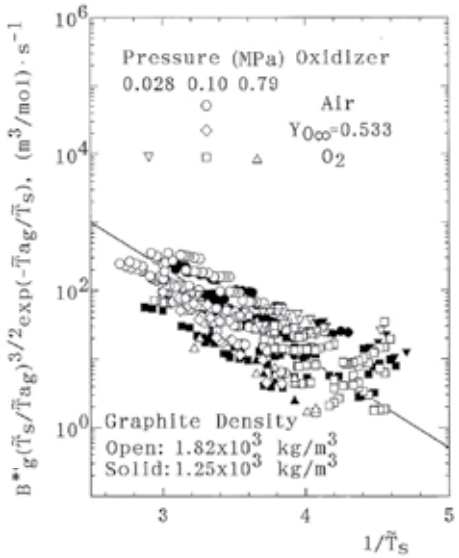

Fig. 7. Arrhenius plot of the global gas-phase reaction (Makino, et al., 1994), obtained from the experimental results of the ignition surface-temperature for the test specimens (1.82×10^3 kg/m^3 and 1.25×10^3 kg/m^3 in graphite density) in oxidizer-flow at various pressures, O_2, and H_2O concentrations .

It is noted that B_g* obtained here is one order of magnitude lower than that of Howard, et al. (1973), which is reported to be B_g* =1.3×10^8 [(mol/m^3)$^{1/2}$·s]$^{-1}$, because the present value is that prior to the appearance of CO-flame and is to be low, compared to that of the "strong" CO-oxidation in the literature. As for the "weak" CO-oxidation, Sobolev (1959) reports B_g* = 3.0×10^6 [(mol/m^3)$^{1/2}$·s]$^{-1}$, by examining data of Chukhanov (1938a, 1938b) who studied the initiation of CO-oxidation, accompanied by the carbon combustion. We see that the value reported by Sobolev (1959) exhibits a lower bound of the experimental results shown in Fig. 7.
It is also confirmed in Fig. 7 that there exists no remarkable effects of O_2 and/or H_2O concentrations in the oxidizer, thereby the assumption for the reaction orders is shown to be appropriate within the present experimental conditions. The choice of reaction orders, however, requires a further comment because another reaction order for O_2 concentration, 0.25 in place of 0.5, is recommended in the literature. Relevant to this, an attempt (Makino, et al., 1994) has further been conducted to compare the experimental data with another ignition criterion, obtained through a similar ignition analysis with this reaction order. However, its result was unfavorable, presenting a much poorer correlation between them.

5.3 Experimental comparisons for the combustion rate

Experimental comparisons have already been conducted in Fig. 2, for test specimens with ρ_C=1.25×10^3 kg/m^3 in graphite density, and a fair degree of agreement has been demonstrated, as far as the trend and approximate magnitude are concerned. Further experimental comparisons are made for test specimens with ρ_C=1.82×10^3 kg/m^3 (Makino, et al., 1994), with kinetic parameters obtained herein. Figure 8(a) compares predicted results with experimental data in airflow of 200 s^{-1} at an atmospheric pressure. The gas-phase Damköhler number is evaluated to be Da_g= 3×10^4 from the present kinetic parameter, while Da_g = 4×10^5 from the value in the literature (Howard, et al., 1973). The ignition surface-temperature is estimated to be $T_{s,ig}$ ≈1476 K from the ignition analysis. We see from Fig. 8(a)

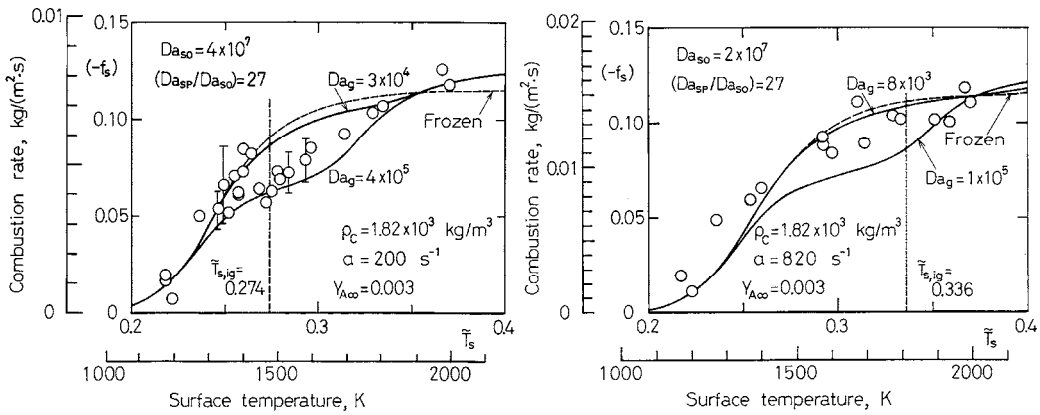

Fig. 8. Experimental comparisons (Makino, et al., 1994) for the combustion rate of test specimen (ρ_C = 1.82×10^3 kg/m^3 in graphite density) in airflow under an atmospheric pressure with H_2O mass-fraction of 0.003; (a) for 200 s^{-1} in stagnation velocity gradient; (b) for 820 s^{-1}. Data points are experimental and solid curves are calculated from theory. The nondimensional temperature can be converted into conventional one by multiplying $q/(c_p\alpha_F)$ = 5387 K.

that up to the ignition surface-temperature the combustion proceeds under the "weak" CO-oxidation, that at the temperature the combustion rate abruptly changes, and that the "strong" CO-oxidation prevails above the temperature.
Figure 8(b) shows a similar plot in airflow of 820 s^{-1}. Because of the lack of the experimental data, as well as the enhanced ignition surface-temperature ($T_{s,ig} \approx 1810$ K), which inevitably leads to small difference between combustion rates before and after the ignition of CO-flame, the abrupt change in the combustion rate does not appear clearly. However, the general behavior is similar to that in Fig. 8(a).
It may informative to note that a decrease in the combustion rate, observed at temperatures between 1500 K and 2000 K, has been so-called the "negative temperature coefficient" of the combustion rate, which has also been a research subject in the field of carbon combustion. Nagel and Strickland-Constable (1962) used the "site" theory to explain the peak rate, while Yang and Steinberg (1977) attributed the peak rate to the change of reaction depth at constant activation energy. Other entries relevant to the "negative temperature coefficient" can be found in the survey paper (Essenhigh, 1981). However, another explanation can be made, as explained (Makino, et al., 1994; Makino, et al., 1996; Makino, et al., 1998) in the previous Sections, that this phenomenon can be induced by the appearance of CO-flame, established over the burning carbon, thereby the dominant surface reaction has been altered from the C-O_2 reaction to the C-CO_2 reaction.
Since the appearance of CO-flame is anticipated to be suppressed at high velocity gradients, it has strongly been required to raise the velocity gradient as high as possible, in order for firm understanding of the carbon combustion, while it has been usual to do experiments under the stagnation velocity gradient less than 1000 s^{-1} (Matsui, et al., 1975; Visser & Adomeit, 1984; Makino, et al., 1994; Makino, et al., 1996), because of difficulties in conducting experiments. In one of the Sections in Part 2, it is intended to study carbon combustion at high velocity gradients.

6. Concluding remarks of part 1

In this monograph, combustion of solid carbon has been overviewed not only experimentally but also theoretically. In order to have a clear understanding, only the carbon combustion in the forward stagnation flowfield has been considered here. In the formulation, an aerothermochemical analysis has been conducted, based on the chemically reacting boundary layer, with considering the surface C-O_2 and C-CO_2 reactions and the gas-phase CO-O_2 reaction. By virtue of the generalized species-enthalpy coupling functions, derived successfully, it has been demonstrated that there exists close coupling between the surface and gas-phase reactions that exerts influences on the combustion rate. Combustion response in the limiting situations has further been identified by using the generalized coupling functions.
After confirming the experimental fact that the combustion rate momentarily reduces upon ignition, because establishment of the CO-flame in the gas phase can change the dominant surface reaction from the faster C-O_2 reaction to the slower C-CO_2 reaction, focus has been put on the ignition of CO-flame over the burning carbon in the prescribed flowfield and theoretical studies have been conducted by using the generalized coupling functions. The asymptotic expansion method has been used to derive the explicit ignition criterion, from which in accordance with experimental results, it has been shown that ignition is facilitated with increasing surface temperature and oxidizer concentration, while suppressed with decreasing velocity gradient.

Then, attempts have been made to estimate kinetic parameters for the surface and gas-phase reactions, indispensable for predicting combustion behavior. In estimating the kinetic parameters for the surface reactions, use has been made of the reduced surface Damköhler number, evaluated by the combustion rate measured in experiments. In estimating the kinetic parameters for the global gas-phase reaction, prior to the appearance of the CO-flame, use has been made of the ignition criterion theoretically obtained, by evaluating it at the ignition surface-temperature experimentally determined. Experimental comparisons have also been conducted and a fair degree of agreement has been demonstrated between experimental and theoretical results.
Further studies are intended to be made in Part 2 for exploring carbon combustion at high velocity gradients and/or in the High-Temperature Air Combustion, in which effects of water-vapor in the oxidizing-gas are also to be taken into account.

7. Acknowledgment

In conducting a series of studies on the carbon combustion, I have been assisted by many of my former graduate and undergraduate students, as well as research staffs, in Shizuoka University, being engaged in researches in the field of mechanical engineering for twenty years as a staff, from a research associate to a full professor. Here, I want to express my sincere appreciation to all of them who have participated in researches for exploring combustion of solid carbon.

8. Nomenclature

General

A	reduced surface Damköhler number
a	velocity gradient in the stagnation flowfield
B	frequency factor
C	constant
c_p	specific heat capacity of gas
D	diffusion coefficient
Da	Damköhler number
d	diameter
E	activation energy
F	function defined in the ignition criterion
f	nondimensional streamfunction
j	j=0 and 1 designate two-dimensional and axisymmetric flows, respectively
k	surface reactivity
L	convective-diffusive operator
$\dot{m}$	dimensional mass burning (or combustion) rate
q	heat of combustion per unit mass of CO
R^o	universal gas constant
R	curvature of surface or radius
s	boundary-layer variable along the surface
T	temperature
Ta	activation temperature
t	time

u velocity component along x
V freestream velocity
v velocity component along y
W molecular weight
w reaction rate
x tangential distance along the surface
Y mass fraction
y normal distance from the surface

Greek symbols

α stoichiometric CO_2-to-reactant mass ratio
β conventional transfer number
γ temperature gradient at the surface
Δ reduced gas-phase Damköhler number
δ product(CO_2)-to-carbon mass ratio
ε measure of the thermal energy in the reaction zone relative to the activation energy
η boundary-layer variable normal to the surface or perturbed concentration
Θ perturbed temperature in the outer region
θ perturbed temperature in the inner region
λ thermal conductivity or parameter defined in the ignition analysis
μ viscosity
ν stoichiometric coefficient
ξ profile function
ρ density
χ inner variable
ψ streamfunction
ω reaction rate

Subscripts

A water vapor or C-H_2O surface reaction
a critical value at flame attachment
C carbon
F carbon monoxide
f flame sheet
g gas phase
ig ignition
in inner region
max maximum value
N nitrogen
O oxygen or C-O_2 surface reaction
out outer region
P carbon dioxide or C-CO_2 surface reaction
s surface
∞ freestream or ambience

Superscripts

j	j=0 and 1 designate two-dimensional and axisymmetric flows, respectively
n	reaction order
~	nondimensional or stoichiometrically weighted
′	differentiation with respect to η
*	without water-vapor effect

9. References

Adomeit, G., Hocks, W., & Henriksen, K. (1985). Combustion of a Carbon Surface in a Stagnation Point Flow Field. *Combust. Flame*, Vol. 59, No. 3, pp. 273-288, ISSN 0010-2180.

Adomeit, G., Mohiuddin, G., & Peters, N. (1976). Boundary Layer Combustion of Carbon. *Proc. Combust. Inst.*, Vol. 16, No. 1, pp. 731-743, ISSN 0082-0784.

Annamalai, K. & Ryan, W. (1993). Interactive Processes in Gasification and Combustion-II. Isolated Carbon, Coal and Porous Char Particles. *Prog. Energy Combust. Sci.*, Vol. 19, No. 5, pp. 383-446, ISSN 0360-1285.

Annamalai, K., Ryan, W., & Dhanapalan, S. (1994). Interactive Processes in Gasification and Combustion-Part III: Coal/Char Particle Arrays, Streams and Clouds. *Prog. Energy Combust. Sci.*, Vol. 20, No. 6, pp. 487-618, ISSN 0360-1285.

Arthur, J. R. (1951). Reactions between Carbon and Oxygen. *Trans. Faraday Soc.*, Vol. 47, pp. 164-178.

Batchelder, H. R., Busche, R. M., & Armstrong, W. P. (1953). Kinetics of Coal Gasification. *Ind. Eng. Chem.*, Vol. 45, No. 9, pp. 1856-1878.

Chelliah, H. K., Makino, A., Kato, I., Araki, N., & Law, C. K. (1996). Modeling of Graphite Oxidation in a Stagnation-Point Flow Field Using Detailed Homogeneous and Semiglobal Heterogeneous Mechanisms with Comparisons to Experiments. *Combust Flame*, Vol. 104, No. 4, pp. 469-480, ISSN 0010-2180.

Chung, P. M. (1965). Chemically Reacting Nonequilibrium Boundary Layers. In: *Advances in Heat Transfer*, Vol. 2, J. P. Hartnett, & T. F. Irvine, Jr. (Eds.), Academic, pp. 109-270, ISBN 0-12-020002-3, New York.

Clark, T. J., Woodley, R. E., & De Halas, D. R. (1962). Gas-Graphite Systems, In: *Nuclear Graphite*, R. E. Nightingale (Ed.), pp.387-444, Academic, New York.

Chukhanov, Z. (1938a). The Burning of Carbon. 1. The Sequence of Processes in the Combustion of Air Suspensions of Solid Fuels. *Tech. Phys. USSR.* Vol. 5, pp. 41-58.

Chukhanov, Z. (1938b). The Burning of Carbon. Part II. Oxidation. *Tech. Phys. USSR.* Vol. 5, pp. 511-524.

Eckbreth, A. C. (1988). *Laser Diagnostics for Combustion Temperature and Species*, Abacus, ISBN 2-88449-225-9, Kent.

Essenhigh, R. H. (1976). Combustion and Flame Propagation in Coal Systems: A Review. *Proc. Combust. Inst.*, Vol. 16, No. 1, pp. 353-374, ISSN 0082-0784.

Essenhigh, R. H. (1981). Fundamentals of Coal Combustion, In: *Chemistry of Coal Utilization*, M. A. Elliott (Ed.), pp. 1153-1312, Wiley-Interscience, ISBN 0-471-07726-7, New York.

Gerstein, M. & Coffin, K. P. (1956). Combustion of Solid Fuels, In: *Combustion Processes*, B. Lewis, R. N. Pease, and H. S. Taylor (Eds.), Princeton UP, Princeton, pp.444-469.

Harris, D. J. & Smith, I. W. (1990), Intrinsic Reactivity of Petroleum Coke and Brown Coal Char to Carbon Dioxide, Steam and Oxygen. *Proc. Combust. Inst.*, Vol. 23, No. 1, pp. 1185-1190, ISSN 0082-0784.

Henriksen, K. (1989). Weak Homogeneous Burning in Front of a Carbon Surface. *Proc. Combust. Inst.*, Vol. 22, No. 1, pp. 47-57, ISSN 0082-0784.

Henriksen, K., Hocks, W., & Adomeit, G. (1988). Combustion of a Carbon Surface in a Stagnation Point Flow Field. Part II: Ignition and Quench Phenomena. *Combust. Flame*, Vol. 71, No. 2, pp. 169-177, ISSN 0010-2180.

Howard, J. B., Williams, G. C., & Fine, D. H. (1973). Kinetics of Carbon Monoxide Oxidation in Postflame Gases. *Proc. Combust. Inst.*, Vol. 14, No. 1, pp. 975-986, ISSN 0082-0784.

Khitrin, L. N. (1962). *The Physics of Combustion and Explosion*, Israel Program for Scientific Translations, Jerusalem.

Khitrin, L. N. & Golovina, E. S. (1964). Interaction between Graphite and Various Chemically Active Gases at High Temperatures. In: *High Temperature Technology*, Butterworths, London, pp. 485-496.

Kurylko, L. and Essenhigh, R. H. (1973). Steady and Unsteady Combustion of Carbon. *Proc. Combust. Inst.*, Vol. 14, No. 1, pp. 1375-1386, ISSN 0082-0784.

Law, C. K. (1978). On the Stagnation-Point Ignition of a Premixed Combustion. *Int. J. Heat Mass Transf.*, Vol. 21, No. 11, pp. 1363-1368, ISSN 0017-9310.

Libby, P. A. & Blake, T. R. (1979). Theoretical Study of Burning Carbon Particles. *Combust. Flame*, Vol. 36, No. 1, pp. 139-169, ISSN 0010-2180.

Liñán, A. (1974). The Asymptotic Structure of Counter Flow Diffusion Flames for Large Activation Energies. *Acta Astronautica*, Vol. 1, No. 7-8, pp. 1007-1039, ISSN 0094-5765.

Maahs, H. G. (1971). Oxidation of Carbon at High Temperatures: Reaction-Rate Control or Transport Control. NASA TN D-6310.

Makino, A. (1990). A Theoretical and Experimental Study of Carbon Combustion in Stagnation Flow. *Combust. Flame*, Vol. 81, No. 2, pp. 166-187, ISSN 0010-2180.

Makino, A. (1992). An Approximate Explicit Expression for the Combustion Rate of a small Carbon Particle. *Combust. Flame*, Vol. 90, No. 2, pp. 143-154, ISSN 0010-2180.

Makino, A. & Law, C. K. (1986). Quasi-steady and Transient Combustion of a Carbon Particle: Theory and Experimental Comparisons. *Proc. Combust. Inst.*, Vol. 21, No. 1, pp. 183-191, ISSN 0082-0784.

Makino, A. & Law, C. K. (1990). Ignition and Extinction of CO Flame over a Carbon Rod. *Combust. Sci. Technol.*, Vol. 73, No. 4-6, pp. 589-615, ISSN 0010-2202.

Makino, A., Araki, N., & Mihara, Y. (1994). Combustion of Artificial Graphite in Stagnation Flow: Estimation of Global Kinetic Parameters from Experimental Results. *Combust. Flame*, Vol. 96, No. 3, pp. 261-274, ISSN 0010-2180.

Makino, A., Kato, I., Senba, M., Fujizaki, H., & Araki, N. (1996). Flame Structure and Combustion Rate of Burning Graphite in the Stagnation Flow. *Proc. Combust. Inst.*, Vol. 26, No. 2, pp. 3067-3074, ISSN 0082-0784.

Makino, A., Namikiri, T., & Araki, N. (1998). Combustion Rate of Graphite in a High Stagnation Flowfield and Its Expression as a Function of the Transfer Number. *Proc. Combust. Inst.*, Vol. 27, No. 2, pp. 2949-2956, ISSN 0082-0784.

Makino, A., Senba, M., Shintomi, M., Fujizaki, H., & Araki, N. (1997). Experimental Determination of the Spatial Resolution of CARS in the Combustion Field – CARS Thermometry Applied to the Combustion Field of Solid Carbon in a Stagnation Flow – . *Combust. Sci. Technol., Jpn.*, Vol. 5, No. 2, pp. 89-101, ISSN 0918-5712. [in Japanese].

Matalon, M. (1980). Complete Burning and Extinction of a Carbon Particle in an Oxidizing Atmosphere. *Combust. Sci. Technol.*, Vol. 24, No. 3-4, pp. 115-127, ISSN 0010-2202.

Matalon, M. (1981). Weak Burning and Gas-Phase Ignition about a Carbon Particle in an Oxidizing Atmosphere. *Combust. Sci. Technol.*, Vol. 25, No. 1-2, pp. 43-48, ISSN 0010-2202.

Matalon, M. (1982). The Steady Burning of a Solid Particle. SIAM J. Appl. Math., Vol. 42, No. 4, pp. 787-803, ISSN 0036-1399.

Matsui, K., Kôyama, A., & Uehara, K. (1975). Fluid-Mechanical Effects on the Combustion Rate of Solid Carbon. *Combust. Flame*, Vol. 25, No. 1, pp. 57-66, ISSN 0010-2180.

Matsui, K. & Tsuji, H. (1987). An Aerothermochemical Analysis of Solid Carbon Combustion in the Stagnation Flow Accompanied by Homogeneous CO Oxidation. *Combust. Flame*, Vol. 70, No. 1, pp. 79-99, ISSN 0010-2180.

Matsui, K., Tsuji, H., & Makino, A. (1983). The Effects of Water Vapor Concentration on the Rate of Combustion of an Artificial Graphite in Humid Air Flow. *Combust. Flame*, Vol. 50, No. 1, pp. 107-118, ISSN 0010-2180.

Matsui, K., Tsuji, H., & Makino, A. (1986). A Further Study of the Effects of Water Vapor Concentration on the Rate of Combustion of an Artificial Graphite in Humid Air Flow. *Combust. Flame*, Vol. 63, No. 3, pp. 415-427, ISSN 0010-2180.

Mulcahy, M. F. & Smith, I. W. (1969). Kinetics of Combustion of Pulverized Fuel: A Review of Theory and Experiment. *Rev. Pure and Appl. Chem.*, Vol. 19, No. 1, pp. 81-108.

Nagel, J. & Strickland-Constable, R. F. (1962). Oxidation of Carbon between 1000-2000°C. *Proc. Fifth Conf. On Carbon*, pp. 154-164, Pergamon, New York.

Rosner, D. E. (1972). High-Temperature Gas-Solid Reactions, *Annual Review of Materials Science*, Vol. 2, pp. 573-606, ISSN 0084-6600.

Sobolev, G. K., (1959). High-Temperature Oxidation and Burning of Carbon Monoxide. *Proc. Combust. Inst.*, Vol. 7, No. 1, pp. 386-391, ISSN 0082-0784.

Spalding, D. B. (1951). Combustion of Fuel Particles. *Fuel*, Vol. 30, No. 1, pp. 121-130, ISSN 0016-2361

Tsuji, H. & Matsui, K. (1976). An Aerothermochemical Analysis of Combustion of Carbon in the Stagnation Flow. *Combust. Flame*, Vol. 26, No. 1, pp. 283-297, ISSN 0010-2180.

Tsuji, H. & Yamaoka, I. (1967). The Counterflow Diffusion Flame in the Forward Stagnation Region of a Porous Cylinder. *Proc. Combust. Inst.*, Vol. 11, No. 1, pp. 979-984. ISSN 0082-0784.

Visser, W. & Adomeit, G. (1984). Experimental Investigation of the Ignition and Combustion of a Graphite Probe in Cross Flow. *Proc. Combust. Inst.*, Vol. 20, No. 2, pp. 1845-1851, ISSN 0082-0784.

Walker, P. L., Jr., Rusinko, F., Jr., & Austin, L. G. (1959). Gas Reaction of Carbon, In: *Advances in Catalysis and Related Subjects*, Vol. 11, D. D. Eley, P. W. Selwood, & P. B. Weisz (Eds.), pp. 133-221, Academic, ISBN 0-12-007811-2, New York.

Yang, R. T. & Steinberg, M. (1977). A Diffusion Cell Method for Studying Heterogeneous Kinetics in the Chemical Reaction/Diffusion Controlled Region. Kinetics of C + CO_2→ 2CO at 1200-1600°C. *Ind. Eng. Chem. Fundam.*, Vol. 16, No. 2, pp. 235-242, ISSN 0196-4313.

13

Mass Transfer Related to Heterogeneous Combustion of Solid Carbon in the Forward Stagnation Region - Part 2 - Combustion Rate in Special Environments

Atsushi Makino
Japan Aerospace Exploration Agency
Japan

1. Introduction

Carbon combustion is a research subject, indispensable for practical utilization of coal combustion, ablative carbon heat-shields, and/or aerospace applications with carbon-carbon composites (C/C-composites). Because of this practical importance, extensive research has been conducted not only experimentally but also theoretically and/or numerically, and several reviews (Batchelder, et al., 1953; Gerstein & Coffin, 1956; Walker, et al., 1959; Clark, et al., 1962; Khitrin, 1962; Mulcahy & Smith, 1969; Maahs, 1971; Rosner, 1972; Essenhigh, 1976, 1981; Annamalai & Ryan, 1993; Annamalai, et al., 1994) describe the accomplishments in this field, as mentioned in Part 1. Nevertheless, because of the complexities involved, there still remain several problems that must be clarified to understand basic nature of carbon combustion.

In Part 1, after describing general characteristics of the carbon combustion, it was intended to represent it by use of some of the basic characteristics of the chemically reacting boundary layers (Chung, 1965; Law, 1978), under recognition that flow configurations are indispensable for proper evaluation of the heat and mass transfer, especially for the situation in which the gas-phase reaction can intimately affect overall combustion response through its coupling to the surface reactions. The flow configuration chosen was that of the stagnation-flow, which is a well-defined, one-dimensional flow, being characterized by a single parameter, called the stagnation velocity gradient, offering various advantages for mathematical analyses, experimental data acquisition, and/or physical interpretations.

Specifically, formulation of the governing equations was first presented in Part 1, based on theories on the chemically reacting boundary layer. Chemical reactions considered were the surface C-O_2 and C-CO_2 reactions and the gas-phase CO-O_2 reaction. Generalized species-enthalpy coupling functions were then derived without assuming any limit or near-limit behaviors, which not only enable us to minimize the extent of numerical efforts needed for generalized treatment, but also provide useful insight into the conserved scalars in the carbon combustion. After that, it was shown that straightforward derivation of the combustion response could be allowed in the limiting situations, such as those for the Frozen, Flame-detached, and Flame-attached modes.

Next, after presenting profiles of gas-phase temperature, measured over the burning carbon, a further analytical study was conducted about the ignition phenomenon, related to finite-rate kinetics in the gas phase, by use of the asymptotic expansion method to obtain a critical condition for the appearance of the CO-flame. Appropriateness of this criterion was further examined by comparing temperature distributions in the gas phase and/or surface temperatures at which the CO-flame could appear. After having constructed these theories, evaluations of kinetic parameters for the surface and gas-phase reactions were then conducted, in order for further comparisons with experimental results.
In this Part 2, it is intended to make use of the information obtained in Part 1, for exploring carbon combustion, further. First, in order to decouple the close coupling between surface and gas-phase reactions, an attempt is conducted to raise the velocity gradient as high as possible, in Section 2. It is also endeavored to obtain explicit combustion-rate expressions, even though they might be approximate, because they are anticipated to contribute much to the foundation of theoretical understanding of carbon combustion, offering mathematical simplifications, just like that in droplet combustion, and to the practical applications, such as designs of ablative carbon heat shields and/or structures with C/C-composites in oxidizing atmospheres.
After having examined appropriateness of the explicit expressions, carbon combustion in the high-temperature airflow is then examined in Section 3, relevant to the High-Temperature Air Combustion, which is anticipated to have various advantages, such as energy saving, utilization of low-calorific fuels, reduction of nitric oxide emission, etc. The carbon combustion in the high-temperature, humid airflow is also examined theoretically in Section 4, by extending formulations for the system with three surface reactions and two global gas-phase reactions. Existence of a new burning mode with suppressed H_2 ejection from the surface can be confirmed for the carbon combustion at high temperatures when the velocity gradient of the humid airflow is relatively low. Some other results relevant to the High-Temperature Air Combustion are further shown in Section 5.
Concluding remarks not only for Part 2 but also for Part 1 are made in Section 6, with references cited and nomenclature tables.

2. Combustion response in high stagnation flowfields

It has been recognized that phenomena of carbon combustion become complicated upon the appearance of CO-flame, as pointed out in Part 1. Then, another simpler combustion response, being anticipated to be observed by suppressing its appearance, by use of the high velocity gradients, would provide useful insight into the carbon combustion, as well as facilitate deeper understanding for it. In addition, under simplified situations, there is a possibility that we could find out an explicit combustion-rate expression that can further contribute much to the foundation of theoretical understanding of the carbon combustion, offering mathematical simplifications, just like that in droplet combustion. Various contributions to practical applications, such as designs of furnaces, combustors, ablative carbon heat-shields, and high-temperature structures with C/C-composites in oxidizing atmosphere, are also anticipated.

2.1 Experimental results for the combustion rate

Figure 1(a) shows the combustion rate (Makino, et al., 1998b) as a function of the surface temperature, with the velocity gradient taken as a parameter. The H_2O mass-fraction in

airflow is set to be 0.003. Data points are experimental and solid curves are results of combustion-rate expressions to be mentioned. When the velocity gradient is 200 s^{-1}, the same trend as those in Figs. 2 and 8 in Part 1 is observed. That is, with increasing surface temperature, the combustion rate first increases, then decreases abruptly, and again increases. In Fig. 1(a), the ignition surface-temperature predicted is also marked.

As the velocity gradient is increased up to 640 s^{-1}, the combustion rate becomes high, due to an enhanced oxidizer supply, but the trend is still the same. A further increase in the velocity gradient, however, changes the trend. When the velocity gradient is 1300 s^{-1}, which is even higher than that ever used in the previous experimental studies (Matsui, et al., 1975; 1983; 1986), the combustion rate first increases, then reaches a plateau, and again increases, as surface temperature increases. Since the ignition surface-temperature is as high as 1970 K, at which the combustion rate without CO-flame is nearly the same as that with CO-flame, no significant decrease occurs in the combustion rate. On the contrary, a careful observation suggests that there is a slight, discontinuous increase in the combustion rate just after the appearance of CO-flame.

Since the ignition surface-temperature strongly depends on the velocity gradient (Visser & Adomeit, 1984; Makino & Law, 1990), as explained in Section 4 in Part 1, the discontinuous change in the combustion rate, caused by the appearance of CO-flame, ceases to exist with

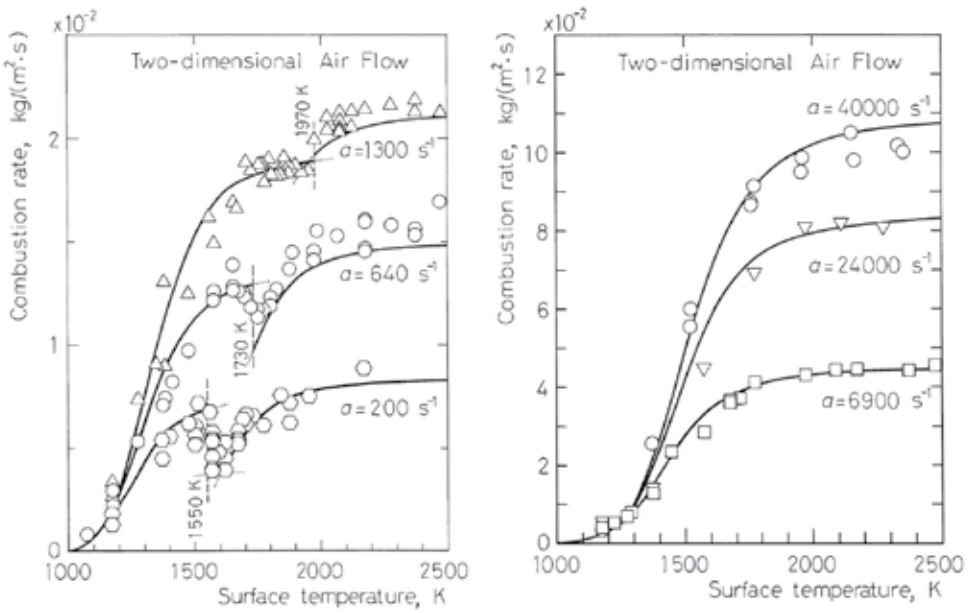

(a) (b)

Fig. 1. Combustion rate as a function of the surface temperature, with the velocity gradient taken as a parameter (Makino, et al., 1998b), (a) when there appears CO-flame within the experimental conditions; (b) when the velocity gradient is at least one order of magnitude higher than that ever used in the previous studies. Oxidizer is air and its H_2O mass-fraction is 0.003. Data points are experimental with the test specimen of 1.25×10^3 kg/m^3 in graphite density; curves are results of the explicit combustion-rate expressions.

increasing velocity gradient, as shown in Fig. 1(b). Here, use has been made of a graphite rod with a small diameter (down to 5 mm), as well as airflow with high velocity (up to 50 m/s). We see that the combustion rate increases monotonically with increasing surface temperature. Note that the velocity gradient used here is at least one order of magnitude higher than those in previous works.

As for the "negative temperature coefficient" of the combustion rate, examined in the literature (*cf.* Essenhigh, 1981), a further comment is required because it completely disappears at high velocity gradients. This experimental fact suggests that it has nothing to do with chemical events, related to the surface reactions, hitherto examined. Although it is described in the literature that some (Nagel and Strickland-Constable, 1962) attributed it to the sites of surface reactions and others (Yang and Steinberg, 1977) did it to the reaction depth, Figs. 1(a) and 1(b) certainly suggest that this phenomenon is closely related to the gas-phase reaction, which can even be blown off when the velocity gradients are high.

2.2 Approximate, explicit expressions for the combustion rate

In order to calculate the combustion rate, temperature profiles in the gas phase must be obtained by numerically solving the energy conservation equation for finite gas-phase reaction kinetics. However, if we note that carbon combustion proceeds with nearly frozen gas-phase chemistry until the establishment of the CO-flame (Makino, et al., 1994; Makino, et al., 1996) and that the combustion is expected to proceed under nearly infinite gas-phase kinetics once the CO-flame is established, analytically-obtained combustion rates (Makino, 1990; Makino, 1992), presented in Section 3 in Part 1, are still useful for practical utility.

However, it should also be noted that the combustion-rate expressions thus obtained are implicit, so that further numerical calculations are required by taking account of the relation, $\beta \equiv (-f_s)/(\xi')_s$, which is a function of the streamfunction f. Since this procedure is slightly complicated and cannot be used easily in practical situations, explicit expressions are anxiously required, in order to make these results more useful.

In order to elucidate the relation between the nondimensional combustion rate $(-f_s)$ and the transfer number β (Spalding, 1951), dependence of $(\xi')_s$ on the profile of the streamfunction f is first to be examined, by introducing a simplified profile of f as

$$f = \begin{cases} f_s & (0 \le \eta \le \eta_*) \\ b\eta + c & (\eta_* \le \eta \le \eta_{**}) \\ \eta + d & (\eta \ge \eta_{**}) \end{cases}, \tag{1}$$

as shown in Fig. 2(a), and then conducting an integration. Here, b, c, and d are constants, $f(\eta_*) = f_s$, and $f(\eta_{**}) = f_o$.

Recalling the definitions of β and $(\xi')_s$, and making use of a relation, $(-f_s) \ll 1$, as is the case for most solid combustion, we have the following approximate relation:

$$1 + \beta \approx \exp[K(-f_s)] \quad \text{or} \quad (-f_s) \approx \frac{\ln(1+\beta)}{K}, \tag{2}$$

where

$$K = \eta_* + \sqrt{\frac{\pi}{2}}\left[\left\{\exp\left(\frac{(b-1){f_o}^2}{2b}\right) - 1\right\} erfc\left(\frac{f_o}{\sqrt{2}}\right) - \left(1 - \frac{1}{\sqrt{b}}\right) erf\left(\frac{f_o}{\sqrt{2}}\right)\right] + \sqrt{\frac{\pi}{2}}. \tag{3}$$

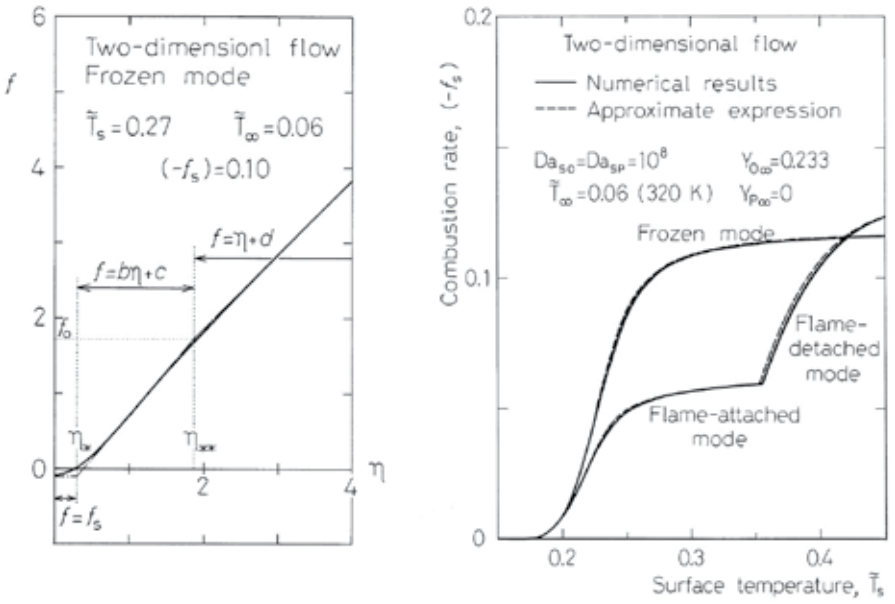

(a) (b)

Fig. 2.(a) A profile of the streamfunction f for the two-dimensional stagnation flow, as a function of the boundary-layer variable η, when the surface temperature $T_s \approx 1450$ K, the ambient temperature $T_\infty \approx 320$ K, and the combustion rate $(-f_s) = 0.10$. The solid curve is the result obtained by a numerical calculation, and the dashed curve is the simplified profile used to find out the approximate expression (Makino, et al., 1998b). (b) Combustion rates for the three limiting modes in the stagnation airflow as a function of the surface temperature when the surface Damköhler number for the C-O_2 reaction, Da_{sO}, and that for the C-CO_2 reaction, Da_{sP}, are 10^8. The solid curves are results of the implicit expressions and dashed curves are those of the explicit expressions.

Equation (2) shows that the combustion rate $(-f_s)$ can be expressed by the transfer number β in terms of the logarithmic term, ln(1+β). Note that the first and second terms in Eq. (3) are one order of magnitude smaller than the third term $(\pi/2)^{1/2}$.
In order to obtain the specific form of the transfer number β, a two term expansion of the exponential function is expected to be sufficient because $(-f_s) << 1$, so that use has been made of the following relation (Makino, 1992; Makino, et al., 1998b).

$$\frac{\beta}{1+\beta} = 1 - \exp\left[-K\left(-f_s\right)\right] \approx K\left(-f_s\right) \tag{4}$$

By virtue of this relation, Eqs. (44), (47), and (55) in Part 1 can yield the following approximate expressions for the transfer number.

Frozen mode:

$$\beta \approx \left(\frac{KA_{s,O}}{1+KA_{s,O}}\right)\left(\frac{\tilde{Y}_{O,\infty}}{\delta}\right) + \left(\frac{KA_{s,P}}{1+KA_{s,P}}\right)\left(\frac{\tilde{Y}_{P,\infty}}{\delta}\right) \tag{5}$$

Flame-detached mode:

$$\beta \approx \left(\frac{KA_{\mathrm{s,P}}}{1+KA_{\mathrm{s,P}}} \right) \left(\frac{\tilde{Y}_{\mathrm{O},\infty} + \tilde{Y}_{\mathrm{P},\infty}}{\delta} \right) \tag{6}$$

Flame-attached mode:

$$\beta \approx \left(\frac{KA_{\mathrm{s,O}}}{1+2KA_{\mathrm{s,O}} - KA_{\mathrm{s,P}}} \right) \left(\frac{\tilde{Y}_{\mathrm{O},\infty}}{\delta} \right) + \left(\frac{KA_{\mathrm{s,P}}}{1+2KA_{\mathrm{s,O}} - KA_{\mathrm{s,P}}} \right) \left(\frac{\tilde{Y}_{\mathrm{P},\infty}}{\delta} \right) \tag{7}$$

Although these are approximate, the transfer number can be expressed explicitly, in terms of the reduced surface Damköhler numbers, $A_{\mathrm{s,O}}$ and $A_{\mathrm{s,P}}$, and O_2 and CO_2 concentrations in the freestream.
In addition, we have

$$KA_{\mathrm{s},i} = k_{\mathrm{s},i} \frac{K}{\sqrt{2^j a \left(\mu_\infty / \rho_\infty \right)}} \; ; \quad k_{\mathrm{s},i} \equiv B_{\mathrm{s},i} \left(\frac{\tilde{T}_\infty}{\tilde{T}_{\mathrm{s}}} \right) \exp\left(-\frac{\tilde{T}a_{\mathrm{s},i}}{\tilde{T}_{\mathrm{s}}} \right) \quad (i = \mathrm{O}, \mathrm{P}) \, , \tag{8}$$

where $k_{\mathrm{s},i}$ is the specific reaction rate constant for the surface reaction. Note that the factor, $K/[2^j a \, (\mu_\infty/\rho_\infty)]^{1/2}$, in Eq. (8) also appears in the combustion rate defined in Eq. (32) in Part 1, by use of the relation in Eq. (2), as

$$\dot{m} \approx \rho_\infty \frac{\sqrt{2^j a \left(\mu_\infty / \rho_\infty \right)}}{K} \ln(1+\beta). \tag{9}$$

2.3 Correction factor K and mass-transfer coefficient

In order to elucidate the physical meaning of the factor, $K/[2^j a \, (\mu_\infty/\rho_\infty)]^{1/2}$, let us consider a situation that $\beta << 1$, with the Frozen mode combustion taken as an example. Then, Eq. (9) leads to the following result:

$$\dot{m} \approx \frac{1}{\dfrac{1}{k_{\mathrm{s},O}} + \dfrac{K}{\sqrt{2^j a \left(\mu_\infty / \rho_\infty \right)}}} \rho_\infty \left(\frac{\tilde{Y}_{\mathrm{O},\infty}}{\delta} \right) + \frac{1}{\dfrac{1}{k_{\mathrm{s},P}} + \dfrac{K}{\sqrt{2^j a \left(\mu_\infty / \rho_\infty \right)}}} \rho_\infty \left(\frac{\tilde{Y}_{\mathrm{P},\infty}}{\delta} \right). \tag{10}$$

We see that this expression is similar to the well-known expression for the solid combustion rate,

$$\dot{m} = \frac{1}{\dfrac{1}{k_s} + \dfrac{1}{h_D}} \left(\rho Y_O \right)_\infty , \tag{11}$$

for the first-order kinetics (Fischbeck, 1933; Fischbeck, et al., 1934; Tu, et al., 1934; Frank-Kamenetskii, 1969). Here, h_D is the overall convective mass-transfer coefficient. It is seen that the factor, $[2^j a \, (\mu_\infty/\rho_\infty)]^{1/2}/K$, corresponds to the mass-transfer coefficient h_{D}, suggesting that the specific form of h_{D} is of use in determining a form of the correction factor K.

Furthermore, by evaluating mass fluxes at the surface and in the gas phase, with the elemental carbon, $(W_C/W_F)Y_F+(W_C/W_P)Y_P$, taken as the transferred substance, and by use of the coupling function in Eq. (33) in Part 1, we have

$$h_D = \left(\frac{\tilde{T}_R}{\tilde{T}_\infty}\right)(\xi')_s \sqrt{2^j a\,(\mu_\infty/\rho_\infty)}\,, \tag{12}$$

suggesting that the correction factor K depends on both $(\xi')_s$ and the representative temperature T_R in the boundary layer.

2.4 Approximate expression for the correction factor K

In obtaining an approximate expression for the factor K, it seems that we can use the accomplishment in the field of heat and mass transfer. The mass-transfer coefficient is given as (Katto, 1982; White, 1988).

Two-dimensional Stagnation Flow:

$$h_D = \left(\frac{\tilde{T}_R}{\tilde{T}_\infty}\right)\frac{0.570}{Sc^{0.6}}\sqrt{a\,(\mu_\infty/\rho_\infty)} \quad \text{from} \quad \frac{Nu_x}{\sqrt{Re_x}} = 0.570\ Sc^{0.4}\,, \tag{13}$$

Axisymmetric Stagnation Flow:

$$h_D = \left(\frac{\tilde{T}_R}{\tilde{T}_\infty}\right)\frac{0.540}{Sc^{0.6}}\sqrt{2a\,(\mu_\infty/\rho_\infty)} \quad \text{from} \quad \frac{Nu_x}{\sqrt{Re_x}} = 0.763\ Sc^{0.4}\,, \tag{14}$$

based on the analogy between heat and mass transfers, where

$$Nu_x = \frac{h_D x}{D_R}, \qquad Re_x = \frac{\rho_R U x}{\mu_R}, \qquad U = ax, \qquad Sc = \frac{\mu/\rho}{D}. \tag{15}$$

However, this kind of expression is far from satisfactory because Eqs. (13) and (14) are originally obtained for heat-transfer problems without mass transfer. In addition, this relation is obtained under an assumption that there is no density change, even though there exist temperature and/or concentration distributions in the gas phase.

Because of the simultaneous existence of temperature and concentration distributions in the carbon combustion, we are required to obtain an approximate expression for the factor K in another way. In this attempt, $(\pi/2)^{1/2}$ in the factor K in Eq. (3) is kept as it is because it is $1/(\xi')_s$ for inviscid stagnation flow without mass ejection from the surface. The remaining part of the factor K is then determined by use of numerical results (Makino, 1990; Makino, et al., 1994; Makino, et al., 1996). In this determination, use has been made of a curve-fitting method, with (T_∞/T_s) taken as a variable, to have a simple function. It has turned out that we can fairly represent the combustion rate for the Frozen and/or Flame-attached modes in two-dimensional stagnation flow with

$$K = \left(\frac{\tilde{T}_\infty}{\tilde{T}_s}\right)\left(1 - \frac{\tilde{T}_\infty}{2\tilde{T}_s}\right) + \sqrt{\frac{\pi}{2}}, \tag{16}$$

within 3% error when the O_2 mass-fraction $Y_{O,\infty}$ is 0.233 (cf. Fig. 2(b); Makino, et al., 1998b); for $Y_{O,\infty}$=0.533, error is within 5%; for $Y_{O,\infty}$=1, error is within 8%. Examinations have been made in the range of the surface Damköhler numbers $Da_{s,O}$ and $Da_{s,P}$ from 10^6 to 10^{10}, that of the surface temperature T_s from 1077 K to 2424 K, and that of the freestream temperature T_∞ from 323 K to 1239 K. The Frozen and Flame-attached modes can fairly be correlated by the single Eq. (16) because the gas-phase temperature profiles are the same. Note that the combustion rate in high O_2 concentrations violates the assumption that $(-f_s)<<1$. Nonetheless, the expressions appear to provide a fair representation because these expressions vary as the natural logarithm of the transfer number.

For axisymmetric stagnation flow, it turns out that the combustion rate in the Frozen and/or Flame-attached modes can fairly be represented with

$$K = \sqrt{\frac{2}{3}\left(\frac{\tilde{T}_\infty}{\tilde{T}_s}\right)\left(1-\frac{\tilde{T}_\infty}{2\tilde{T}_s}\right)} + \sqrt{\frac{\pi}{2}}, \tag{17}$$

within 3% error for $Y_{O,\infty}$=0.233 (Makino, et al., 1998b); within 5% error for $Y_{O,\infty}$=0.7. Difference in the forms between Eq. (16) and Eq. (17) can be attributed to the difference in the flow configuration.

For the combustion rate in the Flame-detached mode, not only the surface and freestream temperatures but also the oxidizer concentration must be taken into account. It has turned out that

$$K = \left(\frac{\tilde{T}_\infty}{\tilde{T}_s}\right)\left(1-\frac{\tilde{T}_\infty}{2\tilde{T}_s}\right) - 0.05\left(1+2\tilde{Y}_{O,\infty}\right) + \sqrt{\frac{\pi}{2}} \tag{18}$$

can fairly represent the combustion rate in two-dimensional stagnation flow, within 4% error when the O_2 mass-fraction $Y_{O\infty}$ is 0.233 and 0.533, although the error becomes 6% near the transition state for the flame attaches. In an oxygen flow, the error is within 6% except for the transition state, while it increases up to 15% around the state.

For axisymmetric stagnation flow, the combustion rate in the Flame-detached mode can be represented with

$$K = \sqrt{\frac{2}{3}\left(\frac{\tilde{T}_\infty}{\tilde{T}_s}\right)\left(1-\frac{\tilde{T}_\infty}{2\tilde{T}_s}\right)} - 0.05\left(1+2\tilde{Y}_{O,\infty}\right) + \sqrt{\frac{\pi}{2}}. \tag{19}$$

The error is nearly the same as that for the two-dimension case.

2.5 Experimental comparisons at high velocity gradients

In order to verify the validity of the explicit combustion-rate expressions, comparisons have been made with their values and the experimental results (Makino, et al., 1998b). Kinetic parameters are those evaluated in Section 5 in Part 1. The values of thermophysical properties are those at T_∞=320 K, which yields $\rho_\infty\mu_\infty=2.12\times10^{-5}$ kg^2/(m^4·s) and $\mu_\infty/\rho_\infty=1.78\times10^{-5}$ m^2/s. Results for the explicit combustion-rate expressions are shown in Figs. 1(a) and 1(b) by solid curves. As shown in Fig. 1(a), up to the ignition surface-temperature, a reasonable prediction can be made by Eq. (2), with the transfer number β for the Frozen mode in Eq. (5) and the correction factor K in Eq. (16), for two-dimensional case.

When the surface temperature is higher than the ignition surface-temperature, Eq. (2) with β for the Flame-detached mode in Eq. (6) and K in Eq. (18) can fairly represent the experimental results, except for the temperatures near the ignition surface-temperature, especially, in airflow with low velocity-gradient, say, 200 s^{-1}. In this temperature range, we can use Eq. (2) with β for the Flame-attached mode in Eq. (7) and K in Eq. (16) although accuracy of this prediction is not so high, compared to the other cases. This is attributed to the fact that we cannot assume the gas-phase reaction rate infinitely fast because the combustion situation is that just after the establishment of CO-flame.
When the velocity gradient is high, as shown in Fig. 1(b), the expression in Eq. (2) with β for the Frozen mode in Eq. (5) and K in Eq. (16) fairly represents the experimental results, up to about 2500 K in the surface temperature.

3. High-temperature air combustion

Here, carbon combustion has been examined, relevant to the High-Temperature Air Combustion, characterized by use of hot air (~1280 K) and attracted as one of the new technology concepts for pursuing energy saving and/or utilization of low-calorific fuels. Although it has been confirmed to reduce NO_x emission through reduction of O_2 concentration in furnaces, without reducing combustion rate of gaseous and/or liquid fuels (Katsuki & Hasegawa, 1998; Tsuji, et al., 2003), its appropriateness for solid-fuel combustion has not been examined fully. Since solid fuels are commonly used as one of the important energy sources in industries, it is strongly required to examine its appropriateness from the fundamental viewpoint. Here, focus is put on examinations for the promoting and suppressing effects that the temperature and water vapor in the airflow have. From the practical point of view, the carbon combustion in airflow at high temperatures, especially, in high velocity gradients, is related to evaluation of ablative carbon heat-shield for atmospheric re-entry. As for that in airflow at high H_2O concentrations, it is related to evaluation of protection properties of rocket nozzles, made of carbonaceous materials, from erosive attacks of water vapor, contained in working fluid for propulsion, as well as the coal/char combustion in such environments with an appreciable amount of water vapor.

3.1 Combustion in relatively dry airflow

Figure 3(a) shows the combustion rate as a function of the surface temperature T_s, with the airflow temperature T_∞ taken as a parameter. The H_2O mass-fraction Y_A=0.003 in the airflow, considered to be dry, practically. The combustion rate in the high-temperature airflow (T_∞=1280 K), shown by a solid diamond, increases monotonically and reaches the diffusion-limited value with increasing T_s. Monotonic change in the combustion rate is attributed to the high velocity gradient (a=3300 s^{-1}), which is too high for the CO-flame to be established (Makino, et al., 2003), so that the combustion here is considered to proceed solely with the surface C-O_2 reaction. Note that this velocity gradient has been chosen, so as to suppress the abrupt changes in the combustion rates, in order to clarify effects of the High-Temperature Air Combustion.
Results in the room-temperature airflow (T_∞=320 K) with the same mass flow rate (a=820 s^{-1}) are also shown. The combustion rate first increases, then decreases abruptly, and again increases, with increasing T_s, as explained in the previous Section. The ignition surface-temperature observed is about 1800 K, in accordance with the abrupt decrease in the

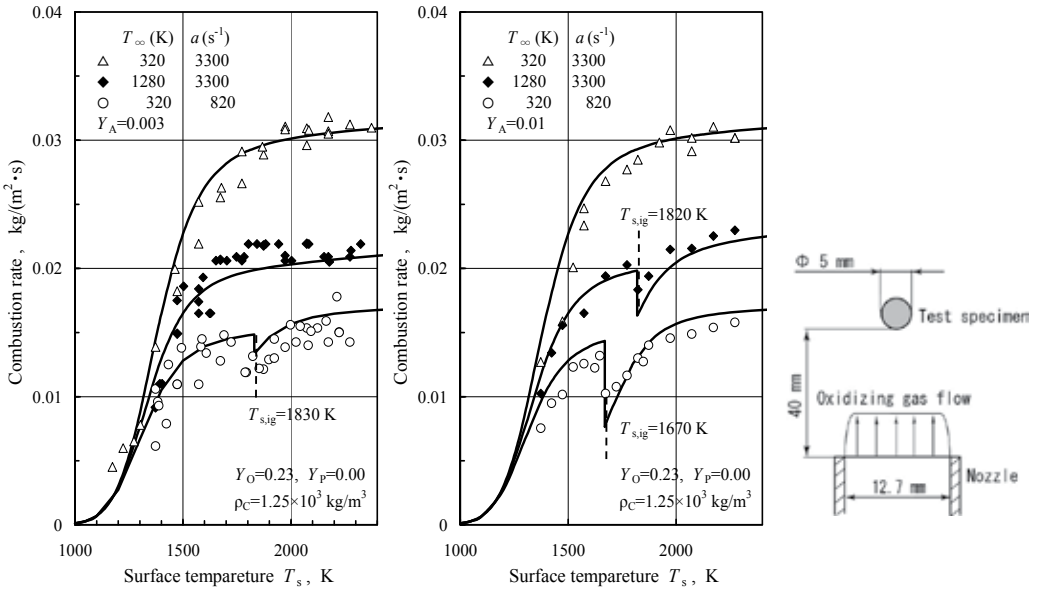

(a) (b)

Fig. 3. Combustion rate in the high-temperature airflow with the velocity gradient a=3300 s^{-1}, as a function of the surface temperature T_s; (a) for the H_2O mass-fraction Y_A=0.003 (Makino, et al., 2003); (b) for Y_A=0.01 (Makino & Umehara 2007). For comparisons, results in the room-temperature airflows with the same mass flow rate and the same velocity gradient are also shown. Data points are experimental with the test specimen of 1.25×10^3 kg/m^3 in graphite density; curves are results of the explicit combustion-rate expressions. Schematical drawing of the experimental setup is also shown.

combustion rate. As for the effect of the high-temperature airflow, we can say that it promotes the combustion rate, because of the elevated transport properties (Makino, et al., 2003) that enhances the mass-transfer rate of oxidizer.

This promoting effect can also be understood by use of a functional form of the combustion rate $\dot{m} \sim (a\rho\mu)^{1/2}$, derived from Eq. (9), for the diffusion-limited conditions. In this situation, we have $a\rho$ = const. when the mass flow rates of air are the same, so that $\dot{m} \sim (\mu)^{1/2}$. Since the viscosity μ, which can also be regarded as the mass diffusivity (ρD) when the Schmidt number is unity, is elevated with increasing air temperature, the combustion rate in the high-temperature airflow is necessarily higher than that in the room-temperature airflow.

Results in the room-temperature airflow with a=3300 s^{-1} are also shown in Fig. 3(a). The combustion rate increases monotonically, in the same manner as that in the high-temperature airflow. Note that when the velocity gradients are the same, the combustion rate in the high-temperature airflow is lower than that in the room-temperature airflow by about 30%, because of the reduced mass-transfer rate of oxygen, due to thickened boundary layer (Makino, et al., 2003), through overcoming an increase in the mass diffusivity ($\rho D \sim \mu$). This situation can easily be understood by use of a functional form of the combustion rate $\dot{m} \sim (\mu/\delta)$, from Eq. (9), for the diffusion-limited conditions, where δ is a measure of the boundary-layer thickness, expressed as $\sim [(\mu/\rho)/a]^{1/2}$ (Schlichting, 1979).

Solid curves are theoretical (Makino, et al., 1998b; 2003). For the airflow with a=3300 s^{-1}, the Frozen mode is used. For the airflow with a=820 s^{-1}, up to the ignition surface-temperature predicted to be 1830 K, the Frozen mode is used, whereas the Flame-detached mode is used above the ignition surface-temperature. It is seen that a fair degree of agreement is demonstrated between experimental and theoretical results, reconfirming the appropriateness to use the Frozen and Flame-detached modes for representing the combustion behavior before and after the establishment of CO-flame, respectively.
As shown in Fig. 3(a), when the mass flow rates of airflows are the same, the combustion rate in the high-temperature airflow is enhanced, so that the advantage of this technique looks trivial. However, its quantitative evaluation is not so straightforward, because there can appear abrupt changes in the combustion rate, related to the establishment of CO-flame that depends on the H_2O mass-fraction in airflow. Furthermore, water vapor can even be an oxidizer for carbon. So, in evaluating the High-Temperature Air Combustion technique, effects of the H_2O concentration are to be examined.

3.2 Combustion in airflow with medium humidity

Figure 3(b) shows similar plots of the combustion rate when the H_2O mass-fraction Y_A = 0.01. Although nearly the same trends are observed, there exist slight differences. Specifically, there exists a slight decrease in the combustion rate, even in the high-temperature airflow, at about 1800 K. This can be attributed to the establishment of CO-flame, facilitated even in the fast airflow with a=3300 s^{-1}, because of the increased H_2O mass-fraction. As for the combustion in the room-temperature airflow with a=820 s^{-1}, the ignition surface-temperature is reduced to be about 1650 K, suggesting that the CO-flame can easily be established. Theoretical results are also shown and fair agreement is demonstrated, suggesting that the Frozen and the Flame-detached modes, respectively, represent the combustion behavior before and after the establishment of CO-flame. The ignition surface-temperature is predicted to be 1820 K for the high-temperature airflow with a=3300 s^{-1} and 1670 K for the room-temperature airflow with a=820 s^{-1}, which are also in accordance with experimental observation.

3.3 Combustion in humid airflow

A further increase in the H_2O mass-fraction can considerably change the combustion behavior (Makino & Umehara, 2007). The H_2O mass-fraction Y_A is now increased to be 0.10, the dew point of which is as high as 328 K (55°C). Note that this H_2O mass-fraction is even higher than that ever used in the previous studies with humid airflow (Matsui, et al., 1983; 1986), by virtue of a small-sized boiler installed in the experimental apparatus. Figure 4(a) shows the combustion rate in the high-temperature airflow with a=3300 s^{-1}, as a function of the surface temperature T_s. The O_2 mass-fraction is reduced, because of the increased H_2O concentration. It is seen that the combustion rate increases first gradually and then rapidly with increasing surface temperature. This trend is quite different from that in Figs. 3(a) or 3(b).
In order to elucidate causes for this trend, theoretical results are obtained, with additional surface C-H_2O and global gas-phase H_2-O_2 reactions taken into the formulation (Makino & Umehara, 2007), which will be explained later. Not only results in the Frozen and Flame-detached modes, but also that in the Flame-attached mode is shown. In the Flame-attached mode, it is assumed that combustion products of the surface reactions can immediately be

oxidized, so that neither CO nor H_2 is ejected into the gas phase. It is seen that experimental results at temperatures lower than about 1500 K are close to the theoretical result of the Flame-attached mode, while those at temperatures higher than about 1700 K are close to the result of the Flame-detached mode. The ignition surface-temperature is predicted to be 1380 K. From these comparisons, we can deduce that because of the high H_2O mass-fraction, as well as the high-temperature airflow, the CO-flame established at 1380 K adheres to the carbon surface. The combustion in the Flame-attached mode prevails until CO-ejection becomes strong enough to separate the CO-flame from the surface. As the surface temperature is increased, the CO-flame detaches, so that the combustion proceeds in the Flame-detached mode. The rapid increase in the combustion rate at high temperatures can be attributed to the participation of the C-H_2O reaction.

Figure 4(b) shows the combustion rate in the room-temperature airflow with the same mass flow rate (a=820 s^{-1}). The airflow temperature, being raised to T_∞=370 K for preventing condensation of water vapor, cannot be called as the "room" temperature, any more, but its terminology is retained to distinguish it from the high-temperature. It is seen that the combustion rate gradually increases with increasing surface temperature. Compared to Fig. 4(a), the combustion rate around 1500 K is nearly the same as that in the high-temperature airflow. So, we can say that when the H_2O concentration is high, there is no merit to use the high-temperature airflow, until the water vapor begins to participate in the surface reaction as another oxidizer at about 1700 K or higher. A difference in the combustion rates at high temperatures becomes large because no remarkable increase in the combustion rate is observed, although the water vapor is anticipated to participate in the surface reaction. A further consideration will be made later.

Theoretical results are also shown in Fig. 4(b). The ignition surface-temperature is now predicted to be 1420 K. We see that the combustion rate experimentally obtained locates in the middle of the theoretical results in the Frozen and Flame-attached modes, after the establishment of CO-flame, suggesting that the gas-phase reaction proceeds in a finite rate, because the airflow is neither fast in velocity nor high in temperature. One more thing to be noted is the combustion behavior at high temperatures, presenting that the combustion rate in the experiment cannot reach the theoretical result that the Flame-detached mode predicts, about which it will be discussed later.

Figure 4(c) shows the combustion rate in the room-temperature airflow with a=3300 s^{-1}. Nearly the same trend as that in Figs. 3(a) and/or 3(b) with low velocity gradient is shown. Because the airflow temperature is low, the establishment of CO-flame is retarded until the surface temperature reaches about 1700 K, and the combustion rate up to this temperature is about double of that in the high-temperature airflow. The rapid increase at high temperatures can be attributed to the contribution of the surface C-H_2O reaction.

Theoretical results are also shown in Fig. 4(c). Until the establishment of CO-flame at T_s = 1690 K predicted, we see again that the Frozen mode can fairly represent the combustion behavior. At high temperatures at which the CO-flame has already been established, the combustion behavior is fairly represented by the Flame-detached mode.

4. Extended formulation for the carbon combustion

Theoretical study (Makino & Umehara, 2007) has been conducted for the system with three surface reactions and two global gas-phase reactions, by extending the previous formulation. Although some of the assumptions introduced in Section 2 in Part 1 are not

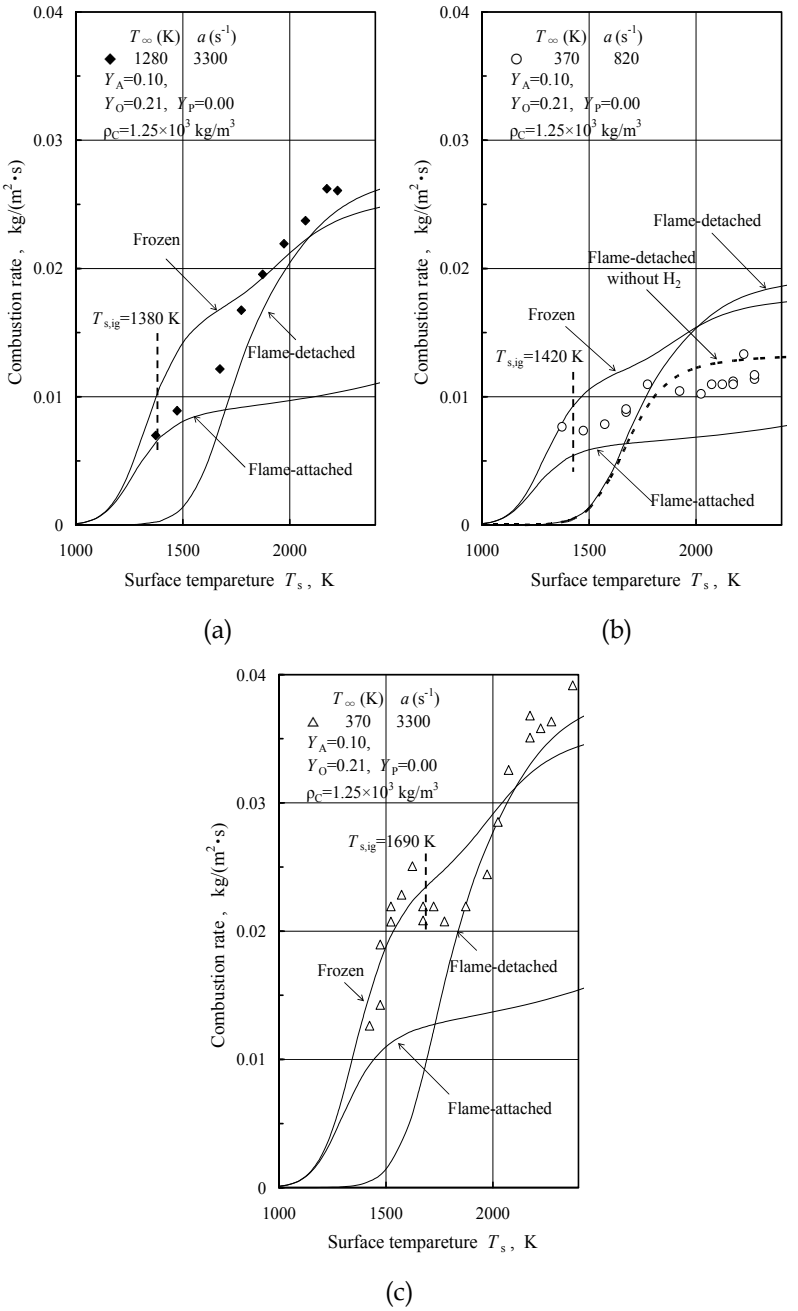

Fig. 4. Combustion rate in humid airflow (Makino & Umehara, 2007) with the H_2O mass-fraction Y_A=0.10, as a function of the surface temperature T_s; (a) in the high-temperature airflow with the velocity gradient a=3300 s^{-1}; (b) in the room-temperature airflow with the same mass flow rate (a=820 s^{-1}); (c) in the room-temperature airflow with the same velocity gradient. Data points are experimental and curves are results of the explicit combustion-rate expressions.

appropriate for systems with hydrogen species, use has been made of those as they are, for tractability, in order to capture fundamental aspects of the carbon combustion under prescribed situations.

4.1 Mass fractions of oxidizers at the carbon surface

By extending Eq. (31) in Part 1, so as to include contribution of the C-H_2O reaction, the combustion rate ($-f_s$) can be expressed as

$$\delta(-f_s) = A_{s,O}\tilde{Y}_{O,s} + A_{s,P}\tilde{Y}_{P,s} + A_{s,A}\tilde{Y}_{A,s}\,. \tag{20}$$

Again, use has been made of an assumption that all the surface reactions are the first-order. The reduced surface Damköhler number $A_{s,i}$, the surface Damköhler number $Da_{s,i}$, and the stoichiometrically weighted mass fraction, relevant to the oxidizing species i (=O, P, A) are also defined in the same manner as those in Section 2 in Part 1.

Although $Y_{i,s}$ must be determined through numerical calculations when the gas-phase kinetics is finite, they can be determined analytically for some limiting cases, as mentioned. One of them is the **Frozen mode,** in which we have

$$\tilde{Y}_{i,s} = \frac{Y_{i,\infty}}{1+\beta+A_{s,i}\left[\beta/(-f_s)\right]} \quad (i = \mathrm{O, P, A}). \tag{21}$$

Another is the **Flame-attached mode** in which CO and H_2 produced at the surface reactions are immediately consumed, so that it looks that the CO-flame adheres to the surface. In the same manner (Makino, et al., 1998b), we have

$$\tilde{Y}_{O,s} = \frac{\tilde{Y}_{O,\infty} - 2\delta\beta}{1+\beta}\,, \quad \tilde{Y}_{P,s} = \frac{\tilde{Y}_{P,\infty} + \delta\beta}{1+\beta}\,, \quad \tilde{Y}_{A,s} = \frac{\tilde{Y}_{A,\infty}}{1+\beta}\,. \tag{22}$$

The third is the **Flame-detached mode** in which the gas-phase reaction is infinitely fast and the CO-flame locates in the gas phase. Although a coupling function

$$\tilde{Y}_{O,s} + \tilde{Y}_{P,s} + \tilde{Y}_{A,s} = \frac{\tilde{Y}_{O,\infty} + \tilde{Y}_{P,\infty} + \tilde{Y}_{A,\infty} - \delta\beta}{1+\beta} \tag{23}$$

can easily be obtained and we can also put $Y_{O,s} = 0$ for this combustion situation, a separation of $Y_{A,s}$ from $Y_{P,s}$ is not straightforward. For this aim, it is needed to take account of another species-enthalpy coupling function, say, (Makino & Umehara, 2007)

$$\tilde{T} + \tilde{Y}_O + (1-\tilde{Q})\tilde{Y}_A\,, \tag{24}$$

then we have

$$\tilde{Y}_{A,s} = \frac{1}{1-\tilde{Q}}\frac{\tilde{T}_\infty - \tilde{T}_s + \tilde{Y}_{O,\infty} + (1-\tilde{Q})\tilde{Y}_{A,\infty} - \gamma}{1+\beta+A_{s,A}\left[\beta/(-f_s)\right]}\,. \tag{25}$$

Here, $\tilde{Q}$ is the ratio of the heats of combustion of the H_2-O_2 and CO-O_2 reactions in the gas phase. For evaluating γ, the temperature profile $T = T_s + (T_f - T_s)(\xi/\xi_f)$ inside the flame has been used, so that we have

$$\gamma = \tilde{T}_\infty - \tilde{T}_s + \tilde{Y}_{O,\infty} + (1-\tilde{Q})\tilde{Y}_{A,\infty} + (1-\tilde{Q})\left(\tilde{Y}_{A,s}\frac{1-\xi_f}{\xi_f} - \frac{\tilde{Y}_{A,f}}{\xi_f}\right), \tag{26}$$

where the coupling function in Eq. (24) is evaluated at the flame. By further using ξ_f and $Y_{A,f}$, determined by use of other coupling functions $\tilde{Y}_O - \tilde{Y}_F - \tilde{Y}_H$ and $\tilde{Y}_H + \tilde{Y}_A$, respectively, we have from Eq. (25) as

$$\tilde{Y}_{A,s} = \frac{\tilde{Y}_{A,\infty}}{1+\beta+A_{s,A}\dfrac{\beta}{(-f_s)}\left(1-\dfrac{\tilde{Y}_{O,\infty}}{2\delta\beta}\right)}. \tag{27}$$

The other mode that has been found (Makino & Umehara, 2007) is the **Flame-detached mode without H_2**, in which there exists no H_2 in the gas phase because it can easily be oxidized. For this mode, we have

$$\tilde{Y}_{O,s} = 0, \quad \tilde{Y}_{P,s} = \frac{\tilde{Y}_{O,\infty} + \tilde{Y}_{P,\infty} - \delta\beta}{1+\beta}, \qquad \tilde{Y}_{A,s} = \frac{\tilde{Y}_{A,\infty}}{1+\beta}, \tag{28}$$

4.2 Approximate, explicit expressions for the combustion rate

By use of the approximate relation in Eq. (4), analytical expressions for β can be obtained as

(I) Frozen mode:

$$\beta \approx \left(\frac{KA_{s,O}}{1+KA_{s,O}}\right)\left(\frac{2W_C}{W_O}Y_{O,\infty}\right) + \left(\frac{KA_{s,P}}{1+KA_{s,P}}\right)\left(\frac{W_C}{W_P}Y_{P,\infty}\right) + \left(\frac{KA_{s,A}}{1+KA_{s,A}}\right)\left(\frac{W_C}{W_A}Y_{A,\infty}\right), \tag{29}$$

(II) Flame-attached mode:

$$\beta \approx \left(\frac{1}{1+2KA_{s,O}-KA_{s,P}}\right)\left(KA_{s,O}\frac{2W_C}{W_O}Y_{O,\infty} + KA_{s,P}\frac{W_C}{W_P}Y_{P,\infty} + KA_{s,A}\frac{W_C}{W_A}Y_{A,\infty}\right), \tag{30}$$

(III) Flame-detached mode:

$$\beta \approx \frac{1}{2}\left\{\frac{KA_{s,P}}{1+KA_{s,P}}\left(\frac{2W_C}{W_O}Y_{O,\infty} + \frac{W_C}{W_P}Y_{P,\infty}\right) + \frac{KA_{s,A}}{1+KA_{s,A}}\left(\frac{W_C}{W_O}Y_{O,\infty} + \frac{W_C}{W_A}Y_{A,\infty}\right)\right\}$$

$$+\frac{1}{2}\left[\left\{\frac{KA_{s,P}}{1+KA_{s,P}}\left(\frac{2W_C}{W_O}Y_{O,\infty} + \frac{W_C}{W_P}Y_{P,\infty}\right) - \frac{KA_{s,A}}{1+KA_{s,A}}\left(\frac{W_C}{W_O}Y_{O,\infty} + \frac{W_C}{W_A}Y_{A,\infty}\right)\right\}^2\right.$$

$$+4\frac{KA_{s,P}}{1+KA_{s,P}}\left(\frac{W_C}{W_O}Y_{O,\infty}+\frac{W_C}{W_P}Y_{P,\infty}\right)\frac{KA_{s,A}}{1+KA_{s,A}}\left(\frac{W_C}{W_A}Y_{A,\infty}\right)\Bigg]^{1/2}, \tag{31}$$

(IV) Flame-detached mode without H_2:

$$\beta\approx\left(\frac{KA_{s,P}}{1+KA_{s,P}}\right)\left(\frac{2W_C}{W_O}Y_{O,\infty}+\frac{W_C}{W_P}Y_{P,\infty}\right)+\left(\frac{KA_{s,A}}{1+KA_{s,P}}\right)\left(\frac{W_C}{W_A}Y_{A,\infty}\right). \tag{32}$$

As the correction factor K for the two-dimensional flow, we have Eq. (16) for the Frozen and Flame-attached modes; Eq. (18) for the Flame-detached mode, regardless of H_2 ejection from the carbon surface.

4.3 Surface kinetic parameters and thermophysical properties

In numerical calculations, use has been made of the kinetic parameters for the surface C-O_2 and C-CO_2 reactions, described in Section 5 in Part 1. For C-H_2O reaction, the frequency factor $B_{s,A}=2\times10^7$ m/s and activation energy $E_{s,A}=271$ kJ/mol, determined after re-examining previous experimental results (Makino, et al., 1998a). As mentioned, effects of porosity and/or other surface characteristics are grouped into the kinetic parameters. Thermophysical properties are $\rho_\infty=1.10$ kg/m^3 and $\mu_\infty=1.95\times10^{-5}$ Pa·s for the room-temperature airflow ($T_\infty=320$ K), while $\rho_\infty=0.276$ kg/m^3 and $\mu_\infty=5.10\times10^{-5}$ Pa·s for the high-temperature airflow ($T_\infty=1280$ K). As for the thermophysical properties of water vapor, $\rho_\infty=0.598$ kg/m^3 and $\mu_\infty=1.22\times10^{-5}$ Pa·s at $T_\infty=370$ K. Wilke's equation (Reid, et al., 1977) has been used in estimating viscosities of humid air.

4.4 Further consideration for experimental comparisons

Experimental results have already been compared with theoretical results in Figs. 3 and 4, and a fair degree of agreement has been demonstrated in general, suggesting appropriateness of the analysis, including the choice of the thermophysical properties. However, Fig. 4(b) requires a further comment because theoretical result of the Flame-detached mode overestimates the combustion rate, especially at high surface temperatures T_s. As assumed in the Flame-detached mode, CO and H_2 produced at the surface reaction are to be transported to the flame and then oxidized. Generally speaking, however, H_2 can easily been oxidized, compared to CO, especially at high temperatures. In addition, the velocity gradient ($a=820$ s^{-1}) in Fig. 4(b) is not so high. In this situation, H_2 produced at the surface reaction is considered to be completely consumed by the water-gas shift reaction ($H_2+CO_2\rightarrow H_2O+CO$), so that the Flame-detached mode without H_2 presented (Makino & Umehara, 2007) seems to be appropriate. A theoretical result is also shown in Fig. 4(b) by a dashed curve. We see that the agreement at high T_s has much been improved, suggesting that this consideration is to the point.

5. Other results relevant to the high-temperature air combustion

As one of the advantages for the High-Temperature Air Combustion, it has been pointed out that oxygen concentration in a furnace can be reduced without reducing combustion rate. In order to confirm this fact, an experiment has been conducted by varying O_2 and CO_2 concentrations in the high-temperature oxidizer-flow (Makino and Umehara, 2007). In

addition, combustion rate of C/C-composite in the high-temperature airflow has been examined (Makino, et al., 2006) in a similar way, relevant to evaluation of protection properties from oxidation. In this Section, those results not presented in previous Sections are shown.

5.1 Effects of O_2 and CO_2 in the oxidizer-flow

Experimental conditions for the O_2 and/or CO_2 concentrations in the high-temperature oxidizer-flow have been chosen to have the same combustion rate as that in the room-temperature airflow, at around T_s=2000 K, shown in Fig. 3(a). Figure 5(a) shows the combustion rate in the high-temperature oxidizer-flow, as a function of the surface temperature T_s. The O_2 and CO_2 mass-fractions are set to be 0.105 and 0.10, respectively. The H_2O mass-fraction Y_A=0.001 or less. Because of the monotonic increase in the combustion rate, the combustion rate at 2000 K is nearly equal to that in the room-temperature airflow, shown in Figs. 3(a) and 3(b), experienced the abrupt decreases in the combustion rate upon the establishment of CO-flame, although it is generally suppressed, because of the reduced O_2 mass-fraction. For comparisons, results in the room-temperature oxidizer-flows with the same mass flow rate and the same velocity gradient are also shown in Fig. 5(a), the general trend of which is in accordance with that in the airflow shown in Figs. 3(a) and 3(b), as far as the combustion rate is concerned.

Figure 5(b) shows the combustion rate as a function of T_s, with CO_2 taken as the only oxidizer. The CO_2 mass-fraction is set to be 0.39. Since CO_2 is the only oxidizer for the

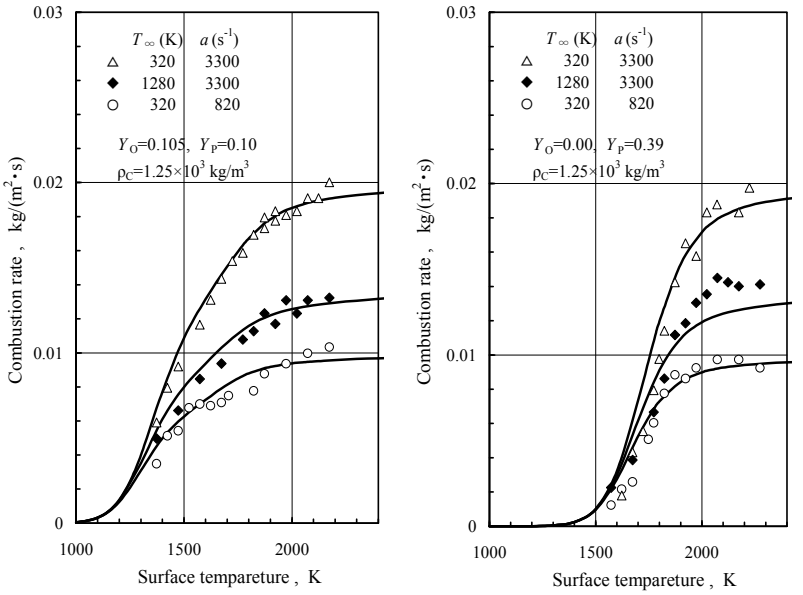

Fig. 5. Combustion rate in the high-temperature oxidizer-flow with the velocity gradient a = 3300 s^{-1}, as a function of the surface temperature (Makino and Umehara, 2007). The H_2O mass-fraction Y_A=0.001 or less. Notation is the same as that in Fig. 3. (a) The O_2 and CO_2 mass-fractions are 0.105 and 0.10, respectively; (b) The CO_2 mass-fraction is 0.39.

surface reaction and there is no gas phase reaction, the monotonic increase in the combustion rate is observed. The same comments as those in Fig. 3(a) can be made for the high-temperature oxidizer-flow although higher surface temperature T_s is required in activating the surface C-CO_2 reaction.

Finally, it is confirmed that as far as the combustion rates at around T_s=2000 K are concerned, those in the high-temperature oxidizer-flows in Figs. 5(a) and 5(b) are nearly the same as that in the room-temperature airflow in Fig. 3(a) with the same mass flow rate. As pointed out (Makino, et al., 2003) that the O_2 mass-fraction can be reduced down to about 0.14 in the High-Temperature Air Combustion, without reducing combustion rate, it has been confirmed that the O_2 mass-fraction can further be reduced (Makino and Umehara, 2007) when there exists CO_2 in the oxidizer-flow.

5.2 Combustion rate of C/C-composite

Figure 6(a) shows the combustion rate as a function of the surface temperature with the velocity gradient taken as a parameter. Use has been made of a test specimen of C/C-composite with rectangular cross section (5 mm width; 8 mm thickness). The velocity gradient used here is defined as $a = 2V_\infty/\ell$, where ℓ is the width; the maximum velocity gradient is limited to be 1300 s^{-1}, because of air-supply system. Other experimental conditions are the same as those in Figs. 1(a) and/or 3(a). An abrupt decrease in the combustion rate, as well as the general combustion response can be observed in the same manner as that of a graphite rod, reported in the previous Sections. Figure 6(b) is a similar plot with the airflow temperature taken as a parameter, presenting the same trend as that in Fig. 3(a).

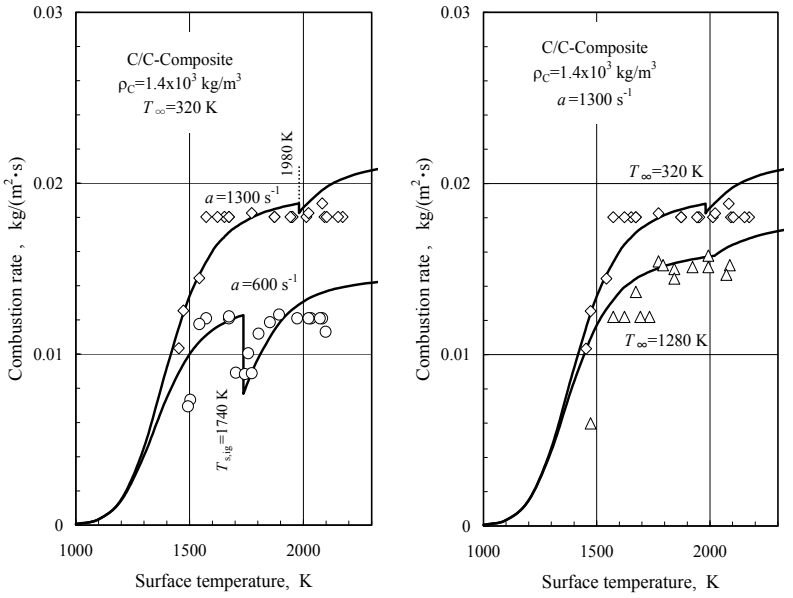

Fig. 6. Combustion rate of C/C-composite (Makino, et al., 2006) as a function of the surface temperature; (a) with the velocity gradient of airflow taken as a parameter; (b) with the airflow temperature taken as a parameter.

Theoretical results are also shown in Figs. 6(a) and 6(b). In obtaining these results, use has been made of kinetic parameters for the artificial graphite with higher density ($\rho_C = 1.82\times10^3$ kg/m^3), after confirming the experimental fact that there appears no remarkable difference in the combustion rates in different graphite densities, because of the prevalence of combustion behavior in the diffusionally controlled regime in the present experimental conditions. As far as the trend and approximate magnitude are concerned, fair agreement is demonstrated, including the ignition surface-temperature. It should be noted that the combustion rate of the C/C-composite is nearly the same as that of artificial graphite when there is no surface coating for protecting oxidation.

6. Concluding remarks

In this monograph, combustion of solid carbon has been overviewed not only experimentally but also theoretically. As explained in Part 1, only the carbon combustion in the forward stagnation flowfield has been considered, in order to have a clear understanding.

In Part 1, by conducting the aerothermochemical analysis, based on the chemically reacting boundary layer, with considering the surface C-O_2 and C-CO_2 reactions and the gas-phase CO-O_2 reaction, the generalized species-enthalpy coupling functions have successfully been derived, which demonstrate close coupling between the surface and gas-phase reactions that can also exert influences on the combustion rate.

Then, focus has been put on the ignition of CO-flame over the burning carbon in the prescribed flowfield, because establishment of the CO-flame in the gas phase can change the dominant surface reaction from the faster C-O_2 reaction to the slower C-CO_2 reaction, causing abrupt changes in the combustion rate. By further conducting the asymptotic expansion analysis, with using the generalized coupling functions, the explicit ignition criterion has been derived, suggesting that ignition is facilitated with increasing surface temperature and oxidizer concentration, while suppressed with decreasing velocity gradient.

Then, attempts have been made to estimate kinetic parameters for the surface and gas-phase reactions, indispensable for predicting combustion behavior, with using theoretical results obtained. A fair degree of agreement has been demonstrated between experimental and theoretical results, through conducting experimental comparisons.

In Part 2, a further study has been conducted in the stagnation flow with high velocity gradient, at least one order of magnitude higher than that ever used, in order to suppress the appearance of CO-flame. It is observed that the combustion rate increases monotonically and reaches the diffusion-limited value with increasing surface temperature when the velocity gradient is high, while there exists a discontinuous change in the combustion rate with increasing surface temperature, due to the establishment of CO-flame when the velocity gradient is low. In addition, an attempt has been made to obtain explicit combustion-rate expressions, presented by the transfer number in terms of the natural logarithmic term, just like that for droplet combustion. For the three limiting cases, explicit expressions have further been obtained by making an assumption of small combustion rate. It has even been found that before the establishment of CO-flame the combustion rate can fairly be represented by the expression in the Frozen mode, and that after the establishment of CO-flame the combustion rate can be represented by the expression in the Flame-attached and/or Flame-detached modes. Since the present expressions are explicit and have fair

accuracy, they are anticipated to make various contributions not only for qualitative and quantitative studies in facilitating understanding, but also for practical utility, such as designs of furnaces, combustors, ablative carbon heat-shields, and high-temperature structures with C/C-composites in various aerospace applications.

Finally, relevant to the High-Temperature Air Combustion, carbon combustion has been studied, by varying H_2O mass-fraction up to 0.10. It has been found that the high H_2O mass-fraction is unfavorable for the enhancement of combustion rate, especially in the medium temperature range, because establishment of the CO-flame is facilitated, and hence suppresses the combustion rate. To the contrary, at high surface temperatures (>2000 K), the high H_2O mass-fraction is favorable because the water vapor participates in the surface reaction as an additional oxidizer. Theoretical results, obtained by additionally introducing the surface C-H_2O reaction and the global gas-phase H_2-O_2 reaction into the previous formulation, have also suggested the usefulness of the explicit expressions for the combustion rate. As for the combustion in the humid airflow with relatively low velocity gradient, it is found that a new mode with suppressed H_2-ejection from the surface can fairly represent the experimental observation.

Although essential feature of the carbon combustion has been captured to some extents, further progresses are strongly required for its firm understanding, because wide attention has been given to carbonaceous materials in various fields.

7. Acknowledgment

In conducting a series of studies on the carbon combustion, I have been assisted by many of my former graduate and undergraduate students, as well as research staffs, in Shizuoka University, being engaged in researches in the field of mechanical engineering for twenty years as a staff, from a research associate to a full professor. Here, I want to express my sincere appreciation to all of them who have participated in researches for exploring combustion of solid carbon.

8. Nomenclature

A	reduced surface Damköhler number
a	velocity gradient in the stagnation flowfield
B	frequency factor
b	constant
c	constant
c_p	specific heat capacity of gas
D	diffusion coefficient
Da	Damköhler number
d	diameter or constant
E	activation energy
F	function defined in the ignition criterion
f	nondimensional streamfunction
h_D	mass-transfer coefficient
j	j=0 and 1 designate two-dimensional and axisymmetric flows, respectively
K	factor
k	surface reactivity

$\mathcal{L}$ convective-diffusive operator
ℓ width
$\dot{m}$ dimensional mass burning (or combustion) rate
Q ratio of heats of combustion in the gas phase
q heat of combustion per unit mass of CO
R^o universal gas constant
R curvature of surface or radius
s boundary-layer variable along the surface
T temperature
Ta activation temperature
t time
u velocity component along x
V freestream velocity
v velocity component along y
W molecular weight
w reaction rate
x tangential distance along the surface
Y mass fraction
y normal distance from the surface

Greek Symbols

α stoichiometric CO_2-to-reactant mass ratio
β conventional transfer number
γ temperature gradient at the surface
Δ reduced gas-phase Damköhler number
δ product(CO_2)-to-carbon mass ratio or boundary-layer thickness
ε measure of the thermal energy in the reaction zone relative to the activation energy
η boundary-layer variable normal to the surface or perturbed concentration
Θ perturbed temperature in the outer region
θ perturbed temperature in the inner region
λ thermal conductivity or parameter defined in the igninition analysis
μ viscosity
ν stoichiometric coefficient
ξ profile function
ρ density
χ inner variable
ψ streamfunction
ω reaction rate

Subscripts

A water vapor or C-H_2O surface reaction
a critical value at flame attachment
C carbon
F carbon monoxide
f flame sheet

g	gas phase
ig	ignition
in	inner region
max	maximum value
N	nitrogen
O	oxygen or C-O_2 surface reaction
out	outer region
P	carbon dioxide or C-CO_2 surface reaction
s	surface
∞	freestream or ambience

Superscripts

a	reaction order
j	*j*=0 and 1 designate two-dimensional and axisymmetric flows, respectively
~	nondimensional or stoichiometrically weighted
′	differentiation with respect to η
*	without water-vapor effect

9. References

Annamalai, K. & Ryan, W. (1993). Interactive Processes in Gasification and Combustion-II. Isolated Carbon, Coal and Porous Char Particles. *Prog. Energy Combust. Sci.*, Vol. 19, No. 5, pp. 383-446, ISSN 0360-1285.

Annamalai, K., Ryan, W., & Dhanapalan, S. (1994). Interactive Processes in Gasification and Combustion-Part III: Coal/Char Particle Arrays, Streams and Clouds. *Prog. Energy Combust. Sci.*, Vol. 20, No. 6, pp. 487-618, ISSN 0360-1285.

Batchelder, H. R., Busche, R. M., & Armstrong, W. P. (1953). Kinetics of Coal Gasification. *Ind. Eng. Chem.*, Vol. 45, No. 9, pp. 1856-1878.

Chung, P. M. (1965). Chemically Reacting Nonequilibrium Boundary Layers. In: *Advances in Heat Transfer*, Vol. 2, J. P. Hartnett, & T. F. Irvine, Jr. (Eds.), Academic, pp. 109-270, ISBN 0-12-020002-3, New York.

Clark, T. J., Woodley, R. E., & De Halas, D. R. (1962). Gas-Graphite Systems, In: *Nuclear Graphite*, R. E. Nightingale (Ed.), pp.387-444, Academic, New York.

Essenhigh, R. H. (1976). Combustion and Flame Propagation in Coal Systems: A Review. *Proc. Combust. Inst.*, Vol. 16, No. 1, pp. 353-374, ISSN 0082-0784.

Essenhigh, R. H. (1981). Fundamentals of Coal Combustion, In: *Chemistry of Coal Utilization*, M. A. Elliott (Ed.), pp. 1153-1312, Wiley-Interscience, ISBN 0-471-07726-7, New York.

Fischbeck, K. (1933). Über das Reaktionsvermögen der Festen Stoffe. *Z. Elektrochem.*, Vol. 39, No. 5, pp. 316-330.

Fischbeck, K., Neundeubel, L. & Salzer, F. (1934). Über das Reaktionsvermögen von Kristallarten. *Z. Elektrochem.*, Vol. 40, No. 7b, pp. 517-522.

Frank-Kamenetskii, D. A. (1969). *Diffusion and Heat Transfer in Chemical Kinetics, 2nd Enlarged/Revised Ed.*, J. P. Appleton (Translation Ed.), Plenum, ISBN0-306-30349-3, New York.

Gerstein, M. & Coffin, K. P. (1956). Combustion of Solid Fuels, In: *Combustion Processes*, B. Lewis, R. N. Pease, and H. S. Taylor (Eds.), Princeton UP, Princeton, pp.444-469.

Katsuki, M. & Hasegawa, T. (1998). The Science and Technology of Combustion in Highly Preheated Air. *Proc. Combust. Inst.*, Vol. 27, No. 2, pp. 3135-3146, ISSN 0082-0784

Katto, Y. (1982a). *An Outline of Heat Transfer*, Yoken-do, Tokyo.

Khitrin, L. N. (1962). *The Physics of Combustion and Explosion*, Israel Program for Scientific Translations, Jerusalem.

Law, C. K. (1978). On the Stagnation-Point Ignition of a Premixed Combustion. *Int. J. Heat Mass Transf.*, Vol. 21, No. 11, pp. 1363-1368, ISSN 0017-9310.

Maahs, H. G. (1971). Oxidation of Carbon at High Temperatures: Reaction-Rate Control or Transport Control. NASA TN D-6310.

Makino, A. (1990). A Theoretical and Experimental Study of Carbon Combustion in Stagnation Flow. *Combust. Flame*, Vol. 81, No. 2, pp. 166-187, ISSN 0010-2180.

Makino, A. (1992). An Approximate Explicit Expression for the Combustion Rate of a small Carbon Particle. *Combust. Flame*, Vol. 90, No. 2, pp. 143-154, ISSN 0010-2180.

Makino, A. & Law, C. K. (1990). Ignition and Extinction of CO Flame over a Carbon Rod. *Combust. Sci. Technol.*, Vol. 73, No. 4-6, pp. 589-615, ISSN 0010-2202.

Makino, A. & Umehara, N. (2007). Combustion Rates of Graphite Rods in the Forward Stagnation Field of the High-Temperature, Humid Airflow. *Proc. Combust. Inst.*, Vol. 31, No. 2, pp. 1873-1880, ISSN 1540-7489.

Makino, A., Araki, N., & Mihara, Y. (1994). Combustion of Artificial Graphite in Stagnation Flow: Estimation of Global Kinetic Parameters from Experimental Results. *Combust. Flame*, Vol. 96, No. 3, pp. 261-274, ISSN 0010-2180.

Makino, A., Fujizaki, H., & Araki, N. (1998a). Combustion Rate of Burning Graphite in a Stagnation Flow of Water Vapor. *Combust. Flame*, Vol. 113, No. 1-2, pp. 258-263, ISSN 0010-2180.

Makino, A., Kato, I., Senba, M., Fujizaki, H., & Araki, N. (1996). Flame Structure and Combustion Rate of Burning Graphite in the Stagnation Flow. *Proc. Combust. Inst.*, Vol. 26, No. 2, pp. 3067-3074, ISSN 0082-0784.

Makino, A., Namikiri, T., & Araki, N. (1998b). Combustion Rate of Graphite in a High Stagnation Flowfield and Its Expression as a Function of the Transfer Number. *Proc. Combust. Inst.*, Vol. 27, No. 2, pp. 2949-2956, ISSN 0082-0784.

Makino, A., Namikiri, T., & Kimura, K. (2003). Combustion Rates of Graphite Rods in the Forward Stagantion Field with High Temperature Airflow. *Combust. Flame*, Vol. 132, No. 4, pp. 743-753, ISSN 0010-2180.

Makino, A., Namikiri, T., & Kimura, K. (2006). Combustion of Solid Carbon with High Density and Carbon/Carbon-Composite in the Stagantion Flow Field. *Trans. Jpn. Soc. Mech. Eng. (Series B)*, Vol. 72, No. 724, pp. 3137-3142, ISSN 0387-5016. [in Japanese].

Matsui, K., Kôyama, A., & Uehara, K. (1975). Fluid-Mechanical Effects on the Combustion Rate of Solid Carbon. *Combust. Flame*, Vol. 25, No. 1, pp. 57-66, ISSN 0010-2180.

Mulcahy, M. F. & Smith, I. W. (1969). Kinetics of Combustion of Pulverized Fuel: A Review of Theory and Experiment. *Rev. Pure and Appl. Chem.*, Vol. 19, No. 1, pp. 81-108.

Nagel, J. & Strickland-Constable, R. F. (1962). Oxidation of Carbon between 1000-2000°C. *Proc. Fifth Conf. On Carbon*, pp. 154-164, Pergamon, New York.

Reid, R. C., Prausnitz, J. M., & Sherwood, T. K. (1977). Viscosities of Gas Mixtures at Low Pressures. *The Properties of Gases and Liquid, 3rd Ed.*, pp. 410-414, McGraw-Hill, ISBN 0-07-051790-8, New York.

Rosner, D. E. (1972). High-Temperature Gas-Solid Reactions, *Annual Review of Materials Science*, Vol. 2, pp. 573-606, ISSN 0084-6600.

Schlichting, H. (1979). *Boundary-Layer Theory, Seventh Ed.*, McGraw-Hill, ISBN 0-07-055334-3, New York.

Spalding, D. B. (1951). Combustion of Fuel Particles. *Fuel*, Vol. 30, No. 1, pp. 121-130, ISSN 0016-2361

Tsuji, H., Gupta, A. K., Hasegawa, T., Katsuki, M., Kishimoto, K., & Morita, M. (2003). *High Temperature Air Combustion from Energy Conservation to Pollution Reduction*, CRC Press, ISBN 0-8493-1036-9, Boca Raton.

Tu, C. M., Davis, H., & Hottel, H. C. (1934). Combustion Rate of Carbon; Combustion of Spheres in Flowing Gas Streams. *Ind. Eng. Chem.*, Vol. 26, No. 7, pp. 749-757.

Visser, W. & Adomeit, G. (1984). Experimental Investigation of the Ignition and Combustion of a Graphite Probe in Cross Flow. *Proc. Combust. Inst.*, Vol. 20, No. 2, pp. 1845-1851, ISSN 0082-0784.

Walker, P. L., Jr., Rusinko, F., Jr., & Austin, L. G. (1959). Gas Reaction of Carbon, In: *Advances in Catalysis and Related Subjects*, Vol. 11, D. D. Eley, P. W. Selwood, & P. B. Weisz (Eds.), pp. 133-221, Academic, ISBN 0-12-007811-2, New York.

White, F. M. (1988). *Heat and Mass Transfer*, Addison-Wesley, ISBN 0-201-17099-X, Reading.

Yang, R. T. & Steinberg, M. (1977). A Diffusion Cell Method for Studying Heterogeneous Kinetics in the Chemical Reaction/Diffusion Controlled Region. Kinetics of C + $CO_2 \rightarrow$ 2CO at 1200-1600°C. *Ind. Eng. Chem. Fundam.*, Vol. 16, No. 2, pp. 235-242, ISSN 0196-4313.

Edited by Jozef Markoš

This book offers several solutions or approaches in solving mass transfer problems for different practical chemical engineering applications: measurements of the diffusion coefficients, estimation of the mass transfer coefficients, mass transfer limitation in separation processes like drying, extractions, absorption, membrane processes, mass transfer in the microbial fuel cell design, and problems of the mass transfer coupled with the heterogeneous combustion. I believe this book can provide its readers with interesting ideas and inspirations or direct solutions of their particular problems.

ISBN 978-953-51-4409-0

Photo by noLimit46 / iStock

IntechOpen